WILEY-VCH
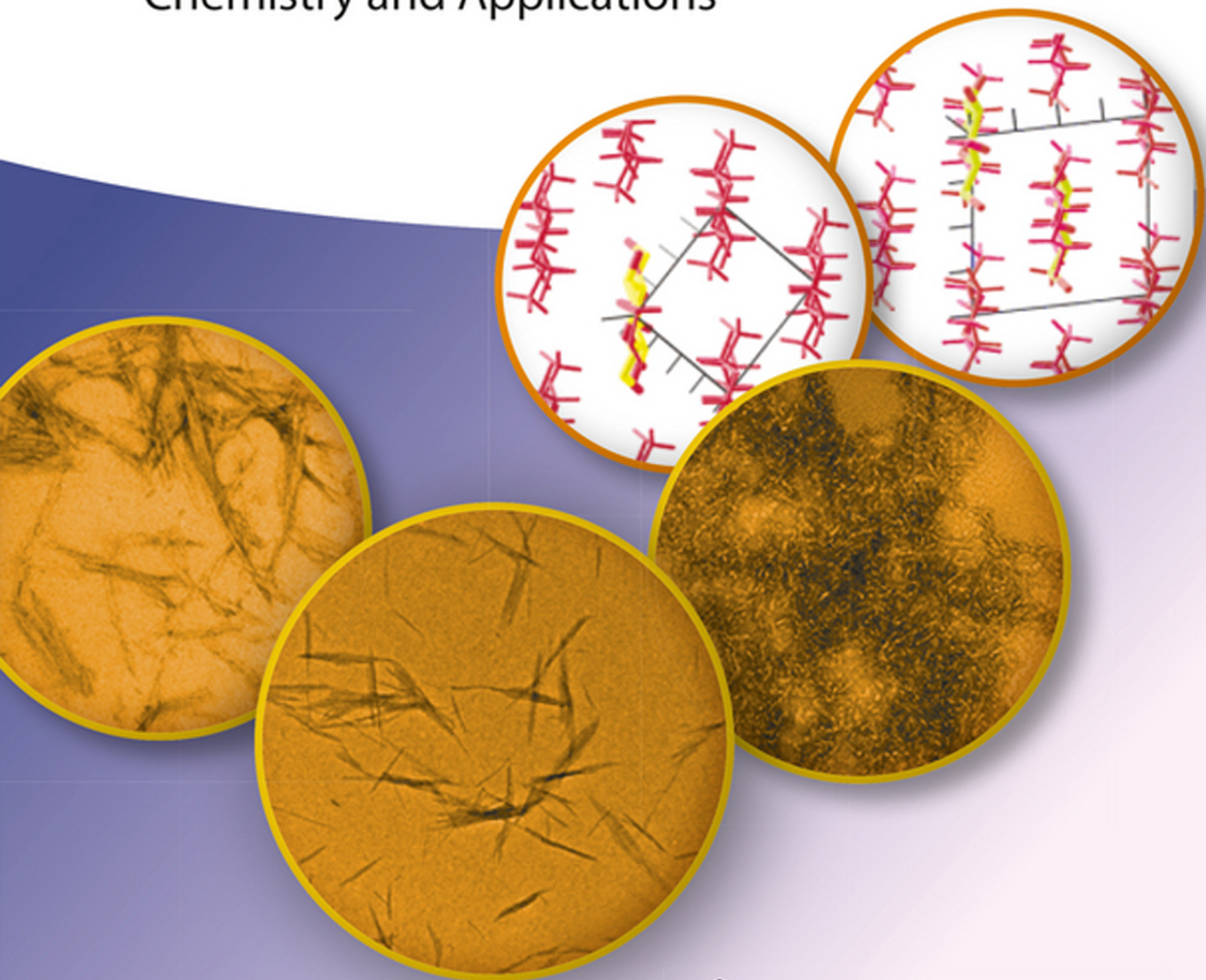
Edited by Jin Huang, Peter R. Chang, Ning Lin, and Alain Dufresne

Polysaccharide-Based Nanocrystals

Chemistry and Applications

Chemical Industry Press

Edited by
Jin Huang, Peter R. Chang, Ning Lin, and
Alain Dufresne

Polysaccharide-Based Nanocrystals

Related Titles

Habibi, Y., Lucia, L.A. (eds.)

Polysaccharide Building Blocks

A Sustainable Approach to the Development of Renewable Biomaterials

2012
Print ISBN: 978-0-470-87419-6

Mittal, V. (ed.)

Renewable Polymers

Synthesis, Processing, and Technology

2012
Print ISBN: 978-0-470-93877-5

Sarmento, B.B., das Neves, J.J. (eds.)

Chitosan-Based Systems for Biopharmaceuticals-Delivery, Targeting and Polymer Therapeutics

2012
Print ISBN: 978-0-470-97832-0

Dufresne, A., Thomas, S., Pothan, L.A. (eds.)

Biopolymer Nanocomposites

Processing, Properties, and Applications

2013
Print ISBN: 978-1-118-21835-8

Tiwari, A., Tiwari, A.

Nanomaterials in Drug Delivery, Imaging, and Tissue Engineering

2013
Print ISBN: 978-1-118-29032-3

Mano, J.F. (ed.)

Biomimetic Approaches for Biomaterials Development

2012
Print ISBN: 978-3-527-32916-8

Thomas, S., Joseph, K., Malhotra, S.K., Goda, K., Sreekala, M.S. (eds.)

Polymer Composites

Volume 2

2013
Print ISBN: 978-3-527-32979-3

Mittal, V. (ed.)

Characterization Techniques for Polymer Nanocomposites

2012
Print ISBN: 978-3-527-33148-2

Thomas, S., Sinturel, C., Thomas, R. (eds.)

Micro- and Nanostructured Epoxy/Rubber Blends

2014
Print ISBN: 978-3-527-33334-9

Vollath, D.

Nanomaterials

An Introduction to Synthesis, Properties, and Applications

2nd Edition
2013
Print ISBN: 978-3-527-33379-0

Gu, Z. (ed.)

Bioinspired and Biomimetic Systems for Drug and Gene Delivery

2014
Print ISBN: 978-3-527-33420-9

Binder, W.H. (ed.)

Self-Healing Polymers

From Principles to Applications

2013
Print ISBN: 978-3-527-33439-1

Pompe, W., Rödel, G., Weiss, H., Mertig, M.

Bio-Nanomaterials

Designing materials inspired by nature

2013
Print ISBN: 978-3-527-41015-6

Edited by Jin Huang, Peter R. Chang, Ning Lin, and Alain Dufresne

Polysaccharide-Based Nanocrystals

Chemistry and Applications

WILEY-VCH

Verlag GmbH & Co. KGaA

Chemical Industry Press

The Editors

Prof. Jin Huang
College of Chemistry, Chemical
Engineering and Life Science
Wuhan University of Technology
122 Luoshi Road
Wuhan 430070
China

Prof. Peter R. Chang
BioProducts and Bioprocesses
National Science Program
Agriculture and Agri-Food Canada
Government of Canada
107 Science Place
Saskatoon SK S7N 0X2
Canada

Mr. Ning Lin
The International School of Paper,
Print Media, and Biomaterials (Pagora)
Grenoble Institute of Technology
(Grenoble INP)
Domaine Universitaire
CS10065, 38402
Saint Martin d'Hères
France

Prof. Alain Dufresne
The International School of Paper, Print
Media, and Biomaterials (Pagora)
Grenoble Institute of Technology
(Grenoble INP)
Domaine Universitaire
CS10065, 38402
Saint Martin d'Hères
France

Contents

List of Contributors

Ishak Ahmad
School of Chemical Sciences and
Food Technology
Faculty of Science and
Technology
Universiti Kebangsan Malaysia
(UKM)
43600, Bangi
Selangor
Malaysia

Debbie P. Anderson
BioProducts and Bioprocesses
National Science Program
Agriculture and Agri-Food
Canada
Government of Canada
107 Science Place
Saskatoon SK S7N 0X2
Canada

Peter R. Chang
Bioproducts and Bioprocesses
National Science Program
Agriculture and Agri-Food
Canada
Government of Canada
107 Science Place
Saskatoon SK S7N 0X2
Canada

and

Department of Chemical and
Biological Engineering
College of Engineering
University of Saskatchewan
Saskatoon SK S7N 5A9
Canada

Youli Chen
College of Chemistry, Chemical
Engineering and Life Science
Wuhan University of Technology
Luoshi Road 122
Wuhan 430070
China

Alain Dufresne
The International School of
Paper, Print Media, and
Biomaterials (Pagora)
Grenoble Institute of Technology
(Grenoble INP)
Domaine Universitaire, CS10065,
38402 Saint Martin d'Hères
France

Shiyu Fu
State Key Laboratory of Pulp and
Paper Engineering
South China University of
Technology
Guangzhou 510641
China

Fei Hu
College of Chemistry, Chemical
Engineering and Life Science
Wuhan University of Technology
Luoshi Road 122
Wuhan 430070
China

Jin Huang
College of Chemistry, Chemical
Engineering and Life Science
Wuhan University of Technology
Luoshi Road 122
Wuhan 430070
China

Hanieh Kargarzadeh
School of Chemical Sciences and
Food Technology
Faculty of Science and
Technology
Universiti Kebangsaan Malaysia
(UKM)
43600, Bangi
Selangor
Malaysia

Ning Lin
The International School of
Paper, Print Media, and
Biomaterials (Pagora)
Grenoble Institute of Technology
(Grenoble INP)
Domaine Universitaire
CS10065, 38402
Saint Martin d'Hères
France

Hou-Yong Yu
College of Materials and Textile
Zhejiang Sci-Tech University
928 Second Avenue, Xiasha
Higher Education Zone
Hangzhou 310018
China

Foreword

Since the beginning of the new century, the development of advanced biobased nanomaterials has been of significant interest in both academia and industry. Polysaccharide nanocrystals, mainly including rod-like cellulose nanocrystals, chitin nanowhiskers, and platelet-like starch nanocrystals, are highly crystalline rigid nanoparticles extracted from biosourced polymers that possess numerous advantages over inorganic nanoparticles. It has been reported that the diverse materials derived from polysaccharide nanocrystals will cover a broad range of properties that are useful in a wide range of applications, for example, in composites, electronics (flexible circuits), energy (flexible batteries, such as Li-ion and solar panels), packaging, coatings, detergents, adhesives, construction, pulp and paper, inks and printing, filtration, medicine and life science (scaffolds in tissue engineering, artificial skin and cartilage, wound healing, and vessel substitutes), optical devices (including reflective properties for security papers and UV or IR reflective barriers), rheological modifiers, and cosmetics. Since the first study on the use of cellulose nanocrystals as a reinforcing filler in nanocomposites about 20 years ago, a huge amount of literature has been devoted to research on polysaccharide nanocrystals in more than 1000 scientific publications.

As a relatively new research area, it is imperative to systematically assemble state-of-the-art technical accomplishments on polysaccharide nanocrystals, particularly with respect to physics, chemistry, materials science, processing, and engineering. This book covers extraction, structure, properties, and surface modification pertaining to polysaccharide nanocrystals. It provides an in-depth description of plastics and composites containing this unique biosourced nanoingredient in terms of structures, properties, manufacturing, and product performance. This book also describes the concept of functional nanomaterials based on polysaccharide nanocrystals and their potential applications. All chapters are contributed by leading experts who have both academic and professional credentials.

It is interesting to note that commercialization/utilization of polysaccharide nanocrystals (especially for cellulose nanocrystals) is finally catching on and is being pursued vigorously by industrial groups, notably in the United States, Canada, and Europe.

Upcoming R&D and relentless pursuit represent well-justified challenges and opportunities for bringing the next generation of polysaccharide nanocrystal-based materials into reality.

Preface

Biobased Polysaccharide Nanocrystals: Chemistry and Applications is the first book that systematically describes the chemistry, properties, processing, and applications of polysaccharide nanocrystals and the nanocomposites/nanomaterials thereby derived.

Development of biobased materials has experienced fast growth in the past two decades thanks to public concern over the environment, climate change, and the depletion of fossil fuels. Over the last 10 years or so, this team of authors has worked collectively and separately with these interesting and yet little known renewable and biodegradable polysaccharide nanocrystals in the cutting edge field of functional nanomaterials and nanocomposites. As such, we are eager to share our knowledge and experience with readers and stakeholders, particularly researchers from academia and industry, policy makers, and the business sector, to foster rapid exploitation and commercialization of these fascinating bioingredients and their derived products, including but not limited to nanocomposites/nanomaterials.

This book is intended to give the reader a comprehensive overview of the present knowledge relating to extraction, structure, properties, surface modification, and the newly derived material of polysaccharide nanocrystals. In addition, it provides an in-depth description of plastics, composites, and nanomaterials specifically procured from cellulose nanocrystals, chitin nanowhiskers, and starch nanocrystals. This is an excellent book for scientists, engineers, graduate students, and industrial researchers in the field of polymeric materials. This book also covers the most recent progress with respect to: (i) the development of a conceptual framework of polysaccharide nanocrystals; (ii) numerous applications in the design and manufacture of nanocomposites and functional nanomaterials; and (iii) the relationship between structure and properties.

The authors sincerely thank Chemical Industry Press and Wiley-VCH press for their kind encouragement and support throughout the project and for publishing this book in both English and Chinese. In addition, the authors wish to acknowledge the continued support toward our research from the National

1

Polysaccharide Nanocrystals: Current Status and Prospects in Material Science

Jin Huang, Peter R. Chang, and Alain Dufresne

1.1

Introduction to Polysaccharide Nanocrystals

Native polysaccharides usually consist of crystalline and amorphous regions; to produce highly crystalline polysaccharide nanocrystals (PNs) the amorphous component is removed through acid hydrolysis. The morphologies and dimensions of PNs strongly depend on the different sources of biomass and different extraction methods. Figure 1.1 depicts the transmission electron microscope (TEM) images of rod-like cellulose and chitin nanocrystals, and platelet-like starch nanocrystals [1]. It is worth noting that the surface properties of PNs are influenced by the extraction methods. The H_2SO_4 hydrolysis protocol usually produces sulfate groups on the surface of PNs, resulting in improved dispersibility in water and lower thermal stability [2, 3]. By comparison, PNs with higher thermal stability may result from HCl hydrolysis, but the resultant suspension aggregates easily in water and shows poor dispersibility [4, 5]. Moreover, PNs with improved dispersibility in water and thermal stability can also be successfully obtained using an acid mixture consisting of hydrochloric acid and an organic acid, such as acetic or butyric acid [6]. In exploring economical routes for enhancing the efficiency and yield of PN production many approaches have been attempted including pretreatments [7], hydrothermal methods [5], microwave- and ultrasonic-assisted technologies [8, 9], and so on.

The rod-like nanocrystals of cellulose and chitin show a predominant characteristic of high aspect ratios, and thus their suspensions display many unique properties, such as cholesteric liquid crystallinity and flow birefringence. These properties showed a dependence on concentration, and phase behavior was affected by electrolytes [10 – 14]. When the suspensions reached a critical concentration, the rod-like nanocrystals exhibited an ordered phase displaying flow birefringence and nematic or chiral nematic structures. Cellulose nanocrystals (CNs) exhibit birefringence not only in aqueous suspensions but also in organic solvents such as dimethylsulfoxide (DMSO), dimethyl formamide (DMF), cyclohexane, and toluene [15, 16]. At the same time, it has been found that surface-modified CNs, that is, carboxymethylated, tetramethyl-piperidin-1-oxyl

(a) (b) (c)
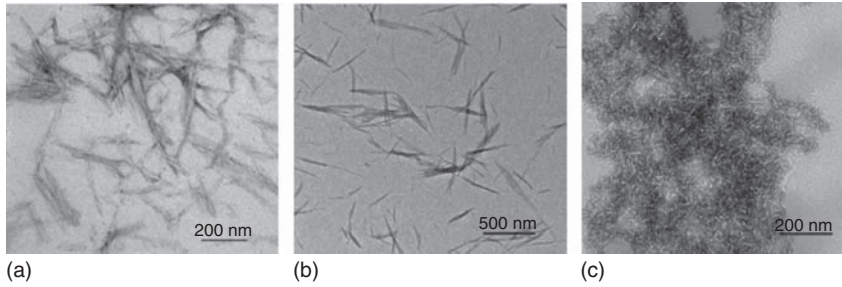
Figure 1.1 TEM images of cellulose nanocrystals from cotton linter with 200–300 nm length and 10–15 nm width (a); chitin nanocrystals from crab shell with 200–600 nm length and 10–20 nm width (b); and pea starch nanocrystals 6–8 nm thick, 40–60 nm in length, and 15–30 nm in width (c).

(TEMPO) oxidized [17], or silylated CNs, displayed birefringence in suspension with tetrahydrofuran (THF) [18]. CN suspensions possess distinctive rheological properties [19] and may form gels from aqueous glycerol suspensions with careful evaporation at 70 °C, when the CN concentration is below 3 wt% [20]. Starch nanocrystals have a unique platelet-like structure and often tend to aggregate in aqueous solution [21], although a stable suspension can be achieved by adjusting the pH [22]. Detailed descriptions of the structure and properties of PNs can be found in Chapter 2.

The abundant hydroxyl groups on the surface of PNs contribute to their positive surface chemical properties and are therefore an essential route to altering surface structure, regulating surface properties, and developing functional materials. The common methodologies for chemical modification of PNs, presented in Figure 1.2, can be classified in three categories: small molecule conjugation, "graft onto," and "graft from" strategies for polymers. There are three main mechanisms of small molecule conjugation, including isocyanation [23], silylation [18, 24], and esterification [25], depending on the availability and activity of the surface hydroxyl groups. In addition, alkynylation and azidation can be used to import alkynyl or azide groups for click chemistry using the Huisgen reaction [26]. The "graft onto" strategy for polymer grafting abides by the mechanism for small molecule conjugation, but the grafting efficiency may be inhibited by the steric hindrance of large polymer chains in contrast with the conjugation efficiency of small molecules [27–29]. In addition, hydroxyl groups on the surface of PNs can directly initiate ring opening polymerization (ROP) of lactones [30] and free radical polymerization (FRP) of olefins to graft polymer chains based on the "graft from" strategy [31]. At the same time, by using small molecule conjugation to import initiating groups, controlled radical polymerization, that is, atom transfer radical polymerization (ATRP), can be achieved using the functionalized Br atom as the initiating point [32]. Detailed surface chemical modification of PNs is described in Chapter 3.
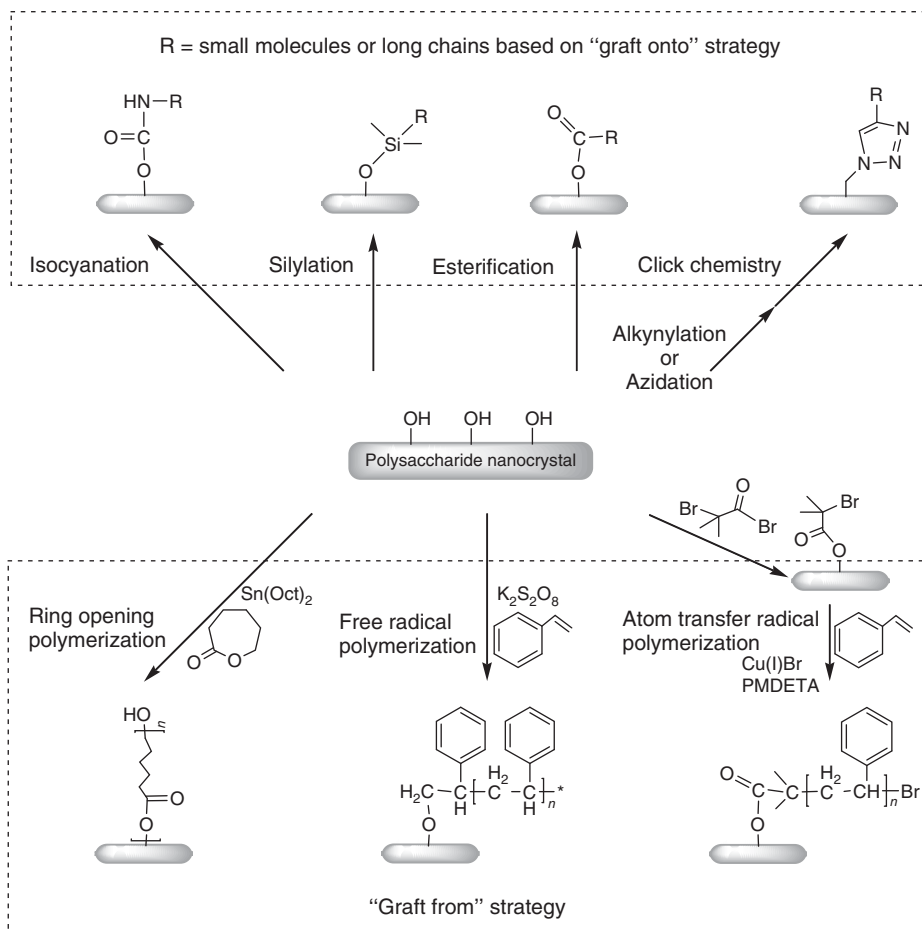
Figure 1.2 Chemical modification methodology and typical examples toward the surface of polysaccharide nanocrystals.

1.2
Current Application of Polysaccharide Nanocrystals in Material Science

PNs have been widely used as a reinforcing biomass-based filler to modify polymeric materials with matrixes of rubber, polyolefin, polyurethane and waterborne polyurethane, polyester, and natural polymer plastics of starch and protein. The reinforcing mechanism depends mainly on the formation of a three-dimensional PN network and the interfacial miscibility between the PN surface and matrix. The former abides by the percolation model and requires PN content to be higher than a critical concentration; the latter can be improved by the formation of strong interfacial interaction or by a co-continuous phase mediated by surface-grafted polymer chains that alter the surface chemical

structure through surface modification of PNs [33–37]. Casting/evaporation processing is the most suitable method for development of the three-dimensional PN network because it provides enough freedom to form hydrogen bonds among PNs before and during solidification of the nanocomposite [37–41]; however, it requires high dispersibility of PNs in the aqueous or organic blending medium during compounding and solvent evaporation. Conversely, melt-compounding and thermoforming methods, such as intensive blending, extrusion, compression molding, and injection molding, may inhibit hydrogen bonding because of the relatively high melting viscosity, and may cleave associations between PNs by shear force and hence fail to construct a three-dimensional network. Furthermore, the commonly used method that uses sulfuric acid hydrolysis for extraction of cellulose and starch nanocrystals results in low thermal stability, which does not match the requirements of thermoprocessing. It is fortunate that physical and chemical modification of the PN surface can significantly enhance thermal stability to contribute to the application of industrial-scale production of PN-modified nanocomposites by thermoprocessing. As mentioned previously, surface physical and chemical modification of PNs play key roles in improving dispersibility in solvent, regulating miscibility with the polymer matrix [37], and enhancing thermal stability to facilitate the enhanced performance of PN-filled nanocomposites together with extension of processing methods and applications [42]. New processing technologies have also been used to develop structural and functional PN-based materials. For example, mats and nanofibers reinforced by PNs have been successfully prepared using electrospinning technology [43–46], while layer-by-layer assembly has been attempted for the preparation of well-defined multilayer films [47–49]. In addition, the sol–gel method can be used to make bulk nanocomposites that inherit the chiral nematic structure of the PN suspension for further development of functional materials. A detailed introduction and relevant preparation methods of PN-modified nanocomposites can be seen in Chapters 4 and 5, respectively. Furthermore, characterization of PN-based materials is key to understanding the structure–properties relationship, as elaborated in Chapter 7.

Many advanced applications for PN-based nanocomposites that depend on surface modification and compounding technologies have been explored. Figure 1.3 depicts the main achievements of PN-based functional materials [36]. PNs with unique rod and platelet structures can act as templates for the controlled preparation of inorganic nanoparticles. For example, TiO_2 nanocubes with high crystallinity and uniform size were synthesized using a template of rod-like CNs [50]. Moreover, via the sol–gel method, the chiral nematic structure inherited from cellulose and chitin nanocrystals in suspension has been used to develop tunable optical biomimetic nanomaterials that are similar to the brilliant iridescent colors of beetle exoskeletons [51]. At the same time, the chiral nematic structure of the CN component in nanocomposites also acted as the template in the preparation of many kinds of silica [52], carbon [53], and titanium-based [54] mesoporous materials. Except for those smart materials with tunable optical functions based on the chiral nematic structure,

Template
function

TiO₂ nanocubes

200 nm

Inorganic nanoparticles   Mesoporous materials

Smart
materials

Relaxed "Soft"   Stiff

Interaction "on"   Interaction "off"   hydrogen bonds

Mechanically adaptive materials

Deliberately
damaged   Partially
healed   Completely
healed

Self-healable materials

Heating in dry oven   Drop cool water   Drop hot water

Shape-memory materials   Optical-tunable materials

Microspheres

Hydrogel

Biomedical
application

PNs-filled drug carriers   Bioimaging probe

1 µm

One-pot
deacetylation

Nanoscaffold

Electrospun fibrous scaffolds

5 µm

Cell scaffold materials

Figure 1.3 Advanced applications of PNs in the field of material sciences. (Reproduced with permission from Refs [36, 50–52, 55, 56, 58, 59, 68]. Copyright 2012, 2007, 2012, 2010, 2010, 2012, 2010, 2011, 2013, Royal Society of Chemistry, Elsevier, Nature Publishing Group, Elsevier, Elsevier, American Chemical Society, Elsevier, American Chemical Society.)

Pollution
decontamination →

PN-based nanofibrous composites

Energy
application →

Substrate of solar cells

Polymer electrolytes

Permselective membrane
applied to the electrodes

Emulsion
stabilizer →

Emulsion stabilization mechanism

Semiconductor
materials →
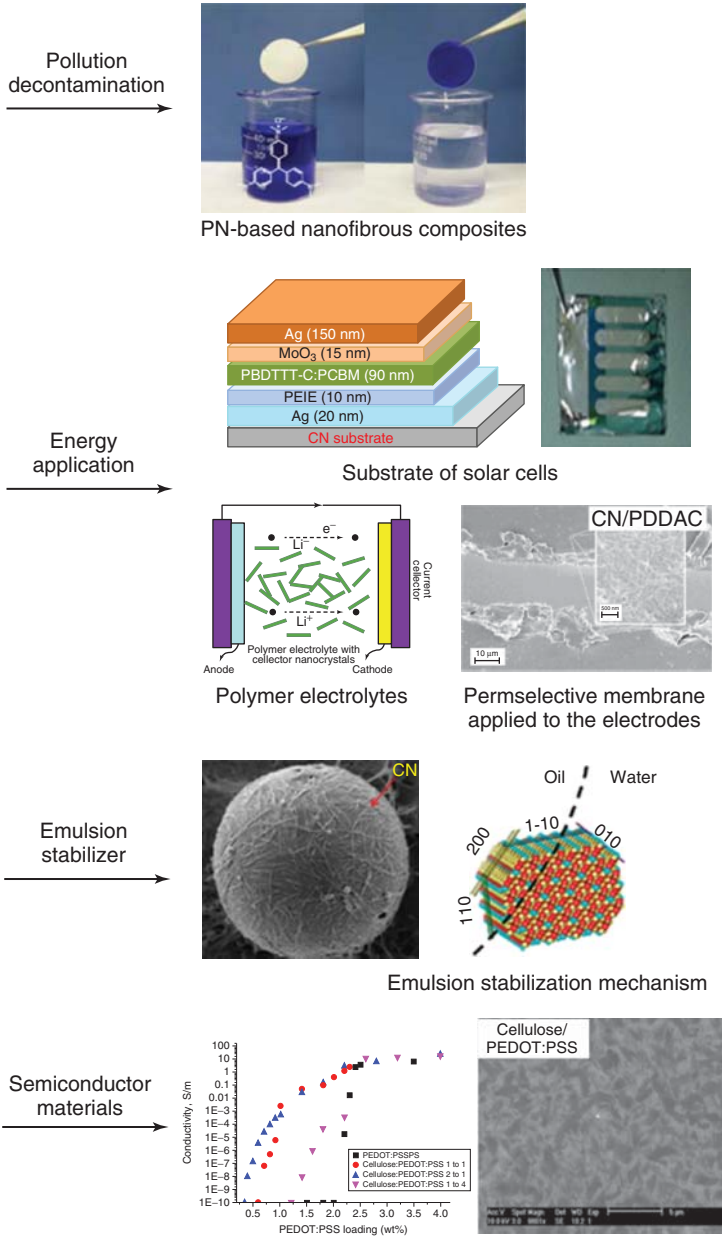
Figure 1.3 *(Continued)*

the moisture sensitivity of the three-dimensional PN network is the driving force for the preparation of mechanically adaptive biomimetic nanomaterials [36, 55]. The moisture-sensitive behavior of the nanocomposites, is ascribed to the formation and decoupling of a three-dimensional CN network, which is similar to what is seen in sea cucumbers that rapidly and reversibly alter the stiffness of their connective tissue under dry and moist conditions. In addition, smart nanocomposites that can self-heal [56] or have shape memory [57] functions have also been developed. For example, CN-filled nanocomposites with a supramolecular motif displayed an intriguing combination of high stiffness, high strength, and rapid and efficient optical healing [56], while in nanocomposites filled with CNs, the formed CNs percolation network provided a fixing force for the temporary shape with regulated reversible formation and disruption [57]. In the field of biomedicine, conjugation of CNs with fluorescent molecules has been attempted for the development of a bioimaging probe that is noncytotoxic and does not interfere with cell membrane integrity [58]. Other attempts made depended on the reinforcing effect of PNs to prepare nanocomposite drug carriers and cell scaffolds. For microsphere [59] and hydrogel [60] drug carriers, the incorporation of PNs could improve the encapsulation efficiency and sustained release profile, and enhance mechanical stability. There are two methods used to prepare PN-based scaffolds: direct one-pot deacetylation of chitin nanowhiskers to produce chitosan nanoscaffold, [61] and electrospinning to prepare fibrous nanoscaffolds reinforced with PNs [62]. In the energy field, the emerging application is the use of PNs as the substrate for solar cells, which displayed good rectification in the dark and reached a power conversion efficiency of 2.7% [63]. At the same time, polymer electrolytes filled with PNs showed high ionic conductivity as well as electrochemical, thermal, and mechanical stability [36], while permselective membranes provided selective binding sites for accumulation and transport of hydrophobic anions [64]. For environmental applications, PNs have been used in pollution decontamination. For example, chemically modified starch nanocrystals that enhanced the adsorption capacity of the nanometric substrate were used as adsorbents for the removal of aromatic organic compounds from water [65]; and a multilayered nanofibrous microfiltration membrane system based on CNs showed high flux, low pressure drop, and high retention capability, and the membrane possessed good mechanical properties as well as high surface charge density [66]. In applications in other fields the hydrophilic surface and nanoscale characteristics of PNs contribute to their function as an emulsion stabilizer, which is promising for the use of CNs to stabilize oil/water interfaces [67]; and a new class of semi-conducting materials was prepared by inducing the formation of a conductive polymer network by templating onto the percolated cellulose nanowhisker network, which is important for reducing the content of the required conducting polymer and increasing the ease of processing for electrical percolation [68]. Chapter 6 presents PN-based functional materials in more detail.

1.3
Prospects for Polysaccharide Nanocrystal-Based Materials

PNs exhibit a wide variety of properties and structures, and have many advantages, such as renewability, low density, biocompatibility, and biodegradability, over inorganic nanoparticles [69]. The opportunities and applications for PNs in new and functional engineered materials are unlimited. The structure of PNs in the matrix, including orientation, three-dimensional network, and interface structure as well as interfacial interaction, is a key issue for the high performance and function of nanocomposites. Although the chiral nematic structure of CNs in suspension can be inherited by the matrix using the sol−gel method [70], creative technologies must be developed in order to develop more nanocomposite systems and applications. The rigid three-dimensional network structure, which forms by strong hydrogen bonding among PNs, helps to reinforce the resultant nanocomposites; however, the network structure forms in solution-blending systems and usually fails in melt-compounding systems and nanocomposites filled with surface-modified PNs. As mentioned previously, PNs in suspension arrange in a chiral nematic structure. It is worth exploring the collaborative effects of PN/solvent, PN/polymer, and polymer/solvent interactions together with the interactions among PNs during evaporation, on the formation of the three-dimensional PN network when the matrix polymer chains are blended with PNs in suspension. This may contribute to the development of strategies for regulating the dispersion and distribution of PNs in the matrix. The failure of the three-dimensional network in melt-compounding is mainly ascribed to cleavage of the interactions between PNs under shear force and lower freedom of PNs under relatively higher melting viscosity. The strong interfacial interaction, which depends on the analogous hydrophilic/hydrophobic character and on the formation of physical interaction/covalent linkages between the PN surface and matrix, is expected to fully exert the reinforcing function of PNs in nanocomposites. The co-continuous structure mediated by the grafted long chains on the PN surface may contribute enough entanglement with the matrix and formation of interactions at multisites, to greatly improve the miscibility between PN and matrix. In addition, the dispersed PNs may act as the crosslinking center to form multicovalent linkages with the matrix to produce a star-like network structure. This structure facilitates stress transfer to achieve balance and enhance mechanical performance. In this case, surface modification of the PN surface is essential, especially chemical modification to enrich the hydroxyl groups on the PN surface. On the other hand, many attempts have shown chemical modification of the PN surface to result in the absence of a three-dimensional network because the modified species inhibited the formation of hydrogen bonds between PNs. As a result, it is a great challenge to achieve the simultaneous fabrication of a three-dimensional PN network and improved interfacial miscibility between the PN and matrix by designing a modified molecular structure and regulating the degree of modification on the PN surface to provide functional groups for hydrogen bonding and show analogous hydrophilic/hydrophobic

properties with the matrix. So far, basic research of PN-based nanocomposites has been profound and exploration into functional applications has made great progress. However, there are two factors that inhibit the large-scale application of PN-based materials: one is the high-yield and high-efficiency "green" extraction technologies of PNs; the other is the industrial production of PN-based materials. With the application of many physical and biological techniques, the PN extraction time has been shortened and the yield greatly increased. Furthermore, surface modification of PNs shows significant positive effects on enhancing the thermal stability of PNs to meet thermoprocessing requirements and improve compatibility with more polymer matrixes. In addition, *in situ* compatibilization may further simplify the preparation process. On the whole, the development and extensive application of PN-based materials strongly depend on breakthroughs in the following scientific theory and key technologies: (i) the structural design and modification methodologies of the PN surface; (ii) the structural design and regulation of PN-filled nanocomposites for high performance and emerging function; and (iii) manufacturing technologies matched with industrial-scale PNs and their materials.

List of Abbreviations

ATRP   atom transfer radical polymerization
CNs   cellulose nanocrystals
DMF   dimethyl formamide
DMSO   dimethylsulfoxide
EVA   polyethylene-co-vinyl acetate
FRP   free radical polymerization
HCl   hydrochloric acid
H_2SO_4 sulfuric acid
PCL   polycaprolactone
PEG   polyethylene glycol
PLA   poly lactic acid
PNs   polysaccharide nanocrystals
PP   polypropylene
PS   polystyrene
ROP   ring opening polymerization
TEMPO   tetramethyl-piperidin-1-oxyl
THF   tetrahydrofuran
TiO_2 titanium dioxide

References

1. Angellier, H., Molina-Boisseau, S., Lebrun, L., and Dufresne, A. (2005) Processing and structural properties of waxy maize starch nanocrystals reinforced natural rubber. *Macromolecules*, **38** (9), 3783–3792.

2. Roman, M. and Winter, W.T. (2004) Effect of sulfate groups from sulfuric acid hydrolysis on the thermal degradation behavior of bacterial cellulose. *Biomacromolecules*, **5** (5), 1671–1677.

3. Wang, N., Ding, E., and Cheng, R. (2007) Thermal degradation behaviors of spherical cellulose nanocrystals with sulfate groups. *Polymer*, **48** (12), 3486–3493.

4. Winter, H.T., Cerclier, C., Delorme, N., Bizot, H., Quemener, B., and Cathala, B. (2010) Improved colloidal stability of bacterial cellulose nanocrystal suspensions for the elaboration of spin-coated cellulose-based model surfaces. *Biomacromolecules*, **11** (11), 3144–3151.

5. Yu, H., Qin, Z., Liang, B., Liu, N., Zhou, Z., and Chen, L. (2013) Facile extraction of thermally stable cellulose nanocrystals with a high yield of 93% through hydrochloric acid hydrolysis under hydrothermal conditions. *J. Mater. Chem. A*, **1** (12), 3938–3944.

6. Braun, B. and Dorgan, J.R. (2008) Single-step method for the isolation and surface functionalization of cellulosic nanowhiskers. *Biomacromolecules*, **10** (2), 334–341.

7. Yang, D., Peng, X.W., Zhong, L.X., Cao, X.F., Chen, W., and Sun, R.C. (2013) Effects of pretreatments on crystalline properties and morphology of cellulose nanocrystals. *Cellulose*, **20** (5), 2427–2437.

8. Tang, L., Huang, B., Lu, Q., Wang, S., Ou, W., Lin, W., and Chen, X. (2013) Ultrasonication-assisted manufacture of cellulose nanocrystals esterified with acetic acid. *Bioresour. Technol.*, **127**, 100–105.

9. Lu, Z., Fan, L., Zheng, H., Lu, Q., Liao, Y., and Huang, B. (2013) Preparation, characterization and optimization of nanocellulose whiskers by simultaneously ultrasonic wave and microwave assisted. *Bioresour. Technol.*, **146**, 82–88.

10. Liu, D., Chen, X., Yue, Y., Chen, M., and Wu, Q. (2011) Structure and rheology of nanocrystalline cellulose. *Carbohydr. Polym.*, **84** (1), 316–322.

11. Araki, J. and Kuga, S. (2001) Effect of trace electrolyte on liquid crystal type of cellulose microcrystals. *Langmuir*, **17** (15), 4493–4496.

12. Gopalan Nair, K. and Dufresne, A. (2003) Crab shell chitin whisker reinforced natural rubber nanocomposites. 1. Processing and swelling behavior. *Biomacromolecules*, **4** (3), 657–665.

13. Nge, T.T., Hori, N., Takemura, A., Ono, H., and Kimura, T. (2003) Phase behavior of liquid crystalline chitin/acrylic acid liquid mixture. *Langmuir*, **19** (4), 1390–1395.

14. Tzoumaki, M.V., Moschakis, T., and Biliaderis, C.G. (2009) Metastability of nematic gels made of aqueous chitin nanocrystal dispersions. *Biomacromolecules*, **11** (1), 175–181.

15. Elazzouzi-Hafraoui, S., Putaux, J.L., and Heux, L. (2009) Self-assembling and chiral nematic properties of organophilic cellulose nanocrystals. *J. Phys. Chem. B*, **113** (32), 11069–11075.

16. Heux, L., Chauve, G., and Bonini, C. (2000) Nonflocculating and chiral-nematic self-ordering of cellulose microcrystals suspensions in nonpolar solvents. *Langmuir*, **16** (21), 8210–8212.

17. Habibi, Y., Chanzy, H., and Vignon, M.R. (2006) TEMPO-mediated surface oxidation of cellulose whiskers. *Cellulose*, **13** (6), 679–687.

18. Goussé, C., Chanzy, H., Excoffier, G., Soubeyrand, L., and Fleury, E. (2002) Stable suspensions of partially silylated cellulose whiskers dispersed in organic solvents. *Polymer*, **43** (9), 2645–2651.

19. Bercea, M. and Navard, P. (2000) Shear dynamics of aqueous suspensions of cellulose whiskers. *Macromolecules*, **33** (16), 6011–6016.

20. Dorris, A. and Gray, D.G. (2012) Gelation of cellulose nanocrystal suspensions in glycerol. *Cellulose*, **19** (3), 687–694.

21. Ren, L., Jiang, M., Wang, L., Zhou, J., and Tong, J. (2012) A method for improving dispersion of starch nanocrystals in water through crosslinking modification with sodium hexametaphosphate. *Carbohydr. Polym.*, **87** (2), 1874–1876.

22. Wei, B., Hu, X., Li, H., Wu, C., Xu, X., Jin, Z., and Tian, Y. (2014) Effect of pHs on dispersity of maize starch nanocrystals in aqueous medium. *Food Hydrocolloids*, **36**, 369–373.

23. Angellier, H., Molina-Boisseau, S., Belgacem, M.N., and Dufresne, A. (2005) Surface chemical modification of waxy maize starch nanocrystals. *Langmuir*, **21** (6), 2425–2433.

24. de Oliveira Taipina, M., Ferrarezi, M.M.F., Yoshida, I.V.P., and do Carmo Gonçalves, M. (2013) Surface modification of cotton nanocrystals with a silane agent. *Cellulose*, **20** (1), 217–226.

25. Sassi, J.F. and Chanzy, H. (1995) Ultra-structural aspects of the acetylation of cellulose. *Cellulose*, **2** (2), 111–127.

26. Sadeghifar, H., Filpponen, I., Clarke, S.P., Brougham, D.F., and Argyropoulos, D.S. (2011) Production of cellulose nanocrystals using hydrobromic acid and click reactions on their surface. *J. Mater. Sci.*, **46** (22), 7344–7355.

27. Siqueira, G., Bras, J., and Dufresne, A. (2009) New process of chemical grafting of cellulose nanoparticles with a long chain isocyanate. *Langmuir*, **26** (1), 402–411.

28. Siqueira, G., Bras, J., and Dufresne, A. (2008) Cellulose whiskers versus microfibrils: influence of the nature of the nanoparticle and its surface functionalization on the thermal and mechanical properties of nanocomposites. *Biomacromolecules*, **10** (2), 425–432.

29. Zoppe, J.O., Peresin, M.S., Habibi, Y., Venditti, R.A., and Rojas, O.J. (2009) Reinforcing poly (ϵ-caprolactone) nanofibers with cellulose nanocrystals. *ACS Appl. Mater. Interfaces*, **1** (9), 1996–2004.

30. Namazi, H. and Dadkhah, A. (2008) Surface modification of starch nanocrystals through ring-opening polymerization of ϵ-caprolactone and investigation of their microstructures. *J. Appl. Polym. Sci.*, **110** (4), 2405–2412.

31. Song, S., Wang, C., Pan, Z., and Wang, X. (2008) Preparation and characterization of amphiphilic starch nanocrystals. *J. Appl. Polym. Sci.*, **107** (1), 418–422.

32. Morandi, G., Heath, L., and Thielemans, W. (2009) Cellulose nanocrystals grafted with polystyrene chains through surface-initiated atom transfer radical polymerization (SI-ATRP). *Langmuir*, **25** (14), 8280–8286.

33. Missoum, K., Belgacem, M.N., and Bras, J. (2013) Nanofibrillated cellulose surface modification: a review. *Materials*, **6** (5), 1745–1766.

34. Lin, N., Huang, J., Chang, P.R., Anderson, D.P., and Yu, J. (2011) Preparation, modification, and application of starch nanocrystals in nanomaterials: a review. *J. Nanomater.*, **2011**, 20.

35. Mincea, M., Negrulescu, A., and Ostafe, V. (2012) Preparation, modification, and applications of chitin nanowhiskers: a review. *Rev. Adv. Mater. Sci.*, **30**, 225–242.

36. Lin, N., Huang, J., and Dufresne, A. (2012) Preparation, properties and applications of polysaccharide nanocrystals in advanced functional nanomaterials: a review. *Nanoscale*, **4**, 3274–3294.

37. Dufresne, A. (2008) Polysaccharide nano crystal reinforced nanocomposites. *Can. J. Chem.*, **86** (6), 484–494.

38. Dufresne, A. (2010) Processing of polymer nanocomposites reinforced with polysaccharide nanocrystals. *Molecules*, **15** (6), 4111–4128.

39. Le Corre, D., Bras, J., and Dufresne, A. (2010) Starch nanoparticles: a review. *Biomacromolecules*, **11** (5), 1139–1153.

40. Zeng, J.B., He, Y.S., Li, S.L., and Wang, Y.Z. (2011) Chitin whiskers: an overview. *Biomacromolecules*, **13** (1), 1–11.

41. Habibi, Y., Lucia, L.A., and Rojas, O.J. (2010) Cellulose nanocrystals: chemistry, self-assembly, and applications. *Chem. Rev.*, **110** (6), 3479–3500.

42. Lin, N. and Dufresne, A. (2013) Physical and/or chemical compatibilization of extruded cellulose nanocrystal reinforced polystyrene nanocomposites. *Macromolecules*, **46** (14), 5570–5583.

43. Ago, M., Okajima, K., Jakes, J.E., Park, S., and Rojas, O.J. (2012) Lignin-based electrospun nanofibers reinforced with cellulose nanocrystals. *Biomacromolecules*, **13** (3), 918–926.

44. Huang, J., Liu, L., and Yao, J. (2011) Electrospinning of Bombyx mori silk fibroin nanofiber mats reinforced by cellulose nanowhiskers. *Fibers Polym.*, **12** (8), 1002–1006.

45. Zhou, C., Wang, Q., and Wu, Q. (2012) UV-initiated crosslinking of electrospun poly (ethylene oxide) nanofibers with pentaerythritol triacrylate: effect of irradiation time and incorporated cellulose nanocrystals. *Carbohydr. Polym.*, **87** (2), 1779–1786.

46. Dong, H., Strawhecker, K.E., Snyder, J.F., Orlicki, J.A., Reiner, R.S., and Rudie, A.W. (2012) Cellulose nanocrystals as a reinforcing material for electrospun poly (methyl methacrylate) fibers: formation, properties and nanomechanical characterization. *Carbohydr. Polym.*, **87** (4), 2488–2495.

47. Aulin, C., Johansson, E., Wågberg, L., and Lindström, T. (2010) Self-organized films from cellulose I nanofibrils using the layer-by-layer technique. *Biomacromolecules*, **11** (4), 872–882.

48. Cranston, E.D. and Gray, D.G. (2006) Formation of cellulose-based electrostatic layer-by-layer films in a magnetic field. *Sci. Technol. Adv. Mater.*, **7** (4), 319–321.

49. Podsiadlo, P., Choi, S.Y., Shim, B., Lee, J., Cuddihy, M., and Kotov, N.A. (2005) Molecularly engineered nanocomposites: layer-by-layer assembly of cellulose nanocrystals. *Biomacromolecules*, **6** (6), 2914–2918.

50. Zhou, Y., Ding, E.Y., and Li, W.D. (2007) Synthesis of TiO$_2$ nanocubes induced by cellulose nanocrystal (CNC) at low temperature. *Mater. Lett.*, **61** (28), 5050–5052.

51. Shopsowitz, K.E., Hamad, W.Y., and MacLachlan, M.J. (2012) Flexible and iridescent chiral nematic mesoporous organosilica films. *J. Am. Chem. Soc.*, **134** (2), 867–870.

52. Shopsowitz, K.E., Qi, H., Hamad, W.Y., and MacLachlan, M.J. (2010) Free-standing mesoporous silica films with tunable chiral nematic structures. *Nature*, **468**, 422–426.

53. Shopsowitz, K.E., Hamad, W.Y., and MacLachlan, M.J. (2011) Chiral nematic mesoporous carbon derived from nanocrystalline cellulose. *Angew. Chem. Int. Ed.*, **50**, 10991–10995.

54. Li, W., Zhao, Y., and Lu, S.X. (2012) Mesoporous TiO2 spheres prepared by an acid catalyzed hydrolysis method using nanocrystalline cellulose as template. *Chin. J. Catal.*, **33** (2), 342–347.

55. Shanmuganathan, K., Capadona, J.R., Rowan, S.J., and Weder, C. (2010) Biomimetic mechanically adaptive nanocomposites. *Prog. Polym. Sci.*, **35** (1), 212–222.

56. Biyani, M.V., Foster, E.J., and Weder, C. (2013) Light-healable supramolecular nanocomposites based on modified cellulose nanocrystals. *ACS Macro Lett.*, **2**, 236–240.

57. Luo, H., Hu, J., and Zhu, Y. (2012) Path-dependent and selective multi-shape recovery of a polyurethane/cellulose-whisker nanocomposite. *Mater. Lett.*, **89**, 172–175.

58. Mahmoud, K.A., Mena, J.A., Male, K.B., Hrapovic, S., Kamen, A., and Luong, J.H.T. (2010) Effect of surface charge on the cellular uptake and cytotoxicity of fluorescent labeled cellulose nanocrystals. *ACS Appl. Mater. Interfaces*, **2**, 2924–2932.

59. Lin, N., Huang, J., Chang, P.R., Feng, L., and Yu, J. (2011) Effect of polysaccharide nanocrystals on structure, properties, and drug release kinetics of alginate-based microspheres. *Colloids Surf., B*, **85**, 270–279.

60. Lin, N. and Dufresne, A. (2013) Supramolecular hydrogels from in situ host−guest inclusion between chemically modified cellulose nanocrystals and cyclodextrin. *Biomacromolecules*, **14**, 871–880.

61. Phongying, S., Aiba, S., and Chirachanchai, S. (2007) Direct chitosan nanoscaffold formation via chitin whiskers. *Polymer*, **48**, 393–400.

62. Zhou, C., Shi, Q., Guo, W., Terrell, L., Qureshi, A.T., Hayes, D.J., and Wu, Q. (2013) Electrospun bio-nanocomposite scaffolds for bone tissue engineering by cellulose nanocrystals reinforcing maleic anhydride grafted PLA. *ACS Appl. Mater. Interfaces*, **5** (9), 3847–3854.

63. Zhou, Y., Fuentes-Hernandez, C., Khan, T.M., Liu, J.-C., Hsu, J., Shim, J.W., Dindar, A., Youngblood, J.P., Moon, R.J., and Kippelen, B. (2013) Recyclable organic solar cells on cellulose nanocrystal substrates. *Sci. Rep.*, **3**, 1536, (5 pages).

64. Bonne, M.J., Edler, K.J., Buchanan, J.G., Wolverson, D., Psillakis, E., Helton, M., Thielemans, W., and Marken, F. (2008) Thin-film modified electrodes with reconstituted cellulose-PDDAC films for the accumulation and detection of triclosan. *J. Phys. Chem. C*, **112** (7), 2660–2666.

65. Alila, S., Aloulou, F., Thielemans, W., and Boufi, S. (2011) Sorption potential of modified nanocrystals for the removal of aromatic organic pollutant from aqueous solution. *Ind. Crops Prod.*, **33**, 350–357.

66. Ma, H., Burger, C., Hsiao, B.S., and Chu, B. (2012) Nanofibrous microfiltration membrane based on cellulose nanowhiskers. *Biomacromolecules*, **13**, 180–186.

67. Kalashnikova, I., Bizot, H., Cathala, B., and Capron, I. (2012) Modulation of cellulose nanocrystals amphiphilic properties to stabilize oil/water interface. *Biomacromolecules*, **13**, 267–275.

68. Tkalya, E., Ghislandi, M., Thielemans, W., van der Schoot, P., de With, G., and Koning, C. (2013) Cellulose nanowhiskers templating in conductive polymer nanocomposites reduces electrical percolation threshold 5-fold. *ACS Macro Lett.*, **2**, 157–163.

69. Dufresne, A. (2006) Comparing the mechanical properties of high performances polymer nanocomposites from biological sources. *J. Nanosci. Nanotechnol.*, **6** (2), 322–330.

70. Desjardin, E., Blaseby, M., and Mann, S. (2003) Synthesis of mesoporous silica by sol–gel mineralisation of cellulose nanorod nematic suspensions. *J. Mater. Chem.*, **13**, 696–699.

2
Structure and Properties of Polysaccharide Nanocrystals

Fei Hu, Shiyu Fu, Jin Huang, Debbie P. Anderson, and Peter R. Chang

2.1
Introduction

Polysaccharide nanocrystals (PNs), the nanoingredient (nanomaterial) with high crystallinity obtained after acid hydrolysis of biosourced polysaccharides, are of economic significance owing to their abundance and functional performance. In contrast to traditional inorganic nanoparticles, PNs exhibit a diverse morphology, high specific strength, a modulus of above 100 GPa (i.e., high rigidity), and a high specific surface area (usually several hundred square meters per gram) [1]. PNs also have attributes that inorganic nanoparticles do not possess, such as renewability, low density, biocompatibility, and biodegradability. They are environmentally friendly and their surfaces are covered with a number of hydroxyl groups that can be chemically modified on the basis of surface hydroxyls. PNs include rod-like or spherical cellulose nanocrystals (CNs), rod-like chitin nanocrystals, and platelet-like starch nanocrystals [2]. It is important to note that the method of preparing PNs inevitably influences their attributes and functional properties. For example, CNs obtained using sulfuric acid exhibit significantly lower thermal stability and higher stability in suspension than their counterparts obtained from hydrochloric acid [3, 4]. Spherical CNs can be derived by using a mixture of sulfuric and hydrochloric acids [5]. Moreover, surface-modified CNs can be generated by using an acid mixture composed of hydrochloric and an organic acid (acetic or butyric acid) [6]. High crystallinity in structure and no *N*-deacetylation were observed in the chitin nanocrystals from TEMPO-oxidized (tetramethyl-piperidin-1-oxyl) chitins. Pretreatment of polysaccharides (prior to acid hydrolysis) affects the hydrolysis time, yield, and structures of the resultant PNs [7]. In this chapter, we cover the preparation, structure, and properties pertaining to nanocrystals derived from biomass-based raw materials such as cellulose, chitin, and starch.

2.2
Cellulose Nanocrystals

2.2.1
Preparation of Cellulose Nanocrystals

2.2.1.1 Acid Hydrolysis Extraction of Cellulose Nanocrystals

CNs are crystalline regions of molecules that are tightly entangled by hydrogen bonding interactions in cellulose. The main process for the isolation of CNs from cellulose fibers is based on acid hydrolysis. In the 1950s, Ranby reported for the first time that CNs could be obtained using sulfuric acid hydrolysis of cellulose fibers [8]. Disordered or paracrystalline regions of cellulose are preferentially hydrolyzed, whereas crystalline regions that have a higher resistance to acid attack remain intact [9, 10]. As such, rod-like CNs are obtained after acid treatment of cellulose. The crystallinity of the cellulose raw material and its corresponding CNs differ according to different sources. The crystallinity of CNs is affected by the preparation technique, pretreatment, or the type of acid [9], and the different cellulose sources result in CNs with distinctive sizes and aspect ratios (see Figure 2.1). For example, CNs from tunicates have a higher aspect ratio than those from plants. Almost all CNs show some degree of aggregation. At the same time, variations in the conditions of acid hydrolysis (e.g., acid type and concentration, hydrolysis time, and temperature) will also impact the physical

(a)　　　　　　　(b)　　　　　　　(c)　　　　　　　(d)

(e)　　　　　　　(f)　　　　　　　(g)
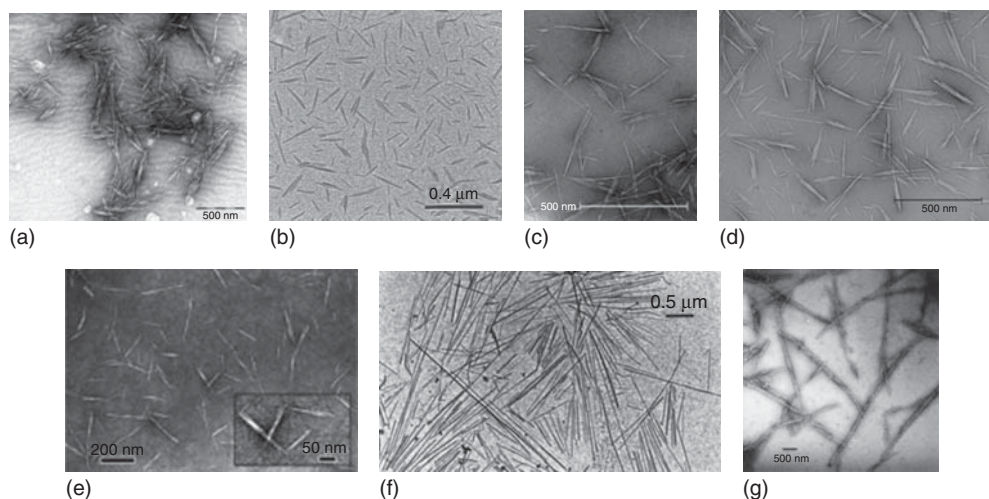
Figure 2.1 TEM images of cellulose nanocrystals derived from: (a) cotton linter, (b) cotton, (c) sisal, (d) ramie, (e) microcrystalline cellulose, (f) tunicate, and (g) bacteria. Reproduced from [12, 13, 14, 15, 16, 17, 11], copyright 2011, 1996, 2008, 2009, 2007, 2000, 2002 © permission from John Wiley & Sons, American Chemical Society, American Chemical Society, Elsevier, American Chemical Society, American Chemical Society, Springer.

attributes/properties of the CNs prepared (i.e., surface charge, size, yield, and birefringence) [11].

Conventionally, CNs were obtained using 64–65% (w/w) sulfuric acid aqueous solution with the ratio of 1 : 8 to 1 : 20 $(g\,ml^{-1})$ of raw material containing cellulose (weight) versus acid (volume) at 45 °C [18–21]. The cellulose fibers from different plants and animals were premixed with sulfuric acid and then stirred for a given time (e.g., 60 min [13, 14]). When the hydrolysis of amorphous cellulose was completed, the suspension was diluted with plenty of deionized water to end the reaction, followed by centrifuging for several minutes to remove the excess acid solution. The obtained precipitates were washed with deionized water and the suspension was centrifuged again. This process was repeated several times and then the suspension was dialyzed with deionized water until the pH of the water was neutral (alternatively, ammonia or NaOH aqueous solution can be used for neutralization prior to dialysis [22, 23]). Afterwards, in order to obtain better dispersed and more homogeneous CN suspensions, mechanical treatment with a high-pressure or high-speed homogenizer was used for the suspension of CNs [20] or the suspension was treated using ultrasound to facilitate dispersion of the CNs in water for more uniformity and stability [18]. Finally, the suspension was freeze-dried to yield dry CNs [21], or a small amount of toluene or chloroform was added into the CN suspension to inhibit bacterial growth, and then directly stored under cold conditions [24, 25]. In addition, the CNs also were transferred to organic solvents (such as methylbenzene, dimethyl formamide (DMF), or dimethylsulfoxide (DMSO), etc.) from the aqueous suspension through ultracentrifugation–redispersion (generally using acetone as an intermediate solvent). Meanwhile, some assisted techniques such as ultrasonic wave and microwave were also used for the extraction of CNs. For example, in the extraction of acid hydrolyzed CNs, using ultrasonic wave and microwave techniques simultaneously can effectively improve the extraction efficiency [26]. It was found that microwave heating to 70 °C for 1.5 h followed by ultrasound, led to a CN yield of 85.75%, which is higher than that reported in other literature, which is in the range of 70–80% [27, 28]. The length of the CNs obtained was in the range of 200–500 nm. The molecular and crystal structure of CNs did not change; crystallinity of the CNs increased from 77% of cellulose fibers to 80% for the CNs obtained.

The mechanism for sulfuric acid hydrolysis of native cellulose is as shown in Figure 2.2a [21]. In sulfuric acid solution, acid hydrolysis of native cellulose occurs through two pathways of rapid protonation: the protonation of glucosidic oxygen or cyclic oxygen by protons from sulfuric acid, followed by water-induced breaking of the glucosidic bonds (see in Figure 2.2a). The hydrolysis process yielded two shorter chain fragments with the basic backbone structure of cellulose. Moreover, besides chain scission, use of sulfuric acid to hydrolyze the native cellulose also involves esterification of the hydroxyl groups (Figure 2.2b). Acid half-esters (so-called "cellulose sulfate") were produced by the esterification reaction. The CNs resulting from sulfuric acid hydrolysis contain sulfonic acid
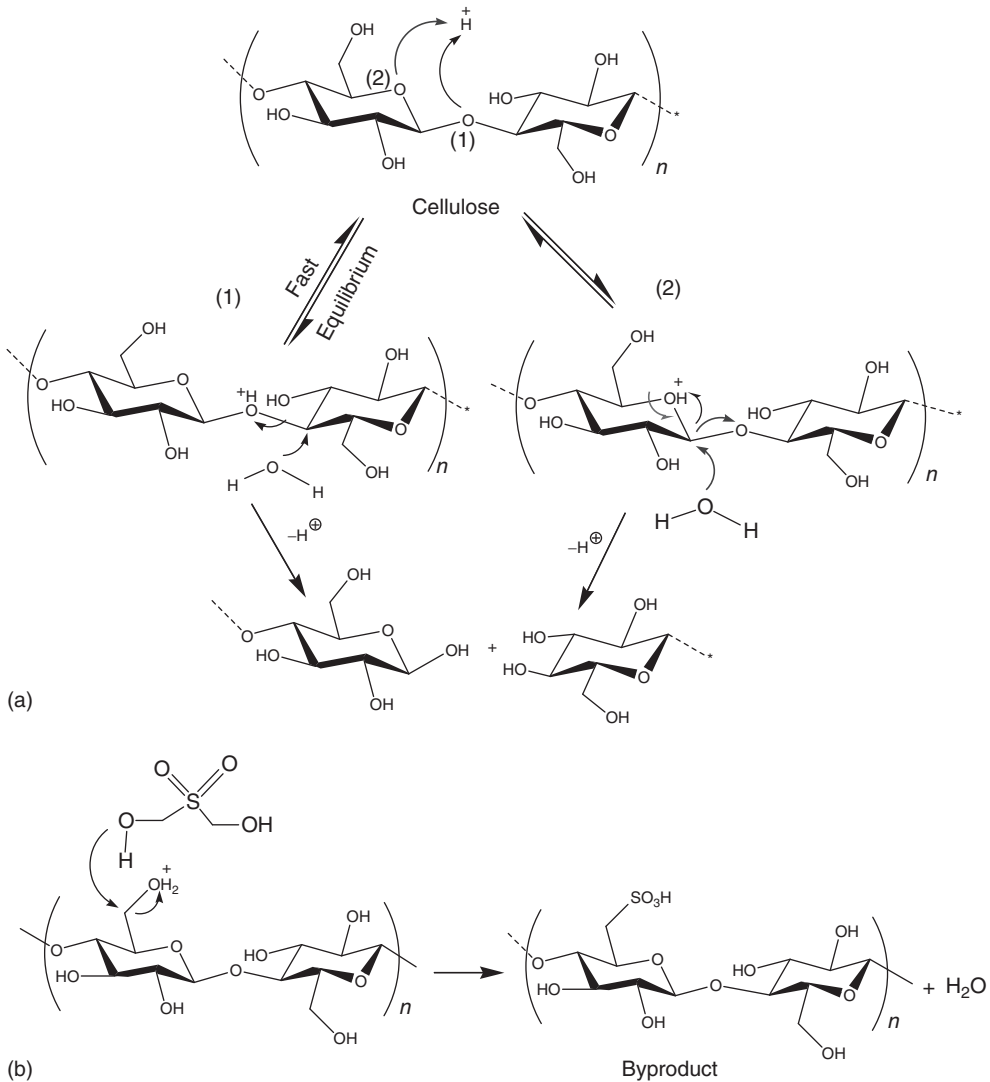
Figure 2.2 (a) Acid hydrolysis mechanism and (b) esterification of cellulose nanocrystal surfaces. Reproduced from [21], copyright 2010 © permission from Elsevier.

groups on the surface, which contribute to the negative charge of the CNs. This negative charge is very efficient in preventing the aggregation of CNs. In general, ultrasonic treatment in an ice bath can avoid possible desulfation of the sulfate groups on the surface of the CNs [21].

CNs obtained under various hydrolysis times have different surface properties and sizes. For example, the final properties and size of CNs changed greatly with different hydrolysis times at 45 °C. With time increasing from 10 to 240 min, both the surface charge and the total sulfur content of CNs increased, but the size of

(a)   (b)
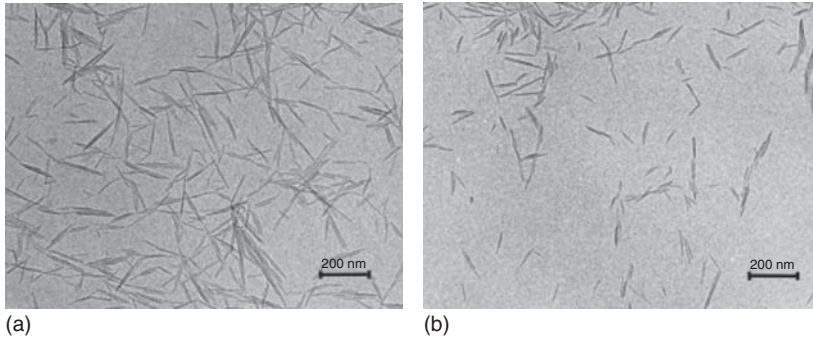
Figure 2.3 TEM images of the CNs. (a) A suspension hydrolyzed for 20 min at 45 °C and (b) a suspension hydrolyzed for 4 h at 45 °C. Reproduced from [29], copyright 1998 © permission from Springer.

CNs decreased. Moreover, the CN suspension became an ordered phase after 20 min. Figure 2.3 shows the TEM (transmission electron microscopy) images of CNs hydrolyzed for 20 min and 4 h at 45 °C respectively. The rod-like nanocrystals are generally larger in Figure 2.3a compared to those in Figure 2.3b − 332 and 177 nm, respectively [29].

2.2.1.2 Effects of Acid Type

In general, sulfuric acid can be replaced with hydrochloric acid to extract CNs; the hydrolysis process using hydrochloric acid is similar to that with sulfuric acid, but there are some differences in acid concentration, solid (weight) versus acid (volume) ratio, and reaction time. CNs can be extracted using $2.5-6\,mol\,l^{-1}$ hydrochloric acid (HCl) aqueous solutions with a certain ratio of cellulose fibers versus acid (e.g., the ratio of $1:30\,g\,ml^{-1}$ of Whatman filter paper versus HCl [30]) at $70-110\,°C$ [4, 30−32] for a preset time. For example, commercial microcrystalline cellulose (MCC) was added to $6\,mol\,l^{-1}$ HCl solution with the ratio of $1:60\,g\,ml^{-1}$ of MCC versus HCl. The obtained suspension was subsequently treated with ultrasound for 10 min in an ice water bath. Then the mixture was transferred to a hydrothermal reaction kettle and placed in an oven at $110\,°C$ for 3 h. After the oven cooled naturally to room temperature, the resultant suspension was diluted with deionized water and neutralized. Finally, the dry CN powder was obtained by freeze-drying [32]. For some cellulose raw materials that are not commercially available, pre-processing should be undertaken to purify cellulose fibers. Bacterial cellulose must first be extracted/recovered from fermentation; broth, and further purified prior to the extraction of bacterial cellulose nanocrystals (BCNs). In one study [4], a nata de coco water/ice suspension was ground to obtain a paste and then was filtered; it was resuspended in 0.5 M NaOH and the suspension transferred into a closed flask at $70\,°C$ with constant stirring for 2 h. This was followed by washing with deionized water and filtering to remove the alkali until the suspension was neutral. The resultant suspension was refluxed with $8.5\,g\,l^{-1}$ $NaClO_2$ in sodium acetate buffer (pH 4.5) at $70\,°C$ for 2 h twice. The purified bacterial cellulose was washed with deionized water to neutrality,

and hydrolyzed using 2.5 M HCl at 70 °C under reflux for 2 h to prepare BCNs. Successive centrifugations were carried out at $10\,000 \times g$ to remove excess HCl, then redispersed in deionized water until the suspension was neutral. Finally, the obtained BCN suspension was treated by ultrasonication for 1 min [4]. The yield of BCNs was about 78% and the rod-like BCNs had lengths of about 855 nm and widths of about 17 nm. The BCNs exhibited strong aggregation and almost all the nanocrystals gathered into bundles [4]. This indicated that CNs obtained after hydrochloric acid hydrolysis aggregated more easily than their counterparts obtained using sulfuric acid.

Very stable turbid colloidal suspensions were obtained by hydrolyzing the cellulose material with hydrochloric acid or sulfuric acid. TEM images showed that the individual nanocrystals were about 3.5 nm in width and 180 ± 75 nm in length (Figure 2.4). The CNs isolated using sulfuric acid showed structure and morphology that were similar to those obtained using hydrochloric acid (as shown in Figure 2.4); however, the degree of aggregation of CNs seen in Figure 2.4a,b is different. Dispersion of CNs hydrolyzed by hydrochloric acid was poor and aggregation became apparent [33]. On the other hand, hydrolysis using sulfuric acid introduced sulfate groups onto the CNs surface and facilitated the dispersion of CNs in water. However, the introduction of sulfate groups resulted in lower degradation temperatures [3].

Hydrobromic acid is a mineral acid stronger than hydrochloric acid which can also be used for extracting CNs. A simplified version of the process used is shown on the left in Figure 2.5 [34]. Typically, cellulose pulp obtained from a Whatman No. 1 filter paper was chopped in a mixer, and then hydrolyzed using 100 ml of 2.5 mol l HBr at 100 °C for 3 h. Either during (every 1 h) or after the reaction, ultrasonication was applied at room temperature. Then the turbid suspension was diluted with deionized water and centrifuged at $1500 \times g$ for 10 min for five cycles to remove the excess hydrobromic acid and water-soluble fragments. Fine cellulose nanoparticles were dispersed in the aqueous solution of pH 4. Finally, to obtain the CNs from the turbid supernatant, further centrifugation at $15\,000 \times g$ for 45 min was required, and the resultant precipitate was freeze-dried to obtain the CN powders. TEM images showed that the rod-like CNs were approximately

(a)   (b)
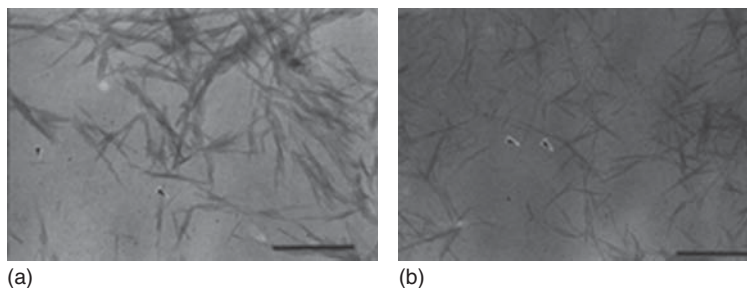
Figure 2.4 TEM images of cellulose nanocrystals extracted by (a) HCl and (b) H_2SO_4 treatments. Typical individual nanocrystals are shown by arrowheads. Scale bars show 500 nm. Reproduced from [33], copyright 1998 © permission from Elsevier.
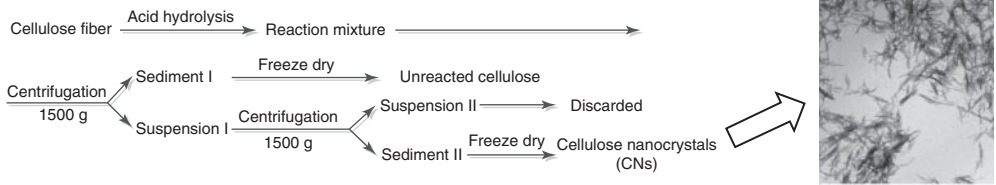
Figure 2.5 Schematic representation of the HBr hydrolysis preparation of cellulose nanocrystals (left) and TEM image of cellulose nanocrystals (right). Reproduced from [34], copyright 2011 © permission from Springer.

100–200 nm in length (right in Figure 2.5) [34]; they also showed aggregation of the CNs.

Although different acids have been used in the preparation of PNs, the principle remains similar in all cases. First, the Whatman No. 1 filter paper was soaked in deionized water for 15 min, and then vigorously stirred to obtain a pulp-like slurry. The blend was transferred to a beaker and treated for 15 min in an ice bath. Using a dropping funnel, phosphoric acid (85% v/v) was added (keeping below 30 °C) slowly until a certain concentration was reached. When the acid addition was completed, the reaction vessel was placed in a preheated 100 °C oil bath and stirred for a preset time. The resulting slightly yellow reaction mixture was cooled in an ice bath to room temperature. Then the CNs were separated from the mixture by centrifugation and washed with deionized water. This process was repeated until the supernatant became colorless. After the centrifugation was completed, the CNs obtained were dispersed in deionized water and then dialyzed against deionized water with the water being changed every day, until the pH was about 7. Finally, the suspension was dispersed by ultrasonication and freeze-dried to obtain the CN powder [35]. The yield of CNs was 76–80%. It was noteworthy that the yield largely depended on the reaction temperature and concentration of phosphoric acid. As shown in Figure 2.6 (Left), it was found that at low concentrations of phosphoric acid (7.8 M), regardless of the reaction time, the hydrolysis was incomplete and inhomogeneous. However, when the concentration of phosphoric acid reached 10.7 M, the hydrolysis reaction was rapid and CNs could be obtained more homogeneously; after 90 min of hydrolysis, the CNs became considerably homogeneous. Therefore, CNs obtained under optimized hydrolysis conditions (at 100 °C with an acid concentration of 10.7 M reacted for 90 min) had an average width of 31 ± 14 nm, length of 316 ± 127 nm, and aspect ratio of 11 ± 1.5, as analyzed by TEM and AFM (atomic force microscopy) images (as shown in right of Figure 2.6) [35].

Spherical CNs were prepared using a mixture of sulfuric and hydrochloric acids to hydrolyze MCC under ultrasonication. TEM images of the commercial MCC and CNs are shown in Figure 2.7 [5]. It was observed that the MCC particles were rod shaped and the average particle length was approximately 20 μm (Figure 2.7a). After hydrolysis and ultrasonic treatment, not only did the size of MCC apparently decrease, but also the shape of CNs changed remarkably. Moreover, because of the evaporation of water in suspension, the CNs exhibited some aggregation.
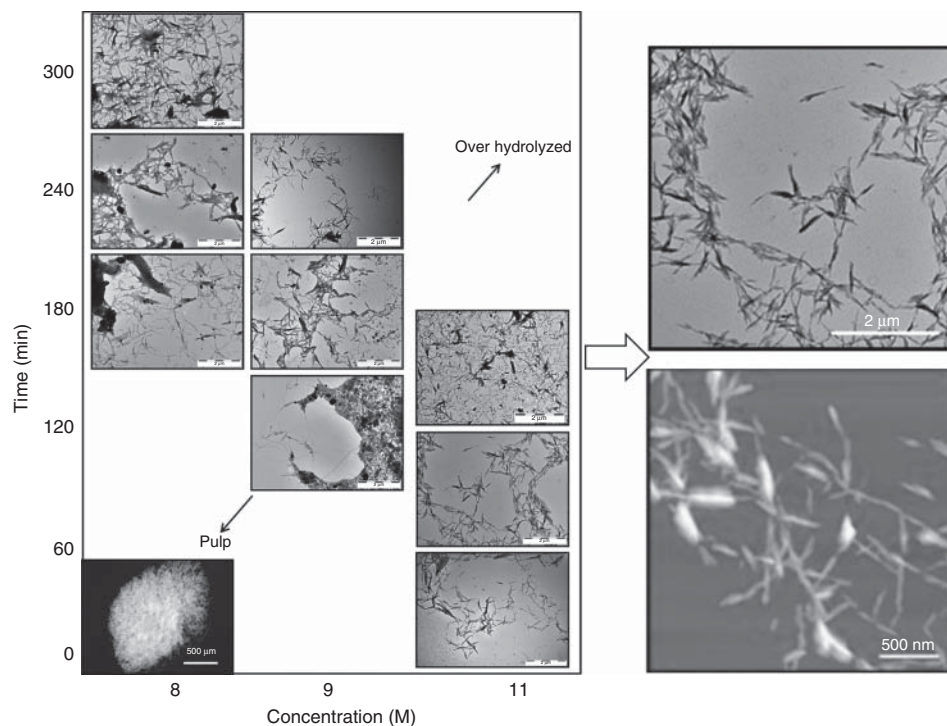
Figure 2.6 TEM images of phosphoric acid hydrolyzed cotton as a function of the hydrolysis time and phosphoric acid concentration (left); TEM (top) and AFM height (bottom) images of CNs isolated from cotton after 90 min of hydrolysis with a 10.7 M phosphoric acid solution at 100 °C (right). Reproduced from [35], copyright 2013 © permission from American Chemical Society.

Compared to rod-like MCC, the average diameter of spherical CNs was about 60 nm (see Figure 2.7b), which was much smaller than the size of the MCC. At the same time, the diverse morphology of CNs obtained by different methods leads to different properties of crystallinity (that of MCC is 83%, and CNs is 78%) and thermal stability. The CNs isolated by hydrolysis using a mixture of sulfuric acid and hydrochloric acid not only showed decreased content of sulfate groups on the surface of CNs as well as increased stability of the suspensions.

Surface-modified CNs were prepared using a one-step acid-catalyzed process with an acid mixture composed of hydrochloric acid and an organic acid (acetic or butyric acid). Hydronium ions resulting from the hydrochloric acid dissociation hydrolyze amorphous cellulose domains and also catalyze the esterification of hydroxyl groups on the exposed cellulose chains. Consequently, isolation and functionalization of CNs can occur simultaneously in a one-step acid-catalyzed process (as opposed to the use of anhydrides), thus eliminating the need for multiple reaction steps, and achieving better atom economy according to the "12 Principles of Green Chemistry" [36]. Figure 2.8 shows the reaction

(a)

(b)
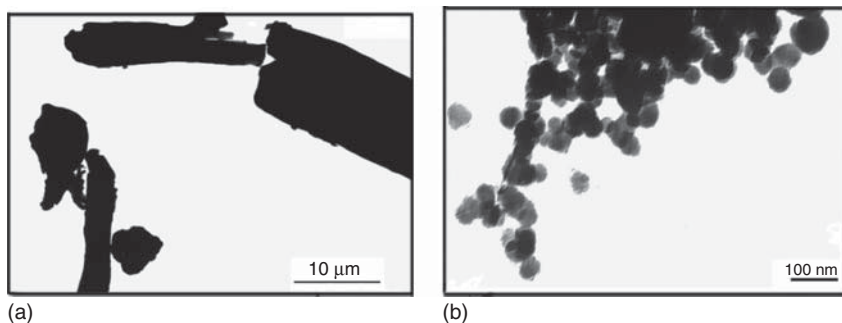
Figure 2.7 (a,b) TEM images of microcrystalline cellulose (MCC) and spherical cellulose nanocrystals. Reproduced from [5], copyright 2007 © permission from Elsevier.

scheme where the hydrolysis and esterification of CNs occur simultaneously (Left) and TEM images of CNs isolated using hydrochloric acid (CNs-HCl) and acetic/hydrochloric acids (CNs-Ac) (Right). It can be observed from the TEM images that the size of CNs isolated by hydrochloric acid was around 200 nm in length and 10–20 nm in diameter, and CNs obtained using the mixed acid systems were similar. Aggregates were clearly present for both CNs-HCl and CNs-Ac [6].
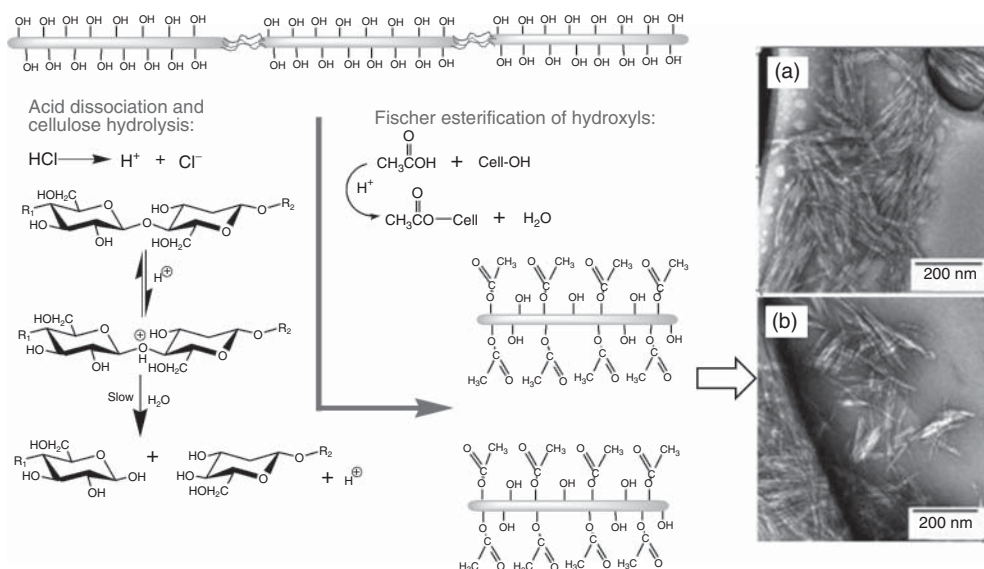
Figure 2.8 Reaction scheme illustrating the simultaneous occurrence of cellulose hydrolysis and esterification of hydroxyl groups using a mixture of acetic and hydrochloric acids (left); and TEM images of CNs isolated using hydrochloric acid alone (CNs-HCl, a) and acetic/hydrochloric (CNs-Ac, b) (right). Reproduced from [6], copyright 2009 © permission from American Chemical Society.

2.2.1.3 **Effects of Pretreatment**

The above-mentioned methods start acid hydrolysis on selected raw materials without pretreatment (for example, freeze-drying, ball-milling, mercerization, *N*-methylmorpholine-*N*-oxide (NMMO), or ionic liquid). Nevertheless, pretreatments lead to great diversity in yield, size, morphology, and crystallinity of CNs. During the freeze-drying process, the hornification of cellulose reduces the accessibility of freeze-dried cellulose fibers [37], which can clearly increase the yield of CNs. For example, cotton linter was immersed in a large quantity of deionized water, stirred for 1 h, and then freeze-dried [38]. It was found that the crystallinity of freeze-dried cellulose decreased slightly to 54.9%, close to that of untreated cellulose (57.2%), indicating that freeze-drying had limited effect on cellulose crystallinity, and that the crystalline structure of cellulose was not changed. After freeze-drying and hydrolyzing with sulfuric acid for 4 h, the crystallinity of CNs increased slightly to 74.1% compared to acid hydrolysis for 4 h without pretreatments, and the yield of CNs has clearly increased, from 7.9% to 12.5%. The dimensions of CNs obtained from freeze-drying cellulose (80–200 nm in length and 30–60 nm in width) were similar to CNs isolated without freeze-drying (length of 100–200 nm and width of 40–60 nm), and both have a rod-like structure (see Figure 2.9a,b) [38]. Theoretically, cellulose fibers can be refined by ball-milling and increase the area of contact between cellulose fibers and acid, thereby facilitating the efficiency of extraction. However, research showed that the crystallinity of ball-milled cellulose fibers decreases dramatically and the cellulose polymorph may be transformed easily in the subsequent extraction process. For example, if the cotton linter was ball-milled at 1000 rpm for 24 h [38], the crystallinity of ball-milled cellulose decreased greatly, to only 21.9%, resulting in an increase in the accessibility of reagents to cellulose; there was no noticeable transformation of the cellulose polymorph. However, the polymorph of CNs obtained from sulfuric acid hydrolysis of the ball-milled cellulose changed slightly (transformed from cellulose crystal I to II) [39]. The obtained CNs were sphere-like with diameters of 100–200 nm (Figure 2.9c), and the crystallinity and yield were 68.4% and 7.7%, respectively.

Cellulose fibers have also been treated by various solvents (e.g., NaOH aqueous solution, NMMO or ionic liquid). Owing to the presence of solvation the crystallinity of cellulose and transformation of cellulose polymorph are changed. For example, when the cotton linter was treated by using 20 wt% NaOH aqueous solutions with a ratio of 1 : 8 (g ml^{-1}) of cotton linter versus NaOH solution at 30 °C for 2 h with stirring at 400 rpm, washed thoroughly with deionized water, and dried in an oven [38], the mercerized cellulose polymorph had transformed from crystal I to II, and the crystallinity of the mercerized cellulose was 46.8%, slightly decreased compared to that of untreated cellulose. When mercerized cellulose was hydrolyzed using sulfuric acid for 4 h, the CNs obtained had a sphere-like morphology with 100–200 nm diameter (Figure 2.9d) [38], and the yield and crystallinity of CNs were 6.3% and 68.9%, respectively. For NMMO pretreatment, the cotton linters were suspended in a 90 wt% NMMO solution with a ratio of 1 : 10 (g ml^{-1}) of cotton linter versus NMMO solution at 80 °C
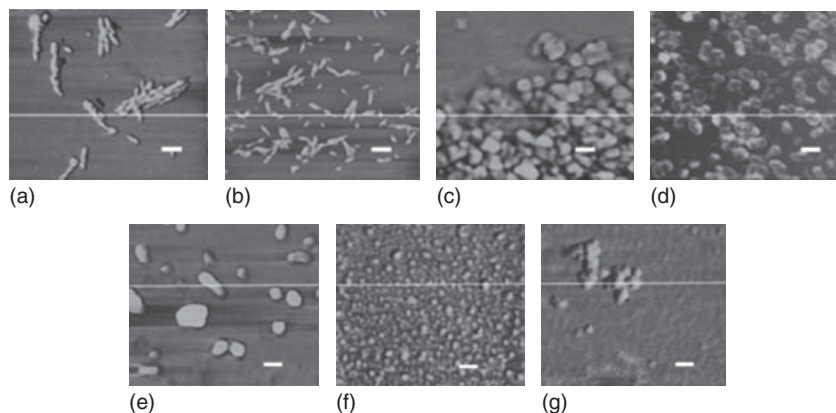
Figure 2.9 AFM images of CNs after pretreatment and hydrolysis by sulfuric acid for 4 h (a–d) and for 2 h (e–g): (a) untreated; (b) freeze-dried; (c) ball-milled; (d) mercerized; (e) untreated; (f) NMMO; and (g) ionic liquid. Reproduced from [38], copyright 2013 © permission from Springer.

for 30 min to be dissolved fully and regenerated by excess deionized water, and then dried in an oven [38]. The obtained cellulose polymorph transformed from crystal I to II, and the crystallinity decreased to 40.1% because of cellulose decrystallization in the NMMO dissolution and regeneration process [40]. Sphere-like CNs with 50–100 nm diameters were obtained after the pretreatment of NMMO and subsequent sulfuric acid hydrolysis for 2 h (Figure 2.9f) [38], but the yield and crystallinity of the CNs declined (as compared to the unpretreated 2-hour hydrolyzed sample in Figure 2.9e) and were only 3.5% and 29.7%, respectively. In addition, ionic liquids can also be used to pretreat cellulose fibers. For example, cotton linter was treated using BmimCl with a concentration of 2 wt% and stirring at 300 rpm at 105 °C for 6 h. Excess ethanol as an anti-solvent was added gradually into the solution. The dissolved/regenerated cellulose was washed thoroughly with deionized water and dried in an oven [38]. The crystallinity of the obtained cellulose decreased significantly to 19.7%. Owing to breakage of inter- and intramolecular hydrogen bonds during ionic liquid dissolution, the original crystalline structures of cellulose were destroyed, and recrystallization in the regeneration process was very limited [41]. Hydrolysis of these CNs with sulfuric acid for 2 h led to sphere-like structures with 50–160 nm diameters (Figure 2.9g) [38], and both the yield and crystallinity were very low.

In summary, the method for preparation of sphere-like CNs was developed using different kinds of pretreatments combined with sulfuric acid hydrolysis. Generally, rod-like CNs were obtained using acid hydrolysis. However, when proper pretreatments were adopted, for example, after the cellulose fibers were mercerized, the acid molecules could quickly penetrate into the inner amorphous regions of the cellulose fibers. Under relatively mild hydrolysis conditions, the cellulose fibers were first hydrolyzed into microlevel fragments and then hydrolyzed to the sphere-like CNs little by little. The increased accessibility of

mercerized and ball-milled cellulose fibers favored the formation of sphere-like CNs. The CNs obtained from freeze-dried cellulose had rod-like structure, which was similar to that obtained using only sulfuric acid hydrolysis, perhaps because of the low accessibility of freeze-dried cellulose. The original crystalline structures of cellulose were destroyed after NMMO and ionic liquid pretreatments, which resulted in a sphere-like structure. In addition, these pretreatments may cause the yield of CNs to decrease.

2.2.2
Structure and Properties of Cellulose Nanocrystals

2.2.2.1 Structure and Rigidity of Cellulose Nanocrystals

At the end of a successful preparation, CNs usually occur as separated/individualized particles. It was found that the structure parameters of the rod-like CNs, length and width, vary widely depending mainly on the cellulose source and the conditions of hydrolysis. In order to reduce the inhomogeneity in size of CNs extracted from a given cellulose source, filtration [16], differential centrifugation [42], and ultra-centrifugation [43] were utilized during hydrolysis. The source and extraction method also influence the size, morphology (refer in particular to the rod-like structure), and crystallinity of CNs. Typical characteristics (i.e., structure parameters, crystallinity, and morphology) for CNs derived from various cellulose sources and extracted by different methods are summarized in Table 2.1. The width of the obtained CNs is usually only a few nanometers, but the length of CNs is distributed over a broad range, from tens of nanometers to several micrometers, and the degree of crystallinity is greater than 70%.

The CNs possess a reactive surface covered with plenty of active hydroxyl groups, which can offer the possibility of modification through the chemical reaction strategy. In recent years, chemical modification of CNs has been studied extensively. The main aim of chemical modification is to make full use of CNs or develop the special functions of CNs in novel nanomaterials, thus expanding the application of CNs in the nanocomposites field. The content of active hydroxyl groups on the CN surface ($n_{\text{surface OH}}$) can be calculated from the CN's molecular structure, as shown in the following (take the rod-like structure, for example, Figure 2.10) [70]:

$$n_{\text{surface OH}} = \left(\frac{N_1 N_2}{N_A} \right) = 3 \left(\frac{w}{\rho_{\text{CNs}} V_{\text{CNs}}} \right) \left(\frac{S_{\text{CNs}}}{S'} \right) \frac{1}{N_A}$$

where

$$N_1 = \left(\frac{w}{\rho_{\text{CNs}}} \right) / V_{\text{CNs}}; \quad N_2 = 3 \left(\frac{S_{\text{CNs}}}{S'} \right); \quad V_{\text{CNs}} = \pi \left(\frac{d}{2} \right)^2 L;$$

$$S_{\text{CNs}} = \pi dL + \pi \left(\frac{d}{2} \right)^2 \approx \pi dL; \quad S' = d'L'$$
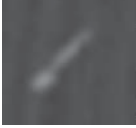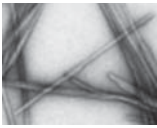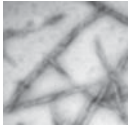
Table 2.1 The fundamental properties of CNs from various sources obtained by different techniques.

Sources	Extraction method	Structural parameters			Moduli (GPa)	Crystallinity (%)	TEM images	References
		L (nm)	w (nm)	E_A	E_T			
Cotton	HCl	100–200	5–10	—	17.7 ± 5.0 [44]	89.3 [45]		[46]
	H_2SO_4	200–300	8			90.5 [45]		[47]
		70–170	~7					[13]
		255	15					[48]
		150–210	5–11					[49]
Cotton linter	H_2SO_4	100–200	10–20			91 [50]		[24]
		25–320	6–70					[16]
		300–500	15–30					[51]
MCC	H_2SO_4	35–265	3–48			84.3 [33]		[16]
	HCl	200–400	10			87.3 [33]		[52]
		250–270	23					[53]
		~500	10					[54]

Table 2.1 (Continued)

Sources	Extraction method	Structural parameters		Moduli (GPa)		Crystallinity (%)	TEM images	References
		L (nm)	w (nm)	E_A	E_T			
Ramie	H_2SO_4	150–250	6–8	90–138 [55–59]		88 [60]		[61]
		134 ± 59	10.8 ± 4.5					[15]
Sisal	H_2SO_4	100–500	3–5			81 [60]		[62]
		150–280	3.5–6.5					[14]
Hemp	H_2SO_4	158.4 ± 63.6	13.2			81.8		[63]
Soft wood	HCl	100–200	3–4	—	24.8 ± 7.0 [44]			[31, 64]
	H_2SO_4	100–150	4–5					[65]

Source	Acid	L (nm)	w (nm)	E_A	E_T		References
Hard wood	H_2SO_4	140–150	4–5				[65]
Tunicate	H_2SO_4	1160	8.8–18.2	143 [1]	2–25 [66]		[67]
		500–1000	16	151 ± 29 [68]			[48]
		1000–3000	10				[17]
		100–1000	15–30				[47]
		1073	15				[16]
Bacterial	H_2SO_4	100–1000	5–50	72			[3, 11, 69]

L = length; w = width; E_A = elastic modulus in the axial direction; and E_T = elastic modulus in transverse direction.
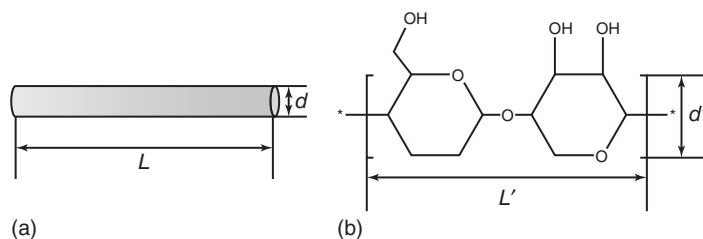
Figure 2.10 Dimensions of (a) individual rod-like cellulose nanocrystal and (b) a single cellulose dextran chain repeat unit. Reproduced from [70], copyright 2012 © permission from Royal Society of Chemistry.

The high crystallization of CNs leads to a higher rigidity. Chapter 7 introduces methods of characterization of the moduli of CNs and involves the different polymorphs of cellulose, but the CNs mentioned here are of the cellulose Iβ type. The moduli of CNs obtained from various cellulose sources using different methods are summarized in Table 2.1. Although the axial (along the axis) elastic modulus (longitudinal modulus, E_A) of CNs from different sources has been under investigation for many years [55–58, 68, 71–78], there are not many reports on the transverse elastic modulus (perpendicular to major axis, E_T) of these materials. Early studies used X-ray diffraction to determine the longitudinal modulus of CNs, which was in the range of 90–138 GPa [55–59]. In 1968 Jaswon *et al.* [72] utilized the theoretical model of cellulose I type to estimate the values of 76, and 51 and 57 GPa of the longitudinal and two transverse moduli, respectively. In the same way, in 1991, the longitudinal and two transverse elastic moduli were predicated to have elastic modulus values of 167, and 11 and 50 GPa, respectively [75]. Furthermore, inelastic X-ray scattering, Raman spectroscopy, and AFM were also used to measure the elastic modulus of CNs. For example, X-ray scattering was used to determine the elastic modulus of CNs and it was found that the transverse modulus of CNs was 15 GPa, much lower than the value of 220 GPa of the longitudinal modulus [79]. Raman spectroscopy was used to determine the elastic moduli of CNs obtained from tunicate (143 GPa, which agrees with the calculated value of the elastic modulus of the theoretical chain structure of 145 GPa [1]) and plant CNs, which was 105 GPa [80]. When AFM was used to determine the modulus of CNs, it was found that the longitudinal modulus of CNs from tunicate was 151 ± 29 GPa [68], and the transverse moduli values of wood, cotton, and tunicate CNs were in the ranges of 18–50 GPa [81], 17.7 ± 5.0 GPa [44], and 2–25 GPa [66], respectively. The various sources, extraction method, and characterization may cause the differences in the modulus among CNs. In addition, X-ray diffraction and Fourier transform infrared (FTIR) spectroscopy could be used to characterize the crystalline structure of CNs. As shown in Figure 2.11, it was found that CNs originating from both cotton and potato have three characteristic diffraction peaks located at $2\theta = 14.7°$, 16.4°, and 22.6°, which belong to the typical planes of cellulose Iβ [82]. This indicated that the polymorph of cellulose was unaltered after acid hydrolysis. The degree of crystallinity of CNs from cotton and potato
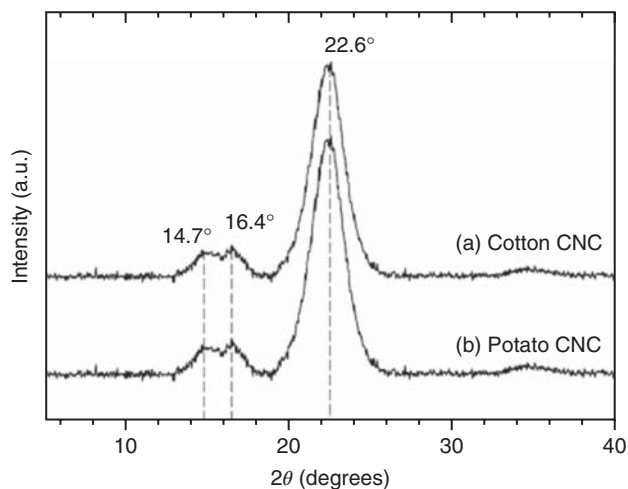
Figure 2.11 X-ray diffraction patterns of CNs derived from (a) cotton and (b) potato peel. Reproduced from [82], copyright 2004 © permission from American Chemical Society.
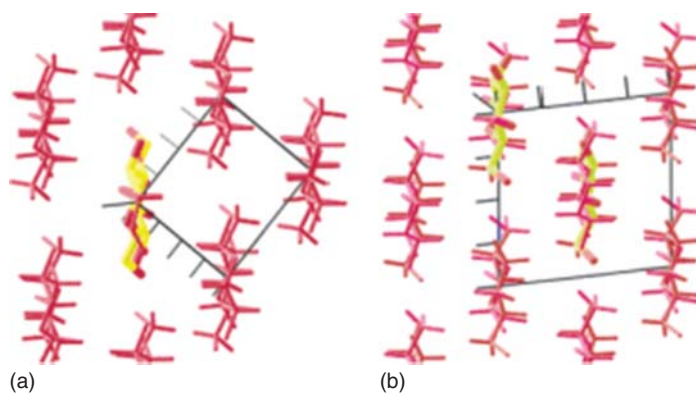
Figure 2.12 The crystal structures of cellulose Iα (a) and Iβ (b). Reproduced from [85], copyright 2004 © permission from American Chemical Society.

peel was 91% and 85%, respectively [83]. For the FTIR spectra of CNs, the O–H stretching and out-of-plane bending bands of celluloses Iα and Iβ were different, that is, located at $3240 \, cm^{-1}$ for the O–H stretching of cellulose Iα, at $3270 \, cm^{-1}$ for Iβ, and at $750 \, cm^{-1}$ for out-of-plane bending of cellulose Iα and $710 \, cm^{-1}$ for Iβ [84]. In general, the characteristic peaks of O–H stretching and O–H out-of-plane bending of CNs extracted by acid hydrolysis were located at 3270 and $710 \, cm^{-1}$, respectively, which indicated that the polymorphs of CNs belonged to the cellulose Iβ type [20]. The crystal structure of cellulose Iα and Iβ are shown in Figure 2.12 [85].

2.2.2.2 Physical Properties of Cellulose Nanocrystals

Water Contact Behavior and Surface Energy of Cellulose Nanocrystals As abundant hydroxyl groups are present on the surface of CNs, the CNs with stronger hydrophilicity can disperse stably in an aqueous solution to form a relatively homogeneous suspension. Hydrophilicity is reflected mainly in the water contact angle of CNs. Generally, the lower the water contact angle, the stronger their hydrophilicity. However, there is some diversity in the water contact angle of CNs prepared from the different cellulose sources and extraction methods, and the results are shown in Table 2.2. Owing to the difference in the surface roughness and liquid–surface interactions between the pellets and films of CNs [86], the water contact angles were not the same for the CN pellets and films; for example, the water contact angle of the CN pellet is about 44.7° [21] and that of the CN film is 10°–15° [30, 87]. Surface energy (γ_S) involves dispersive surface energy (γ^d) and polar surface energy (γ^p). In general, the γ_S of CNs can be calculated by measuring the different contact angles in different solvents, following the equation

$$\gamma_L(1 + \cos\theta) = 2\sqrt{\gamma_L^d \gamma_S^d} + 2\sqrt{\gamma_L^p \gamma_S^p}$$

where, the subscripts L and S refer to the liquid drop and the solid surface, respectively, and θ expresses the contact angle between the solid substrate and the liquid drop. For example, the contact angle values of CNs for water, diiodomethane, and ethylene glycol were 44.60, 19.65, and 17.90, respectively, and according to the above equation the calculated dispersive (γ_S^d) and polar (γ_S^p) surface energies were 39.2 and 21.5 mJ m^{-2}, respectively. So the total surface energy (γ_S) equals the γ_S^d plus the γ_S^p, that is, 60.7 mJ m^{-2} [88]. The surface energy of CNs extracted from different cellulose sources and extraction methods is summarized in Table 2.2. Moreover, water contact angle and surface energy of CNs are critical properties for determining the performance of polymer/CNs nanocomposites. Compatibility between hydrophilic CNs and hydrophobic polymers is relatively poor, and is not conducive to the preparation of nanocomposites based on hydrophobic polymers. Therefore, hydrophobic modification should be carried out for the CNs. For

Table 2.2 Contact angles for water and total surface energy of CNs derived from different sources and extraction methods.

Sources	Extraction method	θ (°)	γ_s^d (mJ m^{-2})	γ_s^p (mJ m^{-2})	γ_s (mJ m^{-2})	References
Cotton linter	H_2SO_4	44.6	39.2	21.5	60.7	[88]
MCC	HCl	30	—	—	—	[89]
Ramie	H_2SO_4	35	35.2	25.3	60.5	[60]
Cotton	H_2SO_4	34	—	—	—	[90]
Soft wood	HCl	12	—	—	—	[30]
Tunicin	H_2SO_4	24	4.9×10^{-6}	94.9	94.9	[67]
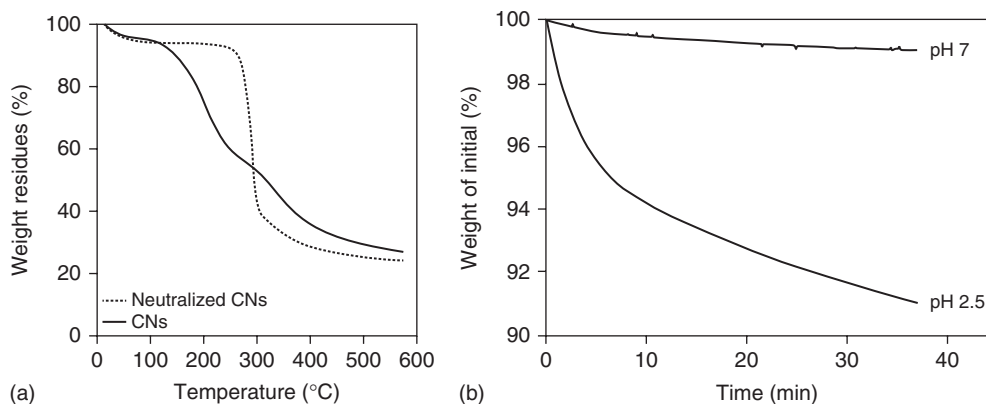
Figure 2.13 TGA curves of CNs and neutralized CNs: (a) the thermal stability of CNs with increasing temperature [62] and (b) at 180 °C the thermal stability of CNs with the time prolonged. Reproduced from [92], copyright 2012 © permission fromSpringer.

example, surface acetylation of CNs can enhance their dispersibility in organic solvents. The measured contact angle for water on the surface of the acetylated CNs is 78°, and the total surface energy is 50 mJ m^{-2} [21].

Thermal Stability of Cellulose Nanocrystals Since conventional thermal processing temperature often exceeds 200 °C, the thermal stability of CNs becomes very important, especially for high temperature matching [91]. In general, the thermal decomposition temperature of cellulose is about 300 °C and meets the requirements of thermal processing. However, as described in Section 2.2.1.1, the normal extraction method uses sulfuric acid for hydrolysis and it is easy to introduce the sulfate ester groups on the surface of the obtained CNs, so that the thermal stability of CNs diminishes and thermal decomposition starts at approximately 200 °C. With increasing sulfate ester content, the degradation temperature becomes lower [3]. Therefore, two methods have been used to improve the thermal stability of CNs: desulfurization to reduce the sulfate ester groups on the surface of CNs, and neutralization of the sulfuric ester groups with alkaline solution. For example, the pH of the solution can be adjusted with sodium hydroxide to neutralize the CNs sulfate ester groups and increase the thermal stability of the CNs [5]. TGA (thermogravimetric analysis) curves of CNs and neutralized CNs are shown in Figure 2.13 [62, 92]. Under a nitrogen atmosphere, the CNs were heated from room temperature to 600 °C at a rate of 10 °C·min^{-1}. The results of TGA obviously displayed a shift in degradation temperature, an increase from 120 to 280 °C, and showed that the neutralized CNs exhibited a different degradation pattern, involving only one pyrolysis process, which is the typical pyrolysis process of cellulose (Figure 2.13a) [62]. In addition, as shown in Figure 2.13b, it can be observed clearly that the CNs neutralized using 0.25 mol l NaOH exhibit a higher thermal stability at 180 °C and the CNs without NaOH neutralization gradually decomposed with time at 180 °C [92]. Meanwhile,
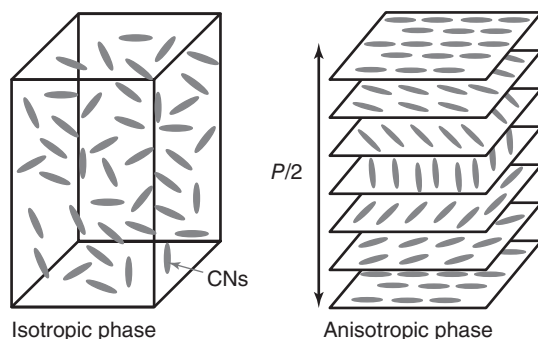
Figure 2.14 Schematic representation of rod-like CNs orientation in both the (a) isotropic and (b) anisotropic (chiral nematic) phases. Reproduced from [49], copyright 2003 © permission from American Chemical Society.

when hydrochloric acid was used instead of sulfuric acid to hydrolyze the native cellulose, sulfate ester groups were not generated on the surface of CNs, and hence the thermal stability of the CNs was enhanced significantly and the thermal degradation onset temperature increased from 234 to 316 °C [31]. This showed that the thermal stability of CNs can be improved with the type of acid extraction. However, the dispersibility of CNs isolated by hydrochloric acid was very poor, and they easily aggregated, compared to those extracted with sulfuric acid. Therefore, physical and chemical surface modification were used to protect the surface of CNs, and research has proved that the thermal stability of CNs improved effectively [93, 94]; Section 3.6.1 introduces this topic in more detail.

Arrangement of Cellulose Nanocrystals in Suspension   In general, the CNs obtained using acid hydrolysis of native cellulose suspensions can spontaneously rearrange from isotropic phase to anisotropic phase above critical concentrations. This anisotropic phase is composed of stacked planes of rod-like CNs aligned along a vector; the orientation of CNs in each plane was rotated at a slight angle around the perpendicular axis from one plane to the next [9, 95] (shown in Figure 2.14 [49]). It is precisely because of this arrangement of CNs in suspension that the CNs exhibit many distinctive structures and properties including cholesteric liquid crystallinity and flow birefringence. The flow birefringence of the CN suspensions is associated with the concentration of CNs. For example, with a relatively low CN concentration only a slight birefringence was observed in the CN colloid suspensions under polarized light (Figure 2.15a) [96]. When the concentration of CNs increased, more birefringence in the suspension was observed. As shown in Figure 2.15b [96], the isotropic and anisotropic (nematic) phases clearly coexisted in CN colloid suspensions with CN concentration of 2.03%. When the CN concentration reached 3.17%, the colloid suspension exhibited birefringence with colors and a clear micro-fingerprint texture (Figure 2.15c) [96], indicating the existence of cholesteric liquid crystalline phases. It is noteworthy that this micro-fingerprint texture was not aligned along a vector but twisting
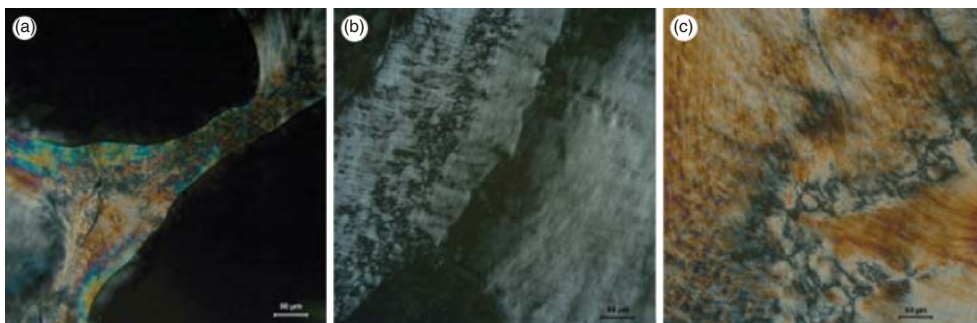
Figure 2.15 Polarized optical micrographs of CN colloids at concentrations of (a) 0.91%, (b) 2.03%, and (c) 3.17%. Reproduced from [96], copyright 2011 © permission from Elsevier.

[96–98]. Moreover, CNs could spontaneously arrange or self-assemble into a highly ordered structure and subsequently form an anisotropic region when a critical concentration of CNs in the colloid suspension was reached. For example, the CN suspensions exhibit shear birefringence, and when allowed to stand for long, they could spontaneously separate into an upper isotropic and a lower anisotropic phase when the CN concentration exceeded the critical concentration of chiral nematic phase formation [9] (shown in Figure 2.16) [69]. This interesting phenomenon is dependent on the surface charge, aspect ratio, and length distribution of CNs. Above the critical concentration, the spontaneous occurrence of this phenomenon was ascribed to the entropically driven self-orientation of rod-like CNs to form the nematic order structure. Compared to the disordered phase, the nematic order phase eliminated volume interactions, resulting in a higher packing entropy [9]. However, the suspensions of CNs prepared by hydrochloric acid do not generate such chiral nematic order because the CNs are not charged; the existence of negative charges on the surface of CNs (from ionized sulfate groups) is thus believed to be beneficial toward phase stability [99]. The threshold/critical concentration for sulfated CNs to form ordered nematic phases in electrolyte-free aqueous suspensions is largely dependent on the charge density and is typically in the range of 1–10% (w/w). As increasing concentration of CNs, the pitch of obtained chiral nematic anisotropic phase decreases and ranges from 20 to 80 μm [9].

Meanwhile, the equilibrium between isotropic and anisotropic phases is sensitive to the presence of electrolytes and counterions. For example, the CNs extracted by sulfuric acid hydrolysis from bacterial cellulose can spontaneously separate into isotropic and anisotropic phases after standing for 1 week at a CN concentration of 0.63% (w/w) (Figure 2.16) [69]. Before this phase separation, the birefringence was maintained for around 7 days. However, when a small amount of electrolyte was added into the suspension, the phase separation was much faster, reaching an obvious boundary in 1 day and attaining equilibrium in 2 days. The presence of an electrolyte also significantly reduced the volume of the lower anisotropic phase [69]. By studying this phase separation and the effect
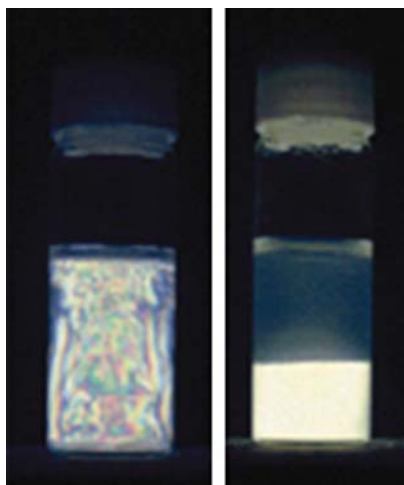
Figure 2.16 Aqueous 0.63% (w/w) CNs suspension observed between crossed polarizers. Immediately after shearing the suspension shows many iridescent birefringence patterns; after 1 week, the suspension separates into the upper isotropic and the lower anisotropic phases. Reproduced from [69], copyright 2001 © permission from American Chemical Society.
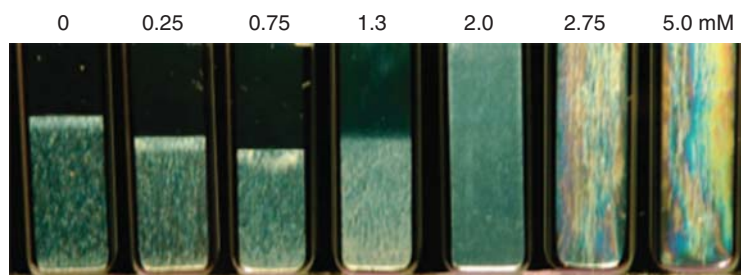
Figure 2.17 Effect of added NaCl on phase separation behavior of the BCNs suspensions for a fixed total cellulose concentration of 3 wt% after standing for 25 days. Reproduced from [100], copyright 2009 © permission from American Chemical Society.

of NaCl (0–5 mM), it was found that the volume fraction of the chiral nematic phase reached a minimum with a NaCl concentration of approximately 1.0 mM. When the concentration of NaCl was varied in the range of 2.0–5.0 mM, the CNs suspensions did not show phase separation and became completely liquid crystalline (Figure 2.17) [100].

As stated previously, when CN suspensions reach a critical concentration, the CNs spontaneously display an ordered phase showing interesting liquid crystalline properties (nematic and chiral nematic). CNs form the structure initially under a minimum electrostatic force (due to the evaporation of water from the suspension); as evaporation continues to progress, the liquid crystal phase develops in the

(a)   (b)
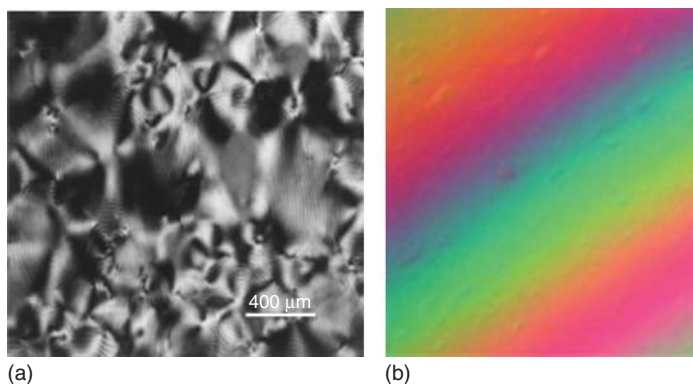
Figure 2.18 (a) Chiral nematic texture of the anisotropic phase of a CNs suspension [47] and (b) solid film of CNs observed between cross-polarizers. Reproduced from [96], copyright 2012 © permission from American Chemical Society.

condensed suspensions. This phenomenon is similar in the non-agglomerated colloid suspensions of other rod-like nanoparticles, for example, the chitin nanocrystals. A cross-polarizing microscope can be used to show this self-organization phenomenon. The existence of the nematic phase transition will give a special "fingerprint texture structure" in the rod-like CNs suspensions, which indicates the ordered chiral nematic structure (Figure 2.18a) [47]. The rod-like morphology and the spiral stacked structure of CNs account for these particular properties. After complete evaporation of the water from the suspension, the chiral nematic structure can be preserved, and an iridescent film obtained, as seen in Figure 2.18b [101, 102].

The dispersion and self-ordering properties of CNs are restricted to aqueous suspensions or a few organic solvents with high dielectric constants, such as DMSO, DMF, and ethylene glycol. In an apolar organic solvent, the inefficient electrostatic repulsion and the strong hydrogen bonds between CNs lead to rapid aggregation of the CNs in suspension. In fact, this electrostatic repulsion that stabilizes the CN suspension can induce stronger chiral interactions between CNs [46]. For example, the dispersion of CNs with different aspect ratios in cyclohexane has been studied, and it was found that the critical concentration at which the suspension spontaneously phase separated into a chiral nematic liquid crystalline phase was higher than that in water. Suspensions of CNs with the highest aspect ratio did not exhibit the phase separation phenomenon, but at relatively high concentrations of CNs (26.3 and 30.8 wt%), the suspension exhibited an anisotropic gel phase (Figure 2.19) [103]. Owing to the presence of stronger chiral interactions in the apolar medium, the chiral nematic pitch was much lower than that measured in water, generally as small as 2 μm [103]. Moreover, because there are plenty of hydroxyl groups on the CN surface, various methods of chemical modification have been used to modify CNs including esterification [104], etherification, oxidation [105], silylation [106, 107], and polymer grafting [108, 109]. Some of the

(a)

(b)
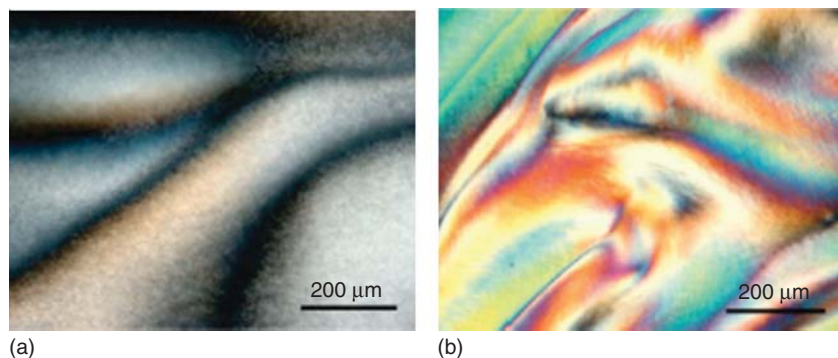
Figure 2.19 Polarized optical micrographs of birefringent gel phases in CN suspensions with high aspect ratios in cyclohexane at total concentrations of (a) 26.3 wt% and (b) 30.8 wt%. Reproduced from [103], copyright 2009 © permission from American Chemical Society.

Figure 2.20 Aqueous 0.53% (w/v) suspensions of CNs observed between crossed polarizers after production by HCl-catalyzed hydrolysis (a), and after their oxidation via TEMPO-mediated reactions (b). Reproduced from [110], copyright 2006 © permission from Springer.

chemically modified CNs retain their birefringence. For example, TEMPO oxidation or carboxymethylation of CN aqueous suspensions exhibited birefringence (shown in Figure 2.20) [110] as did silylated CNs, which can stably disperse in tetrahydrofuran (THF); as shown in Figure 2.21, under shearing or shaking, THF suspension of the modified CNs would appear as bright and black areas [106].

Figure 2.21 Polarized optical micrographs of the silylated CN suspension in THF. Reproduced from [106], copyright 2002 © permission from Elsevier.

Rheological Properties of Cellulose Nanocrystal Suspensions Suspensions of CNs have the unique property of liquid crystal phase transition as well as distinctive rheological properties [111]. Under different CN concentrations and shear rates. At the beginning, the behavior was mainly shear thinning and it was thought that at this stage the network, constructed by strong hydrogen or ionic bonding interactions among CNs, was broken by increasing shear strength. When the critical shear rates and concentrations were exceeded, however, the viscosity of suspensions increased. At this stage, the CNs rearranged to form an ordered network, thus leading to a sudden increase in viscosity. This is the typical rheological behavior of liquid crystalline polymers [112]. The viscosity (η) of CN suspensions of various concentrations at room temperature as a function of shear rate ($d\gamma/dt$) is shown in Figure 2.22 [96]. It was clearly observed that the viscosity of CN suspension increased as the CN concentration increased, and at lower shear rates, the viscosity of CN suspension decreased linearly as the shear rates increased. This stage indicated a shear thinning behavior of the CN suspension. At higher shear rates (above the critical shear rates), the viscosity increased with increasing shear rates [96]. However, the suspension of CNs prepared by sulfuric acid and hydrochloric acid exhibited different rheological properties. The viscosity of suspensions of CNs extracted by sulfuric acid displayed no time dependence; yet the suspension of CNs from hydrochloric acid hydrolysis was thixotropic above concentrations of 0.5% (w/w) and anti-thixotropic below 0.3% (w/w) [32]. Furthermore, the CN suspension could form an equilibrium chiral
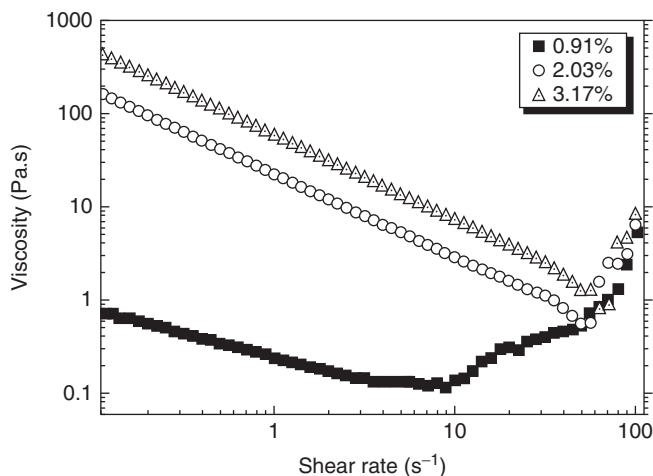
Figure 2.22 Viscosity as a function of shear rate for CN suspensions of different concentrations [96].
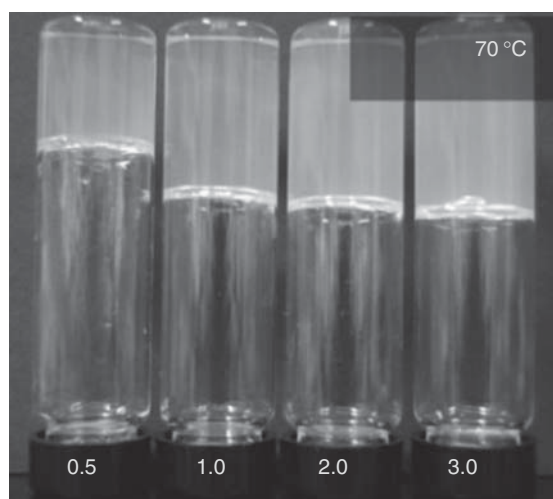
Figure 2.23 Inverted sample tubes containing 0.5, 1.0, 2.0, and 3.0 wt% CN gel in glycerol, prepared under evaporation at 70 °C. Reproduced from [113], copyright 2012 © permission from Springer.

nematic phase above the critical concentration, if the stability of the suspension declined; for example, if the charge density on the CNs surface or the properties of the suspending medium were changed, the suspension tended to form a gel or aggregation. In general, direct addition of the unmodified CNs into organic solvents often resulted in aggregation of CNs. However, on evaporation of water slowly from the water–glycerol suspension of CNs, thixotropic gels can be obtained, at below 3 wt% concentration of the CNs (Figure 2.23) [113].

2.3
Chitin Nanocrystals

2.3.1
Preparation of Chitin Nanocrystals

2.3.1.1 **Extraction of Chitin Nanocrystals by Acid Hydrolysis**

Unlike CNs, chitin nanocrystals are derived from biological tissue and therefore include impurities such as protein and other organic compounds [114]. Thus, chitin must be treated to remove impurities before extraction of chitin nanocrystals. The common method for preparation of chitin nanocrystals is acid hydrolysis with a strong acid, followed by mechanical disintegration of the products [115, 116]: Chitin was suspended in an alkali solution of a certain concentration (generally was 5% KOH [117, 118] or 0.5 M NaOH [119]) and stirred for a certain time to remove most of the protein and other impurities; the suspension was stirred overnight at room temperature. It was then filtered and washed with deionized water several times. Subsequently, $NaClO_2$ aqueous solution containing sodium acetate buffer was used to bleach for a preset time at a certain temperature. Finally, the suspension was soaked in KOH aqueous solution to remove the residual protein and centrifuged to obtain the purified chitin. The chitin nanocrystal suspension was obtained by using a certain amount of HCl to hydrolyze the purified chitin at the ratio of $1:30$ $(g\,ml^{-1})$ of chitin versus acid under boiling conditions for a given time [117, 118, 120, 121] while stirring. Then, the suspension was washed with deionized water and centrifuged, and the process repeated several times. Subsequently, the suspension was dialyzed with deionized water until the pH was 4. Finally, the suspension was dispersed by ultrasonication, and after adding sodium azide into the suspension to avoid bacterial growth, stored at $6\,°C$ [117]. As with CNs, chitin nanocrystals had a rod-like structure and the source influenced their structure, morphology, and size. Figure 2.24 shows TEM images of chitin nanocrystals extracted from crab

(a)   L = 270 nm d = 20 nm   (b)   L = 200 nm d = 15 nm
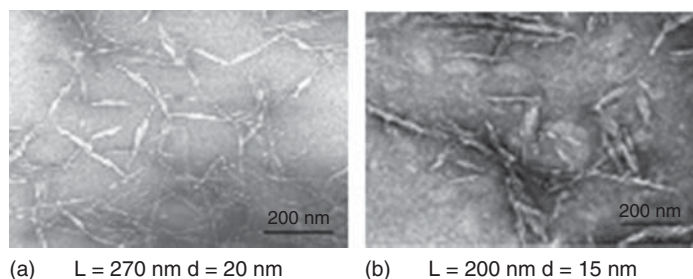
Figure 2.24 TEM images of chitin nanocrystals derived from (a) crab Reproduced from [118], copyright 2003 © permission from American Chemical Society and (b) shrimp. Reproduced from [2], copyright 2010 © permission from Elsevier.

and shrimp. Both of the chitin nanocrystals had a rod-like structure with only a slight difference in size.

2.3.1.2 Extraction of Chitin Nanocrystals by TEMPO Oxidation

The process used for TEMPO oxidation is as follows: First, chitin was added into deionized water that contained TEMPO and sodium bromide. A certain amount of NaClO solution was added to the suspension at the beginning of the oxidation procedure. The pH of the suspension was maintained at 10 by continuous addition of 0.5 M NaOH. When the alkali solution was no longer consumed, small amounts of ethanol were added to terminate the oxidation reaction. Then the pH of the suspension was adjusted to 7 with hydrochloric acid and centrifuged to obtain the precipitate. The precipitate was washed with deionized water and the procedure repeated. Finally, the obtained chitin nanocrystal suspension was stored at 4 °C before using. TEM images of the chitin nanocrystal suspension with different amounts of NaClO are shown in Figure 2.25 [7]. When the ratio of NaClO versus chitin was 2.5 mmol g^{-1}, it was observed clearly that most of the rod-like chitin nanocrystals were gathered into large bundles. Some of the smaller bundles and individual nanocrystals were attached to the large bundles. As the content of NaClO was increased to 5.0 mmol (per gram of chitin), the number of individual chitin nanocrystals increased, but the bundles of nanocrystals remained in the suspension of chitin nanocrystals. When the ratio of NaClO versus chitin was 10 mmol g^{-1}, more individual nanocrystals were observed in the suspension, and the lengths of these chitin nanocrystals were obviously smaller. Compared to chitin nanocrystals prepared by hydrochloric acid hydrolysis, the crystal structure and crystallinity of the obtained chitin nanocrystals were preserved. Also, regardless of the amount

TEMPO-oxidized chitins (the amount of NaClO added)

| (2.5 mmol/g) | (5.0 mmol/g) | (10.0 mmol/g) |
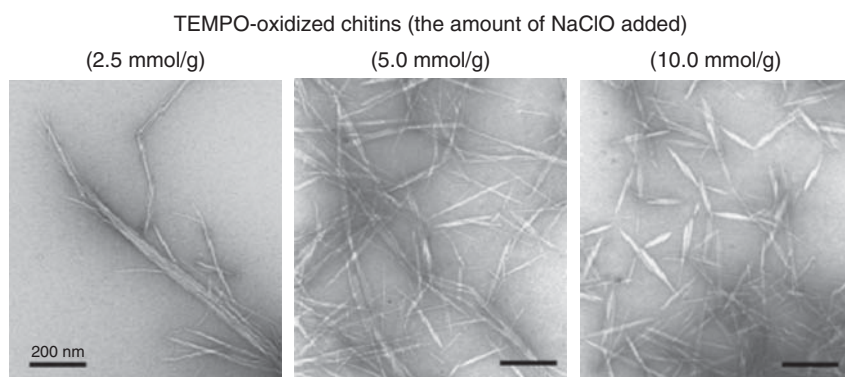
Figure 2.25 TEM images of TEMPO-oxidized chitin nanocrystals prepared under different conditions. Reproduced from [7], copyright 2008 © permission from American Chemical Society.

of NaClO added into the TEMPO oxidation chitin system, *N*-deacetylation did not occur during the procedure [7].

2.3.2
Structure and Properties of Chitin Nanocrystals

2.3.2.1 Structure and Rigidity of Chitin Nanocrystals
In general, the diameter of chitin microfibrils derived from the epidermis of arthropods and the cell walls of fungi was in the range of 2.5–2.8 nm, and the diameter of chitin microfibrils derived from the epidermis of crustaceans was up to 25 nm [115]. Native chitin is a crystalline polymer and has three crystal structures (*α*, *β*, *Υ*), which depends on the source of chitin [122, 123]. The *Υ* crystal structure is occasionally found, and is often obtained by a transformation of the *α* crystal structure [124]. The crystal structures of *α*-chitin and *β*-chitin are shown in Figure 2.26 [125]. In order to extract chitin nanocrystals with high crystallinity, it is necessary to remove the protein and low crystallinity components. Chitin nanocrystals have a highly ordered atomic arrangement, and have a high strength modulus – generally the longitudinal modulus is 150 GPa and the transverse modulus about 15 GPa [116]. Table 2.3 summarizes the basic structural parameters (length and width), crystallinity, and morphology of chitin nanocrystals prepared from different sources and extraction methods.
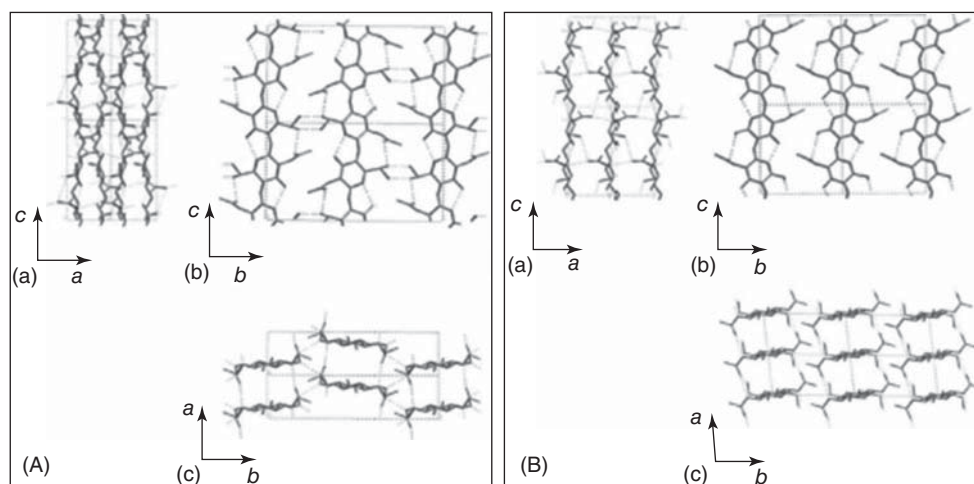
Figure 2.26 Crystals structures of (A) *α*-chitin and (B) *β*-chitin. Reproduced from [125], copyright 2006 © permission from Elsevier.

Table 2.3 Effect of extraction method and chitin source on fundamental properties of chitin nanocrystals.
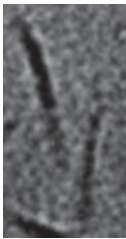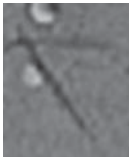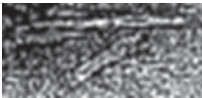
Chitin sources	Extraction method	Structural parameters		Crystall-inity (%)	TEM images	References
		Length (nm)	Width (nm)			
Crab shells	HCl hydrolysis	50–300 100–600 100–650	6–8 4–40 10–80			[115] [118] [117] [126]
	TEMPO-oxidation	200–500 340	5–20 8	93		[7]
Chitin powder	HCl hydrolysis	255 ± 56 250 ± 140	31 ± 6 6.2 ± 1.1			[126] [127]
Shrimp shells	HCl hydrolysis	200–500 231–969 180–820 110–975	10–15 12–65 8–74 8–73	84		[119] [128] [121] [120]

Table 2.3   (*Continued*)

Chitin sources	Extraction method	Structural parameters		Crystall-inity (%)	TEM images	References
		Length (nm)	Width (nm)			
Squid pen	HCl hydrolysis	50–300	18			[116]
Riftia tubes	HCl hydrolysis	500–10 000	~18			[129]

2.3.2.2   Properties of Chitin Nanocrystal Suspensions

As with CNs, the suspension of chitin nanocrystals obtained by acid hydrolysis also displays birefringence (Figure 2.27) [118] due to the presence of a positive charge (NH_3^+) that is derived from protonation of amino (NH_2) groups on the chitin nanocrystal surface. The phase behavior of a ternary system of chitin nanocrystals, water, and acrylic acid was studied [130]. At an acrylic acid concentration of 3.74% and chitin nanocrystal concentration of 6.41%, a cholesteric texture was observed (Figure 2.28a) [130]. However, at higher acrylic acid concentrations, owing to increased viscosity, fingerprint texture was not seen although a stable flow-birefringence glassy phase could be observed, as in Figure 2.28b–e [130]. When the chitin nanocrystal concentration was increased
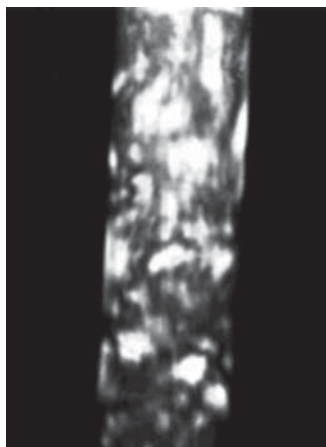
Figure 2.27   Photograph of birefringence of the chitin nanocrystals suspension. Reproduced from [118], copyright 2003 © permission from American Chemical Society.

E (AA-3.74%)-chitin 6.41%

(a)

D (AA-9.36%)-chitin 6.41%

(b)

C (AA-18.72%)-chitin 6.41%

(c)

B (AA-28.08%)-chitin 6.41%

(d)

A (AA-37.44%)-chitin 6.41%

(e)

B (AA-26.79%)-chitin-10.70%

(f)
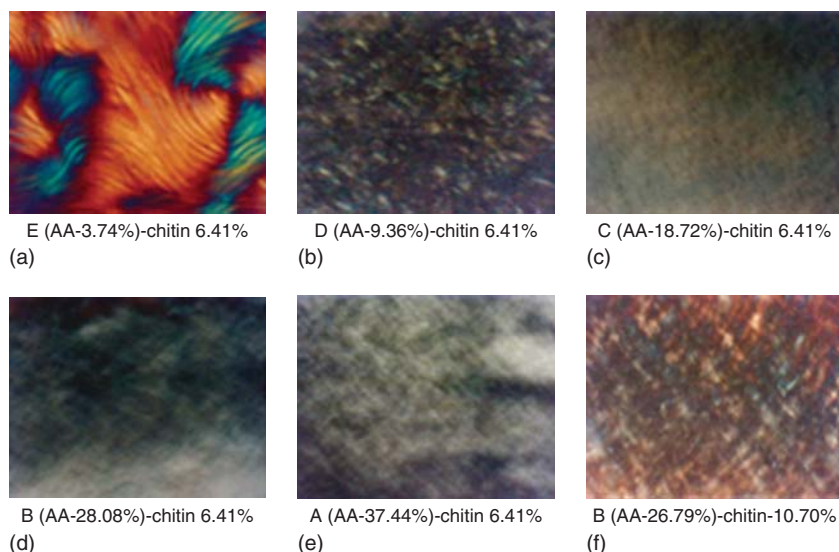
Figure 2.28 Polarized optical micrographs of liquid crystal chitin/AA mesophase with 6.41% (w/w) chitin from (a) to (e): (a) the fingerprint-like pattern, chiral nematic texture and (f) optical texture of anisotropic phases 10.70% (w/w) chitin. Reproduced from [130], copyright 2003 © permission from American Chemical Society.

to 10.70%, the chitin nanocrystal suspension exhibited an anisotropic phase and a distinct birefringence (Figure 2.28f) [130]. Furthermore, the birefringent behavior of chitin nanocrystal suspension was affected by the concentration of the chitin nanocrystal, ionic strength, and pH [131]. It was found that chitin nanocrystal suspensions displayed a nematic gel-like behavior with increasing chitin nanocrystal concentration, which could be ascribed to interactions between the chitin nanocrystals. As shown in Figure 2.29a [131], the 2.4% (w/w) suspension displayed no or only slight birefringence but when the chitin nanocrystal concentration increased to 3.6% and 4.6% (w/w), the suspension exhibited clear birefringence, and no apparent cholesteric structures, possibly because of the formation of the network that hindered the growth of ordered nanocrystal aggregates [132]. In addition, at increasing ionic strength and pH, the interactions between the chitin nanocrystals increased and a stronger gel was formed. The suspension containing only 1.8% (w/w) chitin nanocrystals did not show any birefringence, whereas it displayed a birefringent behavior when 15 and 100 mM NaCl were added to the chitin nanocrystal suspension (Figure 2.29b) [131]. When the pH of the 1.8% (w/w) chitin nanocrystal suspension was 3.0, no clear birefringence could be observed. However, when the pH was closer to the isoelectric point of the chitin nanocrystal suspension (6.3) [115], it displayed a birefringent nematic-like structure (Figure 2.29c) [131].
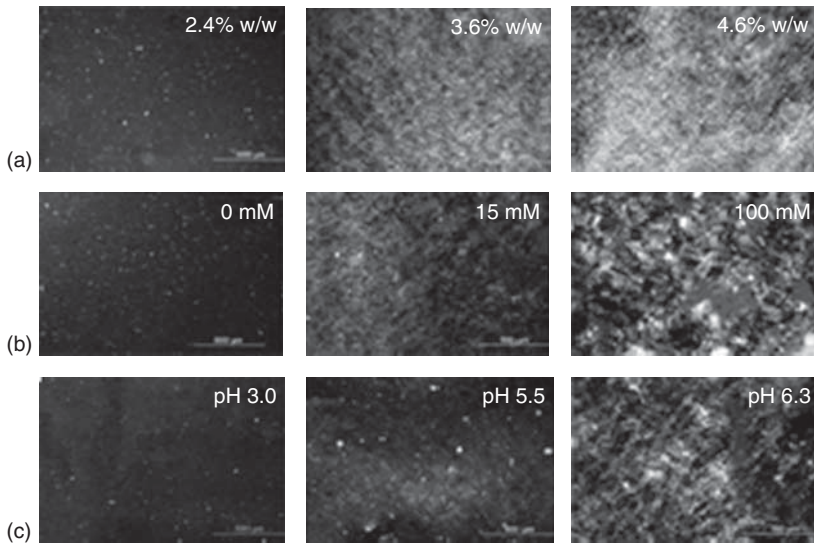
Figure 2.29 Polarized optical micrographs of (a) aqueous suspension containing different concentrations of chitin nanocrystals; (b) effect of ionic strength on the microstructure of a 1.8% (w/w) chitin nanocrystal aqueous suspension; and (c) effect of pH on the microstructure of a 1.8% (w/w) chitin nanocrystal aqueous suspension (scale bar 500 μm). Reproduced from [131], copyright 2010 © permission from American Chemical Society.

2.4
Starch Nanocrystals

2.4.1
Preparation of Starch Nanocrystals

2.4.1.1 Extraction of Starch Nanocrystals by Acid Hydrolysis

As shown in Figure 2.30, the commonly accepted model for a starch granule structure is a concentric semicrystalline (i.e., alternating amorphous and crystalline regions) multiscale structure. Hydrolysis of starch could be described as a "peeling process" [133]. Conventional methods for the preparation of starch nanocrystals use sulfuric acid or hydrochloric acid to catalyze the hydrolysis as follows: A given weight of native waxy maize starch granules was mixed with diluted acid (2.2 N HCl or $1.5-4$ M H_2SO_4). The suspensions were kept at $35-40\,°C$ and continuously stirred. After different hydrolysis times the insoluble residues were washed by successive centrifugation in distilled water until neutrality. They were then mechanically treated for given time to disperse aggregates formed during centrifugation. The resulting aqueous suspensions were stored at $4\,°C$ [134–136]. In fact, the temperature has a great influence on the hydrolysis of starch nanocrystals. For example, Kim *et al.* researched waxy maize starch hydrolysis using 3.16 M sulfuric acid at 40 or $4\,°C$, or at cycled temperatures
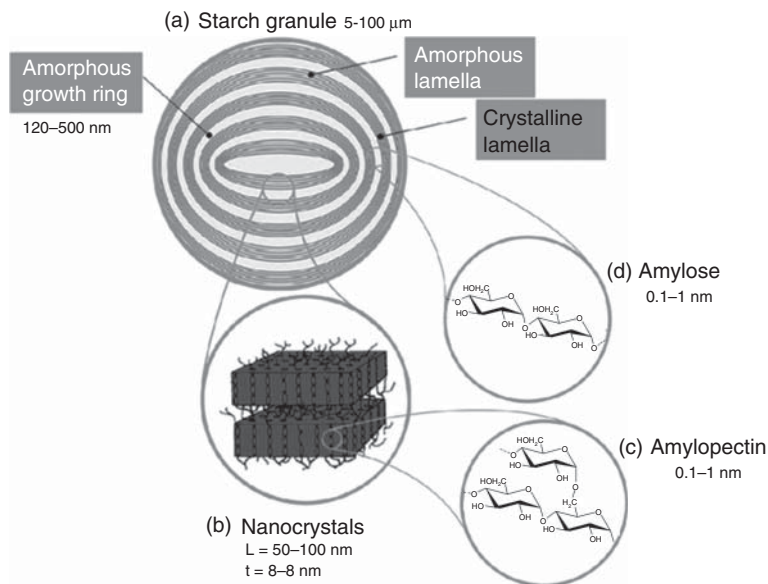
Figure 2.30 Starch granule structures. Reproduced from [133], copyright 2011 © permission from American Chemical Society
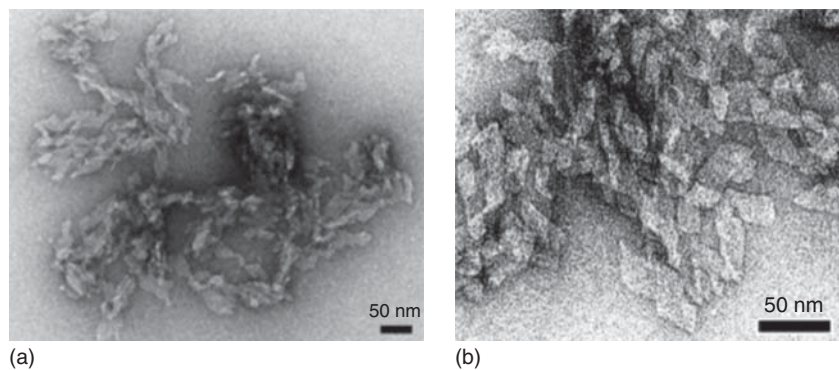
Figure 2.31 TEM images of starch nanocrystals prepared using (a) sulfuric acid [134] and (b) hydrochloric acid. Reproduced from [136], copyright 2004 © permission from American Chemical Society.

of 4/40 °C. They found that the yield of starch nanocrystals extracted at 4 °C was much higher than that at 40 °C during the 6 days of hydrolysis. The yield at a cycled temperature of 4/40 °C was between that at 4 and 40 °C. However, the crystallinity of starch nanocrystals increased with increasing hydrolysis temperature [137]. In general, the starch nanocrystals obtained using sulfuric or hydrochloric acid under certain conditions have a platelet-like structure and they are 6–8 nm thick, 40–60 nm in length, and 15–30 nm wide [138]. Figure 2.31 shows TEM images of starch nanocrystals prepared using sulfuric
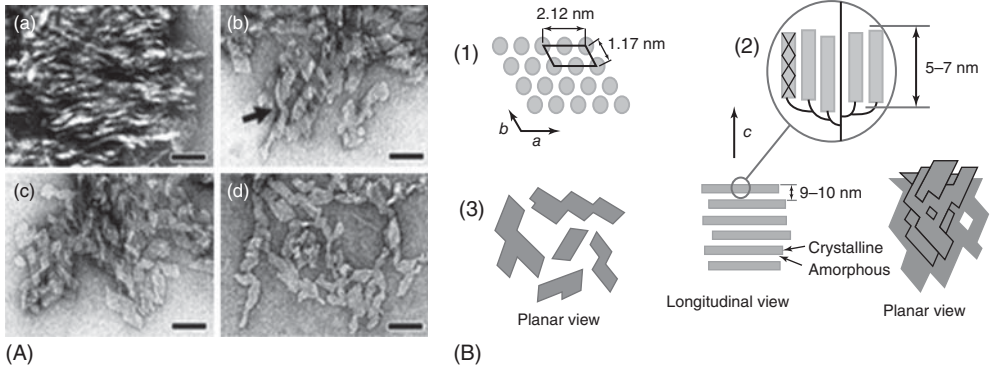
Figure 2.32 (A) TEM images of starch nanocrystals: (a–c) the starch nanocrystals after 2 weeks hydrolysis; in (b,c), the parallelepiped platelets can be seen; the arrow in (b) indicates a pyramidal stack of crystals. (d) The starch nanocrystals after 6 weeks hydrolysis. (B) The schematic diagram of extracted starch nanocrystals. Reproduced from [136], copyright 2004 © permission from American Chemical Society.

or hydrochloric acid. Nanoplatelets were generally observed in the two samples with some difference in size.

In addition, hydrolysis time affects the lamellar structures of starch nanocrystals. Putaux *et al.* [136] researched the morphology of starch nanocrystals extracted from waxy maize starch by using hydrochloric acid under different hydrolysis times. After hydrolyzing for 2 weeks, some compact fragments of 200–500 nm were found. As shown in TEM images of Figure 2.32a, starch nanocrystals with a lamellar structure consisting of a stack of fragments, with a width of 5–7 nm, can be clearly observed. In TEM images of Figure 2.31b,c, the parallelepipedal platelets with sharp 60°–65° acute angles were observed and also stacked in a pyramidal style (indicated by an arrow in TEM images of Figure 2.32b) or more randomly distributed (shown in TEM images Figure 2.32c). On hydrolysis for 6 weeks, an insoluble residue was obtained and the polygonal structure of the starch nanocrystals was similar to those shown in TEM images of Figure 2.32b,c, but it is hard to find completely individual nanocrystals (shown in TEM images of Figure 2.32d). The general extraction process of starch nanocrystals is schematized in the Figure 2.32B, parts (2) and (3). The "idealized" individual platelet of starch nanocrystals is seen in Figure 2.32B (1).

2.4.1.2 Effect of Ultrasonic Treatment

Starch nanocrystals isolated using sulfuric or hydrochloric acid easily tended to aggregate the microparticles formed, especially when drying the starch nanocrystals to form powders [139]. Moreover, the hydrolysis time usually exceeded 5 days and the yield of obtained starch nanocrystals was too low, below 20%. Ultrasonic treatment not only shortened the hydrolysis duration and enhanced the yield of starch nanocrystals but also effectively broke up the aggregates. There are generally two methods of ultrasonication to treat

starch nanocrystal suspension; one is to use ultrasonication once a day on the suspension during hydrolysis; the other is to apply ultrasonication to the re-dispersion of starch precipitates obtained from the native starch hydrolysis. The first type of ultrasonic treatment may prevent the formation of aggregates of starch nanocrystals and detach them from the aggregates during the hydrolysis of starch. The yield of starch nanocrystals increased clearly with this method. The second ultrasonic treatment could cause the microparticles to convert to nanoparticles. Ultrasonic treatment during acid hydrolysis retains the crystalline structure of the native starch, but it is damaged by the ultrasonic treatment to re-disperse the microparticles [140]. Thereby, the use of the ultrasonication during acid hydrolysis of starch granules can effectively increase the yield of starch nanocrystals. On the basis of the effect of low temperature on the yield, ultrasonic treatments can be considered in combination with low temperature to achieve large-scale extraction of starch nanocrystals.

2.4.1.3 Effect of Pretreatment

Currently, using the common method of preparation, starch nanocrystals are extracted from native starch granules by using sulfuric acid to hydrolyze the amorphous regions. However, so far, the optimized process for isolating starch nanocrystals still involves 5 days or more [134]; therefore, it is necessary to undertake pretreatments that could greatly shorten the hydrolysis time. A desired pretreatment would break the starch granule, or create pores in the starch granule, so that better acid diffusion occurs through the starch granule. The use of enzymes may solve the problem, as seen in Figure 2.33, which shows SEM (scanning electron microscope) images of waxy maize starch granules after a 2 h enzymatic hydrolysis pretreatment [141]. There are many holes on the surface of the pretreated starch granules, which allow more acid molecules to penetrate into the interior of starch granules. Thus, compared with the common method for preparing starch nanocrystals, the pretreated starch method is much faster. The extent of hydrolysis normally reached in 24 h is obtained after only 6 h, and the regular final yield (15% after 5 days) is reached in 45 h [142].

2.4.2
Structure and Properties of Starch Nanocrystals

2.4.2.1 Structure of Starch Nanocrystals

Natural starch granules are composed of crystalline and amorphous phases. The disordered or low ordered regions of starch granules are preferentially hydrolyzed, whereas the crystalline regions that have a higher resistance and are water insoluble remain [143]. The starch source, type of crystallization, and relative proportion of crystalline amylose and amylopectin commonly determine the structure and morphology of the extracted starch nanocrystals [144]; the size and yield of starch nanocrystals is affected by the hydrolysis conditions (such as acid type,
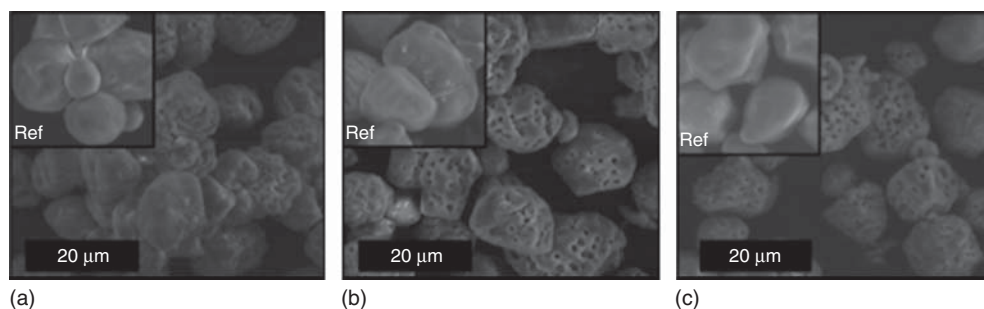
Figure 2.33 SEM images of waxy maize starch granules after a 2 h enzymatic hydrolysis pretreatment with (a) α-amylase, (b) β-amylase, and (c) glucoamylase. Reproduced from [141], copyright 2012 © permission from American Chemical Society.

Table 2.4 Effect of different extraction methods and starch sources on starch nanocrystals size [141].

Starch source	Concentration of acid for hydrolysis	Temperature (°C)	Duration (d)	Structural parameters (nm)	Characterization	References
Waxy corn starch	2.2 mol l^{-1} HCl	36	40	$L = 20-40$ $w = 15-30$ $T = 5-7$	TEM	[136]
	3.16 mol l^{-1} H$_2$SO$_4$	40	5	$L = 40-60$ $w = 15-30$	TEM	[134]
	3.16 mol l^{-1} H$_2$SO$_4$	40	5	$T = 6-8$ $L = 70-100$	TEM	[145]
Corn starch	2.87 mol l^{-1} H$_2$SO$_4$	45	7	$L = 50$	SEM	[146]
Pea starch	3.16 mol l^{-1} H$_2$SO$_4$	40	5	$L = 60-150$ $w = 15-30$	TEM	[147, 148] [149]
	3.16 mol l^{-1} H$_2$SO$_4$	40	5	$L = 30-80$	TEM	
Potato starch	3.16 mol l^{-1} H$_2$SO$_4$	40	5	$L = 40-70$ $w = 10-20$	TEM	[150]
	2.2 mol l^{-1} HCl	35	15	—	TEM	[151]

Data for structural parameters are length (L), width (W), and thickness (T) of starch nanocrystals.

acid concentration, temperature, and time). The structure parameters of starch nanocrystals derived from diverse sources and extracted under a variety of hydrolysis conditions are summarized in Table 2.4 [141].

2.4.2.2 Properties of Starch Nanocrystal Suspensions

As the surface energy of starch nanocrystals is in an unstable state, nanoparticles tend to aggregate easily through van der Waals forces and hydrogen bonding. In aqueous solvents, starch nanocrystals with surface polarity easily aggregate

(a)   (b)

Figure 2.34 Dispersion of starch nanocrystals in water (a) settled 0 min and (b) settled 30 min. Reproduced from [152], copyright 2012 © permission from Elsevier.

and ultrasound must generally be used to assist dispersion. Dispersions of starch nanocrystals in water are shown in Figure 2.34 [152]. It can be seen clearly that because of aggregation, the starch nanocrystals started to settle within several minutes, and wholly precipitated to the bottom of the vessel in 30 min (Figure 2.34b). However, it was observed that a stable suspension of starch nanocrystals extracted by sulfuric acid can be obtained by controlling the suspension pH [153]. It was found that a stable suspension was obtained when the pH was above 5.38. As the sulfate esters and carboxyl could become protonated at pH below 5.38, the resultant repulsive forces were much weaker than hydrogen bonding and van der Waals forces. In suspension, the starch nanocrystals aggregated quickly. When the pH of the suspension increased, the sulfate esters and carboxyl were deprotonated, and the repulsive forces were much stronger, so that a stable starch nanocrystal suspension could be obtained.

2.5
Conclusion and Prospects

PNs were generally extracted by acid hydrolysis; the different methods of extraction and sources would have an effect on the structure, morphology, and surface properties of PNs. Of course, the properties may be affected by using different kinds of acids. The thermal stability of PNs obtained using sulfuric acid was much lower than that obtained using hydrochloric acid. Pretreatments mainly improve the efficiency of native polysaccharide hydrolysis to obtain a higher yield of PNs. In addition, new and greener methods for extraction of PNs could be explored to achieve higher yield as well as controlling the size, surface structure, and properties to make PNs suitable for wider application.
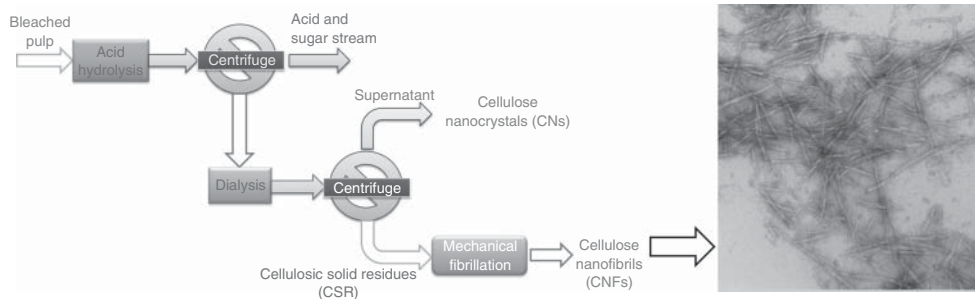
Figure 2.35 (Left) Schematic process flow diagram of the extraction and preparation of CNs and CNFs. (Right) TEM images of the CNFs produced from CSR. Reproduced from [154], copyright 2012 © permission from Springer.

Low yields of the extracted CNs lead to wasted cellulose raw materials. Therefore, the waste materials containing cellulose (e.g., the waste from bio-ethanol preparation) can be used to extract CNs or the solid residue obtained from CNs extraction can be used to prepare other cellulose nanoparticles to attain near 100% utilization. Both methods can help promote the application and development of cellulose in the materials field, at least to reduce the cost of extracting CNs. For example, when the yield of CNs is lower, in order to make full use of cellulose resource, cellulose nanofibrils (CNFs) can be prepared by optimizing the process, so that the conversion ratio of cellulose to CNs and CNFs can reach nearly 100% with no decline in the yield of CNs [154]. A schematic flow diagram for the extraction and preparation of CNs and CNFs is shown in Figure 2.35a [154]. TEM imaging indicated that the lengths of the CNFs were between 200 and 400 nm (Figure 2.35b) [154]. The rod-like CNFs were different from CNFs from other preparation methods such as enzymatic hydrolysis [155] or TEMPO-mediated oxidation [156], but could form a network structure. However, the practical performance and properties of CNFs need further exploration.

List of Abbreviations

AA	acrylic acid
AFM	atomic force microscopy
BCNs	bacterial cellulose nanocrystals
CNFs	cellulose nanofibrils
CNs	cellulose nanocrystals
DMF	dimethyl formamide
DMSO	dimethylsulfoxide
FTIR	Fourier transform infrared spectroscopy
HCl	hydrochloric acid
H_2SO_4	sulfuric acid
KOH	potassium hydroxide

MCC   microcrystalline cellulose
NaCl   sodium chloride
NaClO   sodium hypochlorite
NaClO$_2$ sodium chlorite
NaOH   sodium hydroxide
NMMO   *N*-methylmorpholine-*N*-oxide
PNs   polysaccharide nanocrystals
SEM   scanning electron microscope
TEM   transmission electron microscopy
TEMPO   tetramethyl-piperidin-1-oxyl
TGA   thermogravimetric analysis
THF   tetrahydrofuran

References

1. Šturcová, A., Davies, G.R., and Eichhorn, S.J. (2005) Elastic modulus and stress-transfer properties of tunicate cellulose whiskers. *Biomacromolecules*, **6** (2), 1055–1061.

2. Zhang, X., Huang, J., Chang, P.R., Li, J., Chen, Y., Wang, D., and Chen, J. (2010) Structure and properties of polysaccharide nanocrystal-doped supramolecular hydrogels based on cyclodextrin inclusion. *Polymer*, **51** (19), 4398–4407.

3. Roman, M. and Winter, W.T. (2004) Effect of sulfate groups from sulfuric acid hydrolysis on the thermal degradation behavior of bacterial cellulose. *Biomacromolecules*, **5** (5), 1671–1677.

4. Winter, H.T., Cerclier, C., Delorme, N., Bizot, H., Quemener, B., and Cathala, B. (2010) Improved colloidal stability of bacterial cellulose nanocrystal suspensions for the elaboration of spin-coated cellulose-based model surfaces. *Biomacromolecules*, **11** (11), 3144–3151.

5. Wang, N., Ding, E., and Cheng, R. (2007) Thermal degradation behaviors of spherical cellulose nanocrystals with sulfate groups. *Polymer*, **48** (12), 3486–3493.

6. Braun, B. and Dorgan, J.R. (2008) Single-step method for the isolation and surface functionalization of cellulosic nanowhiskers. *Biomacromolecules*, **10** (2), 334–341.

7. Fan, Y., Saito, T., and Isogai, A. (2007) Chitin nanocrystals prepared by TEMPO-mediated oxidation of α-chitin. *Biomacromolecules*, **9** (1), 192–198.

8. Rånby, B.G. (1951) Fibrous macromolecular systems. Cellulose and muscle. The colloidal properties of cellulose micelles. *Discuss. Faraday Soc.*, **11**, 158–164.

9. Habibi, Y., Lucia, L.A., and Rojas, O.J. (2010) Cellulose nanocrystals: chemistry, self-assembly, and applications. *Chem. Rev.*, **110** (6), 3479–3500.

10. Angles, M.N. and Dufresne, A. (2001) Plasticized/tunicin whiskers nanocomposites materials. 2. Mechanical behavior. *Macromolecules*, **34** (9), 2921–2931.

11. Grunert, M. and Winter, W.T. (2002) Nanocomposites of cellulose acetate butyrate reinforced with cellulose nanocrystals. *J. Polym. Environ.*, **10** (1–2), 27–30.

12. Lin, N., Yu, J., Chang, P.R., Li, J., and Huang, J. (2011) Poly (butylene succinate)-based biocomposites filled with polysaccharide nanocrystals: structure and properties. *Polym. Compos.*, **32** (3), 472–482.

13. Dong, X.M., Kimura, T., Revol, J.F., and Gray, D.G. (1996) Effects of ionic strength on the isotropic-chiral nematic phase transition of suspensions of cellulose crystallites. *Langmuir*, **12** (8), 2076–2082.

14. Siqueira, G., Bras, J., and Dufresne, A. (2008) Cellulose whiskers versus microfibrils: influence of the nature of the nanoparticle and its surface functionalization on the thermal and mechanical properties of nanocomposites. *Biomacromolecules*, **10** (2), 425–432.

15. Junior de Menezes, A., Siqueira, G., Curvelo, A.A., and Dufresne, A. (2009) Extrusion and characterization of functionalized cellulose whiskers reinforced polyethylene nanocomposites. *Polymer*, **50** (19), 4552–4563.

16. Elazzouzi-Hafraoui, S., Nishiyama, Y., Putaux, J.L., Heux, L., Dubreuil, F., and Rochas, C. (2007) The shape and size distribution of crystalline nanoparticles prepared by acid hydrolysis of native cellulose. *Biomacromolecules*, **9** (1), 57–65.

17. Angles, M.N. and Dufresne, A. (2000) Plasticized starch/tunicin whiskers nanocomposites. 1. Structural analysis. *Macromolecules*, **33** (22), 8344–8353.

18. Urena-Benavides, E.E., Brown, P.J., and Kitchens, C.L. (2010) Effect of jet stretch and particle load on cellulose nanocrystal–alginate nanocomposite fibers. *Langmuir*, **26** (17), 14263–14270.

19. Pakzad, A., Simonsen, J., and Yassar, R.S. (2012) Gradient of nanomechanical properties in the interphase of cellulose nanocrystal composites. *Compos. Sci. Technol.*, **72** (2), 314–319.

20. Edwards, J.V., Prevost, N.T., Condon, B., French, A., and Wu, Q. (2012) Immobilization of lysozyme-cellulose amide-linked conjugates on cellulose I and II cotton nanocrystalline preparations. *Cellulose*, **19** (2), 495–506.

21. Lu, P. and Hsieh, Y.L. (2010) Preparation and properties of cellulose nanocrystals: rods, spheres, and network. *Carbohydr. Polym.*, **82** (2), 329–336.

22. Lin, N., Huang, J., Chang, P.R., Feng, J., and Yu, J. (2011) Surface acetylation of cellulose nanocrystal and its reinforcing function in poly (lactic acid). *Carbohydr. Polym.*, **83** (4), 1834–1842.

23. Espino-Pérez, E., Bras, J., Ducruet, V., Guinault, A., Dufresne, A., and Domenek, S. (2013) Influence of chemical surface modification of cellulose nanowhiskers on thermal, mechanical, and barrier properties of poly (lactide) based bionanocomposites. *Eur. Polym. J.*, **49** (10), 3144–3154.

24. Roohani, M., Habibi, Y., Belgacem, N.M., Ebrahim, G., Karimi, A.N., and Dufresne, A. (2008) Cellulose whiskers reinforced polyvinyl alcohol copolymers nanocomposites. *Eur. Polym. J.*, **44** (8), 2489–2498.

25. Cranston, E.D. and Gray, D.G. (2006) Morphological and optical characterization of polyelectrolyte multilayers incorporating nanocrystalline cellulose. *Biomacromolecules*, **7** (9), 2522–2530.

26. Lu, Z., Fan, L., Zheng, H., Lu, Q., Liao, Y., and Huang, B. (2013) Preparation, characterization and optimization of nanocellulose whiskers by simultaneously ultrasonic wave and microwave assisted. *Bioresour. Technol.*, **146**, 82–88.

27. Tang, L., Huang, B., Lu, Q., Wang, S., Ou, W., Lin, W., and Chen, X. (2013) Ultrasonication-assisted manufacture of cellulose nanocrystals esterified with acetic acid. *Bioresour. Technol.*, **127**, 100–105.

28. Tang, L.R., Huang, B., Ou, W., Chen, X.R., and Chen, Y.D. (2011) Manufacture of cellulose nanocrystals by cation exchange resin-catalyzed hydrolysis of cellulose. *Bioresour. Technol.*, **102** (23), 10973–10977.

29. Dong, X.M., Revol, J.F., and Gray, D.G. (1998) Effect of microcrystallite preparation conditions on the formation of colloid crystals of cellulose. *Cellulose*, **5** (1), 19–32.

30. Rusli, R., Shanmuganathan, K., Rowan, S.J., Weder, C., and Eichhorn, S.J. (2011) Stress transfer in cellulose nanowhisker composites–influence of whisker aspect ratio and surface charge. *Biomacromolecules*, **12** (4), 1363–1369.

31. Salajková, M., Berglund, L.A., and Zhou, Q. (2012) Hydrophobic cellulose nanocrystals modified with quaternary ammonium salts. *J. Mater. Chem.*, **22** (37), 19798–19805.

32. Yu, H., Qin, Z., Liang, B., Liu, N., Zhou, Z., and Chen, L. (2013) Facile

extraction of thermally stable cellulose nanocrystals with a high yield of 93% through hydrochloric acid hydrolysis under hydrothermal conditions. *J. Mater. Chem. A*, **1** (12), 3938–3944.

33. Araki, J., Wada, M., Kuga, S., and Okano, T. (1998) Flow properties of microcrystalline cellulose suspension prepared by acid treatment of native cellulose. *Colloids Surf., A Physicochem. Eng. Asp.*, **142** (1), 75–82.

34. Sadeghifar, H., Filpponen, I., Clarke, S.P., Brougham, D.F., and Argyropoulos, D.S. (2011) Production of cellulose nanocrystals using hydrobromic acid and click reactions on their surface. *J. Mater. Sci.*, **46** (22), 7344–7355.

35. Camarero Espinosa, S., Kuhnt, T., Foster, E.J., and Weder, C. (2013) Isolation of thermally stable cellulose nanocrystals by phosphoric acid hydrolysis. *Biomacromolecules*, **14** (4), 1223–1230.

36. Anastas, P.T. and Warner, J.C. (2000) *Green Chemistry: Theory and Practice*, Oxford University Press.

37. Esteghlalian, A.R., Bilodeau, M., Mansfield, S.D., and Saddler, J.N. (2001) Do enzymatic hydrolyzability and Simons' stain reflect the changes in the accessibility of lignocellulosic substrates to cellulase enzymes? *Biotechnol. Prog.*, **17** (6), 1049–1054.

38. Yang, D., Peng, X.W., Zhong, L.X., Cao, X.F., Chen, W., and Sun, R.C. (2013) Effects of pretreatments on crystalline properties and morphology of cellulose nanocrystals. *Cellulose*, **20** (5), 2427–2437.

39. Ago, M., Endo, T., and Hirotsu, T. (2004) Crystalline transformation of native cellulose from cellulose I to cellulose ID polymorph by a ball-milling method with a specific amount of water. *Cellulose*, **11** (2), 163–167.

40. Gao, Q., Shen, X., and Lu, X. (2011) Regenerated bacterial cellulose fibers prepared by the $NMMO/H_2O$ process. *Carbohydr. Polym.*, **83** (3), 1253–1256.

41. Zhang, H., Wu, J., Zhang, J., and He, J. (2005) 1-Allyl-3-methylimidazolium chloride room temperature ionic liquid: a new and powerful nonderivatizing

solvent for cellulose. *Macromolecules*, **38** (20), 8272–8277.

42. Bai, W., Holbery, J., and Li, K. (2009) A technique for production of nanocrystalline cellulose with a narrow size distribution. *Cellulose*, **16** (3), 455–465.

43. de Souza Lima, M.M. and Borsali, R. (2002) Static and dynamic light scattering from polyelectrolyte microcrystal cellulose. *Langmuir*, **18** (4), 992–996.

44. Pakzad, A., Simonsen, J., Heiden, P.A., and Yassar, R.S. (2012) Size effects on the nanomechanical properties of cellulose I nanocrystals. *J. Mater. Res.*, **27** (03), 528–536.

45. Gu, J., Catchmark, J.M., Kaiser, E.Q., and Archibald, D.D. (2013) Quantification of cellulose nanowhiskers sulfate esterification levels. *Carbohydr. Polym.*, **92** (2), 1809–1816.

46. Araki, J., Wada, M., and Kuga, S. (2001) Steric stabilization of a cellulose microcrystal suspension by poly (ethylene glycol) grafting. *Langmuir*, **17** (1), 21–27.

47. Heux, L., Chauve, G., and Bonini, C. (2000) Nonflocculating and chiral-nematic self-ordering of cellulose microcrystals suspensions in nonpolar solvents. *Langmuir*, **16** (21), 8210–8212.

48. de Souza Lima, M.M., Wong, J.T., Paillet, M., Borsali, R., and Pecora, R. (2003) Translational and rotational dynamics of rodlike cellulose whiskers. *Langmuir*, **19** (1), 24–29.

49. Miller, A.F. and Donald, A.M. (2003) Imaging of anisotropic cellulose suspensions using environmental scanning electron microscopy. *Biomacromolecules*, **4** (3), 510–517.

50. Morais, J.P.S., Rosa, M.D.F., Nascimento, L.D., do Nascimento, D.M., and Cassales, A.R. (2013) Extraction and characterization of nanocellulose structures from raw cotton linter. *Carbohydr. Polym.*, **91** (1), 229–235.

51. Li, Q., Zhou, J., and Zhang, L. (2009) Structure and properties of the nanocomposite films of chitosan reinforced with cellulose whiskers. *J. Polym. Sci. B*, **47** (11), 1069–1077.

52. Bondeson, D., Mathew, A., and Oksman, K. (2006) Optimization of the isolation of nanocrystals from microcrystalline cellulose by acid hydrolysis. *Cellulose*, **13** (2), 171−180.

53. Capadona, J.R., Shanmuganathan, K., Trittschuh, S., Seidel, S., Rowan, S.J., and Weder, C. (2009) Polymer nanocomposites with nanowhiskers isolated from microcrystalline cellulose. *Biomacromolecules*, **10** (4), 712−716.

54. Pranger, L. and Tannenbaum, R. (2008) Biobased nanocomposites prepared by in situ polymerization of furfuryl alcohol with cellulose whiskers or montmorillonite clay. *Macromolecules*, **41** (22), 8682−8687.

55. Sakurada, I., Nukushina, Y., and Ito, T. (1962) Experimental determination of the elastic modulus of crystalline regions in oriented polymers. *J. Polym. Sci.*, **57** (165), 651−660.

56. Sakurada, I., Ito, T., and Nakamae, K. (1964) Elastic moduli of polymer crystals for the chain axial direction. *Makromol. Chem.*, **75** (1), 1−10.

57. Matsuo, M., Sawatari, C., Iwai, Y., and Ozaki, F. (1990) Effect of orientation distribution and crystallinity on the measurement by X-ray diffraction of the crystal lattice moduli of cellulose I and II. *Macromolecules*, **23** (13), 3266−3275.

58. Nishino, T., Takano, K., and Nakamae, K. (1995) Elastic modulus of the crystalline regions of cellulose polymorphs. *J. Polym. Sci. B*, **33** (11), 1647−1651.

59. Ishikawa, A., Okano, T., and Sugiyama, J. (1997) Fine structure and tensile properties of ramie fibers in the crystalline form of cellulose I, II, III$_I$ and IV$_I$. *Polymer*, **38** (2), 463−468.

60. Habibi, Y., Hoeger, I., Kelley, S.S., and Rojas, O.J. (2009) Development of langmuir−Schaeffer cellulose nanocrystal monolayers and their interfacial behaviors. *Langmuir*, **26** (2), 990−1001.

61. Habibi, Y., Goffin, A.L., Schiltz, N., Duquesne, E., Dubois, P., and Dufresne, A. (2008) Bionanocomposites based on poly (ε-caprolactone)-grafted cellulose nanocrystals by ring-opening polymerization. *J. Mater. Chem.*, **18** (41), 5002−5010.

62. De Rodriguez, N.L.G., Thielemans, W., and Dufresne, A. (2006) Sisal cellulose whiskers reinforced polyvinyl acetate nanocomposites. *Cellulose*, **13** (3), 261−270.

63. Kargarzadeh, H., Ahmad, I., Abdullah, I., Dufresne, A., Zainudin, S.Y., and Sheltami, R.M. (2012) Effects of hydrolysis conditions on the morphology, crystallinity, and thermal stability of cellulose nanocrystals extracted from kenaf bast fibers. *Cellulose*, **19** (3), 855−866.

64. Araki, J., Wada, M., Kuga, S., and Okano, T. (1999) Influence of surface charge on viscosity behavior of cellulose microcrystal suspension. *J. Wood Sci.*, **45** (3), 258−261.

65. Beck-Candanedo, S., Roman, M., and Gray, D.G. (2005) Effect of reaction conditions on the properties and behavior of wood cellulose nanocrystal suspensions. *Biomacromolecules*, **6** (2), 1048−1054.

66. Wagner, R., Moon, R., Pratt, J., Shaw, G., and Raman, A. (2011) Uncertainty quantification in nanomechanical measurements using the atomic force microscope. *Nanotechnology*, **22** (45), 455703.

67. Terech, P., Chazeau, L., and Cavaille, J.Y. (1999) A small-angle scattering study of cellulose whiskers in aqueous suspensions. *Macromolecules*, **32** (6), 1872−1875.

68. Iwamoto, S., Kai, W., Isogai, A., and Iwata, T. (2009) Elastic modulus of single cellulose microfibrils from tunicate measured by atomic force microscopy. *Biomacromolecules*, **10** (9), 2571−2576.

69. Araki, J. and Kuga, S. (2001) Effect of trace electrolyte on liquid crystal type of cellulose microcrystals. *Langmuir*, **17** (15), 4493−4496.

70. Lin, N., Huang, J., and Dufresne, A. (2012) Preparation, properties and applications of polysaccharide nanocrystals in advanced functional nanomaterials: a review. *Nanoscale*, **4** (11), 3274−3294.

71. Meyer, K.H. and Lotmar, W. (1936) On the elasticity of the cellulose. (On the constitution of partially crystallized

cellulose IV). *Helv. Chim. Acta*, **19** (1), 68–86.

72. Jaswon, M.A., Gillis, P.P., and Mark, R.E. (1968) The elastic constants of crystalline native cellulose. *Proc. R. Soc. London, Ser. A Math. Phys. Sci.*, **306** (1486), 389–412.

73. Tashiro, K. and Kobayashi, M. (1985) Calculation of crystallite modulus of native cellulose. *Polym. Bull.*, **14** (3–4), 213–218.

74. Kroon-Batenburg, L.M.J., Kroon, J., and Northolt, M.G. (1986) Chain modulus and intramolecular hydrogen bonding in native and regenerated cellulose fibers. *Polym. Commun.*, **27** (10), 290–292.

75. Tashiro, K. and Kobayashi, M. (1991) Theoretical evaluation of three-dimensional elastic constants of native and regenerated celluloses: role of hydrogen bonds. *Polymer*, **32** (8), 1516–1526.

76. Guhados, G., Wan, W., and Hutter, J.L. (2005) Measurement of the elastic modulus of single bacterial cellulose fibers using atomic force microscopy. *Langmuir*, **21** (14), 6642–6646.

77. Tanaka, F. and Iwata, T. (2006) Estimation of the elastic modulus of cellulose crystal by molecular mechanics simulation. *Cellulose*, **13** (5), 509–517.

78. Cheng, Q. and Wang, S. (2008) A method for testing the elastic modulus of single cellulose fibrils via atomic force microscopy. *Composites Part A*, **39** (12), 1838–1843.

79. Diddens, I., Murphy, B., Krisch, M., and Müller, M. (2008) Anisotropic elastic properties of cellulose measured using inelastic X-ray scattering. *Macromolecules*, **41** (24), 9755–9759.

80. Rusli, R. and Eichhorn, S.J. (2008) Determination of the stiffness of cellulose nanowhiskers and the fiber-matrix interface in a nanocomposite using Raman spectroscopy. *Appl. Phys. Lett.*, **93** (3), 033111.

81. Lahiji, R.R., Xu, X., Reifenberger, R., Raman, A., Rudie, A., and Moon, R.J. (2010) Atomic force microscopy characterization of cellulose nanocrystals. *Langmuir*, **26** (6), 4480–4488.

82. Wada, M., Heux, L., and Sugiyama, J. (2004) Polymorphism of cellulose I family: reinvestigation of cellulose IVI. *Biomacromolecules*, **5** (4), 1385–1391.

83. Chen, D., Lawton, D., Thompson, M.R., and Liu, Q. (2012) Biocomposites reinforced with cellulose nanocrystals derived from potato peel waste. *Carbohydr. Polym.*, **90** (1), 709–716.

84. Wada, M., Kondo, T., and Okano, T. (2003) Thermally induced crystal transformation from cellulose Iα to Iβ. *Polym. J.*, **35** (2), 155–159.

85. Nishiyama, Y., Sugiyama, J., Chanzy, H., and Langan, P. (2003) Crystal structure and hydrogen bonding system in cellulose Iα from synchrotron X-ray and neutron fiber diffraction. *J. Am. Chem. Soc.*, **125** (47), 14300–14306.

86. Khoshkava, V. and Kamal, M.R. (2013) Effect of surface energy on dispersion and mechanical properties of polymer/nanocrystalline cellulose nanocomposites. *Biomacromolecules*, **14** (9), 3155–3163.

87. Dankovich, T.A. and Gray, D.G. (2011) Contact angle measurements on smooth nanocrystalline cellulose (I) thin films. *J. Adhes. Sci. Technol.*, **25** (6-7), 699–708.

88. Shang, W., Huang, J., Luo, H., Chang, P.R., Feng, J., and Xie, G. (2013) Hydrophobic modification of cellulose nanocrystal via covalently grafting of castor oil. *Cellulose*, **20** (1), 179–190.

89. Yu, H.Y. and Qin, Z.Y. (2014) Surface grafting of cellulose nanocrystals with poly (3-hydroxybutyrate-co-3-hydroxyvalerate). *Carbohydr. Polym.*, **101**, 471–478.

90. Morandi, G., Heath, L., and Thielemans, W. (2009) Cellulose nanocrystals grafted with polystyrene chains through surface-initiated atom transfer radical polymerization (SI-ATRP). *Langmuir*, **25** (14), 8280–8286.

91. Glasser, W.G., Taib, R., Jain, R.K., and Kander, R. (1999) Fiber-reinforced cellulosic thermoplastic composites. *J. Appl. Polym. Sci.*, **73** (7), 1329–1340.

92. Bondeson, D. and Oksman, K. (2007) Dispersion and characteristics of surfactant modified cellulose whiskers

nanocomposites. *Compos. Interfaces*, **14** (7-9), 617–630.

93. Ben Azouz, K., Ramires, E.C., Van den Fonteyne, W., El Kissi, N., and Dufresne, A. (2011) Simple method for the melt extrusion of a cellulose nanocrystal reinforced hydrophobic polymer. *ACS Macro Lett.*, **1** (1), 236–240.

94. Lin, N. and Dufresne, A. (2013) Physical and/or chemical compatibilization of extruded cellulose nanocrystal reinforced polystyrene nanocomposites. *Macromolecules*, **46** (14), 5570–5583.

95. Beck, S., Bouchard, J., Chauve, G., and Berry, R. (2013) Controlled production of patterns in iridescent solid films of cellulose nanocrystals. *Cellulose*, **20** (3), 1401–1411.

96. Liu, D., Chen, X., Yue, Y., Chen, M., and Wu, Q. (2011) Structure and rheology of nanocrystalline cellulose. *Carbohydr. Polym.*, **84** (1), 316–322.

97. Majoinen, J., Kontturi, E., Ikkala, O., and Gray, D.G. (2012) SEM imaging of chiral nematic films cast from cellulose nanocrystal suspensions. *Cellulose*, **19** (5), 1599–1605.

98. Roman, M. and Gray, D.G. (2005) Parabolic focal conics in self-assembled solid films of cellulose nanocrystals. *Langmuir*, **21** (12), 5555–5561.

99. Revol, J.F., Bradford, H., Giasson, J., Marchessault, R.H., and Gray, D.G. (1992) Helicoidal self-ordering of cellulose microfibrils in aqueous suspension. *Int. J. Biol. Macromol.*, **14** (3), 170–172.

100. Hirai, A., Inui, O., Horii, F., and Tsuji, M. (2008) Phase separation behavior in aqueous suspensions of bacterial cellulose nanocrystals prepared by sulfuric acid treatment. *Langmuir*, **25** (1), 497–502.

101. Picard, G., Simon, D., Kadiri, Y., LeBreux, J.D., and Ghozayel, F. (2012) Cellulose nanocrystal iridescence: a new model. *Langmuir*, **28** (41), 14799–14807.

102. de Souza Lima, M.M. and Borsali, R. (2004) Rodlike cellulose microcrystals: structure, properties, and applications. *Macromol. Rapid Commun.*, **25** (7), 771–787.

103. Elazzouzi-Hafraoui, S., Putaux, J.L., and Heux, L. (2009) Self-assembling and chiral nematic properties of organophilic cellulose nanocrystals. *J. Phys. Chem. B*, **113** (32), 11069–11075.

104. Sassi, J.F. and Chanzy, H. (1995) Ultrastructural aspects of the acetylation of cellulose. *Cellulose*, **2** (2), 111–127.

105. Montanari, S., Roumani, M., Heux, L., and Vignon, M.R. (2005) Topochemistry of carboxylated cellulose nanocrystals resulting from TEMPO-mediated oxidation. *Macromolecules*, **38** (5), 1665–1671.

106. Goussé, C., Chanzy, H., Excoffier, G., Soubeyrand, L., and Fleury, E. (2002) Stable suspensions of partially silylated cellulose whiskers dispersed in organic solvents. *Polymer*, **43** (9), 2645–2651.

107. de Oliveira Taipina, M., Ferrarezi, M.M.F., Yoshida, I.V.P., and do Carmo Gonçalves, M. (2013) Surface modification of cotton nanocrystals with a silane agent. *Cellulose*, **20** (1), 217–226.

108. Zhao, B. and Brittain, W.J. (2000) Polymer brushes: surface-immobilized macromolecules. *Prog. Polym. Sci.*, **25** (5), 677–710.

109. Ljungberg, N., Bonini, C., Bortolussi, F., Boisson, C., Heux, L., and Cavaillé, J.Y. (2005) New nanocomposite materials reinforced with cellulose whiskers in atactic polypropylene: effect of surface and dispersion characteristics. *Biomacromolecules*, **6** (5), 2732–2739.

110. Habibi, Y., Chanzy, H., and Vignon, M.R. (2006) TEMPO-mediated surface oxidation of cellulose whiskers. *Cellulose*, **13** (6), 679–687.

111. Urena-Benavides, E.E., Ao, G., Davis, V.A., and Kitchens, C.L. (2011) Rheology and phase behavior of lyotropic cellulose nanocrystal suspensions. *Macromolecules*, **44** (22), 8990–8998.

112. Bercea, M. and Navard, P. (2000) Shear dynamics of aqueous suspensions of cellulose whiskers. *Macromolecules*, **33** (16), 6011–6016.

113. Dorris, A. and Gray, D.G. (2012) Gelation of cellulose nanocrystal suspensions in glycerol. *Cellulose*, **19** (3), 687–694.

114. Morganti, P., Muzzarelli, R.A., and Muzzarelli, C. (2006) Multifunctional use of innovative chitin nanofibrils for skin care. *J. Appl. Cosmetol.*, **24**, 105–114.

115. Revol, J.F. and Marchessault, R.H. (1993) In vitro chiral nematic ordering of chitin crystallites. *Int. J. Biol. Macromol.*, **15** (6), 329–335.

116. Paillet, M. and Dufresne, A. (2001) Chitin whisker reinforced thermoplastic nanocomposites. *Macromolecules*, **34** (19), 6527–6530.

117. Lu, Y., Weng, L., and Zhang, L. (2004) Morphology and properties of soy protein isolate thermoplastics reinforced with chitin whiskers. *Biomacromolecules*, **5** (3), 1046–1051.

118. Gopalan Nair, K. and Dufresne, A. (2003) Crab shell chitin whisker reinforced natural rubber nanocomposites. 1. Processing and swelling behavior. *Biomacromolecules*, **4** (3), 657–665.

119. Goodrich, J.D. and Winter, W.T. (2007) α-chitin nanocrystals prepared from shrimp shells and their specific surface area measurement. *Biomacromolecules*, **8** (1), 252–257.

120. Watthanaphanit, A., Supaphol, P., Tamura, H., Tokura, S., and Rujiravanit, R. (2008) Fabrication, structure, and properties of chitin whisker-reinforced alginate nanocomposite fibers. *J. Appl. Polym. Sci.*, **110** (2), 890–899.

121. Wongpanit, P., Sanchavanakit, N., Pavasant, P., Bunaprasert, T., Tabata, Y., and Rujiravanit, R. (2007) Preparation and characterization of chitin whisker-reinforced silk fibroin nanocomposite sponges. *Eur. Polym. J.*, **43** (10), 4123–4135.

122. Rudall, K.M. and Kenchington, W. (1973) The chitin system. *Biol. Rev.*, **48** (4), 597–633.

123. Paralikar, K.M. and Balasubramanya, R.H. (1984) Electron diffraction study of α-chitin. *J. Polym. Sci.*, **22** (10), 543–546.

124. Atkins, E. (1985) Conformations in polysaccharides and complex carbohydrates. *J. Biosci.*, **8** (1–2), 375–387.

125. Rinaudo, M. (2006) Chitin and chitosan: properties and applications. *Prog. Polym. Sci.*, **31** (7), 603–632.

126. Yamamoto, Y., Nishimura, T., Saito, T., and Kato, T. (2010) CaCO$_3$/chitin-whisker hybrids: formation of CaCO3 crystals in chitin-based liquid-crystalline suspension. *Polym. J.*, **42** (7), 583–586.

127. Fan, Y., Saito, T., and Isogai, A. (2010) Individual chitin nano-whiskers prepared from partially deacetylated α-chitin by fibril surface cationization. *Carbohydr. Polym.*, **79** (4), 1046–1051.

128. Junkasem, J., Rujiravanit, R., and Supaphol, P. (2006) Fabrication of α-chitin whisker-reinforced poly (vinyl alcohol) nanocomposite nanofibres by electrospinning. *Nanotechnology*, **17** (17), 4519.

129. Morin, A. and Dufresne, A. (2002) Nanocomposites of chitin whiskers from Riftia tubes and poly (caprolactone). *Macromolecules*, **35** (6), 2190–2199.

130. Nge, T.T., Hori, N., Takemura, A., Ono, H., and Kimura, T. (2003) Phase behavior of liquid crystalline chitin/acrylic acid liquid mixture. *Langmuir*, **19** (4), 1390–1395.

131. Tzoumaki, M.V., Moschakis, T., and Biliaderis, C.G. (2009) Metastability of nematic gels made of aqueous chitin nanocrystal dispersions. *Biomacromolecules*, **11** (1), 175–181.

132. Belamie, E., Davidson, P., and Giraud-Guille, M.M. (2004) Structure and chirality of the nematic phase in α-chitin suspensions. *J. Phys. Chem. B*, **108** (39), 14991–15000.

133. LeCorre, D., Bras, J., and Dufresne, A. (2011) Evidence of micro-and nanoscaled particles during starch nanocrystals preparation and their isolation. *Biomacromolecules*, **12** (8), 3039–3046.

134. Angellier, H., Choisnard, L., Molina-Boisseau, S., Ozil, P., and Dufresne, A. (2004) Optimization of the preparation of aqueous suspensions of waxy maize starch nanocrystals using a response surface methodology. *Biomacromolecules*, **5** (4), 1545–1551.

135. Angellier, H., Putaux, J.L., Molina-Boisseau, S., Dupeyre, D., and Dufresne, A. (2005) Starch nanocrystal

fillers in an acrylic polymer matrix. *Macromol. Symp.*, **221** (1), 95–104.

136. Putaux, J.L., Molina-Boisseau, S., Momaur, T., and Dufresne, A. (2003) Platelet nanocrystals resulting from the disruption of waxy maize starch granules by acid hydrolysis. *Biomacromolecules*, **4** (5), 1198–1202.

137. Kim, H.Y., Park, D.J., Kim, J.Y., and Lim, S.T. (2013) Preparation of crystalline starch nanoparticles using cold acid hydrolysis and ultrasonication. *Carbohydr. Polym.*, **98** (1), 295–301.

138. Angellier, H., Molina-Boisseau, S., Lebrun, L., and Dufresne, A. (2005) Processing and structural properties of waxy maize starch nanocrystals reinforced natural rubber. *Macromolecules*, **38** (9), 3783–3792.

139. Dufresne, A. (2008) Polysaccharide nano crystal reinforced nanocomposites. *Can. J. Chem.*, **86** (6), 484–494.

140. Kim, H.Y., Han, J.A., Kweon, D.K., Park, J.D., and Lim, S.T. (2013) Effect of ultrasonic treatments on nanoparticle preparation of acid-hydrolyzed waxy maize starch. *Carbohydr. Polym.*, **93** (2), 582–588.

141. LeCorre, D., Vahanian, E., Dufresne, A., and Bras, J. (2011) Enzymatic pretreatment for preparing starch nanocrystals. *Biomacromolecules*, **13** (1), 132–137.

142. Lin, N., Huang, J., Chang, P.R., Anderson, D.P., and Yu, J. (2011) Preparation, modification, and application of starch nanocrystals in nanomaterials: a review. *J. Nanomater.*, **2011**, 20.

143. Wang, Y.J., Truong, V.D., and Wang, L. (2003) Structures and rheological properties of corn starch as affected by acid hydrolysis. *Carbohydr. Polym.*, **52** (3), 327–333.

144. Angellier-Coussy, H., Putaux, J.L., Molina-Boisseau, S., Dufresne, A., Bertoft, E., and Perez, S. (2009) The molecular structure of waxy maize starch nanocrystals. *Carbohydr. Res.*, **344** (12), 1558–1566.

145. Namazi, H. and Dadkhah, A. (2010) Convenient method for preparation of hydrophobically modified starch nanocrystals with using fatty acids. *Carbohydr. Polym.*, **79** (3), 731–737.

146. Song, S., Wang, C., Pan, Z., and Wang, X. (2008) Preparation and characterization of amphiphilic starch nanocrystals. *J. Appl. Polym. Sci.*, **107** (1), 418–422.

147. Zheng, H., Ai, F., Chang, P.R., Huang, J., and Dufresne, A. (2009) Structure and properties of starch nanocrystal-reinforced soy protein plastics. *Polym. Compos.*, **30** (4), 474–480.

148. Yu, J., Ai, F., Dufresne, A., Gao, S., Huang, J., and Chang, P.R. (2008) Structure and mechanical properties of poly (lactic acid) filled with (Starch nanocrystal)-graft-poly (ε-caprolactone). *Macromol. Mater. Eng.*, **293** (9), 763–770.

149. Chen, Y., Cao, X., Chang, P.R., and Huneault, M.A. (2008) Comparative study on the films of poly (vinyl alcohol)/pea starch nanocrystals and poly (vinyl alcohol)/native pea starch. *Carbohydr. Polym.*, **73** (1), 8–17.

150. Chen, G., Wei, M., Chen, J., Huang, J., Dufresne, A., and Chang, P.R. (2008) Simultaneous reinforcing and toughening: new nanocomposites of waterborne polyurethane filled with low loading level of starch nanocrystals. *Polymer*, **49** (7), 1860–1870.

151. Namazi, H. and Dadkhah, A. (2008) Surface modification of starch nanocrystals through ring-opening polymerization of ε-caprolactone and investigation of their microstructures. *J. Appl. Polym. Sci.*, **110** (4), 2405–2412.

152. Ren, L., Jiang, M., Wang, L., Zhou, J., and Tong, J. (2012) A method for improving dispersion of starch nanocrystals in water through crosslinking modification with sodium hexametaphosphate. *Carbohydr. Polym.*, **87** (2), 1874–1876.

153. Wei, B., Hu, X., Li, H., Wu, C., Xu, X., Jin, Z., and Tian, Y. (2014) Effect of pHs on dispersity of maize starch nanocrystals in aqueous medium. *Food Hydrocolloids*, **36**, 369–373.

154. Wang, Q.Q., Zhu, J.Y., Reiner, R.S., Verrill, S.P., Baxa, U., and McNeil, S.E. (2012) Approaching zero cellulose loss in cellulose nanocrystal (CNC) production: recovery and characterization of cellulosic solid residues (CSR) and CNC. *Cellulose*, **19** (6), 2033–2047.

155. Zhu, J.Y., Sabo, R., and Luo, X. (2011) Integrated production of nano-fibrillated cellulose and cellulosic biofuel (ethanol) by enzymatic fractionation of wood fibers. *Green Chem.*, **13** (5), 1339–1344.

156. Saito, T., Okita, Y., Nge, T.T., Sugiyama, J., and Isogai, A. (2006) TEMPO-mediated oxidation of native cellulose: microscopic analysis of fibrous fractions in the oxidized products. *Carbohydr. Polym.*, **65** (4), 435–440.

3
Surface Modification of Polysaccharide Nanocrystals

Ning Lin and Alain Dufresne

3.1
Introduction

Natural polysaccharides, such as cellulose, chitin, and starch, consist of crystalline and amorphous regions. The amorphous regions are highly susceptible to hydrolysis and, under controlled conditions, may be removed leaving the rigid crystalline regions intact. The recovered material occurs in the form of polysaccharide nanocrystals (PNs), most commonly rod-like cellulose nanocrystals (CNs) (also called cellulose (nano)whiskers, nanocrystalline cellulose, etc.), chitin nanowhiskers (ChWs), and platelet-like starch nanocrystals (SNs). The advantages of natural PNs over inorganic nanoparticles have been reported in many papers, and mainly consist of availability, biocompatibility, biodegradability, comparatively easy processability, nanoscale effects, low cost, high specific strength, and modulus as well as relatively reactive surface. The outstanding properties and characteristics of PNs lead to their potentially wide applications in the field of material science. Therein, most researchers focus on the utilization of PNs with possible physical and chemical surface modifications to reinforce all kinds of matrices, and the main purpose of the modification is to change the surface property of PNs to adapt their potential applications. Unlike previous reviews or books, this chapter discusses in detail the surface modification of PNs with a new framework according to the category of modified groups. In this context, comparison of the influence and effect among various modified groups or molecules is clearly discussed and investigated.

3.2
Surface Chemistry of Polysaccharide Nanocrystals

3.2.1
Surface Hydroxyl Groups

PNs possess a reactive surface covered with numerous active hydroxyl groups, which provide the possibility of modification via physical or chemical reaction.
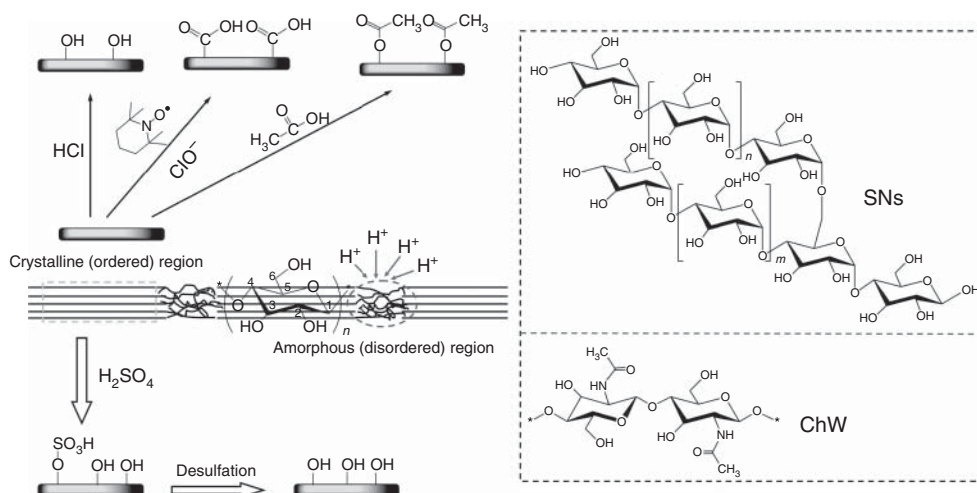
Figure 3.1 Chemical structures of CNs, SNs, and ChW; different extraction methods of CNs provide for distinctive surface chemistry: hydrochloric acid treatment provides hydroxyl, acetic acid provides acetyl, TEMPO mediated hypochlorite treatment provides carboxylic acid, and sulfuric acid treatment provides sulfate esters as well as the hydroxyl with desulfation of treatment.

For each anhydroglucose unit, the reactivity of active hydroxyl groups on different positions is heterogeneous. Taking cellulose as an example, the hydroxyl group at the 6 position acts as a primary alcohol, whereas the hydroxyl groups in the 2 and 3 positions behave as secondary alcohols (as shown in Figure 3.1). Indeed, the carbon atom that carries the hydroxyl group in the 6 position is only attached to one alkyl group, while the carbons with the hydroxyl groups in the 2 and 3 positions are joined directly to two alkyl groups, which will induce steric effects derived from the supramolecular structure of cellulose and the reacting agent [1]. It has been reported that the hydroxyl group at the 6 position can react 10 times faster than the other OH groups [2] while the reactivity of the hydroxyl group in the 2 position was found to be twice that of the hydroxyl group at the 3 position.

In light of inherent chemical structure, polysaccharide is a carbohydrate, which has chemical similarity with sugars. However, due to the highly ordered arrangement of the crystalline structure, the reactivity of PNs is different from that of a macromolecular polysaccharide, which should not be simply regarded as that of a multihydroxyl alcohol. The reactions between hydroxyl groups and reagents only occur or are controlled on the surface of PNs. Geometrical considerations obtained from microscopic observations are generally used to determine the content of active hydroxyl groups on the surface of nanocrystals ($n_{\text{Surface OH}}$). Taking rod-like CNs as an example and calculating according to the Connely surface methodology, around 3.8 mmol g^{-1} available hydroxyl groups can be obtained for cotton CNs with average width $d = 4$ nm and average length $L = 250$ nm [3]. Using

a similar method, the content of hydroxyl groups present on the surface of platelet-like SNs was estimated to be about $2.5\,mmol\,g^{-1}$ [4]. However, even for these surface polysaccharide chains, not all hydroxyl groups are accessible, as some are oriented toward the inner side of the nanoparticle. Indeed, because of the different orientation of some hydroxyl groups and high crystallinity of nanocrystals, as well as large difference in reactivity of hydroxyl groups (such as 10 times more reactive C6-OH than compared to C3-OH of CNs), it was assumed that the fraction of hydroxyl groups available on the surface for the chemical modification was only one third for nanocrystals [5]. An important parameter to characterize the extent or efficiency of reaction of PNs is the degree of substitution (DS). It indicates the average number of hydroxyl groups of anhydroglucose moiety that are substituted after the reaction. The DS value ranges between 0 and 3 and the maximum value of 3 indicates that all three hydroxyl groups are substituted.

Another issue that should be emphasized is the solvent medium used for the reaction of PNs. Most modification reactions are performed with a suspension of PNs in water or common organic solvents by heterogeneous reaction. Only a few solvent systems, such as ionic liquids [6] or alkali/urea solution [7], can be used to completely dissolve cellulose or chitin to induce a homogeneous reaction. However, for these solvents, some drawbacks exist, such as the high cost or uncontrollable degradation resulting from an undefined mechanism.

3.2.2
Surface Groups Originating from Various Extraction Methods

The main process for the isolation of PNs from natural polysaccharide is based on acid hydrolysis. Disordered or paracrystalline regions of polysaccharide are preferentially hydrolyzed, whereas crystalline regions that have a higher resistance to acid attack remain intact. The surface chemistry of PNs, especially surface groups, is governed by the type of acid used for the hydrolysis procedure. Considering the preparation of CNs as an example, Figure 3.1 shows the different surface groups on CNs provided by various extraction methods. Hydrolysis of cellulose with hydrochloric acid preserves the hydroxyl groups of the native fibers but leads to less stable aqueous suspensions [8]. With a combination of TEMPO (2,2,6,6-tetramethylpiperidine-1-oxyl) and hypochlorous acid, surface hydroxyl groups of CNs can be effectively transformed into carboxyl groups, which may be useful in realizing the subsequent reaction during the surface modification. Moreover, an acid mixture composed of hydrochloric and an organic acid (acetic acid) was used to prepare CNs through hydrolysis and modification in a single-step process [9]. The CNs obtained directly bear hydrophobic acetyl groups on the surface.

Sulfuric acid has been more extensively used for the hydrolysis of PNs (including CNs, SNs, and ChW derived from various natural materials) since Marchessault *et al.* first applied it to extract cellulose crystallites in 1959 [10]. When sulfuric acid is used as the hydrolyzing agent, it reacts with the surface hydroxyl groups on PNs to yield charged surface sulfate esters that promote dispersion of nanocrystals in water [11]. The concentration of surface sulfate moieties on the surface of CNs is

very low, and it was determined by sulfur elemental analyses to be only 0.85, 0.76, and 0.80% on dry matter for sisal, ramie, and cotton CNs, respectively [12]. However, the introduction of these charged sulfate groups induces thermal degradation of nanocrystals and compromises the thermostability of ensuing composites [13]. Therefore, the treatment of desulfation for the removal of sulfate groups on the surface of CNs was proposed [14]. Solvolytic desulfation of H_2SO_4-hydrolyzed CNs in DMSO (dimethyl sulfoxide) via a pyridinium salt produced nanocrystals with virtually no sulfate groups on the surface and slightly increased the crystallite dimension of CNs. Under the same condition of sulfuric acid hydrolysis, Thielemans *et al.* detected the presence of adsorbed low molecular weight organic compounds on the surface of the nanocrystals during the extraction process, which can block the available reactive sites [15]. It was reported that Soxhlet extraction treatment using ethanol was effective in removing the adsorbed species and promoting improved reproducibility of surface modification reactions.

With some mild reactions on the surface of PNs, hydroxyl groups can be converted to active amino groups ($-NH_2$) [16], mercapto groups (–SH) [17], and carboxyl groups (–COOH) (discussed in Section 3.5.2) without destruction of the original crystalline property.

3.3
Approaches and Strategies for Surface Modification

3.3.1
Purpose and Challenge of Surface Modification

Efficiency of nanofiller dispersion in a continuous matrix and adequacy of nanofiller–matrix interfacial interactions are widely known to critically affect material physical and mechanical properties. Hydroxyl groups present in the native polysaccharide and sulfate ester units introduced during hydrolysis with sulfuric acid both contribute to the hydrophilic character of PNs. In comparison with the weak dispersibility of neutral nanocrystals obtained by HCl hydrolysis, PNs extracted with sulfuric acid hydrolysis show a good dispersibility level in aqueous-based mixtures and in several organic solvents with high dielectric constants, such as dimethylformamide (DMF), DMSO, and ethylene glycol. It was shown that in these solvents, such as DMF with N atom in the structure, the interchain bonding in PNs is weakened, allowing the formation of a new hydrogen bond structure, such as O–H···N between the hydroxyl groups on the PNs and the N atom of the solvent molecules [18]. However, owing to the electrostatic character and high ionic strength of PNs, it is difficult to achieve a good dispersion level of PNs in most common non-water organic solvents or nonpolar polymeric matrices. The reasons stem primarily from the inefficient electrostatic repulsion and establishment of strong hydrogen bonds between nanocrystals, which induces the rapid aggregation or flocculation of the colloidal suspension in highly hydrophobic media [10]. An experiment was conducted on

freeze-dried CN samples, which can be homogeneously dispersed by sonication in DMF. The addition of a small amount of water to DMF led to the aggregation of nanoparticles [19].

To prevent self-aggregation (sometimes referred to as hornification) and promote efficient dispersion in non-aqueous media, the surface of PNs can be modified with hydrophobic compounds using covalent or non-covalent coupling techniques. Specific approaches and strategies of modification are described in the next section. The purpose of the modification of PNs consists in reducing the surface energy and improving the degree of dispersion by transforming the polar hydroxyl groups present at the surface of the nanocrystals into moieties capable of enhancing interactions with nonpolar polymers. All modifications of PNs can be conducted mainly to (i) introduce stable negative or positive electrostatic charges on the surface of PNs to obtain better dispersion; (ii) tune the surface energy characteristics of PNs to improve compatibility, especially when used in conjunction with nonpolar or hydrophobic matrices in nanocomposites; and (iii) tailor the nanoparticles to impart specific functional groups on PNs for advanced functional nanomaterials. The main challenge for surface modification of PNs is to choose a reagent and reaction medium that enable modification of PNs in such a way that it only changes the surface of CNs, while preserving the original morphology to avoid any undesired bulk changes [20] and polymorphic conversion, and to maintain the integrity of the crystal [21]. In addition, it should be noted that a potential drawback of surface modification in some systems is the possibility that the distinctive properties of PNs may be lost on modification. For example, mechanical properties could be compromised by surface chemical modification of ChW to reinforce the NR (natural rubber) matrix as a result of the disruption of the three-dimensional nanocrystal network [22].

3.3.2
Comparison of Different Approaches and Strategies of Surface Modification

Surface modification of PNs can be achieved by attaching small molecules or polymers via covalent bonds or physical interactions. A wide variety of surface modification techniques can be conducted on the surface of PNs, including physical absorption of surfactants, chemical derivatization of coupling hydrophobic small molecules, or chemical grafting of polymeric chains and advanced functional molecules (as shown in Figure 3.2). These modification methods have generally been borrowed from larger pulp and paper processes, and rely on the surface functionality such as hydroxyl groups in native polysaccharide or on functionality derived from synthesis of the nanoparticles as a "handle" for modification [23]. Among these methods, physical absorption of surfactant or polymer coating, a convenient operation and procedure, is the simplest method in comparison with chemical modification. However, this method was developed for improving dispersibility of PNs in organic solvents and is not expected to be effective in composite applications because of the lack of covalent bonding between the hydroxyl groups from PNs and alkyl groups from surfactants.
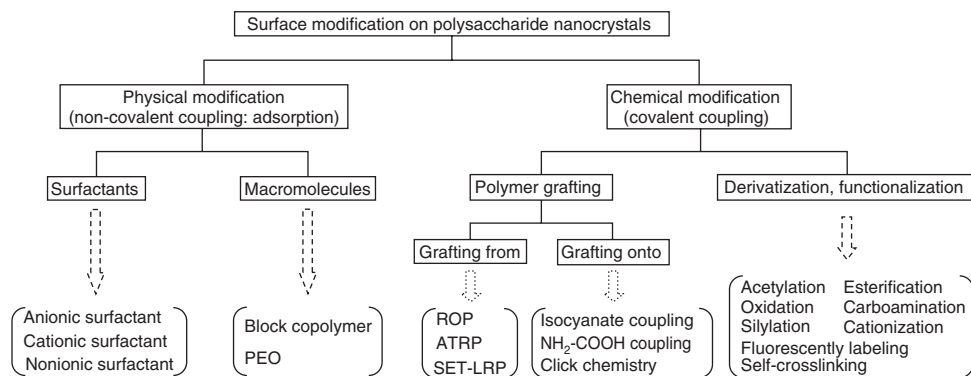
Figure 3.2 Diverse surface modifications on polysaccharide nanocrystals.

In the field of chemical modification, derivatization is the most effective means to change the surface properties of PNs, such as hydrophilicity, surface charge, and density, which can be carried out with covalent conjunction between PNs and hydrophobic small molecules. In spite of its easy achievement, more attention should be paid to the degree of derivatization on PNs to avoid the destruction of the substrate if the reaction is pushed too far. Modification consisting of the introduction of functional molecules on PNs is a rather new field that depends largely on the unique property of PNs. Most studies were performed on CNs, which have a more stable structure than other PNs. Some novel techniques such as "click chemistry" have been used in the functional modification on CNs, which endows nanocrystals with advanced functions, such as fluorescent labeling, gene delivery, or photobactericidal effect.

Another chemical modification, consisting of polymer grafting, can be realized using two strategies, namely "grafting onto" and "grafting from." The "grafting onto" approach involves attachment of pre-synthesized polymer chains, carrying reactive end groups, to the surface of PNs, whereas the "grafting from" approach consists in mixing nanocrystals with a monomer and an initiator agent to induce the polymerization of the monomer from the nanoparticle surface. The schematic representation of diverse approaches of modification of PNs is shown in Figure 3.3. In the first approach, a common "carboxylation–amidation reaction" consisting in creating a covalent amide bond between a primary amine-terminated polymer and carboxylated PNs by COOH–NH$_2$ coupling and an "isocyanate-mediated reaction" depending on the different reactivity of isocyanate groups are widely used to graft polymeric chains onto the surface of PNs. The grafted polymers can be fully characterized before grafting on the surface, offering the possibility of controlling the properties of the resulting material. However, one cannot expect high grafting densities because of steric hindrance and blocking of reactive sites by the already grafted polymer chains using the "grafting onto" method. "Grafting from" has been proved to be a very effective approach to creating high grafting densities and well-controlled polymer structures on different kinds of surfaces. Surface-initiated ring-opening polymerization (ROP) and living radical polymerization
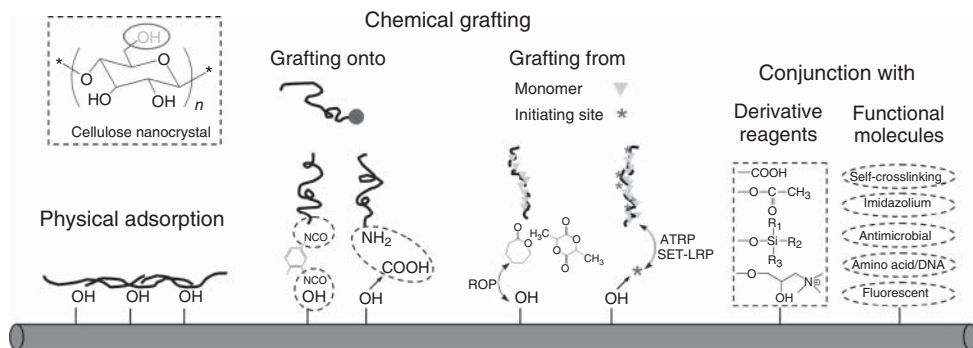
Figure 3.3 Comparison of different modifications on polysaccharide nanocrystals.

(LRP) are two methods that can be used for the strategy of "grafting from." In ROP, the hydroxyl groups on the surface of PNs act as initiator and the ratio of monomer (such as ε-caprolactone (CL) or L-lactide) to initiating groups determines the DP of the grafted polymer chains. As for LRP modification, such as atom transfer radical polymerization (ATRP) and single electron transfer-living radical polymerization (SET-LR), two steps are involved, which are the initial formation of initiating sites for LRP with the immobilized initiator on PNs and the reaction of the initiator-modified nanoparticles with a monomer to induce the polymerization. Because of the lower viscosity of the medium and limitation of steric hindrance, this strategy has proved to be a very effective way to creating high grafting densities on the surface. However, the drawback of this approach is the difficulty in precisely determining and characterizing the molecular weight of grafted polymers. To solve this problem, some studies recently reported some methods of cleaving the polymeric chains from the cellulose backbone, such as dissolving PS-grafted (polystyrene) CNs [24] or PDMAEMA-grafted (poly(*N,N*-dime-thylaminoethyl methacrylate)) CNs [25] in acidic condition with acid hydrolysis or saponification treatment to cleave grafted PNiPAAm (poly(*N*-isopropylacrylamide)) polymeric chains on the surface of CNs [26].

Recently, some new strategies for the surface modification on PNs has been proposed, such as grafting amine compounds or drug molecules to CNs through the change of glucose structure with periodate oxidation, while keeping the crystalline integrality of nanocrystals [27, 28].

It should be pointed out that dozens of reviews and book chapters have described the surface modification of PNs (especially for chemical modification of CNs), and almost all of them introduced this topic in the catalog of modification methods. In this chapter, surface modification of PNs is discussed according to the category of modified groups. Under this framework, comparison of the influence and effect among various modified groups or molecules is analyzed in detail.

3.4
Adsorption of Surfactant

In order to obtain non-flocculated dispersion of PNs in nonpolar solvents, the easiest approach is to coat the surface of nanocrystals with surfactants having polar heads and long hydrophobic tails. With the simple mixing in solvent, non-covalent physical absorption of surfactant on PNs will be a much more controllable and easily operated process than delicate chemical modification. Surfactants are usually amphiphilic organic compounds, containing both the water-insoluble (oil soluble) component for hydrophobic groups (so-called tails) and the water-soluble component for hydrophilic groups (so-called heads). The hydrophilic end of the surfactant molecule may adsorb on the surface of PNs, whereas the hydrophobic end may extend out providing a nonpolar surface and lowering the surface tension of the nanoparticles. With this process, the ensuing surfactant-coated nanoparticles display reduced surface energy and improved dispersibility or compatibility with nonpolar organic media.

3.4.1
Anionic Surfactant

Since the surfactant Beycostat NA (BNA) was applied as stabilizing agent to prepare stable suspension of CNs in nonpolar solvents [29], there were more studies focusing on the influence and properties of BNA-modified CNs. BNA is a commercial anionic surfactant, and its chemical structure involves a phosphoric ester of polyoxyethylene (PEO) nonylphenyl ether. It was shown that the mixing ratio of surfactant and CNs should be cautiously controlled. A low surfactant level is not sufficient to obtain a good dispersion in organic solvents, whereas too high a level may induce self-aggregation of nanoparticles during the mixing process. Generally, the initial suspension is mixed with the surfactant in the proportion of 4/1, 2/1, or 1/1 (w/w) of BNA to CNs. It was shown that the ratio of adsorbed surfactant on the surface of CNs was 0.7 for cotton CNs and 1.5 for tunicin CNs. Stable dispersions of BNA-adsorbed CNs in toluene or cyclohexane can be obtained, and suspensions with modified CNs exhibit strong birefringence, mixed structure of isotropic and anisotropic phases, and chiral-nematic structure [29]. Meanwhile, using small angle neutron scattering, it was observed that a surfactant layer 15 Å thick coated the surface of CNs, which indicated the effective adsorption of BNA and folded conformation of the surfactant molecule on the surface of CNs [30]. In further studies, using the same preparation method, the properties of BNA-adsorbed CNs, such as morphology, and self-assembling and chiral nematic property, were investigated. Various techniques including atomic force microscopy (AFM), bright-field transmission electron microscopy (TEM), and field emission scanning electron microscopy (FESEM) were used to observe the morphology and dimensions of CNs [31]. The chiral nematic ordering of BNA-adsorbed CNs suspensions in cyclohexane with different concentrations was investigated [32]. When using these surfactant modified CNs as nanofiller to reinforce polymeric

matrix (such as PLA (poly (lactic acid)) or PP (polypropylene)), the presence of surfactant on the surface of nanocrystals was found to facilitate the dispersion of the nanofiller in the matrix and improve the nucleation effect of the matrix for the ensuing materials [33–35].

3.4.2
Cationic Surfactant

Unlike the hydrophilic–hydrophobic mechanism for the absorption of common surfactants, cationic surfactants (such as dioctadecylammonium bromide: DODA-Br) can be adsorbed on the surface of PNs through strong electrostatic interactions between the negative charge of sulfate groups on CNs generated from sulfuric acid hydrolysis and cationic charge of the surfactant. DODA (dioctade-cylammonium) is a cationic surfactant that has been widely used in Langmuir films to investigate the adsorption and binding processes involving anionic polyelectrolytes at the air/water interface. Rojas *et al.* applied cationic surfactant DODA to modify the surface of CNs, and used this surfactant as the carrier of CN nanoparticles [12]. With the Langmuir–Schaefer (LS) technique, the precursor CNs–DODA complexes were subsequently used to prepare CN monolayer films. Owing to the low concentration of surface sulfate moiety on the surface of CNs (<1%), the weight ratio of CNs to DODA was much higher than for other CN/surfactant systems, which was 125, 250, 375, or 500 (wt(CNs)/wt(DODA)). When transferring the CN–DODA complexes from the air/liquid interface to the surface of a hydrophobic solid substrate (alkanethiol-modified gold), the adhesion between the DODA molecule (carrying the CNs) and the alkyl chains coating the gold surface was expected to have been developed from strong, long-range hydrophobic interactions when they were in contact, which was the basis of subsequent LS process.

3.4.3
Nonionic Surfactant

A nonionic surfactant, such as sorbitan monostearate, was also used to improve the dispersion of CNs in organic solvents and to prevent self-aggregation [36]. From the results of turbidity experiment performed on 0.3 and 0.6 wt% CN suspension in THF (tetrahydrofuran), it was reported that surfactant concentration determined the stability of modified CNs in the solvent. For high concentrations of surfactant, the surfactant molecules self-aggregate and probably do not adhere to the surface of CNs, which probably caused the weak stress transfer effect when using CNs as a reinforcing filler. In another study, the same absorbed surfactant, that is, nonionic surfactant sorbitan monostearate, was adsorbed to improve the dispersion of CNs in a PS matrix and to produce bead-free electrospun composite webs [37]. As a small surfactant molecule, *tert*-butanol was also adsorbed on the surface of CNs [38]. It was reported that *tert*-butanol was able to limit the aggregation of CNs during the freeze-drying process and promote more loose conditions

in comparison with pristine CNs. Meanwhile, *tert*-butanol-modified CNs showed flow birefringence in chloroform, and exhibited homogeneous dispersion in PLA matrix.

3.5
Hydrophobic Groups Resulting from Chemical Derivatization

As mentioned in Section 3.2.2, because of their high surface area and hydrophilic nature, PN nanoparticles tend to seriously aggregate through hydrogen bonding. For instance, stable CN suspensions can only be obtained in water and polar aprotic solvents such as DMF or DMSO [19, 39]. However, PNs cannot be easily dispersed in apolar solvents and are poorly compatible with hydrophobic matrices. The inefficient reinforcement resulting from poor dispersion induced by poor interfacial interaction between pristine PNs and nonpolar polymer matrices makes imperative the modification of surface properties of PNs. Considering various chemical modifications on PNs, derivatization is one of the simplest and immediate approaches that led to the use of commercial cellulose derivatives as the reference (such as cellulose acetate). Chemical derivatization is mainly divided into five categories – acetylation and esterification, oxidation, carboamination, silylation, and cationization.

3.5.1
Acetyl and Ester Groups with Acetylation and Esterification

Surface esterification is the most common method for chemical derivatization of PNs. It is a reaction that introduces an ester functional group COO on the surface of PNs by condensation of a carboxylic acid group COOH and an alcohol group OH. As one of the simplest methods of esterification, acetylation that introduces an acetyl group $COCH_3$ on the surface of PNs has been well studied generally using acid anhydrides as the acetylating agent. Modification by acetylation and esterification of PNs from various sources is summarized in Table 3.1.

In 1995, Sassi and Chanzy first investigated the effect and influence of surface acetylation of tunicin nanocrystals, especially focusing on the change of morphology, crystallinity, and structure [40]. It was shown that during the process of modification, there was a reduction in the diameter of CNs while their length was reduced to a lower extent. It was supposed that nanocrystals break down laterally but not longitudinally upon acetylation (peeling effect). In a further study, the relative reactivity of the I_α and I_β phases of cellulose toward partial acetylation was investigated. It was shown that the reactivity of the I_α phase was substantially higher than that of the corresponding I_β component at the beginning of acetylation [43]. Similar results were reported in the study of vinyl acetate (VA) acetylation of CNs with potassium carbonate as the catalyst. The degree of acetylation of CNs can be monitored with the reaction time. The nanostructure of CNs, such as their dimensions and crystallinity, was preserved during the modification only when

Table 3.1 Acetylation and esterification on polysaccharide nanocrystals.

Types	Sources	Reagents	DS	Solvents for stable dispersion	Matrices	References
CNs	Tunicin	AA in acetic acid	0.2, 0.4, 0.8, 2.3	—	—	[40]
		iso-ODSA or n-TDSA in water	0.0165	Various apolar solvents[a]	PS	[41]
	Valonia cell wall	Palmitoyl chloride	0.15–1.17	—	—	[42]
	MCC	AA in acetic acid	0.15, 0.3, 0.9	—	—	[40, 43]
		AA in isopropyl alcohol	0.031	Dilute acetic acid	—	[44]
		VA/K$_2$CO$_3$ in DMF	—	THF	—	[45]
		Tos-Cl/pyridine	—	Chloroform	PHB	[46]
	Cotton linter	AA in pyridine	—	Methylene chloride, acetone, toluene, THF, DMF	PLA	[47]
		AA in pyridine	—	THF	PU	[48]
		Castor oil/TDI	0.215	Ethyl ether, toluene, acetone, DMF, ethanol, water, THF	—	[49]
		Acetic/hydrochloric acid or butyric/hydrochloric acid	0.09–1.59	EA, toluene	—	[9, 50]
	Ramie fiber	Organic acid chloride/TEA in toluene[b]	0.68, 0.32, 0.31	—	LDPE	[51]
	Grass *Zoysia*	MA/diisopropyl amine	—	Chloroform	PLA	[52]
	Eucalyptus wood pulp	MAC/TEA	—	EA, DMF, THF	CAB	[53]
		MAC/TEA	0.15, 0.25	EA, DMF, THF, water, acetone	Chitosan	[54]
	Wood pulp filter paper	Acetic acid	0.22–0.47	—	—	[55]
	Whatman filter paper	10-Undecenoyl chloride/DMAP/pyridine/ acetonitrile	—	THF	PBD	[56]

(continued overleaf)

Table 3.1 (Continued)

Types	Sources	Reagents	DS	Solvents for stable dispersion	Matrices	References
SNs	Corn starch	AA/MSA in glacial acetic acid	0.16, 0.99, 2.45	DMF, acetone, CTC, toluene	—	[57]
	Waxy maize starch	ASA/DAP in toluene	—	Methylene chloride	—	[4]
		Stearic acid chloride/TEA in MEK	—	—	—	[58]
		Fatty acid chloride in water[c]	0.13, 0.09, 0.08	Chloroform	—	[59]
ChW	Crab shell	ASA/DAP in dioxane	—	Toluene	NR	[22]
		AA in pyridine	—	Dichloromethane	PLA	[60]

CTC, carbon tetrachloride; LDPE, low density polyethylene; MA, maleic anhydride; MEK, methyl ethyl ketone; MAC, methyl adipoyl chloride; MSA, methanesulphonic acid; PBD, poly(butadiene); and PU, polyurethane.

a) Acetylated CNs in this work can be well dispersed in various apolar solvents including DMAc (*N*,*N*-dimethylacetamide), methanol, ethanol, acetone, 1-butanol, dichloroethane, dichloromethane, THF, chloroform, toluene, and 1,4-dioxane.

b) Three organic acid chlorides used in this work were hexanoyl chloride (C6), lauroyl chloride (C12), and stearoyl chloride (C18).

c) Three fatty acid chlorides were synthesized with octanoic acid (C8), nonanoic acid (C9), and decanoic acid (C10) with thionyl chloride.

short reaction times were used (less than 2 h). With increasing reaction time, the inner crystallites were gradually attacked by the VA molecules, leading to higher substitution, and also to the erosion of the CNs structure and loss of crystallinity [45]. Surface acetylation of CNs was also performed with *iso*-octadecenyl succinic anhydride (*iso*-ODSA) or *n*-tetradecenyl succinic anhydride (*n*-TDSA), which are used as sizing agents in papermaking [41]. It is interesting that because of surface acylation, modified CNs can readily disperse in 11 solvents of medium or low polarity (as listed in footnote in Table 3.1). A more common acetylating agent, acetic anhydride, was widely used in the acetylation of CNs and SNs. Lin *et al.* [47] performed this reaction in anhydrous pyridine, and used the acetylated CNs to reinforce PLA. The moderate substitution of hydroxyl groups with acetyl groups on the surface of CNs improved the dispersion in organic solvents and significantly reduced the polarity, which was beneficial for the interfacial adhesion between filler and matrix. A similar experiment was conducted for the modification of SNs. However, despite much improved dispersibility in common organic solvents, acetylation caused the change of platelet-like SNs to spherical shape and transformation of crystalline structure from A-type to V-type [57]. To avoid complex synthetic routes, Braun and Dorgan reported a single-step process with simultaneous hydrolysis of amorphous cellulose chains and acetylation of accessible hydroxyl groups on the surface of CNs [9]. The reaction was carried out in an acid mixture composed of hydrochloric acid and an organic acid (acetic or butyric acid). When the cellulose suspension was heated to 105 °C, the hydronium ions resulting from the hydrochloric acid dissociation hydrolyzed amorphous cellulose domains and also catalyzed the acetylation of hydroxyl groups on the exposed cellulose chains. More than half of the hydroxyl groups located on the CN surface were substituted under this reaction condition, and acetylated CNs with narrower diameter polydispersity indices as well as good dispersion in ethyl acetate (EA) and toluene were obtained.

Apart from acetylating agents, other chemicals, such as organic acid chloride and alkenyl succinic anhydride (ASA), were also applied for the surface esterification of PNs. In the structure of the former reagent, special acid chloride groups (COCl) can react with the hydroxyl groups via halide substitution. Triethylamine (TEA) is commonly used as the catalyst to remove the byproduct of hydrogen chloride in this reaction. Thielemans *et al.* [58] first used stearic acid chloride to modify the surface of SNs. Interestingly, after the modification the polar surface energy (γ^{P}) (contribution of polar component to the surface energy) of modified SNs decreased to zero, which was attributed to efficient surface coverage by the stearate aliphatic chain ends on SNs. Meanwhile, a study using X-ray diffraction showed extensive crystallization of the stearate moieties grafted onto SN, forming a crystalline hydrophobic shell around the hydrophilic surface of SNs. These property changes induced by modification had a large effect on the individualization of nanocrystals because of reduced hydrogen bonding and polar interactions between the individual particles. In a further study, three organic acid chlorides with different lengths of aliphatic chains (C6, C12, C18) were used to chemically modify the surface of CNs with a similar esterification reaction [51].

It was reported that the polar character of modified CNs decreased with increase in aliphatic acid length, which was shown through the gradual decrease of γ^p for the three modified CNs (12.5, 2.9, 0.2 mJ m^{-2} for C6-CNs, C12-CNs, C18-CNs, respectively, in comparison with 35.2 mJ m^{-2} for unmodified CNs). The change from polar to nonpolar nature of the modified CNs further affected their interactions with matrix in the ensuing nanocomposites, which exhibited increased homogeneity of the material when increasing the length of the grafted chains. Covalently bonded aliphatic acid chains were able to crystallize at the surface of CNs when using stearoyl chloride of the longest carbon chains (C18). To avoid the use of organic solvents such as toluene in the modification of PNs with organic acid chloride, a reaction of the esterification of SNs in aqueous medium was conducted using octanoyl (C8), nonanoyl (C9), and decanoyl chloride (C10) [59]. By introducing fatty acids, modified SNs possessed higher affinity toward organic solvents (chloroform) rather than aqueous media, and showed higher thermal stability.

Esterification was also carried out through ring-opening reaction of small molecules such as ASA as the esterifiable agent for both SNs and ChW surface modifications. Both studies were conducted in organic solvent to avoid hydrolysis of ASA with DAP (dimethyl amino pyridine) as catalyst. A stable suspension of ASA-modified ChW was obtained in toluene, which was used to reinforce NR with improved dispersion within the matrix [22]. In another study, the property change of ASA-modified SNs was investigated with a smart wettability experiment, in which pristine and modified SNs were ploughed into an immiscible solvent system consisting of both water and methylene chloride [4]. This solvent system with two different polarities and densities gave rise to two phases, the upper one corresponding to the water phase ($d = 1$) and the lower one to the organic phase ($d = 1.32$). By adding ASA-modified SNs in this solvent system, the modified nanoparticles migrated toward the methylene chloride phase, whereas unmodified SNs migrated in the water phase, which suggested the lower polar nature of the nanocrystal surface after chemical modification. In addition, the platelet shape of modified SNs became ambiguous after surface chemical modification with ASA, which was attributed to being closely surrounded by ASA.

To realize the solvent-free derivatization of CNs, a novel method of gas-phase surface esterification was achieved on the surface of CNs with palmitoyl chloride [42]. The reaction between the solid-state cellulosic substrate and palmitoyl chloride was carried out in a vacuum oven at controlled temperature and pressure. As the temperature was raised, a fraction of the reagent, which was in large excess, evaporated and diffused through the cellulosic substrate. During its diffusion, the acid chloride reacted with the hydroxyl groups of CNs to form hydrophobic ester bonds, while liberating hydrogen chloride. In a subsequent step, further gaseous palmitoyl chloride can readily diffuse in the newly formed layer of cellulose palmitate and thus reach the underlying layer of unreacted chains, which in turn become esterified, leading to further esterification. The esterification proceeded essentially from the skin to the core of nanocrystals with partial or full esterification. The pressure was controlled with a continuous slow nitrogen stream, and was also used

to eliminate the hydrogen chloride formed. By changing the pressure and reaction temperature, the DS of CNs can be tuned, and esterified CNs with different hydrophobic surfaces obtained with minimum environmental impact.

3.5.2
Carboxyl Groups Resulting from TEMPO-Mediated Oxidation

Since de Nooy *et al.* [61] first applied TEMPO-mediated oxidation to native polysaccharide such as starch, amylodextrin, and pullulan for regioselective conversion of C6 primary hydroxyls to carboxylate groups in 1995, this technique has been widely used in the derivatization of natural polymers, especially cellulose. In general, there are three targets for the utilization of TEMPO-mediated oxidation of polysaccharides. The first aim is the change of surface properties of PNs, which is described here. The second one is the transformation of surface hydroxyl groups to carboxyl groups, which can be used for subsequent introduction of functional molecules or for grafting polymeric chains with carboxylation–amidation reaction. For example, it was reported that the new carboxyl groups on the surface of CNs induced by chemical oxidization can provide the possibility of participating in the construction of an alginate-based sponge's structure and played a fundamental role in the structural and mechanical stability of the ensuing sponges [62]. This issue is discussed in the following sections. The third target consists in using TEMPO-mediated oxidation for the conversion and preparation of native cellulose to micro- or nanofibers coupled with low-speed mechanical treatment. In this reaction, together with the oxidation of TEMPO radical as a catalyst, the chemical reaction helps in degrading the material through successive mild disintegration in water [63]. In view of the topic of this chapter, this section focuses on the process, degree, and influence on surface properties induced by TEMPO-mediated oxidation of PNs.

TEMPO and its analogs are water soluble, commercially available, and stable nitroxyl radicals. With the TEMPO catalytic oxidation, the C6 primary hydroxyls of cellulose are expected to be oxidized to C6 carboxylate groups by TEMPO/NaBr/NaClO or TEMPO/NaClO/NaClO$_2$ oxidation systems in water at pH 10–11 [64, 65]. The oxidation process can be monitored from the pattern of aqueous NaOH consumption, which is continuously added to the reaction mixture to maintain the pH at 10 during oxidation. The oxidized products have almost homogeneous chemical structures of sodium $(1 \rightarrow 4)$-β-D-poly-glucuronate or sodium salt of cellouronic acid consisting of D-glucuronosyl units alone. Hence, the C6 primary hydroxyls of cellulose can be entirely and selectively converted to C6 sodium carboxyl groups by TEMPO-mediated oxidation [66].

Araki *et al.* first applied TEMPO-mediated oxidation to introduce carboxyl groups and then grafted PEG (poly(ethylene glycol)) chains onto the surface of CNs. It was a pity that this study only focused on the effect of grafting polymers, and on changes in dispersion state and fingerprint texture of oxidized CNs [67]. Montanari *et al.* systematically investigated the degree and size influence of the TEMPO-mediated oxidation of cotton linter CNs. The degree of oxidation (DO)
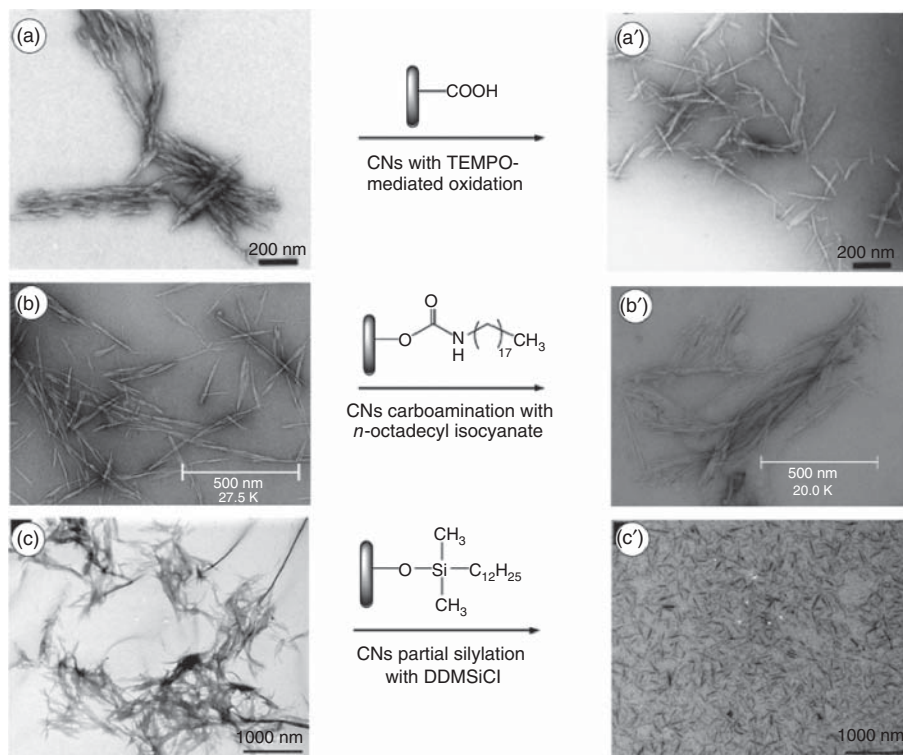
Figure 3.4 (a,a′) TEM images of cotton CNs and oxidized CNs. Reproduced with permission from Ref. [68] Copyright © 2005, American Chemical Society. (b,b′) TEM images of sisal CNs and carboaminated CNs. Reproduced with permission from Ref. [71] Copyright © 2010, American Chemical Society. (c,c′) TEM images of cotton CNs and silylated CNs dispersed in THF. Reproduced with permission from Ref. [72] Copyright © 2010, Elsevier.

was determined by conductometric titration as 0.24. During TEMPO-mediated oxidation, a decrease of the crystal size occurred, and the introduction of negative charges on the surface of the crystalline domains induced a better individualization and dispersion of the crystallites [68], as shown in Figure 3.4a,a′. In another study, the maximum degree of oxidation (DO_{max}) of CNs was calculated as 0.095 (roughly 0.1) with a simplified rectangle model. With the change of NaClO/anhydroglucose unit ratio, the DO of CNs varied from partial oxidation (DO = 0.029) to nearly complete oxidation (DO = 0.097). Oxidization provided a number of negative charges on the surface of CNs, and as a consequence modified CNs were easily dispersible in water as birefringent non-flocculated suspensions [69]. The method of TEMPO-mediated oxidation can be directly used for the preparation of oxidized ChW including the hydrolysis of native chitin. It was shown that the amount of NaClO added to native chitin/water mixture might be the key factor for controlling the amount and position of carboxylate groups

formed on ChW. When 5.0 mmol of NaClO per gram of chitin was used, the weight percentage of the water-insoluble fraction in the TEMPO-oxidized chitin (crystalline chitin) was preserved as high as 90%, and the carboxyl content reached 0.48 mmol g^{-1}. The oxidized ChW obtained with this one-step method mostly exhibited individualization and homogeneous dispersion in water after ultrasonic treatment [70].

3.5.3
Derivatization with Isocyanate Carboamination

Through the reaction between the isocyano group and the hydroxyl group, isocyanate possessing a single isocyano group can be coupled onto the surface of PNs. Chemical modification with isocyanate as coupling agent presents some advantages such as (i) relatively high reaction rate; (ii) absence of secondary products; and (iii) chemical stability of urethane moiety [73]. Isocyanates used for the derivatization modification of PNs are mainly phenyl isocyanate (PI), isopropenyl-α,α′-dimethylbenzyl isocyanate (TMI), and *n*-octadecyl isocyanate (C$_{18}$H$_{37}$NCO). The former reagents (PI and TMI) are isocyanates bearing a rigid phenyl in their chemical structure. The reactivity of isocyanate with OH group is higher than that of anhydride; on the other hand, the aromatic NCO group is more reactive than the aliphatic one. It was reported that the modification on ChW with PI or TMI significantly improved the dispersion of nanocrystals in toluene [22]. When applying PI to modify the surface of SNs, it was shown that the modified PI molecules induced a partial solubilization of starch molecules, which caused a slight decrease in the size of the nanoparticles compared with unmodified SNs. Meanwhile, chemical modification using PI as a coupling agent to introduce hydrophobic phenyl on the surface of SNs effectively reduced the polar surface energy and improved dispersibility in organic solvents (dichloromethane) [4]. For the modification of CNs using long-chain *n*-octadecyl isocyanate, Siqueira *et al.* reported a new treatment involving an *in situ* solvent exchange procedure before the chemical reaction, which avoided the problem of CN dispersion in the reaction solvent. It was shown that a DS of 0.07 can be achieved (as shown in Figure 3.4b,b′) and that chemical modification improved the dispersion of CNs in dichloromethane [5, 71]. Recently, a new isocyanate agent, UPy-NCO (2-(6-isocyanatohexylaminocarbonyl amino)-6-methyl-4[1*H*]pyrimidinone), was used in the surface modification of CNs, which will provide active UPy motifs for further reactions [74].

3.5.4
Silyl Groups Resulting from Silylation

Silylation consists in the introduction of substituted silyl groups on the surface of PNs. The chemical structure of organosilanes (R$_1$R$_2$R$_3$SiX) presents two kinds of functional groups, namely, hydrophobic aliphatic groups with different lengths of carbon chains (R$_1$R$_2$R$_3$) and functional groups (X) for coupling with the hydroxyl

groups of PNs. In the structure of most silylating agents used for the derivatization of PNs, R_1 and R_3 are generally methoxy, and R_2 varies from 1 carbon chains to 12 carbon chains (CH_3, i-C_3H_7, n-C_4H_9, n-C_8H_{17}, n-$C_{12}H_{25}$). X is a hydrolyzable group, typically alkoxy, acyloxy, amine, or more commonly chlorine. During the silylation reaction of PNs, the bond between X and the silicon atom in the coupling agent is replaced by the bond between the polysaccharide substrate and the silicon atom, and provides the hydrophobic organosilane groups on the surface of PNs.

Trimethylsilylation was first applied to CNs derived from bacterial cellulose [75]. The topochemically trimethylsilylated derivatization of CNs reduced their hydrophilicity and improved their dispersion in acetone, and silylated CNs were used to reinforce cellulose acetate butyrate (CAB). However, the degree and mechanism of silylation of CNs were not investigated. Goussé *et al.* carefully studied the process of silylation modification of CNs and proposed a mechanism model to describe the influence of silylation on CN structure. Four alkyldimethylchlorosilane silylating agents (IPDMSiCl (isopropyldimethylchlorosilane), BDMSiCl (n-butyldimethylchlorosilane), ODMSiCl (n-octyldimethylchlorosilane), and DDMSiCl (n-dodecyldimethylchlorosilane)), with alkyl moieties ranging from isopropyl to n-butyl, n-octyl, and n-dodecyl, were used to prepare more stable silylated CNs [76]. It was shown that with a surface DS of the order of $0.6-1$, the nanocrystals retained their morphological integrity; owing to their surface silylation, they became readily dispersible in solvents of medium polarity such as acetone and THF. The resulting suspensions did not flocculate and appeared birefringent when viewed between cross polars. However, for surface DS higher than 1, the core of the nanocrystals became also silylated, leading to loss of their crystal character, and it was no longer possible to obtain birefringent suspensions. According to a report on this study, under low degree of silylation, just a few silyl groups are distributed randomly on the surface of CNs, which provides them the structural integrity but unchanged hydrophilic property. If too much of the silylating agent or too long a reaction time is used, excessive silylation breaks up the cellulose chains and causes the solubilization of CNs in the reaction medium. Therefore, silylated derivatization of CNs should be controlled in the moderate degree range to provide a sufficient number of silyl groups and confer a change on the hydrophobic surface but not induce the destruction of the original structure of CNs. With the same silylating agent DDMSiCl, Pei *et al.* [72] conducted partial silylation of cotton CNs in toluene, and used the modified CNs to reinforce PLA. Besides improved stability of silylated CNs when dispersed in organic solvents (as shown in Figure 3.4c,c′), the addition of surface silylated CNs in PLA also induced an increase in the crystallization rate of the matrix. It was shown that silane treatment of CNs improved nucleation efficiency and that silylated CNs can be used as biobased nucleating agent for PLA. The effect of methacryloxypropyltrimethoxysilane (MPS) as silylating agent on the surface modification of CNs was also investigated [77]. Recently, γ-methacryloxypropyl trimethoxy silane (A-174) as a new silane coupling agent for the surface silylation of CNs was reported. This special silylating agent can provide vinyl groups on the surface of CNs acting as the initiators for successive free radical polymerization [78].

3.5.5
Cationic Groups Resulting from Cationization

CNs prepared by hydrolysis of native cellulose with sulfuric acid bear negatively charged surface acid groups, which induce the electrostatic stabilization of nanocrystals in aqueous medium. Most attempts have focused on promoting the hydrophobic surface property of H_2SO_4-hydrolyzed CNs, such as the chemical derivatization discussed earlier or creating layer-by-layer (LBL) films between CNs and cationic matrices via electrostatic interactions between two layers, such as DODA, poly(diallyldimethylamonium chloride) (PDDA), polyethyleneimine (PEI), and so on. However, only a few studies were conducted on the surface cationic modification of CNs, such as through a reaction with epoxypropyltrimethylammonium chloride (EPTMAC) as the cationization agent [79]. Surface cationization of CNs with EPTMAC proceeds through the nucleophilic addition of the alkali-activated cellulose hydroxyl groups to the epoxy moiety of EPTMAC. The cationization process reversed the surface charge from -39 ± 3 mV before to $+30 \pm 5$ mV after treatment with EPTMAC, and led to a reduction in the total surface charge density from 0.41 to $0.26\,e\,nm^{-2}$. The modification also promoted the formation of stable dispersions, and cationized CNs were more spreadable than pristine CNs on flat mica surfaces. In addition, these cationic nanocrystals can form thixotropic gels and exhibit unexpected gelling and rheological properties, such as shear thinning. GTMAC (glycidyltrimethylammonium chloride) and quaternary ammonium salts were also reported to be used as cationic agents for surface cationization of CNs [80, 81]. Different from the common electrostatic adsorption method, a chemical grafting method was proposed to introduce cationic PEI polymers on the surface of CNs. The synthesis of PEI grafted CNs included three steps, which were surface modification of CNs using tosyl chloride, cationic ring opening grafting polymerization of 2-ethyl-2-oxazoline monomer with tosylated CNs as macroinitiators, and, finally, obtaining cationic PEI-modified CNs through hydrolysis in acidic condition [82].

3.6
Polymeric Chains from Physical Absorption or Chemical Grafting

As mentioned, the practical application of PNs faced many obstacles, mainly related to poor dispersibility in common nonpolar solvents and interfacial incompatibility between the hydrophobic components and hydrophilic PNs. To prevent aggregation and improve the compatibility of PNs in diverse matrices, polymer chain grafting seems to be of interest because the grafted polymer chains can act as compatibilizer, particularly when they are of the same nature as the matrix, which can improve interfacial adhesion and maximize compatibility between both components. On the other hand, grafting special polymers on PNs may endow these natural nanoparticles with advanced functional applications.

Polymer grafting can be accomplished by utilizing different approaches such as "grafting onto" or "grafting from" strategies. Polymer adsorption can also promote interfacial interactions with a polymeric matrix.

3.6.1
Hydrophilic Polymer

PNs are hydrophilic and therefore have limited ability to disperse in hydrophobic solvents and polymer matrices [83]. To restrain the coagulation of nanoparticles in polar solvents, the method of grafting or adsorption of hydrophilic polymers on the surface of PNs was proposed. This modification involves the steric colloidal stabilization of PN suspension, which results from the hindrance of direct contact between nanoparticles and therefore inhibition of suspension coagulation. As a promising candidate, PEG, a water-soluble polymer, consists of hydrophilic and flexible long chains. Four synthetic routes were proposed to introduce PEG (or PEO) on the surface of PNs, which were mainly based on the strategy of "grafting onto" and physical absorption, as shown in Figure 3.5. As mentioned in Section 3.3.2, one of the drawbacks of the "grafting onto" approach is the increase in the viscosity of the reaction medium, especially for polymeric chains with high molecular weight (M_n). Therefore, the M_ns of PEG grafted onto PNs in these systems were lower than $2500 \, \text{g mol}^{-1}$. In 2001, Araki *et al.* first reported the steric stabilization of CN suspensions by PEG
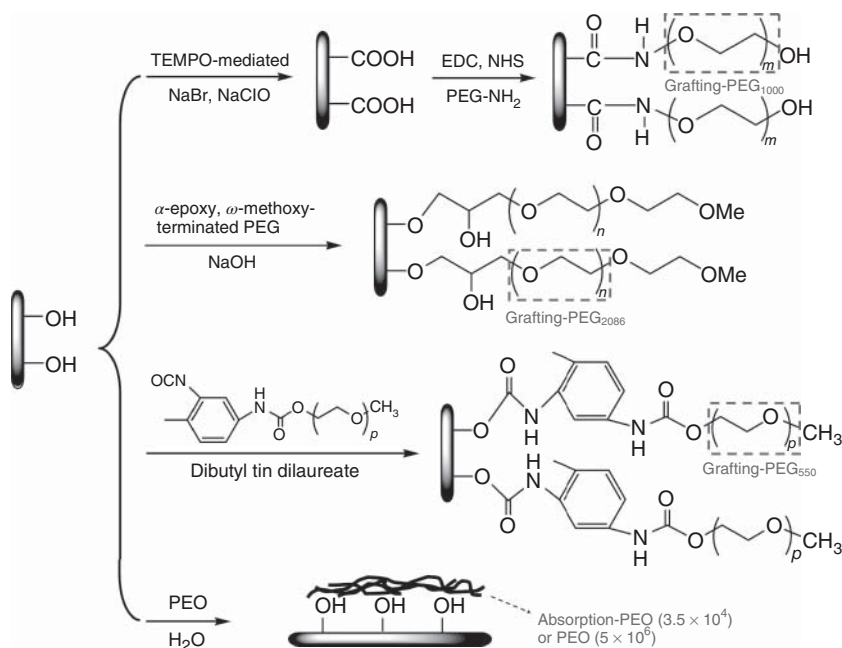
Figure 3.5 Different methods of introducing PEG chains on the surface of CN.

grafting using a carboxylation–amidation procedure. By grafting PEG in a ratio of 0.2–0.3 g/g of cellulose on CN, the modified CNs showed drastically enhanced dispersion stability and ability to redisperse into either water or chloroform from the freeze-dried state [67]. However, owing to uncompleted reaction between surface carboxyl groups and amino groups (only 20–30% carboxyl consumption in the amidation step), the improved stability effect induced by the modification could not exactly be proved. For these reasons, Kloser and Gray proposed an alkaline epoxide ring-opening method for the surface grafting of PEG onto CNs. Desulfation of sulfuric acid-prepared nanocrystals was carried out and the nanoparticles were modified with α-epoxy, ω-methoxy-terminated PEG under alkaline conditions. Aqueous dispersions of PEG-grafted CNs were stable over time and exhibited similar phase behavior as the initial electrostatically stabilized CN suspensions, with the onset of chiral nematic phase separation occurring at 5% w/w [84]. Using the end hydroxyl groups of PEGME (poly(ethylene glycol) methyl ether) and toluene 2,4-diisocyanate (2,4-TDI) as coupling agents, PEG can also be grafted onto SNs. Surface grafted-PEG chains reduced hydrogen bonding and polar interactions between the individual nanoparticles, which improved the individualization of the particles in solvents [58].

Physical absorption of PEG in water was performed to introduce high molecular weight PEG (PEO) on the surface of CNs. Unlike grafting low M_n PEG, adsorbed long PEO chains wrapped the nanoparticles and promoted the interactions between CNs and the apolar matrix, which improved the dispersibility and thermal stability of CNs [85].

Recently, Lin and Dufresne reported the strategy of surface modification involving two PEG/PEO layers on the surface of cellulose nanocrystals using both chemical grafting and physical adsorption. Using a carboxylation–amidation reaction, short chain PEG ($M_n = 5000$) was first grafted on the surface of nanocrystals, followed by the treatment of immobilizing long PEO ($M_n = 5 \times 10^6$) chains on modified nanocrystals through physical adsorption and entanglement. With the possibility of entanglements and cocrystallization between short PEG chains and long PEO chains, two polymeric layers can closely wrap and protect the surface of the nanocrystals, further improving the thermal stability and compatibility of CNs and the apolar matrix (PS) [86].

3.6.2
Polyester

Aliphatic polyesters constitute the most versatile group of degradable polymers, which are often biocompatible and hydrophobic with low glass transition temperature. In the family of polyesters, poly(caprolactone) (PCL) and PLA are the most common materials, which can be traditionally synthesized by ROP of cyclic CL and L-lactide monomers. Therefore, grafting of PCL and PLA polymeric chains (especially PCL) on the surface of PNs was widely investigated.

In the initial stage, several studies on the introduction of PCL to PNs mainly focused on grafting onto PCL chains with an isocyanate-mediated reaction. This

chemical modification is based on the different reactivity of the two isocyanate groups from 2,4-TDI, the isocyanate at the 4-position being seven times more reactive than the isocyanate at the 2-position [87]. Grafting PCL onto the surface of PNs involves a three-step process. The first step requires the reaction of PCL on the isocyanate group of phenylisocyanate. The second step involves the reaction of PCL, now protected, with 4-position isocyanate group of 2,4-TDI. During the third step, the unreacted 2-position isocyanate group of 2,4-TDI is reacted with the surface hydroxyl groups of the PNs to graft the PCL chain onto the nanoparticles [88]. PCL chains with various molecular weights (such as 10 000, 42 500, 80 000, and 2000 g mol^{-1}) were grafted onto CNs or SNs for the reinforcement of co-continuous nanocomposites or electrospinned nanofibers [89, 90]. It was shown that the grafting efficiency decreased with the length of the polymeric chain, and that there was stronger reinforcing effect for long chain PCL-modified PNs due to chain entanglements and co-crystallization.

Because of the ease of achieving the highest grafting density and the possibility of chain length control, the strategy of "grafting from" is generally preferred for most studies aimed at grafting PCL chains on the surface of PNs. For this modification, the hydroxyl groups on the PN surface act as initiator to induce the polymerization of cyclic CL monomer, and the ratio of monomer to initiating groups determines the DP of the grafted polymer chains. The grafting reaction was performed under predetermined conditions and stopped by adding a few drops of dilute hydrochloric acid solution. The non-grafted PCL homopolymer can be removed by solubilization−centrifugation or Soxhlet extraction. Surface grafting of hydrophobic PCL moieties on PNs can facilitate the dispersibility of nanoparticles in hydrophobic systems. Habibi *et al.* and Goffin *et al.* applied Sn(Oct)$_2$-catalyzed ROP grafting of PCL on CNs to reinforce a PCL matrix using casting/evaporation [91] and extrusion [92]. Excellent dispersion of PCL-modified nanocrystals within the hydrophobic matrix and entanglement of the surface-grafted polyester chains with matrix chains significantly improved the thermomechanical properties of ensuing nanomaterials. In another study, Lin *et al.* performed microwave irradiation to assist PCL surface ROP on CNs, and prepare filaceous PCL-grafted CNs that were used to reinforce PLA matrix [93].

Grafting of PCL chains was also attempted on SNs and ChW. PCL-grafted SNs were synthesized through ROP of CL in the presence of Sn(Oct)$_2$ as catalyst. The introduction of PCL chains increased the range of melting temperature for starch; meanwhile, chemical modification caused the degradation of SNs in a broader temperature range [94]. Huang *et al.* applied a microwave-assisted technique to promote the polymerization of the CL monomer on the surface of SNs. When adding these PCL-grafted SNs in PLA and waterborne polyurethane (WPU) matrix, the rubbery PCL component provided enough flexibility to enhance the matrix, inducing the effect of simultaneous enhancement of strength and elongation at break of the ensuing nanomaterials [95, 96]. Similarly, PCL-grafted ChW with high grafting efficiency can be prepared. It was interesting that the grafted nanoparticles can be directly injection-molded as a thermoformable nanocomposite without any matrix component, which may be attributed to

numerous long "plasticizing" PCL tails on ChW surface [97]. Reactive conditions and grafting efficiency of diverse chemical modification for grafted-PCL on PNs are summarized in Table 3.2.

Recently, two studies investigated the reproducibility and interfacial molecular modeling of PCL grafting on the surface of PNs. It was reported that the process of Soxhlet extraction using ethanol before modification can effectively remove the adsorbed low molecular weight organic compounds produced during the hydrolysis, which may block the reactive sites of CNs and cause variable surface composition [15]. Molecular dynamics simulation was used to estimate the work of adhesion based on surface energies with different amounts of grafted CL. Cellulose interfaces with water and CL medium were modeled with different amounts of grafted CL. The modifications lead to an increased work of adhesion between the surface and its surrounding medium. The interaction between cellulose and the surrounding medium is dominated by Coulomb interactions, predominantly as hydrogen bonds. Hydrogen bonds were formed extensively between the grafted CL and the surrounding medium [100].

In recent research, citric acid was reported to be used as a benign alternative to metal catalyst in the surface-initiated ROP of grafting PCL on CNs. With "green" citric acid as catalyst, grafting efficiency of PCL on the surface of CNs was up to 58 wt%, about four times higher than earlier reported PCL grafted CNs using the common catalyst of $Sn(Oct)_2$ [98]. Carlsson *et al.* reported the monitoring of CN surfaces grafting from PCL using TBD (1,5,7-triazabicyclo[4.4.0]dec-5-ene) as catalyst by the quartz crystal microbalance technique, which provided a tool to regulate the polymerization reactions [101].

Another biodegradable polyester, PLA, was chemically grafted on the surface of CNs using the "grafting from" strategy of $Sn(Oct)_2$-catalyzed ROP of L-lactide initiated from the hydroxyl groups available at the CN surface [102]. The grafting reaction was performed in toluene at 80 °C for 24 h, and the grafting efficiency of PLA chains was determined by gravimetry as 83%. The effect of covalent bonding of PLA chains on CNs was investigated by a dispersion experiment in organic solvent (chloroform) in comparison with ungrafted CNs and CNs with physically adsorbed PLA chains. It was shown that hydrophobic PLA chains grafted on the CN surface were highly solvated, maintaining the nanoparticles in a more stable and homogeneous suspension in the apolar solvent. Another study investigated the strategy of grafting from high molecular weight PLA chains with partial pre-acetylation of surface hydroxyl groups to control the grafting density, while maintaining sufficient interparticle contact for efficient stress transfer within a percolating network [103].

3.6.3
Polyolefin

Since the mid-1990s, LRPs such as ATRP and single-electron transfer living radical polymerization (SET-LRP) have been used extensively as a tool for the development of novel macromolecular structures [104, 105]. Originating from

Table 3.2 Reactive conditions of various grafted poly(caprolactone) (PCL) on the surface of PNs (L = length, W = width, T = thick, D = diameter).

Types	Sources	Dimensions (nm)	Methods	Catalyst/coupling agents	Solvents	Conditions	Grafting efficiency (%)	References
CNs	Ramie fiber	L = 150–250 D = 6–8	Grafting onto	2,4-TDI	Toluene	70–80 °C, 7 d	—	[89]
	Ramie fiber	L = 100–250 D = 3–10	Grafting onto	2,4-TDI	Toluene	75 °C, 24 h	30	[90]
	Ramie fiber	L = 150–250 D = 6–8	Grafting from	Sn(Oct)$_2$	Toluene	95 °C, 24 h	85	[91, 92]
	Cotton linter	L = 200–300 D = 10–20	Grafting from-microwave	Sn(Oct)$_2$	—	Several minutes	85.09	[93]
SNs	Cotton wool	—	Grafting from	Citric acid	—	120 °C, 24 h	58	[15, 98]
	Waxy maize starch	L = 20–40 W = 15–30 T = 5–7	Grafting onto	2,4-TDI	Toluene	70–80 °C, 7 d	54.45	[88, 89]
	Pea starch	L = 60–150 W = 15–30	Grafting from-microwave	Sn(Oct)$_2$	—	Several minutes	84.16	[95, 96]
	Potato starch	—	Grafting from	Sn(Oct)$_2$	—	75 °C	39.9	[94]
ChW	Crab shell	L = several hundred nm D = 20	Grafting from-microwave	Sn(Oct)$_2$	—	Several minutes	89.60	[99]

the attributes of "livingness," control, and robustness from LRP, the techniques of surface-initiated atom transfer radical polymerization (SI-ATRP) and SET-LRP (SI-SET-LRP) were developed to "graft from" polymer chains or brushes on the surface of PNs (especially for CNs). It proved to be a versatile technique to synthesize well-defined polymers with high surface grafting density and low polydispersity on the CN surface. Copper-mediated LRP is generally chosen for its versatility with respect to monomer choice and ease of synthesis. Depending on the reaction conditions, the reactive mechanisms of two methods, ATRP and SET-LRP, are slightly different. In both cases, Cu(I) salts can be added to control the polymerization. However, SET-LRP is favored in polar reaction media and for strongly coordinating ligands, whereupon Cu(I) spontaneously and near-quantitatively disproportionates into Cu(0) and Cu(II). Subsequently, an outer-sphere electron transfer is thought to occur, and Cu(0) activates the dormant chains. On the contrary, in ATRP, the Cu(I) salt directly reacts with the alkyl halide initiator fragment, favorable under conditions where Cu(I) is stable in less polar solvents. Generally, two steps are involved in the chemical modification of grafting polymeric chains on CNs, as shown in Figure 3.6. The first step is the initial formation of initiating sites for LRP, in which an initiator is immobilized on the nanoparticles and a macromolecular initiator of CNs-Br can be obtained. It should be pointed out that 2-bromoisobutyryl bromide (BriB) is always chosen for the esterification of nanocrystals and provides the initiating sites. To prevent the destruction of the crystalline structure of CNs, this reaction should be performed at low temperature (sometimes with ice bath), which can exclude superfluous heat. The second step involves reaction of the initiator-modified nanoparticles with a monomer (C=C groups from alkene molecules) to induce polymerization.

First reports on using SI-ATRP to graft polyolefin polymeric chains on CNs surface were published by Zhang *et al.* concerning PS [24], poly{6-[4-(4-methoxyphenylazo) phenoxy] hexyl methacrylate} (PMMAZO) [99], and PDMAEMA [25]. All modifications were performed on CNs extracted from filter paper, and the focus of these studies was on liquid crystal phase behavior and
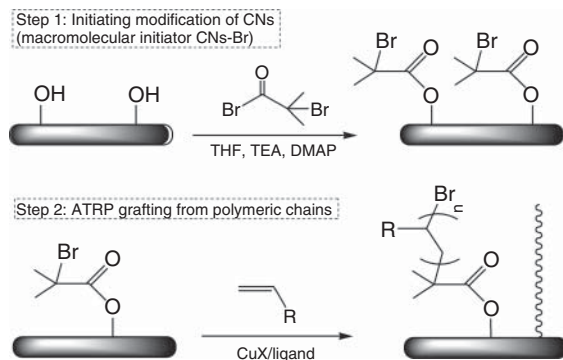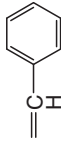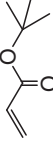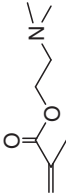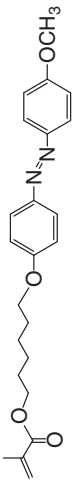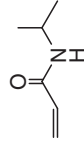
Figure 3.6 Synthetic routes of grafting polyolefin chains on CNs with the technique of ATRP.

fingerprint texture. It was a pity that the amount of bromine in the initiator-modified CNs was very low (just 0.6 wt%) in these studies, which restricted the subsequent grafting reaction. On the other hand, the issue of grafting polymeric chains with different lengths, which implies a controllable feature of ATRP, was not investigated. By altering the extent of initiator surface modification through polymerization control, Morandi *et al.* [106] produced PS-grafted CNs with varying grafting densities and different polymer brush lengths. Various grafting densities of PS on the surface of CNs were realized by controlling the final content of initiating sites under different conditions (time and temperature of BriB/CNs reactions). It was shown that a good coverage of PS layer can form on the surface of CNs, which exhibited the capacity to absorb the equivalent of 50% of the weight of the organic pollutant. They further reported a method of grafting a photosensitive moiety bearing initiating sites onto the surface of CNs, followed by grafting from PS chains with ATRP. This new pathway for the synthesis of PS-grafted CNs provided a possibility to degraft the PS chains using UV irradiation and exactly investigate grafted polymer brush length and molecular weights [107]. Walther *et al.* reported an effective method of chemical vapor deposition (CVD) and continued esterification to improve the initiator density for CNs surface [108]. The simple CVD pretreatment of BriB for CNs was conducted for 24 h at room temperature (5 wt% bromine content), which promoted subsequent esterification to obtain more initiating sites (15 wt% bromine content). Whereafter, poly(acrylic acid) (PAA) polyelectrolyte chains were grafted from CNs via Cu-mediated surface initiated-ATRP of *tert*-butyl acrylate (tBA) and subsequent hydrolysis. Via the technique of SI-SET-LRP at room temperature [26], CNs derived from ramie fiber can be grafted with thermoresponsive PNiPAAm brushes. It was shown that the suspension stability, interfacial interactions, and friction for grafted CNs can be controlled by changing the temperature, which could be explained by local heterogeneities shifting the SET-LRP equilibrium to the active state. In a further study, based on these grafting copolymers, an ultrathin and temperature-responsive material was prepared without the need for an anchoring polymeric matrix [109].

With the method of HCl hydrolysis or saponification, grafted polyolefin chains can be cleaved from the surface of CNs, and the properties of grafted polymers, such as molecular weight (M_n) and polydispersity, can be carefully investigated through gel permeation chromatography (GPC) or size exclusion chromatography (SEC). The diverse monomers, reactive conditions, and properties of grafted polyolefin chains on CNs are summarized in Table 3.3.

Despite the advantages of control and high grafting density for surface-initiated LRP, there are some shortcomings for this technique, which are the inconvenience of experimental operation (with three freeze-pump-thaw or vacuum-nitrogen cycles) and rigorous reactive conditions of anaerobic circumstances. Some studies exploited other approaches to graft polyolefin on the surface of PNs. Harrisson *et al.* [110] grafted PS and poly(*t*-butyl acrylate) (PtBA) chains on CNs via the carbodiimide-mediated amidation reaction between the terminal amine groups from polyolefin polymers and carboxylic acid groups on the surface of oxidized

Table 3.3 Reactive conditions and properties of various grafted polyolefin chains on CNs with the technique of ATRP and SET-LRP.

Monomers	Polymeric chains	Catalyst/ ligands	Solvents	Conditions	Grafting efficiency[a] (%)	Grafted polymer (M_n)	PDI[b]	References
	PS	Cu(I)Br/ HMTETA	—	110 °C, 12 h	68	74 700	1.21	[24]
		Cu(I)Br/ PMDETA	Anisole	30° or 70 °C 16 or 24 h	24–40	2 800–17 800	1.09– 1.13	[106]
	PtBA (PAA)	Cu(I)Br/ PMDETA	DMF	75 °C	—	6 200–36 300	1.10	[108]
	PDMAEMA	Cu(I)Br/ HMTETA	CH$_3$OH	55 °C, 12 h	53	10 200	1.38	[25]
	PMMAZO	Cu(I)Br/ HMTETA	Chloro- benzene	90 °C, 24 h	74.6	—	—	[99]
	P(NiPAAm)	Cu(I)Br/ PMDETA	H$_2$O: MeOH	25 °C, 24 h	—	10 630–42 860	1.20	[26]

a) The grafting efficiency listed here is determined according to the weight percent of grafted polymer in the modified-CNs.
b) PDI is polydispersity index, which represents the uniform degree of M_n from grafted polymers on CNs.
PMDTA, N,N,N',N',N''-pentamethyldiethylenetriamine

CNs. With ATRP, PS or PtBA polymers were first synthesized on a chemical of *N*-(2-(2-bromoisobutyryl)ethoxy) ethyl phthalimide, which provided the terminal amine groups through subsequent deprotection reaction. Whereafter, the hydrophobic polymer was grafted onto the surface of oxidized CNs with the amidation reaction. The polymer-grafted microcrystals can be readily dispersed in nonpolar solvents such as acetone and toluene, and form an interesting class of rigid, rod-shaped, polymeric nanoparticles. Another study was an attempt at grafting PS chains on SNs using the method of graft copolymerization [111]. Although the prepared PS-grafted SNs exhibited uniform dispersion both in water and in organic solvents (toluene, dichloromethane), this reaction displayed low grafting efficiency and weak combination between nanoparticles and polymeric chains.

Recently, a novel approach of *in situ* free-radical grafting polymerization of polyacrylamide (PAM) chains on the surface of CNs was developed [112]. Potassium persulfate (KPS) together with sodium bisulfite (SBS) were used as the redox initiator in the grafting reaction, because $[SO_4^-\cdot]$ radical can react directly with the polymeric backbone of cellulose to produce the requisite radicals [113]. When the KPS/SBS redox initiator was added into the CN suspension, it induced a hydroxyl group on the surface of CNs to produce radicals. After the addition of acrylamide (AM) monomer and *N, N′*-methylenebisacrylamide (NMBA) cross-linker, the free radicals formed on the CN surface then reacted with the double bonds of AM monomer, resulting in grafting points (covalent bond C–O) between the CN and the PAM chain. Simultaneously, other free radicals existing in the solution initiated the homopolymerization of AM to grow PAM macromolecule chains, which were also cross-linked by the NMBA. Finally, based on PAM network and *in situ* grafting of CNs, the hydrogel was formed with good CN dispersion in PAM as well as enhanced interfacial interaction between these two components [114]. Another study reported *in situ* radical polymerization of methacrylic groups of the adsorbed coating to form a PHEMA (poly(2-hydroxyethylmethacrylate)) network on the CN surface [115]. The double bonds at the CN surface introduced through the monomer layer were proposed to be grafting sites for PHEMA polymer chains. It was a convenient method for the modification of some polymers on PNs, but the surface grafting reaction was not proved and the degree of grafting and effect of polymeric chains on CNs were not studied.

3.6.4
Block Copolymer

Besides the introduction of hydrophilic polymers (such as PEG) and hydrophobic polymers (such as polyolefin), block copolymers including both hydrophilic and hydrophobic segments were grafted on the PN surface (mainly CNs). A kind of saccharide-based amphiphilic triblock copolymer, xyloglucan oligosaccharide-poly (ethylene glycol)-polystyrene (XGO-*co*-PEG-*co*-PS), was used for the surface modification of CN [116]. The triblock copolymer was pre-synthesized and

physically adsorbed on CNs in the solvent DMF/H$_2$O (1 : 100 v/v). The weight fraction of the adsorbed copolymer on CNs was determined as 45% by TGA (thermogravimetric analysis). In this system, PEG was used as a compatible block between the carbohydrate (XGO, xyloglucan oligosaccharide) and hydrophobic (PS) blocks and to increase the hydrophilicity of the copolymer, whereas the hydrophobic PS chains facilitated property change of the CN surface. The modified CNs adsorbed with the triblock copolymer were easily redispersed in the organic solvent (toluene), and the chiral nematic self-ordering of the modified CNs was investigated in a nonpolar solvent. In another study, Azzam *et al.* [117] introduced PPG-*co*-PEG copolymers on the CN surface using the grafting onto approach. Coupling reaction was performed between the carboxyl groups from oxidized CNs and amine-terminated groups from Jeffamine copolymers either in water or in DMF. It was shown that in DMF, the copolymer with low molecular weight can be grafted onto CNs with a high grafting density (DS = 0.1049). Individual nanocrystals were decorated by a shell of polymer chains, which induced the steric stabilization, surface-active, and thermoreversible aggregation of modified nanoparticles. However, owing to the limitation of "grafting onto" strategy, only copolymers of low M_n (1000 or 2070 g mol^{-1}) were used in this chemical modification. Via the chlorination reaction, PHBV (poly(3-hydroxybutyrate-co-3-hydroxyvalerate)) can be grafted onto the surface of ChW, and the effects of original ChW and PHBV-grafted-ChW on the crystallizing and melting behavior were investigated [118].

3.6.5
Polyurethane and Waterborne Polyurethane

As promising materials possessing low viscosity at high molecular weight, nontoxicity, and good applicability, WPUs are a hot topic in both academia and industry. As is well known, to prepare high performance materials from a hydrophobic matrix and hydrophilic PN, the major issues to address are adequate dispersion and strong interfacial adhesion between the matrix and the filler. Obviously, the most ideal and effective way is through covalent attachment of WPU chains to the stiff PN surface [119]. However, most studies just involved the physical blending of PNs for the nano-reinforcement of WPU matrix, except two research studies focusing on the grafting of WPU chains on PN and co-construction of the materials. Cao *et al.* [120] prepared WPU/CNs nanocomposites via a one-pot synthetic reaction between the exposed hydroxyl groups on the CN surface and isocyanate from the ends of the WPU prepolymer. It was reported that the presence of the grafted WPU chains on the CN surface provided a crystalline environment that induced the crystallization of the WPU polymeric chains from the matrix surrounding CNs. This co-crystallization phenomenon induced the formation of a co-continuous phase, which significantly facilitated good dispersion and enhanced interfacial adhesion between WPU and CNs. In another study, chemical grafting of WPU chains onto the surface of SNs was performed, and used as the nano-phase to prepare the nanocomposites [121]. It was a pity

that both studies did not provide powerful proofs to validate the presence of WPU-grafted chains on CNs or SNs. Meanwhile, the degree of grafting and the state of modified nanocrystals in the network of WPU matrix also need to be investigated.

3.6.6
Other Hydrophobic Polymer

PP is a common hydrophobic polymer that is always used as a representative apolar matrix. A comparison of the reinforcing effect of CN grafted with maleated PP and CN dispersed with the surfactant BNA into atactic PP as the matrix was reported [122]. It was shown that PP-grafted CNs tended to aggregate in the matrix and reduced the ductility of the ensuing nanocomposites, whereas surfactant-coated CNs showed good dispersion in the matrix (transparent films) and improved ductility. In another study, hydrophobic poly(propylene glycol) monobutyl ether (PPGBE) or poly(tetrahydrofuran) (PTHF) chains were grafted onto the surface of SNs using 2,4-TDI as the coupling agent [88]. It was shown that the grafting of PPGBE chains on SNs was quite efficient because 7.27% of the hydroxyl groups from the surface have been substituted by the polymeric chain, whereas the grafting of PTHF chains displayed a much lower efficiency with only 0.68%. The surface chemical modification allowed enhancement of the nonpolar nature of the original SNs, which showed an obvious decrease in polar surface energy from $32.71 \, \text{mN m}^{-1}$ (pristine SNs) to $4.12 \, \text{mN m}^{-1}$ (PTHF grafted SNs) or $0.14 \, \text{mN m}^{-1}$ (PPGBE grafted SNs), respectively. Through the carboxylation–amidation procedure, hydrophobic chains of polypropylene glycol (PPG, $M_n = 600$) can also be grafted onto the surface of CNs through covalent reaction between carboxylated CNs and amine-terminated PPG [123]. The approach involving direct "grafting onto" modification for the introduction of hydrophobic polymers on PNs seems to be inefficient, which may be attributed to the weak interaction resulting from the compulsive conjunction between hydrophilic nanocrystals and hydrophobic long chains. As mentioned in Section 3.3.2, the low grafting density rooting resulting from steric hindrance and blocking of reactive sites by the already grafted polymer chains is one of the main drawbacks of the "grafting onto" method.

3.7
Advanced Functional Groups and Modification

Intensive exploration and research has been conducted on PNs in the past two decades, which mainly focused originally on their use as the reinforcing nanophase in nanocomposites. Recently, more investigations have led to the emergence of diverse potential applications of PNs as advanced functional nanomaterials, which are closely associated with modification from common derivatization or polymer grafting to provide hydrophobic surface for the

introduction of advanced functional groups for special applications of PNs [3]. The preparation and application of functional nanomaterials based on PNs is systematically discussed in Chapter 6, and this section just focuses on the reaction and process of modification of PNs (generally CNs). Chemical structures of various functional groups and modification of CNs are shown in Figure 3.7.
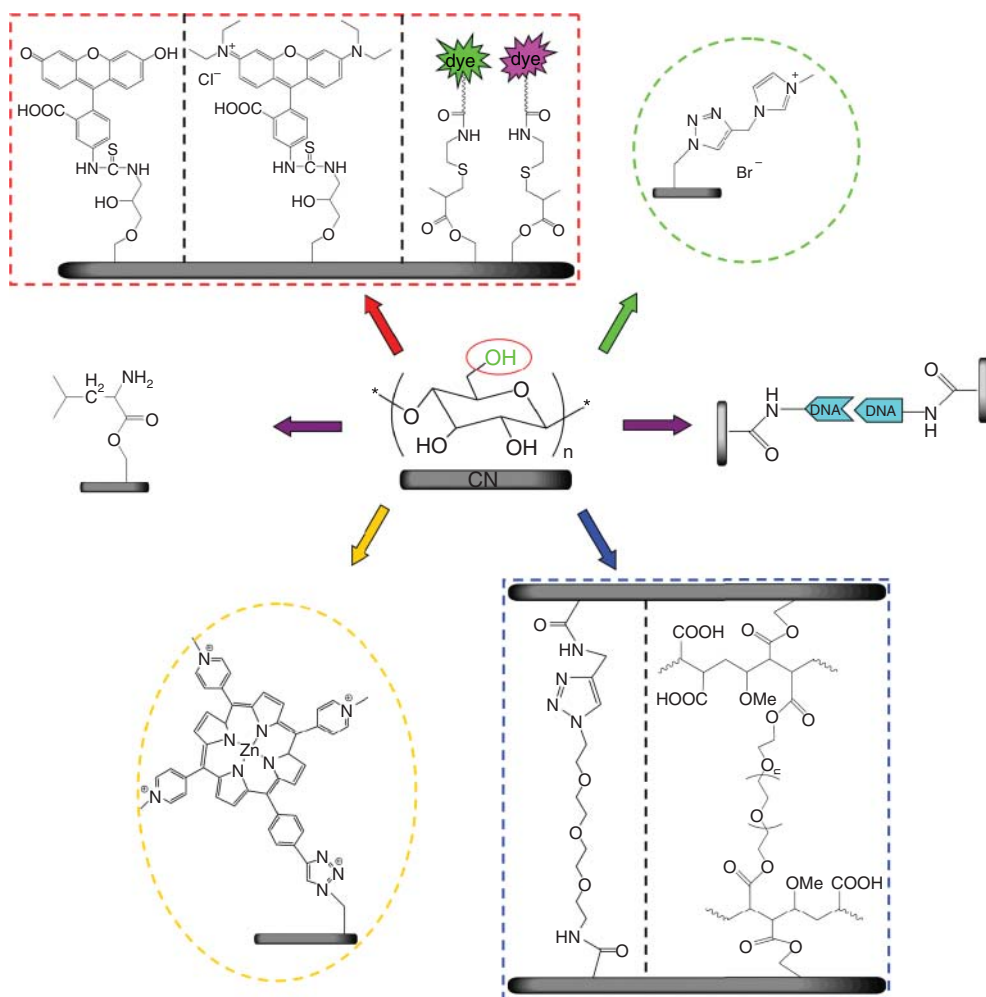
Figure 3.7 Examples of advanced functional modifications of CNs: grafting fluorescent or dye molecules (as directed with red arrows); grafting imidazolium molecule (as directed with green arrows); grafting amino acid or DNA oligonucleotide (as directed with purple arrows); grafting photobactericidal porphyrin (as directed with yellow arrows); and self-crosslinking of CNs via click chemistry or with PMVEMA and PEG (as directed with blue arrows).

3.7.1
Fluorescent and Dye Molecules

In covalent conjunction with nanoparticles, fluorophores can be used to label these nanoparticles not only for fluorescence bioassay and bioimaging applications but also for the investigation of bioeffects and safety of nanoparticles inside cells or human beings. For the first time, Dong and Roman [124] introduced the fluorescent molecule FITC on the surface of CNs via a three-step approach. First, the surface of the nanocrystals was decorated with epoxy functional groups via reaction with epichlorohydrin. Then, the epoxy ring was opened with ammonium hydroxide to introduce primary amino groups on CNs. Finally, the primary amino group was reacted with the isothiocyanate group of FITC, in which covalent association between CNs and FITC was realized via the formed thiourea groups. It was shown that the unlabeled suspension was colorless and slightly opaque, whereas the FITC-labeled CN suspension appeared clear and yellow. Meanwhile, according to the results of UV/vis spectroscopy, FITC-labeled nanocrystals showed absorption maxima of both the dianionic (490 nm) and the anionic (453 and 472 nm) forms of FITC, whereas unlabeled CNs did not show any absorption peaks in the wavelength range 200–600 nm. In another study, using a similar method two fluorescent molecules (FITC and RBITC) were introduced on the surface of CNs; the study investigated the effects of cellular uptake and cytotoxicity for different fluorescent CNs [125]. The suspension of RBITC-labeled CNs appeared wine red and displayed the excitation wavelength at 540 nm attributed to RBITC. It was worth noting that in comparison with free RBITC aqueous solution, there was a red shift (from 577 to 584 nm) for the fluorescence emission of RBITC-labeled CNs, which was attributed to the influence of the fluorescent molecules covalently attached to nanocrystals. Fluorescent terpyridine molecules [126, 127] and pyrene molecules [128] were also reported to be modified on the surface of CNs.

Eyley and Thielemans [129] developed two synthetic approaches to introduce two fluorescent or dye molecules on CNs for the preparation of dual fluorescent labeled CNs. The first approach employed a similar procedure as that of Dong and Roman, involving the reaction between amino CNs and both isothiocyanate FITC and RBITC. The amount of FITC and RBITC on dual fluorescent labeled CNs was estimated to be 2.8 and 2.1 $\mu mol\, g^{-1}$. To avoid the use of scarce isothiocyanate fluorescent molecules, a new three-step procedure was performed on CNs, which was the introduction of a double bond on CNs via esterification, followed by thiol–ene Michael addition and, finally, coupling with the succinimidyl ester dyes. Two different pH-sensitive dyes, FAM-SE (5-(and-6)-carboxyfluorescein succinimidyl ester) and OG-SE (Oregon green 488 carboxylic acid, succinimidyl ester), were grafted onto CNs along with the reference TAMRA-SE (fluorophore 5, 6-carboxytetram-ethylrhod-amine succinimidyl ester) dye, which is brighter than Rhodamine B, and only available as a succinimidyl ester. The average amounts of dyes on labeled CNs were 10.4 $\mu mol\, g^{-1}$ FAM-SE, 4.7 $\mu mol\, g^{-1}$ TAMRA-SE, 7.3 $\mu mol\, g^{-1}$ OG-SE, and 4.2 $\mu mol\, g^{-1}$ TAMRA-SE, respectively.

The dual fluorescent labeled CNs (FITC and RBITC labeled CNs) and two dual dyes labeled CNs (FAM-SE and TAMRA-SE labeled CNs as well as OG-SE and TAMRA-SE labeled CNs) all exhibited pH sensing in McIlvaine buffers with varying pH conditions.

3.7.2
Amino Acid and DNA

As the natural rigid nanocrystals, PNs are expected to be a good candidate for the construction of biocompatible and biologically active nanomaterials, such as drug carrier and gene delivery. The anchoring of amino acid or DNA molecules to the surface of CNs allows the creation of a binding site to which drugs or targeting molecules can be attached. The chemical modification of L-leucine on CNs was performed through a two-step process involving the reaction between Fmoc (fluorenylmethyloxycarbonyl chloride)-protected L-leucine and thereafter the removal of the Fmoc protecting group. The first step consisted in the reaction between CNs and Fmoc−L-leucine by using DMAP (dimethyl amino pyridine) as the catalyst and EDC·HCl (*N*-ethyl-*N*′-(3-dimethylami-nopropyl) carbodiimide hydrochloride) as the coupling agent. The removal of the protecting Fmoc group was performed by stirring Fmoc-L-leucine CNs in piperidine/DMF solution [130]. Mangalam *et al.* [131] developed the synthetic route of grafting different single-stranded oligonucleotides with an amino modifier on CNs, and subsequent duplexing of complementary oligonucleotides formed with individual modified CNs via the molecular recognition ability of the oligomeric base pairs. The reaction of grafting amino-modified ssDNA on CNs was carried out using the carboxylation−amidation procedure. Two kinds of oligonucleotides modified CNs, both strand A and strand B modified CNs, were mixed together in water for the preparation of duplexed DNA-modified CNs. It was shown that complementary strands of DNA bonded to separate populations of CNs hybridized under suitable conditions to form bonded structures and this hybridization was reversible by raising the temperature above the melting temperature of the duplexed DNA.

3.7.3
Self-Cross-linking of Polysaccharide Nanocrystals

Different from the traditional application of CN as the reinforcing filler, some studies utilize CNs themselves to be the matrix for the construction of self-cross-linked materials. Goetz *et al.* first developed the self-cross-linking of CNs extracted from MCC (microcrystalline cellulose) with PMVEMA (poly(methyl vinyl ether comaleic acid)) and PEG as the cross-linking agents by reacting varying amounts of CNs (0−100%) [132, 133]. PMVEMA is a polycarboxylic acid containing a polymer that was recently used as a bioadhesive polymer for drug delivery applications. The cross-linking of CNs with PMVEMA and PEG was anticipated to occur via an esterification reaction between the hydroxyl

groups of cellulose, terminal hydroxyl groups of PEG, and the carboxylic acid groups of PMVEMA. The cross-linking between the three components trapped the nanocrystals in the cross-linked network, preventing aggregation and subsequently producing CNs self-cross-linked nanomaterials with the intramolecular and interchain reactions. The CNs self-cross-linked material was found to consist of mobile chain portions between cross-linked junction points and immobilized chain segments near or at those junction points whose relative fraction increased on further incorporation of CNs. The nanoscale morphology of the films showed a multiphased system and there was an indication through the phase images that one of the phases was forming a network in the second phase with a relatively homogeneous distribution of the phases.

In another study, a three-step route of click chemistry was utilized for the synthesis and formation of cellulose nanoplatelet gels with the regular self-cross-linking of CNs [134]. Initially, the primary hydroxyl groups on the surface of CNs were selectively activated by converting them to carboxylic acids through the use of TEMPO-mediated oxidation. Further reactions using the oxidized CNs were carried out via carbodiimide-mediated formation of an amide linkage between precursors carrying the amine groups and the carboxylic acid groups on the surface of oxidized CNs. Finally, with two kinds of modified CNs containing the azide derivative or the alkyne derivative on their surface, the click chemistry reaction of Cu(I)-catalyzed Huisgen 1,3-dipolar cycloaddition between the azide and the alkyne was performed on CNs, bringing together the nanocrystalline materials in a unique regularly packed arrangement demonstrating a degree of molecular control for creating self-cross-linked CNs nanomaterials. The cycloaddition linking reaction in an organized manner between individual CNs was proved by the uniform vertical arrangement of nanocrystals and observed vertical arrays in a larger rectangular shape.

Inspired by the water-enhanced mechanical gradient character of the squid beak, Fox *et al.* recently reported a mechanical gradient nanocomposite made from modified tunicate CNs by CN–CN cross-linking in a PVA (polyvinyl alcohol) matrix. CNs were first modified by the introduction of allyl moieties on the surface. With the addition of a small molecule tetra-thiol cross-linker and radical photoinitiator, modified CNs will self-cross-link under the exposure of UV irradiation via photoinduced thiolene chemistry reaction. Furthermore, with the control of UV exposure duration, the degree of cross-linking for nanocrystals can be regulated, and mechanical gradient nanocomposites fabricated [135].

3.7.4
Photobactericidal Porphyrin Molecule

With the benefits of biocompatibility and biodegradability of PNs, this kind of natural nanoparticles have been more studied in the application of biomedical materials. Feese *et al.* [136] developed surface-modified CNs with the cationic porphyrin via the Cu(I)-catalyzed Huisgen–Meldal–Sharpless 1,3-dipolar cycloaddition "click reaction" occurring between azide groups on the cellulosic

surface and porphyrinic alkynes. In the reaction, about 50% of all azide groups on the surface of modified CNs were substituted by porphyrin molecules. Covalent attachment of the porphyrin molecule to the surface of CNs will potentially contribute to longer lasting or permanent antimicrobial property, minimizing the leaching of the biocidal agent into the surrounding environment. In a further study, using visible light (400–700 nm) experiment, the specific property of photoinactivate antimicrobial for porphyrin-modified CNs toward different genera of bacteria was investigated, which showed an impressive 6 log units of reduction in viable cells for methicillin-resistant *Staphylococcus aureus* (gram-positive), 5–6 log units for *Acinetobacter baumannii* and MDRAB (multidrug-resistant Acinetobacter baumannii) (gram-negative), and about 2.5 log units for *Pseudomonas aeruginosa* (gram-negative), when using a 20 μM suspension of porphyrin-modified CNs and illuminated with visible light (400–700 nm; 118 J cm^{-2}) [137].

3.7.5
Imidazolium Molecule

As shown in Figure 3.7, the imidazolium salt can be grafted onto CNs with a three-step synthetic route of copper(I) catalyzed azide–alkyne cycloaddition "click" reaction [129]. First, CNs were azidated to allow grafting of an alkyne terminated ionic liquid ([MPIM][Br], 1-methyl-3-propargylimidazolium bromide). Instead of tosylation, chlorination was chosen as the azidation process to activate the nanocrystals, because of the inconsistent results of heterogeneous tosylation reactions on cotton [138]. The chlorinated nanocrystals were subsequently azidated using sodium azide in DMF. Finally, imidazolium molecule was grafted to the azido CNs in an aqueous solution using copper(II) sulfate (5 mol%) as a pre-catalyst and sodium ascorbate (10 mol%) as the reductant. The value of DS for imidazolium grafting was calculated using nitrogen concentration to be 0.36, assuming that all azide moieties were converted to triazoles. The ζ-potential of imidazolium-grafted CNs was determined to be +47 mV (−9.49 mV for pristine CNs), which showed the change of cationic surface with positive surface charge for imidazolium-grafted CNs. Meanwhile, the concentration of imidazolium residues on the surface of CNs was calculated as 0.53 mmol g^{-1}, giving a surface charge density of 1.17 e nm^{-2}. Recently, with the reaction of azide–alkyne cycloaddition, ferrocene was reported to be decorated onto CNs by the grafting of ethynylferrocene onto azide modified CNs, which showed potential in the development of bioelectrochemical devices [139].

3.7.6
Cyclodextrin Molecule and Pluronic Polymer

Using grafted β-cyclodextrin as target sites, Pluronic polymers were reported to be introduced on the surface of CNs by means of inclusion interaction between grafted β-cyclodextrin and the hydrophobic segment of the polymers. Because of steric stabilization effect, the PEG chains introduced from Pluronic facilitate

the dispersion and compatibility of nanocrystals. Meanwhile, uncovered PEG segments render the participating inclusion of α-cyclodextrin for the architecture of *in situ* supramolecular hydrogels [140].

3.8
Concluding Remarks

As discussed, there are two fields focusing on the study of PNs, which are the use as nano-reinforcing fillers in composites, and novel applications in advanced functional nanomaterials. No matter which application, it requires diverse surface modifications to convert or endow new properties on these ageless nanocrystals. For the former application, mass production of PNs in some institutes or companies (such as 10 kg week^{-1} CNs from FPInnovations [141] and 100 kg year^{-1} CNs from Western Economic Partnership Agreement (WEPA) [142]) provides the possibility of PNs as common biomass nanofiller in future materials. It is worth noting that besides the fundamental research on the introduction of PNs for the relationship between structure and property of nanocomposites, different preparation or treatment techniques, such as melting extrusion, also deserve more investigation. Recently, another application regarding the development of functional nanomaterials from PNs has attracted more and more researchers to explore this new field, such as advanced optical materials, biomedical materials, mechanically adaptive materials based on CNs, and so on. For example, there was a report on the interesting attempt to cultivate the growth of nerve cells on nanocellulose, which was expected to allow the preparation of artificial gristle or even artificial blood vessel [143]. In spite of numerous applications, the potential security of PNs should be seriously studied; but there are just a few reports on the toxicological evaluation of PNs currently [144, 145], and there is no research investigating the influence of PNs on nanomaterials.

List of Abbreviations

AA	acetic anhydride
ASA	alkenyl succinic anhydride
ATRP	atom transfer radical polymerization
BDMSiCl	*n*-butyldimethylchlorosilane
BriB	2-bromoisobutyryl bromide
CAB	cellulose acetate butyrate
ChW	chitin nanowhiskers
CNs	cellulose nanocrystals
CTC	carbon tetrachloride
DAP (DMAP)	dimethyl amino pyridine
DDMSiCl	*n*-dodecyldimethylchlorosilane
DMAc	*N*,*N*-dimethylacetamide

DMF	*N,N*-dimethylformamide
DMSO	dimethyl sulfoxide
DP	degree of polymerization
DODA	dioctadecyldimethylammonium
DS	degree of substitution
EA	ethyl acetate
EDC·HCl	*N*-ethyl-*N′*-(3-dimethylami-nopropyl) carbodiimide hydrochloride
EPTMAC	(2,3-epoxypropyl)trimethylammonium chloride
IPDMSiCl	isopropyldimethylchlorosilane
FAM-SE	5-(and-6)-carboxyfluorescein succinimidyl ester
FITC	fluorescein-5′-isothiocyanate
GTMAC	glycidyltrimethylammonium chloride
LDPE	low density polyethylene
LRP	living radical polymerization
MA	maleic anhydride
MCC	microcrystalline cellulose
MEK	methyl ethyl ketone
M_n	molecular weight
[MPIM][Br]	1-methyl-3-propargylimidazolium bromide
MAC	methyl adipoyl chloride
MSA	methanesulphonic acid
NR	natural rubber
ODMSiCl	*n*-octyldimethylchlorosilane
iso-ODSA	*iso*-octadecenyl succinic anhydride
OG-SE	Oregon Green 488 carboxylic acid, succinimidyl ester
PAA	poly(acrylic acid)
PBD	poly(butadiene)
PCL	poly(caprolactone)
PDDA	poly(diallyldimethylammonium chloride)
PDMAEMA	poly(*N,N*-dimethylaminoethyl methacrylate)
PEG	poly(ethylene glycol)
PEI	poly(ethyleneimine)
PEO	poly(oxyethylene)
PHBV	poly(3-hydroxybutyrate-*co*-3-hydroxyvalerate)
PHEMA	poly(2-hydroxyethylmethacrylate)
PI	phenyl isocyanate
PLA	poly(lactic acid)
PMMAZO	poly{6-[4-(4-methoxyphenylazo) phenoxy] hexyl methacrylate}
PMVEMA	poly(methyl vinyl ether comaleic acid)
PNs	polysaccharide nanocrystals
PNiPAAm	poly(*N*-isopropylacrylamide)
PP	polypropylene
PPGBE	poly(propylene glycol) monobutyl ether
PS	polystyrene

PTHF	poly(tetrahydrofuran)
PU	polyurethane
RBITC	rhodamine B isothiocyanate
ROP	ring-opening polymerization
SET-LRP	single-electron transfer living radical polymerization
SNs	starch nanocrystals
TAMRA-SE	fluorophore 5, 6-carboxytetram-ethylrhod-amine succinimidyl ester
2,4-TDI	toluene 2,4-diisocyanate
n-TDSA	*n*-tetradecenyl succinic anhydride
tBA	*tert*-butyl acrylate
TBD	1,5,7-triazabicyclo[4.4.0]dec-5-ene
TEA	triethylamine
TEMPO	2,2,6,6-tetramethylpiperidine-1-oxyl
THF	tetrahydrofuran
TMI	isopropenyl-α,α′-dimethylbenzyl isocyanate
Tos-Cl	*p*-toluensulfonyl chloride
UPy-NCO	2-(6-isocyanatohexylaminocarbonyl amino)-6-methyl-4[1*H*]pyrimidinone
VA	vinyl acetate
WPU	waterborne polyurethane

References

1. Wakelyn, P.J. (1998) in *Handbook of Fiber Chemistry* (eds M. Levin and E.M. Pearce), Marcel Dekker, New York, pp. 642–654.

2. Hebeish, A. and Guthrie, J.T. (1981) *The Chemistry and Technology of Cellulosic Copolymers*, Springer-Verlag, Berlin.

3. Lin, N., Huang, J., and Dufresne, A. (2012) Preparation, properties and applications of polysaccharide nanocrystals in advanced functional nanomaterials: a review. *Nanoscale*, **4**, 3274–3294.

4. Angellier, H., Molina-Boisseau, S., Belgacem, M.N., and Dufresne, A. (2005) Surface chemical modification of waxy maize starch nanocrystals. *Langmuir*, **21**, 2425–2433.

5. Siqueira, G., Bras, J., and Dufresne, A. (2009) Cellulose whiskers versus microfibrils: influence of the nature of the nanoparticle and its surface functionalization on the thermal and mechanical properties of nanocomposites. *Biomacromolecules*, **10**, 425–432.

6. Pinkert, A., Marsh, K.N., Pang, S., and Staiger, M.P. (2009) Ionic liquids and their interaction with cellulose. *Chem. Rev.*, **109**, 6712–6728.

7. Cai, J., Zhang, L.N., Chang, C.Y., Cheng, G.Z., Chen, X.M., and Chu, B. (2007) Hydrogen-bond-induced inclusion complex in aqueous cellulose/LiOH/urea solution at low temperature. *ChemPhysChem*, **8**, 1572–1579.

8. Beck-Candanedo, S., Roman, M., and Gray, D.G. (2005) Effect of reaction conditions on the properties and behavior of wood cellulose nanocrystal suspensions. *Biomacromolecules*, **6**, 1048–1054.

9. Braun, B. and Dorgan, J.R. (2009) Single-step method for the isolation and surface functionalization of cellulosic nanowhiskers. *Biomacromolecules*, **10**, 334–341.

10. Marchessault, R.H., Morehead, F.F., and Walter, N.M. (1959) Liquid crystal

systems from fibrillar polysaccharides. *Nature*, **184**, 632–633.

11. Dong, X.M., Revol, J.-F., and Gray, D.G. (1998) Effect of microcrystallite preparation conditions on the formation of colloid crystals of cellulose. *Cellulose*, **5**, 19–32.

12. Habibi, Y., Hoeger, I., Kelley, S.S., and Rojas, O.J. (2010) Development of Langmuir-Schaeffer cellulose nanocrystal monolayers and their interfacial behaviors. *Langmuir*, **26**, 990–1001.

13. Roman, M. and Winter, W.T. (2004) Effect of sulfate groups from sulfuric acid hydrolysis on the thermal degradation behavior of bacterial cellulose. *Biomacromolecules*, **5**, 1671–1677.

14. Jiang, F., Esker, A.R., and Roman, M. (2010) Acid-catalyzed and solvolytic desulfation of H_2SO_4-hydrolyzed cellulose nanocrystals. *Langmuir*, **26**, 17919–17925.

15. Labet, M. and Thielemans, W. (2011) Improving the reproducibility of chemical reactions on the surface of cellulose nanocrystals: ROP of ϵ-caprolactone as a case study. *Cellulose*, **18**, 607–617.

16. Way, A.E., Hsu, L., Shanmuganathan, K., Weder, C., and Rowan, S.J. (2012) pH-responsive cellulose nanocrystal gels and nanocomposites. *ACS Macro Lett.*, **1**, 1001–1006.

17. Lokanathan, A.R., Nykänen, A., Seitsonen, J., Johansson, L.-S., Campbell, J., Rojas, O.J., Ikkala, O., and Laine, J. (2013) Cilia-mimetic hairy surfaces based on end-immobilized nanocellulose colloidal rods. *Biomacromolecules*, **14**, 2807–2813.

18. Wu, Q., Henriksson, M., Liu, X., and Berglund, L.A. (2007) A high strength nanocomposite based on microcrystalline cellulose and polyurethane. *Biomacromolecules*, **8**, 3687–3692.

19. Azizi Samir, M.A.S., Alloin, F., Sanchez, J.-Y., Kissi, N.E., and Dufresne, A. (2004) Preparation of cellulose whiskers reinforced nanocomposites from an organic medium suspension. *Macromolecules*, **37**, 1386–1393.

20. Klemm, D., Kramer, F., Moritz, S., Lindström, T., Ankerfors, M., Gray, D., and Dorris, A. (2011) Nanocelluloses: a new family of nature-based materials. *Angew. Chem. Int. Ed.*, **50**, 5438–5466.

21. Habibi, Y., Lucia, L.A., and Rojas, O.J. (2010) Cellulose nanocrystals: chemistry, self-assembly, and applications. *Chem. Rev.*, **110**, 3479–3500.

22. Gopalan Nair, K. and Dufresne, A. (2003) Crab shell chitin whiskers reinforced natural rubber nanocomposites. 3. Effect of chemical modification of chitin whiskers. *Biomacromolecules*, **4**, 1835–1842.

23. Moon, R.J., Martini, A., Nairn, J., Simonsen, J., and Youngblood, J. (2011) Cellulose nanomaterials review: structure, properties and nanocomposites. *Chem. Soc. Rev.*, **40**, 3941–3994.

24. Yi, J., Xu, Q., Zhang, X., and Zhang, H. (2008) Chiral-nematic self-ordering of rodlike cellulose nanocrystals grafted with poly(styrene) in both thermotropic and lyotropic states. *Polymer*, **49**, 4406–4412.

25. Yi, J., Xu, Q., Zhang, X., and Zhang, H. (2009) Temperature-induced chiral nematic phase changes of suspensions of poly(*N*,*N*-dimethylaminoethyl methacrylate)-grafted cellulose nanocrystals. *Cellulose*, **16**, 989–997.

26. Zoppe, J.O., Habibi, Y., Rojas, O.J., Venditti, R.A., Johansson, L.-S., Efimenko, K., Österberg, M., and Laine, J. (2010) Poly(*N*-isopropylacrylamide) brushes grafted from cellulose nanocrystals via surface-initiated single-electron transfer living radical polymerization. *Biomacromolecules*, **11**, 2683–2691.

27. Dash, R., Elder, T., and Ragauskas, A.J. (2012) Grafting of model primary amine compounds to cellulose nanowhiskers through periodate oxidation. *Cellulose*, **19**, 2069–2079.

28. Dash, R. and Ragauskas, A.J. (2012) Synthesis of a novel cellulose nanowhisker-based drug delivery system. *RSC Adv.*, **2**, 3403–3409.

29. Heux, L., Chauve, G., and Bonini, C. (2000) Nonflocculating and chiral-nematic self-ordering of cellulose microcrystals suspensions in nonpolar solvents. *Langmuir*, **16**, 8210–8212.

30. Bonini, C., Heux, L., Cavaillé, J.-Y., Lindner, P., Dewhurst, C., and Terech, P.

(2002) Rodlike cellulose whiskers coated with surfactant: a small-angle neutron scattering characterization. *Langmuir*, **18**, 3311–3314.

31. Kvien, I., Tanem, B.S., and Oksman, K. (2005) Characterization of cellulose whiskers and their nanocomposites by atomic force and electron microscopy. *Biomacromolecules*, **6**, 3160–3165.

32. Elazzouzi-Hafraoui, S., Putaux, J.-L., and Heux, L. (2009) Self-assembling and chiral nematic properties of organophilic cellulose nanocrystals. *J. Phys. Chem. B*, **113**, 11069–11075.

33. Bondeson, D. and Oksman, K. (2007) Dispersion and characteristics of surfactant modified cellulose whiskers nanocomposites. *Compos. Interfaces*, **14**, 617–630.

34. Fortunati, E., Armentano, I., Zhou, Q., Iannoni, A., Saino, E., Visai, L., Berglund, L.A., and Kenny, J.M. (2012) Multifunctional bionanocomposite films of poly(lactic acid), cellulose nanocrystals and silver nanoparticles. *Carbohydr. Polym.*, **87**, 1596–1605.

35. Ljungberg, N., Cavaillé, J.-Y., and Heux, L. (2006) Nanocomposites of isotactic polypropylene reinforced with rodlike cellulose whiskers. *Polymer*, **47**, 6285–6292.

36. Kim, J., Montero, G., Habibi, Y., Hinestroza, J.P., Genzer, J., Argyropoulos, D.S., and Rojas, O.J. (2009) Dispersion of cellulose crystallites by nonionic surfactants in a hydrophobic polymer matrix. *Polym. Eng. Sci.*, **49**, 2054–2061.

37. Rojas, O.J., Montero, G.A., and Habibi, Y. (2009) Electrospun nanocomposites from polystyrene loaded with cellulose nanowhiskers. *J. Appl. Polym. Sci.*, **113**, 927–935.

38. Petersson, L., Kvien, I., and Oksman, K. (2007) Structure and thermal properties of poly(lactic acid)/cellulose whiskers nanocomposite materials. *Compos. Sci. Technol.*, **67**, 2535–2544.

39. Viet, D., Beck-Candanedo, S., and Gray, D.G. (2007) Dispersion of cellulose nanocrystals in polar organic solvents. *Cellulose*, **14**, 109–113.

40. Sassi, J.F. and Chanzy, H. (1995) Ultrastructural aspects of the acetylation of cellulose. *Cellulose*, **2**, 111–127.

41. Yuan, H., Nishiyama, Y., Wada, M., and Kuga, S. (2006) Surface acylation of cellulose whiskers by drying aqueous emulsion. *Biomacromolecules*, **7**, 696–700.

42. Berlioz, S., Molina-Boisseau, S., Nishiyama, Y., and Heux, L. (2009) Gas-phase surface esterification of cellulose microfibrils and whiskers. *Biomacromolecules*, **10**, 2144–2151.

43. Sassi, J.F., Tekely, P., and Chanzy, H. (2000) Relative susceptibility of the I_α and I_β phases of cellulose towards acetylation. *Cellulose*, **7**, 119–132.

44. Wang, N., Ding, E., and Cheng, R. (2007) Surface modification of cellulose nanocrystals. *Front. Chem. Eng. Chin.*, **1**, 228–232.

45. Çetin, N.S., Tingaut, P., Ozmen, N., Henry, N., Harper, D., Dadmun, M., and Sebe, G. (2009) Acetylation of cellulose nanowhiskers with vinyl acetate under moderate conditions. *Macromol. Biosci.*, **9**, 997–1003.

46. Zhang, R., Zhu, C., Shan, X., Xia, J., Zhu, Q., and Hu, Y. (2013) Study on the poly(3-hydroxybutyrate-*co*-4-hydroxybutyrate)-based nanocomposites reinforced by surface modified nanocrystalline cellulose. *J. Appl. Polym. Sci.*, **130**, 2015–2022.

47. Lin, N., Huang, J., Chang, P.R., Feng, J., and Yu, J. (2011) Surface acetylation of cellulose nanocrystal and its reinforcing function in poly(lactic acid). *Carbohydr. Polym.*, **83**, 1834–1842.

48. Lin, S., Huang, J., Chang, P.R., Wei, S., Xu, Y., and Zhang, Q. (2013) Structure and mechanical properties of new biomass-based nanocomposite: castor oil-based polyurethane reinforced with acetylated cellulose nanocrystal. *Carbohydr. Polym.*, **95**, 91–99.

49. Shang, W., Huang, J., Luo, H., Chang, P.R., Feng, J., and Xie, G. (2013) Hydrophobic modification of cellulose nanocrystal via covalently grafting of castor oil. *Cellulose*, **20**, 179–190.

50. Sobkowicz, M.J., Braun, B., and Dorgan, J.R. (2009) Decorating in green: surface

esterification of carbon and cellulosic nanoparticles. *Green Chem.*, **11**, 680–682.

51. de Menezes, A.J., Siqueira, G., Curvelo, A.A.S., and Dufresne, A. (2009) Extrusion and characterization of functionalized cellulose whiskers reinforced polyethylene nanocomposites. *Polymer*, **50**, 4552–4563.

52. Pandey, J.K., Chu, W.S., Kim, C.S., Lee, C.S., and Ahn, S.H. (2009) Bio-nano reinforcement of environmentally degradable polymer matrix by cellulose whiskers from grass. *Composites Part B*, **40**, 676–680.

53. Blachechen, L.S., de Mesquita, J.P., de Paula, E.L., Pereira, F.V., and Petri, D.F.S. (2013) Interplay of colloidal stability of cellulose nanocrystals and their dispersibility in cellulose acetate butyrate matrix. *Cellulose*, **20**, 1329–1342.

54. de Mesquita, J.P., Donnici, C.L., Teixeira, I.F., and Pereira, F.V. (2012) Bio-based nanocomposites obtained through covalent linkage between chitosan and cellulose nanocrystals. *Carbohydr. Polym.*, **90**, 210–217.

55. Tang, L., Huang, B., Lu, Q., Wang, S., Ou, W., Lin, W., and Chen, X. (2013) Ultrasonication-assisted manufacture of cellulose nanocrystals esterified with acetic acid. *Bioresour. Technol.*, **127**, 100–105.

56. Rosilo, H., Kontturi, E., Seitsonen, J., Kolehmainen, E., and Ikkala, O. (2013) Transition to reinforced state by percolating domains of intercalated brush-modified cellulose nanocrystals and poly(butadiene) in cross-linked composites based on thiol–ene click chemistry. *Biomacromolecules*, **14**, 1547–1554.

57. Xu, Y., Ding, W., Liu, J., Li, Y., Kennedy, J.F., Gu, Q., and Shao, S. (2010) Preparation and characterization of organic-soluble acetylated starch nanocrystals. *Carbohydr. Polym.*, **80**, 1078–1084.

58. Thielemans, W., Belgacem, M.N., and Dufresne, A. (2006) Starch nanocrystals with large chain surface modifications. *Langmuir*, **22**, 4804–4810.

59. Namazi, H. and Dadkhah, A. (2010) Convenient method for preparation of hydrophobically modified starch nanocrystals with using fatty acids. *Carbohydr. Polym.*, **79**, 731–737.

60. Zhang, Q., Wei, S., Huang, J., Feng, J., and Chang, P.R. (2013) Effect of surface acetylated-chitin nanocrystals on structure and mechanical properties of poly(lactic acid). *J. Appl. Polym. Sci.* doi: 10.1002/APP.39809

61. de Nooy, A.E.J., Besemer, A.C., and van Bekkum, H. (1995) Highly selective nitroxyl radical-mediated oxidation of primary alcohol groups in water-soluble glucans. *Carbohydr. Res.*, **269**, 89–98.

62. Lin, N., Bruzzese, C., and Dufresne, A. (2012) TEMPO-oxidized nanocellulose participating as crosslinking aid for alginate-based sponges. *ACS Appl. Mater. Interfaces*, **4**, 4948–4959.

63. Saito, T., Hirota, M., Tamura, N., Kimura, S., Fukuzumi, H., Heux, L., and Isogai, A. (2009) Individualization of nano-sized plant cellulose fibrils by direct surface carboxylation using TEMPO catalyst under neutral conditions. *Biomacromolecules*, **10**, 1992–1996.

64. Hirota, M., Tamura, N., Saito, T., and Isogai, A. (2009) Oxidation of regenerated cellulose with $NaClO_2$ catalyzed by TEMPO and NaClO under acid-neutral conditions. *Carbohydr. Polym.*, **78**, 330–335.

65. Fujisawa, S., Isogai, T., and Isogai, A. (2010) Temperature and pH stability of cellouronic acid. *Cellulose*, **17**, 607–615.

66. Isogai, A., Saito, T., and Fukuzumi, H. (2011) TEMPO-oxidized cellulose nanofibers. *Nanoscale*, **3**, 71–85.

67. Araki, J., Wada, M., and Kuga, S. (2001) Steric stabilization of a cellulose microcrystal suspension by poly(ethylene glycol) grafting. *Langmuir*, **17**, 21–27.

68. Montanari, S., Roumani, M., Heux, L., and Vignon, M.R. (2005) Topochemistry of carboxylated cellulose nanocrystals resulting from TEMPO-mediated oxidation. *Macromolecules*, **38**, 1665–1671.

69. Habibi, Y., Chanzy, H., and Vignon, M.R. (2006) TEMPO-mediated surface oxidation of cellulose whiskers. *Cellulose*, **13**, 679–687.

70. Fan, Y., Saito, T., and Isogai, A. (2008) Chitin nanocrystals prepared by

TEMPO-mediated oxidation of α-chitin. *Biomacromolecules*, **9**, 192–198.

71. Siqueira, G., Bras, J., and Dufresne, A. (2010) New process of chemical grafting of cellulose nanoparticles with a long chain isocyanate. *Langmuir*, **26**, 402–411.

72. Pei, A., Zhou, Q., and Berglund, L.A. (2010) Functionalized cellulose nanocrystals as biobased nucleation agents in poly(L-lactide) (PLLA)–Crystallization and mechanical property effects. *Compos. Sci. Technol.*, **70**, 815–821.

73. Gandini, A. and Belgacem, M.N. (2008) *Monomers, Polymers and Composites from Renewable Resources*, 1st edn, Elsevier, Kidlington, Oxfordshire, UK, pp. 419–432.

74. Biyani, M.V., Foster, E.J., and Weder, C. (2013) Light-healable supramolecular nanocomposites based on modified cellulose nanocrystals. *ACS Macro Lett.*, **2**, 236–240.

75. Grunert, M. and Winter, W.T. (2002) Nanocomposites of cellulose acetate butyrate reinforced with cellulose nanocrystals. *J. Polym. Environ.*, **10**, 27–30.

76. Goussé, C., Chanzy, H., Excoffier, G., Soubeyrand, L., and Fleury, E. (2002) Stable suspensions of partially silylated cellulose whiskers dispersed in organic solvents. *Polymer*, **43**, 2645–2651.

77. Raquez, J.-M., Murena, Y., Goffin, A.-L., Habibi, Y., Ruelle, B., DeBuyl, F., and Dubois, P. (2012) Surface-modification of cellulose nanowhiskers and their use as nanoreinforcers into polylactide: a sustainably-integrated approach. *Compos. Sci. Technol.*, **72**, 544–549.

78. Yang, J., Han, C.-R., Duan, J.-F., Ma, M.-G., Zhang, X.-M., Xu, F., and Sun, R.-C. (2013) Synthesis and characterization of mechanically flexible and tough cellulose nanocrystals–polyacrylamide nanocomposite hydrogels. *Cellulose*, **20**, 227–237.

79. Hasani, M., Cranston, E.D., Westman, G., and Gray, D.G. (2008) Cationic surface functionalization of cellulose nanocrystals. *Soft Matter*, **4**, 2238–2244.

80. Zaman, M., Xiao, H., Chibante, F., and Ni, Y. (2012) Synthesis and characterization of cationically modified nanocrystalline cellulose. *Carbohydr. Polym.*, **89**, 163–170.

81. Salajková, M., Berglund, L.A., and Zhou, Q. (2012) Hydrophobic cellulose nanocrystals modified with quaternary ammonium salts. *J. Mater. Chem.*, **22**, 19798–19805.

82. Tehrani, A.D. and Neysi, E. (2013) Surface modification of cellulose nanowhisker throughout graft polymerization of 2-ethyl-2-oxazoline. *Carbohydr. Polym.*, **97**, 98–104.

83. de Souza Lima, M.M. and Borsali, R. (2004) Rodlike cellulose microcrystals: structure, properties, and applications. *Macromol. Rapid Commun.*, **25**, 771–787.

84. Kloser, E. and Gray, D.G. (2010) Surface grafting of cellulose nanocrystals with poly(ethylene oxide) in aqueous media. *Langmuir*, **26**, 13450–13456.

85. Azouz, K.B., Ramires, E.C., den Fonteyne, W.V., El Kissi, N., and Dufresne, A. (2012) Simple method for the melt extrusion of a cellulose nanocrystal reinforced hydrophobic polymer. *ACS Macro Lett.*, **1**, 236–240.

86. Lin, N. and Dufresne, A. (2013) Physical and/or chemical compatibilization of extruded cellulose nanocrystal reinforced polystyrene nanocomposites. *Macromolecules*, **46**, 5570–5583.

87. Belgacem, M.N., Quillerou, J., and Gandini, A. (1993) Urethanes and polyurethanes bearing furan moieties—3. Synthesis, characterization and comparative kinetics of the formation of diurethanes. *Eur. Polym. J.*, **29**, 1217–1224.

88. Labet, M., Thielemans, W., and Dufresne, A. (2007) Polymer grafting onto starch nanocrystals. *Biomacromolecules*, **8**, 2916–2927.

89. Habibi, Y. and Dufresne, A. (2008) Highly filled bionanocomposites from functionalized polysaccharide nanocrystals. *Biomacromolecules*, **9**, 1974–1980.

90. Zoppe, J.O., Peresin, M.S., Habibi, Y., Venditti, R.A., and Rojas, O.J. (2009) Reinforcing poly(ϵ-caprolactone)

nanofibers with cellulose nanocrystals. *ACS Appl. Mater. Interfaces*, **9**, 1996–2004.

91. Habibi, Y., Goffin, A.-L., Schiltz, N., Duquesne, E., Dubois, P., and Dufresne, A. (2008) Bionanocomposites based on poly(ε-caprolactone)-grafted cellulose nanocrystals by ring-opening polymerization. *J. Mater. Chem.*, **18**, 5002–5010.

92. Goffin, A.-L., Raquez, J.-M., Duquesne, E., Siqueira, G., Habibi, Y., Dufresne, A., and Dubois, P. (2011) Poly(ε-caprolactone) based nanocomposites reinforced by surface-grafted cellulose nanowhiskers via extrusion processing: morphology, rheology, and thermo-mechanical properties. *Polymer*, **52**, 1532–1538.

93. Lin, N., Chen, G., Huang, J., Dufresne, A., and Chang, P.R. (2009) Effects of polymer-grafted natural nanocrystals on the structure and mechanical properties of poly(lactic acid): a case of cellulose whisker-*graft*-polycaprolactone. *J. Appl. Polym. Sci.*, **113**, 3417–3425.

94. Namazi, H. and Dadkhah, A. (2008) Surface modification of starch nanocrystals through ring-opening polymerization of ε-caprolactone and investigation of their microstructures. *J. Appl. Polym. Sci.*, **110**, 2405–2412.

95. Yu, J., Ai, F., Dufresne, A., Gao, S., Huang, J., and Chang, P.R. (2008) Structure and mechanical properties of poly(lactic acid) filled with (starch nanocrystal)-graft-poly(ε-caprolactone). *Macromol. Mater. Eng.*, **293**, 763–770.

96. Chang, P.R., Ai, F., Chen, Y., Dufresne, A., and Huang, J. (2009) Effects of starch nanocrystal-*graft*-polycaprolactone on mechanical properties of waterborne polyurethane-based nanocomposites. *J. Appl. Polym. Sci.*, **111**, 619–627.

97. Feng, L., Zhou, Z., Dufresne, A., Huang, J., Wei, M., and An, L. (2009) Structure and properties of new thermoforming bionanocomposites based on chitin whisker-graft-polycaprolactone. *J. Appl. Polym. Sci.*, **112**, 2830–2837.

98. Labet, M. and Thielemans, W. (2012) Citric acid as a benign alternative to metal catalysts for the production of cellulose-grafted-polycaprolactone copolymers. *Polym. Chem.*, **3**, 679–684.

99. Xu, Q., Yi, J., Zhang, X., and Zhang, H. (2008) A novel amphotropic polymer based on cellulose nanocrystals grafted with azo polymers. *Eur. Polym. J.*, **44**, 2830–2837.

100. Bergenstråhle, M., Mazeau, K., and Berglund, L.A. (2008) Molecular modeling of interfaces between cellulose crystals and surrounding molecules: effects of caprolactone surface grafting. *Eur. Polym. J.*, **44**, 3662–3669.

101. Carlsson, L., Utsel, S., Wågberg, L., Malmström, E., and Carlmark, A. (2012) Surface-initiated ring-opening polymerization from cellulose model surfaces monitored by a quartz crystal microbalance. *Soft Matter*, **8**, 512–517.

102. Goffin, A.-L., Raquez, J.-M., Duquesne, E., Siqueira, G., Habibi, Y., Dufresne, A., and Dubois, P. (2011) From interfacial ring-opening polymerization to melt processing of cellulose nanowhisker-filled polylactide-based nanocomposites. *Biomacromolecules*, **12**, 2456–2465.

103. Braun, B., Dorgan, J.R., and Hollingsworth, L.O. (2012) Supramolecular ecobionanocomposites based on polylactide and cellulosic nanowhiskers: synthesis and properties. *Biomacromolecules*, **13**, 2013–2019.

104. Wang, J.-S. and Matyjaszewski, K. (1995) Controlled/"living" radical polymerization. Atom transfer radical polymerization in the presence of transition-metal complexes. *J. Am. Chem. Soc.*, **117**, 5614–5615.

105. Matyjaszewski, K. (2012) Atom transfer radical polymerization (ATRP): current status and future perspectives. *Macromolecules*, **45**, 4015–4039.

106. Morandi, G., Heath, L., and Thielemans, W. (2009) Cellulose nanocrystals grafted with polystyrene chains through surface-initiated atom transfer radical polymerization (SI-ATRP). *Langmuir*, **25**, 8280–8286.

107. Morandi, G. and Thielemans, W. (2012) Synthesis of cellulose nanocrystals bearing photocleavable grafts by ATRP. *Polym. Chem.*, **3**, 1402–1407.

108. Majoinen, J., Walther, A., McKee, J.R., Kontturi, E., Aseyev, V., Malho, J.M.,

Ruokolainen, J., and Ikkala, O. (2011) Polyelectrolyte brushes grafted from cellulose nanocrystals using Cu-mediated surface-initiated controlled radical polymerization. *Biomacromolecules*, **12**, 2997–3006.

109. Zoppe, J.O., Österberg, M., Venditti, R.A., Laine, J., and Rojas, O.J. (2011) Surface interaction forces of cellulose nanocrystals grafted with thermoresponsive polymer brushes. *Biomacromolecules*, **12**, 2788–2796.

110. Harrisson, S., Drisko, G.L., Malmström, E., Hult, A., and Wooley, K.L. (2011) Hybrid rigid/soft and biologic/synthetic materials: polymers grafted onto cellulose microcrystals. *Biomacromolecules*, **12**, 1214–1223.

111. Song, S., Wang, C., Pan, Z., and Wang, X. (2008) Preparation and characterization of amphiphilic starch nanocrystals. *J. Appl. Polym. Sci.*, **107**, 418–422.

112. Zhou, C., Wu, Q., and Zhang, Q. (2011) Dynamic rheology studies of in situ polymerization process of polyacrylamide–cellulose nanocrystal composite hydrogels. *Colloid Polym. Sci.*, **289**, 247–255.

113. Bhattacharya, A. and Misra, B.N. (2004) Grafting: a versatile means to modify polymers: techniques, factors and applications. *Prog. Polym. Sci.*, **29**, 767–814.

114. Zhou, C., Wu, Q., Yue, Y., and Zhang, Q. (2011) Application of rod-shaped cellulose nanocrystals in polyacrylamide hydrogels. *J. Colloid Interface Sci.*, **353**, 116–123.

115. Karaaslan, M.A., Tshabalala, M.A., Yelle, D.J., and Buschle-Diller, G. (2011) Nanoreinforced biocompatible hydrogels from wood hemicelluloses and cellulose whiskers. *Carbohydr. Polym.*, **86**, 192–201.

116. Zhou, Q., Brumer, H., and Teeri, T.T. (2009) Self-organization of cellulose nanocrystals adsorbed with xyloglucan oligosaccharide-poly(ethylene glycol)-polystyrene triblock copolymer. *Macromolecules*, **42**, 5430–5432.

117. Azzam, F., Heux, L., Putaux, J.-L., and Jean, B. (2010) Preparation by grafting onto, characterization, and properties of thermally responsive polymer-decorated cellulose nanocrystals. *Biomacromolecules*, **11**, 3652–3659.

118. Wang, J., Wang, Z., Li, J., Wang, B., Liu, J., Chen, P., Miao, M., and Gu, Q. (2012) Chitin nanocrystals grafted with poly(3-hydroxybutyrate-*co*-3-hydroxyvalerate) and their effects on thermal behavior of PHBV. *Carbohydr. Polym.*, **87**, 784–789.

119. Cao, X., Habibi, Y., Magalhães, W.L.E., Rojas, O.J., and Lucia, L.A. (2011) Cellulose nanocrystals-based nanocomposites: fruits of a novel biomass research and teaching platform. *Curr. Sci.*, **100**, 1172–1176.

120. Cao, X., Habibi, Y., and Lucia, L.A. (2009) One-pot polymerization, surface grafting, and processing of waterborne polyurethane-cellulose nanocrystal nanocomposites. *J. Mater. Chem.*, **19**, 7137–7145.

121. Chen, G., Wei, M., Chen, J., Huang, J., Dufresne, A., and Chang, P.R. (2008) Simultaneous reinforcing and toughening: new nanocomposites of waterborne polyurethane filled with low loading level of starch nanocrystals. *Polymer*, **49**, 1860–1870.

122. Ljungberg, N., Bonini, C., Bortolussi, F., Boisson, C., Heux, L., and Cavaillé, J.Y. (2005) New nanocomposite materials reinforced with cellulose whiskers in atactic polypropylene: effect of surface and dispersion characteristics. *Biomacromolecules*, **6**, 2732–2739.

123. Peng, B., Han, X., Liu, H., Berry, R.C., and Tam, K.C. (2013) Interactions between surfactants and polymer-grafted nanocrystalline cellulose. *Colloid Surf., A*, **421**, 142–149.

124. Dong, S. and Roman, M. (2007) Fluorescently labeled cellulose nanocrystals for bioimaging applications. *J. Am. Chem. Soc.*, **129**, 13810–13811.

125. Mahmoud, K.A., Mena, J.A., Male, K.B., Hrapovic, S., Kamen, A., and Luong, J.H.T. (2010) Effect of surface charge on the cellular uptake and cytotoxicity of fluorescent labeled cellulose nanocrystals. *ACS Appl. Mater. Interfaces*, **2**, 2924–2932.

126. Hassan, M.L., Moorefield, C.M., Elbatal, H.S., and Newkome, G.R. (2012) New metallo-supramolecular terpyridine-modified cellulose functional

nanomaterials. *J. Macromol. Sci. Part A*, **49**, 298–305.

127. Hassan, M.L., Moorefield, C.M., Elbatal, H.S., Newkome, G.R., Modarelli, D.A., and Romano, N.C. (2012) Fluorescent cellulose nanocrystals via supramolecular assembly of terpyridine-modified cellulose nanocrystals and terpyridine-modified perylene. *Mater. Sci. Eng., B*, **177**, 350–358.

128. Zhang, L., Li, Q., Zhou, J., and Zhang, L. (2012) Synthesis and photophysical behavior of pyrene-bearing cellulose nanocrystals for Fe^{3+} sensing. *Macromol. Chem. Phys.*, **213**, 1612–1617.

129. Eyley, S. and Thielemans, W. (2011) Imidazolium grafted cellulose nanocrystals for ion exchange applications. *Chem. Commun.*, **47**, 4177–4179.

130. Cateto, C.A. and Ragauskas, A. (2011) Amino acid modified cellulose whiskers. *RSC Adv.*, **1**, 1695–1697.

131. Mangalam, A.P., Simonsen, J., and Benight, A.S. (2009) Cellulose/DNA hybrid nanomaterials. *Biomacromolecules*, **10**, 497–504.

132. Goetz, L., Mathew, A., Oksman, K., Gatenholm, P., and Ragauskas, A.J. (2009) A novel nanocomposite film prepared from crosslinked cellulosic whiskers. *Carbohydr. Polym.*, **75**, 85–89.

133. Goetz, L., Foston, M., Mathew, A.P., Oksman, K., and Ragauskas, A.J. (2010) Poly(methyl vinyl ether-co-maleic acid)-polyethylene glycol nanocomposites cross-linked in situ with cellulose nanowhiskers. *Biomacromolecules*, **11**, 2660–2666.

134. Filpponen, I. and Argyropoulos, D.S. (2010) Regular linking of cellulose nanocrystals via click chemistry: synthesis and formation of cellulose nanoplatelet gels. *Biomacromolecules*, **11**, 1060–1066.

135. Fox, J.D., Capadona, J.R., Marasco, P.D., and Rowan, S.J. (2013) Bioinspired water-enhanced mechanical gradient nanocomposite films that mimic the architecture and properties of the squid beak. *J. Am. Chem. Soc.*, **135**, 5167–5174.

136. Feese, E., Sadeghifar, H., Gracz, H.S., Argyropoulos, D.S., and Ghiladi, R.A. (2011) Photobactericidal porphyrin-cellulose nanocrystals: synthesis, characterization, and antimicrobial properties. *Biomacromolecules*, **12**, 3528–3539.

137. Carpenter, B.L., Feese, E., Sadeghifar, H., Argyropoulos, D.S., and Ghiladi, R.A. (2012) Porphyrin-cellulose nanocrystals: a photobactericidal material that exhibits broad spectrum antimicrobial activity. *J. Photochem. Photobiol.*, **88**, 527–536.

138. McCormick, C.L., Dawsey, T.R., and Newman, J.K. (1990) Competitive formation of cellulose *p*-toluenesulfonate and chlorodeoxycellulose during homogeneous reaction of *p*-toluenesulfonyl chloride with cellulose in *N,N*-dimethylacetamide-lithium chloride. *Carbohydr. Res.*, **208**, 183–191.

139. Eyley, S., Shariki, S., Dale, S.E.C., Bending, S., Marken, F., and Thielemans, W. (2012) Ferrocene-decorated nanocrystalline cellulose with charge carrier mobility. *Langmuir*, **28**, 6514–6519.

140. Lin, N. and Dufresne, A. (2013) Supramolecular hydrogels from in situ host–guest inclusion between chemically modified cellulose nanocrystals and cyclodextrin. *Biomacromolecules*, **14**, 871–880.

141. Guilbault, N. and Bouchard, J. (2011) FPInnovations Inaugurates its New Research Facilities for Nanocrystalline Cellulose, *http://www.newswire.ca/en/story/795699/fpinnovations-inaugurates-its-new-research-facilities-for-nanocrystalline-cellulose* (accessed 20 June 2014).

142. Capstick, K., Kinley, D., and Prefontaine, E. (2011) New Facility to Produce Wonder Material from Forests and Farms, *http://www.wd.gc.ca/eng/77_12990.asp* (accessed 20 June 2014).

143. Gatenholm, P. (2012) Nerve Cells Grow on Nanocellulose, *http://www.chalmers.se/en/news/Pages/Nerve-cells-grow-on-nanocellulose.aspx* (accessed 20 June 2014).

144. Kovacs, T., Naish, V., O'Connor, B., Blaise, C., Gagné, F., Hall, L., Trudeau, V., and Martel, P. (2010) An ecotoxicological characterization of nanocrystalline cellulose (NCC). *Nanotoxicology*, **4**, 255–270.

145. Ni, H., Zeng, S., Wu, J., Cheng, X., Luo, T., Wang, W., Zeng, W., and Chen, Y. (2012) Cellulose nanowhiskers: preparation, characterization and cytotoxicity evaluation. *Bio-Med. Mater. Eng.*, **22**, 121–127.

4
Preparation of Polysaccharide Nanocrystal-Based Nanocomposites

Hou-Yong Yu, Jin Huang, Youli Chen, and Peter R. Chang

4.1
Introduction

Nanoparticles with high crystallinity can be procured by the removal of the amorphous component of biosourced polysaccharides such as starch, cellulose, and chitin via a conventional acidolysis method. Polysaccharide nanocrystals (PNs) are rigid, biodegradable, biocompatible, and renewable, and are generally regarded as eco-friendly materials. PNs have many virtues including high modulus (greater than 100 GPa), high specific surface area (greater than hundreds of $m^2\,g^{-1}$), high aspect ratio, plentiful surface hydroxyl groups, and low density, and they have been used to enhance the performance of polymer composites [1]. Fabrication methods greatly affect the structure and properties of the resultant composites, so different fabrication methods have been developed according to the desired attributes/characteristics of the PNs, the properties of the polymers, and the application requirements. Current fabrication methods include solution casting, melt blending, electrospinning, sol−gel, and self-assembly techniques [2−6].

Homogeneous dispersion of PNs in the polymeric matrix is essential as it facilitates the formation of strong hydrogen bonds between the polymer and PNs, and leads to better performance of the ultimate PN/polymer nanocomposites. Poor compatibility between the hydrophilic surface of the PNs and the hydrophobic polymers (in most cases) initially causes intramolecular hydrogen bond interactions to occur between PNs, and subsequently, the PNs tend to agglomerate in the polymer matrix. Agglomeration is observed during melt processing of nanocomposites and weakens the reinforcing effect of PNs. Not surprisingly, homogeneous dispersion of PNs in the hydrophobic matrix is a great challenge [2].

In order to efficiently improve the reinforcing effect of PNs, plasticization or surface modification of PNs was adopted to reduce the internal intramolecular hydrogen bond interaction and to improve dispersion in the hydrophobic polymer matrix. Polymer blending and surface modification are usually used to improve compatibility between the polymer matrix and PNs; however, most of the PNs prepared by sulfuric acid hydrolysis exhibit poor thermal stability owing to residual

sulfate groups, and would further prevent processing through the use of several melt processing techniques such as injection molding, twin−screw compounding, and extrusion. The prevailing problems of PNs, such as agglomeration and poor thermal stability, cannot be solved simply by introducing a third polymer component. Although a third polymer component usually contributes to better mechanical properties of the matrix, it usually shows selective/strong affinity to PNs.

Surface modification of PNs, including physical adsorption, small molecule reaction, and grafting of polymers based on "graft onto" and "graft from" strategies [4] seems to afford a practical solution to the above problems. The introduction of hydrophobic chains to the surface of PNs enhances interfacial compatibility between the PNs and matrix, extending their application. Sol−gel processing could mitigate poor interface interactions and serve as a template for preparing chiral porous materials. Interestingly, in spite of strong hydrogen bond interactions among PNs resulting in self-agglomeration, the hydrogen bond interactions can be used as the driving force in the preparation of pure PN self-assembly materials. This chapter covers the preparation and fabrication of PN-based nanocomposites and discusses the relationship between structure and properties of these materials as well as the recent progress in their application.

4.2
Casting/Evaporation Processing

4.2.1
Solution Casting/Evaporation Processing

A new direction for research on composites has been developed owing to the emergence of biosourced PNs. High-performance nanocomposites can be achieved by introducing PNs via solution casting/evaporation processing, as shown in Figure 4.1. The properties of nanocomposites were found to be dependent on the dispersion of PNs in the solvent/matrix, the matching polarity/nonpolarity of the PNs/matrix, and the formation of an intermolecular hydrogen bond network. Some advantages of solution casting/evaporation processing are the good dispersion of PNs in the aqueous or organic medium and the formation of a three-dimensional network structure by solvent evaporation or heat treatment (Figure 4.1), which can significantly enhance the mechanical and thermal properties of the polymer matrix [5]. However, with an increase in the PN content, self-aggregation of PNs occurred and resulted in an increase in the nanophase-structure size, which was not conducive to the formation of the three-dimensional network structure and induced a decrease in the mechanical properties of the nanocomposites. This resulted mainly from the abundant hydroxyl groups on the PN surface, which easily dispersed in the polar solvent and had an affinity for water. This would restrict the range of application as green nanocomposites.
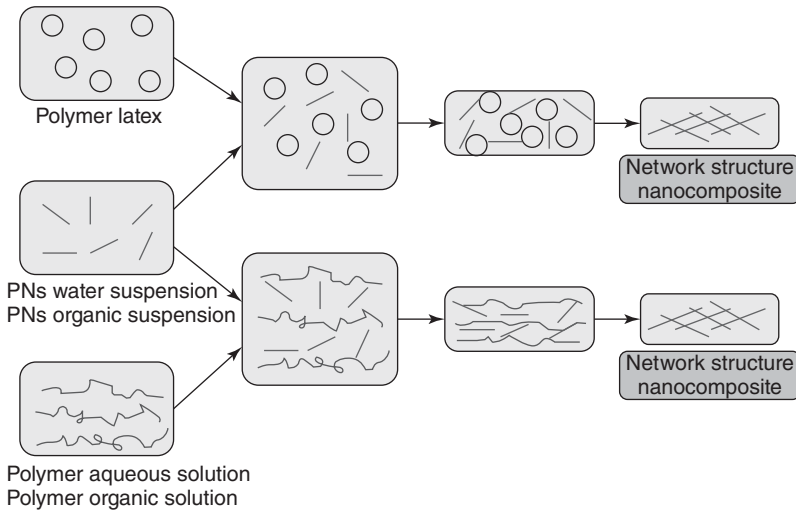
Figure 4.1 Solution casting/evaporation process for PN-based nanocomposites.

4.2.2
Solution Casting in Aqueous Medium

4.2.2.1 Dispersion Stability of Polysaccharide Nanocrystals in Aqueous Medium

PNs can be prepared by sulfuric acid hydrolysis of biosourced polysaccharides. PNs procured by this method are usually well dispersed in the aqueous medium after ultrasonication because of the electrostatic repulsion of residual sulfate groups. PNs have been found to exhibit birefringence [5–10]. Habibi *et al.* [6] prepared a cellulose nanocrystal (CN) suspension by pretreatment of ramie fiber with sodium hydroxide solution, followed by hydrolysis of 65 wt% sulfuric acid. Shear birefringence was observed between crossed polarizers in a 0.63 wt% suspension of rodlike CNs. Once the shear was removed, the solution spontaneously separated into an upper isotropic and a lower anisotropic phase, which was ascribed to self-orientation of the rodlike CNs. The liquid crystal phase formed because the negatively charged sulfate groups on the CNs caused the electrostatic repulsion of CNs to change their structure from a flat cylinder into a twisted rod [7]; this configuration led to parallel packing of the rods to form a nematic phase as well as the appearance of birefringence. Wang *et al.* [8] obtained spherical CNs through H_2SO_4/HCl hydrolysis of microcrystalline cellulose with ultrasonication. With an increase in the solids content, the birefringence of the CN suspension became apparent and the liquid crystal phase was observed. Formation of the liquid crystal phase was due mainly to polydispersity (up to 49%) of spherical CNs and the introduction of sulfate groups on their surface.

Formation of three-dimensional network structure between PNs is usually inhibited and consequently self-aggregation often occurs. For example, starch nanocrystals can be dispersed in an aqueous medium with sonication, but starch

nanocrystals with polar groups will agglomerate easily [11–14]. Lin *et al.* [11] overcame the self-aggregation of PNs using a three-dimensional network structure from alginate gel to improve their dispersibility and the reinforcing effect of PNs in nanocomposites. However, the surface energy of starch nanocrystals was unstable, and nanoparticles easily agglomerated in water because of hydrogen bonding and van der Waals forces [12, 13]. The FE-SEM (field emission scanning electron microscopy) image in Figure 4.2 shows that different particle size distributions of starch nanocrystals were achieved by tailoring centrifugation speed and storage time. With an increase of storage time, self-aggregation of the starch nanocrystals became obvious; the greater the centrifugal rate, the narrower the particle size distribution obtained [13].

4.2.2.2 Blending with Hydrophilic Polymers

PNs produced from renewable resources have many advantages, such as high strength, high modulus, and biodegradability. PNs also have a large number of hydrophilic hydroxyl groups, and as a result they are used to enhance hydrophilic polymers, such as waterborne polyurethane (WPU) [15–18], polyvinyl alcohol (PVA) [19–21], soy protein isolate (SPI) [22–25], and chitosan (CS) [26]
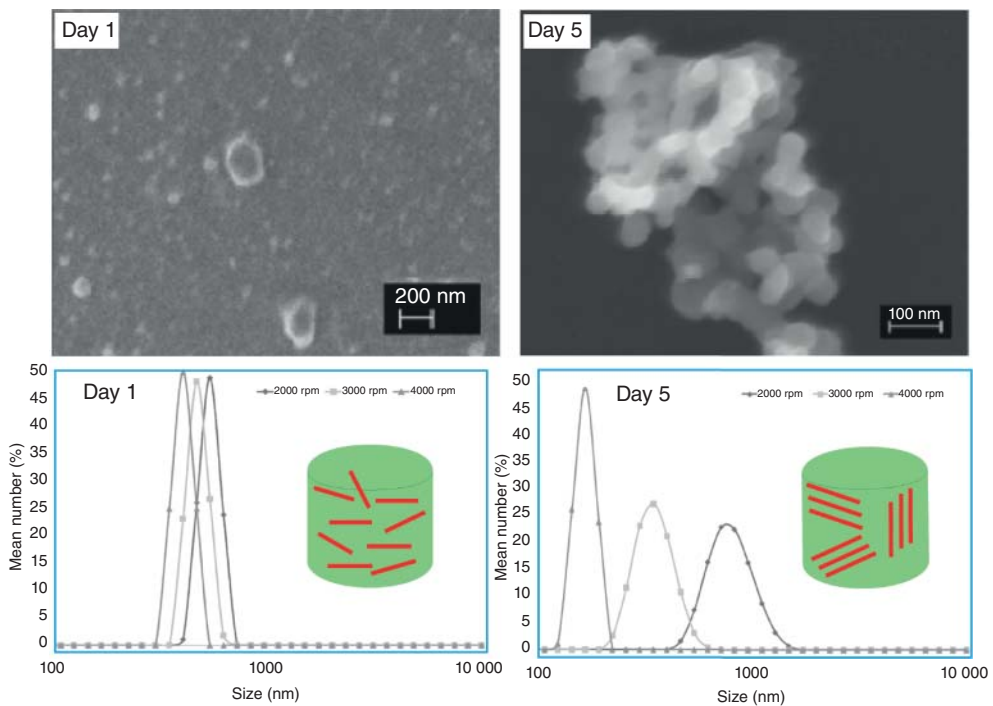
Figure 4.2 Particle size distribution (centrifugation rates of 2000, 3000, and 4000 rpm) and FE-SEM images (4000 rpm) of starch nanocrystals at 1 and 5 days. Reprinted with permission from Ref. [13].
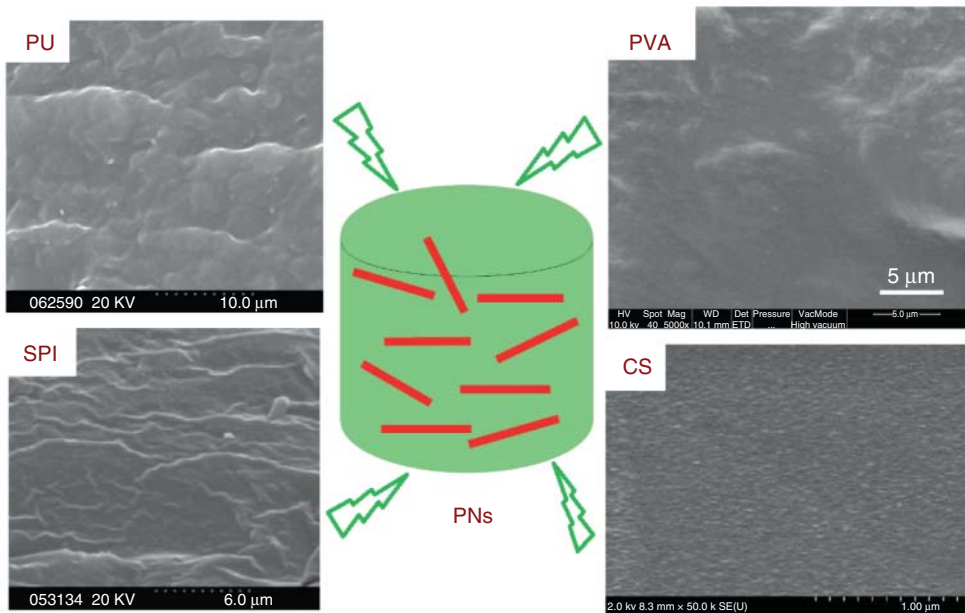
Figure 4.3 SEM images of nanocomposites containing PNs with PU, PVA, SPI, and CS. Reprinted with permission from Refs. [15, 19, 25, 26].

(Figure 4.3). Conceivably, the quantity and surface chemistry of PNs, the nature of the polymeric matrix, and the fabrication method all have significant impact on the structure and properties of nanocomposites. Cao *et al.* reported that 0–30 wt% flax CNs were added to polyurethane (PU) by direct solution blending, and the mechanical properties of the nanocomposites were obviously improved. This was due to interaction between CNs and the WPU matrix, but phase separation between CNs and the matrix became more serious as CN content increased [15]. Subsequently, isocyanate groups were introduced onto the CN surface to successfully prepare water-soluble CN/PU copolymer by grafting polycaprolactone (PCL) oligomers via *in situ* polymerization [16]. Increasing the CN concentration accelerated crystallization of the soft PCL chain segments, and cocrystallization between grafting chains and matrix chains occurred. This induced the formation of a continuous phase between the CNs and the matrix, and led to significant improvement in the mechanical strength of the nanocomposites; however, the toughness of the nanocomposites was reduced.

Regulation of the PN fractions also plays an important role in the structure and performance of nanocomposites. When starch nanocrystals and CNs were introduced into WPU, the two types of PNs combined to form strong hydrogen bond networks, leading to the synergistic reinforcement of WPU [17].

Surface activity and rigidity of PNs are important factors that affect the performance of nanocomposites. Chen *et al.* grafted polyols onto starch nanocrystals using diisocyanate as a coupling agent, and prepared modified

starch nanocrystal/PU nanocomposite films by solution casting. With an increase in starch nanocrystal content, cross-linking between hard and soft chain segments occurred, and as a result, physical interaction and cross-link density of nanocomposites were significantly changed. When 2 wt% starch nanocrystals were added, the strength and toughening of PU were enhanced. Compared to pure PU, maximum elongation at break and strength of the nanocomposites were increased by 170 and 260%, respectively. This result could be attributed to effective stress transfer due to rigid starch nanocrystals, and to strong interaction between the starch nanocrystals and PU matrix resulting from uniform dispersion of the starch nanocrystals [18].

The influence of the degree of hydrolysis of PVA on the interfacial interaction between CNs and the matrix was investigated by Roohani *et al.* [19]. It was found that fully hydrolyzed PVA had better affinity with CNs, allowing stronger filler/matrix interactions to occur as compared to partially hydrolyzed samples. Improved interfacial compatibility led to the enhanced mechanical properties of the fully hydrolyzed PVA nanocomposite. Paralikar *et al.* [20] prepared PVA barrier membranes reinforced by different amounts of CNs and poly(acrylic acid) (PAA) added as a cross-linking agent to provide water resistance. Heat treatment allowed the formation of ester groups between PAA and PVA and for the CNs to disperse well in the polymer matrix; moreover, cross-linking of PVA and PAA, and CNs and PVA occurred, resulting in improved barrier and mechanical properties of the nanocomposites. Barrier membranes with 10% CNs/10% PAA/10% PVA were synergistic and possessed the highest tensile strength and tensile modulus.

The influence of the size effect of pea starch nanocrystals on the structure and performance of PVA were investigated by Chen *et al.* [21] who found that pea starch nanocrystals of smaller size were better dispersed in the PVA matrix. Also, smaller nanocrystals formed more hydrogen bonds, creating stronger hydrogen bond interactions than those of the PVA/native pea starch nanocomposites, showing greater potential for pea starch nanocrystals as a reinforcing material.

Regulation of the interfacial structure between PNs and the polymer matrix is an effective method for improving the properties of nanocomposites. Modification of the plasticizer, cross-linking agent, and surface functionalization were found to directly influence the interfacial structure of nanocomposites. Wang *et al.* [25] prepared environmentally friendly thermoplastic protein composites with 0−30 wt% cotton CNs and glycerol as the plasticizer that showed that with high levels of CNs the cross-linked structure formed easily in the plasticizer-rich soy protein isolate (SPI) matrix. The hydrogen bond network structure formed through the strong force of hydrogen bonds between the CNs and SPI matrix, thus the mechanical properties of the nanocomposites increased significantly, while the water resistance also obviously improved. Mathew *et al.* [27] presented a chemical cross-linking post-treatment to improve the barrier properties and stability of CS-based nanocomposites. First, chitin nanocrystal/CS composites were immersed in glutaraldehyde solution at room temperature for 48 h. The glutaraldehyde molecules induced chemical cross-linking in the reactive groups
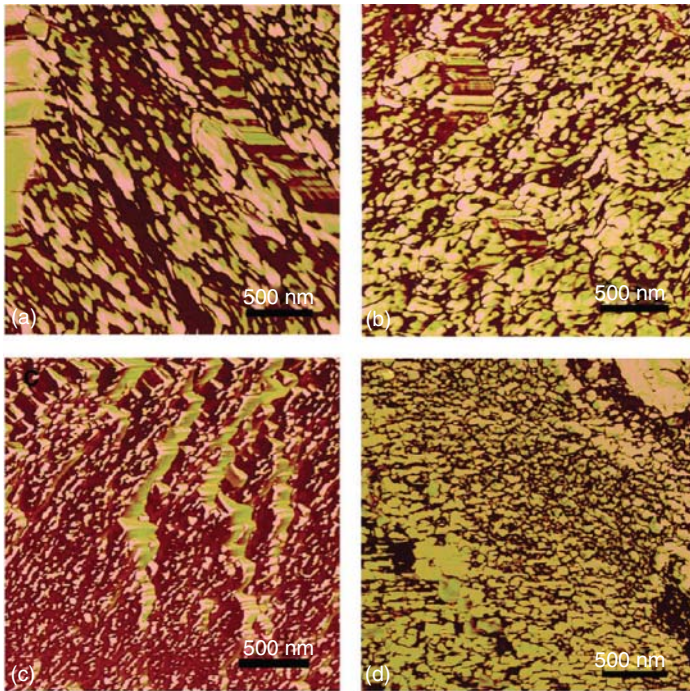
Figure 4.4 AFM images of composite containing different chitin nanocrystal contents: (a) composites with 5 wt% chitin nanocrystals without cross-linking; (b) composites with 10 wt% chitin nanocrystals without cross-linking; (c) composites with 5 wt% chitin nanocrystals after cross-linking; and (d) composites with 10 wt% chitin nanocrystals after cross-linking. Reprinted with permission from Ref. [27].

(e.g., amino, carboxyl groups) of the nanocomposite. Figure 4.4 shows the AFM (atomic force microscopy) images of the composite structures before and after cross-linking. The above-stated chemical cross-linking contributed not only to lower water resistance but also to higher stability to acids in the resultant nanocomposites. Wang and Roman [28] reported that the obtained polyelectrolyte macromolecules with different structures could be regulated through the ratio of CN sulfate groups and CS amino groups. Particles that formed with amino/sulfate group molar ratios greater than 1 were nearly spherical in shape and positively charged, whereas particles that formed at ratios less than 1 had well-defined nonspherical shapes and were negatively charged. In short, the nanocomposites could adjust the CNs/CS ratio to control their morphology, showing the attractive potential for application in drug release. In addition, Zhang *et al.* [29] and Zhang [30] prepared several kinds of supramolecular hydrogels modified by PNs and found that the elasticity modulus and viscosity of supramolecular hydrogels were increased greatly by the introduction of rigid PNs, and showed outstanding drug release behavior.

4.2.2.3 Blending with Hydrophobic Polymers

Highly dispersed PNs offer potential reinforcing effects to some specific hydrophobic polymers. Poly(styrene-co-butyl acrylate) (poly(S-*co*-BuA)) [31−37] and natural rubber (NR) [38−43] were modified by physical blending or emulsion polymerization with PNs to improve reinforcement and toughening. It was found that movement of the macromolecular chain and formation of hydrogen bond interactions in nanocomposites were dependent on the structure of the percolation network between PNs and the structural design of the matrix. In 1995, Favier *et al.* [31] prepared poly(S-*co*-BuA) nanocomposite with CNs as the reinforcing material for the first time. A CN content of 6 wt% embedded into the poly(S-*co*-BuA) matrix (Figure 4.5) led to a strong hydrogen bond network being formed between the CNs and poly(S-*co*-BuA), which greatly improved the shear modulus of the nanocomposites [32]. Meanwhile, Alain Dufresne [1] prepared novel poly(S-*co*-BuA) nanocomposites using potato starch nanocrystals as the reinforcing material. By increasing the starch nanocrystal content, a percolation network structure easily formed with a percolation threshold of 20%. The glass transition temperature (T_g) of nanocomposites was higher than that of poly(S-*co*-BuA). When the starch nanocrystal content was more than 20%, the interfacial thickness between reinforcing materials and the matrix was reduced because of overlapping. Vulcanization of NR also influenced the structure and properties of PN-modified nanocomposites [37]. It was found that a hydrogen bond network formed relatively easily between chitin nanocrystals and unvulcanized NR so that at the same concentration the reinforcing effect of chitin
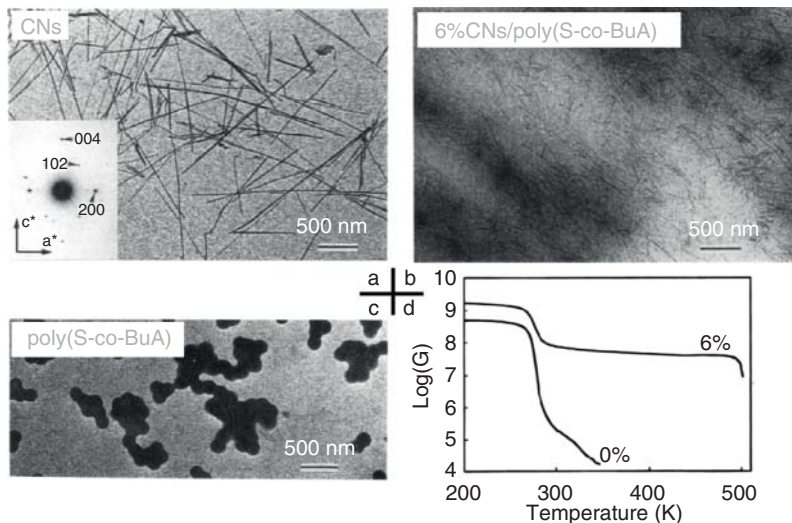

Figure 4.5 (a) TEM image of CNs; (b) TEM image of poly (S-*co*-BuA) colloidal particles; (c) TEM image of 6% CN/poly(S-*co*-BuA) composite; and (d) dynamic mechanics curve of pure poly(S-*co*-BuA) and 6% CN/poly(S-*co*-BuA). Reprinted with permission from Ref. [29].

nanocrystals on the mechanical and thermal properties of unvulcanized NR was more apparent than those of vulcanized NR. In addition, a study on the effect of starch nanocrystals (from waxy rice starch) and traditional carbon black on the properties of NR material was carried out [38]. The glass transition temperature of nanocomposites with 20 wt% glutinous rice starch nanocrystals was 75 times higher than that of unmodified rubber, and its strength was equivalent to that of nanocomposites with 26.6 wt% carbon black, proving even more potential for starch nanocrystals as a reinforcing agent of rubber materials than carbon black.

The aspect ratio of PNs is also an important parameter for the structure and properties of nanocomposites. Visakh *et al.* [39, 40] prepared NR nanocomposites with bamboo pulp cellulose microfiber and CNs with different aspect ratios and investigated the permeation behavior of three aromatic organic solvents (benzene, toluene, and xylene), and the diffusion coefficient, absorption coefficient, and permeability coefficient were calculated. The results showed that mobility of the interface molecular chains was prompted by interaction between high aspect ratio cellulose microfiber and rubber, improving the penetration of organic solvent molecules. The permeation resistance for toluene was better than that of nanocomposites with CNs, but the permeation resistance for xylene was poor. In addition, when the CN content was less than 10 wt%, it dispersed well in the matrix and strong interactions between the CNs and matrix occurred. As a result, the thermal stability and mechanical properties of nanocomposites were improved. However, when the CN content increased to 10 wt%, the nanocomposite properties were reduced because of agglomeration of the CNs. This suggests that development of a compatibilizer for nanocomposites is necessary.

4.2.3
Solution Casting in Organic Medium

4.2.3.1 Dispersion Stability of Polysaccharide Nanocrystals in Organic Medium
Although PNs (with polar groups) disperse easily in water, their reinforcing effects in hydrophobic polymers rely upon their dispersibility in organic solvents. It has been reported that PNs prepared by sulfuric acid hydrolysis dispersed well in the aqueous phase because of electrostatic repulsion from sulfate groups on CNs; however, electrostatic repulsion between CNs was limited in nonpolar organic solvents. Studies have shown that freeze-dried CNs disperse only in solvents such as dichloromethane, *N*,*N*-dimethylformamide (DMF), and dimethyl sulfoxide (DMSO) [42–44], and are difficult to disperse in most other organic solvents.

Recently, a solvent exchange method attracted attention because of the avoidance of agglomeration of freeze-dried CNs, and the high dispersion of CNs achieved by centrifugation [42–45]. Generally, the solvent exchange process involved two steps: (i) CNs were exchanged from water to acetone suspension and (ii) CNs were exchanged from acetone to polymer organic solvent. Good dispersion of CNs in the polymer was achieved via this method, which enabled the properties of the nanocomposites to be greatly improved. However, solvent exchange consumed large amounts of solvent, the long-term stability of the CN

suspensions was not good, and importantly, the loading levels of CNs within the polymer matrix were low because of self-aggregation [43, 45]. Therefore, surface modification of PNs is required to improve dispersion in organic solvents.

So far, some modification methods such as adding surfactants [46], compatibilizer [47], or chemical grafting [48–52] have been used to improve the dispersion of CNs in organic solvents. Good dispersion of CNs in organic solvents or polymer matrices is due to the affinity between surfactants or compatibilizer on the CN surface and the solvent or polymer matrix. De Mesquita *et al.* [48] prepared methyl adipose chloride modified CNs by grafting methyl adipoyl chloride (MAC) onto the CNs, and then compared the dispersion of unmodified CNs and MAC-modified CNs (MA-CNs) in different organic solvents. Dispersion stability of MA-CNs in various organic solvents was indeed better than that of unmodified CNs (Figure 4.6). This was ascribed to surface grafting of hydrophobic small molecules onto CNs, endowing them with good dispersion in organic solvents. Lin N. [42] and Lin S. [50] effectively improved the dispersion of modified CNs in organic solvents through surface acetylation. Their group also used benzoyl chloride to be grafted on the surface of konjac glucan-mannan chitosan nanocrystals (KGM), which reduced the surface energy of nanocrystals, making it disperse well in the organic solvent. Xu [52] modified the surface of chitin nanocrystals by grafting from L-lactide using tin(II) ethylhexanoate $(Sn(Oct)_2)$ as a catalyst for ring-opening polymerization to improve the compatibility of nanocrystals. The grafted copolymers kept the original morphology and crystal structure of CNs, but their hydrophobic properties and stability improved, as did their dispersion in organic solvents.

4.2.3.2 Blending with Polymers in Organic Solvent

As mentioned earlier, PNs have good dispersion in a limited number of solvents, so research has focused on polymers that can dissolve in the above solvents to develop into fully biodegradable nanocomposites. Jiang *et al.* [53] and Ten *et al.* [54] obtained well-dispersed CNs in DMF by ultrasonication, which were then added into poly(3-hydroxybutyrate-*co*-3-hydroxyvalerate) (PHBV) to obtain nanocomposites by solution casting. Moreover, the influence of
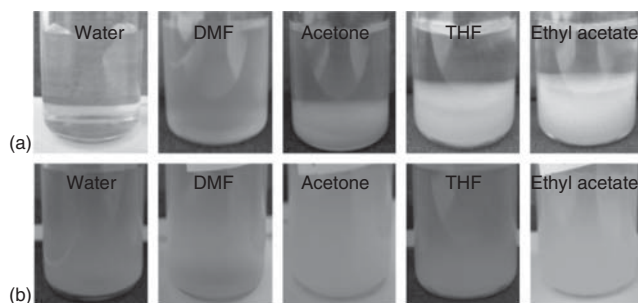

Figure 4.6 Pictures of dispersions of (a) unmodified CNs and (b) MA-CNs in water and different organic solvents. Reprinted with permission from Ref. [48].

PHBV/CN nanocomposites prepared by solution casting and melt blending on the dispersion state and properties was compared. When 5 wt% CN was added into a PHBV matrix through solution casting, its tensile strength increased from 14.1 to 26.1 MPa, which was higher than that of nanocomposites prepared by melt blending. It was found that better dispersion of CNs in the PHBV matrix was achieved by solution casting, whereas microphase separation occurred because of agglomeration of CNs during melt blending – which was not conducive to effectively absorbing stress transfer [53]. It was obvious that good dispersion of CNs in polymers was helpful for improving the physical properties of nanocomposites. In order to improve the dispersion of CNs in the PHBV matrix, polyethylene glycol (PEG) was introduced as a compatibilizer into the nanocomposites. As expected, the tensile strength and modulus of the nanocomposites containing 5 wt% CNs obviously improved [54], but their thermal stability did not enhance; compared to neat PHBV, the maximum thermal degradation temperature decreased from 295 to 290 °C. Although PEG improved the dispersion of CNs in organic solvents and in the polymer matrix, it hindered the formation of interactions between CNs and PHBV, leading to poor thermal stability. Yu *et al.* [55–58] obtained good dispersion of CNs in PHBV using solvent exchange without compatibilizer, and as a result had more hydrogen bond interactions forming between the CNs and PHBV; meanwhile, the more significant nucleation effect was achieved because of the homogeneous dispersion of CNs in the PHBV matrix. When the CN content was 10 wt%, significant enhancement of the mechanical and thermal properties of nanocomposites was achieved. Compared to neat PHBV, the tensile strength and Young's modulus of nanocomposites increased by 149 and 250%, respectively, and the maximum thermal degradation temperature (T_{max}) increased by 47.1 °C. This illustrated that the hydrogen bond interaction between CNs and PHBV restricted the formation of the six-member ring ester during the PHBV degradation process (Figure 4.7) to significantly improve the thermal stability [55–57]. However, compared with pure PHBV, when 1 wt% CN was added, there was a slight decrease in the thermal stability of the nanocomposites, which was due to residual sulfuric acid groups on the CN surface [55, 56]. CNs without acid groups were prepared using a novel hydrothermal method, and the reinforcing effect on PHBV of these and of those prepared using a sulfuric acid method was compared [58, 59]. The effect of CNs prepared by the hydrothermal method was more significant, and the CNs contained a large number of rich hydroxyl groups, which could form strong hydrogen bond interactions with PHBV and avoid the introduction of acid radical groups. Therefore, the thermal stability of the nanocomposite was greatly improved. In short, solvent exchange improved the dispersion of PNs in organic solvents and in the polymer matrix, thus enhancing the mechanical and thermal properties of the nanocomposites. However, due to rich polar groups on the PN surface the loading levels in the nanocomposites were less than 10 wt%, and poor compatibility with the polymer matrix and weak interfacial effects between the two components occurred [58, 60–63].

Research has been carried out to overcome problems related to the high activity of PN hydroxyl groups, poor compatibility with biodegradable polyesters, and low
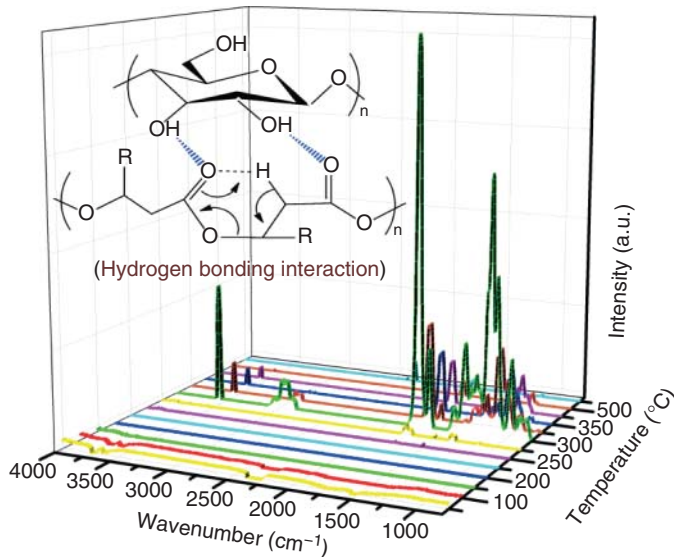
Figure 4.7 TG/FT–IR stack plots for nanocomposite with 10 wt% CNs. (Authors' own original artwork for this chapter according to Ref. [55].)

loading levels. Grafted small molecules (acetic anhydride, castor oil) on PNs led to an increase in the surface hydrophobicity of PNs, and improved compatibility with the hydrophobic biopolyester [60–63]. Subsequently, with the addition of 6 wt% acetylated CNs, the Young's modulus of the nanocomposites increased by 1.5 times, mainly because of the improved interfacial interaction between the CNs and the polymer matrix [62]. However, a slight agglomeration of CNs occurred when the CN content was greater than 10 wt%. This problem led researchers to graft PCL to the PNs by adopting "grafting from" and "grafting to" strategies, which were used to prepare fully biodegradable nanocomposites with high loading levels [5, 64]. "Grafting from" refers to the fact that polymer brushes can be grown *in situ* from initiation sites on the CN surface to react with reactive monomers. "Grafting to" involves the reaction between hydroxyl groups on the CN surface and functional end-groups of macromolecules or polymer chains. PCL/CN copolymers were prepared using the "grafting from" method. Even 40 wt% graft copolymer was added to the PCL matrix, the mechanical properties of nanocomposites were better than those of unmodified CN/PCL nanocomposites. This could be attributed to the continuous structure and cocrystallization formed between the PCL graft side chains and PCL, leading to significant improvement in polymer properties. PCL with different molecular weights was also grafted onto CNs and starch nanocrystals using the "grafting to" strategy. Incorporation of 50 wt% graft copolymer led to a great increase in the mechanical properties of the nanocomposites, which was due to chain entanglement between the grafted side chain and the polymer chains. Wang *et al.* [65] grafted PHBV onto chitin nanocrystals using a chlorination process (similar to "grafting to") and the modified chitin

nanocrystals were dispersed into a PHBV matrix. It was found that interfacial interaction of the nanocomposite obviously improved, but the heterogeneous nucleation effect of the modified chitin nanocrystals on the crystallization process was decreased. More importantly, the surface hydroxyl was replaced by polymer chains, weakening the hydrogen bond interactions of the nanocomposites. Nair *et al.* [66] proved that surface modification of chitin nanocrystals was not beneficial to the formation of hydrogen bond interactions and the chitin nanocrystal three-dimensional network. In this work, phenyl isocyanate (PI), alkenyl succinic anhydride (ASA), and 3-isopropenyl-dimethylbenzyl isocyanate (TMI) were introduced to reinforce NR. Results showed that the mechanical properties of modified chitin nanocrystal-based nanocomposites were poorer than those of nanocomposites with unmodified chitin nanocrystals. It indicated that surface modification of PNs improved the interfacial interaction between the filler and the polymer matrix, but it was not enough to improve the mechanical properties. The modified PNs was not beneficial to form the hydrogen bond interaction and three-dimensional network, resulting in no obvious property enhancement [66].

Solution casting is a technique commonly used for the preparation of nanocomposites because of its low cost and simplicity. However, the key to preparing high-performance PN nanocomposites is the dispersion of PNs within the polymer, the formation of a hydrogen bond network, and interfacial compatibility between the two components. Therefore, future development of a simple process for the preparation of surface-functionalized PNs is important.

4.3
Thermoprocessing Methods

4.3.1
Thermoplastic Materials Modified with Polysaccharide Nanocrystals

Thermoprocessing methods, such as extrusion, melt compounding, compression, and injection molding, are the most commonly used technologies for industrial-scale production of nanocomposites. These technologies are expected to promote large-scale manufacturing and wider application of CN-filled nanocomposites; however, CNs prepared by conventional sulfuric acid hydrolysis present low thermal stability and poor miscibility with the hydrophobic polymer matrix, thereby preventing the application of thermoprocessing technologies in the production of CN-filled nanocomposites [67]. It has been proved that small amounts of sulfate groups caused a considerable decrease in degradation temperature [68]. In this case, the sulfate groups generally induced rapid degradation of CNs at 180 °C, but neutralization by NaOH aqueous solution greatly enhanced the thermal stability of CNs. Therefore, an alternative method can be used to extract CNs from raw biomass materials using hydrochloric acid instead of sulfuric acid, which avoids

the formation of sulfate groups on the CN surface, causing thermal instability. With hydrochloric acid hydrolysis the as-prepared CNs have an obvious tendency toward aggregation [69] and do not favor dispersion and distribution in the matrix. As a result, surface modification of CNs has been considered to be a good way to enhance thermal stability by shielding sulfate groups and to simultaneously improve miscibility with the matrix and dispersion in the matrix.

4.3.2
Influence of Surface Modification of Polysaccharide Nanocrystals on Nanocomposite Thermoprocessing

Recently, great effort has been devoted to solving the problem of mismatch between the thermal stability of CNs and the thermoprocessing temperature. Physical modification was first attempted as a simple, easy method. It has been reported that attaching homopolymers to the surface of CNs, such as hydrophilic poly(oxyethylene) (PEO), can improve thermal stability because of the covering and wrapping of PEO on the CN surface together with the shielding of sulfate groups. Figure 4.8 shows the TGA (thermogravimetric analysis) curves of freeze-dried CNs and CNs physically attached to PEO of different molecular weights, as well as photographs of the extruded low density polyethylene (LDPE) films with and without both neat and modified CNs. For neat CNs, a gradual weight loss over the $200-400\,°C$ range was observed after an initial weight loss at less than $100\,°C$ owing to moisture removal. Obviously, attaching PEO to the CN surface caused the degradation process to shift to a higher temperature, over a narrower temperature range. At the same time, the appearance of the extruded LDPE films filled with neat and modified CNs indicated that the thermal stability did not match the $160\,°C$ temperature of thermal extrusion of LDPE. Owing to
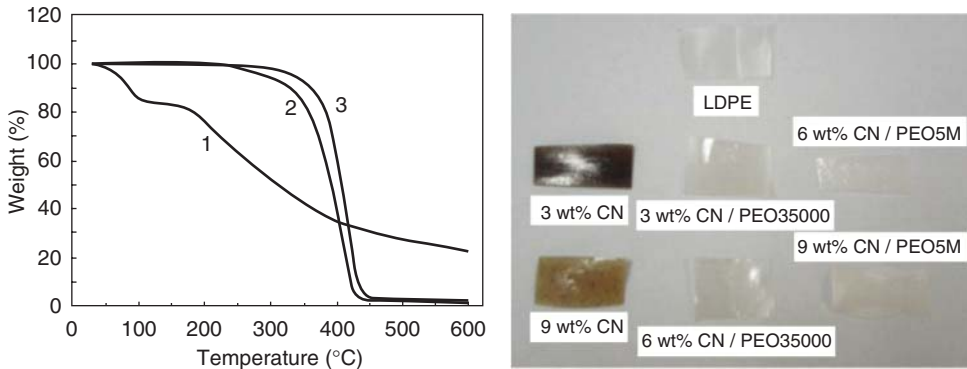

Figure 4.8 (a,b) TGA curves of freeze-dried CNs (1) and CNs physically attached by PEO (the weight ratio of CN vs. PEO as 80 : 20) of molecular weight $3.5 \times 10^4\,g·mol^{-1}$ (2) and $5 \times 10^6\,g·mol^{-1}$ (3); and photographs of extruded LDPE films filled with or without neat CNs and PEO-attached CNs at various loading levels. Reprinted with permission from Ref. [70].

thermal degradation of neat CNs, the LDPE film containing 3 wt% CNs presented a homogeneous darkness. With an increase in the CN content, poor miscibility between CNs and LDPE resulted in an inhomogeneous dispersion of CNs in the matrix, shown as black dots (CN aggregates) distributed in the brown substrate. However, the appearance of the LDPE films filled with PEO-attached CNs was similar to the translucent unfilled LDPE film. This was ascribed to the fact that the attached PEO improved the miscibility between CNs and LDPE to give uniform distribution and enhanced thermal stability by shielding the surface sulfate groups. In this case, the use of high molecular weight PEO was key [70]. When the molecular weight of the PEO used was low, the attached PEO layer was pulled from the CN surface during extrusion and failed to compatibilize the CNs with the matrix to enhance the thermal stability [53]. On the other hand, the strong affinity between the polymer on the CN surface and the polymer matrix was also a possible factor in the peeling off of the attached polymers from the CN surface. For example, PHBV was filled with CNs by extrusion and injection molding using low molecular weight PEO as a compatibilizer. The PEO/PHBV interaction was stronger than that of PEO/CN, and that together with the PEO not wrapping adequately on CNs because of the lower molecular weight, resulted in the removal of PEO from the CN surface, which then blended into the PHBV matrix during high shear twin-screw compounding [53]. Another water-soluble polymer, PVA, was used to encapsulate CNs and compound them with the poly(lactic acid) (PLA) matrix via dry-mixing of lyophilized PVA/CN with PLA prior to extrusion or pumping of the PVA/CN suspension directly into an extruder. The differences in interactions between the CN and PVA or PLA caused immiscibility between PVA and PLA resulting in a two-phase separated structure with the CNs primarily located in the discontinuous PVA phase. A negligible quantity of CNs was located in the continuous PLA phase leading to poor performance of the resultant nanocomposites [68]. It can be concluded from this that the effects of physical modification of homopolymers strongly depends on wrapping and shielding (confirmed by the high molecular weight of the homopolymer) and balancing of interactions involving the CN/matrix, CN/homopolymer, and the homopolymer/matrix.

Amphiphilic surfactants have been used to coat the CN surface to produce freeze-dried solids from suspension for melt compounding. The lyophilisate of CN coated with Beycostat A B09 was melt-compounded with PLA by a twin-screw micro extruder to process as a film. The maximum kneading temperature was controlled at 185 °C. The nanocomposites maintained the transparency of the PLA matrix and the presence of the surfactant favored the dispersion of CNs in the matrix. The nucleation effect was remarkably enhanced, inducing an increase in the Young's modulus [45]. In one study, a masterbatch was prepared with CNs preloaded into a polymer for subsequent melt compounding with the same polymer as the matrix. The CNs were mixed with polyvinylacetate (PVAc) in an aqueous solution, and then freeze-dried to obtain the masterbatch. Uniform dispersion of the CNs was expected in the masterbatch. Subsequently, the masterbatch containing the CNs was melt-compounded together with PVAc
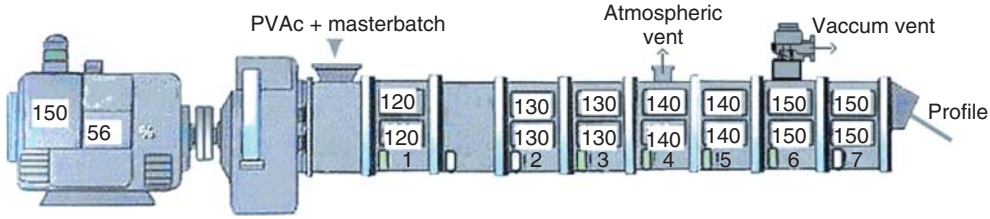
Figure 4.9 Schematic illustration of the feeding zone of the masterbatch and PVAc, and the temperature profile for the extrusion process for the CN/PVAc nanocomposites. (Authors' own original artwork for this chapter according to Ref. [45].)

by extrusion. The CNs showed good dispersion in the nanocomposites prepared using the extrusion process [71], which is schematically depicted in Figure 4.9.

The "dispersed nano-objects protective encapsulation" (DOPE) process was used to encapsulate the CNs during the cross-linking of alginate by Ca^{2+}. The DOPE method can be considered to be a good technology for production of the precursor containing CNs for thermoprocessing. The resultant capsules were compounded with a plasticizer-free thermoplastic material made of BASFs ecoflex® and potato starch, that is, commercial Bioplast GF 106/02, by twin-screw extrusion. However, the capsules did not disperse uniformly in the resultant nanocomposites and kept their integrity, so poor mechanical performance occurred [72]. In spite of the initial results being unsatisfactory, the DOPE strategy extends the concept of preloading CNs in one precursor to inhibit the self-aggregation of CNs in melt compounding.

Although physical modification of the CN surface is helpful to enhance thermal stability and compatibility with the hydrophobic matrix, these effects usually fail under the shear of thermoprocessing owing to cleavage of the association between CNs and the modified species. Furthermore, strong affinity between the matrix and the species used in physical modification may destroy the association between the CN and the modified species, while immiscibility between the matrix and the physically modified species on the CN surface may form two separate phases assigned to the matrix and the modified species. As a result, chemical modification has been considered to immobilize the designed functionality on the CN surface and hence eliminate the interference of the shear force. For instance, silylation contributed various functional groups, such as alkyl, amino, acryloyloxy, and methacryloxy, to the CN surface and the resultant silylated CNs were compounded with PLA using extrusion technology. In contrast to the dark color of injection-molded PLA filled with unmodified CNs, the nanocomposites prepared by melt processing remained colorless, suggesting that silylation of the CN surface reduced the thermosensitivity of CNs to allow its implementation via extrusion. Light-transmittance observation revealed good dispersion of the silylated CNs in the PLA matrix together with a few aggregates, which contributed to an increase in crystallinity and thermomechanical properties of the PLA matrix [23]. Esterification has also been used to modify the CN surface and introduce various lengths of aliphatic chains (C_6, and C_{12} and C_{18}) [70]. The
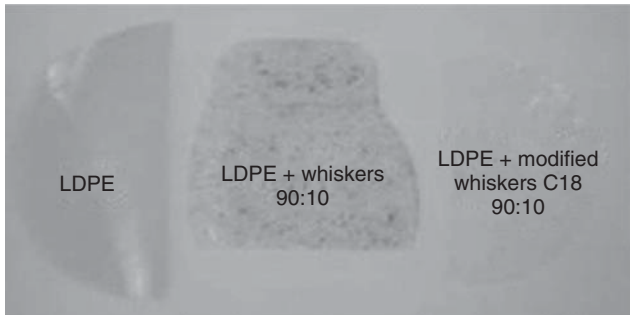
Figure 4.10 Photographs of unfilled LDPE film and LDPE films filled with 10 wt% unmodified CNs and CNs modified by stearoyl chloride. (In this figure "whiskers" means CN and "modified whiskers C18" means CNs modified by stearoyl chloride.) Reprinted with permission from Ref. [73].

modified CNs were melt-compounded with LDPE using twin-screw extrusion and subsequently hot-pressed into films. Figure 4.10 shows photographs of the unfilled LDPE film and the LDPE films filled with 10 wt% unmodified CNs and CNs modified by stearoyl chloride. The addition of 10 wt% CNs resulted in many black dots dispersed throughout the nanocomposite film in contrast to the translucent film of neat LDPE. This was ascribed to inhomogeneous dispersion that resulted from poor miscibility between the hydrophobic LDPE and the hydrophilic CN surface, and to low thermal stability of the CNs in the LDPE matrix due to sulfate groups on the CN surface. Silylation of the CNs with stearoyl chloride eliminated aggregation of the CNs [73], and the introduction of aliphatic chains compatibilized the CN and LDPE matrix, resulting in a translucent film similar to the neat LDPE film. This indicated that thermal stability was improved by surface silylation of the CNs. Furthermore, the CNs were not orientated via melt extrusion, and the homogeneity of the ensuing nanocomposites was found to increase with the length of the introduced aliphatic chain. Silylation on the CN surface resulted in an increase in tensile strength and elongation at break. In particular, the longest aliphatic chain derived from stearoyl chloride gave a significant increase in elongation at break [74].

In view of the contributions of long chains to the mechanical properties and miscibility with matrix mentioned above [70, 73, 74], polymer-grafted CNs were used to modify the polymeric materials via melt-processing technologies. For example, PCL-grafted and PLA-grafted CNs were melt-compounded with the corresponding PCL and PLA matrices using extrusion technology. Polymer grafting enhanced the thermal stability of the CNs and hence matched the temperature of the extrusion process. It was observed that PLA-grafted CNs eliminated the dark color resulting from thermal degradation of CNs, and the resultant nanocomposites appeared colorless and transparent [75]. The enhanced thermal stability was ascribed to the protection of grafted PLA and its mediated entanglement with the matrix, similar to a shell for sulfate groups on the CN surface [75]. In these two nanocomposite systems, improved miscibility between

the CNs and matrix not only depended on the affinity of the same molecular structure of the grafted chain and matrix but was also ascribed to entanglement with the matrix and the formation of a physical chain network mediated with grafted long chains [35], which was absent in systems containing CNs modified by small molecules and short chains. The effects of the co-continuous structure induced by grafted long chains is discussed in a later section. Besides the common reinforcing effect, polymer-grafted CNs could contribute to plasticization derived from grafted long chains [75]. Furthermore, polymer-grafted CNs may become nucleation sites to enhance the crystallinity of the nanocomposites [35].

Recently, the synergistic effect of physical and chemical modification of CNs has been verified to be very predominant for compatibilization with the hydrophobic matrix and for enhancing thermal stability [76]. A series of surface-modified CNs involving PEO attachment, PEG grafting, and both together were prepared and it was observed that modification by both PEO attachment and PEG grafting showed the highest thermal stability and the highest contact angle. Furthermore, PEG-grafted CNs displayed roughly two times higher PEO adsorption capacity than pristine CN because of the possibility of the formation of entanglements between the grafted PEG chains and the attached PEO chains. These surface-modified CNs were respectively melt-compounded with polystyrene (PS) by twin-screw extrusion at 200 °C. As shown in Figure 4.11, in contrast to the dark PS filled with pristine CNs, the PS filled with modified CNs was transparent owing to the enhanced thermal stability of surface physical/chemical modification, and to the cooperation of surface grafting and the subsequent attaching, which gave optimal light transmittance. This indicated that surface physical/chemical modification resulted in matching thermal stability to thermoprocessing temperature. Moreover, surface modification contributed to good dispersion of CNs in the matrix and compatibility with the hydrophobic PS matrix. Hence, mechanical reinforcement
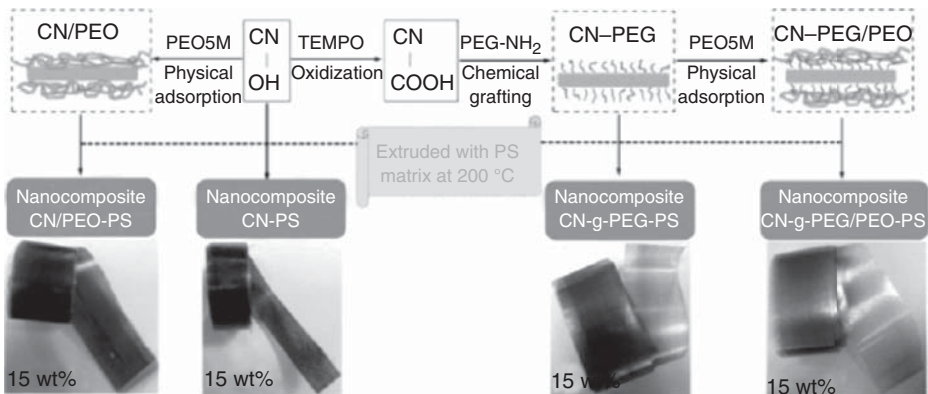

Figure 4.11 Schematic illustration of physical attachment and/or chemical grafting on the CN surface with PEO and PEG, respectively; photographs of the corresponding PS-based nanocomposites containing 15 wt% pristine and modified CNs. Reprinted with permission from Ref. [76].

and improved barrier properties were achieved, and the combination of surface grafting and subsequent attaching achieved optimal results [76].

On the whole, surface modification is an effective method for enhancing the thermal stability of CNs, and is expected to overcome key challenges for large-scale thermoprocessing of CN-based nanocomposites as industrial products. Furthermore, the improved miscibility between hydrophilic CNs and the hydrophobic matrix by surface modification can contribute to good mechanical performance and other properties. On the other hand, surface modification strategies and optimization of modification conditions need continued exploration, and the interfacial effect induced by surface modification and the corresponding regulation mechanism require more understanding. *In situ* surface modification of CNs in melt compounding with the matrix, such as the use of coupling CNs with polymer chains in the matrix by reactive small molecules and graft polymerization of monomers from the CN surface based on the "graft from" strategy, is expected to simplify the procedure and increase production efficiency.

4.4
Preparation of Nanofibers by Electrospinning Technology

4.4.1
Electrospinning Technology

4.4.1.1 Concepts
Nowadays, it is well known that electrospinning is the stretching of a polymer melt or solution under a high-voltage electrostatic field. The basic idea for commercialization of electrospinning began in 1900s, and then a number of patents for high voltage electrospinning equipment have been awarded [77–79], and subsequently an electrospinning device for polymer fibers was invented. In fact, in 1882 Rayleigh [80] focused on the problem of instability of charged liquid droplets, and put forward the question of how many charges the surface tension of a droplet needed to overcome. In 1952, Vonnegut and Neubauer [81] produced uniform droplets with a diameter of about 0.1 mm. In 1981, Larrondo and St John Manley [82] successfully produced polyethylene (PE) and polypropylene fibers using an electrospinning process and found that the diameter of the fiber was dependent on the electrical field, solution viscosity, and operating temperature. At the same time, electrospinning of thermoplastic polymers was invented. In the 1990s, with the development of nanoscience and nanotechnology, the huge potential for application of nanofiber products attracted more and more attention [83]. In recent years, electrospinning, as a simple and common method of producing continuous fiber with a submicron diameter, has become one of the most common methods for preparation of nanofibers [84–89]. The resulting nanofiber materials have been used in filtration membranes, catalytic materials, sensors, and tissue engineering

scaffolds [88–91]. Recently, because of their advantages of high porosity, large specific surface area, high fiber uniformity, and large aspect ratios, electrospun nanofibers have been used to prepare nonwoven fabrics, which have broad applications as high-performance filtration materials [91].

4.4.1.2 Formation Process of Nanofibers

Electrospinning is a method of inducing the formation of very fine fibers from a liquid jet using high voltage. Figure 4.12a shows a schematic diagram for the formation of nanofibers using a traditional electrospinning device. Nanofibers are formed from a liquid polymer solution or melt that is fed through a syringe needle or capillary tube into a region of high electric field. The electric field is most commonly generated by connecting a high-voltage power source in the kilovolt range to the syringe needle [92]. When electrostatic forces overcome the surface tension of the liquid, a Taylor cone is formed (Figure 4.12b) and a thin jet is rapidly accelerated to different collecting plates. Instabilities in this jet would induce violent whipping motions that elongate and thin the jet, allowing
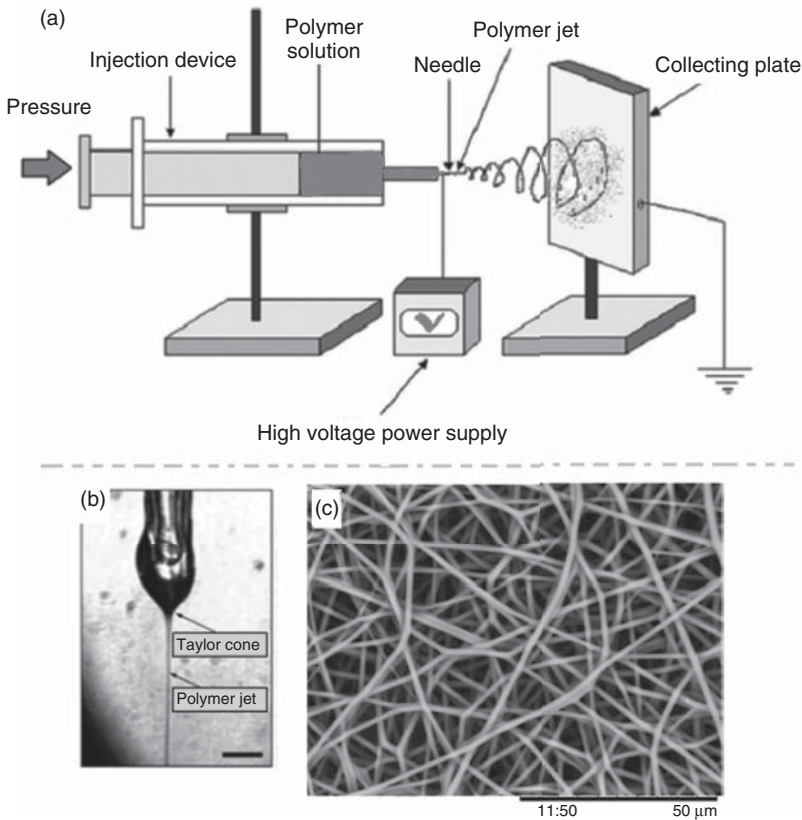

Figure 4.12 (a) Traditional electrospinning device; (b) formation of the Taylor cone; and (c) morphology of nonwoven fiber. Reprinted with permission from Refs. [87, 92].

the evaporation of some of the solvent or cooling of the melts to form solid nanofibers on the collecting plate (Figure 4.12c). Finally, the random non-woven films or uniaxially aligned sheets or arrays consisting of electrospun nanofibers are usually collected [87–92].

4.4.1.3 Basic Electrospinning Parameters and Devices

The typical electrospinning jet is a very complex fluid dynamics process, in which several electrospin processing parameters, such as solution viscosity, voltage, feed rate, solution conductivity, capillary-to-collector distance, orifice size, temperature, and humidity, would influence the size and microstructure of the nanofibers [87, 92–94]. For example, solvents with different volatilities will affect the fiber morphology as a highly volatile solvent would easily form a porous structure in the hydrophobic polymer nanofibers [93, 94]. In addition, the proportion of solvents in the solvent system would also affect fiber size.

In addition to processing parameters, the selection of the electrospinning device is the best way to produce controllable structure and properties of nanofibers [95–101]. As shown in Figure 4.13, a typical electrospinning device is composed of a high voltage power supply, solution storage and injection, and collecting devices [95]. The diversity of the device is mainly reflected by the differences in the position and shape of the collecting plates. No matter which position of collecting plates (vertical direction or keeping a certain angle between the needle and the collecting plates) was employed [95, 96], it is usually observed
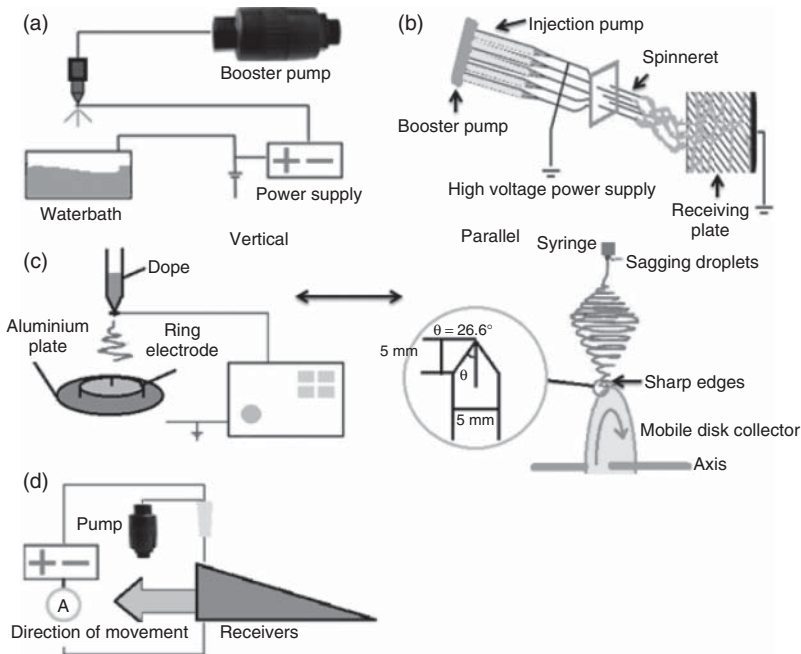

Figure 4.13 (a–d) Different electrospinning devices.

that randomly oriented fiber mats are obtained when a simple static collecting surface is used, while highly oriented fiber mats are commonly collected with a high-speed rotating roller used as the collecting device when the parallel collecting plate is used [96].

As electrospinning techniques developed, the conventional electrospinning device not only showed low production and low efficiency but also exhibited difficulty in preparing nanofibers of particular structures, such as core-shell structures, parallel arrangements, hollow structures, and internal hole structures [97–101]. To overcome the above problems, a novel electrospinning device emerged. Theron *et al.* obtained more fiber using multiple jets and adding realistic configurations of the external electric field between the electrodes, in which a decrease in the internozzle distances would lead to greater repulsion between the jets, reducing the edge effect of the fibers due to the repulsive force between jets [97, 98], as shown in Figure 4.13b. Fiber yarns with better orientation can be achieved using rotary collecting plates at high speed (Figure 4.13c) [99]. Theron *et al.* [100] used a blade-shaped edge as the collecting plate to form fiber bundles. Because of the limited area on the blade edge, only a small amount of fiber was recovered. Owing to the mutual repulsion between the same charges, the orientation of fiber decreased with an increase in the amount of collected fibers. Han *et al.* [101] observed various buckling instabilities of electrospinning jets when the grounded collector plate was tilted between 0° and 45° (Figure 4.13d). In addition, it was found that the buckling frequency was influenced by the velocity, diameter, density, and viscosity of the electrospinning jets. Moreover, different features of the electrical bending circles and buckling patterns can be tailored by changing interelectrode distances. Since the interelectrode distance was increased with time because of the lateral motion of the inclined collector, these patterns of fibers were collected along the slope of the moving collector.

4.4.1.4 Newly Emerging Electrospinning Techniques

1) Blend electrospinning involves two processing methods. The first one is that the two different polymer solutions do not mix in advance, but jet coaxially through the same capillary or syringe needle under the drive of the electrical field force, resulting in a continuous composite fiber with a core-shell structure [95]. Coaxial composite spinning equipment and the fiber core-shell structure are shown in Figure 4.14a,b. The second method involves two stages as follows: two kinds of polymers that were initially dissolved in the same solvent, and were subsequently electrospun using the same traditional electrospinning device. The resulting nanofiber materials from the second method may contain many ingredients, and could improve the physical and chemical properties of each fiber; however, the nanofibers were in a state of random distribution because of difficulty controlling the distribution of components [105, 106].

2) Multijet electrospinning uses multinozzle electrospinning and a high-speed collection drum as the collecting plate to form a hybrid nanofiber containing

(a)
Electrode
Air pressure inlet of the inner chamber
Rubber band
Air pressure inlet of the outer chamber
Inner and outer polymer solution
Out chamber outlet
Inner chamber outlet

(b)

(c)
Moving stage (perpendicular to motion of conveyor)
3D plotter
Electrodes
Spinnerets
Grounded Substrate

(d)
3D plotter
Electrospinning
Hybrid scaffold

(e)
Ethanol
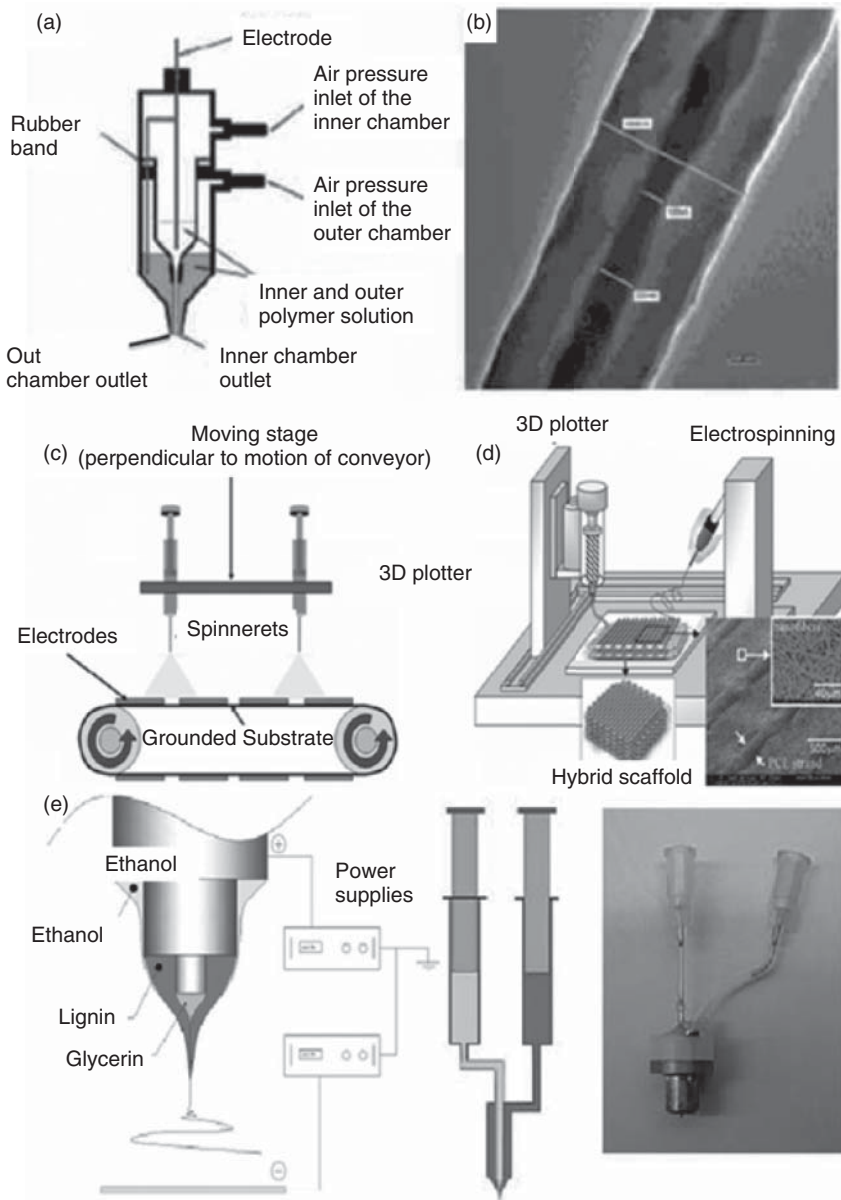Power supplies
Ethanol
Lignin
Glycerin

Figure 4.14 Schematic diagram of (a) a coaxial blend electrospinning device, (b) composite fiber morphology, (c) a multi-jet electrospinning device, (d) a multilayer nanometer composite scaffold prepared by multijet electrospinning, and (e) a coaxial electrospinning device. Reprinted with permission from Refs. [95, 102–104].

different polymers [107, 108] (Figure 4.14c). The production efficiency of electrospinning could be improved by the multijet electrospinning method, speeding up the industrial electrospinning process. This device can produce high yield and uniform nanofiber mats; however, a wide distribution of fiber diameter would happen because of interference between the electrode electric field of the jets, which could be improved by increasing the distance between the jets or decreasing the numbers of jets.

3) Multilayer electrospinning involves electrospinning with different polymer solutions (Figure 4.14d) to deposit the materials on the collecting plates and form nanofiber mats. Kidoaki *et al.* [109] proposed the concepts of multilayer and mixed electrospinning. During the electrospinning process, two or more different polymers are deposited onto a reception roller from two or more jets while rotating the reception roller at high speed to obtain cross-woven composite nanofiber membranes.

4) Coaxial electrospinning uses a coaxial composite jet instead of a single jet (Figure 4.14e). The shell-core fiber prepared by this method performs as two different polymers. The electrospinning solution may be added only to the outer layer to form a hollow tubular fiber [110, 111]. When the hollow structure was loaded with drugs, the resulting drug-loaded fibers showed great pontential in drug release, tissue engineering scaffolds, and drug-loaded wound dressing [111].

4.4.2
Nanocomposite Nanofibers Filled with Polysaccharide Nanocrystals

Recently, PNs have been used in many applications for biomedicine, food, and cosmetics because of their excellent characteristics of biodegradability, biocompatibility, high strength (Young's modulus of 150 GPa), abundant hydrophilic hydroxyl groups, and small size [3, 112]. Mahmoud *et al.* [112] found that cells adhering to the surface of CNs grew well, and implantation of CNs is harmless to human tissues. Currently, CNs are widely used as a starting material in electrospun nanofiber materials aiming for potential application in tissue engineering (Figure 4.15) [113–122, 125, 126].

4.4.2.1 Electrospun Nanofibers in Aqueous Medium
Peresin *et al.* [113, 125, 126] used electrospinning to prepare uniform PVA/CN composite nanofibers with different CN contents. It was found that with an increase in the CN content, the diameter of the composite nanofibers decreased, but the mechanical strength was significantly enhanced. With the addition of 15 wt% CNs, the diameter of the CN/PVA composite nanofibers decreased from 235 nm in the neat PVA nanofibers to 188 nm, and the storage modulus increased from 15.45 to 57.30 MPa. In addition, a percolation network formed easily because of strong hydrogen bond interactions that improved the performance of the composite nanofibers. Subsequently, the effect of humidity on the reinforcing effect of CN/PVA nanofibers was investigated. With the addition
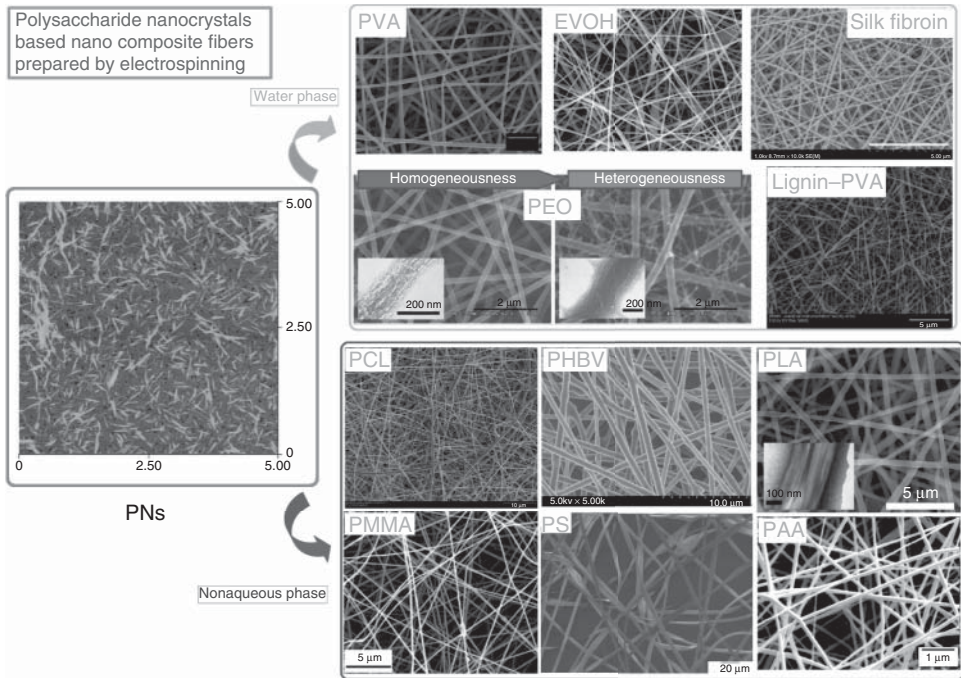
Figure 4.15 PN-based composite nanofibers prepared by electrospinning in aqueous and non-aqueous phases. Reprinted with permission from Ref. [113–124].

of CNs, even under high humidity, not only was the morphological stability of composite nanofiber maintained but also the strength increased as the humidity increased. This was attributed to the formation of a continuous phase structure under high humidity. After repeated treatment in high humidity (80%) and low humidity (0%), the performance of pure PVA nanofibers was very poor, but the mechanical properties of composite nanofibers remained stable. In fact, with increasing number of high and low humidity cycles, the mechanical strength of the composite nanofiber gradually increased, which was mainly due to the plasticizing effect induced by moisture and the reinforcing effect of CNs. The influence of CN content on lignin/PVA composite nanofibers has also been studied and it was found that increasing the lignin content was beneficial for obtaining bead-free nanocomposite fibers, while the increasing CN content changed spherical beads to spindles. More importantly, the introduction of CNs improved the thermal stability of lignin/PVA composite nanofibers through the strong hydrogen bond interaction between CNs and lignin/PVA, as seen in the IR results [113]. Martinez-Sanz *et al.* [114] prepared composite nanofibers of ethylene/vinyl alcohol copolymer (EVOH) with 5 wt% CNs. Compared to the multibeaded structure of neat EVOH fibers, the diameter of composite nanofibers without a beaded structure increased, and the glass transition temperature of the composite nanofibers increased as the CN content increased. Huang *et al.*

[115] successfully prepared CN/silkworm silk fibroin (SF) composite nanofibers. It was found that by increasing the CN content, the strength and modulus of the composite nanofibers increased, but the elongation at break decreased. Composite nanofibers containing CNs and PEO were prepared by Zhou *et al.* [116]. The microstructure of the fibers was modulated by changing the PEO fraction and the CN content. When the PEO fraction was 5 wt%, an increase in the CN content caused the composite nanofibers to become smaller and the structure was uniform; when 7 wt% PEO was used secondary nanofibers appeared (Figure 4.15).

Cross-linked polymers formed between PEO and pentaerythritol triacrylate (PETA), which was used as a photoinitiator [117]. The optimal UV irradiation cross-linking time was 40 min which had little impact on the diameter of the composite nanofibers. However, when the CN content was 10 wt% the diameter of the composite nanofibers decreased significantly. When the CN content was more than 10 wt%, the mechanical performance improved significantly as compared to PEO without cross-linking; the maximum tensile stress and Young's modulus of cross-linked PEO/CN composite fibers increased by 377.5 and 190.5%, respectively. Yu *et al.* [118] prepared biodegradable cellulose nanocrystal-grafted polyethylene glycol copolymer (CNs-*g*-PEG) using CNs as the skeleton, PEG as the functional side chain, and nontoxic oxalate as the coupling agent. The average diameter of the resulting nanofiber was about 910 nm. Moreover, the nanofibers could store and release energy during the heating and cooling processes (or phase change process). Meanwhile the nanofibers showed excellent solid–solid phase change behavior and a phase transition enthalpy of $88.2\,\mathrm{J\,g^{-1}}$. As a result, such nanofibers show potential as solid–solid phase change energy storage material.

4.4.2.2 Electrospun Nanofibers in Non-aqueous Medium

Rojas *et al.* [119] successfully obtained CN/PS composite nanofibers in a non-aqueous medium (THF, tetrahydrofuran) with electrostatic spinning. It was easy to get PS nanofibers with multibeaded structures under low voltage, but under high voltage the nanofibers obtained were smooth and unbeaded. The addition of both CNs and surfactant to the PS nanofibers favored the elimination of the beaded structure of the composite nanofibers and a smaller diameter. Besides, with an increase in electrospinning voltage, the nanocomposite fibers gave highly porous structures. Recently, they applied unmodified CNs and modified CNs (PCL short chain grafted CNs) to reinforce PCL nanofibers [120]. By adding unmodified CNs, sulfate groups on the CN surface could increase the charge density of the electrospinning solution, so the diameter of the uniformly sized composite nanofibers decreased significantly, and the mechanical properties improved. Surprisingly, the "annealing structure" continuous phase of composite nanofibers occurred because of the instability of the electrospinning solution and interference from grafted short chains [120]. Lu and Hsieh [121] used electrospinning to prepare CN/PAA composite nanofibers in ethanol solution. The influence of the PAA fraction (4, 6, 8, and 10%) on the structure of the composite nanofibers was investigated. Uniform nanofibers were achieved in the

4% PAA solution. The influence of CN content on the structure and performance of composite nanofibers was also investigated. The incorporation of CNs reduced the diameter of PAA nanofibers and their uniformity improved. When the CN content was increased to 20 wt%, the diameter decreased from 349 to 69 nm. Compared to neat PAA nanofiber, the modulus and strength of the thermally cross-linked composite nanofiber membrane with 20 wt% CNs improved by 77 and 58 times, respectively. Dong *et al.* [122] prepared polymethyl methacrylate (PMMA) nanofibers reinforced with different CN contents (5–41 wt%). It was found that the nanofiber diameter in the composite decreased when the CN content increased, and the thermal and mechanical properties improved.

Subsequently, new composite nanofibers have been developed for application in drug release and bone tissue scaffolds. Yu *et al.* [123] and Qin *et al.* [124] adopted an electrospinning method to prepare CN/PHBV composite nanofibers. It was found that with the introduction of CNs, the thermal stability and mechanical properties of the composite nanofibers were enhanced and that drug-loaded composite nanofibers were released steadily because of strong interactions between CNs and small molecule drugs (e.g., tetracycline hydrochloride). Zhou *et al.* [127] successfully prepared CN/PLA composite nanofibers of uniform diameter in which the thermal and mechanical performance could be controlled by varying the CN content. Moreover, the composite nanofibers were nontoxic to human adult adipose tissue-derived stromal cells (hASCs) and promoted their growth. In addition, the composite nanofibers had strong potential for application in bone tissue engineering materials. Wei *et al.* [128] prepared chitin nanocrystal/PLA composite nanofiber membranes with the ability to keep food fresh by adding chitin nanocrystals with a PLA fraction of 7% and a trace amount of Span 80 emulsifier. The PE film, pure PLA nanofiber membranes, and chitin nanocrystal/PLA composite nanofibers were comparatively studied as packaging for strawberries. Results showed that the chitin nanocrystal/PLA composite nanofiber membrane delayed weight loss, inhibited the decrease in titratable acidity and vitamin C mass fraction, and had a significant antibacterial effect.

Although electrospun PN-based composite nanofibers have great potential for applications in biomedicine, electrospinning has many problems such as low production capacity and large energy consumption, there is difficultly developing it for industrial applications, and the strength of the composite nanofibers does not meet the needs of the application. Therefore, application and development of electrospun PN composite nanofibers have a long way to go.

4.5
Sol–Gel Method

4.5.1
Concepts of Sol–Gel Process

Unmodified PNs are generally used to reinforce polymer matrixes with many polar chemical groups through solution casting. For nonpolar polymers (without

groups), amphiphilic polymer physical coating or chemical modification of the PN surface is needed because poor interfacial compatibility of the composite materials, microphase separation, and agglomeration will lead to a significant decrease in the mechanical properties [129]. A sol–gel method can overcome these shortcomings, allowing unmodified PNs dispersed in water or solvent to form three-dimensional self-assembled structures. PNs have a high specific surface area of up to $1000 \, m^2 \, g^{-1}$ after forming a three-dimensional network structure, but too large a specific surface area will produce a significant tendency for self-association. Recently, Capadona *et al.* introduced a sol–gel approach to nanocomposite fabrication. The process is based on the formation of a three-dimensional template scaffold of well-individualized CNs, which is subsequently filled with a polymer of choice [130]. During the sol-gel process, the important step is the formation of a CN template involving the formation of a homogeneous aqueous CN dispersion followed by gelation through solvent exchange with a water-miscible solvent (routinely acetone).

A diagram for the preparation of PN nanomaterials using the sol–gel method is shown in Figure 4.16. The method includes five steps: (i) a nonsolvent is added to a dispersion of CNs in the absence of any polymer, (ii) solvent exchange promotes the self-assembly of a gel of CNs, (iii) the gelled CN scaffold is interpenetrated with a polymer by immersion in a polymer solution, before the nanocomposite is (iv) dried and (v) compacted [130].

4.5.2

Polysaccharide Nanocrystal-Based or -Derived Nanocomposites Prepared by Sol–Gel Method

CNs were dispersed in a hydrophilic solvent (acetone) using a solvent exchange method to form a three-dimensional network gel in acetone that restricted the migration rate of CNs. When CN gels were impregnated with a hydrophobic polymer PS solution, the PS molecule dissolved, or partly dissolved, in the acetone solution. The organogel films containing polymers were wiped with paper towels
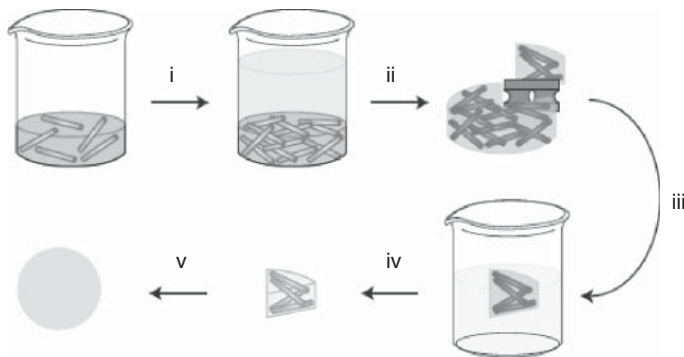

Figure 4.16 Synthesis of CNs/ polymer composite materials by sol–gel method. Reprinted with permission from Ref. [130].

and clamped between a pair of rectangular metal frames, to prevent lateral and longitudinal shrinkages, and dried in ambient air. It was found that the resulting composites showed dense filling of the cellulose gel voids with PS polymers. A result, a network formed as a result of entanglements between the CN molecular chains and the polymer molecular chains, and high-performance nanocomposites were obtained by taking advantage of the rigidity of CNs and specific interaction between cellulose and aromatic groups of PS. When the PS content was 20 wt%, the mechanical properties of the PS/CN material was significantly improved over original PS polymers. The Young's modulus and tensile strength of CN/PS nanocomposites reached 75 GPa and 75 MPa, respectively [131]. In addition, the coefficient of thermal expansion (30 ppm K^{-1}) was about one-third of the pure polymers, which indicated that the regenerated cellulose network was effective in suppressing thermal expansion of the synthetic polymers. Recently, CN organogels with three-dimensional structure were prepared by exchanging from aqueous dispersions, to acetone, and finally DMF using a solvent exchange sol–gel process. CN/epoxy resin nanocomposites were prepared by mixing CNs with oligomeric diglycidyl ether and multifunctional amine cross-linkers [132]. Using the sol–gel method, CNs were used not only to prepare nanocomposites with high mechanical properties but also to synthesize inorganic materials and chiral porous materials by using CNs with a chiral phase structure as a template for applications of chiral separation, asymmetric catalysis, chiral recognition, and optical materials.

4.5.3
Chiral Nanocomposites Using Cellulose Nanocrystal Template

4.5.3.1 Inorganic Chiral Materials Based on Cellulose Nanocrystal Template

It has been reported that polysaccharides exhibited chirality at the molecular level. Introducing chirality into porous inorganic solids is considered to produce new types of materials that could be useful for chiral separation, stereospecific catalysis, chiral recognition (sensing), and photonic materials [133–137]. For example, mesoporous silica-based inorganic chiral materials were synthesized by sol–gel mineralization using nematic liquid crystalline templates consisting of rod-like CNs. Firstly, the CNs were evaporated onto glass slides to form nematic liquid crystals. Secondly, an aqueous alkaline solution of pre-hydrolyzed tetramethoxysilane (TMOS) was added to the CN droplets to achieve a birefringent cellulose–silica composite. Finally, the composite was subsequently calcined at 400 °C for 2 h to remove the cellulose nanorod template, and a birefringent silica replica with patterned mesoporosity was produced owing to the presence of co-aligned cylindrical pores [133–135]. Mann *et al.* [134] first used CNs as a template to obtain birefringent silica, but no long-range helical ordering was observed and no porosity was measured. Shopsowitz *et al.* [133] showed that free-standing mesoporous silica films with long-range chiral nematic ordering may be obtained using a template-based approach (chiral nematic phase of CNs as a template), in which a condensation reaction between the surface hydroxyl
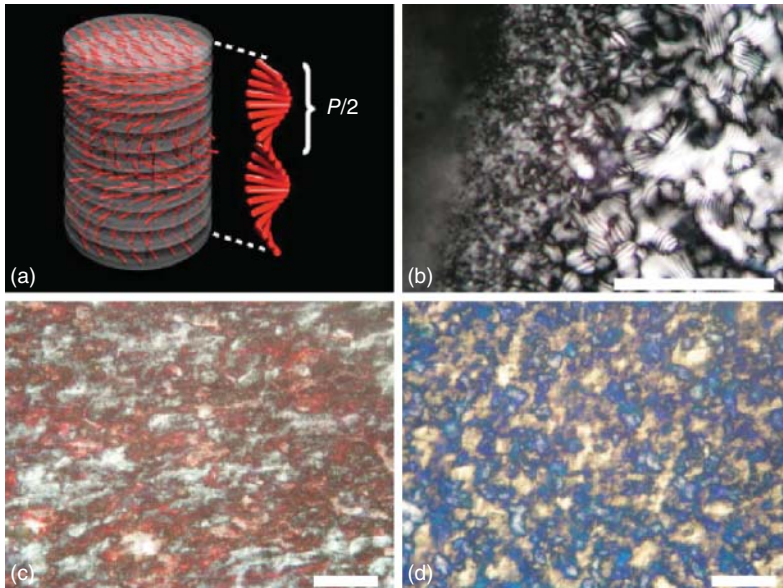
Figure 4.17 (a) Schematic of the chiral nematic ordering present in CN, along with an illustration of the half-helical pitch P/2 (150–650 nm); (b) polarized optical microscopy (POM) image of a CN/TEOS suspension observed during slow evaporation at room temperature (22 °C) clearly shows a fingerprint texture characteristic of chiral nematic ordering; (c) POM image of an CN/silica composite film. Strong birefringence and domains with different orientations are present; and (d) POM image of the mesoporous silica film obtained from the calcination of the film in (c). A shift in color from red to blue was observed, while the overall texture remained essentially unchanged. All micrographs were taken with crossed polarizers (scale bar, 100 mm). Reprinted with permission from Ref. [133].

groups of CNs and tetraethyl orthosilicate (TEOS) was carried out. After calcination of the composite films at 540 °C under air, the remaining chiral nematic structure was retained and was used to prepare porous inorganic materials with chiral nematic structures. As shown in Figure 4.17, after solvent evaporation, a fingerprint texture of the CNs/TEOS suspension was observed, indicating that the chiral nematic phase was established during drying in the presence of the silica precursor. After drying, free-standing composite films were obtained; meanwhile, the calcined films showed strong birefringence and a texture similar to that of the composite films. Moreover, the chiral nematic organization and high surface area of CNs were accurately replicated in the inorganic solid. The helical structure of the mesoporous films results in chiral reflectance that can be modulated across the entire visible spectrum and into the near-infrared [133].

4.5.3.2 Chiral Porous Materials

As mentioned earlier, CN/TMOS nanocomposites with a chiral structure can be prepared by the sol–gel method. At pH 2.4, the TMOS on the surface of the

CNs hydrolyzed and formed a uniform chiral nematic structure, and the chiral nematic structure of CNs was not destroyed [133]. After solvent evaporation, CN templates were calcined at 540 °C to prepare inorganic silicon dioxide thin film materials. Nitrogen adsorption test results showed that the pore size distribution was between 3.5 and 4 nm, and pores of greater than 8 nm were very few [133]. This result was consistent with the pore size of 5 nm for wood CNs, which further proves that the chiral structure of CNs was maintained by the condensation reaction of TMOS and the CN hydroxyl groups. Circular dichroism (CD) tests confirmed that the left-handed chiral nematic structure from CNs was preserved in the mesoporous silica films. SEM (scanning electron microscopy) results provide further confirmation of the replication of chiral nematic organization in pure silica films (Figure 4.18). The top surface of the thin film material was very smooth, but perpendicular to the surface a layered structure with defects that arose from changes in the direction of the helical axis of the chiral nematic phase
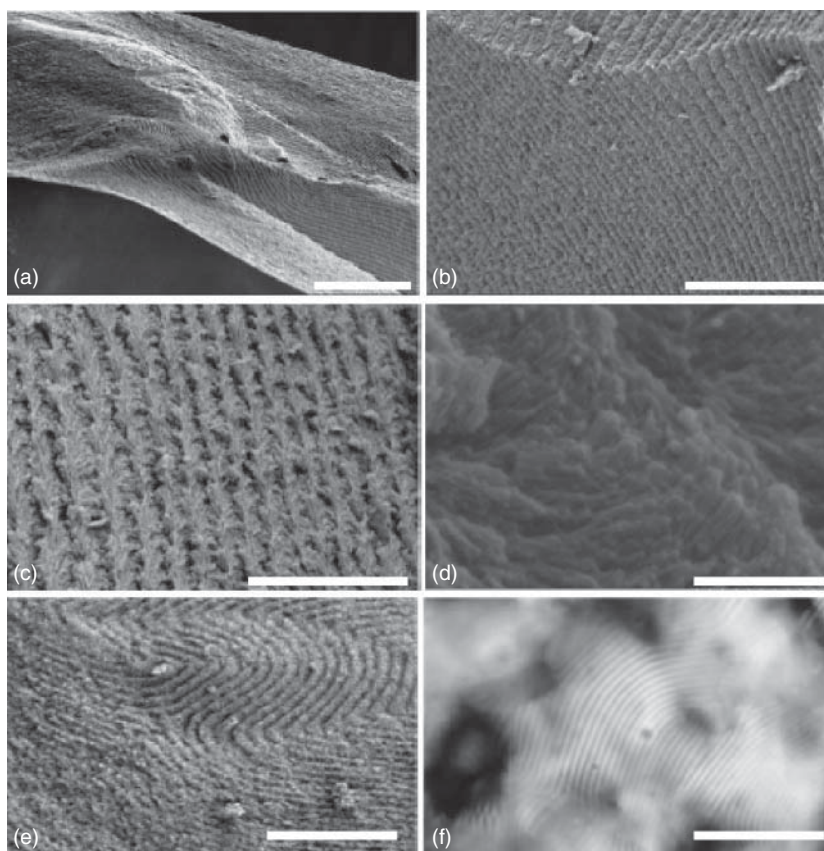

Figure 4.18 SEM photographs of silicon thin film material with chiral porous structure (a–e) and the corresponding polarized light microscopy of CN/TEOS mixture (f). Reprinted with permission from Ref. [133].

was observed (Figure 4.18a). This could be ascribed to macroscopic alignment not being performed on the samples. Moreover, the size of the repeating structure appeared to be a of few hundred nanometers (Figure 4.18b,c). With further magnification, a twisting rod-like morphology (Figure 4.18d) was observed. Throughout the sample, this twisting appears to occur in a counterclockwise direction when moving away from the viewer, consistent with a left-handed helical organization [133]. In some locations defects can be seen that correspond to a condensed version of those observed by polarized optical microscopy (POM) in the liquid crystal phase (Figure 4.18e,f). Therefore, this provides direct evidence that the chiral nematic organization of CNs has been faithfully replicated in the mesoporous silica films.

Recently, mesoporous anatase TiO_2 materials with high specific surface areas and optical structures have opened up a new direction for research. Shopsowitz *et al.* [136] reported the synthesis of mesoporous anatase TiO_2 using chiral nematic mesoporous silica films as a hard template (Figure 4.19), in which the silicon film materials were prepared by condensation reaction between hydrolyzed TMOS and the CN surface, resulting in the surrounding of SiO_2 on CNs with a chiral nematic organization. In addition, CNs were initially removed from the CN−silica composite films by calcination at $540\,°C$ to give chiral nematic mesoporous silica films. This is the first example of organizing a crystalline metal oxide into a chiral nematic structure. Moreover, it was found that free-standing films of mesoporous titania with high specific surface areas ($150−230\,m^2\,g^{-1}$) were achieved, which was determined by the porosity of the starting silica template [136]. Meanwhile, the mesoporous titania material selectively reflects left-handed circularly polarized light, indicating a chiral nematic organization of the titania crystallites. Such highly porous films of titania show great potential

Mesoporous silica   Mesoporous titania

1. TiCl$_4$ infiltration
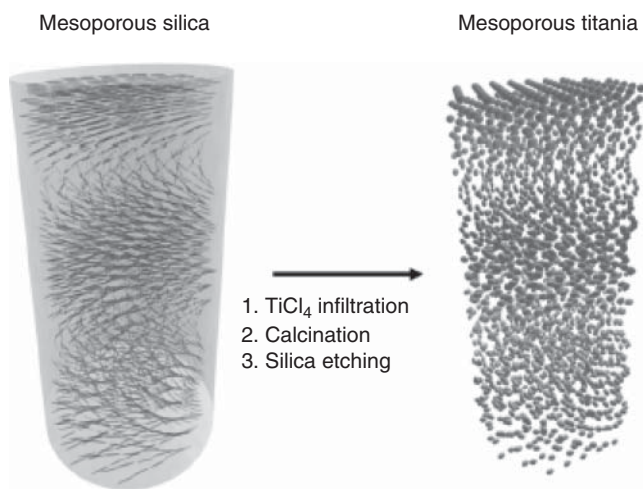2. Calcination
3. Silica etching

Figure 4.19 Synthesis of titanium dioxide material with chiral nematic silica material as rigid template. Reprinted with permission from Ref. [136].

applications in dye-sensitized solar cells, photocatalysts, sensors, and batteries [134].

4.5.3.3 Chiral Porous Carbon Materials

The combination of a mesoporous material (pore size 2–50 nm) with a carbon material is a new direction in research that shows great potential for macromolecular adsorption, double layer capacitors, lithium ion batteries, catalyst carriers, and field effect transistors [137–143]. Porous carbon materials with chiral nematic structures were synthesized using chiral mesoporous CN–silica composite films as the rigid template. The CN–silica composite films were then pyrolyzed under nitrogen at 900 °C to give carbon–silica composite films because of the removal of CNs from these films (Figure 4.20). In the final step, the silica was dissolved with aqueous NaOH to yield free-standing carbon films with centimeter dimensions and a glossy black appearance (Figure 4.21a). The conversion of CN into carbon proceeded in approximately 30% yield, as determined by TGA [137].

Table 4.1 shows that the porosity of the CN-derived porous carbon materials was analyzed by nitrogen adsorption/desorption [137]. CMC-1 (carboxymethyl cellulose) is the blank sample without any silicon component. Compared to that of CMC-1, the surface area and pore volume increased to 1460 $m^2\,g^{-1}$ and 1.22 $cm^3\,g^{-1}$, for the 65% CN–silica composite (CMC-3, Figure 4.21b), repectively. In addition, it was observed that CMC-3 showed no significant micropores in the carbon walls, indicating a highly ordered structure of the individual CNs prior to carbonization. The microporosity of CMC-1 may result from spaces that formed between the individual CNs during carbonization. Moreover, the mesopores of CMC-3 observed in TEM (transmission electron microscope) showed locally aligned pores, agreeing with the local nematic organization expected for a chiral nematic pore structure, but CMC-1 showed much smaller and more disordered pores (Figure 4.21c,d).

SEM images show that the long-range chiral nematic structure of CMC-3 was preserved, and that the porous carbon membrane material had a repetitive structure with a smooth surface and duplicate layers [137]. Under high magnification it can be seen that the rodlike CNs were retained in the carbon, and twisting in
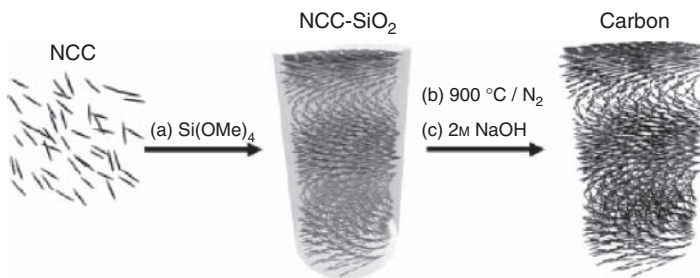

Figure 4.20 Diagram of the porous carbon materials with chiral nematic structure. Reprinted with permission from Ref. [137].
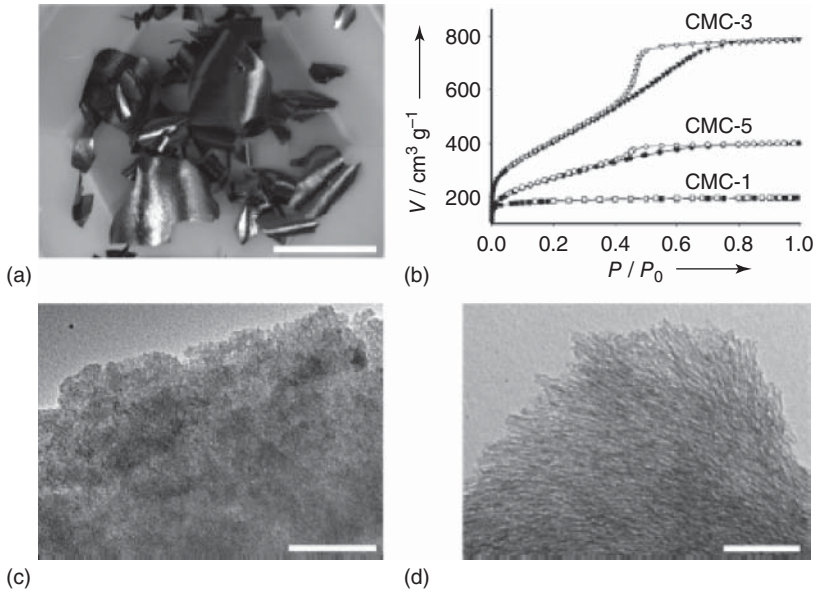
(a)

(b)

(c)

(d)

Figure 4.21 Carbon materials with different chiral nematic structures: (a) the morphology of CMC-3 porous carbon material (scale is 2 cm); (b) nitrogen adsorption isotherm curves for CMC-1, CMC-3, CMC-5; (c) TEM image of CMC-1 (scale is 200 nm); and (d) TEM image of CMC-3 (scale is 200 nm). Reprinted with permission from Ref. [137].

Table 4.1 Nitrogen adsorption data of carbon content material samples with the different CNs contents.

Sample	wt% NCC in composite	BET surface area $(m^2\,g^{-1})$	Micropore area $(m^2\,g^{-1})$	Pore volume $(cm^3\,g^{-1})$
CMC-1	100	616	488	0.30
CMC-2	76	578	37	0.38
CMC-3	65	1465	11	1.22
CMC-4	56	1230	128	0.96
CMC-5	43	932	132	0.62

NCC, nanocrystalline cellulose; BET, Brunauer, Emmett and Teller.

Reprinted with permission from Ref. [137].

a counterclockwise direction was observed, which was consistent with the left-handed chiral nematic structure of the CN template (Figure 4.22). However, carbon films prepared from chiral nematic CN films without silica showed no retention of chiral nematic ordering. In addition to the introduction of mesoporosity into the samples, the silica was also necessary for preserving long-range structural organization in the CN films during carbonization [137]. Recently, Shopsowitz *et al.* [144] showed that CNs were used to template free-standing films
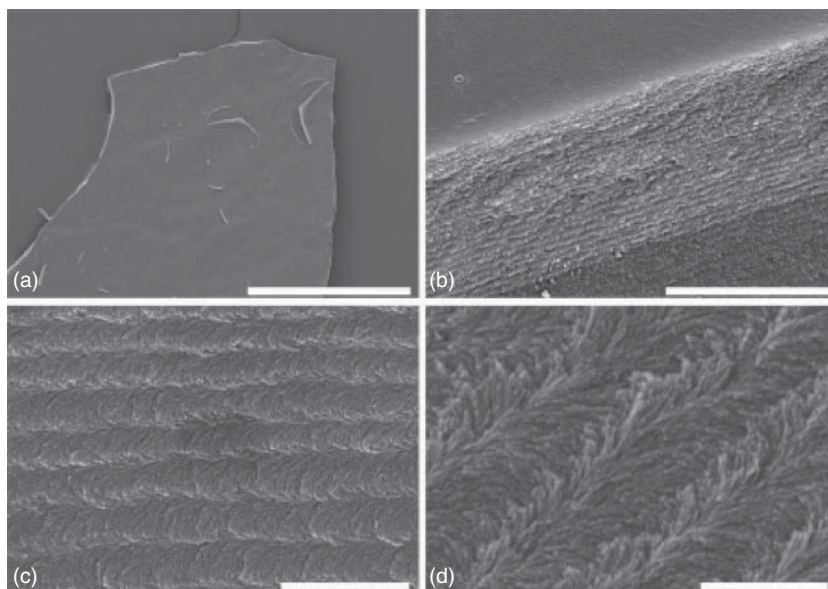
Figure 4.22 SEM images (weight ratio of CN in the composite is 65 wt%) of CMC-3. (a) The vertical image under low magnification (scale is 500 μm). (b) The lateral plane of fracture (scale is 5 μm). (c) The fracture under high magnification (scale is 2 μm). (d) The high magnification of the fracture showing sinistral chiral structure (scale is 500 nm). Reprinted with permission from Ref. [137].

of ethylene-bridged mesoporous organosilica with a chiral nematic structure by using $(MeO)_3SiRSi(OMe)_3$ as organosilica precursors. Moreover, it was found that the incorporation of an ethylene bridge into the mesoporous organosilica films induced a great improvement in mechanical properties and flexibility compared to pure silica.

4.5.3.4 Metal Nanoparticle-Decorated Chiral Nematic Materials

It is well known that chiral nematic CNs can be used as a template to prepare a variety of new sol–gel derived materials with chiral nematic structure and optical properties [133–137]. Removal of the CNs produces mesoporous free-standing films that retain the chiral nematic structure of the CN template. Kelly *et al.* investigated the influence of ionic strength (various metal salt solutions) on the self-assembly of CN/silica sol–gel films, and prepared chiral nematic mesoporous materials decorated with metal nanoparticles using the templated self-assembly of CN/silica materials [145]. From Figure 4.23, it can be seen that when 1–5 ml of $HAuCl_4$ solution was added to the CN/TMOS composites, the reflection wavelength appeared to blueshift from 975 to 450 nm before solvent volatilization. The magnitude of the blueshift in reflectance as a function of ion concentration varied with the change in ionic strength. In addition, when the ionic strength was low, CN/TMOS suspensions showed a chiral nematic texture. With an increase
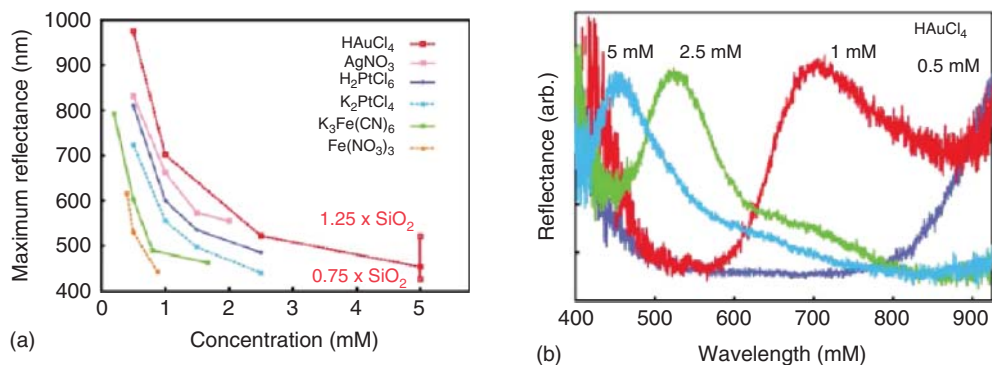
Figure 4.23 Maximum reflected wavelength as a function of ion concentration (a) and specular reflectance from HAuCl4-loaded CN/SiO_2 composite films (b). Reprinted with permission from Ref. [145].

in ionic strength, the chiral nematic characteristic gradually disappeared. At high ionic strength, the CN/TMOS mixture easily formed colloids that became transparent after drying. SEM of the transparent colloid confirmed that it no longer had a chiral nematic structure and had formed a disordered layered structure. It is worth noting that the reflection peak of the chiral nematic composite will appear to redshift by increasing the amount of silicon in the material. Adding 5 mM $HAuCl_4$ solution can also make the reflected light wavelength appear to redshift, from 425 to 520 nm by changing the proportion of TMOS (28−40 wt%). Therefore, by changing the ionic strength or the Si content one is able to control the reflection wavelength [145]. Moreover, the Ag and Au nanoparticles included in the silica show induced circular dichroism (CD) signals associated with their plasmon resonances, which were also sensitive to changes in their local environments, and could be used as the basis for sensing applications.

4.6
Self-Assembly Method

4.6.1
Overview of Self-Assembly Method

Self-assembly is a process whereby molecules and nanoparticles spontaneously create an aggregate with thermodynamic stability derived by non-covalent bond forces (electrostatic interaction, van der Waals force, hydrophobic interaction, and hydrogen bonding), which is beneficial for the preparation of new high-performance materials [129, 146−152]. Molecular self-assembly, the most common self-assembly technology, is the process used to spontaneously form molecules, molecular aggregates, or supramolecular structures with a particular function by non-covalent bonding. Compared with other techniques,

self-assembly not only has the advantage of precise control over film thickness, as in a Langmuir–Blodgett membrane (LB), but also has the advantages of simple equipment and convenient operation. This technology is suitable for producing thin film devices with large areas; meanwhile, it perfectly solves the issue of the junction between functional materials and the substrate electrode to obtain a high-performance membrane with structural stability [148]. At present, preparation methods contain self-assembly membrane technology based on chemical adsorption; ionic self-assembly membrane technology (ISAM) based on physical adsorption; spin-coating; slow solvent evaporation; film grafting; organic molecular self-assembly on the matrix; and supramolecular synthetic technology based on supermolecular recognition [146–148]. Layer-by-layer self-assembly (LBL) is a simple, easy, and multifunctional interface supramolecular assembly method that was developed in the 1990s. The layers spontaneously deposited to form a molecular aggregation or supramolecular structure by virtue of the weak interaction between the layer of molecules (electrostatic forces, hydrogen bonding, coordination bonding) [149]. LBL technology can be divided into electrostatic, hydrogen bonding, and other LBL technologies (coordination effect, charge transfer, and specific molecular recognition) according to the driving force behind its assembly. LBL has found wide application in electronics, optics, separation, catalysis, biomedical materials, biological sensors, and sustained-release drugs. With the high-speed development of nanotechnology, the self-assembly technique for the preparation of PNs has been emerging. Because PNs possess many advantages, such as nanometer scale, abundant hydroxyl groups, and strong adsorption capacity due to high specific surface area, the self-assembly behavior of PNs in aqueous or organic medium has been studied and some interesting PN functional materials developed.

4.6.2
Self-Assembly Method Toward Polysaccharide Nanocrystal-Modified Materials

4.6.2.1 Self-Assembly of Polysaccharide Nanocrystals in Aqueous Medium
Researchers found a crosshatch pattern in a PN suspension when observed by POM (Figure 4.24a), suggesting the formation of a birefringent glassy phase in post-sulfonated PN suspensions rather than the fingerprint pattern in chiral nematic phases typical of directly sulfated PNs [152]. More exciting was that after the water evaporated, a rainbow film with chiral nematic structure was retained. The formation mechanism of the special film was investigated and it was found that the optical properties could not be reproduced in printing and copying, which is very important in applications of decorative and coating materials for anti-counterfeiting [150]. Much research has also been carried out on the formation mechanism of PN self-assembly in aqueous media, especially the self-assembly behavior of CNs. Generally, CN self-assembly was caused by a change in the spiral structure in natural cellulose materials. Owing to the asymmetry of the chiral nematic stack, the spiral structure of the suspension was easily rearranged. Habibi *et al.* [5] comparatively studied the self-assembly
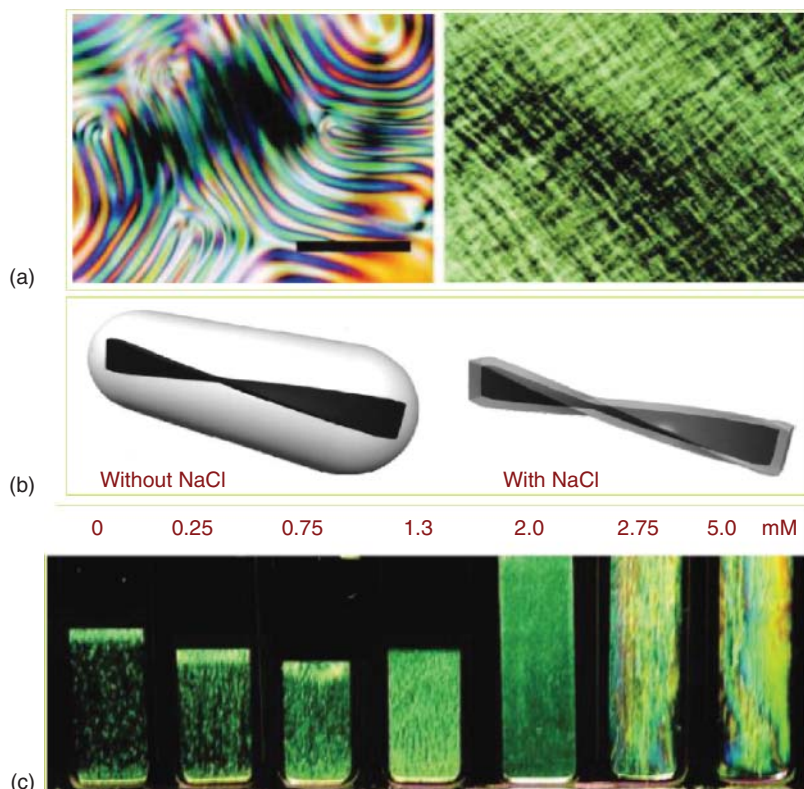
Figure 4.24 (a) POM of PN suspension: (left) fingerprint pattern in the chiral nematic liquid crystal phase of the PN suspension (initial solids content, 5.4%) directly prepared by H_2SO_4 and (right) the cross-hatch pattern of post-sulfated CN suspension (solids content, 7.1%) [152]. (b) Schematic illustration of bacterial cellulose nanocrocrystals with surface charge, showing the change in effective particle shape: (left) in water, repulsion by surface charge extends to long-range, resulting in an apparently nonchiral rod and (right) addition of NaCl decreases repulsion range and the effective particle becomes a twisted rod [6, 7]. (c) Influence of added NaCl on the phase behavior of CN suspension with a concentration of 3 wt% CNs [153]. Reprinted with permission from Ref. [6, 7, 152, 153].

behavior of CNs prepared by hydrochloric acid and sulfuric acid methods. CN suspensions without charge did not form a chiral nematic liquid crystal phase. The negative charge produced by sulfate groups on CNs obtained by the sulfuric acid method maintained the chiral nematic liquid crystal phase. However, in the presence of an electrolyte or surface charge, the CN suspension assumed chiral nematic order. This phenomenon was explained by nontrivial morphological changes in the CN, that is, from a plain cylindrical configuration to a twisted rod, as a result of the screening of surface charge [6, 7]. Orts *et al.* [151] and Araki and Kuga [7] proved that CNs have a spiral rod-shaped configuration. The CNs did not form a chiral nematic phase in suspension without electrolytes; however,

when electrolytes were present, suspensions developed a chiral nematic order. This phenomenon was considered to be an abnormal configuration change of CNs that was due to the change in shape from a flat cylindrical structure to a twisted rod that was induced by surface electrostatic repulsion, as shown in Figure 4.24b. In fact, without electrolytes, CN swelling caused by surface charge repulsion hides the chiral configuration, forming an effectively stick straight and smooth shape. This structure formed a chiral nematic liquid crystal phase through parallel stacking of rods. Incorporation of electrolytes will cause the particle effective size to shrink, leading to distortion of the cellulose nanorods and weakening the CN orientation, and then formation of the chiral nematic liquid crystal phase.

The self-assembly behavior of CNs is dependent on the aspect ratio of the nanocrystal, the charge density, and the nature of the charge and osmotic pressure [6, 152–154]. The critical concentration for sulfating CNs to form an orderly nematic liquid crystal phase in an aqueous suspension without electrolyte was about 1–10 wt%, which depended largely on the charge density. With increasing CN concentration, the pitch (20–80 μm) of the anisotropic chiral nematic liquid crystal phase correspondingly lowered [6]. The isotropic–anisotropic balance was sensitive to the character of the electrolyte and counterion, and the component ratio of the two phase coexistence changed with the concentrations of electrolyte and counterion [6, 155]. Increasing the amount of added electrolyte reduced the formation of the anisotropic phase because of the smaller pitch of the chiral nematic liquid crystal phase as the electrolyte concentration increased [6]. The phase became more highly twisted, reducing the thickness of the electrical double layer, which was not conducive to the formation of a chiral liquid crystal phase. For inorganic counterions, the critical concentration of ordered phase formation was in the order $H^+ < Cs^+ < K^+ < Na^+$ [6]. For organic counterions such as NH_4^+, $(CH_3)_4 N^+$, and $(CH_3CH_2)_4 N^+$ the critical concentration depended on hydrophobic attraction and steric repulsion. In general, the critical concentration of the liquid crystal phase increased with increasing counterion size. Moreover, the influence of different NaCl concentrations on the CN phase separation and on the chiral nematic liquid crystal phase were investigated [153]. It was found that with a NaCl concentration of about 1.0 mM, the volume fraction of the chiral nematic phase reached a minimum. When the NaCl concentration increased from 2.0 to 5.0 mM, no phase separation appeared, but the suspension turned into liquid crystal (Figure 4.24c). When the NaCl concentration increased from 0 to 2.75 mM, the size of the ordered anisotropic phase decreased. At 2.75 mM NaCl, only the tactoids were observed, and at 5.0 mM NaCl, the chiral nematic phase was not observed.

The nature of the charge and density on the surface of CNs also can affect formation of the chiral nematic phase. After the epoxypropyltrimethylammonium chloride cation was grafted to the CNs, shear birefringence of the suspension was observed, but a chiral nematic liquid crystal phase was not observed. This may be due to a restriction in the formation of the liquid crystal phase by its high viscosity

[156]. The influence of H_2SO_4-hydrolyzed CNs and HCl-hydrolyzed CNs on chiral nematic phase formation was also compared [151]. Post-sulfated suspensions first formed a birefringent glassy phase with a crosshatch pattern rather than a fingerprint pattern indicative of chiral nematic phases typical of directly sulfated CNs (Figure 4.24a), and indicating the formation of a chiral nematic phase. More interestingly, a high viscosity suspension of post-sulfated CNs does not yield a chiral nematic phase, which is most likely due to low charge content on the CN surface.

4.6.2.2 Self-Assembly of Polysaccharide Nanocrystals in Organic Medium

Heux *et al.* [157] provided the first description of self-assembly of CNs in apolar solvents. In their preliminary study, a surfactant coating was used to disperse CNs and thereby obtain a chiral nematic structure. The pitch of the chiral nematic phase was about 4 μm, which was significantly less than the pitch of a CN aqueous suspension (pitch: 20–80 μm), and at higher CN concentrations (up to 36%) good dispersion of CNs was achieved. These results were attributed to steric stabilization exerted by the surfactant coating. A correlation between the CN's aspect ratio and its dispersion in nonpolar solvent with the chiral nematic structure has been reported. The critical concentration where separation into chiral nematic mesophase occurs spontaneously was higher than that in water, and the mutual affinity between the cellulose nanorods was stronger in the nonpolar medium, which resulted in a decrease in the chiral nematic pitch to less than 2 μm. In addition, the CN suspension with a high aspect ratio did not show any phase separation, but produced an anisotropic gel phase at high concentrations [158]. Zhou *et al.* [159] successfully prepared a xyloglucan oligosaccharide-PEG-PS triblock copolymer, and the chiral nematic phase self-assembly behavior in nonpolar solvents was investigated by adsorbing them onto the CNs' surface. The chiral nematic pitch of CNs with xyloglucan oligosaccharide-PEG-PS triblock copolymer was about 17 μm in toluene, which was significantly higher than the pitch of CNs in other nonpolar solvents, further confirming that formation of the chiral nematic phase of CNs in nonpolar solvents resulted from chiral interactions between rods rather than the chirality or the surface charge of nanorods.

4.6.2.3 Self-Assembly of Polysaccharide Nanocrystals in Solid Film

CN suspensions easily undergo chiral nematic ordering to give rise to iridescent solid cellulosic films with tunable optical properties by simply controlling the evaporation of the CN suspension under ambient conditions in small PS Petri dishes [160, 161]. The liquid crystalline order of these suspensions was preserved in the solid films and the chiral nematic pitch of the films was on the same scale as the wavelength of visible light. As an interference device, this unique system has the capacity to reflect circularly polarized light over a specific wavelength range. Because the wavelength of reflected light determines its spectral or intrinsic color, the perceived color of the film depends on the pitch of the cholesteric order and the angle of incidence of the light. The microstructure of such films is very sensitive to the drying conditions. Moreover, the perceived
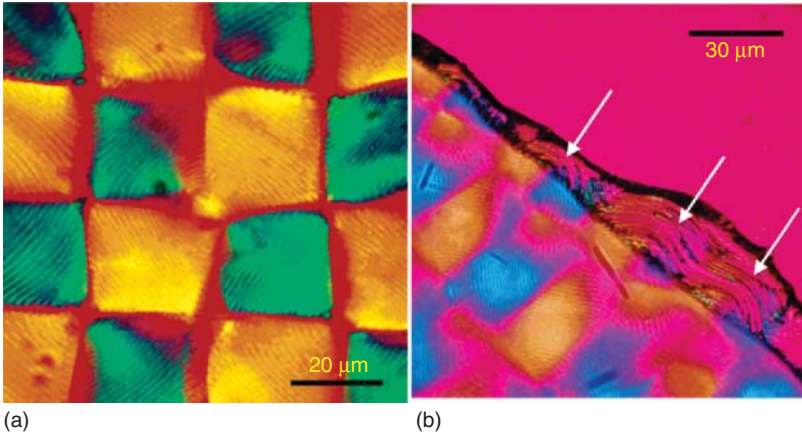
(a)   (b)

Figure 4.25 (a) Square lattice with crossed
polars and full-wave retardation plate
inserted into the microscope. Scale bar
20 μm and (b) layered conical structures
(white arrows) observed at a film fracture
line. Crossed polars, full-wave retardation
plate. Scale bar 30 μm. Reprinted with per-
mission from Ref. [160].

color of the reflected polarized light is "tunable" because the final pitch can
be varied depending on processing conditions (aspect ratio of CNs and the
amount of electrolyte added). Roman and Gray [160] reported a self-assembled
film with a parabolic focal conic (PFC) structure (a symmetrical form of focal
conic defects in which the line defects form a pair of perpendicular, antiparallel,
and confocal parabolas) (Figure 4.25). The texture with its symmetrical array
of line defects is well known for thin layers of smectic and chiral nematic
molecular and polymeric liquid crystalline phases between flat surfaces. A series
of layered half-cone structures were observed on the fracture surface edge of
the solid membrane. It is suggested that CNs show a chiral nematic directional
orientation in solid films, leading to the anisotropic mechanical properties of
materials. In addition, the application of a magnetic field during the drying
process increased the CNs' chiral nematic areas and improved the orientation
of the film surface screw axis [161]. Csoka *et al.* [162] prepared ultrathin
membranes of highly oriented CNs by self-assembly under low electric fields.
Orientation of the CNs depended on the electric field intensity and frequency.
It was found that low field strength led to the special anisotropic structure of
the ultrathin membranes. Zhang *et al.* [163] successfully prepared CS oxide
self-assembled films by reacting sodium periodate and CS at room temperature
for 2 h with stirring in the dark. Chitosan aldehyde groups were produced
by oxidation of sodium periodate and regulated by controlling the amount of
sodium periodate added. The C=N double bond was generated by a Schiff base
reaction with the CS amino group, leading to self-cross-linking. High water
resistance and high tensile strength can be obtained in CS oxide self-assembled
films.

4.6.3
Polysaccharide Nanocrystal-Modified Materials Prepared by LBL Method

Podsiadlo *et al.* [164] reported for the first time that CN multilayer composites with poly(diallyldimethylammonium chloride) (PDDA) were prepared using an LBL technique. The multilayer film had uniform coverage and a densely packed cellulose crystal surface. A novel, highly porous architecture reminiscent of a "flattened matchsticks pile" was prepared from tunicin CNs and polyethyleneimine (PEI). The obtained film had strong antireflective performance (transmittance of almost 100%) and better mechanical properties compared to pure PEI, exhibiting great potential for application in semiconductor nanowires [165]. Cranston and Gray [166] prepared an LBL self-assembled film of poly(allylamine) hydrochloride (PAH)/CNs by taking advantage of the negative magnetic anisotropy of CNs and the stable chiral nematic liquid crystal phase that formed when above the critical concentration under a magnetic field. To prepare the LBL self-assembled film the anionic silicon surface was coated with polycation membranes and then a layer of anionic CNs was adsorbed under a magnetic field to slowly orient the nanocrystalline layer. De Mesquita *et al.* [167] selected a positively charged polymer-CS with high deacetylation and negatively charged sulfate ester groups on the CN surface to prepare an LBL self-assembled film. The driving force behind the LBL self-assembled film was hydrogen bonding and electrostatic interaction between negatively charged sulfate ester groups on the CN surface and ammonium groups of the CS. The self-assembled film could be used in fully biodegradable nanocomposites, which have great potential in biomedicine and food packaging. A stable self-assembled hybrid multilayer film was produced using LBL self-assembly technology with eucalyptus wood CNs derived from plants and collagen derived from animals as raw materials [168]. It was demonstrated that the driving forces of electrostatic interaction and hydrogen bond interaction were not mutually repulsive in building LBL self-assembled films. For the collagen/CNs LBL self-assembled membrane system, electrostatic interaction contributed little to building the LBL films, while hydrogen bond interactions between the amide of the collagen and the hydroxyl groups of CNs played an important role in construction.

Currently, preparation of PN LBL self-assembled films is limited, but the effects of interactions between PNs and polyelectrolytes on the structure and performance of LBL self-assembled films has attracted more attention [169–171]. Sui *et al.* [169] adopted LBL self-assembly deposition techniques to embed CN polyanions into PDDA and deacetylated CS in the preparation of two composite membranes. The in-plane and out-of-plane elastic constants of the composites were measured using Brillouin light scattering as a function of film thickness and CN content. It was found that incorporation of CNs increased the stiffness of polymer films more significantly in the in-plane direction as compared to the out-of-plane direction, resulting in elastic anisotropy. For the highest CN loadings, the out-of-plane moduli for PDDA/CN films show an improvement from cast PDDA films, while the out-of-plane moduli for CS/CN films were similar to those of the cast CS film. This suggests better adhesion and therefore better

stress transfer between PDDA and CNs. Aulin *et al.* [170] used LBL self-assembly to prepare anionic/cationic modified CN multilayer films and PEI/anionic modified CN multilayer films. The adsorption behavior of anionic/cationic CNs was compared with that of PEI/anionic CNs. When the number of film layers was more than five, the water content of the anionic/cationic CN composite membranes (70%) was greater than that of the PEI/CN composite membranes (50%). AFM images confirmed that the fibrous structure in the PEI/CN composite membranes was more compact than the CN composite membranes (Figure 4.26a,b). The existing repulsion between the electrostatic and steric forces in the anionic/cationic CN composite membranes led to its intact structure. It was also found that the separation energy of PEI/CN multilayer membranes was more than that of anionic/cationic CN multilayer films. Qi *et al.* [171] reported that anionic CNs TEMPO oxidized CNs (TOCN) were obtained by the
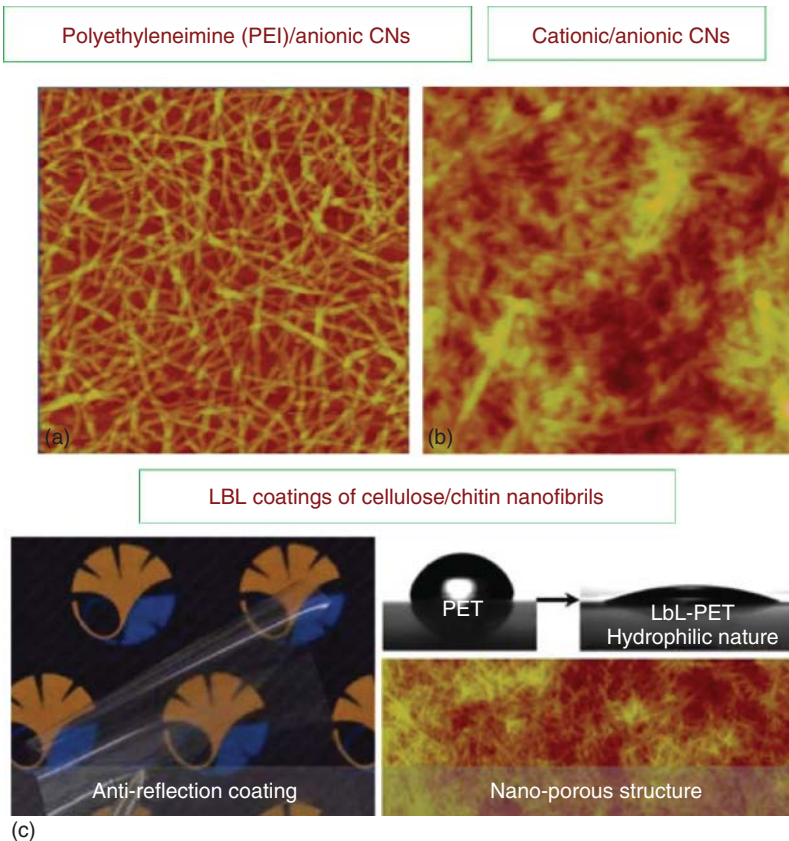

Figure 4.26 AFM images of the anion/cation CN composite membrane (a) and the PEI/CN composite membrane (b) [170]; multifunctional films prepared by the deposition of CNs and chitin nanofibers on the PET through LBL self-assembly (c) [171]. Reprinted with permission from Ref. [170, 171].

2,2,6,6-tetramethylpiperidine-1-oxyl radical (TEMPO)-mediated oxidation of native cellulose (TOCN), and then deposited with cationic beta-chitin nanofibers (BCN) on poly (ethylene terephthalate) (PET) films with electrostatic attraction and hydrogen bonding as the driving forces for production of multifunctional LBL self-assembled composite membranes. The films showed high transmission, flexibility, and hydrophilicity, and had a nanoporous structure (Figure 4.26c). This versatile coating can adsorb charged dye molecules through ionic bonds or hydrophobic interactions. In addition, TOCN/BCN LBL-PET films have unique antireflective properties to visible light, depending on the number of layers and the wavelength of the incident light. The LBL coating process was completely free from organic solvents. This LBL multilayer membrane could be developed and applied in new highly functional materials as antireflective or antifog coatings and as scaffolds for functional molecules.

4.7
Other Methods and Prospects

PNs have been used to prepare versatile nanocomposites, such as aerogels, bio-based microspheres, and nonwoven microfiltration membranes [172, 173]. Aerogels, as the lightest solid, have a great potential for application in energy storage and heat preservation, and as catalytic carriers and sound-absorbing materials. Heath and Thielemans [172] first reported on a method for preparation of CN aerogels involving sonicating CNs in water to form a hydrogel, followed by solvent exchange with ethanol, and supercritical CO_2 drying to eliminate the alcohol that resulted in a porous light aerogel. The specific surface area of the aerogels reached $605 \, \text{m}^2 \, \text{g}^{-1}$, and the density was as low as $0.078 \, \text{g} \, \text{cm}^{-3}$. In addition, aerogels that were kept for several weeks retained their mechanical integrity and did not show visible degradation.

Recently, PN-based microspheres have received attention for use in the fields of biological medicine, food, and cosmetics. Lin *et al.* dispersed three kinds of PNs (CNs, chitin nanocrystals, and starch nanocrystals) in sodium alginate solution (SA), and the as-prepared sols containing SA and PNs were injected into 10 wt% $CaCl_2$. Thus, the SA component would be cross-linked by the Ca^{2+} to produce nanocomposite microspheres [11]. The free Ca^{2+} on the surface or in the inner cavity was removed from the microspheres after repeated washing. Moreover, the drug release behavior of drug-loaded composite microspheres was examined using theophylline as a model drug. The introduction of rigid PNs not only enhanced the mechanical properties of composite materials but also improved the stability and density of the alginate three-dimensional structure, hindering the escape route of drug molecules and exhibiting prominent sustained release profiles.

Kalashnikova *et al.* [173] produced a Pickering emulsion with outstanding stability in oil/water by emulsion polymerization of cotton CNs and bacterial CNs with the PS. Studies showed that the electrostatic repulsion of the PN surface was

a key factor in controlling the oil/water interface stability, and the surface charge density of PNs was modulated by various postsulfation/desulfation treatments.

In recent years, with the rapid development of nonwoven technology (acupuncture, spunlace, melt-blown), a variety of nonwoven composite technologies have been exploited. Qi *et al.* [171] developed a combination of electrospinning technology and nonwoven technology that not only overcame the shortcomings of high energy consumption and small scale of electrospinning but also decreased the tensile strength of electrospun nanofibers. High value-added applications for PN-based composite materials have been developed. Electrospinning with polyacrylonitrile (PAN) as the solution and an acupuncture polyester (PET) nonwoven as the receiving cathode was used to develop a PAN/PET composite nonwoven membrane [91]. CN suspensions of different loading levels were injected into the nonwoven membrane and heated to 100 °C for 10 min to form a cross-linked network in the membrane that could be used in commercial microfiltration. Further, it was found that the average pore size and pore size distribution of the obtained microfiltration membranes could be adjusted with the CN content. The film not only had better mechanical properties compared to pure PAN film but also had a high surface charge density, high adsorption capacity for cationic dye (compared to commercial common microfiltration membrane), and a strong barrier effect to bacteria.

List of Abbreviations

ASA	alkyenyl succinic anhydride
BCN	beta-chitin nanofibers
CD	circular dichroism
CNs	cellulose nanocrystals
CS	chitosan
DMF	*N*,*N*-dimethylformamide
DMSO	dimethyl sulfoxide
EVOH	ethylene/vinyl alcohol copolymer
HASCs	human adult adipose tissue-derived stromal cells
ISAM	ionic self-assembly membrane technology
KGM	konjac glucan-mannan chitosan nanocrystals
LB	Langmuir–Blodgett membrane
LBL	layer-by-layer self-assembly
LDPE	low density polyethylene
MAC	methyl adipoyl chloride
MA-CN	Methyl adipose chloride modified CNs
NR	natural rubber
PAA	poly(acrylic acid)
PAH	poly(allylamine) hydrochloride
PAN	polyacrylonitrile
PCL	poly(caprolactone)
PDDA	poly(diallyldimethylammonium chloride)

PEG	poly(ethylene glycol)
PEI	poly(ethyleneimine)
PEO	poly(oxyethylene)
PET	poly(ethylene terephthalate)
PHBV	poly(3-hydroxybutyrate-*co*-3-hydroxyvalerate)
PI	phenyl isocyanate
PLA	poly(lactic acid)
PMMA	polymethyl methacrylate
PNs	polysaccharide nanocrystals
Poly(S-*co*-BuA)	poly(styrene-co-butyl acrylate)
PS	polystyrene
PETA	pentaerythritol triacrylate
PU	polyurethane
PVA	polyvinyl alcohol
SA	sodium alginate solution
SF	silkworm silk fibroin
SPI	soy protein isolate
TEMPO	2,2,6,6-tetramethylpiperidine-1-oxyl
TEOS	tetraethyl orthosilicate
T_g	glass transition temperature
THF	tetrahydrofuran
TMI	isopropenyl-α, α'-dimethylbenzyl isocyanate
T_{max}	the maximum thermal degradation temperature
TMOS	tetramethoxysilane
TOCN	TEMPO oxidized CNs
WPU	waterborne polyurethane

References

1. Dufresne, A. (2003) Interfacial phenomena in nanocomposites based on polysaccharide nanocrystals. *Compos. Interfaces*, **10** (4-5), 369–387.

2. Dufresne, A. (2008) Polysaccharide nano crystal reinforced nanocomposites. *Can. J. Chem.*, **86** (6), 484–494.

3. Lin, N., Huang, J., and Dufresne, A. (2012) Preparation, properties and applications of polysaccharide nanocrystals in advanced functional nanomaterials: a review. *Nanoscale*, **4** (11), 3274–3294.

4. Lin, N., Yu, J.H., Chang, P.R., Li, J.L., and Huang, J. (2011) Poly(butylene succinate)-based biocomposites filled with polysaccharide nanocrystals: structure and properties. *Polym. Compos.*, **32** (3), 472–482.

5. Habibi, Y., Goffin, A.L., Schiltz, N., Duquesne, E., Dubois, P., and Dufresne, A. (2008) Bionanocomposites based on poly(ϵ-caprolactone)-grafted cellulose nanocrystals by ring-opening polymerization. *J. Mater. Chem.*, **18** (41), 5002–5010.

6. Habibi, Y., Lucia, L.A., and Rojas, O.J. (2010) Cellulose nanocrystals: chemistry, self-assembly, and applications. *Chem. Rev.*, **110** (6), 3479–3500.

7. Araki, J. and Kuga, S. (2001) Effect of trace electrolyte on liquid crystal type of cellulose microcrystals. *Langmuir*, **17** (15), 4493–4496.

8. Wang, N., Ding, E., and Cheng, R.S. (2008) Preparation and liquid crystalline properties of spherical cellulose nanocrystals. *Langmuir*, **24** (1), 5–8.

9. Marchessault, R.H., Morehead, F.F., and Koch, M.J. (1961) Some hydrodynamic properties of neutral suspensions of cellulose crystallites as related to size and shape. *J. Colloid Sci.*, **16** (4), 327–344.

10. Marchessault, R.H., Morehead, F.F., and Walter, N.M. (1959) Liquid crystal systems from fibrillar polysaccharides. *Nature*, **184**, 632–633.

11. Lin, N., Huang, J., Chang, P.R., Feng, L.D., and Yu, J.H. (2011) Effect of polysaccharide nanocrystals on structure, properties, and drug release kinetics of alginate-based microspheres. *Colloids Surf., B*, **85** (2), 270–279.

12. Liu, D.G., Wu, Q.L., Chen, H.H., and Chang, P.R. (2009) Transitional properties of starch colloid with particle size reduction from micro- to nanometer. *J. Colloid Interface Sci.*, **339** (1), 117–124.

13. LeCorre, D., Bras, J., and Dufresne, A. (2011) Evidence of micro- and nanoscaled particles during starch nanocrystals preparation and their isolation. *Biomacromolecules*, **12** (8), 3039–3046.

14. Wang, Z.F., Lin, H., Huang, J., Li, K.M., and Liu, J.K. (2010) Study on structure of cassava starch nanocrystals. *Chem. Eng.*, **11**, 1–3.

15. Cao, X.D., Dong, H., and Li, C.M. (2007) New nanocomposite materials reinforced with flax cellulose nanocrystals in waterborne polyurethane. *Biomacromolecules*, **8** (3), 899–904.

16. Cao, X.D., Habibi, Y., and Lucia, L.A. (2009) One-pot polymerization, surface grafting, and processing of waterborne polyurethane-cellulose nanocrystal nanocomposites. *J. Mater. Chem.*, **19** (38), 7137–7145.

17. Wang, Y.X., Tian, H.F., and Zhang, L.N. (2010) Role of starch nanocrystals and cellulose whiskers in synergistic reinforcement of waterborne polyurethane. *Carbohydr. Polym.*, **80** (3), 665–671.

18. Chen, G.J., Wei, M., Chen, J.H., Huang, J., Dufresne, A., and Chang, P.R. (2008) Simultaneous reinforcing and toughening: new nanocomposites of waterborne polyurethane filled with low loading level of starch nanocrystals. *Polymer*, **49** (7), 1860–1870.

19. Roohani, M., Habibi, Y., Belgacem, N.M., Ebrahim, G., Karimi, A.N., and Dufresne, A. (2008) Cellulose whiskers reinforced polyvinyl alcohol copolymers nanocomposites. *Eur. Polym. J.*, **44** (8), 2489–2498.

20. Paralikar, S.A., Simonsen, J., and Lombardi, J. (2008) Poly(vinyl alcohol)/cellulose nanocrystal barrier membranes. *J. Membr. Sci.*, **320** (1-2), 248–258.

21. Chen, Y., Cao, X., Chang, P.R., and Huneault, M.A. (2008) Comparative study on the films of poly(vinyl alcohol)/pea starch nanocrystals and poly(vinyl alcohol)/native pea starch. *Carbohydr. Polym.*, **73** (1), 8–17.

22. Lu, Y.S., Weng, L.H., and Zhang, L.N. (2004) Morphology and properties of soy protein isolate thermoplastics reinforced with chitin whiskers. *Biomacromolecules*, **5** (3), 1046–1051.

23. Chen, G.F.S. (2009) *Preparation and Properties of Cellulose Nanofiber Reinforced Soybean Protein Isolated Transmitting Composite Materials*, Fujian Normal University.

24. Zheng, H., Ai, F., Chang, P.R., Huang, J., and Dufresne, A. (2009) Structure and properties of starch nanocrystal-reinforced soy protein plastics. *Polym. Compos.*, **30** (4), 474–480.

25. Wang, Y.X., Cao, X.D., and Zhang, L.N. (2006) Effects of cellulose whiskers on properties of soy protein thermoplastics. *Macromol. Biosci.*, **6** (7), 524–531.

26. Khan, A., Khan, R.A., Salmieri, S., Le Tien, C., Riedl, B., Bouchard, J., Chauve, G., Tan, V., Kamal, M.R., and Lacroix, M. (2012) Mechanical and barrier properties of nanocrystalline cellulose reinforced chitosan based nanocomposite films. *Carbohydr. Polym.*, **90** (4), 1601–1608.

27. Mathew, A.P., Laborie, M.P.G., and Oksman, K. (2009) Cross-linked chitosan/chitin crystal nanocomposites with improved permeation selectivity and pH stability. *Biomacromolecules*, **10** (6), 1627–1632.

28. Wang, H.Z. and Roman, M. (2011) Formation and properties of chitosan-cellulose nanocrystal polyelectrolyte-macroion complexes for drug delivery applications. *Biomacromolecules*, **12** (5), 1585–1593.

29. Zhang, X.L., Huang, J., Chang, P.R., Li, J.L., Chen, Y.M., Wang, D.X., Yu, J.H., and Chen, J.H. (2010) Structure and properties of polysaccharide nanocrystal-doped supramolecular hydrogels based on cyclodextrin inclusion. *Polymer*, **51** (19), 4398–4407.

30. Zhang, Q.X. (2011) *Building and Performance of the Response Model Drug Delivery System*, Wuhan University of Technology.

31. Favier, V., Canova, G.R., Cavaillé, J.Y., Chanzy, Y.H., Dufresne, A., and Gauthier, C. (1995) Nanocomposite materials from latex and cellulose whiskers. *Polym. Adv. Technol.*, **6** (5), 351–355.

32. Favier, V., Chanzy, H., and Cavaille, J.Y. (1995) Polymer nanocomposites reinforced by cellulose whiskers. *Macromolecules*, **28** (18), 6365–6367.

33. Samir, M.A.S.A., Alloin, F., Paillet, M., and Dufresne, A. (2004) Tangling effect in fibrillated cellulose reinforced nanocomposites. *Macromolecules*, **37** (11), 4313–4316.

34. Hajji, P., Cavaille, J.Y., Favier, V., Gauthier, C., and Vigier, G. (1996) Tensile behavior of nanocomposites from latex and cellulose whiskers. *Polym. Compos.*, **17** (4), 612–619.

35. Dufresne, A., Cavaille, J.Y., and Helbert, W. (1996) New nanocomposite materials: microcrystalline starch reinforced thermoplastic. *Macromolecules*, **29** (23), 7624–7626.

36. Paillet, M. and Dufresne, A. (2001) Chitin whisker reinforced thermoplastic nanocomposites. *Macromolecules*, **34** (19), 6527–6530.

37. Nair, K.G. and Dufresne, A. (2003) Crab shell chitin whisker reinforced natural rubber nanocomposites. 2. Mechanical behavior. *Biomacromolecules*, **4** (3), 666–674.

38. Angellier, H., Molina, B.S., Lebrun, L., and Dufresne, A. (2005) Processing and structural properties of waxy maize starch nanocrystals reinforced natural rubber. *Macromolecules*, **38** (9), 3783–3792.

39. Visakh, P.M., Thomas, S., Oksman, K., and Mathew, A.P. (2012) Cellulose nanofibers and cellulose nanowhiskers based natural rubber composites: diffusion, sorption, and permeation of aromatic organic solvents. *J. Appl. Polym. Sci.*, **124** (2), 1614–1623.

40. Visakh, P.M., Thomas, S., Oksman, K., and Mathew, A.P. (2012) Crosslinked natural rubber nanocomposites reinforced with cellulose whiskers isolated from bamboo waste: processing and mechanical/thermal properties. *Composites Part A: Appl. Sci. Manuf.*, **43** (4), 735–741.

41. Zhang, W.Y., Wang, C., Xu, D.M., Pan, Z.L., and Wang, X.F. (2009) Preparation and properties of starch nanocrystals/natural rubber composites. *China Synth. Rubber Ind.*, **32** (4), 330.

42. Lin, N. (2011) *Structure and Properties of Polysaccharide Nanocrystals Composite Modified Biomass Materials*, Wuhan University of Technology.

43. Viet, D., Beck-Candanedo, S., and Gray, D.G. (2007) Dispersion of cellulose nanocrystals in polar organic solvents. *Cellulose*, **14** (2), 109–113.

44. Siqueira, G., Bras, J., and Dufresne, A. (2009) Cellulose whiskers versus microfibrils: influence of the nature of the nanoparticle and its surface functionalization on the thermal and mechanical properties of nanocomposites. *Biomacromolecules*, **10** (2), 425–432.

45. Shang, W.L. (2012) *Physical and Chemical Modified Materials of Polysaccharide Nanocrystals*, Wuhan University of Technology.

46. Isogai, A. and Kato, Y. (1998) Preparation of polyuronic acid from cellulose by TEMPO-mediated oxidation. *Cellulose*, **5** (3), 153–164.

47. Petersson, L., Kvien, I., and Oksman, K. (2007) Structure and thermal properties of poly(lactic acid)/cellulose whiskers nanocomposite materials. *Compos. Sci. Technol.*, **67** (11-12), 2535–2544.

48. De Mesquita, J.P., Donnici, C.L., Teixeira, I.F., and Pereira, F.V. (2012)

Bio-based nanocomposites obtained through covalent linkage between chitosan and cellulose nanocrystals. *Carbohydr. Polym.*, **90** (1), 210–217.

49. Goussé, C., Chanzy, H., Excoffier, G., Soubeyranda, L., and Fleury, E. (2002) Stable suspensions of partially silylated cellulose whiskers dispersed in organic solvents. *Polymer*, **43** (9), 2645–2651.

50. Lin, S. (2012) Acetylated modification of cellulose nanocrystals. *Anhui Chem. Ind.*, **38** (5), 48–50.

51. Yang, Z.Y., Wang, W.J., Shao, Z.Q., and Li, Y.H. (2013) Surface acetylation of cellulose nanowhiskers and its reinforcing function in cellulose acetate. *Chem. J. Chin. Univ.*, **34** (4), 1021–1026.

52. Xu, Y. (2010) *Preparation, Modification and its Performance of Polysaccharide Nanocrystals*, Chinese Academy of Sciences Graduate Student.

53. Jiang, L., Morelius, E., Zhang, J., Wolcott, M., and Holbery, J. (2008) Study of the poly (3-hydroxybutyrate-co-3-hydroxyvalerate)/cellulose nanowhisker composites prepared by solution casting and melt processing. *J. Compos. Mater.*, **42** (24), 2629–2645.

54. Ten, E., Turtle, J., Bahr, D., Jiang, L., and Wolcott, M. (2010) Thermal and mechanical properties of poly(3-hydroxybutyrate-co-3-hydroxyvalerate)/cellulose nanowhiskers composites. *Polymer*, **51** (12), 2652–2660.

55. Yu, H.Y., Qin, Z.Y., Liu, Y.N., Chen, L., Liu, N., and Zhou, Z. (2012) Simultaneous improvement of mechanical properties and thermal stability of bacterial polyester by cellulose nanocrystals. *Carbohydr. Polym.*, **89** (3), 971–978.

56. Yu, H.Y., Qin, Z.Y., and Zhou, Z. (2011) Cellulose nanocrystals as green fillers to improve crystallization and hydrophilic property of poly(3-hydroxybutyrate-co-3-hydroxyvalerate). *Prog. Nat. Sci.-Mater. Int.*, **21** (6), 478–484.

57. Yu, H.Y. and Qin, Z.Y. (2012) Effect of cellulose nanocrystal on crystallization behavior of poly(3−hydroxybutyrate−co−3−

hydroxyvalerate). *Adv. Mater. Res.*, **430-432**, 20–23.

58. Yu, H.Y., Qin, Z.Y., Liu, L., Yang, X.G., Zhou, Y., and Yao, J.M. (2013) Comparison of the reinforcing effects for cellulose nanocrystals obtained by sulfuric and hydrochloric acid hydrolysis on the mechanical and thermal properties of bacterial polyester. *Compos. Sci. Technol.*, **87** (18), 22–28.

59. Yu, H.Y., Qin, Z.Y., Liang, B.L., Liu, N., Zhou, Z., and Chen, L. (2013) Facile extraction of thermally stable cellulose nanocrystals with a high yield of 93% through hydrochloric acid hydrolysis under hydrothermal conditions. *J. Mater. Chem. A*, **1** (12), 3938–3944.

60. Yu, J.H., Ai, F.J., Dufresne, A., Gao, S.J., Huang, J., and Chang, P.R. (2008) Structure and mechanical properties of poly(lactic acid) filled with (starch nanocrystal)-graft-poly(epsilon-caprolactone). *Macromol. Mater. Eng.*, **293** (9), 763–770.

61. Chen, G.J., Dufresne, A., Huang, J., and Chang, P.R. (2009) A novel thermo-formable bionanocomposite based on cellulose nanocrystal-graft-poly(epsilon-caprolactone). *Macromol. Mater. Eng.*, **294** (1), 59–67.

62. Lin, N., Huang, J., Chang, P.R., Feng, J.W., and Yu, J.H. (2011) Surface acetylation of cellulose nanocrystal and its reinforcing function in poly(lactic acid). *Carbohydr. Polym.*, **83** (4), 1834–1842.

63. Shang, W.L., Huang, J., Luo, H., Chang, P.R., Feng, J.W., and Xie, G.Y. (2013) Hydrophobic modification of cellulose nanocrystal via covalently grafting of castor oil. *Cellulose*, **20** (1), 179–190.

64. Habibi, Y. and Dufresne, A. (2008) Highly filled bionanocomposites from functionalized polysaccharide nanocrystals. *Biomacromolecules*, **9** (7), 1974–1980.

65. Wang, J., Wang, Z., Li, J., Wang, B., Liu, J., Chen, P., Miao, M., and Gu, Q. (2012) Chitin nanocrystals grafted with poly(3−hydroxybutyrate−co−3−hydroxyvalerate) and their effects on thermal behavior of PHBV. *Carbohydr. Polym.*, **87** (1), 784–789.

66. Nair, K.G. and Dufresne, A. (2003) Crab shell chitin whiskers reinforced

natural rubber nanocomposites. 3. Effect of chemical modification of chitin whiskers. *Biomacromolecules*, **4** (6), 1835–1842.

67. Petersson, L. and Oksman, K. (2006) Biopolymer based nanocomposites: comparing layered silicates and microcrystalline cellulose as nanoreinforcement. *Compos. Sci. Technol.*, **66** (13), 2187–2196.

68. Bondeson, D. and Oksman, K. (2007) Dispersion and characteristics of surfactant modified cellulose whiskers nanocomposites. *Compos. Interfaces*, **14** (7-9), 617–630.

69. Araki, J., Wada, M., Kuga, S., and Okano, T. (1998) Flow properties of microcrystalline cellulose suspension prepared by acid treatment of native cellulose. *Colloids Surf. A Physicochem. Eng. Asp.*, **142** (1), 75–82.

70. Azouz, K.B., Ramires, E.C., Van den Fonteyne, W., Kissi, N.E., and Dufresne, A. (2012) Simple method for the melt extrusion of a cellulose nanocrystal reinforced hydrophobic polymer. *ACS Macro Lett.*, **1** (1), 236–240.

71. Mathew, A.P., Gong, G., Bjorngrim, N., Wixe, D., and Oksman, K. (2011) Moisture absorption behavior and its impact on the mechanical properties of cellulose whiskers-based polyvinylacetate nanocomposites. *Polym. Eng. Sci.*, **51** (11), 2136–2142.

72. Lemahieu, L., Bras, J., Tiquet, P., Augier, S., and Dufresne, A. (2011) Extrusion of nanocellulose-reinforced nanocomposites using the dispersed nano-objects protective encapsulation (DOPE) process. *Macromol. Mater. Eng.*, **296** (11), 984–991.

73. Menezes, A.J., Siqueira, G., Curvelo, A.A.S., and Dufresne, A. (2009) Extrusion and characterization of functionalized cellulose whiskers reinforced polyethylene nanocomposites. *Polymer*, **50** (19), 4552–4563.

74. Raquez, J.M., Murena, Y., Goffin, A.L., Habibi, Y., Ruelle, B., DeBuyl, F., and Dubois, P. (2012) Surface-modification of cellulose nanowhiskers and their use as nanoreinforcers into polylactide: a sustainably-integrated approach. *Compos. Sci. Technol.*, **72** (5), 544–549.

75. Goffin, A.L., Raquez, J.M., Duquesne, E., Siqueira, G., Habibi, Y., Dufresne, A., and Dubois, P. (2011) From interfacial ring-opening polymerization to melt processing of cellulose nanowhisker-filled polylactide-based nanocomposites. *Biomacromolecules*, **12** (7), 2456–2465.

76. Lin, N. and Dufresne, A. (2013) Physical and/or chemical compatibilization of extruded cellulose nanocrystal reinforced polystyrene nanocomposites. *Macromolecules*, **46** (14), 5570–5583.

77. Formhals, A. (1934) Process and apparatus for preparing artificial thread. US Patent 1975504, Oct. 2, 1934.

78. Formhals, A. (1937) Production of artificial fibers. US Patent 2, 077, 373.

79. Formhals, A. (1939) Method and apparatus for the production of artificial fibers. US Patent 2, 158, 416.

80. Rayleigh, L. (1882) On the equilibrium of liquid conducting masses charged with electricity. *Philos. Mag.*, **14** (87), 184–186.

81. Vonnegut, B. and Neubauer, R.L. (1952) Production of monodisperse liquid particles by electrical atomization. *J. Colloid Sci.*, **7** (6), 616–622.

82. Larrondo, L. and St John Manley, R. (1981) Electrostatic fiber spinning from polymer melts. I. Experimental observations on fiber formation and properties. *J. Polym. Sci.: Polym. Phys. Ed.*, **19** (6), 909–920.

83. Doshi, J. and Reneker, D.H. (1995) Electrospinning process and applications of electrospun fibers. *J. Electrostat.*, **35** (2-3), 151–160.

84. Reneker, D.H. and Chun, I. (1996) Nanometre diameter fibers of polymer produced by electrospinning. *Nanotechnology*, **7** (3), 216–223.

85. Thayer, P.S., Dimling, A.F., Plessl, D.S., Hahn, M.R., Guelcher, S.A., Dahlgren, L.A., and Goldstein, A.S. (2014) Cellularized cylindrical fiber/hydrogel composites for ligament tissue engineering. *Biomacromolecules*, **15** (1), 75–83.

86. Li, Y.C., Ceylan, M., Shrestha, B., Wang, H.B., Lu, Q.R., Asmatulu, R., and Yao, L. (2014) Nanofibers support oligo-dendrocyte precursor cell growth and function as a neuron-free model for myelination study. *Biomacromolecules*, **15** (1), 319–326.

87. Sun, D., Chang, C., Li, S., and Lin, L. (2006) Near-field electrospinning. *Nano Lett.*, **6** (4), 839–842.

88. Huang, Z.M., Zhang, Y.Z., Kotaki, M., and Ramakrishna, S. (2003) A review on polymer nanofibers by electrospinning and their applications in nanocomposites. *Compos. Sci. Technol.*, **63** (15), 2223–2253.

89. Serp, P., Corrias, M., and Kalck, P. (2003) Carbon nanotubes and nanofibers in catalysis. *Appl. Catal. Gen.*, **253** (2), 337–358.

90. Sadek, A.Z., Wlodarski, W., Kalantar-Zadeh, K., Baker, C., and Kaner, R.B. (2007) Doped and dedoped polyaniline nanofiber based conductometric hydrogen gas sensors. *Sens. Actuators, A*, **139** (1-2), 53–57.

91. Ma, H.Y., Burger, C., Hsiao, B.S., and Chu, B. (2012) Nanofibrous microfiltration membrane based on cellulose nanowhiskers. *Biomacromolecules*, **13** (1), 180–186.

92. Beachley, V. and Wen, X. (2010) Polymer nanofibrous structures: fabrication, biofunctionalization, and cell interactions. *Prog. Polym. Sci.*, **35**, 868–892.

93. Lin, J.Y., Ding, B., Yu, J.Y., and Hsieh, Y. (2010) Direct fabrication of highly nanoporous polystyrene fibers via electrospinning. *ACS Appl. Mater. Interfaces*, **2** (2), 521–528.

94. Dayal, P., Liu, J., Kumar, S., and Kyu, T. (2007) Experimental and theoretical investigations of porous structure formation in electrospun fibers. *Macromolecules*, **40** (21), 7689–7694.

95. Hu, P., Zhang, L., Fang, Z.X., Yang, D.Z., and Qi, H.X. (2004) Electrospinning and its application in biomedical materials. *Text. Sci. Res.*, **2**, 26–32 (Chinese journal).

96. Beachley, V. and Wen, X. (2009) Effect of electrospinning parameters on the nanofiber diameter and length. *Mater. Sci. Eng., C*, **29** (3), 663–668.

97. Theron, S.A., Yarin, A.L., Zussman, E., and Kroll, E. (2005) Multiple jets in electrospinning: experiment and modeling. *Polymer*, **46** (9), 2889–2899.

98. Kim, G.H., Cho, Y., and Kim, W.D. (2006) Stability analysis for multi-jets electrospinning process modified with a cylindrical electrode. *Eur. Polym. J.*, **42** (9), 2031–2038.

99. Liu, C.K., Sun, R.J., Lai, K., Sun, C.Q., and Wang, Y.W. (2008) Preparation of short submicron-fiber yarn by an annular collector through electrospinning. *Mater. Lett.*, **62** (29), 4467–4469.

100. Theron, A., Zussman, E., and Yarin, A.L. (2001) Electrostatic field-assisted alignment of electrospun nanofibers. *Nanotechnology*, **12** (3), 384–390.

101. Han, T., Reneker, D.H., and Yarin, A.L. (2007) Buckling of jets in electrospinning. *Polymer*, **48** (20), 6064–6076.

102. Li, Y. and Huang, Z.M. (2006) Electrostatic spinning of polymers. *Polym. Bull.*, **5**, 12–20.

103. Greiner, A. and Wendorff, J.H. (2007) Electrospinning: a fascinating method for the preparation of ultrathin fibers. *Angew. Chem. Int. Ed.*, **46** (30), 5670–5703.

104. Kim, G.H., Son, J.G., Park, S.A., and Kim, W.D. (2008) Hybrid process for fabricating 3d hierarchical scaffolds combining rapid prototyping and electrospinning. *Macromol. Rapid Commun.*, **29** (19), 1577–1581.

105. Sundarrajan, S., Venkatesan, A., and Ramakrishna, S. (2009) Fabrication of nanostructured self-detoxifying nanofiber membranes that contain active polymeric functional groups. *Macromol. Rapid Commun.*, **30** (20), 1769–1774.

106. Bhattarai, N., Li, Z.S., Gunn, J., Leung, M., Cooper, A., Edmondson, D., Veiseh, O., Chen, M.H., Zhang, Y., Ellenbogen, R.G., and Zhang, M.Q. (2009) Natural-synthetic polyblend nanofibers for biomedical applications. *Adv. Mater.*, **21** (27), 2792–2797.

107. Ding, B., Kimura, E., Sato, T., Fujita, S., and Shiratori, S. (2004) Fabrication of blend biodegradable nanofibrous nonwoven mats via multi-jet electrospinning. *Polymer*, **45** (6), 1895–1902.

108. Hong, Y., Fujimoto, K., Hashizume, R., Guan, J.J., Stankus, J.J., Tobita, K., and Wagner, W.R. (2008) Generating elastic, biodegradable polyurethane/poly(lactide-co-glycolide) fibrous sheets with controlled antibiotic release via two-stream electrospinning. *Biomacromolecules*, **9** (4), 1200–1207.

109. Kidoaki, S., Kwon, I.K., and Matsuda, T. (2005) Mesoscopic spatial designs of nano- and microfiber meshes for tissue-engineering matrix and scaffold based on newly devised multilayering and mixing electrospinning techniques. *Biomaterials*, **26** (1), 37–46.

110. Wei, M., Kang, B., Sung, C., and Joey, M. (2006) Core-sheath structure in electrospun nanofibers from polymer blends. *Macromol. Mater. Eng.*, **291** (11), 1307–1314.

111. Kalra, V., Lee, J.H., Park, J.H., Marquez, M., and Joo, Y.L. (2009) Confined assembly of asymmetric block-copolymer nanofibers via multiaxial jet electrospinning. *Small*, **5** (20), 2323–2332.

112. Mahmoud, K.A., Mena, J.A., Male, K.B., Hrapovic, S., Kamen, A., and Luong, J.H.T. (2010) Effect of surface charge on the cellular uptake and cytotoxicity of fluorescent labeled cellulose nanocrystals. *ACS Appl. Mater. Interfaces*, **2** (10), 2924–2932.

113. Ago, M., Okajima, K., Jakes, J.E., Park, S., and Rojas, O.J. (2012) Lignin-based electrospun nanofibers reinforced with cellulose nanocrystals. *Biomacromolecules*, **13** (3), 918–926.

114. Martinez-Sanz, M., Olsson, R.T., Lopez-Rubio, A., and Lagaron, J.M. (2011) Development of electrospun EVOH fibers reinforced with bacterial cellulose nanowhiskers. Part I: characterization and method optimization. *Cellulose*, **18** (2), 335–347.

115. Huang, J., Liu, L., and Yao, J.M. (2011) Electrospinning of Bombyx mori silk fibroin nanofiber mats reinforced by cellulose nanowhiskers. *Fibers Polym.*, **12** (8), 1002–1006.

116. Zhou, C.J., Chu, R., Wu, R., and Wu, Q.L. (2011) Electrospun polyethylene oxide/cellulose nanocrystal composite nanofibrous mats with homogeneous and heterogeneous microstructures. *Biomacromolecules*, **12** (7), 2617–2625.

117. Zhou, C., Wang, Q., and Wu, Q. (2012) UV–initiated crosslinking of electrospun poly(ethylene oxide) nanofibers with pentaerythritol triacrylate: effect of irradiation time and incorporated cellulose nanocrystals. *Carbohydr. Polym.*, **87** (2), 1779–1786.

118. Yu, H.Y., Zhou, Z., and Qin, Z.Y. (2010) Electrospun solid–solid phase change nanofibers of poly(ethylene glycol) grafted onto the surface of cellulose nanocrystals. *Nanosci. Nanotechnol.*, **7** (6), 50–54.

119. Rojas, O.J., Montero, G.A., and Habibi, Y. (2009) Electrospun nanocomposites from polystyrene loaded with cellulose nanowhiskers. *J. Appl. Polym. Sci.*, **113** (2), 927–935.

120. Zoppe, J.O., Peresin, M.S., Habibi, Y., Venditti, R.A., and Rojas, O.J. (2009) Reinforcing poly(ϵ–caprolactone) nanofibers with cellulose nanocrystals. *ACS Appl. Mater. Interfaces*, **1** (9), 1996–2004.

121. Lu, P. and Hsieh, Y.L. (2009) Cellulose nanocrystal-filled poly(acrylic acid) nanocomposite fibrous membranes. *Nanotechnology*, **20** (41), 415604.

122. Dong, H., Strawhecker, K.E., Snyder, J.F., Orlicki, J.A., Reiner, R.S., and Rudie, A.W. (2012) Cellulose nanocrystals as a reinforcing material for electrospun poly(methyl methacrylate) fibers: formation, properties and nanomechanical characterization. *Carbohydr. Polym.*, **87** (4), 2488–2495.

123. Yu, H.Y., Zhou, Z., Liu, Y.N., and Qin, Z.Y. (2011) Cellulose nanocrystal-reinforced electrospun poly(3-hydroxybutyrate-co-3-hydroxyvalerate) nanofibers. Proceedings of International Conference on Advanced Fibers and Polymer Materials, Shanghai.

124. Qin, Z.Y., Yu, H.Y., and Tian, F. (2012) A Biodegradable Drug Sustained Release Nanofiber Membrane Used in the Treatment of Periodontitis and its Preparation Method, Publication Number: CN102423506A.

125. Peresin, M.S., Habibi, Y., Zoppe, J.O., Pawlak, J.J., and Rojas, O.J. (2010) Nanofiber composites of polyvinyl

alcohol and cellulose nanocrystals: manufacture and characterization. *Biomacromolecules*, **11** (3), 674–681.

126. Peresin, M.S., Habibi, Y., Vesterinen, A.H., Rojas, O.J., Pawlak, J.J., and Seppala, J.V. (2010) Effect of moisture on electrospun nanofiber composites of poly(vinyl alcohol) and cellulose nanocrystals. *Biomacromolecules*, **11** (9), 2471–2477.

127. Zhou, C.J., Shi, Q.F., Guo, W.H., Terrell, L., Qureshi, A.T., Hayes, D.J., and Wu, Q.L. (2013) Electrospun bio-nanocomposite scaffolds for bone tissue engineering by cellulose nanocrystals reinforcing maleic anhydride grafted PLA. *ACS Appl. Mater. Interfaces*, **5** (9), 3847–3854.

128. Wei, J., Wan, Y.Q., Wang, H.B., and Gao, W.D. (2012) Effect of Chitin nanowhisker/polylactic acid nanofiber film on the preservation of strawberry. *J. Food Sci. Biotechnol.*, **31** (11), 1184–1188.

129. Revol, J.F., Bradford, H., Giasson, J., Marchessault, R.H., and Gray, D.G. (1992) Helicoidal self-ordering of cellulose microfibrils in aqueous suspension. *Int. J. Biol. Macromol.*, **14** (3), 170–172.

130. Capadona, J.R., Van Den Berg, O., Capadona, L.A., Schroeter, M., Rowan, S.J., Tyler, D.J., and Weder, C. (2007) A versatile approach for the processing of polymer nanocomposites with self-assembled nanofiber templates. *Nat. Nanotechnol.*, **2** (12), 765–769.

131. Isobe, N., Sekine, M., Kimura, S., Wada, M., and Kuga, S. (2011) Anomalous reinforcing effects in cellulose gel-based polymeric nanocomposites. *Cellulose*, **18** (21), 327–333.

132. Tang, L. and Weder, C. (2010) Cellulose whisker/epoxy resin nanocomposites. *ACS Appl. Mater. Interfaces*, **2** (14), 1073–1080.

133. Shopsowitz, K., Qi, H., Hamad, W., and MacLachlan, M. (2010) Free-standing mesoporous silica films with tunable chiral nematic structures. *Nature*, **468**, 422–425.

134. Dujardin, E., Blaseby, M., and Mann, S. (2003) Synthesis of mesoporous silica by sol-gel mineralization of cellulose nanorod nematic suspensions. *J. Mater. Chem.*, **13**, 696–699.

135. Thomas, A. and Antonietti, M. (2003) Silica nanocasting of simple cellulose derivatives: towards chiral pore systems with long-range order and chiral optical coatings. *Adv. Funct. Mater.*, **13** (10), 763–766.

136. Shopsowitz, K., Stahl, A., Hamad, W., and MacLachlan, M. (2012) Hard templating of nanocrystalline titanium dioxide with chiral nematic ordering. *Angew. Chem. Int. Ed.*, **51** (28), 6886–6890.

137. Shopsowitz, K., Hamad, W., and MacLachlan, M. (2011) Chiral nematic mesoporous carbon derived from nanocrystalline cellulose. *Angew. Chem. Int. Ed.*, **50** (46), 10991–10995.

138. Lytle, J., Yan, H., Turgeon, R., and Stein, A. (2004) Multistep, low-temperature pseudomorphic transformations of nanostructured silica to titania via a titanium oxyfluoride intermediate. *Chem. Mater.*, **16** (20), 3829–3837.

139. Han, S., Sohn, K., and Hyeon, T. (2000) Fabrication of new nanoporous carbons through silica templates and their application to the adsorption of bulky dyes. *Chem. Mater.*, **12** (11), 3337–3341.

140. Lee, J., Yoon, S., Hyeon, T., Oh, S.M., and Kim, K. (1999) Synthesis of a new mesoporous carbon and its application to electrochemical double-layer capacitors. *Chem. Commun.*, **21**, 2177–2178.

141. Adelhelm, P., Hu, Y., Chuenchom, L., Antonietti, M., Smarsly, B., and Maiter, J. (2007) Generation of hierarchical meso- and macroporous carbon from mesophase pitch by spinodal decomposition using polymer templates. *Adv. Mater.*, **19** (22), 4012–4017.

142. Ji, X., Lee, K.T., and Nazar, L.F. (2009) A highly ordered nanostructured carbon-sulphur cathode for lithium-sulphur batteries. *Nat. Mater.*, **8**, 500–506.

143. Joo, S.H., Choi, S.J., Oh, I., Kwak, J., Liu, Z., Terasaki, O., and Ryoo, R. (2001) Ordered nanoporous arrays of carbon supporting high dispersions of platinum nanoparticles. *Nature*, **412**, 169–172.

144. Shopsowitz, K., Hamad, W., and MacLachlan, M. (2012) Flexible and iridescent chiral nematic mesoporous organosilica films. *J. Am. Chem. Soc.*, **134** (2), 867–870.

145. Kelly, J., Shopsowitz, K., Ahn, J., Hamad, W., and MacLachlan, M. (2012) Chiral nematic stained glass: controlling the optical properties of nanocrystalline cellulose-templated materials. *Langmuir*, **28** (50), 17256–17262.

146. Liu, Z.M., Wu, P., and Xie, C. (2013) Layer-by-layer self-assembly and characterization of polyvinyl alcohol/nanocellulose/polyvinyl alcohol. *Mater. Eng.*, **1**, 45–51 (Chinese journal).

147. Li, Q., Cui, Y., Zhang, W.X., Zou, Y.L., Li, M., and Zhang, C.Y. (2004) Methods and applications of molecular self-assembly. *Polym. Mater. Sci. Eng.*, **20** (6), 33–36, 41.

148. Zeng, P.J., Liu, Y.Q., Hu, W.P., and Zhu, D.B. (1999) Film forming techniques of molecular self-assembly. *Physics*, **28** (12), 713–719.

149. Li, J.B. and Xu, Q. (2007) Development and application of layer-by-layer self-assembly technology. *World Sci.-Tech.*, **29** (3), 31–38 (Chinese journal).

150. Godbout, D.L., Gray, D.G., and Revol, J.F. (1997) Solidified liquid crystals of cellulose with optically variable properties. US Patent 5,629,055.

151. Orts, W.J., Godbout, L., Marchessault, R.H., and Revol, J.F. (1998) Enhanced ordering of liquid crystalline suspensions of cellulose microfibrils: a small angle neutron scattering study. *Macromolecules*, **31** (17), 5717–5725.

152. Araki, J., Wada, M., Kuga, S., and Okano, T. (2000) Birefringent glassy phase of a cellulose microcrystal suspension. *Langmuir*, **16** (6), 2413–2415.

153. Hirai, A., Inui, O., Horii, F., and Tsuji, M. (2009) Phase separation behavior in aqueous suspensions of bacterial cellulose nanocrystals prepared by sulfuric acid treatment. *Langmuir*, **25** (1), 497–502.

154. Dong, X.M., Kimura, T., Revol, J.F., and Gray, D.G. (1996) Effects of ionic strength on the isotropic−chiral nematic phase transition of suspensions of cellulose crystallites. *Langmuir*, **12** (8), 2076–2082.

155. Dong, X.M. and Gray, D.G. (1997) Effect of counterions on ordered phase formation in suspensions of charged rodlike cellulose crystallites. *Langmuir*, **13** (8), 2404–2409.

156. Hasani, M., Cranston, E.D., Westmana, G., and Gray, D.G. (2008) Cationic surface functionalization of cellulose nanocrystals. *Soft Matter*, **4**, 2238–2244.

157. Heux, L., Chauve, G., and Bonini, C. (2000) Nonflocculating and chiral-nematic self-ordering of cellulose microcrystal suspensions in nonpolar solvents. *Langmuir*, **16**, 8210–8212.

158. Elazzouzi-Hafraoui, S., Putaux, J.L., and Heux, L. (2009) Self-assembling and chiral nematic properties of organophilic cellulose nanocrystals. *J. Phys. Chem. B*, **113**, 11069–11075.

159. Zhou, Q., Brumer, H., and Teeri, T.T. (2009) Self-organization of cellulose nanocrystals adsorbed with xyloglucan oligosaccharide-poly(ethylene glycol)-polystyrene triblock copolymer. *Macromolecules*, **42**, 5430–5432.

160. Roman, M. and Gray, D.G. (2005) Parabolic focal conics in self-assembled solid films of cellulose nanocrystals. *Langmuir*, **21**, 5555–5561.

161. Revol, J.F., Godbout, L., Dong, X.M., Gray, D.G., Chanzy, H., and Maret, G. (1994) Chiral nematic suspensions of cellulose crystallites; phase separation and magnetic field orientation. *Liq. Cryst.*, **16**, 127–134.

162. Csoka, L., Hoeger, I.C., Peralta, P., Ilona, P., and Rojas, O.J. (2011) Dielectrophoresis of cellulose nanocrystals and alignment in ultrathin films by electric field-assisted shear assembly. *J. Colloid Interface Sci.*, **363**, 206–212.

163. Zhang, T., Yang, J.H., Liang, K., and Du, Y. (2007) Preparation and performance of chitosan oxide self-assembly films. *J. Anal. Sci.*, **23** (2), 125–128 (Chinese journal).

164. Podsiadlo, P., Choi, S.Y., Shim, B., Lee, J., Cuddihy, M., and Kotov, N.A. (2005) Molecularly engineered nanocomposites: layer-by-layer assembly of cellulose

nanocrystals. *Biomacromolecules*, **6**, 2914–2918.

165. Podsiadlo, P., Sui, L., Elkasabi, Y., Burgardt, P., Lee, J., Miryala, A., Kusumaatmaja, W., Carman, M.R., Shtein, M., Kieffer, J., Lahann, J., and Kotov, N.A. (2007) Layer-by-layer assembled films of cellulose nanowires with antireflective properties. *Langmuir*, **23**, 7901–7906.

166. Cranston, E.D. and Gray, D.G. (2006) Formation of cellulose-based electrostatic layer-by-layer films in a magnetic field. *Sci. Technol. Adv. Mater.*, **7**, 319–321.

167. De Mesquita, J.P., Donnici, C.L., and Pereira, F.V. (2010) Biobased nanocomposites from layer-by-layer assembly of cellulose nanowhiskers with chitosan. *Biomacromolecules*, **11**, 473–480.

168. De Mesquita, J.P., Patrıcio, P.S., Donnici, C.L., Petri, D.F.S., de Oliveira, L.C.A., and Pereira, F.V. (2011) Hybrid layer-by-layer assembly based on animal and vegetable structural materials: multilayered films of collagen and cellulose nanowhiskers. *Soft Matter*, **7**, 4405–4413.

169. Sui, L., Huang, L., Podsiadlo, P., Kotov, N.A., and Kieffer, J. (2010) Brillouin light scattering investigation of the mechanical properties of layer-by-layer assembled cellulose nanocrystal films. *Macromolecules*, **43**, 9541–9548.

170. Aulin, C., Johansson, E., Wågberg, L., and LindstrÖm, T. (2010) Self-organized films from cellulose I nanofibrils using the layer-by-layer technique. *Biomacromolecules*, **11**, 872–882.

171. Qi, Z.D., Saito, T., Fan, Y., and Isogai, A. (2012) Multifunctional coating films by layer-by-layer deposition of cellulose and chitin nanofibrils. *Biomacromolecules*, **13**, 553–558.

172. Heath, L. and Thielemans, W. (2010) Cellulose nanowhisker aerogels. *Green Chem.*, **12** (8), 1448–1453.

173. Kalashnikova, I., Bizot, H., Cathala, B., and Capron, I. (2012) Modulation of cellulose nanocrystals amphiphilic properties to stabilize oil/water interface. *Biomacromolecules*, **13** (1), 267–275.

5

Polysaccharide Nanocrystal-Reinforced Nanocomposites

Hanieh Kargarzadeh and Ishak Ahmad

5.1
Introduction

Over the past few years, natural polymers have increasingly attracted attention, and much effort has been made to use polymer nanocrystals as reinforcing fillers. Among the important biological nanocompounds, polysaccharides (cellulose, chitin, and starch) are one of the most promising sources of nanocrystals because of their renewability, biodegradability, versatility, availability, high aspect ratio, and so on. The extraction of polysaccharide nanocrystals can be accomplished by a simple process based on the acid hydrolysis of biomass under controlled conditions.

Cellulose structure consists of mainly a crystalline cellulose core and amorphous domains including hemicellulose, lignin, wax, and pectin. Amorphous regions have lower density than the crystalline regions. Therefore, when cellulose fibers are subjected to acid treatment, the amorphous region dissolves, releasing the individual crystallites. The resulting cellulose nanocrystals (CNCs) are rigid rod-like crystals with a diameter in the range 10−20 nm and length of approximately a few hundred nanometers [1]. The properties of CNCs depend on various factors, such as the sources, reaction time and temperature, and the types of acid used for hydrolysis [2]. Because of the distinctive properties of CNCs, they are an important class of renewable nanomaterials with many useful applications; their most important application is the reinforcement of polymeric matrices.

Chitin is a naturally occurring polysaccharide and consists of 2-acetamido-2-deoxy-D-glucose via β-1,4-linkages similar to cellulose. It is the second most abundant semicrystalline polysaccharide and widely used as the substitute for inorganic nanoparticles in reinforcing polymer nanocomposites. Compared to cellulose whiskers, chitin has been rarely studied. Chitin nanowhiskers (ChWs) are also obtained by the acid hydrolysis of chitin from various sources.

Starch nanocrystals (SNCs) are also obtained from starch by acid hydrolysis. Unlike rod-like CNCs and slender ChWs, SNCs are platelet-like, combining the advantages of bulk polymers and nanosized effects [3]. Similar to CNCs and

ChWs, the structure and yield of lamella-like nanocrystals formed by acid hydrolysis depend on properties of starch, including its origin, type of crystallinity, relative amylose/amylopectin ratio, granule morphology, and the acid hydrolysis conditions (acid type and concentration, temperature, and duration) [4].

In general, the addition of polysaccharide nanoparticles to polymer matrix may improve the mechanical properties, thermal properties, surface appearance, and change in the gas and water permeability of the resulting materials. However, the main challenges are the homogeneous dispersion within a polymeric matrix and the poor interfacial adhesion between cellulosic fibers because polar materials in a nonpolar medium act as polymeric materials.

This chapter focuses on the use of polyester, rubber, polyolefin, polyurethane (PU), starch, and protein as the polymer matrices for the preparation of polysaccharide nanocrystal-based nanocomposites because less attention has been paid to the recent findings on these nanocomposites. The important findings on the mechanical, thermal, morphological, and other unique properties of these nanocomposites are discussed.

5.2
Rubber-Based Nanocomposites

Rubber is an elastic, insulated substrate obtained from the latex of rubber trees and can be vulcanized and transformed into various products. Both natural rubber (NR) and synthetic rubber show excellent mechanical properties and are widely used in industrial, technological, and engineering areas such as tires, mountings, gaskets, and seals [5]. The unique mechanical properties of NR result from both its highly stereoregular microstructure and the rotational freedom of α-methylene C−C bonds contributing to the high elasticity [6, 7].

The mechanical properties of NR have been improved by reinforcing with fillers with various chemical surface modification and aggregate size/aspect ratio to suit the concerned application. Carbon black (CB), silica, and clay are the conventional fillers for NR compounds. CB is the most important reinforcing filler used in the rubber industry. Because CB originates from petroleum, its processing is cumbersome and contaminates the end products; moreover, CB makes the rubber black [8]. Silica is an excellent reinforcing filler because of its ability to reduce heat build-up and rolling resistance. However, silica has some disadvantages such as long processing time, high energy consumption, and environment pollution during the processing [9]. Therefore, there is an urgent need to search for suitable substrates that are environment friendly and energy saving to replace CB and silica in NR processing.

Over the past few years, natural polymers have increasingly attracted our attention and much effort has been made to use the nanocrystals obtained from them as reinforcing fillers. Among the important biological nanocompounds, polysaccharides (cellulose, chitin, and starch) are one of the most promising sources of nanocrystals.

The applications of CNCs and cellulose nanofibrils (CNFs) in plastic matrices have been widely studied; in contrast, those for rubber have been rarely reported [5, 10, 11]. The nanocomposites were obtained by casting and water evaporation. The protocol shown in Figure 5.1 is one of the common methods to prepare rubber nanocomposites [12, 13].

Figure 5.2 shows the scanning electron microscopic (SEM) images of CNC and microfibrillated cellulose (MFC)/NR-based films. The fractured surface of a neat NR film (a) is smooth and uniform, whereas those of the nanocomposite
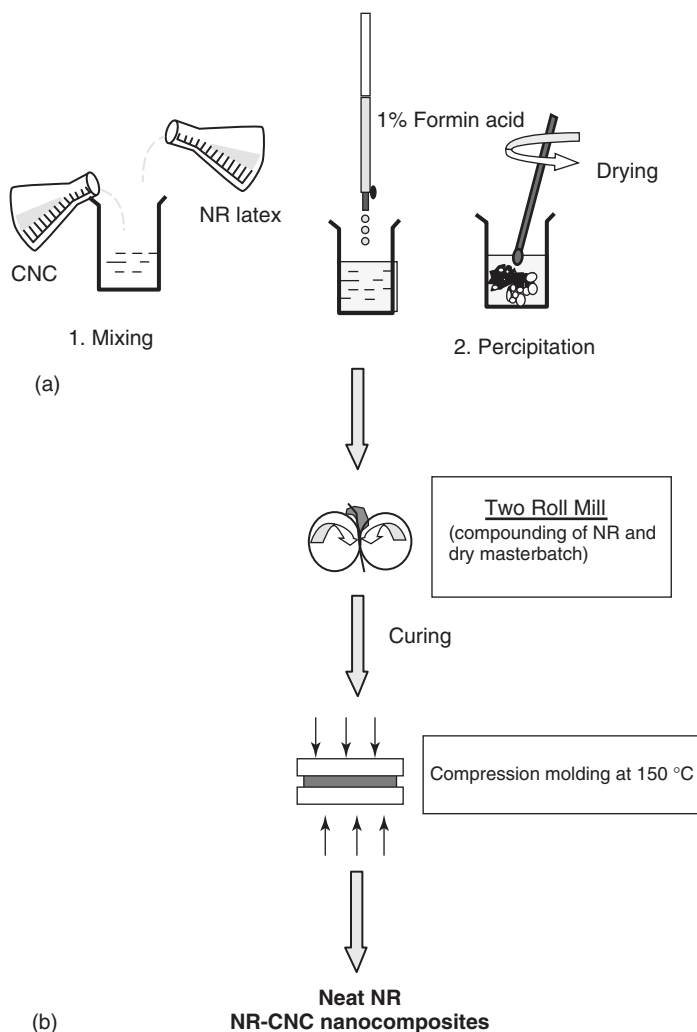
Figure 5.1   Schematic diagram for the preparation natural rubber/cellulose nanocrystal nanocomposites. (a) Masterbatch preparation and (b) nanocomposite preparation. Reproduced from [14], copyright 2011 © permission from Wiley Periodicals.
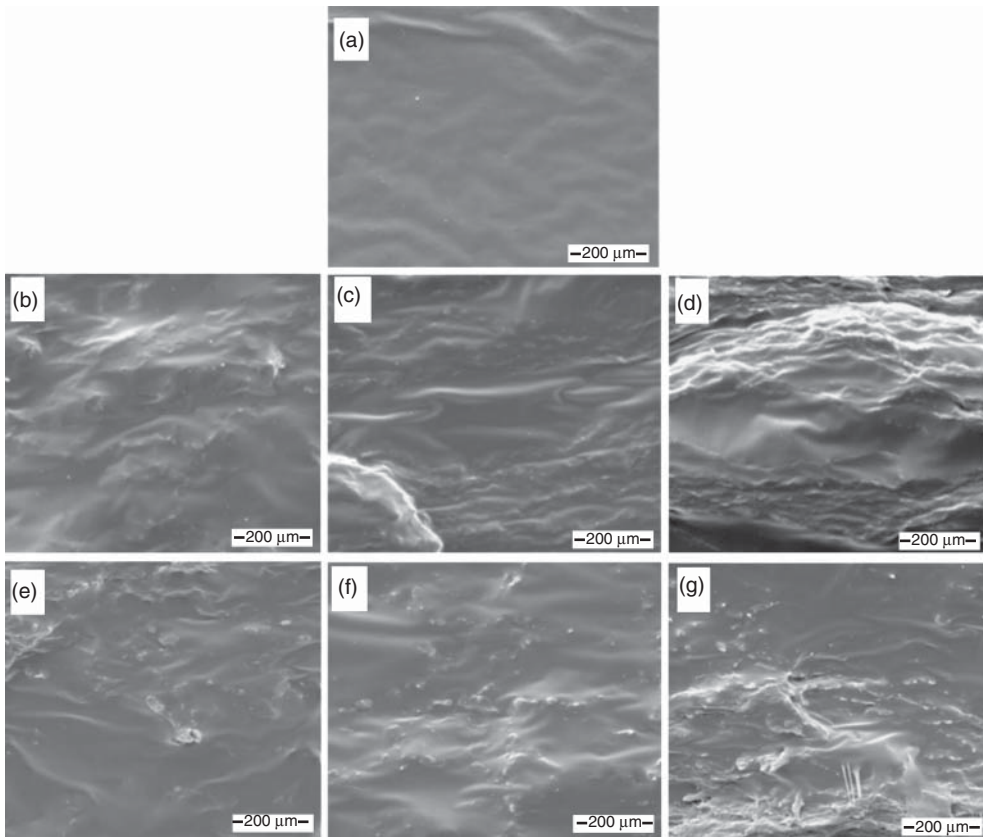
Figure 5.2 Scanning electron microscopy micrographs of the fractured surfaces of natural rubber (NR)-based films reinforced with cellulose nanocrystals (CNCs) extracted from the rachis of date palm tree: (a) neat NR matrix, (b) NR/CNC1, (c) NR/CNC5, (d) NR/CNC15, (e) NR/MFC1, (f) NR/MFC5, and (g) NR/MFC15. Reproduced from [13], copyright 2010 © permission from Elsevier.

films (CNC, b–d; MFC, e–g) show a rough surface. This is probably because of the brittleness of the nanocomposites under nitrogen. The CNCs are hardly distinguishable; however, the aggregated nanoparticles are more visible for the MFC-based nanocomposites. This is probably because of the entanglements of hairy flexible MFCs during the processing [13].

The effects of temperature and frequency on the mechanical properties of the elastic material were investigated by dynamic thermomechanical analysis (DMA). The global evolution of the nanocomposite film is similar to that of the neat matrix. At a low temperature, that is, below the glass-transition temperature (T_g), the reinforcing effect of CNCs was low, justifying the normalization of the modulus. Therefore, the films were relatively soft, and a constant and precise thickness along these samples was difficult to obtain. Above the T_g, the nanoparticles were significantly reinforced because of the mechanical percolation phenomenon of CNCs

[13]. Pasquini *et al.* [12] reported that the storage modulus upon filler addition at the rubbery state increased from 2.2 MPa for the unfilled NR matrix to 154 MPa for the NR film reinforced with 10 wt% Cassava bagasse CNC. On the other hand, a comparison of the two types of nanoparticles showed that MFC had a higher reinforcing effect of up to 5 wt%, whereas the opposite trend was observed above this concentration. The results of DMA and successive tensile test confirmed that the reinforcing effect was higher for MFCs than for CNCs [12]. This was attributed to the high aspect ratio and possible entanglement of the CNCs. The presence of residual lignin, extractive substance, and fatty acid at the surface of the MFC also suggested promoting a higher adhesion level with the polymeric matrix.

Because CNCs are nanosized, they are easily aggregated and cannot be dispersed finely in a rubber matrix. Surface modification and chemical grafting can be used to improve the dispersion and reinforce the interfacial effect between CNC and rubber. Xu *et al.* [9] reported the effect of partial replacement of silica with surface-modified cellulose nanocrystal (MCNC) on the properties of NR nanocomposites. A comparison of the vulcanization characteristics, processing properties of compounds and mechanical properties, compression fatigue properties, and dynamic mechanical performance of NR/MCNC/silica and NR/CNC/silica nanocomposites showed that MCNC is more efficient than CNC. MCNC could activate the vulcanization process; suppress the Payne effect; increase 300% modulus, tear strength, and hardness; and reduce the heat build-up and compression set. Moreover, fine MCNC dispersion and strong interfacial interaction could be achieved by using NR/MCNC/silica nanocomposites [9].

Bendahou *et al.* [13] investigated the swelling properties of NR-based nanocomposite films in toluene and water. Figure 5.3 shows the toluene (a and b) and water uptake (c and d) vs. time about CNC (a and c) and MFC (b and d)-reinforced NR compositions. The swelling behavior of the polymeric matrix in toluene strongly decreased even in the presence of only 1 wt% CNCs and was almost independent of the filler content [13].

Visakh *et al.* [14] studied the diffusion, sorption, and permeation of aromatic organic solvents in CNC- and MFC-based NR to investigate the interactions between nanocomposite structure and matrix filler. Both the nanoparticles decreased the uptake of aromatic solvents in nanocomposite membranes; the effect was more significant for nanofibers than for nanowhiskers. Furthermore, the uptake decreased with increasing penetrant size, being the highest for benzene and the lowest for *p*-xylene. Transport parameters such as diffusion coefficient, sorption coefficient, and permeation coefficient were calculated. Comparison of the experimental values of the equilibrium solvent uptake with the predicted values indicated that both the nanocelluloses restricted the molecular mobility at the interphase, thereby decreasing the transport of solvents through the materials; this effect was more significant in the case of nanofibers. The results showed that both the cellulosic nanomaterials acted as functional additives capable of manipulating and tailoring the transport of organic solvents through elastomeric membranes, even at concentrations as low as 2.5 wt%. Research has the potential
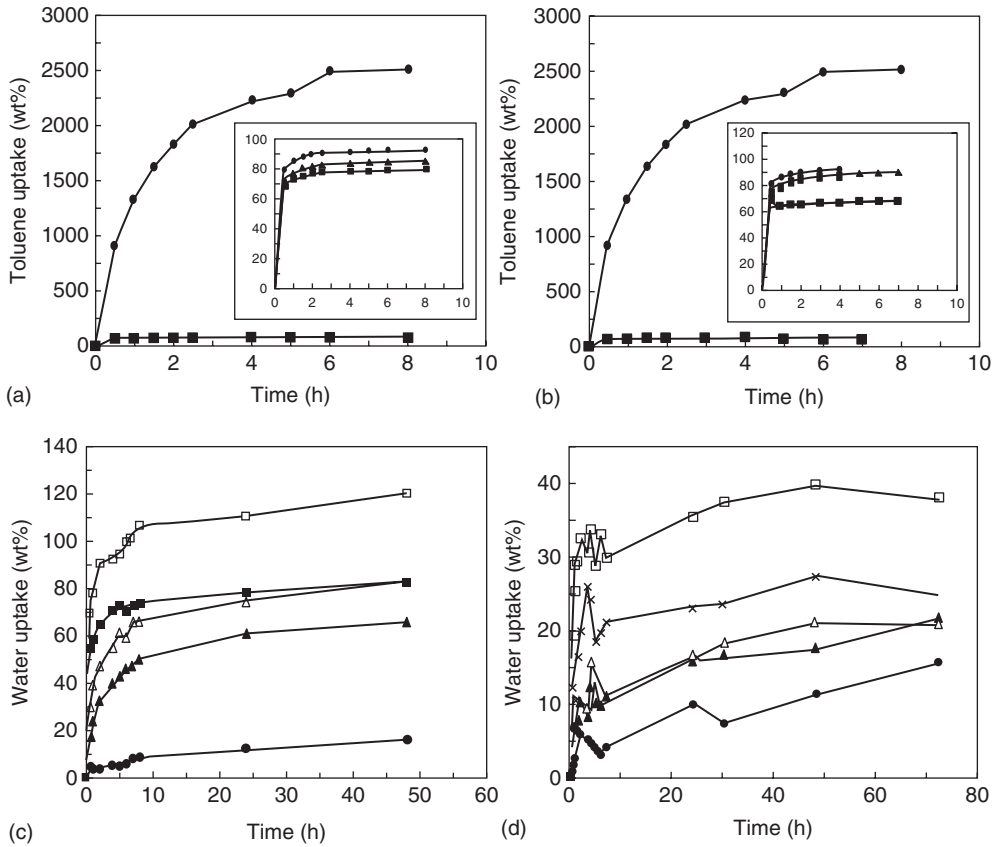
Figure 5.3 Evolution of (a,b) toluene uptake and (c,d) water uptake as a function of time at room temperature for NR (●), NR-CNC1/NR-MFC1 (○), NR-CNC2.5/NR-MFC2.5 (▲), NR-CNC5/NR-MFC5 (△), NR-CNC7.5/NR-MFC7.5 (✕), NR-CNC10/NR-MFC10 (■), and NR-CNC15/NR-MFC15 (□).

Panels (a,c) correspond to CNC-reinforced nanocomposite films and panels (b,d) correspond to MFC-reinforced nanocomposite films. NR = natural rubber; CNC = cellulose nanocrystal; and MFC = microfibrillated cellulose. Reproduced from [13], copyright 2010 © permission from Elsevier.

to develop the materials as permeable or semipermeable membranes for the selective separation or fractionation of liquid or gaseous mixtures [14].

ChW-reinforced NR nanocomposites were developed from the colloidal suspension of ChWs and latex of both vulcanized and prevulcanized NR. The nanocomposite films can be prepared either by freeze-drying and hot-pressing or by casting and evaporating [5]. Figure 5.4 shows the SEM micrograph of the chitin from crab shells, and the transmission electron micrograph (TEM) of a dilute suspension of ChW. The average length and width were estimated to be ~240 and 15 nm, respectively [5].

The cryo-fractured surface of ChW/NR composites was examined using SEM. Panels a and b of Figure 5.5 show the SEM images of unfilled evaporated natural
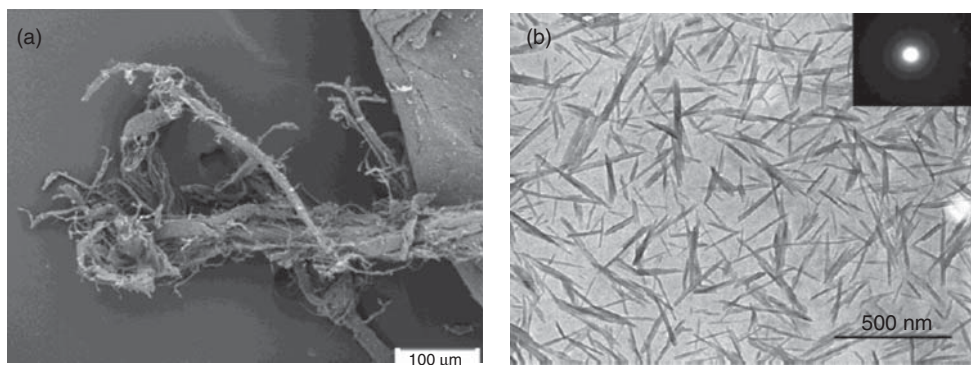
Figure 5.4 (a) Scanning electron micrograph of chitin from crab shell and (b) transmission electron micrograph of chitin nanowhiskers from crab shell. Reproduced from [5], copyright 2003 © permission from American Chemical Society.

rubber (NRev) (water evaporation technique) and NRL (freeze-drying and hot-pressing technique) films, respectively. The surface of the unvulcanized NRev (Figure 5.5a) shows uniform-phase morphology, whereas the NRL (Figure 5.5b) shows nonuniform-phase morphology. The nonuniform-phase morphology results from the quenching prior to freeze-drying, and the lyophilized film shows the imperfection introduced by evaporating traces of entrapped water in the freeze-dried rubber during hot-pressing.

The surface of the prevulcanized natural rubber evaporated film (PNRev, Figure 5.5c) was not as uniform as that of NRev because of certain spherical granular domains. This is probably due to the retention of some original particulate structure formed because of the faster cross-linking nature of surface molecules of the individual particles present in the prevulcanized latex [5]. Different processing methods had no effect on the whisker distribution as can be seen by comparing panels d and e. There is no obvious difference between the two. However, broader smooth unfilled regions are observed in Figure 5.5e. This probably indicates poorer whisker distribution in the freeze-dried and hot-pressed composites.

DMA results showed a small percentage of crystallinity in the evaporated samples only. The rubbery modulus of unvulcanized NRev improved significantly by incorporating ChWs. In contrast, the reinforcing effect was lower than that of the hot-pressed sample. Tensile and successive tensile tests indicated that the mechanical properties improved on adding ChWs and by the presence of the three-dimensional (3D) network within the evaporated samples. The mechanical properties of the modified ChWs were inferior to those of the unmodified samples. This is different from the modified cellulosic nanocomposites. Although the modification increased filler–matrix interaction, the destruction of the 3D network of ChWs may have decreased the mechanical properties [5, 7, 15].

The swelling process and its kinetics provide information about the capacity of a cross-linked polymer in different liquids and vapor media. The mass and dimensions of polymer systems may change because of the penetration of solvents into
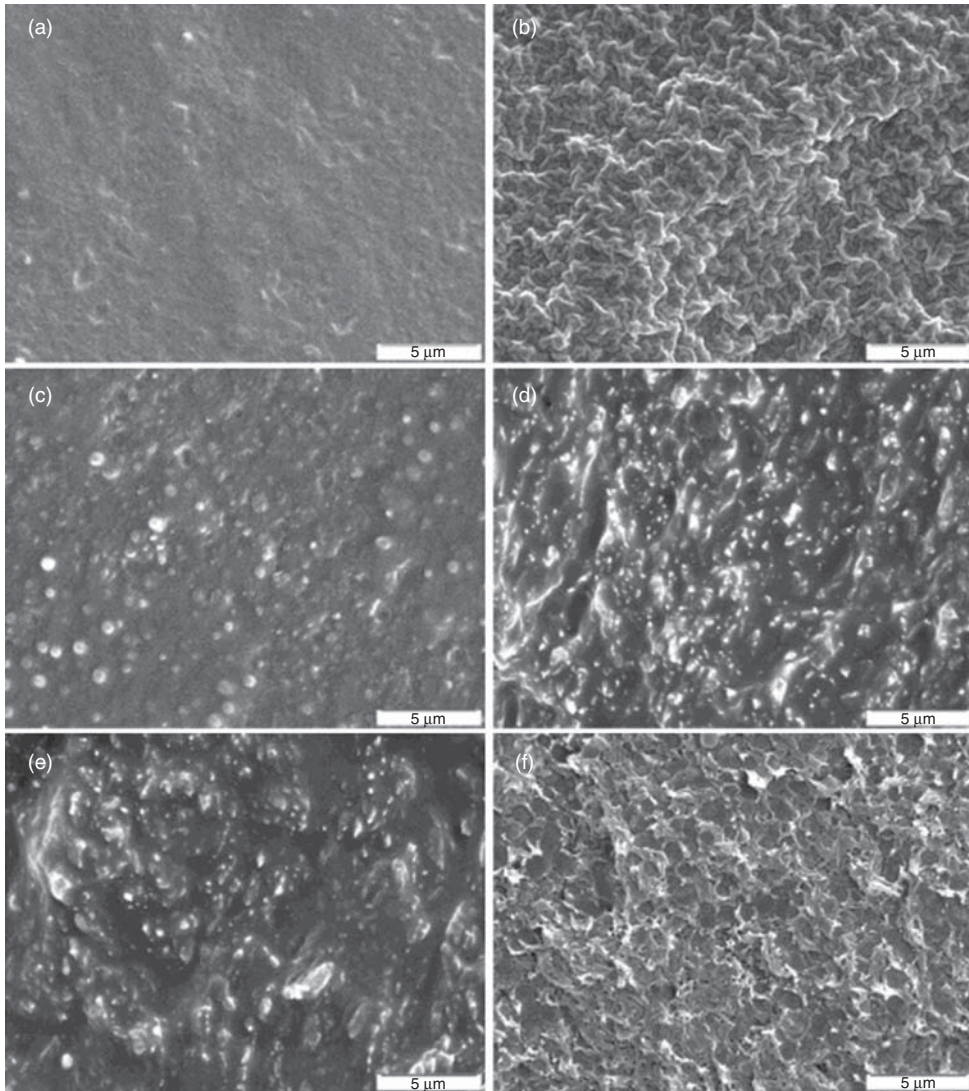
Figure 5.5 Scanning electron micrographs of the cryo-fractured surfaces of (a) NRev, (b) NRL, (c) PNRev, (d) NCH20ev, (e) NCH20L, and (f) PCH20ev films; NRev = evaporated NR; NRL = freeze-dried and hot-pressed NR; PNRev = prevulcanized NRev; and NCH = chitin nanowhiskers. Reproduced from [5], copyright 2003 © permission from American Chemical Society.

the swollen specimen. Nair and Dufresne [5] investigated the swelling behavior of toluene in the ChW-based nanocomposites and concluded that a chitin–chitin 3D network exists in the evaporated samples. The 3D network resulted from the strong hydrogen bonding between the whiskers in the evaporation step, similarly
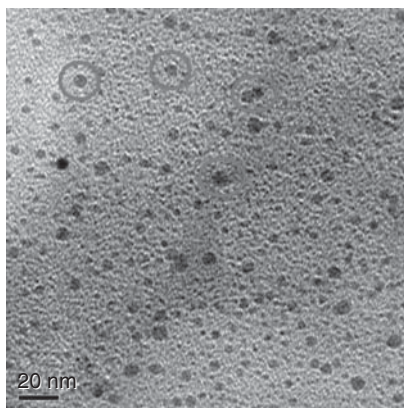
Figure 5.6 Transmission electron microscopic image of starch potato nanocrystals. The marked portions show the nanoparticles. Particles are well dispersed in the solution. Reproduced from [16], copyright 2011 © permission from Elsevier.

to the cellulose nanowhiskers. The rigid network prevented the swelling of the polymeric nanocomposites and resulted in a lower degree of swelling exhibited by the evaporated samples than the hot-pressed samples. In each method, the degree of swelling in the samples decreased with increasing whisker content. The decrease in the swelling of the freeze-dried samples with increasing whisker content was attributed to the higher rigidity of the material because of the high amount of filler–matrix interaction. Both filler–matrix interaction and chitin network are responsible for the low degree of swelling with increasing whisker content in the evaporated sample. The processing technique controls the mechanical properties of ChW-reinforced NR nanocomposites [5].

SNC-reinforced NR nanocomposites were prepared by casting/evaporating from a mixture of SNC suspensions and rubber latex in different proportions. Figure 5.6 shows the TEM image of a starch potato nanocrystal (filler content, 5%) [16], and Figure 5.7 shows the SEM image of the SNC-reinforced NR (filler
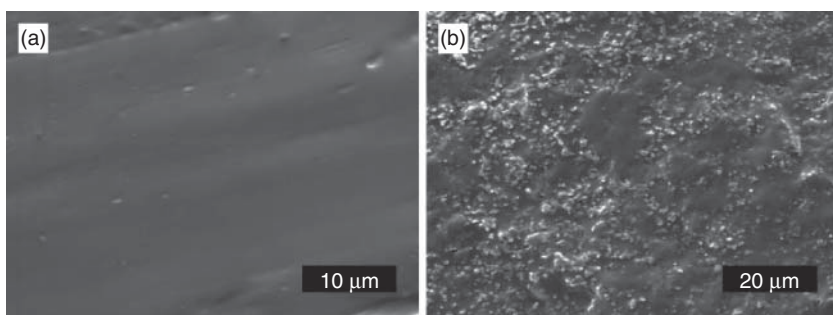
Figure 5.7 Scanning electron micrographs of the fractured cross-sections of (a) NR100, (b) M27-NR70; M27 = waxy maize starch with 27% amylose. Reproduced from [11], copyright 2012 © permission from Wiley-VCH Verlag GmbH & Co. KGaA, Weinheim.
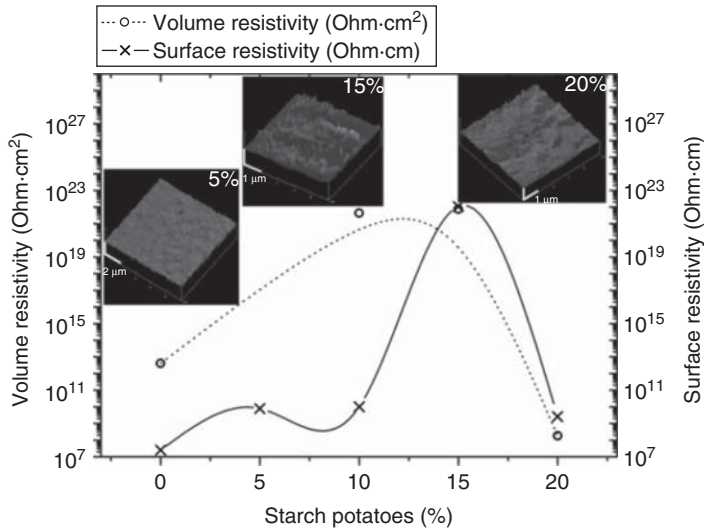
Figure 5.8 Effect of starch potato nanocrystal composition on the volume and surface electrical resistivity of the nanocomposites. Also, the atomic force microscopic images of 5, 15, and 20% starch are shown. Reproduced from [5], copyright 2003 © permission from American Chemical Society.

content, 30%) [11]. The atomic force microscopic (AFM) image in Figure 5.8 shows that at a lower filler content, a uniform distribution of the nanocrystals is obtained, whereas agglomeration is observed when the content is >15% [16]. The values of the electrical resistivity measured on the surface and volume are reported in Figure 5.8. The electrical surface resistivity increased for 15% w/w, whereas the values decreased with increasing filler content. The volume electrical resistivity increased even though a small amount of starch was added; however, the same threshold was observed for a composition close to 15% w/w of starch. The increase in electrical resistance indicates that nanoparticles act as a barrier to the electrical charge movements. This is an important result because it is often proposed to add nanoparticles for creating a conductive pathway (hopping conduction) at a percolation threshold, as reported by Huang *et al.* [17]. Furthermore, the values of the electrical resistances obtained for the filler content >15% w/w are identical to those of the matrix alone, clearly proving the agglomeration of starch nanoparticles at high filler content. This threshold was also observed by Angellier *et al.* [18, 19] from the mechanical characterization of a similar nanocomposite with the same composition, thus confirming the existence of a threshold in the physical behavior of potato SNC/rubber nanocomposites [18, 19].

SNCs were found to be effective reinforcing agents for NR at temperatures higher than the T_g of the matrix. The addition of only 10 wt% starch nanoparticles to NR induced a reinforcing effect similar, in terms of rigidity, to that observed with 26.6 wt% CB. Up to 20 wt% of this new filler effectively reinforced NR without significantly decreasing the elongation-at-break of the material. All the results

showed that particle–particle interactions play a crucial role in the properties of SNC-filled NR. Any deterioration of these interactions dramatically decreased the mechanical performances of the resulting composite. Furthermore, high SNC content preserved the elastic behavior of NR-based composites in contrast to CB. In conclusion, although SNCs are not better than organoclays, they are clearly a good substitute for CB. The mechanical properties of the modified SNC-based composites are lower than those of unmodified SNC-based composites.

The amylose content of the starch plays an important role in the application of SNC-based NR composites. The structure and mechanical properties of SNC-reinforced NR composites, with the SNCs extracted from various sources such as waxy maize starch, normal maize starch, amylomaize, potato starch, and wheat starch, have been investigated [11]. SEM micrographs (Figure 5.7) and solvent uptake experiments showed that (i) from 5 wt% onwards, a percolation network is gradually formed as shown by the correlation to specific surface area and (ii) at 30 wt%, some SNCs are "homogeneously aggregated." In addition, for rubber, a highly hydrophobic matrix, the SNC has a detrimental effect on water vapor permeation (WVP), particularly at a high filler content. Regarding the mechanical properties, at 5 wt% SNC loading, although the properties were improved, no significant difference was observed between the nanocomposites reinforced by SNCs extracted from different sources. However, at 30 wt% SNC, the general trend was as follows: The greater the amylose content of the starch used for preparing SNC, the lower was the reinforcing effect (except for potato starch) maintaining the ductility of the material. The SNCs produced from a higher amylose content starch may release loosely bonded amylose chains during the preparation and/or soaking in water, thus producing fewer SNCs to participate in the formation of a reinforcing and diffusing network [11].

5.3
Polyolefin-Based Nanocomposites

Polyolefins are synthetic polymers of olefinic monomers and are produced from oil or natural gas by polymerization, where the short chains of chemicals (monomers) are joined in the presence of a catalyst to afford long chains (polymers). Polyolefins may be classified on the basis of their monomeric unit and chain structures, such as ethylene-based polyolefins, propylene-based polyolefins, higher polyolefins (the names of the former three suggesting the dominant monomer type), and polyolefin elastomers. Polyolefins are used in diverse applications, including grocery bags, containers, toys, adhesives, home appliances, engineering plastics, automotive parts, medical applications, and prosthetic implants. Polyolefins are also recyclable, and significant improvement in properties is possible using blending and composite technologies [20].

Polypropylene (PP) is one of the most useful polyolefins owing to the low price and favorable properties such as good rigidity, lightweight, good weathering ability, design flexibility, and good mechanical properties. PP matrix composites can

be produced from many different types of fillers using widely applied processing techniques such as injection and compression moldings. Recent developments in natural filler-reinforced composites have shown that it is possible to obtain high-performance materials utilizing environment-friendly reinforcements. PP is among the most utilized polymer matrix because of its recyclability and low processing costs. To improve the competitiveness of PP for engineering plastic applications, it is an important objective in PP compounding to simultaneously increase its dimensional stability, heat distortion temperature and rigidity, strength, and impact resistance without sacrificing ease of processing [21].

One of the main challenges of utilizing CNCs with the PP matrix is their different polarities. CNC with a considerable amount of OH groups on its surface is more hydrophilic than PP with hydrophobic nature. The dispersion of CNCs in nonpolar solvents, incorporating it into new polymeric matrix, has been reported previously [22, 23].

The surface modification of CNCs is another way to enhance the compatibility of CNC with a nonpolar matrix. Ljungberg *et al.* [24, 25] treated CNCs with a surfactant and maleic anhydride-grafted polypropylene (MAPP) and applied them to PP, a nonpolar matrix [24, 25]. All the types of CNCs studied improved the mechanical properties for both tensile testing and DMA compared to neat PP. They concluded that at a large deformation, the mechanical properties depended strongly on the degree of dispersion of the whiskers. Agarwal *et al.* [26] studied the spatial distribution of CNCs in extruded PP composite filaments using Raman spectroscopy. They found that CNCs were poorly dispersed in the PP, even though the addition of MAPP slightly improved the situation because of the functionalization of PP with polar groups. The tensile modulus and strength of CNC-reinforced MAPP improved significantly compared to those of neat PP [26].

Bahar *et al.* [27] achieved a uniform distribution of CNC by dissolving the matrix polymer (PP) in toluene by sonication and magnetic stirring. The SEM micrographs of the film samples (2 ma 15 CNC, Figure 5.9) showed some micropores (voids) and white dots representing CNC domains, which are generally <200 nm, indicating slight agglomeration of the CNCs in the composite film. The use of 0.8 wt% of maleic anhydride (MA) increased both rigidity and strength;
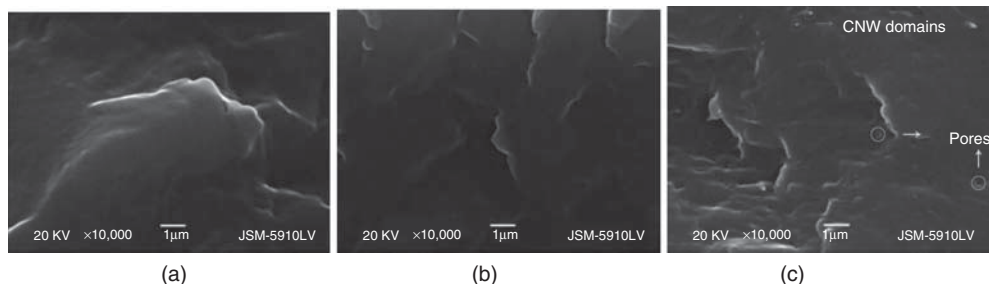
Figure 5.9 Scanning electron micrographs of (a) (PP reference), (b) (2 ma reference), and (c) (2 wt% MA-15 CNC). Reproduced from [27], copyright 2011 © permission from Wiley Periodicals, Inc.

however, 2 wt% MA increased the rigidity but decreased the strength of the PP nanocomposite. Compared to neat PP, the tensile strength of the composite improved by 70–80% by the addition of CNCs. Crystallinity has also been improved by ~50% in the CNC-reinforced samples. An increase in the CNC content in the composite resulted in higher thermal degradation temperatures, hydrophilicity, and thermal conductivity [27].

A nanocomposite of PP, CNCs, and nanosilicate layers has been prepared by Pandey *et al.* [28] using the melt-blending process. A comparison has been made between layered silica modified with crystalline cellulose (named as nanowood clay, NWC), wood flour (WF) and clay, and reinforced PP. They found that the tensile strength of the composites prepared from NWC was greater than that of the PP-clay and PP-WF composites at 5% filler concentration, whereas the mechanical properties deteriorated when the clay and WF were used alone for reinforcement [28].

The endothermic heat flow data are shown in Figure 5.10. The samples exhibited single peaks, and the melting temperature (T_m) of PP was 164 °C. The T_m of the samples increased after reinforcing with cellulose-modified clays, and the highest T_m was obtained for NWC5. The T_m increased significantly with 10% and 20% NWC concentrations; however, it was not very high for NWC5. The results showed that the filler dispersion was more important than the filler concentration for affecting the melting of polymer chains. The addition of reinforcing phases changed the crystallization and onset temperatures for the PP matrix. Cellulose
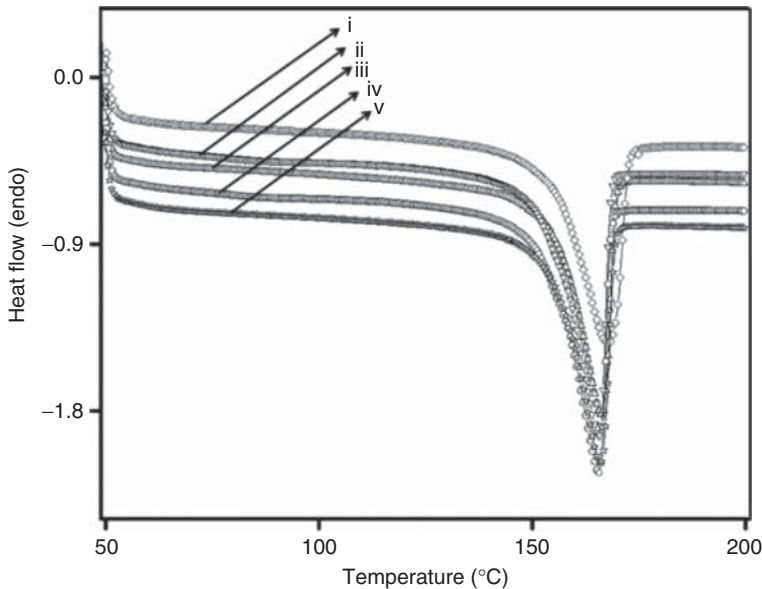
Figure 5.10 DSC thermograms of composites showing the variations in the melting temperature (i–v represent NWC5, 10, 20, CL 10, and PP, respectively). Reproduced from [28], copyright 2012 © permission from Wiley Periodicals, Inc.

has been shown to nucleate PP and affect transcrystallinity with decreasing spherulite size. The WF composites showed higher crystallization temperatures at all the concentrations, and the peaks were sharper than those of the composites prepared by mixing only clay to the matrix. Thus, the nucleating effect of WF was greater than that of clay in these composites. However, when clay is modified with an organic modifier and mixed with PP, it is reported to induce crystallization and it may act as a nucleating agent. The extent of intercalation between MA-g-PP chains and silicate galleries decreased with increasing clay loading. The dispersed clay particles acted as nucleating agents and lowered the spherulite size. The increase in the crystallization temperature observed for NWC5 was lower than that with NWC10 or NWC15. This behavior can be explained by the probable encapsulation of crystalline cellulose through the interaction of layered silicates and WF that may have decreased its nucleating effect. Thus, the chain mobility in NWC5 was reduced owing to better wetting with the polymer matrix than with other samples.

5.4
Polyurethane and Waterborne Polyurethane-Based Nanocomposites

PU is a polymer family with a chain of organic units joined by carbamate (urethane) links and obtained by reacting isocyanates, bearing at least two isocyanate groups per molecule, with polyols, bearing two or more OH groups per molecule, in the presence of a catalyst [29, 30]. The polymers are mainly in the form of films, foams, and rigid materials. The properties of PUs are greatly influenced by the types of isocyanates and polyols. PUs have interesting intrinsic properties such as low density, low thermal conductivity, high strength-to-weight ratio, good dimensional stability, and low cost, and are relatively environment friendly. Thus, they find wide use in industries and our daily life such as in the form of high-resilience foam seating, rigid foam insulation panels, microcellular foam seals and gaskets, durable elastomeric wheels and tires (such as roller coaster wheels), automotive suspension bushings, electrical potting compounds, high-performance adhesives, surface coatings, and surface sealants.

In addition, PU has also been used in biomedical applications, for example, elastic bandage and artificial heart. Despite the significant benefits of PU, it has disadvantages such as poor degradability and toxicity caused by isocyanates, motivating studies to find more environment-friendly starting materials. The mechanical and thermal properties of pristine PU are not superior to other synthetic polymers (e.g., polystyrene). Therefore, studies have been conducted to overcome these limitations by reinforcing the matrix to create new composites [29, 31–35].

The ingredients, ratio, and types of isocyanates and polyols greatly affect the properties of PUs. Difunctional polymers are preferred for a linear or low-cross-linked PU as shown in Figure 5.11. Marcovich *et al.* [36] used a mixture of di- and multifunctional polyols and polymeric 4,4′-diphenyl methane diisocyanate (MDI) [36]. Auad *et al.* [37] selected polyethylene glycol (PEG), MDI, and 1,4-butanediol
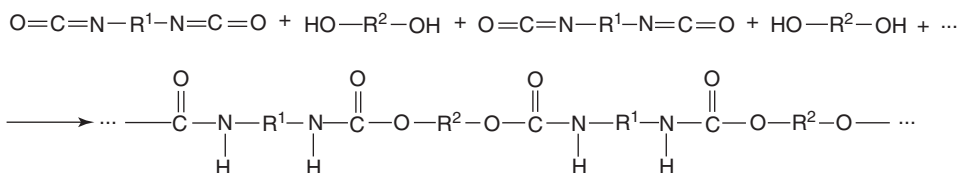
$$O=C=N-R^1-N=C=O \ + \ HO-R^2-OH \ + \ O=C=N-R^1-N=C=O \ + \ HO-R^2-OH \ + \ \cdots$$

$$\longrightarrow \cdots \underset{\underset{H}{|}}{\overset{\overset{O}{\|}}{C}}-N-R^1-\underset{\underset{H}{|}}{N}-\overset{\overset{O}{\|}}{C}-O-R^2-O-\overset{\overset{O}{\|}}{C}-\underset{\underset{H}{|}}{N}-R^1-\underset{\underset{H}{|}}{N}-\overset{\overset{O}{\|}}{C}-O-R^2-O-\cdots$$

Figure 5.11 Synthesis of linear polyurethanes . Reproduced from [42], copyright 2011 © permission from Wiley Periodicals, Inc.

(BDO) as the raw materials [37]. Waterborne polyurethanes (WPUs) have been prepared from a diol such as polycaprolactone (PCL) and polypropylene glycol (PPG), an isocyanate such as isophorone diisocyanate (IPDI) and 2,4-toluene diisocyanate (TDI), an organic acid such as dimethylol propionic acid (DMPA), and a catalyst such as triethylamine (TEA) [38–40]. In contrast, rigid PU foams with a highly cross-linked structure are prepared from multifunctional polyols and isocyanates. Moreover, a foaming catalyst is used along with the cross-linking catalyst, and a surfactant is often added to reduce the surface tension and obtain a high content of closed cells. For example, sucrose- and glycerol-based polyols with a functionality of 4.4 and 3.0, respectively; polymeric MDI with a functionality of 2.7; dimethylcyclohexylamine; 1-methyl-4-(2-dimethylaminoethyl) piperazine; silicone surfactant; and pentane were used by Li *et al.* [41]. To meet the challenge of oil exhaustion and environmental concerns, a series of green PUs have been synthesized. The above-mentioned polyols have been replaced by those obtained from soybean and castor oils to prepare novel PUs [29, 31, 32]. Ethanol organosolv lignin-based PU foams have also been prepared [30].

In general, reinforcements usually consist of inorganic and organic fillers. In recent years, the effects of fillers on the properties of PU have been extensively investigated. Inorganic fillers have shown significant effects on the physical properties of PU. PPG phosphate ester-modified nanosilica improved the hardness of PU [43]. Silane coupling agent functionalized nanosilica improved the thermal stability and water resistance of PU [44]. Vinyl isocyanate-modified nanosilica was used to synthesize PU nanocomposite; the mechanical properties of the resulting coating were enhanced [45]. The water vapor and gas permeabilities of the modified PU were enhanced by adding nano-TiO$_2$ [46]. The tensile strength and elongation of PU were enhanced by adding surface-modified nanocarbon particles [47].

With increasing environmental concerns, rapidly diminishing petroleum resources, and various economic factors, polysaccharides, including cellulose, chitin, and starch, have attracted more attention. In recent years, CNCs have been widely used as the fillers to reinforce PUs, such as those prepared from bacterial cellulose [29, 31], microcrystaline cellulose (MCC) [33], flax fiber [39], cotton liner pulp [38, 40], and bleached softwood kraft pulp [41] by acid hydrolysis as proposed by Dong *et al.* [48]. The main limitation for CNCs to reinforce PUs is to disperse CNCs well in the PU matrix and improve the interfacial contraction. On the other hand, processing techniques significantly affect the final properties of the composites. Therefore, several studies classified the processing methods in
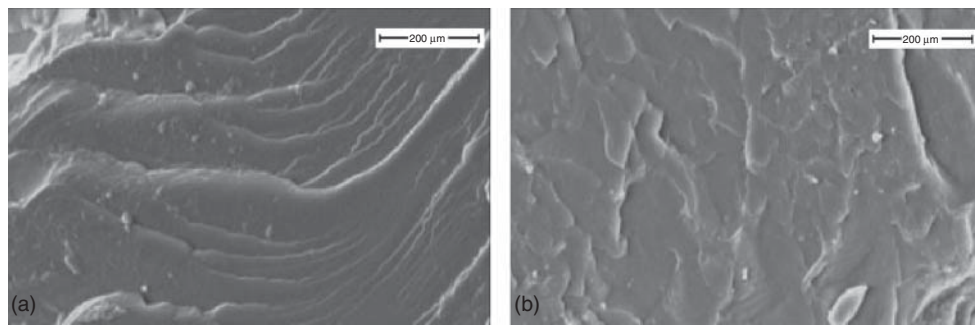
Figure 5.12 Scanning electron microscopic images of segmented polyurethane (SPU) 2000-23 containing 0 wt% (a) and 1 wt% (b) cellulose incorporated during the synthesis. Reproduced from [37], copyright 2012 © permission from Wiley Periodicals, Inc.

the ascending order of their reinforcement efficiency as follows: extrusion < hot-pressing < evaporation, associated to probable breakage and/or orientation of CNC during processing [5, 49, 50].

PU films have been prepared mostly by evaporating/casting. First, a suspension of whiskers in dimethyl formamide (DMF) was added to a polyol or a mixture of polyols with stirring, followed by ultrasonic treatment and solvent evaporation at 70 °C. Next, isocyanate was added until a selected isocyanate/OH ratio was reached and mixed thoroughly. Because isocyanate is a very reactive chemical and reacts with traces of water present in the starting materials and/or reacts with itself forming trimers, a molar ratio of isocyanate to OH groups >1.0 is often used. The mixture was then cast into an open mold and cured under varying conditions [42]. The morphology and surface of PU nanocomposites were investigated by SEM, TEM, and AFM, as shown in Figures 5.12–5.14, respectively.

Fourier transform infrared (FTIR) spectral analysis of the PU–CNC nanocomposites shows the peaks of unreinforced PU at 2900, 1690, and 1376 cm^{-1} corresponding to the C–H, carbonyl (C=), and C–N stretching vibrations, respectively (Figure 5.15). The peak at 2271 cm^{-1} was attributed to the free, unreacted isocyanate group. The completion of the reaction of the cellulose OH groups with MDI was proved by the detection of new bands at 1646 and 1510 cm^{-1}, corresponding to the absorption of C=O groups and N–H bending deformation combined with C–N asymmetric stretching vibration, respectively. The intensities of these absorption bands increased with increasing CNC content [51].

The thermal properties of PU nanocomposites have been investigated by differential scanning calorimetry (DSC) [32, 37, 52] and thermogravimetric analysis (TGA) [30, 32, 35]. The DSC images showed a two-phase structure [37, 53–55]: (i) crystalline soft-segment (SS) phase and (ii) hard-segment (HS) phase with a weak crystallization endothermic peak. Brunette and coworkers [56] studied a model of the HS compound, BDO-MDI, using DSC and FTIR to determine the temperature dependence of hydrogen bonding, and concluded that sufficient annealing at 150 °C effectively converted the noncrystalline domain structure to the crystalline state, producing a well-defined high-temperature transition at
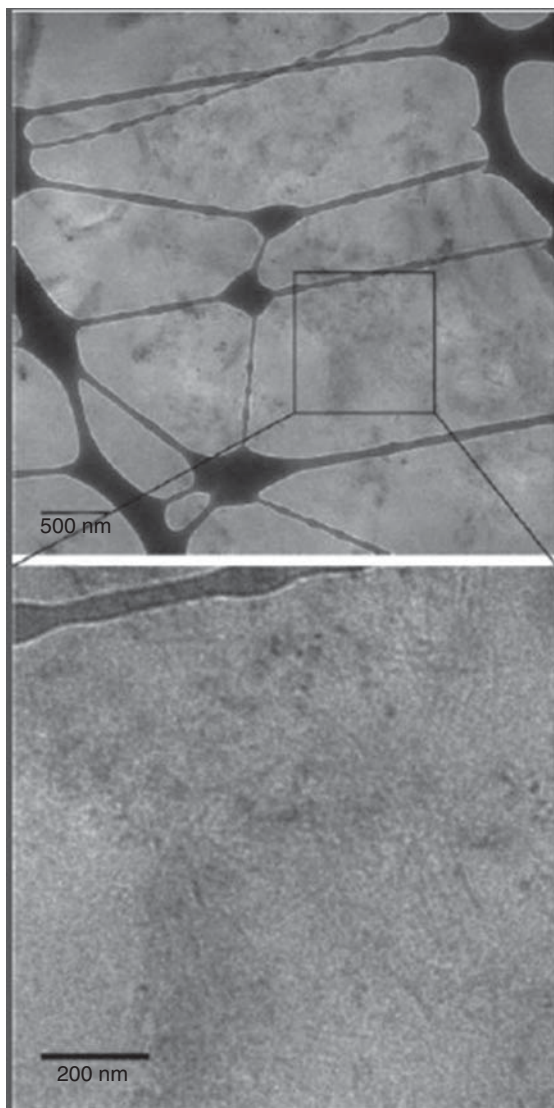
Figure 5.13 Transmission electron microscopy of the ultrathin cryo cross section of polyurethane nanocomposites with 5 wt% of cellulose nanocrystals. Reproduced from [51], copyright 2011 © permission from American Chemical Society.

200–230 °C. Therefore, the crystallization of HS phase was found to be related to the thermal history and particular composition [56]. PU has the same temperature transitions and endotherm that confirmed the nucleation effect of CNCs [52]. The results showed that CNCs favored crystallization in both SS and HS that may have originated from the maximization of matrix–cellulose interactions by well-dispersed nanoreinforcements [55] through hydrogen bonding, by taking
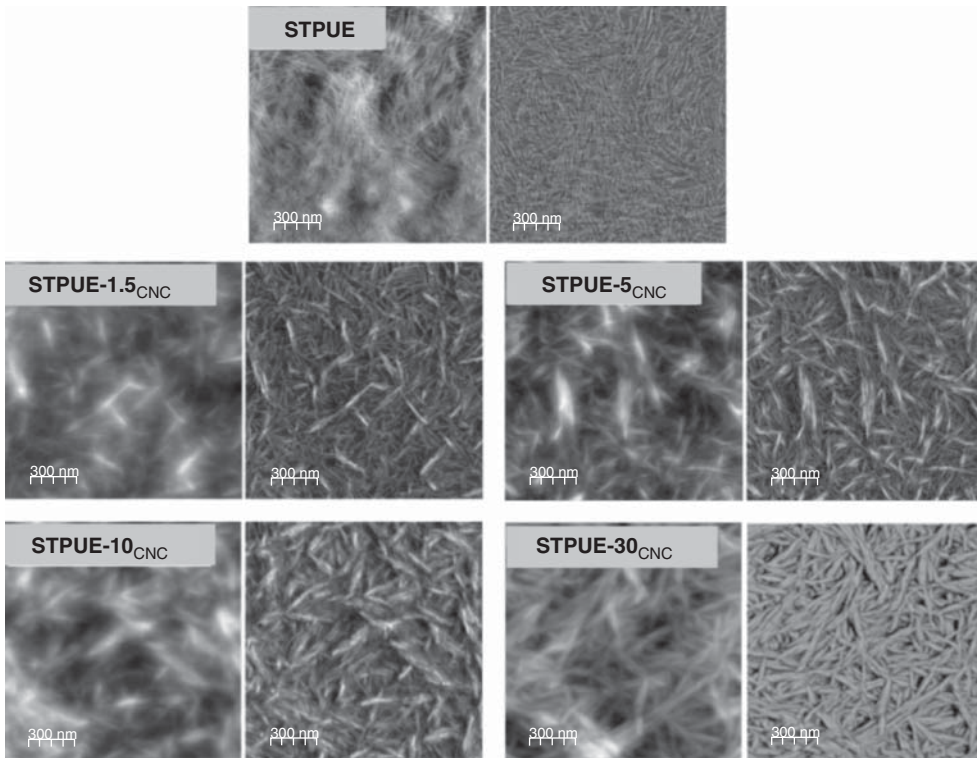
Figure 5.14 Atomic force microscopy height (left) and phase (right) images of annealed polyurethane and polyurethane nanocomposites at 100 °C for 12 h(2). Reproduced from [33], copyright 2013 © permission from Elsevier.

advantage of the abundant OH groups on the surface of CNCs and C=O groups in both PU segments [33]. The enhancement of the thermal stability was clearly shown by adding CNCs. However, when the CNC content is too low (0.5%), the reinforcement did not occur [30].

TGA results showed that thermal stability was enhanced compared to neat PU or CNC [30, 32, 35, 53]. For example, small addition of CNC in the shape memory polyurethane (SMPU) matrix improved the thermal stability of the nanocomposite. In particular, 1.97 and 3.81 wt% (N-2 and N-4) CNC improved the decomposition temperature of 80% weight loss to high temperature. Instead, the pure MCC and SMPU (N-0) showed poorer thermal stability than the nanocomposite series and CNC-5.

The mechanical properties of PU nanocomposites have been widely investigated by DMA [32, 35, 37, 52–54], tensile test [35, 53], and cycle tensile test [53]. The dramatic effect of CNCs on the tensile and thermomechanical properties of PU nanocomposites is shown in Figure 5.16. The introduction of CNCs as the reinforcing filler in PU remarkably improved the tensile strength, strain-to-failure, Young's modulus, and work-to-fracture of the nanocomposites, as summarized
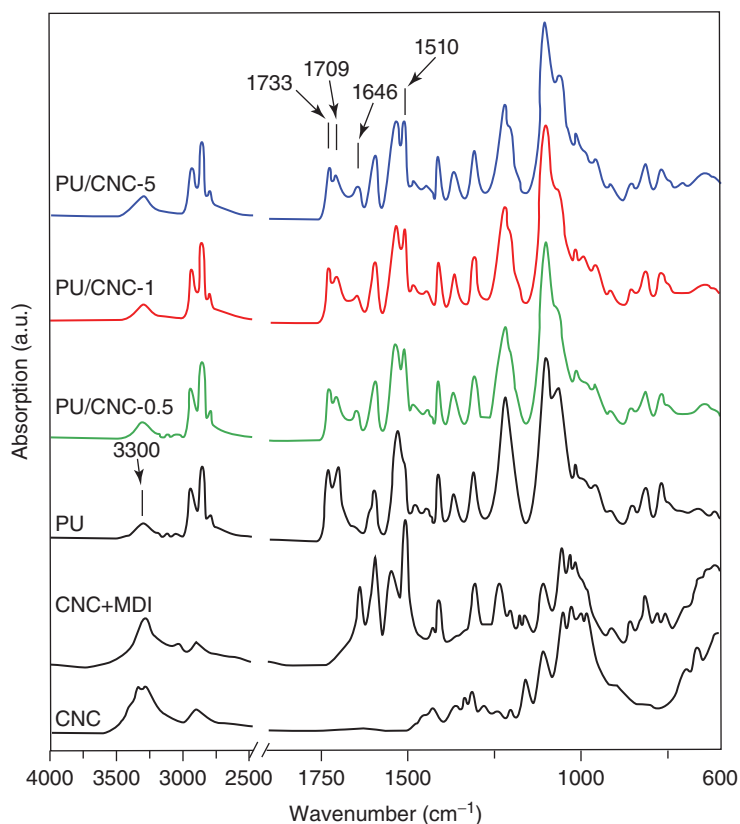
Figure 5.15 Fourier transform infrared spectra of cellulose nanocrystals (CNCs), pure polyurethane (PU), PU/CNC nanocomposites, and a mixture of CNCs and 4,4′-diphenylmethane diisocyanate MDI (control). Reproduced from [51], copyright 2011 © permission from American Chemical Society.

in Table 5.1. Figure 5.16a shows that pure PU exhibits a stress–strain curve without obvious strain hardening, whereas the PU nanocomposites exhibited strain hardening, particularly at larger elongations [51].

The tensile strength increased from 7.5 (1.0 MPa) for neat PU to 26.9 (1.5 MPa) for PU/CNC-0.5 and further to 61.5 (4.8 MPa) for PU/CNC-1 containing only 1 wt% CNCs. The Young's modulus increased with CNC content and reached the highest value of 44.9 (2.4 MPa at 5 wt% CNCs, >5 times higher than that of pure PU). It is very unusual to improve the modulus while significantly improving the strength and toughness. The results showed that CNCs preferentially reinforced the HSs rather than the SSs of PU, thus avoiding the undesired hardening of the soft domain and maintaining the large strain-to-failure of the PU composites. In addition, the high strength indicates that CNCs oriented strongly at high strains and also induced synergistic PU orientation effects contributing to dramatic strength enhancement. To the best of our knowledge, this is the first time that

(a)

(b)
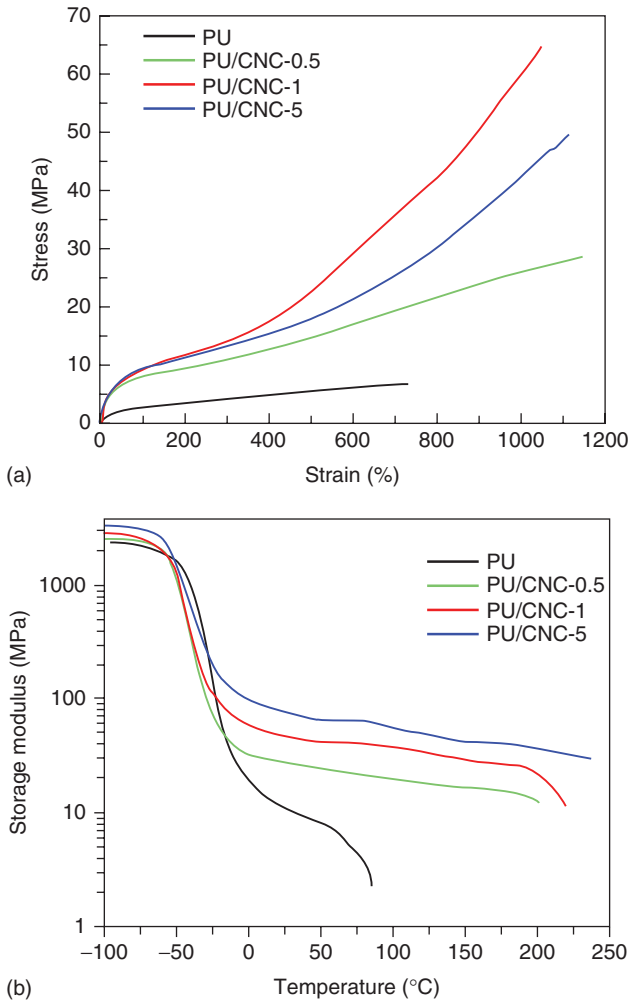
Figure 5.16 (a) Stress–strain curves of pure PU and PU/CNC nanocomposites. (b) Storage modulus of the PU and PU/CNC nanocomposites as a function of temperature. Reproduced from [51], copyright 2011 © permission from American Chemical Society.

such a significant improvement in mechanical properties was achieved with only 1 wt% of nanoscale CNC reinforcement for the rubbery matrix [51].

The DMA results showed the effect of CNC on the dynamic mechanical properties in terms of temperature and also the strong interfacial interactions between CNC and the PU matrix. A remarkable improvement in the storage modulus was achieved by introducing CNCs into the PU matrix as shown in Figure 5.16b. The moduli of the nanocomposites were slightly higher than that of the neat PU matrix below T_g. However, a significant reinforcement effect was observed in the low-modulus region above T_g. The reinforcement mechanism is attributed to the CNC

Table 5.1 Mechanical properties of polyurethane/cellulose nanocrystal (PU/CNC) nanocomposites [51].

Sample	Young's modulus (MPa)	Tensile strength (MPa)	Strain-to-failure (%)	Work-to-fracture (MJ m^{-3})
PU	8.2 ± 0.9	7.5 ± 1.0	751.4 ± 31.4	37.0 ± 6.2
PU/CNC-0.5	40.9 ± 3.3	26.9 ± 1.5	1087.0 ± 61.9	161.2 ± 9.3
PU/CNC-1	42.4 ± 3.0	61.5 ± 4.8	994.2 ± 75.3	317.7 ± 36.2
PU/CNC-5	44.9 ± 2.4	49.8 ± 6.6	1110.3 ± 101.1	290.2 ± 50.8

reinforcement and increased effective cross-link density of the rubber network because of the PU–CNC interactions.

For the neat PU, as the reference, the modulus in Figure 5.16b showed a sharp decrease during the glass–rubber transition, and the modulus decreased with temperature in the rubbery region because of the thermoplastic nature of the material. In the nanocomposites, the decrease in the storage modulus dramatically reduced as the PU covalently linked to CNCs. The modulus of the nanocomposites containing only 1 wt% cellulose was 400%, 1200% higher than those of pure PU at 20 and 80 °C, respectively. In addition, the introduction of CNCs also provided the nanocomposites with outstanding thermal stability up to 210–230 °C, the temperature at which cellulose starts to degrade. The reason for such mechanical reinforcing and thermal stability enhancement was the formation of a rigid network by the cellulose whiskers in the host polymer matrix, which was governed by the percolation mechanism. In this mechanism, the network may form above the critical volume fraction at the percolation threshold, VRc, which depends on the aspect ratio (L/d) of the filler. In our case, the aspect ratio of CNCs from cotton was 10–30, resulting in a VRc value of 2.3–5.0 vol%, that is, 3.3–7.0 wt%. However, the PU/CNC nanocomposite with ultra-high tensile strength and strain-to-failure was obtained from only 0.5 wt% of CNCs, which is much lower than the calculated percolation value. Thus, such a significant modulus reinforcement effect without the formation of a cellulose network was because of the introduction of a discrete reinforcement phase of nanoscale rod-like stiff CNCs, combined with increased effective rubber cross-link density owing to the covalent linking of CNCs to the PU HSs [51].

Despite the appealing properties of the PUs seen in the conventional PU products, they usually contain organic solvents and even free isocyanate monomers [38, 39]. Therefore, considering the health, safety, and environmental factors, PUs have been replaced by WPUs gradually in recent years [38, 39]. In addition, WPUs possess several advantages associated with conventional organic solvent-borne PU, such as low viscosity at high molecular weight, nontoxicity, and good applicability without the accompanying problems mentioned above [38]. However, the thermal stability, insolubility, and mechanical properties of
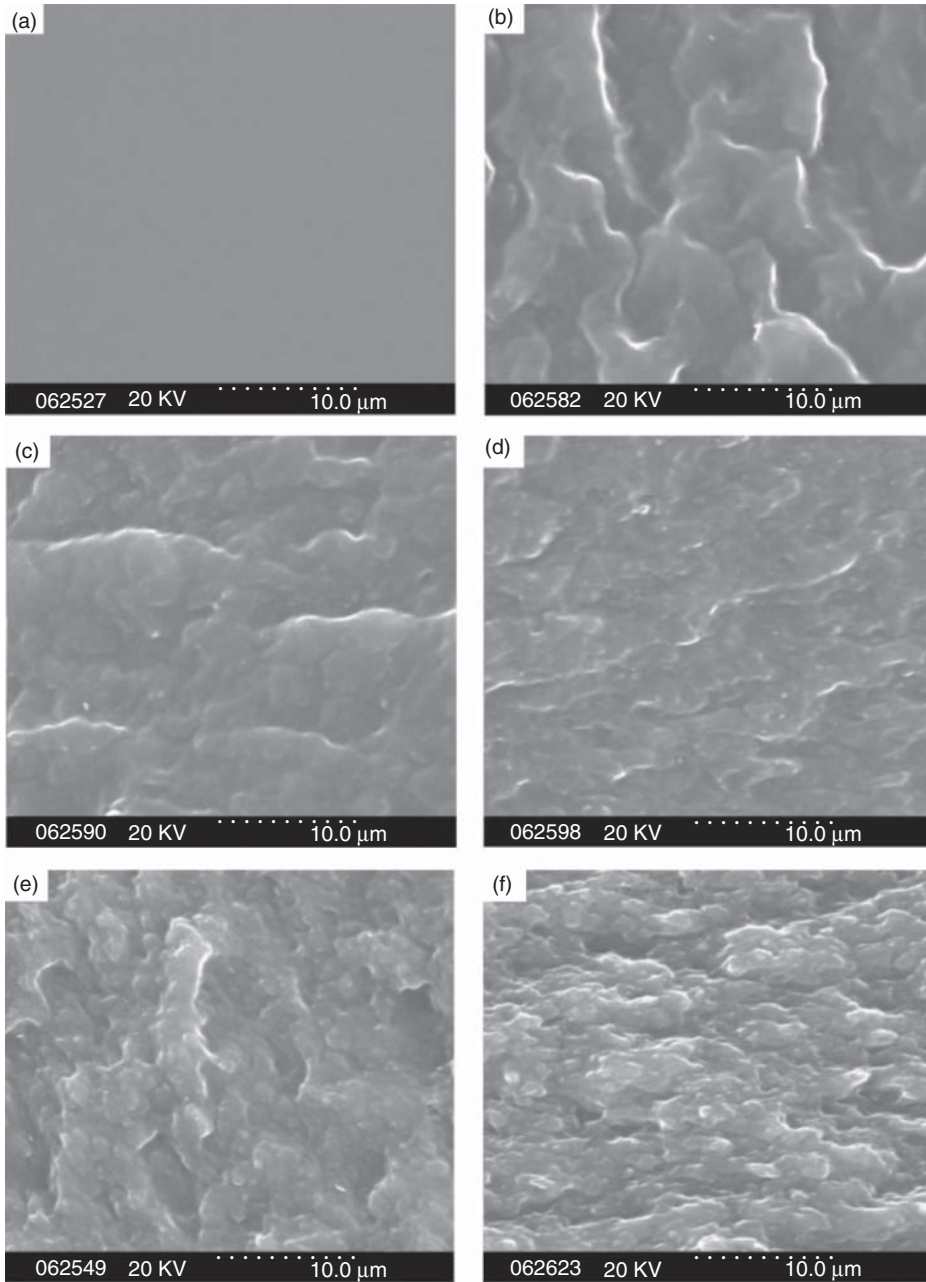
Figure 5.17 Scanning electron microscopic images of the waterborne polyurethane/cellulose nanocrystal (WPU/CNC)nanocomposites with different CNC content: (a) 0 wt%; (b) 10 wt%; (c) 15 wt%; (d) 20 wt%; (e) 25 wt%; and (f) 30 wt%. Reproduced from [39], copyright 2007 © permission from American Chemical Society.

the WPU are still lower than those of the organic solvent-borne PU and need to be improved. Nanosized particle additives are used as an effective strategy to enhance the properties of WPU [39]. To the best of our knowledge, however, two critical challenges still exist in nanocomposite reinforcement [51]: (i) to obtain well-dispersed reinforcing nanocrystals in polymer matrix and (ii) to increase the strength without remarkable decrease in their high extensibility [39, 57]. The nanocomposites have been prepared by casting/evaporating methods. The morphology of the nanocomposites has been investigated by SEM [38, 39, 58]. The SEM results, as shown in Figure 5.17, indicate that the nanoparticles are well dispersed, and no large aggregates exist in the matrix, implying good adhesion between the nanocrystal fillers and the matrix. This can be attributed to the hydrophilicity of both WPU and CNCs and the hydrogen-bonding interactions between the filler/filler and filler/matrix. Such an even and uniform distribution of the fillers in the matrix played an important role in improving the mechanical performance of the resulting nanocomposite films and their antifelting effects [58]. Infrared spectrometer is a powerful instrument for investigating the hydrogen-bonding behavior in PU [39].

Multiple hydrogen bonds can be formed between polar groups where one group serves as a proton "donor," and the other serves as a proton "acceptor." Two different types of proton "donors" (urethane N−H and urea N−H) and four different types of proton "acceptors" (urethane CO, urea CO, ester CO of castor oil, and C−O−C of PEG) exist in WPU. Moreover, the O−H groups introduced by Eucalyptus globules in CNCs can strongly interact with the WPU matrix [39]. Several vibrational modes are sensitive to hydrogen bonding in PU; however, the N−H and C−O stretching modes at $3600-3100$ and $1600-1760\,\mathrm{cm}^{-1}$, respectively, are most informative (Figure 5.18) [57]. The nanoscale structural changes characterized by attenuated total reflectance−Fourier transform infrared (ATR-FTIR) analysis show that the incorporation of CNCs favors microphase separation between the HSs and SSs; however, new CNCs/WPU hydrogen bonds formed largely within the hard domain, leading to higher hydrogen bond density in the hard domain and less reduction of elongation-at-break [57]. The results indicated that CNCs exhibited well reinforcement of PU/WPU nanocomposites.

Chitin/chitosan (CS) nanowhiskers have also been used to improve the mechanical properties and thermal stability of PUs. On the basis of the hydrophilic nature of chitin/CS, PU/WPU exhibits good compatibility with them. CS possesses amine groups that can react with isocyanate groups in PU-prepolymers. The nanocomposites have been prepared by casting/evaporating [59−61].

Morphological studies were also performed by SEM as shown in Figure 5.19 [59, 60]. When the ChW loading level was <2 wt%, the WPU/ChW nanocomposites (Figures 5.19b,c) showed a fluctuant fractured surface similar to that of neat WPU (Figure 5.19a). This is because at a lower loading level, ChW uniformly dispersed in the WPU matrix and had almost no effect on the original structure and fractured behavior of the WPU matrix.
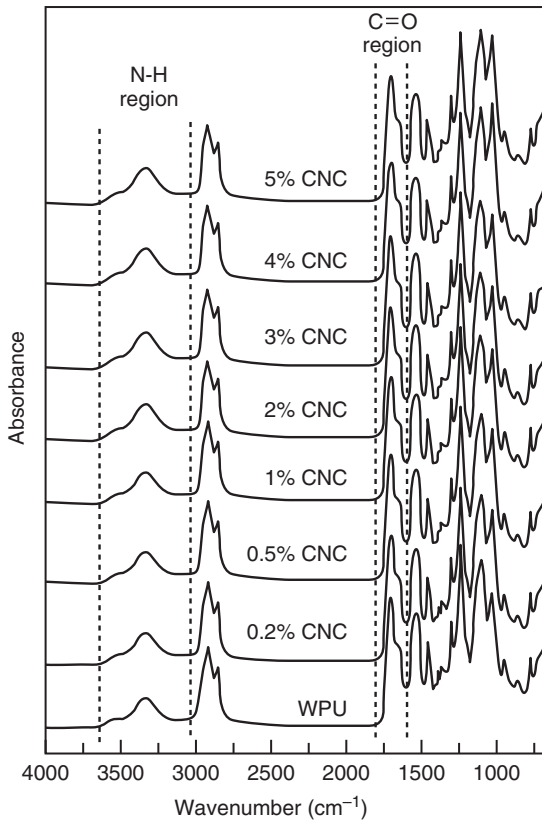
Figure 5.18 Attenuated total reflectance–Fourier transform infrared spectra of the CNC/WPU nanocomposite films with pure WPU. Reproduced from [57], copyright 2012 © permission from Elsevier.

However, with increasing ChW loading, fracture morphologies gradually became smooth surfaces with regular and compact thin stripes. This brittle–fracture characteristic agreed with the decrease in strength and elongation-at-break and was attributed to the breakage of the original structure of the WPU matrix after adding more ChWs. In addition, with increasing ChW loading, the ChW nanophase in the WPU matrix was observed as many white dots dispersed across the fracture surface. SEM images confirmed the effects of increasing ChW loading on the increasing number and expanded size of the ChW nanophase in the nanocomposites [60]. The resulting WPU/ChW nanocomposites prominently enhanced both the strength and Young's modulus and maintained an elongation of greater than about 500%. The 3 wt% ChW loading showed the maximum tensile strength (28.8 MPa) and enhanced the Young's modulus (6.5 MPa), about 1.8- and 2.2-folds higher than those of neat WPU. The active surface and rigidity of ChW formed the interface for stress transfer and contributed to higher stress endurance. With increasing ChW loading, the
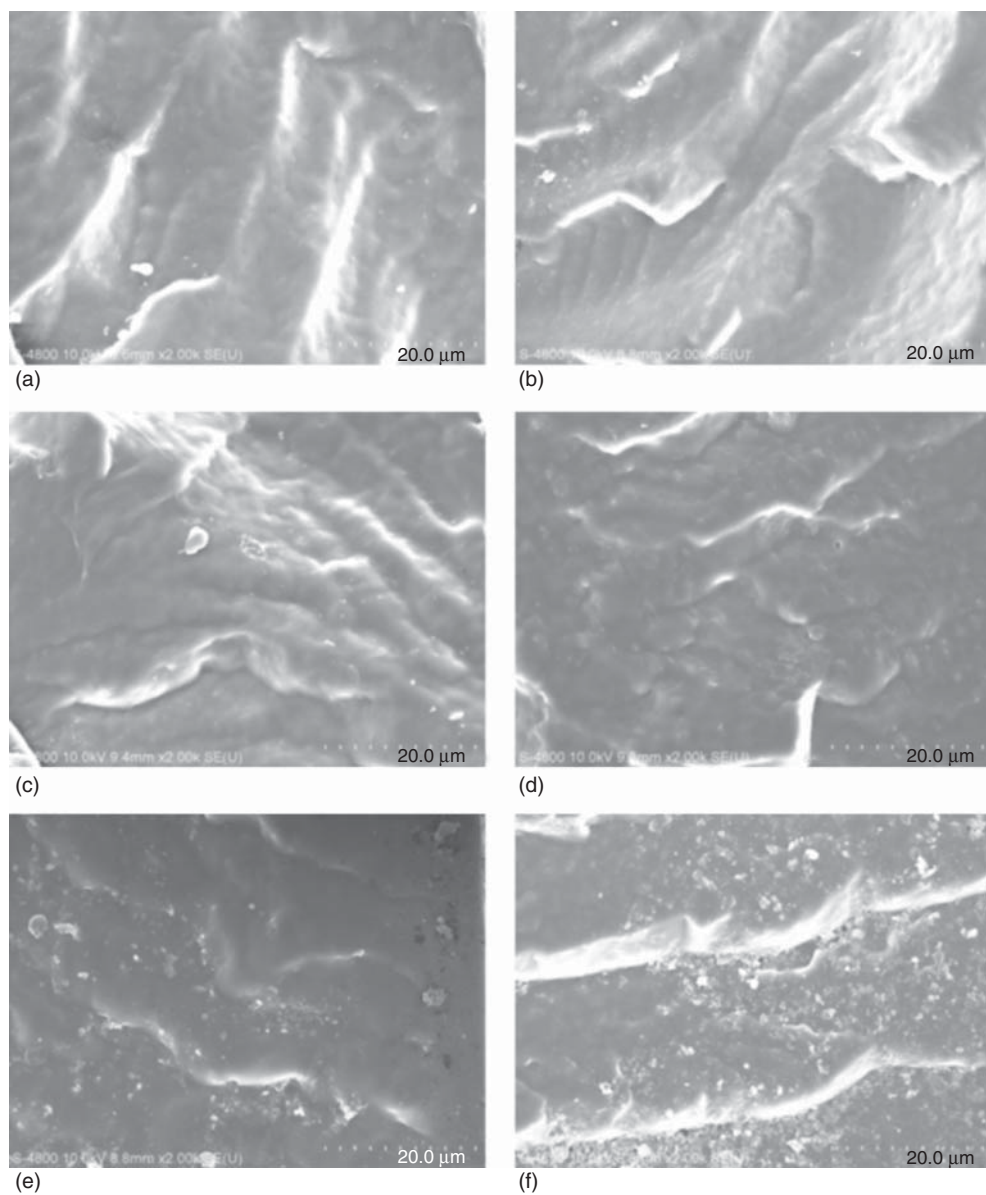
Figure 5.19 Scanning electron microscopic images of fractured surfaces of WPU/ChW nanocomposites with various ChW loading levels and WPU as the reference. (a) WPU; (b) WPU/ChW-1; (c) WPU/ChW-2; (d) WPU/ChW-3; (e) WPU/ChW-4; and (f) WPU/ChW-5. Reproduced from [60], copyright 2011 © permission from Express Polymer Letters.

self-aggregation of ChWs decreased the strength; however, the rigidity of ChW increased the Young's modulus. The nanocomposites containing 5 wt% ChWs had the highest Young's modulus (9.6 MPa). This study achieved high mechanical performance of WPU-based nanocomposites by introducing natural nanofillers; these high-performance "green" bionanocomposites have great potential.

PUs are one of the most versatile polymeric materials with respect to both processing methods and mechanical properties. However, conventional PU products usually contain a significant amount of organic solvents and even free isocyanate monomers. Therefore, these solvent-based PUs have been gradually replaced by WPUs because of the increasing need to reduce the volatile organic compounds (VOCs) and hazardous air pollutants (HAPs) [62]. WPUs show many advantages such as being nontoxic, non-flammable, pollution free, having low viscosity at high molecular weight, and good applicability, and are now one of the most rapidly developing and active branches of PU chemistry and technology [63]. Recently, a series of studies focused on the addition of nanosized particles, particularly polysaccharide nanocrystals, in the WPU matrix to improve the thermal resistance and mechanical properties of WPU materials [3, 39, 64–66]. These novel materials are eco-friendly and biodegradable and have potential application in medicine and biology [40]. Nanocomposites of polysaccharide nanocrystal-based WPU have been prepared by casting/evaporating and mechanical blending [40, 67].

Despite the different content of SNCs, nanocomposites show the same fracture morphology (Figure 5.20). The nanophase dispersed well in the matrix as the loading increased at low content levels. SEM images confirmed the effects of increasing SNC loading level on the increasing number and expanded size of the starch nanophase in the nanocomposites [68]. Moreover, the strength, elongation, and Young's modulus were simultaneously enhanced. Herein, two nanocomposite films of SNC-filled WPU (US) are worth noting: (i) US-2 containing only 2 wt% SNCs had the maximum elongation (1406.6%) and enhanced tensile strength (28.6 MPa), about 1.7- and 2.6-fold higher than those of neat WPU, respectively and (ii) US-5 filled with 5 wt% SNCs. The SNCs had the highest tensile strength (51.5 MPa) and increased Young's modulus (5.2 MPa), which were enhanced by about 370% and about 93%, respectively, with increasing elongation (981.9%). The significant improvement in the mechanical performances, that is, simultaneous reinforcing and toughening, was attributed to the enduring stress of rigid SNCs and stress transfer mediated by the strong interaction at the interfaces between SNC nanofillers and the WPU matrix. Moreover, preservation of the original structure and interaction in WPU matrix was the second crucial factor for further enhancement in the mechanical performances. Furthermore, chemical grafting did not enhance the strength and elongation by inhibiting the physical interaction on the SNC surface and increasing the network density of the nanocomposites [3]. The nanoparticles aggregate at high loading. Zou *et al.* [68] reported good dispersion of starch nanoparticles in the composites even when the nanoparticle loading reached 30%. Furthermore, the resulting composites prominently enhanced both the strength and Young's modulus and maintained an elongation of >300%.
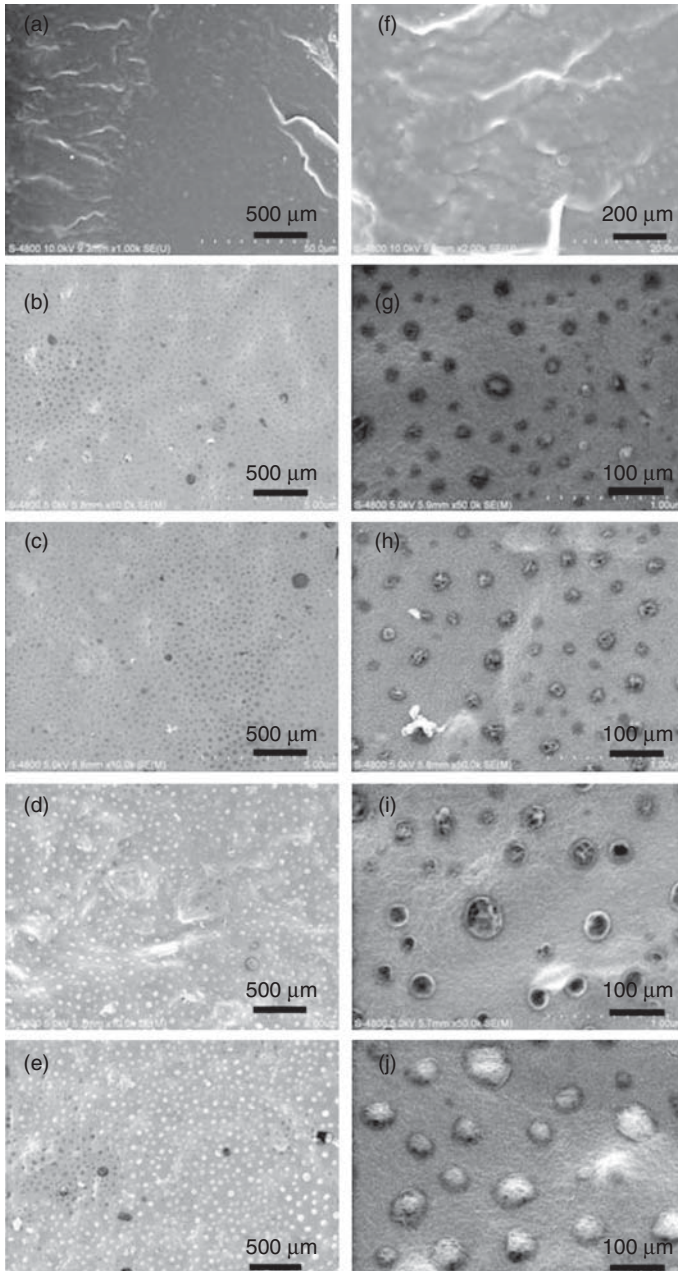
Figure 5.20   Scanning electron microscopic images of fractured surfaces of WPU/SNC nanocomposites with various SNC loading levels and WPU film reference. (a) WPU, (b) WPU/SNC-5, (c) WPU/SNC-10, (d) WPU/SNC-20, (e) WPU/SNC-30; and (f–j) are high multiple electron micrographs corresponding to (a–e). Scale bar: 20 min (a) and 10 min (f); 2 min (b–e); and 400 min (g–j). Reproduced from [68], copyright 2011 © permission from Elsevier.

A 10 wt% SNC loading showed the maximum tensile strength (31.1 MPa) and an enhanced Young's modulus, 1.8- and 35.7-folds higher than those of neat WPU, respectively. The active surface and rigidity of SNC formed an interface for stress transfer and contributed to higher stress endurance. As the SNC loading increased, the self-aggregation of SNCs decreased the strength; however, the rigidity of SNC increased the Young's modulus, which was highest in the nanocomposites containing 30 wt% SNCs. Thus, high-performance WPU-based "green" bionanocomposites were obtained [68]. An interesting and innovative study on the synergistic reinforcement of cellulose nanowhiskers and SNCs has been reported. With the incorporation of 1 wt% SNC and 0.4 wt% CNC, the tensile strength, Young's modulus, and tensile energy at break of the WPU-based nanocomposites were significantly enhanced by 135%, 252%, and 136%, respectively, and the elongation-at-break remained the same as that of pure WPU. The WPU/1%−SN/0.4% CNC system also exhibited a much better reinforcing effect than all the WPU/SNC and WPU/CNC systems. Furthermore, WPU-based nanocomposites exhibited greater thermal resistance. The results clearly showed that the different polysaccharide nanocrystals and whiskers combined to form strong hydrogen-bonding networks, synergistically reinforcing WPU. This study provides a new eco-friendly pathway to prepare polymer nanocomposites with a high performance using both natural nanocrystals and whiskers [40]. To decrease nanoparticle aggregation, SNCs were modified to improve their dispersity in the matrix. Chen *et al.* [3] investigated the reinforcement of starch nanocrystal-grafted-polycaprolactone (SNC-g-PCL) on WPU [3].

The WPU/SNC-g-PCL with the lowest loading of 5 wt% SNC-g-PCL showed the maximum tensile strength and elongation higher than those of neat WPU. In this case, the simultaneous enhancement in strength and elongation was attributed to the uniform dispersion of the nanoscale SNC-g-PCL, increasing entanglements mediated by the grafted PCL chains, and the reinforcing function of rigid SNC. However, with increasing SNC-g-PCL content, the SNC-g-PCL self-aggregated as crystalline domains, hindering the improvement in tensile strength and elongation-at-break, even though the Young's modulus was significantly enhanced. To the best of our knowledge, this is the first report on the modification of WPU based on polymer-grafted natural nanocrystal. Moreover, the same origin for SS in WPU matrix and grafted polymer chains onto SNC has been considered as the key factor in enhancing the mechanical properties. Moreover, the high mechanical performances of such new nanocomposite materials based on biodegradable compositions may have great potential applications [67].

5.5
Polyester-Based Nanocomposites

Polyesters are polymers with ester functional groups on the main chain, for example, polyethylene terephthalate (PET) and polybutylene terephthalate (PBT). Polyesters are obtained both from the cut in plant cuticles and by synthetic

methods involving the polycondensation reaction of purified terephthalic acid (PTA) or its dimethyl ester, dimethyl terephthalate (DMT), and monoethylene glycol (MEG). Depending on the chemical structure, polyesters are of two types: thermoplastic and thermosetting. Polyesters are widely used in our daily life and industry such as in apparel and home furnishings, bottles, films, insulating tapes, and safety belts. As mentioned above, the addition of nanofillers into the polymeric matrix improved the mechanical properties, thermal properties, surface appearance, and gas and water permeability of the resulting materials. Therefore, many studies used inorganic nanofillers such as carbon nanotubes (CNTs) and nanosilica [69, 70].

Polysaccharide (cellulose, chitin, and starch) nanoparticles have attracted increased attention to replace the inorganic nanoparticles because of their renewability, biodegradability, versatility, availability, high aspect ratio, and so on. However, the reinforcing effect of nanocrystals depends not only on their nature, content, and state of dispersion within the polymeric matrix but also on the intermolecular interactions between the matrix and the nanofillers. To investigate the reinforcement effects of the polysaccharide nanoparticles on polyesters, several studies have been conducted.

Green materials are prepared by adding polysaccharide nanoparticles into the polyester matrix. Polysaccharide nanoparticle-based polyester nanocomposites have been prepared by solution casting, melt-processing [71], microwave irradiation [72], and electrospinning methods [73, 74]. The materials prepared by different methods differ in their properties [71]. Recently, Wolcott *et al.* [75] reported that the melt-processed nanocomposites exhibited a lower strength than that of solution-processed nanocomposites during the study of the tensile strength improvement of the CN-modified poly(3-hydroxybutyrate-co-3-hydroxyvalerate) PHBV. This may be because of the better dispersion of CNCs in the PHBV matrix through a solution casting process [75].

In addition, simultaneous improvement in the mechanical properties and thermal stability of CNC-based bacterial polyester PHBV has been achieved. Compared to pristine PHBV, 149% improvement in the tensile strength and 250% increase in the Young's modulus were obtained for the nanocomposites with 10 wt% CNCs; moreover, the T0, T5%, T_{max}, and T_f increased by 51.4, 36.5, 47.1, and 52.9 °C, respectively. Such a reinforcing effect can be attributed to the high modulus and high strength of the CNCs as the nanoscale reinforcement. Good crystallization properties, and most importantly, strong intermolecular hydrogen-bonding interactions was due to the excellent dispersions of CNCs in the PHBV matrix via solvent exchange procedure [71].

Lin *et al.* [76] studied the reinforcing effect of CNC and SNC on the mechanical properties of polybutylene succinate (PBS) [76]. CNC and SNC were isolated by the acid hydrolysis of native linter and pea starch granules, respectively. PBS is a biodegradable aliphatic polyester with a low modulus, typically 300 – 500 MPa. The tensile strength and tensile energy at break of CNC/PBS and SNC/PBS increased with 2 and 5 wt% of fillers. Moreover, the modulus increased gradually with increasing filler content. The reason was the strong interfacial adhesion
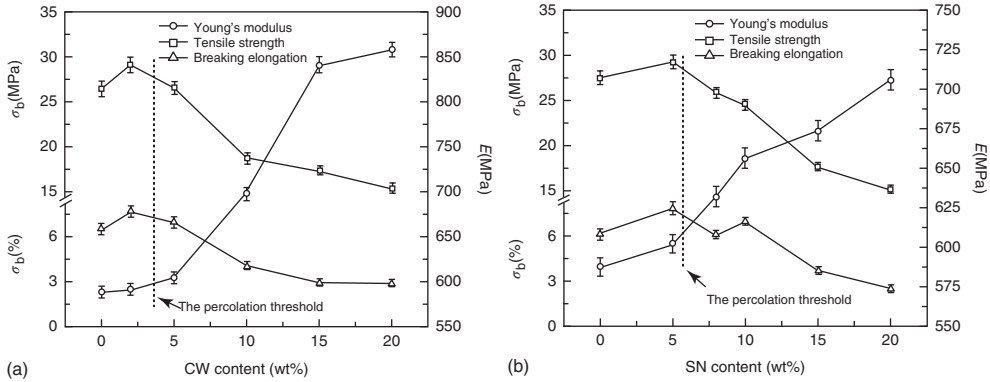
(a)

(b)

Figure 5.21 Effects of CNC and SNC contents on tensile strength (rb), elongation-at-break (eb), and Young's modulus (E) for the PBS/CNC-series (a) and PBS/SNC-series (b) nanocomposites. Reproduced from [76], copyright 2011 © permission from Society of Plastics Engineers.

between the fillers and matrix below the percolation threshold. However, above the percolation threshold, the rigid three-dimensional (3D) continuous network structure, namely, percolating network, formed with the strong interaction of hydrogen bonds between the nanoparticles that eventually contributed to the reinforcement of nanocomposites. They claimed that the percolating network did not form by adding only 2 wt% CNC or 5 wt% SNC filler, and the interactions between CNC or SNC nanoparticles and PBS polymer molecules were stronger than the interactions between the nanofillers themselves, preserving the intact and ordered structure of the PBS matrix. The reported results are shown in Figure 5.21.

DSC and X-ray diffraction (XRD) analyses showed that the presence of rigid nanoparticles increased the T_m of the nanocomposites and crystallinity below the percolation threshold. In fact, the presence of rigid particles and increase in the crystallinity of the nanocomposites inhibited the free motion of PBS polymer chains and demanded more energy for the thermal transformation, increasing the T_m of PBS/CNC-2 and PBS/SNC-5 nanocomposites compared to the neat PBS-F. However, above the percolation threshold, T_m decreased gradually with increasing filler loading. This is probably because the 3D continuous network structure formed, and the filler–filler interactions were stronger than the filler–matrix interactions. The presence of the continuous network structure helped endure and absorb more energy in the thermal behavior of the nanocomposites, thereby improving the thermal stability of the entire system by shifting the T_g to a higher temperature as observed from the dynamic mechanical thermal analysis (DMTA) test. However, the rigid network inevitably destroyed the PBSs original structure and disordered the crystalline structure of the PBS matrix. Moreover, the emerging interface between the network and amorphous or crystalline region also degraded the thermal performance of the nanocomposites, as shown by the obvious decrease in the T_m.
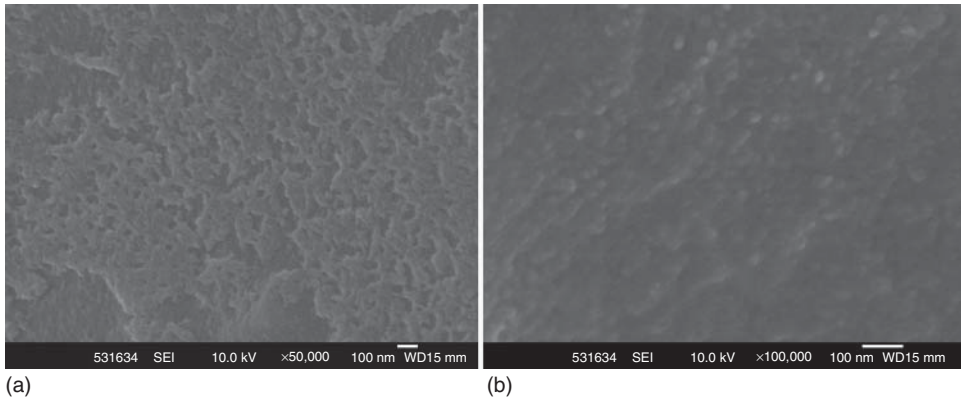
Figure 5.22 Field emission-scanning electron microscopic morphologies of alkali-etched (a) and CNC-grafted PET (b) fabrics [77].

PET reinforced with CNCs by surface modification "graft onto" has been investigated [77]. The morphology and thermal properties of the alkali-etched and CNC-grafted PET fabrics were investigated by field emission scanning electron microscopy (FE-SEM) and TGA, as shown in Figures 5.22 and 5.23.

As shown in Figure 5.22, the alkali-etched PET fabrics are porous, and the CNC-grafted PET fabrics contain nanoparticles. The TGA thermograms in Figure 5.23 show that the untreated PET fiber has only one thermal weight loss peak during $350-500\,°C$, and the alkali-treated PET fiber has two peaks in the range $300-350$ and $350-500\,°C$, respectively. The CNC-g-PET fibers show three thermal weight loss peaks in the ranges $120-200$, $300-350$, and $350-500\,°C$, respectively. CNC-g-PET showed less weight loss in the range $300-350\,°C$ than the alkali-treated PET fibers, which was caused by the cross-linking effect of the CNC particles with multi-ended reactive groups.

Zaman *et al.* [78] cationically grafted CNC using glycidyl trimethyl ammonium chloride (GTMAC), and applied it on the PET fabric using a rolling–drying–curing process. The hypothesis of this modification was to develop a durable hydrophilic surface finishing system to improve the hydrophilic properties of polyester. The hydrophobicity of polyester originated from the lack of polar functional groups (OH, COOH, NH_2, etc.) on its polymer backbone. Polyester keeps human perspiration trapped against the body. Because of the hydrophobicity, polyester is also more electrostatic than natural fibers. The electrostatic nature of polyester is highly undesirable because it makes clothes cling to each other. The surface properties of polyester fabric were changed from hydrophobic to hydrophilic after heat treatment with CNC grafted by GTMAC [78].

The wettability of specimens is evaluated by wicking test and contact angle analysis. Figure 5.24 shows the wicking distance of CNC-treated fabric after multiple washing. The untreated fabric showed a wicking distance of 6 mm, whereas

(a)

(b)

(c)
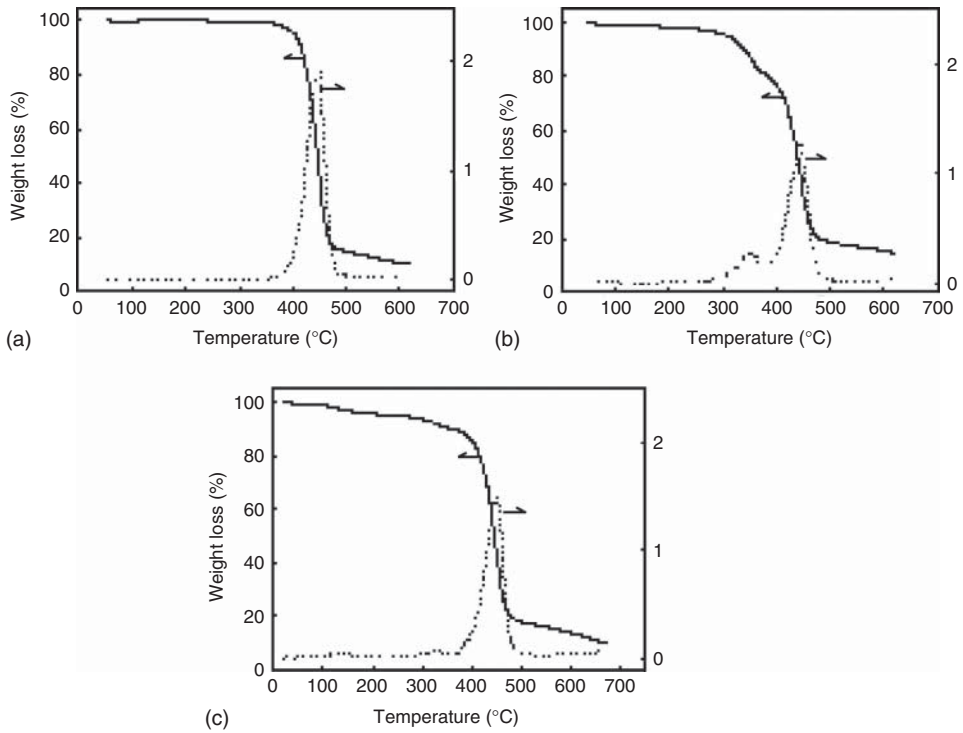
Figure 5.23 TGA of pristine (a), alkali-etched (b), and CNC-grafted PET fibers (c) [77].
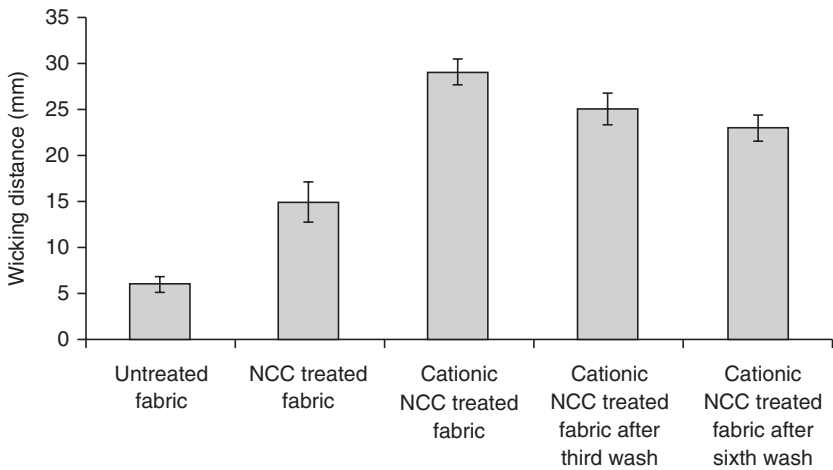
Figure 5.24 Wicking distance of both untreated and CNC-treated fabric after multiple washing. Reproduced from [78], copyright 2013 © permission from Elsevier.

Contact angle: 132°

(a)

Contact angle: 93°

(b)

Contact angle: 42°

(c)
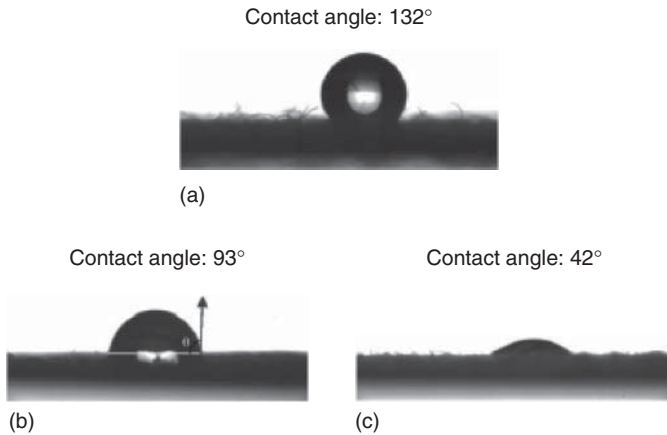
Figure 5.25 Water contact angle : (a) untreated PET; (b) original, CNC-treated PET; and (c) cationic CNC-treated PET. Reproduced from [78], copyright 2013 © permission from Elsevier.

the original and cationic CNC-treated fabric showed a much higher wicking distance of 15 and 29 mm, respectively. The higher hydrophilicity of the cationic CNC-treated fabric can be attributed to the presence of quaternary ammonium groups, which is well known for enhancing the water uptake of polymers and resins. Despite the decrease in wicking distance after multiple washing, the wicking distance of 23 mm after six washing cycles for the cationic CNC-treated fabric was still remarkably higher than that of the untreated fabric.

Water contact angle analysis was also performed to investigate the wetting behavior of the treated fabrics. The water droplet on the surface of untreated PET fabric formed a contact angle of ~132°, which was because of its highly hydrophobic nature (Figure 5.25). However, the CNC-treated fabric and cationic CNC showed a significant reduction in the water contact angle to 93° and 42°, respectively. The increase in hydrophilicity of the treated PET fabric can be attributed to the presence of hydrophilic CNC on the fabric surface. The OH and quaternary ammonium groups on the CNC surface favored the formation of hydrogen bonds on contact with water, increasing the hydrophilicity of the fabric. The author claimed that cationic CNC coating is one of the most effective surface treatment methods for improving the hydrophilicity and durability of polyester fabric among other existing techniques.

Peng *et al.* [79] utilized CNC grafting on PET, used as a hydrophilic substrate and morphology-influencing agent, to promote the nucleation and crystal growth of TiO_2 [79]. The lack of polar functional groups, such as COOH and OH, on the main chains of PET leads to its low surface free energy, low wettability, and poor adhesion [77, 80]. Thus, CNC with a surface full of hydrophilic groups acted as morphology-inducing and coordinating agent, providing coordination sites with titanium atoms to promote the nucleation and crystal growth of TiO_2 nanoflowers at a low temperature. On the other hand, hydrogen bonding strengthened the interfacial interaction between the PET and TiO_2.

The common technique for obtaining rutile TiO_2 required high-temperature calcination, unavoidably causing agglomeration and reducing the photoactivity of the prepared TiO_2. However, in the suggested system by Peng *et al.* [79], the rutile TiO_2 nanocrystals *in situ* grown on PET fabrics were obtained at 70 °C using CNC without any special equipment. Moreover, the presence of CNC saved the trouble of separating TiO_2 powders in aqueous solution. The hybrid nanocomposites exhibited an excellent self-cleaning performance, which has a good potential for commercialization [79].

In another study reported by Li and Ding [80], CNC was grafted with low-molecular-weight PEG and immobilized on the surface of PET fabric to produce a fabric comfortable for difficult climate. CNCs were prepared by hydrolyzing small squares of a cotton filter paper with a mixture of H_2SO_4 and hydrochloric acid. The dimension of spherical CNC particles was in the range 30–50 nm. Dimensional memory measurements showed that when deionized water was absorbed completely, the deformation after absorbing water declined from 11% for the PET fabrics covered by CNC-free coating to 6.5% for the PET fabrics with CNC-loaded coating. In other words, the deformation decreased by about 41% in the presence of CNC; therefore, the former exhibited better shape-stability than the latter. This result showed that CNC particles served as a multifunctional reactant and reinforcing filler, forming the cross-linking network and improving the shape-stability of the PET fabrics. The CNCs widened the phase change temperature range, thus increasing the phase change enthalpy [80].

PET nanocomposite has been prepared by the layer-by-layer (LBL) assembly of two biopolymers, CS and CNC, on an amorphous PET [81]. Multiple-layer structures were clearly observed, as shown in Figure 5.26a, confirming that the nanoscale layers were created by LBL assembly. The average thickness of the 30 bilayers CS/CNs coating was ~800 nm. Figure 5.26b demonstrates the high transparency of CS/CNCs nanocomposite coating by eye inspection.

For the ($CSpH_4$/$CNCspH_2$) condition, the oxygen permeability coefficient of CS/CNCs coating and the oxygen permeability of the coated PET are shown in
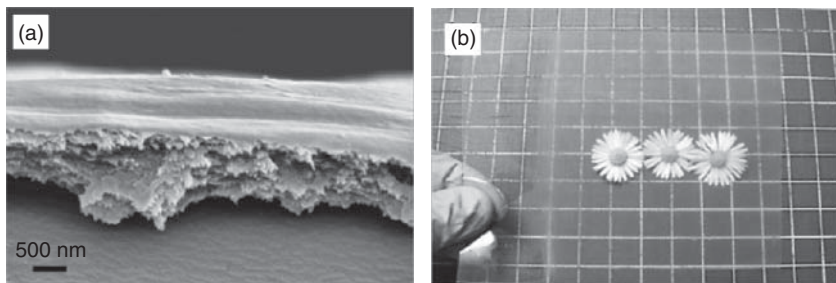
Figure 5.26 (a) Scanning electron microscopic image of the multilayer cross section, after cutting it with blade and coating it with a few nanometer Au layer. The average thickness of the multilayer was ~800 nm. (b) Optical property of coated A-PET. CS, chitosan and CNCs, cellulose nanocrystals. Reproduced from [81], copyright 2013 © permission from Elsevier.
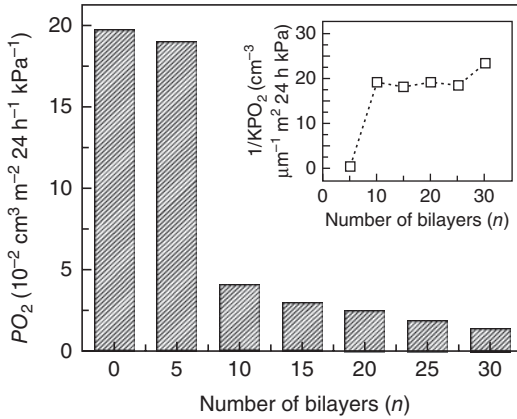
Figure 5.27 Oxygen permeability (PO_2, $cm^3\,m^{-2}\,24\,h^{-1}\,kPa^{-1}$) for a 180 µm A-PET substrate coated with increasing numbers of (CSpH4/CNCspH2)n bilayers ($n = 0$, 5, 10, 15, 20, 25, and 30). Reproduced from [81], copyright 2013 © permission from Elsevier.

Figure 5.27, according to the number of bilayers (n), which varies from 0 to 30. The oxygen permeability (PO_2) value of the coated PET decreased dramatically with increasing thickness of the LBL coating. For example, at 30 bilayers, the PO_2 value of coated PET reduced by ~94% than the uncoated PET, from ~0.2 to ~0.013 $cm^3\,m^{-2}\,24\,h^{-1}\,kPa^{-1}$ because of the strong electrostatic interaction and hydrogen bonding between CS and CNs. However, from 10 to 30 bilayers, the reciprocal of the oxygen permeability coefficient (KPO_2) remains constant. Thus, both the oxygen diffusion coefficient and the oxygen solubility changes in the CS/CNCs nanocomposite, are independent of the thickness and the number (n) of bilayers (for $n \geq 10$).

Chen *et al.* [72] first reported thermoformable bionanocomposites based on cellulose nanocrystal-grafted-poly(e-caprolactone) (CNC-g-PCL); they were synthesized by the ring-opening polymerization of PCL monomers on the surface of microcrystalline cellulose under microwave irradiation [72]. The "graft from" strategy contributed to long and dense "plasticizing" tails of PCL on the CNC surface, which were the key for thermoforming. In this case, the long grafted PCL chains entangled with each other in the melting process of thermoforming, producing molded sheets with good mechanical strength. Furthermore, the shielding of PCL grafted onto the surface of CNC contributed to the high hydrophobicity of the bionanocomposite material. Such new bionanocomposite materials may have a great number of potential applications in biomedical or environment-friendly materials. This method may be used to produce biocomposite material-based polymer-grafted natural nanocrystals as the matrix and/or nanofiller by a continuous process of polymerization, compounding, and molding. They also developed nanocomposites using cellulose nanocrystal-grafted-PCL (CNC-g-PCL) and SNC-g-PCL as fillers to reinforce poly(lactic acid) [82, 83]. The results showed simultaneous improvement in the strength and elongation, ability of rigid CNC nanoparticles to endure higher stress, and the essential associations of the facile

transfer of the stress to the CNC nanoparticles mediated by grafted PCL chains. Furthermore, the prominent enchantment in the elongation and the reduction of the modulus, was due to the rubbery PCL component.

5.6
Starch-Based Nanocomposites

Starch is a biomass consisting of many granules, namely, amylase and amylopectin. Amylase is primarily a linear polymer composed of ~1000 1,4-linked α-D-glucopyranosyl units. Amylopectin is a very large molecule (105−106 glucose units) comprising 1,4-linked α-D-glucopyranose chains with α-1,6 branches.

Starch is obtained from many sources such as corn, wheat, potato, and cassava. Being a natural polymer, the properties of starch depend on the molecular weight and ratios of the branched chains to the straight chains. Studies showed that the starch with a high amylose content was compatible to prepare plastic, materials with better mechanical properties. In general, in the studies on starch-based biodegradable plastics, starch was directly used as the fillers to reinforce plastics, and starch blends with synthesized polymers to develop plastics and total starch plastics (thermal plastics) [84].

In recent years, plasticized starch (PS) has attracted considerable attention and has offered an interesting alternative for synthetic polymers, where long-term durability is not needed and rapid degradation is an advantage [85]. However, compared to conventional synthetic thermoplastics, biodegradable products based on starch, unfortunately, still have many disadvantages such as water sensitivity, brittleness, and poor mechanical properties [86]. Starch-based bio-nanocomposites have been extensively studied, which can be obtained by filling a thermoplastic starch matrix with nanofillers such as layer silicates, CNTs, CB, cellulose, and SNCs. CNCs or whiskers have been used to reinforce starchy material [87−89]. Recently, polysaccharide nanoparticles have been widely used as fillers to improve thermoplastic starch. Polysaccharide nanoparticles, mainly cellulose, chitin, and starch nanoparticles, not only inherit the properties of the biomass such as abundance, renewability, biodegradability, low cost, and easy processing, but also add the nanometer size effect such as high aspect ratio, improved mechanical properties, high elastic modulus, and high Young' modulus [85]. SEM images (Figure 5.28) showed that the neat thermoplastic starch film was rather smooth, compared to the nanocomposites films. With increasing nanoparticle content, no large aggregation and homogeneous distribution were observed, indicating good adhesion between fillers and matrix. This was attributed to good compatibility resulting from the chemical similarities between starch and cellulose and the hydrogen-bonding interactions existing in the interface between fillers and matrix. Such even and uniform distribution of the fillers in the matrix played an important role in improving the mechanical performance of the resulting nanocomposite films as discussed later.
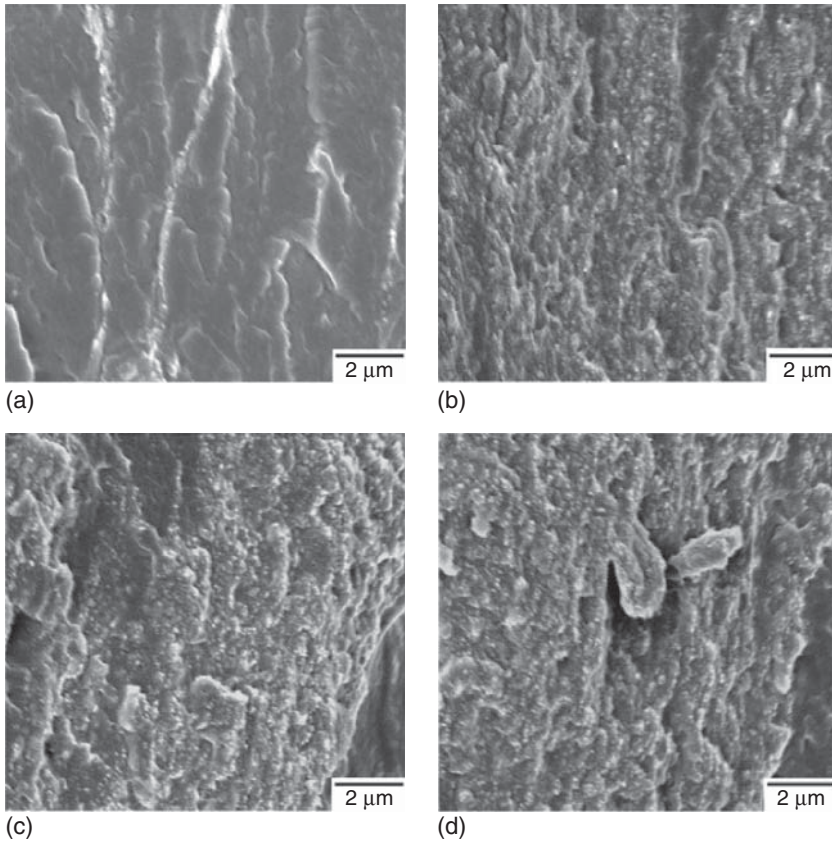
(a)

(b)

(c)

(d)

Figure 5.28 FE-scanning electron microscopic images of the failure surfaces of the PS and PS/CNCs nanocomposites with different CNCs content: (a) 0 wt%; (b) 10 wt%; (c) 20 wt%; and (d) 30 wt% (scale bar: 2.0 μm). Reproduced from [86], copyright 2008 © permission from Express Polymer Letters.

XRD results of nanocomposites showed improvement in crystallinity by adding nanofibrils [90]. Wide-angle X-ray diffraction (WAXRD) images (Figure 5.29) show that typical starch granules involve alternating amorphous and crystalline lamellae in which two main components, amylose and amylopectin, are embedded. When starch granules are destroyed by heat and shear force during processing, amylose, an essentially linear polymer, dissociates out of the granule and crystallizes into several single helical crystal structures. Thermoplastic starch is characterized by a broad hump centered on 19°, indicating that the material is fully amorphous [91]. This showed that the crystalline structure of native starch granules disappeared during the processing. The magnitude of the peaks at 16.7° and 22.5° increased with increasing CNF content, indicating a crystalline structure with the preservation of the crystallinity of SNCs during the processing (Figure 5.29) [90].
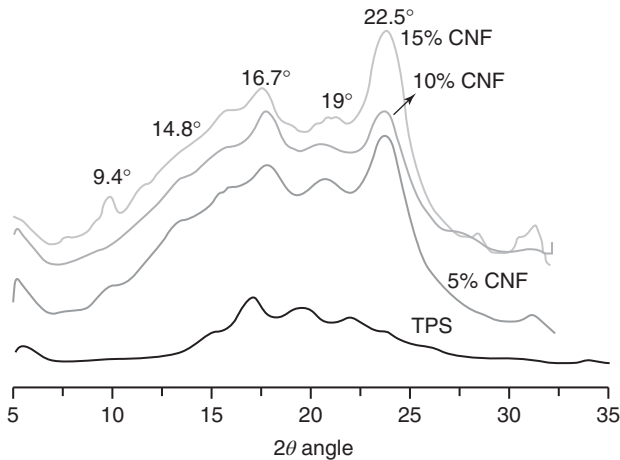
Figure 5.29 XRD spectra of thermoplastic starch (TPS) cellulose nanofibril nanocomposites with 5%, 10%, and 15% nanofibrils. Reproduced from [90], copyright 2010 © permission from Elsevier.

Different types of (ligno-) cellulose fibers or microfibrils were tested along with plasticized starch: microfibrils from potato pulp, bleached leafwood fibers, fibers from bleached eucalyptus pulp, and flax and jute fibers. Several studies have shown high compatibility between starch and fibers. For instance, Averous and Boquillon [92] found a strong increase in T_g by adding cellulose fibers into a plasticized starch (PS) matrix [92]. This behavior was attributed to the fiber–matrix interactions that decreased the mobility of starch chains. After mixing, a large improvement in the material performance properties was observed. Some of these enhancements were linked to typical matrix reinforcement, and some others were linked to fiber–matrix interface interactions [93]. For instance, compared to biopolyester-based biocomposites, starch-based biocomposites (i) exhibited superior mechanical properties attributed to higher interactions between the matrix and filler; (ii) exhibited higher thermal resistance because of the transition shift of T_g and an increase in the rubber plateau; (iii) showed reduced water sensitivity because of fiber–matrix interactions and higher hydrophobic character of the cellulose, which is attributed to its high crystallinity; and (iv) showed reduced post-processing aging because of the formation of a 3D network between the different matrix–filler carbohydrates based on hydrogen bonds.

Different nanofillers will lead to different improvements in properties, such as the mechanical properties, barrier properties, or change in the thermal properties and electrical conductivity. Geometry, surface area, and surface chemistry affected the reinforcement [94]. Starch plastics have been reinforced using rod-like CNCs [86]. The mechanical properties were investigated by tensile test and DMA. The results showed that the content of the nanoparticles greatly affected the mechanical properties. The tensile strength increased from 3.9 to 11.9 MPa. The Young's modulus increased significantly from 31.9 to

498.2 MPa with increasing filler content from 0 to 30 wt%, respectively, whereas the elongation-at-break decreased from 68.2% to 7.2%. This may be explained by the reinforcement effect from the homogeneously dispersed high-performance CNC fillers in the PS matrix and the strong hydrogen-bonding interactions between CNCs and PS molecules. The CNCs from flax fiber showed a similar effect as that of ramie-based nanocomposites on the mechanical properties in the PS-based nanocomposites [86].

Humidity is one of the most important factors affecting the mechanical properties of thermoplastic starch. Liu *et al.* [94] studied the spherical-like CNC-reinforced thermoplastic starch and improved its properties [94]. When bamboo CNCs (BCCs) were added, the water uptake of the starch/BCC nanocomposite (SBC) decreased. When the BCC content was >8%, the water uptake decreased very slowly. The water uptake of SBC20 was slightly higher than that of SBC15, which was probably because of the increasing interspace between BCC and starch, as shown by the SEM micrograph. Because of the macro-phase separation caused by the severe congregation of BCCs, more water could easily penetrate/diffuse into the interspace. With increasing BCC content, both the tensile strength and Young's modulus increased. When the size of particles was reduced significantly, many interesting phenomena occurred because of the larger surface area and higher surface energy. CNCs have a high modulus, up to 134 GPa, and a strong tensile strength of >4 GPa [95]. An 8% BCC content was quite sufficient to obtain a profound reinforcing effect comparable to the starch composites reinforced with 30–50% cellulose fibers [96, 97]. When the BCC content was >10%, interface adhesion was not sufficient to withstand the imposed high stretching forces, decreasing the tensile strength. Obviously, the decreased water uptake also accounted for the increase in the modulus and strength of water-sensitive starch-based biocomposites [94].

Studies also showed that the water sensitivity was lowered mainly because of the low water uptake of CNC itself and the strong hydrogen-bonding interactions between matrix and fillers, or fillers and fillers [86]. DSC results showed that the stability of starch-based nanocomposites improved to some degree by adding CNCs. In DSC experiments, T_g is generally taken as the inflection point of the specific heat increment at the glass–rubber transition. Figure 5.30 clearly show that all the samples display two distinct specific heat increments, corresponding to the glass transitions of the PS matrix. As Angles and Dufresne [87] previously reported, the PS plasticized by glycerol is a complex heterogeneous system comprising glycerol-rich domains dispersed in a starch-rich continuous phase, and each phase exhibits its own T_g [87]. Therefore, the transitions located in the temperature ranges −80 to −50 and 30–60 °C can be assigned to the T_{g1} of glycerol-rich phase and T_{g2} of starch-rich phase, respectively. With increasing CNC fillers from 0 to 30 wt%, no obvious change in the T_{g1} value at low temperature for the glycerol-rich phase was observed. However, the T_{g2} for starch-rich phase shifted to a higher temperature from 43.3 to 48.8 °C, indicating that CNCs restrict the mobility of starch chains because of the strong intermolecular interactions between starch and rigid CNCs [86].
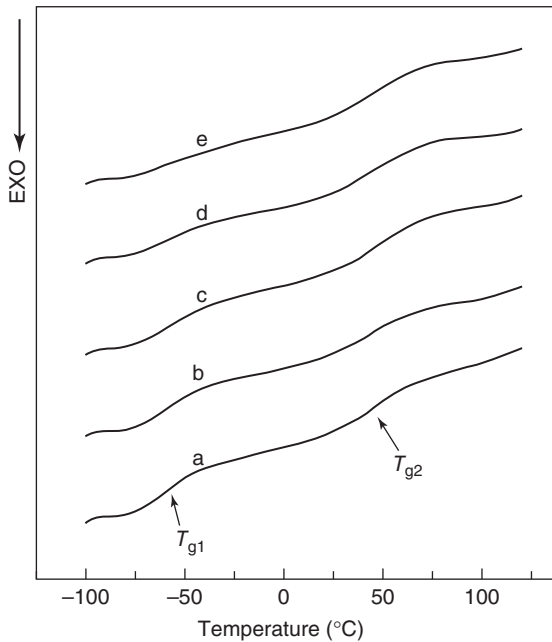
Figure 5.30 DSC thermograms of PS and PS/CNCs nanocomposites with different CNC content: (a) 0 wt%; (b) 5 wt%; (c) 10 wt%; (d) 20 wt%; and (e) 30 wt% [86].

Zainuddina *et al.* [98] prepared biocomposite films by mixing starch and glycerol/sorbitol with various filler compositions. A comparison between raw kenaf fiber-reinforced starch nanocomposite and CNC-based starch nanocomposite was evaluated. Compared to kenaf fiber, the tensile strength and tensile modulus were enhanced by 134% and 85%, respectively. This significant improvement in starch thermoplastic-reinforced CNC was mainly because of the high specific area and high aspect ratio, which provided better reinforcement capability compared to raw kenaf fiber. This also confirmed the strong interfacial interaction between starch and cellulose. The ability of the nanocellulose to hinder matrix mobility also contributed to this improvement. The high crystallinity and rigidity of the CNCs was also another reason for enhancing tensile modulus [98].

5.7
Protein-Based Nanocomposites

Proteins are highly complex polymers made up of 20 different amino acids. The constituents are linked by substituted amide bonds. Protein molecules are amphoteric and can easily be located at oil/water or air/water interfaces. The molecules can have multiple functionalities in addition to localized charges. Compared to starch, proteins have better gas barrier properties, but lower water vapor permeabilities [99]. Proteins are widely used as nanoparticles and act as

efficient drug delivery vehicles [99]. They can be used as the matrix to produce biodegradable composites. This part of the chapter focuses on the application of protein as the matrix for polysaccharide nanoparticles.

Gelatin is one of the proteins obtained by denaturing the triple-helix structure of collagen into single-strain molecules. When an aqueous solution of gelatin was cooled to below 35 °C, physically thermoreversible gels were formed because of the partial recovery of collagen triple-helix structure by disorder–order rearrangement [100].

However, the application of gelatin is typically limited at higher temperatures (above 35 °C), where the disruption of the secondary bonding structure destroys the physical network. This leads to poor thermal and mechanical properties and has thus far limited further application of gelatin, a readily available, and relatively inexpensive material. Therefore, chemical cross-links between the protein chains of gelatin are used to stabilize these gels, often referred as chemical gelatin gels [101]. Dash *et al.* [100] used oxidized CNC to improve the thermal and mechanical properties of gelatin hydrogels. They have reported an increased degree of chemical cross-linking (0.14–17%) between gelatin and nanowhiskers with increased aldehyde contents (0.062–0.230 mmol g^{-1}) [100].

^{1}H nuclear magnetic resonance (NMR) spin–spin (T_2) relaxation experiments on swollen hydrogels showed that the systems consisting of both gelatin and cellulose nanowhiskers displayed a higher percentage of "ridge" protons, attributed in part to increasing chemical cross-linking junction points between gelatin and nanowhiskers. This increase in hydrogel rigidity modified local chain dynamics and influenced gel swelling, indicating relatively reduced water uptake ability than that of the neat gelatin. Rheological measurements confirmed a 150% improvement in the storage modulus of the cross-linked hydrogels compared to neat gelatin. Chemical cross-linking also increased the resistance of the gels toward thermal degradation above the T_m of gelatin as observed by thermal scanning experiments [100].

Figure 5.31 shows the images of the transverse cross-sectional surfaces of the gels with different degrees of cross-linking; the pore structures depend on the degree of cross-linking. A relatively open network structure with interconnected pores of various sizes was observed in the gelatin samples. However, the cross-linking affected the openness of the network structure as the pore size of the cross-linked gels became smaller and more regular in shape than the control samples. For 17% cross-linking, the interior appeared to be more compact with the smallest pore size. The gradual decrease in the pore size and increase in the compactness of the cross-linked gels was attributed to the effect of increased degree of cross-linking that offers more intermolecular association forming more junction points, which in turn affects the pore structure, size, and its distribution.

Soy protein is one of the few natural polymers that can be thermoplastically processed [102]; however, water sensitivity, high rigidity, and poor rheological properties hinder the development and applications of soy protein-based plastics. Furthermore, although plasticization generally improves the toughness and processability, the decrease in tensile strength and modulus are inevitable. Among all
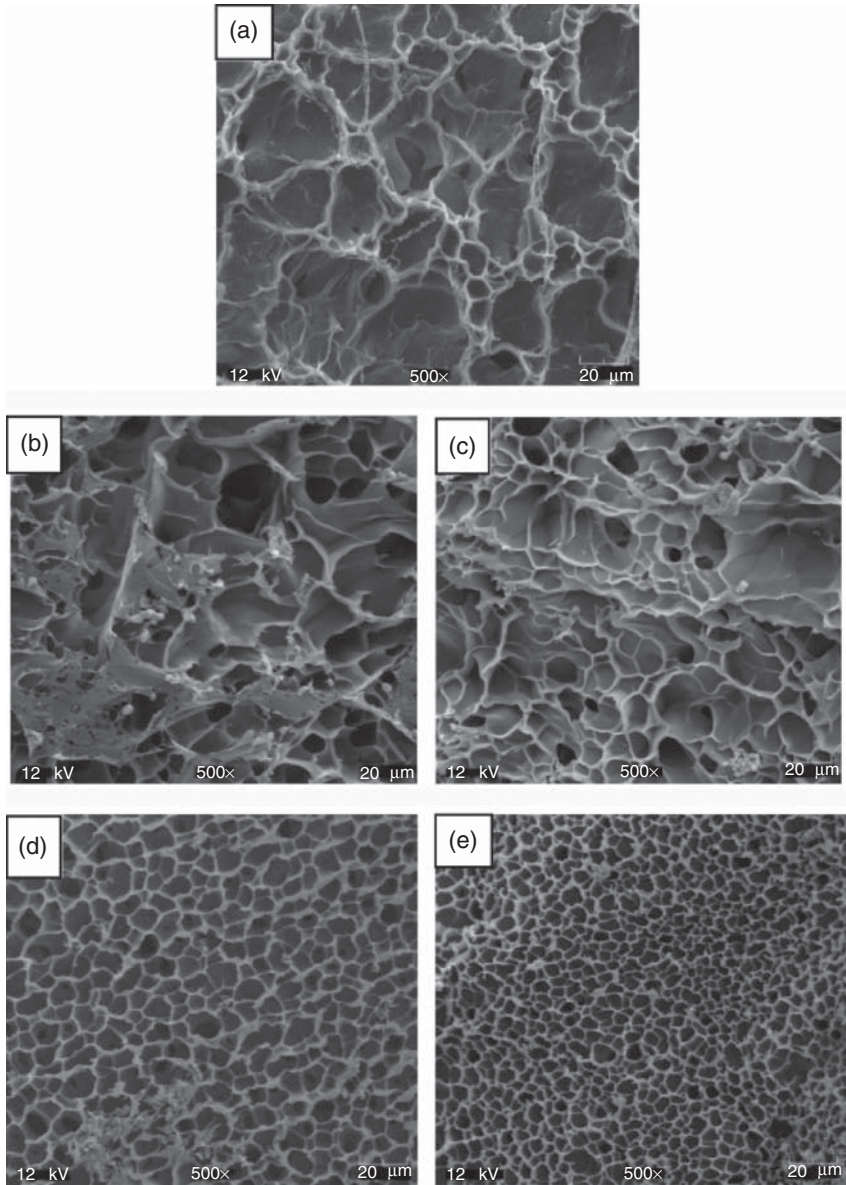
Figure 5.31 Cross-sectional morphologies of (a) gelatin and (b) 0.14%, (c) 4.32%, (d) 13.02%, and (e) 17.30% cross-linked gels (scale bar 20 μm). Reproduced from [100], copyright 2013 © permission from Elsevier.
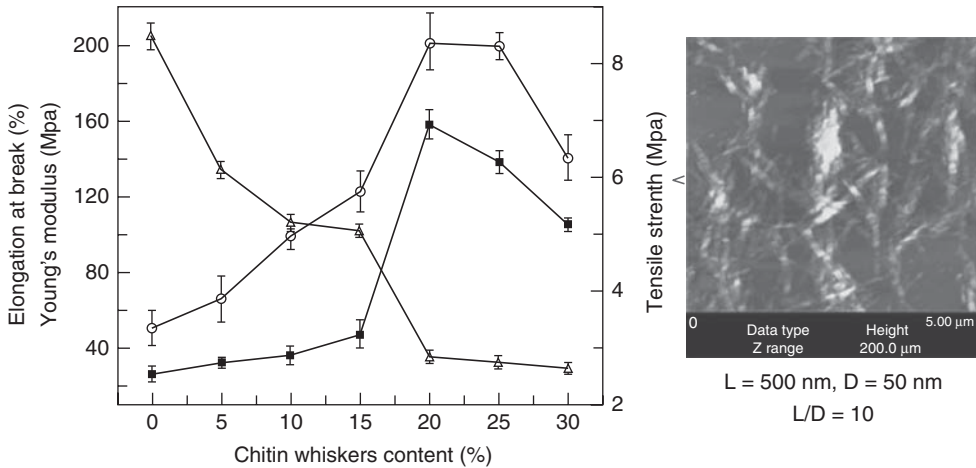
Figure 5.32 Effects of ChW (as shown in the atomic force microscopy image) loading level on mechanical properties of nanocomposites. Reproduced from [104], copyright 2004 © permission from American Chemical Society.

the protein resources, soy protein is regarded as a readily renewable biopolymer and potential source for biodegradable plastics, textile fibers, biodegradable membranes, and adhesives; further, it can be acetylated, trans glutaminase-treated, and blended with organic or inorganic nanoparticles [103].

Lu *et al.* [104] reported a simultaneous increase in the tensile strength and Young's modulus when ChWs were added to the soy protein isolate (SPI), containing more than 90% protein and 18 diverse amino acids [104]. Compared to the neat SPI sheet, the Young's modulus and tensile strength of the SPI/ChW composites increased from 26 to 158 MPa, and from 3.3 to 8.4 Mpa, respectively, with increasing loading to 20 wt% (Figure 5.32). With increasing ChW loading, the water resistance and thermal stability of the nanocomposites also gradually increased. Meanwhile, 3D ChW networks that formed above the percolation threshold significantly decreased the water diffusion coefficient. The properties of nanocomposites improved because the ChWs self-constructed 3D hydrogen-bonding networks and interacted strongly with the SPI chains [104].

Gao *et al.* [105] reported soybean meal-based adhesive-reinforced cellulose nanowhiskers [105]. They found that the incorporation of CNC in the adhesive formulation improved the water resistance of the plywood by 20%. SEM analysis of the cross section of the cured neat adhesive showed holes and cracks compared to that with CNC. These holes and cracks may be caused by the gasification of water in the adhesive during hot pressing, reducing the water resistance of the adhesive. After the incorporation of CNC, fewer holes and cracks were observed on the cross section of the cured adhesive, indicating that the use of CNC reduced the water gasification in the adhesive (Figure 5.33).

Pea SNCs have also been incorporated into SPI to form SPI/SNC composites [106]. As shown in Figure 5.34, the optimal SNC loading level was only 2 wt%.

(a)   A (×1000)

(b)   B (×1000)
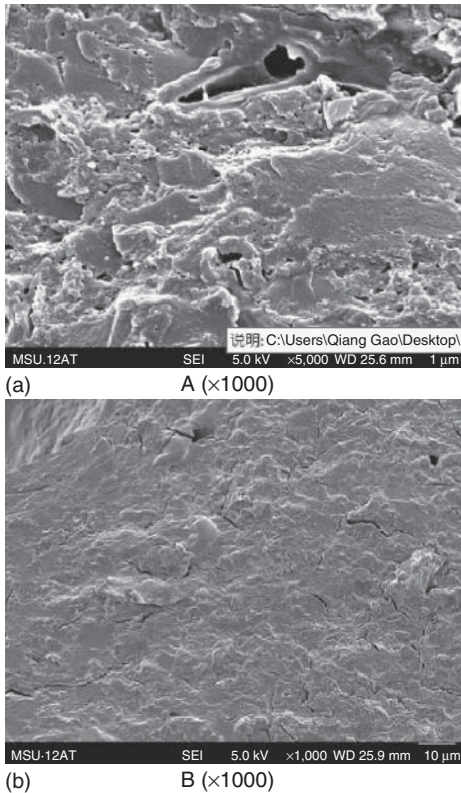
Figure 5.33 Cross section of the cure adhesives (a) soybean meal adhesive and (b) soybean meal/CNC adhesive. Reproduced from [105], copyright 2012 © permission from Bioresources.

At this loading level, the nanocomposite showed the maximum tensile strength of 10.39 MPa and the maximum Young's modulus enhanced by ∼200% than the neat SPI sheet. These improvements were attributed to the uniform dispersion of SNCs and the strong interfacial interaction between the active SNC surface and SPI matrix.

Tzoumaki *et al.* [107] claimed that the addition of whey protein isolate (WPI) to an aqueous dispersion of ChWs, which initially did not behave elastically, formed a network; the gel strength increased by increasing either WPI or ChW concentration. They believed that the gel structure was attributed to phase separation phenomena, possibly because of thermodynamic incompatibility of the macromolecular components; that is, when the WPI globular biopolymers were excluded from the interspace between the ChW colloidal particles, the imbalance in osmotic pressure finally led to attractive forces between the colloidal particles [107].

Rheological investigations showed that the heating of the ChW – WPI mixed dispersions further increased the storage modulus, which was irreversible upon
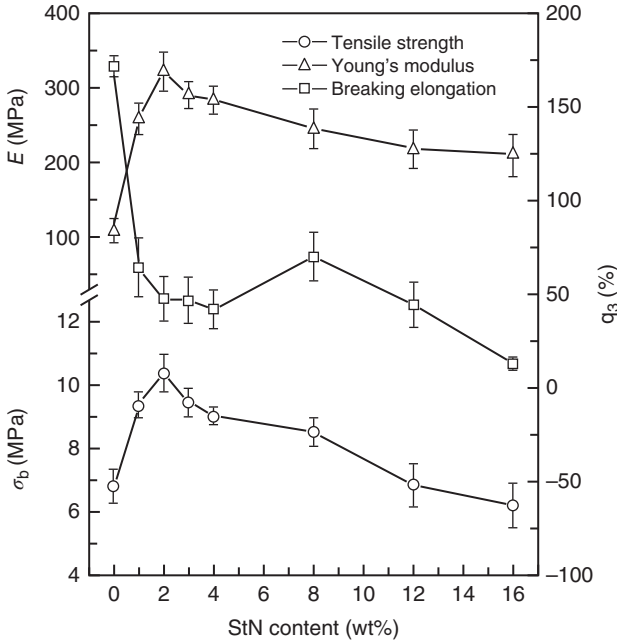
Figure 5.34 Effects of the SNC content on the mechanical properties of the SPI/SNC nanocomposite and SPI sheets. Reproduced from [106], copyright 2009 © permission from John Wiley & Sons.

cooling; the magnitude of the increase depended mostly on the ChW concentration. The increase in the storage modulus may be attributed to the ChW network "strengthening" with increasing temperature. Thus, the addition of WPI in ChW dispersions was an effective way to modify the rheological properties of ChW aqueous dispersions; moreover, heating, even at temperatures that do not cause protein denaturation, can be another method to enhance the elastic character of the mixed ChW–WPI dispersions [107].

Silk fibroin (SF) is a fibrous protein isolated from the cocoon fiber of Bombyx mori (B. mori) silkworm. It has wide application in biomaterials such as film, 3D scaffolds, hydrogels, and non-woven mats. The SF films from regenerated SF solution usually have silk I crystalline structure, leading to brittleness and poor flexibility. However, the mechanical properties of SF films were enhanced by blending SF with other polymers such as PEG and cellulose nanowhiskers [108]. The incorporation of CNC substantially increased the storage modulus of the PEG-plasticized SF film, which may be attributed to the formation of rigid whisker network controlled by a percolation mechanism within the host matrix (Figure 5.35a). A shift in the T_g toward high temperature was also observed with increasing CNC content, indicating a reduced mobility of the amorphous SF chains in the presence of interactions between the CNCs and the matrix. On the other hand, the altitude of tan δ peak at T_g decreased with increasing CNC
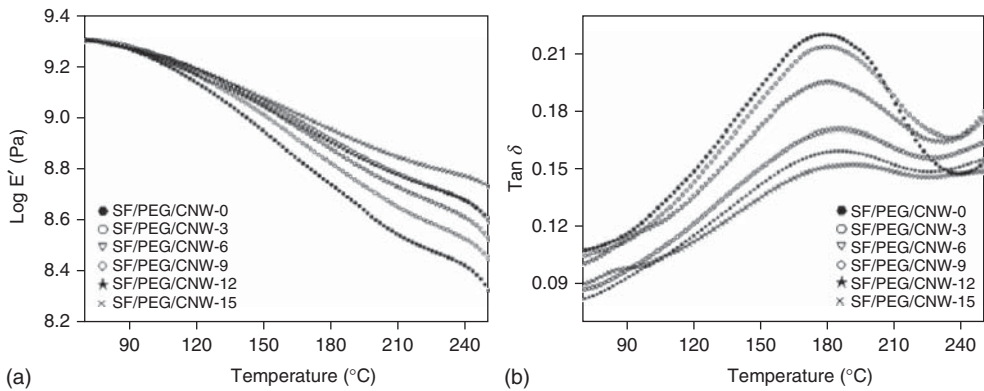
Figure 5.35 Evolution of (a) storage modulus and (b) tan d as a function of temperature from DMA analysis of different composite films. Reproduced from [108], copyright 2012 © permission from Wiley Periodicals.
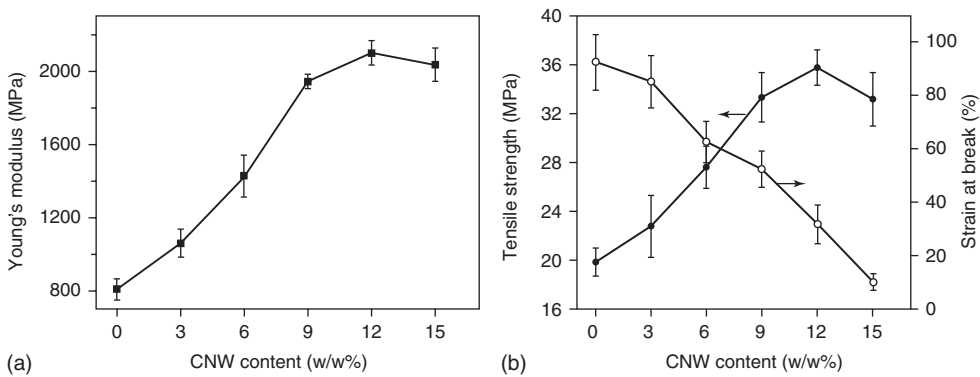
Figure 5.36 (a) Young's modulus and (b) tensile strength and strain-at-break for the composite films prepared with different CNC contents. Reproduced from [108], copyright 2012 © permission from Wiley Periodicals.

content as shown in Figure 5.35b, which may be attributed to the decrease in the mobile units of SF participating in the relaxation process.

The Young's modulus of the composite films remarkably increased with increasing CNC content. The Young's modulus of SF/PEG/CNC-9 was more than 2.5 times higher than that of SF/PEG/CNC-0. However, it slightly reduced at higher CNC content because of the aggregation of CNCs in the SF matrix (Figure 5.36). Similar to the evolution of the Young's modulus, the tensile strength of the composite films increased significantly from 20 to 36 MPa with increasing CNC content from 0 to 12 w/w%, followed by a decrease to 33 MPa when the CNC content was 15 w/w%. Moreover, the strain-at-break decreased from 92 to 10% as shown in Figure 5.36 [108].

5.8
Concluding Remarks

Polysaccharide nanocrystals (CNC, chitin nanocrystals, and SNCs) have great potential as reinforcements in nanocomposites because of their abundance, high strength and rigidity, and low weight and biodegradability. The surface chemical modification and nanosized dimensions of polysaccharide nanocrystals have been extensively used in diverse applications, for example, packaging, adhesives, and electronic display materials. This review summarizes some selected studies in polysaccharide nanocrystals extracted from different sources and their influences on the thermal, mechanical, and other unique properties of rubber, polyester, polyolefin, PU, starch, plastic, and protein nanocomposites. The combination of these highly rigid crystals with a polymeric matrix has been shown to provide excellent mechanical, thermal, and barrier properties for the above-mentioned polymeric nanocomposites. However, the key issue is to balance the interfacial interaction between the nanocrystals and polymer matrix. The properties of polysaccharide nanocrystal-based nanocomposites were directly affected by the source and extraction technique of the nanocrystals and the preparation techniques of the nanocomposites. Polysaccharide nanocrystal-based nanocomposites may become the next-generation novel eco-friendly nanocomposites.

List of Abbreviations

CNC   cellulose nanocrystal
ChW   chitin nanowhiskers
SNC   starch nanocrystal
PU   polyurethane
NR   natural rubber
CB   carbon black
CNF   cellulose nanofibril
SEM   scanning electron microscopy
MFC   microfibrillated cellulose
DMA   dynamic thermomechanical analysis
T_g glass-transition temperature
MCNC   surface-modified CNC
TEM   transmission electron microscopy
AFM   atomic force microscopy
WVP   water vapor permeation
PP   polypropylene
MA   maleic anhydride
MAPP   maleic anhydride-grafted polypropylene
NWC   nanowood clay
WF   wood flour
T_m melting temperature
DSC   differential scanning calorimetry

MDI	4,4′-diphenyl methane diisocyanate
WPUs	waterborne PUs
PEG	polyethylene glycol
BD	1,4-butanediol
PCL	polycaprolactone
PPG	polypropylene glycol
IPDI	isophorone diisocyanate
TDI	2,4-toluene diisocyanate
DMPA	dimethylol propionic acid
TEA	triethylamine
MCC	microcrystaline cellulose
DMF	dimethyl formamide
SPU	segmented polyurethane
FTIR	Fourier transform infrared
TGA	thermogravimetric analysis
SS	soft-segment
HS	hard-segment
BDO	butanediol
SMPU	shape memory polyurethane
ATR	attenuated total reflectance
VOC	volatile organic compound
HAP	hazardous air pollutant
PET	polyethylene terephthalate
PBT	polybutylene terephthalate
PTA	purified terephthalic acid
DMT	dimethyl terephthalate
MEG	monoethylene glycol
CNT	carbon nanotube
PHBV	poly(3-hydroxybutyrate-*co*-3-hydroxyvalerate
PBS	polybutylene succinate
XRD	X-ray diffraction
DMTA	mechanical thermal analysis
FE-SEM	field emission SEM
GTMAC	glycidyl trimethyl ammonium chloride
CS	chitosan
KPO_2	oxygen permeability coefficient
PS	plasticized starch
WAXRD	wide-angle XRD
TPS	thermoplastic starch
PS	plasticized starch
BCC	bamboo CNC
NMR	^{1}H nuclear magnetic resonance
SPI	soy protein isolate
WPI	whey protein isolate
SF	silk fibroin

References

1. Peng, B.L., Dhar, N., Liu, H.L., and Tam, K.C. (2011) Chemistry and applications of nanocrystalline cellulose and its derivatives: a nanotechnology perspective. *Can. J. Chem. Eng.*, **98**, 1191–1206.

2. Kargarzadeh, H., Ahmad, I., Abdullah, I., Dufresne, A., Zainudin, S.Y., and Sheltami, R.M. (2012) Effects of hydrolysis conditions on the morphology, crystallinity, and thermal stability of cellulose nanocrystals extracted from kenaf bast fibers. *Cellulose*, **19**, 855–866.

3. Chen, G., Wei, M., Chen, J., Huang, J., Dufresne, A., and Chang, P.R. (2008) Simultaneous reinforcing and toughening: new nanocomposites of waterborne polyurethane filled with low loading level of starch nanocrystals. *Polymer*, **49**, 1860–1870.

4. Chang, P.R., Huang, J., and Lin, N. (2011) in *Nanocomposites with Biodegradable Polymers: Synthesis, Properties and Future Perspectives* (ed. V. Mittal), Oxford University Press, New York, pp. 71–100.

5. Nair, K.G. and Dufresne, A. (2003) Crab shell chitin whisker reinforced natural rubber nanocomposites. 1. Processing and swelling behavior. *Biomacromolecules*, **4**, 657–665.

6. Valodkar, M. and Thakore, S.I. (2012) Biopolymers as effective fillers in natural rubber: composites versus biocomposites. *J. Appl. Polym. Sci.*, **124**, 3815–3820.

7. Nair, K.G. and Dufresne, A. (2003) Crab shell chitin whisker reinforced natural rubber nanocomposites. 2. Mechanical behavior. *Biomacromolecules*, **4**, 666–674.

8. Praveen, S., Chattopadhyay, P.K., Albert, P., Dalvi, V.G., Chakraborty, B.C., and Chattopadhyay, S. (2009) Synergistic effect of carbon black and nanoclay fillers in styrene butadiene rubber matrix: development of dual structure. *Composites Part A*, **40**, 309–316.

9. Xu, S.H., Gu, J., Luo, Y.F., and Jia, D.M. (2012) Effects of partial replacement of silica with surface modified nanocrystalline cellulose on properties of natural rubber nanocomposites. *eXPRESS Polym. Lett.*, **6**, 14–25.

10. Ismail, H., Shaari, S.M., and Othman, N. (2011) The effect of chitosan loading on the curing characteristics, mechanical and morphological properties of chitosan-filled natural rubber (NR), epoxidised natural rubber (ENR) and styrene-butadiene rubber (SBR) compounds. *Polym. Test.*, **30**, 784–790.

11. LeCorre, D.S., Bras, J., and Dufresne, A. (2012) Influence of the botanic origin of starch nanocrystals on the morphological and mechanical properties of natural rubber nanocomposites. *Macromol. Mater. Eng.*, **297**, 969–978.

12. Pasquini, D., Teixeirab, E.M., Curvelob, A.A.S., Belgacemc, M.N., and Dufresne, A. (2010) Extraction of cellulose whiskers from cassava bagasse and their applications as reinforcing agent in natural rubber. *Ind. Crops Prod.*, **32**, 486–490.

13. Bendahou, A., Kaddami, H., and Dufresne, A. (2010) Investigation on the effect of cellulosic nanoparticles' morphology on the properties of natural rubber based nanocomposites. *Eur. Polym. J.*, **46**, 609–620.

14. Visakh, P.M., Thomas, S., Oksman, K., and Mathew, A.P. (2012) Cellulose nanofibres and cellulose nanowhiskers based natural rubber composites: diffusion, sorption, and permeation of aromatic organic solvents. *J. Appl. Polym. Sci.*, **124**, 1614–1623.

15. Nair, K.G. and Dufresne, A. (2003) Crab shell chitin whiskers reinforced natural rubber nanocomposites. 3. Effect of chemical modification of chitin whiskers. *Biomacromolecules*, **4**, 1835–1842.

16. Bouthegourd, E., Rajisha, K.R., Kalarical, N., Saiter, J.M., and Thomas, S. (2011) Natural rubber latex/potato starch nanocrystal nanocomposites: correlation morphology/electrical properties. *Mater. Lett.*, **65**, 3615–3617.

17. Huang, X., Jiang, P., and Kim, C. (2007) Electrical properties of polyethylene/aluminum nanocomposites. *J. Appl. Phys.*, **102**, 124103–124108.

18. Angellier, H., Molina-Boisseau, S., Lebrun, L., and Dufresne, A. (2005) Processing and structural properties of waxy maize starch nanocrystals reinforced natural rubber. *Macromolecules*, **38**, 3783–3792.

19. Angellier, H., Boisseau, S.M., and Dufresne, A. (2005) Mechanical properties of waxy maize starch nanocrystal reinforced natural rubber. *Macromolecules*, **38**, 9161–9170.

20. Nwabunma, D. (2008) in *Polyolefin Blends* (eds D. Nwabunma and T. Kyu), John Wiley & Sons, Inc., Hoboken, NJ, pp. 3–26.

21. Yang, H.S., Gardner, D.J., and Nader, J.W. (2011) Characteristic impact resistance model analysis of cellulose nanofibril-filled polypropylene composites. *Composites Part A*, **42**, 2028–2035.

22. Goussé, C., Chanzy, H., Excoffier, G., Soubeyrand, L., and Fleury, E. (2002) Stable suspensions of partially silylated cellulose whiskers dispersed in organic solvents. *Polymer*, **43**, 2645–2651.

23. Heux, L., Chauve, G., and Bonini, C. (2000) Nonflocculating and chiral-nematic self-ordering of cellulose microcrystals suspensions in nonpolar solvents. *Langmuir*, **16**, 8210–8212.

24. Ljungberg, N., Cavaillé, J.-Y., and Heux, L. (2006) Nanocomposites of isotactic polypropylene reinforced with rod-like cellulose whiskers. *Polymer*, **47**, 6285–6292.

25. Ljungberg, N., Bonini, C., Bortolussi, F., Boisson, C., Heux, L., and Cavaillé, J.-Y. (2005) New nanocomposite materials reinforced with cellulose whiskers in atactic polypropylene: effect of surface and dispersion characteristics. *Biomacromolecules*, **6**, 2732–2739.

26. Agarwal, U.P., Sabo, R., Reiner, R.S., Clemons, C.M., and Rudie, A.W. (2012) Spatially resolved characterization of cellulose nanocrystal– polypropylene composite by confocal Raman microscopy. *Appl. Spectrosc.*, **66**, 750–756.

27. Bahar, E., Ucar, N., Onen, A., Wang, Y., Oksüz, M., Ayaz, O., Ucar, M., and Demir, A. (2012) Thermal and mechanical properties of polypropylene nanocomposite materials reinforced with cellulose nano whiskers. *J. Appl. Polym. Sci.*, **125**, 2882–2889.

28. Pandey, J.K., Lee, S., Kim, H.J., Takagi, H., Lee, C.S., and Ahn, S.H. (2012) Preparation and properties of cellulose-based nano composites of clay and polypropylene. *J. Appl. Polym. Sci.*, **125**, E651–E660.

29. Seydibeyoğlu, M.Ö., Misra, M., Mohanty, A., Blaker, J.J., Lee, K.Y., Bismarck, A., and Kazemizadeh, M. (2013) Green polyurethane nanocomposites from soy polyol and bacterial cellulose. *J. Mater. Sci.*, **48**, 2167–2175.

30. Li, Y. and Ragauskas, A.J. (2012) Ethanol organosolv lignin-based rigid polyurethane foam reinforced with cellulose nanowhiskers. *RSC Adv.*, **2**, 3347–3351.

31. Juntaro, J., Ummartyotin, S., Saina, M., and Manuspiya, H. (2012) Bacterial cellulose reinforced polyurethane-based resin nanocomposite: a study of how ethanol and processing pressure affect physical, mechanical and dielectric properties. *Carbohydr. Polym.*, **87**, 2464–2469.

32. Floros, M., Hojabri, L., Abraham, E., Jose, J., Thomas, S., Pothan, L., Leao, A.L., and Narine, S. (2012) Enhancement of thermal stability, strength and extensibility of lipid-based polyurethanes with cellulose-based nanofibers. *Polym. Degrad. Stab.*, **97**, 1970–1978.

33. Rueda, L., Saralegui, A., Fernández D'arlas, B., Zhou, Q., Berglund, L.A., Corcuera, M.A., Mondragon, I., and Eceiza, A. (2013) Cellulose nanocrystals/polyurethane nanocomposites. Study from the viewpoint of microphase separated structure. *Carbohydr. Polym.*, **92**, 751–757.

34. Zhang, H., She, Y., Song, S., Chen, H., and Pu, J. (2012) Improvements of mechanical properties and specular gloss of polyurethane by modified nanocrystalline cellulose. *Bioresources*, **7**, 5190–5199.

35. Wik, V.M., Aranguren, M.I., and Mosiewicki, M.A. (2011) Castor oil-based polyurethanes containing cellulose nanocrystals. *Polym. Eng. Sci.*, **51**, 1389–1396.

36. Marcovich, N.E., Auad, M.L., Bellesi, N.E., Nutt, S.R., and Aranguren, M.I. (2006) Cellulose micro/nanocrystals reinforced polyurethane. *J. Mater. Res.*, **21**, 870–881.

37. Auad, M.L., Mosiewicki, M.A., Richardson, T., Aranguren, M.I., and Marcovich, N.E. (2010) Nanocomposites made from cellulose nanocrystals and tailored segmented polyurethanes. *J. Appl. Polym. Sci.*, **115**, 1215–1225.

38. Cao, X.D., Habibi, Y., and Lucia, L.A. (2009) One-pot polymerization, surface grafting, and processing of waterborne polyurethane-cellulose nanocrystal nanocomposites. *J. Mater. Chem.*, **19**, 7137–7145.

39. Cao, X.D., Dong, H., and Li, C.M. (2007) New nanocomposite materials reinforced with flax cellulose nanocrystals in waterborne polyurethane. *Biomacromolecules*, **8**, 899–904.

40. Wang, Y.X., Tian, H.F., and Zhang, L.N. (2010) Role of starch nanocrystals and cellulose whiskers in synergistic reinforcement of waterborne polyurethane. *Carbohydr. Polym.*, **80**, 665–671.

41. Li, Y., Ren, H.F., and Ragauskas, A.J. (2010) Rigid polyurethane foam reinforced with cellulose whiskers: synthesis and characterization. *Nano-Micro Lett.*, **2**, 89–94.

42. Li, Y. and Ragauskas, A.J. (2011) Cellulose nano whiskers as a reinforcing filler in polyurethanes. *Algae*, **75**, 10–15.

43. Blagojevic, S.L., Buhin, Z., Pustak, A., and Kovaic, R.L. (2012) Influence of nanosilica on the morphology, thermal and mechanical properties of polyurethane elastomer. *Appl. Polym. Sci.*, **125**, 181–190.

44. Sun, D.X., Miao, X., Zhang, K.J., Kim, H., and Yuan, Y.G. (2011) Triazole-forming waterborne polyurethane composites fabricated wit h silane coupling agent functionalized nano-silica. *J. Colloid Interface Sci.*, **361**, 483–490.

45. Nikje, M.M.A. and Tehrani, Z.M. (2010) Novel modified nanosilica-based on synthesized dipodal silane and its effects on the physical properties of rigid polyurethane foams. *Des. Monomers Polym.*, **13**, 249–260.

46. Sabzi, M., Mirabedini, S.M., Zohuriaan-Mehr, J., and Atai, M. (2009) Surface modification of TiO2 nanoparticles with silane coupling agent and investigation of its effect on the properties of polyurethane composite coating. *Prog. Org. Coat.*, **65**, 222–228.

47. Liu, X.H., Zhao, Y., Liu, Z., Wang, D.J., Wu, J.G., and Xu, D.F. (2008) Preparation and characterization of modified nano carbon black/polyurethane composites. *Chem. J. Chin. Univ.*, **29**, 2096–2100.

48. Dong, X.M., Kimura, T., Revol, J.F., and Gray, D.G. (1996) Effects of ionic strength on the isotropic-chiral nematic phase transition of suspensions of cellulose crystallites. *Langmuir*, **12**, 2076–2082.

49. Hajji, P., Cavaillé, J.-Y., Favier, V., Gauthier, C., and Virgier, G. (1996) Tensile behavior of nanocomposites from latex and cellulose whiskers. *Polym. Compos.*, **17**, 612–619.

50. Morin, A. and Dufresne, A. (2002) Nanocomposites of chitin whiskers from Riftia tubes and poly(caprolactone). *Macromolecules*, **35**, 2190–2199.

51. Pei, A., Malho, J.M., Ruokolainen, J., Zhou, Q., and Berglund, L.A. (2011) Strong nanocomposite reinforcement effects in polyurethane elastomer with low volume fraction of cellulose nanocrystals. *Macromolecules*, **44**, 4422–4427.

52. Rueda, L., Fernández D'arlas, B., Zhou, Q., Berglund, L.A., Corcuera, M.A., Mondragon, I., and Eceiza, A. (2011) Isocyanate-rich cellulose nanocrystals and their selective insertion in elastomeric polyurethane. *Compos. Sci. Technol.*, **71**, 1952–1960.

53. Han, J., Zhu, Y., Hu, J., Luo, H., Yeung, L.Y., Li, W., Meng, Q., Ye, G., Zhang, S., and Fan, Y. (2012) Morphology, reversible phase crystallization, and thermal sensitive shape memory effect

of cellulose whisker/SMPU nano-composites. *J. Appl. Polym. Sci.*, **123**, 749–762.

54. Luo, H., Hu, J., and Zhu, Y. (2012) Path-dependent and selective multi-shape recovery of a polyurethane/cellulose-whisker nanocomposite. *Mater. Lett.*, **89**, 172–175.

55. Auad, M.L., Contos, V.S., Nutt, S., Aranguren, M.I., and Marcovich, N.E. (2008) Characterization of nanocellulose reinforced shape memory polyurethanes. *Polym. Int.*, **57**, 651–659.

56. Brunette, C., Hsu, S., and Macknight, W. (1982) Hydrogen-bonding properties of hard-segment model compounds in polyurethane block copolymers. *Macromolecules*, **15**, 71–77.

57. Gao, Z., Peng, J., Zhong, T., Sun, J., Wang, X., and Yue, C. (2012) Bio-compatible elastomer of waterborne polyurethane based on castor oil and polyethylene glycol with cellulose nanocrystals. *Carbohydr. Polym.*, **87**, 2068–2075.

58. Zhaoa, Q., Sun, G., Yana, K., Zhoua, A., and Chena, Y. (2013) Novel bio-antifelting agent based on waterborne polyurethane and cellulose nanocrystals. *Carbohydr. Polym.*, **91**, 169–174.

59. Nikje, M.M.A. and Tehrani, Z.M. (2010) Synthesis and characterization of waterborne polyurethane-chitosan nanocomposites. *Polym. Plast. Technol. Eng.*, **49**, 812–817.

60. Huang, J., Zou, J.W., Chang, P.R., Yu, J.H., and Dufresne, A. (2011) New waterborne polyurethane-based nanocomposites reinforced with low loading levels of chitin whisker. *Express Polym. Lett.*, **5**, 362–373.

61. Zeng, M., Gao, H., Wu, Y., Fan, L., and Li, A. (2010) Preparation and characterization of nanocomposite films from chitin whisker and water-borne poly(ester-urethane) with or without ultra-sonification treatment. *J. Macromol. Sci. Part A.*, **47**, 867–876.

62. Lu, Y. and Larock, R.C. (2010) in *Green Polymer Chemistry: Biocatalysis and Biomaterials* (eds H.N. Cheng and R.A.

Gross), American Chemical Society, New York, pp. 87–102.

63. Jeon, H.T., Jang, M.K., Kim, B.K., and Kim, K.H. (2007) Synthesis and characterizations of waterborne polyurethane–silica hybrids using sol–gel process. *Colloids Surf., A*, **302**, 559–567.

64. Lee, H. and Lin, L. (2006) Waterborne polyurethane/clay nanocomposites: novel effects of the clay and its inter-layer ions on the morphology and physical and electrical properties. *Macromolecules*, **39**, 6133–6141.

65. Wu, Q., Henriksson, M., Liu, X., and Berglund, L. (2007) A high strength nanocomposite based on microcrys-talline cellulose and polyurethane. *Biomacromolecules*, **8**, 3687–3692.

66. Wang, Y. and Zhang, L. (2008) High-strength waterborne polyurethane reinforced with waxy maize starch nanocrystals. *J. Nanosci. Nanotechnol.*, **8**, 5831–5838.

67. Chang, P.R., Ai, F., Chen, Y., Dufresne, A., and Huang, J. (2009) Effects of starch nanocrystal-graft-polycaprolactone on mechanical properties of waterborne polyurethane-based nanocomposites. *J. Appl. Polym. Sci.*, **111**, 619–627.

68. Zou, J., Zhang, F., Huang, J., Chang, P.R., Sub, Z., and Yud, J. (2011) Effects of starch nanocrystals on structure and properties of waterborne polyurethane-based composites. *Carbohydr. Polym.*, **85**, 824–831.

69. Chen, C., Justice, R.S., Schaefer, D.W., and Baur, J.W. (2008) Highly dispersed nanosilica–epoxy resins with enhanced mechanical properties. *Polymer*, **49**, 3805–3815.

70. Gojny, F., Wichmann, M., Köpke, U., Fiedler, B., and Schulte, K. (2004) Carbon nanotube-reinforced epoxy-composites: enhanced stiffness and fracture toughness at low nanotube content. *Compos. Sci. Technol.*, **64**, 2363–2371.

71. Yu, H.-Y., Qin, Z.-Y., Liu, Y.-N., Chen, L., Liu, N., and Zhou, Z. (2012) Simul-taneous improvement of mechanical properties and thermal stability of bacterial polyester by cellulose

nanocrystals. *Carbohydr. Polym.*, **89**, 971–978.

72. Chen, G., Dufresne, A., Huang, J., and Chang, P.R. (2009) A novel thermo-formable bionanocomposite based on cellulose nanocrystal-graft-poly (ɛ-caprolactone). *Macromol. Mater. Eng.*, **294**, 59–67.

73. Liu, X., Lin, T., Gao, Y., Xu, Z., Huang, C., Yao, G., Jiang, L., Tang, Y., and Wang, X. (2012) Antimicrobial electrospun nanofibers of cellulose acetate and polyester urethane composite for wound dressing. *Soc. Biomater.*, **100B**, 1556–1565.

74. Jung, K.H., Huh, M.W., Meng, W., Yuan, J., Hyun, S.H., Bae, J.S., Hudson, S.M., and Kang, I.K. (2007) Preparation and antibacterial activity of PET/Chitosan nanofibrous mats using an electrospinning technique. *J. Appl. Polym. Sci.*, **105**, 2816–2823.

75. Jiang, L., Morelius, E., Zhang, J., Wolcott, M., and Holbery, J. (2008) Study of the poly (3-hydroxybutyrate-co-3-hydroxyvalerate)/cellulose nanowhisker composites prepared by solution casting and melt processing. *J. Compos. Mater.*, **42**, 2629–2645.

76. Lin, N., Yu, J., Chang, P.R., Li, J., and Huang, J. (2011) Poly(butylene succinate)-based biocomposites filled with polysaccharide nanocrystals: structure and properties. *Polym. Compos.*, **32**, 472–482.

77. Weidong, L. and Enyong, D. (2006) Characterization of PET fabric surface modified by graft cellulose nano-crystal using TGA, FE-SEM and XPS. *Surf. Rev. Lett.*, **13**, 819–823.

78. Zaman, M., Liua, H., Xiaoa, H., Chibantec, F., and Ni, Y. (2013) Hydrophilic modification of polyester fabric by applying nanocrystalline cellulose containing surface finish. *Carbohydr. Polym.*, **91**, 560–567.

79. Peng, X., Ding, E., and Xue, F. (2012) In situ synthesis of TiO2/polyethylene terephthalate hybrid nanocomposites at low temperature. *Appl. Surf. Sci.*, **258**, 6564–6570.

80. Li, W.D. and Ding, E.Y. (2007) Preparation and characterization of poly(ethylene tereph-thalate) fabrics

treated by blends of cellulose nanocrystals and polyethylene glycol. *J. Appl. Polym. Sci.*, **105**, 373–378.

81. Li, F., Biagionib, P., Finazzib, M., Silvia Tavazzic, S., and Piergiovannia, L. (2013) Tunable green oxygen barrier through layer-by-layer self-assembly of chitosan and cellulose nanocrystals. *Carbohydr. Polym.*, **92**, 2128–2134.

82. Yu, J., Ai, F., Dufresne, A., Gao, S., Huang, J., and Chang, P.R. (2008) Structure and mechanical properties of poly (lactic acid) filled with (Starch nanocrystal)-graft-poly (ɛ-caprolactone). *Macromol. Mater. Eng.*, **293**, 763–770.

83. Lin, N., Chen, G., Huang, J., Dufresne, A., and Chang, P.R. (2009) Effects of polymer-grafted natural nanocrystals on the structure and mechanical properties of poly (lactic acid): a case of cellulose whisker-graft-polycaprolactone. *J. Appl. Polym. Sci.*, **113**, 3417–3425.

84. Zhang, Z. and Ren, P. (2008) Research status of starch-based biodegradable plastic. *Mater. Rev.*, **7**, 013.

85. Chen, Y., Liu, C., Chang, P.R., Anderson, D.P., and Huneault, M.A. (2009) Pea starch-based composite films with pea hull fibers and pea hull fiber-derived nanowhiskers. *Polym. Eng. Sci.*, **49**, 369–378.

86. Cao, X., Chen, Y., Chang, P.R., Muir, A.D., and Falk, G. (2008) Starch-based nanocomposites reinforced with flax cellulose nanocrystals. *eXPRESS Polym. Lett.*, **2**, 502–510.

87. Angles, M.N. and Dufresne, A. (2000) Plasticized starch/tunicin whiskers nanocomposites 1. Structural analysis. *Macromolecules*, **33**, 8344–8353.

88. Angles, M.N. and Dufresne, A. (2001) Plasticized starch/tunicin whiskers nanocomposite materials 2. Mechanical behavior. *Macromolecules*, **34**, 2921–2931.

89. Kvien, I., Sugiyama, J., Votrubec, M., and Oksman, K. (2007) Characterization of starch based nanocomposites. *J. Mater. Sci.*, **42**, 8163–8171.

90. Kaushik, A., Singh, M., and Verma, G. (2010) Green nanocomposites based on thermoplastic starch and steam exploded cellulose nanofibrils from

wheat straw. *Carbohydr. Polym.*, **82**, 337–345.

91. Angellier, H., Molina-Boisseau, S., Dole, P., and Dufresne, A. (2006) Thermoplastic starch-waxy maize starch nanocrystals nanocomposites. *Biomacromolecules*, **7**, 531–539.

92. Averous, L. and Boquillon, N. (2004) Biocomposites based on plasticized starch: thermal and mechanical behaviours. *Carbohydr. Polym.*, **56**, 111–122.

93. Avérous, L. and Halley, P.J. (2009) Biocomposites based on plasticized starch. *Biofuels, Bioprod. Biorefin.*, **3**, 329–343.

94. Liu, D., Zhong, T., Chang, P.R., Li, K., and Wu, Q. (2010) Starch composites reinforced by bamboo cellulosic crystals. *Bioresour. Technol.*, **101**, 2529–2536.

95. Sakurada, I., Nukushina, Y., and Ito, T. (1962) Experimental determination of the elastic modulus of crystalline regions in oriented polymers. *J. Polym. Sci.*, **57**, 651–660.

96. Eichhorn, S.J., Baillie, C.A., Zafeiropoulos, N., Mwaikambo, L.Y., Ansell, M.P., Dufresne, A., Entwistle, K.M., Herrera-Franco, P.J., Escamilla, G.C., Groom, L., Hughes, M., Hill, C., Rials, T.G., and Wild, P.M. (2001) Review: current international research into cellulosic fibres and composites. *J. Mater. Sci.*, **36**, 2107–2131.

97. Bogoeva-Gaceva, G., Avella, M., Malinconico, M., Buzarovska, A., Grozdanov, A., Gentile, G., and Errico, M.E. (2007) Natural fiber eco-composites. *Polym. Compos.*, **28**, 98–107.

98. Zainuddina, S.Y.Z., Ahmad, I., Kargarzadeh, H., Abdullah, I., and Dufresne, A. (2013) Potential of using multiscale kenaf fibers as reinforcing filler in cassava starch-kenaf biocomposites. *Carbohydr. Polym.*, **92**, 2299–2305.

99. Ojijo, V. and Ray, S.S. (2013) Processing strategies in bionanocomposites. *Prog. Polym. Sci.*, **38**, 1543–1589.

100. Dash, R., Foston, M., and Ragauskas, A.J. (2013) Improving the mechanical and thermal properties of gelatin hydrogels cross-linked by cellulose nanowhiskers. *Carbohydr. Polym.*, **91**, 638–645.

101. Draye, J.P., Delaey, B., Van De Voorde, A., Van Den Bulcke, A., Bogdanov, B., and Schacht, E. (1998) In vitro release characteristics of bioactive molecules from dextran dialdehyde cross-linked gelatin hydrogel films. *Biomaterials*, **19**, 99–107.

102. Huang, J., Lin, N., Chen, Y., Chang, P.R., and Yu, J. (2011) in *Nanocomposites with Biodegradable Polymers: Synthesis, Properties and Future Perspectives* (ed. V. Mittal), Oxford University Press, New York, pp. 261–282.

103. Xiang, L.X., Tang, C.Y., Cao, J., Wang, C.Y., Wang, K., Zhang, Q., and Fu, Q. (2009) Preparation and characterization of soy protein isolate (SPI)/montmorillonite (MMT) bionanocomposites. *Chin. J. Polym. Sci.*, **27**, 843–849.

104. Lu, Y., Weng, L., and Zhang, L. (2004) Morphology and properties of soy protein isolate thermoplastics reinforced with chitin whiskers. *Biomacromolecules*, **5**, 1046–1051.

105. Gao, Q., Li, J., Shi, S.Q., Liang, K., and Zhang, X. (2012) Soybean meal-based adhesive reinforced with cellulose nanowhiskers. *Bioresources*, **7**, 5622–5633.

106. Zheng, H., Ai, F., Chang, P.R., Huang, J., and Dufresne, A. (2009) Structure and properties of starch nanocrystal-reinforced soy protein plastics. *Polym. Compos.*, **30**, 474–480.

107. Tzoumaki, M.V., Moschakis, T., and Biliaderis, C.G. (2011) Mixed aqueous chitin nanocrystal–whey protein dispersions: microstructure and rheological behaviour. *Food Hydrocolloids*, **25**, 935–942.

108. Li, R., Zhang, Y., Zhu, L., and Yao, J. (2012) Fabrication and characterization of silk fibroin/poly(ethylene glycol)/cellulose nanowhisker composite films. *J. Appl. Polym. Sci.*, **124**, 2080–2086.

6

Polysaccharide Nanocrystals-Based Materials for Advanced Applications

Ning Lin, Jin Huang, and Alain Dufresne

6.1
Introduction

Materials, together with energy and information, are regarded as the key industries in the world economy of the twenty-first century. With the recent development of nanotechnology, a new scientific field of materials chemistry and physics that emphasizes on the rational synthesis and study of nanoscale materials has emerged. Functional nanomaterials are especially an attractive topic because they enable the creation of materials with new or improved properties by mixing multiple constituents and exploiting synergistic effects, such as electronic, optical, magnetic, and catalytic properties or bioactivity, selective permeation, adsorption, and so on. With a special property or several remarkable functions, functional nanomaterials are a type of high added-value materials possessing potential applications in specific fields [1]. Polysaccharides such as cellulose and chitin are naturally occurring polymers found abundantly in nature as structural building blocks. Other polysaccharides (such as starch) provide stored solar energy in the form of sugar for fuel cells. As indicated by the European Polysaccharide Network of Excellence (EPNOE), research on polysaccharide has attracted tremendous academic interest and fundamental understanding that will boost the development of applications, not only limited to replacing the present oil-based chemistry but also opening up new fields and markets [2].

With the mechanically and/or chemically induced destructuring strategies [3], highly crystalline polysaccharide nanocrystals (PNs) can be obtained, most commonly rod-like cellulose nanocrystals (CNs), chitin nanowhiskers (ChWs), and platelet-like starch nanocrystals. The advantages of natural PNs over inorganic nanoparticles have been reported in many reviews, mainly consisting of availability, biocompatibility, biodegradability, comparatively easy processability, and low cost. Meanwhile, as described in detail in Chapter 2, special structures and properties appear on PNs, such as diverse surface characteristics including active hydroxyl groups, negative charges, rigid nanoparticles; unique nano-reinforcing

effects; special chiral nematic ordering phenomenon; and promising barrier property. The application and role of PNs in various functional materials are closely related to these interesting physical and chemical properties.

6.2
Surface Characteristics Induced Functional Nanomaterials

Even the most rigorous researcher will be attracted by the diverse and interesting surface characteristics of PNs. First of all, PNs possess a reactive surface covered with numerous active hydroxyl groups (–OH), which provide the possibility of modification via a chemical reaction strategy. Through the chemical grafting routes, various functional molecules or polymeric chains (such as fluorescent molecules, DNA, peptide, etc.) can be introduced on the surface of nanocrystals, with the aim of tailoring physicochemical properties and achieving novel functions. In addition, surface hydroxyl groups of PNs (especially CNs) can be used for anchoring and stabilizing sites, which provides a preferential template or scaffold for these natural nanocrystals during the synthesis of various inorganic nanoparticles. On the other hand, the negatively charged surface (sulfated groups $-OSO_3H$) of CNs from H_2SO_4 hydrolysis induces electrostatic stabilization of nanoparticles in aqueous medium and also provides the feasibility to perform electrostatic adsorption or grafting. Using the reactions of the surface charges, CNs, chitin whiskers, or starch nanocrystals can be constructed as high-efficiency adsorbing materials and emulsion nanostabilizers. Finally, as nanoscaled particles, CNs and starch nanocrystals exhibited promising bioactivity and biocompatibility in cellar cultivation and high surface area for application in water decontamination.

6.2.1
Active Groups

As discussed in Chapter 3, PNs are active chemicals because of the presence of hydroxyl groups in each anhydroglucose unit. These surface hydroxyl groups are therefore responsible for the physical or chemical reactions of PNs in introducing functional groups or molecules on the surface of nanocrystals.

6.2.1.1   Importing Functional Groups or Molecules
Since the first report on the fluorescent labeling of CNs with fluorescein-5′-isothiocyanate (FITC) molecules [4], more and more researchers have investigated fluorescent modifications on the surface of CNs. Modification on CNs with fluorescent labeling enables the potential use of nanocrystals in the field of biomedical applications, such as optical bioimaging, biosensors, bioprobes, and photodynamic therapy (PDT), together with diverse fluorescence techniques, such as spectrofluorometry, fluorescence microscopy, and flow cytometry. Besides the most common FITC reagent, attempts have been made to covalently attach many other fluorescent molecules on the surface of CNs, such as rhodamine B

isothiocyanate (RBITC) [5], pyrene dyes [6], terpyridine and its derivatives [7, 8], tryptophan-based peptides [9], 1-pyrenebutyric acid *N*-hydroxysuccinimide ester (PSE) [10], 5-(and-6)-carboxyfluorescein succinimidyl ester (FAM-SE), 5-(and-6)-carboxytetramethylrhod-amine succinimidyl ester (TAMRA-SE), Oregon Green 488 carboxylic acid, succinimidyl ester (OG-SE) [11], and polyethylenimine (PEI)-chlorin *p6* derivatives [12]. So far, however, most studies focused on the pathway to introduce fluorescent molecules on CNs, but rarely covered the *in vivo* or even clinic research. Consequently, there is a long way to go before the practical application of fluorescent PNs in biomedical materials.

The immobilization and recognition of enzymes and proteins on a carrier matrix is a powerful technique and hot topic in biomedical applications. An ideal matrix for enzyme/protein immobilization should be biocompatible without compromising the protein structure and biological activity. Furthermore, this carrier material should be easily processed to enhance the enzyme/protein loading and activity as well as the stability in both operation and storage. As a material that is nontoxic, noncarcinogenic, biocompatible, and in no way injurious in the biological environment, PNs meet the rigid medical requirements of suitable carriers for the immobilization of enzyme and protein. Another key point in enzyme/protein immobilization is the selection of immobilization methods, such as adsorption, entrapment, and covalent binding. Available hydroxyl groups and negative charges on the surface of PNs provide the possibility of enzyme/protein immobilization on the basis of chemical conjunction and electrostatic adsorption. As for the approach of chemical conjunction, some studies directly immobilized enzymes/proteins on CNs with chemical grafting, such as immobilization of lysozyme on aminoglycine-CN with carbodiimide activation coupling reaction [13]; and peroxidase on CN with the activation of cyanogen bromide treatment [14]. Another approach consists in first functionalizing with smaller nanoparticles (generally gold nanoparticles Au), and then realizing the immobilization of enzyme/protein on CNs with the aid of inorganic nanoparticles. Luong *et al.* investigated Au/CN as a catalytic platform for enzyme immobilization, which exhibited significant biocatalytic activity and preservation of original activity. The recovered specific activities were ~70% and 95% for enzymes of CGTase and alcohol oxidase [15]. A more complicated carrier based on CN/PEI/Au was developed to immobilize glucose oxidase enzyme [16]. Mahmoud *et al.* developed a special nanocomposite consisting of magnetite nanoparticles (Fe_3O_4) and Au nanoparticles embedded on CNs used as a magnetic support for the covalent conjugation of papain and facilitated recovery of this immobilized enzyme [17]. The conjugated material retained high enzyme activity and good stability and reusability. On the basis of a similar strategy of enzyme/protein immobilization, labeled DNA or enzyme was immobilized on CNs as a probe; this material can be used for the identification or recognition of target DNA sequence and enzyme molecules, and as a platform for immunoassays and diagnostics [18, 19]. Recently, Edwards *et al.* reported a colorimetric approach to the detection of human neutrophil elastase (HNE) using peptide conjugated cotton CNs. A HNE tripeptide substrate was covalently attached to glycine-esterified CNs and

compared with a similar tetrapeptide analog for colorimetric HNE sensor activity. According to the study, colorimetric detection of HNE requires the use of only a few milligrams of the peptide–CN complex to yield a visually detectable response at HNE levels previously reported in chronic wounds [20].

There are some reports focusing on the functional modification of PNs (especially for CNs) for potential biological application. Surface grafting of amino acid molecules can offer biologically active building blocks on CNs, which may contribute to the potential of CNs to be used as nanocarrier for drug delivery applications [21]. Using the molecular recognition ability of DNA oligomeric base pairs, duplexing complementary DNA oligonucleotides can be grafted onto CNs, which produces special DNA-based biocompatible nanomaterials [22]. Ferrocene-decorated CNs can be prepared by grafting ethynylferrocene onto azide functionalized CNs using azide–alkyne cycloaddition reaction, which can be assembled in three-dimensional structures for application in biosensors and bioelectrochemical assemblies [23]. Click chemistry has also been utilized for the grafting of imidazolium salt ([MPIM][Br] (1-methyl-3-propargylimidazolium bromide)) on the surface of CNs. The bromide anion on the modified nanocrystals can be used for ion exchange of bistriflimide and the anionic dye, which provides the opportunity to synthesize a wide variety of ion exchange systems or catalysts using PNs as a support medium [24]. CNs can be covalently grafted on cationic porphyrin groups, which showed excellent efficiency of photodynamic inactivation toward bacteria. This strategy can be used in the development of potential photobactericidal nanomaterials [25, 26].

6.2.1.2 Template for Synthesizing Inorganic Nanoparticles

The strategy of using natural nanocrystals as templates for synthesizing inorganic nanoparticles breaks new ground to make optimum use of inorganic materials, such as rare noble metal resources, in association with the most abundant and renewable bioresources. As a promising template in the synthesis of inorganic nanoparticles, PNs (mainly CNs) always play the roles of reducing agent, structure-directing agent, and stabilizer during the reactions.

Using partially ordered rod-like CN suspensions as the template, mesoporous silica (Si and SiO_2) nanoparticles can be fabricated by sol–gel mineralization, which exhibit aligned cylindrical pores with a diameter of 13–18 nm [27–30]. Shin *et al.* prepared biomorphic silicon carbide (SiC) materials, which were typical aggregations of β-SiC nanoparticles with thermal treatment of wood/silicic acid at high temperature in the absence of oxygen. It is worth noting that in comparison with the different roles of three natural biotemplates (lignin, amorphous bleached cellulose, and CNs) during the synthesis of SiC nanoparticles, only the template of CNs can produce clean and uniform SiC nanowires (70 nm in diameter, >100 μm in length) without the camelback structure [31]. A homogeneous hybrid nanomaterial composed of inorganic calcium carbonate ($CaCO_3$) nanoparticles and organic CNs can be produced with the template of natural nanocrystals. This organic–inorganic hybrid material exhibited an even distribution of different nanoparticles, promoting an optically transparent and relatively hard surface [32].

Synthesis of silver (Ag) nanoparticles was carried out by 2,2,6,6-tetra-methylpiperidine-1-oxyradical (TEMPO)-mediated oxidation of CNs as the scaffold by reducing metallic cations using $NaBH_4$. The carboxyl and hydroxyl groups of carboxylated CNs provided a coordination effect to adsorb metallic cations and reduce Ag^+ to Ag^0 [18]. Similarly, under mild alkaline conditions, the periodate oxidation of CNs generating aldehyde functions can also reduce silver ions to form Ag nanoparticles [33]. Using bacterial CNs, Ag nanoparticles can be template-prepared by a method involving an ion-exchange reaction of sodium with the silver salt and its thermal reduction, leading to the production of stable silver particles with a controlled size distribution and high density on the surface of CNs [34]. Gold (Au) nanoparticles can be obtained on crystalline cellulose single nanofibers with a topochemical reduction reaction. It is particularly worth noting that the Au@CN exhibited an excellent catalytic efficiency in comparison with conventional polymer-supported Au nanoparticles [35, 36]. Uniform Au−Ag alloy nanoparticles have been synthesized on CNs by the co-reduction of the corresponding metal ions. The composition of alloy nanoparticles can affect the dimension of the resultant nanoparticles, which increases with increase in Ag content [37]. Recently, with the same method, Ag−Pd alloy nanoparticles were synthesized with carboxylated CNs as the scaffold, and the morphology and dimension were similar to Au−Ag alloy nanoparticles [38]. Padalkar *et al.* systemically investigated the effects of the concentration of the surfactant, salt solution, reaction time, and pH of the salt solution on the average size of synthesized inorganic nanoparticles (Ag, Cu, Au, and Pt) and coverage on CNs [39].

Using a hydrothermal process (400−500 °C) nickel (Ni) nanocrystals were simply prepared on carbon through a thermal reduction process after Ni(II) ions were deposited and stabilized on a CN surface [31]. Another study reported the synthesis of platinum (Pt) nanoparticles at relatively low temperatures in aqueous solution from hexachloroplatinic acid using CNs as reducing agents. The synthesis involves heating an aqueous solution of H_2PtCl_6 containing CNs at only 80 °C [40]. In addition, by introducing a carbon support into the synthesis and removing the cellulose by burning it after the reaction, it was possible to produce carbon-supported Pt particles [41]. Similarly, in the hydrothermal process at 120−160 °C, CNs can also be used as the template in the synthesis of selenium (Se) nanoparticles [42]. The reaction temperature affects the dimension of interfacially bound Se nanoparticles. Under mild conditions, the synthesis of monodispersed palladium (Pd) nanoparticle consisted of the reduction reaction with homogeneous colloidal CNs. The excellent active catalyst effect of the Pd@CN nanoparticles in the Heck coupling of styrene and iodobenzene was investigated, which proved the possibility of using colloidal CNs as an efficient support for catalysis [43]. The synthesis of cadmium sulfide (CdS), zinc sulfide (ZnS), and lead sulfide (PbS) nanoparticles on tunicate CN templates can be accomplished by the reaction of the precursor salt, namely, the cationic surfactant cetyltrimethylammonium bromide (CTAB) [44]. The dimensions and packing densities of semiconductor nanoparticles on the surface of CNs could be controlled by variation of the precursor concentration and the pH of the salt solution. Titania (Ti) core−shell and hollow nanoparticles with

different aspect ratios were synthesized using layer-by-layer (LBL) assembly and sol–gel nanocoating method with CNs as the template. It is shown that the overall shape and aspect ratio of Ti nanoparticles can be controlled by choosing different sizes of templates and coating thickness during LBL or sol–gel templating synthesis [45]. When using only $TiCl_4$ and CNs as the starting materials, TiO_2 nanocubes can be synthesized. The introduction of CNs that acted as morphology inducer and coordinating agent results in acceleration of the crystal growth of TiO_2 particles and promotes the formation of nanocube morphology [46]. The preparation of porous TiO_2 nanocluster with different shapes [42], low-temperature synthesis of flower-like TiO_2 nanocrystals [47] using CNs as the template, and investigation of the photocatalytic activity of TiO_2/CNs are also reported [48]. Figure 6.1 shows the different morphologies and dimensions of various inorganic nanoparticles obtained through templated synthesis with CNs.
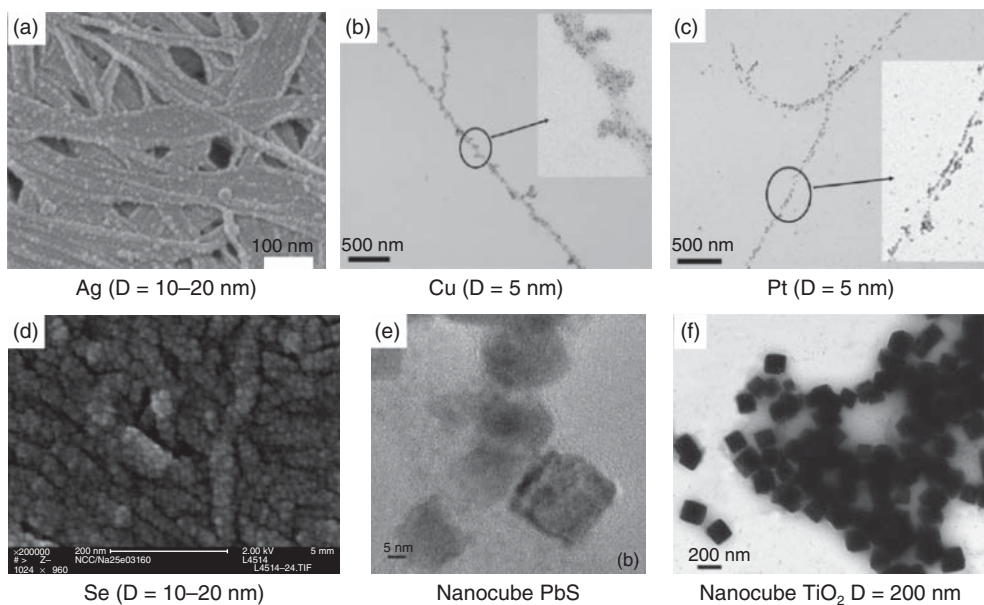
Figure 6.1 Morphologies and dimensions of inorganic nanoparticle templated synthesis with cellulose nanocrystals. (a) Ag nanoparticles. Reproduced from [34], copyright 2009 © permission from The American Chemical Society. (b) Cu nanoparticles. Reproduced from [39], copyright 2010 © permission from The American Chemical Society. (c) Pt nanoparticles. Reproduced from [39], copyright 2010 © permission from The American Chemical Society. (d) Se nanoparticles. Reproduced from [42], copyright 2007 © permission from Elsevier (e) PbS nanoparticles. Reproduced from [44], copyright 2011 © permission from Springer. (f) TiO_2 nanocubes. Reproduced from [46], copyright 2007 © permission from Elsevier.

On the basis of template synthesis of inorganic nanoparticles with PNs, some organic/inorganic hybrid nanomaterials were reported. Especially for the combination of Ag nanoparticles and CNs, the ensuing materials exhibited antimicrobial property from nano-Ag and enhanced mechanical performance from CNs [49, 50].

6.2.2
Surface Charges and Hydrophilicity

Three kinds of PNs are generally prepared by sulfuric acid hydrolysis inducing the formation of sulfate ester groups ($-OSO_3^-/H^+$) on the surface of the nanoparticles via an esterification process. These charged moieties, the density of which increases with the severity (acid concentration, time, temperature) of the treatment, induce the formation of a negative electrostatic layer covering the nanocrystals and promote high stability of the H_2SO_4-prepared nanocrystal aqueous suspensions. Meanwhile, surface negative charge provides accessibility to electrostatic adsorption and conjunction with cationic groups or molecules. With the negative charges on the surface of PNs, some structural materials (such as LBL assembled nanomaterials) and functional materials (such as emulsion nanostabilizers and adsorbed or permselective materials) can be realized.

6.2.2.1 Emulsion Nanostabilizer

Research efforts on the development of sustainable, biodegradable, and nontoxic solid particle emulsion stabilizers have not stopped since several decades ago. Capron and coworkers first introduced CNs in emulsion and investigated their effects on stabilizing the emulsion. CNs were dispersed in water with the required concentration, and hexadecane was added later. The oil/aqueous phase ratio of the prepared emulsion was controlled to be 30/70 (v/v), and the aqueous and oil phase biphasic system can form the emulsion. Capron and coworkers observed that because of their hydrophilic surface and nanoscale, CNs that promote monodispersed oil (hexadecane) in water droplets around 4 mm in diameter were stable for several months, which proved the promising ability of CNs to stabilize the hexadecane–water interface [51]. A subsequent study proved the fact that neutral CNs dispersed in water can stabilize oil/water interfaces and produce Pickering emulsions with outstanding stability, whereas sulfated nanocrystals did not show this interfacial property [52]. Surface charge density of CNs can be modulated by various postsulfation/desulfation treatments. Regardless of the crystalline origin, electrostatic interaction played a major role in the control of the interface of oil and water. CNs with a surface charge density above $0.03 \, e/nm^2$ were not able to efficiently stabilize at the oil/water interface, whereas a decreasing surface charge density led to stable emulsions. Recently, Capron and Cathala investigated the formation of gel structure from oil-in-water high internal phase emulsions by colloidal network of CNs. They found that this high internal phase emulsions is only possible when a Pickering emulsion is prepared first, suggesting that a reorganization of CNs at the oil/water interface occurs as

the volume of the internal phase and the interfacial area increases [53]. Zoppe *et al.* compared different nanostabilized effects of CNs before and after polymer brushes grafting. Water-continuous Pickering emulsions produced by thermoresponsive poly(NIPAM) (poly(*N*-isopropylacrylamide)) brushes grafted onto CNs can be stable during the time of observation for 4 months, whereas unmodified nanocrystals were unable to stabilize heptane-in-water emulsions [54].

Biliaderis and coworkers studied the oil-in-water emulsion stabilizing ability of chitin nanocrystals, the factors that affect the properties of emulsion systems, and *in vitro* lipid digestion of chitin nanocrystal stabilized oil/water emulsions [55, 56]. Chitin nanocrystals were proved to be quite effective in stabilizing oil/water emulsions against coalescence over a period of 1 month, which can be attributed to the inter-droplet network structure and the formation of a chitin nanocrystal network in the continuous phase from the adsorption of the nanocrystals at the oil–water interface. At the same time, it was shown that the increase in chitin nanocrystal concentration, NaCl concentration, pH, and temperature led to smaller droplets, higher stability to creaming, and enhancement of the emulsion elastic structure.

Platelet-like starch nanocrystals also possess the ability of emulsion nanostabilization. Using starch nanocrystals as emulsifier at concentrations above 0.02 wt%, oil-in-water emulsions of 50 vol% paraffin liquid that are stable over months can be obtained. The size of the droplets decreased with increase in the starch nanocrystals' concentrations [57]. The potential of starch nanocrystals to stabilize emulsion droplets was used to promote miniemulsion polymerization. During the polymerization, starch nanocrystals can provide a synergistic stabilization effect when used together with a cationic surfactant, reducing the required surfactant amount by a factor of 4. Stabilized monomer emulsion droplets remained stable throughout the polymerization reaction and did not show any sign of Ostwald ripening [58].

6.2.2.2 High-Efficiency Adsorption

As the surface of PNs is negatively charged, their direct application should involve adsorption against positively charged molecules. On the basis of this strategy, Hsiao and coworkers developed some efficiently adsorbed membranes from cellulose nanofibers and nanocrystals and chitin nanofibers [59, 60]. Generally, CNs were anchored on the matrix surface, forming a cross-linked nanostructured mesh with very high surface-to-volume ratio and a negatively charged surface. The mean pore size and pore size distribution of this system could be adjusted by the loading of CNs, where the resulting membrane not only possessed good mechanical properties but also high surface charge density. The CN-based membrane thus prepared exhibited 16 times higher adsorption capacity against a positively charged dye over a commercial nitrocellulose-based membrane [61].

6.2.2.3 Permselective Membrane

The negatively charged sulfate groups on the surface of CNs can be used to develop permselective membranes, which are attributed to the inhibition of negatively charged species but admission of positively charged species. A suspension

of cotton CNs (1.5 wt%) was used to form membranes at glassy carbon electrodes with simple drop-coating procedures. Stable nanoporous thin membranes can be formed at the electrode surface with the interparticle hydrogen bonding between the negatively charged nanocrystals. The drop-coated CNs formed a porous layer with 50–100 nm pores visible throughout the layer. Owing to the negatively charged surface, this nanostructured membrane exhibits permselective behavior toward substances with different charge properties. It was shown that positively charged ruthenium hexamine [$Ru(NH_3)_6^{3+}$] was significantly adsorbed by the membrane, with a large value of permeability (P) of 216%, whereas the negatively charged potassium hexachloroiridate [$IrCl_6^{3-}$] was almost excluded by the membrane, with a P value of only 33.9%. From the charge transport process, partition of redox species, and effect of deposition time on cation partition into the membrane, it was proved that the diffusion of the cationic and neutral mediators was not significantly impeded by the CN membrane, whereas for the anionic mediator it was just the opposite [62].

6.2.3
Nanoscale and High Surface Area

Because of the properties of porosity, biocompatibility, and right mechanical property similar to natural tissue, PN-based biomaterials (especially for CNs) can provide a cell-friendly environment to encourage attachment and proliferation of cells as a special tissue bioscaffold. Furthermore, derived from the nanoscale dimensions, PNs have a high surface area (several hundred square meters per gram), which is useful and efficient to adsorb organic molecules and other nanoparticles for water purification.

6.2.3.1 Surface Cell Cultivation
As for the CN-based mediums for the cultivation of cells, most studies applied conventional suspensions of unmodified or fluorescent-modified nanocrystals as the environment for cells. From insect cells S*f*9 and Hamster lung fibroblast V79 to human foreskin fibroblasts and human embryonic kidney cells HEK-293, no significant cytotoxicity to various cell models was found, and promising cellular uptake and proliferation were reported in these studies [5, 63, 64]. Recently, using a spin-coating method, Dugan *et al.* prepared a submonolayer film with oriented surfaces of adsorbed CNs. Owing to the shape and nanoscale dimensions of CNs, murine myoblast cells C2C12 adopted increasingly oriented morphologies in response to more densely adsorbed and oriented nanocrystal surfaces (Figure 6.2). With a mean feature height of only 5–6 nm, CN surfaces presented the smallest features ever reported to induce contact guidance in skeletal muscle myoblasts [65, 66].

6.2.3.2 Water Decontamination
The abundant availability, particularly high specific surface area, of PNs, coupled with their low cost, renewability, wide variability in processing options, and

(a) (b)
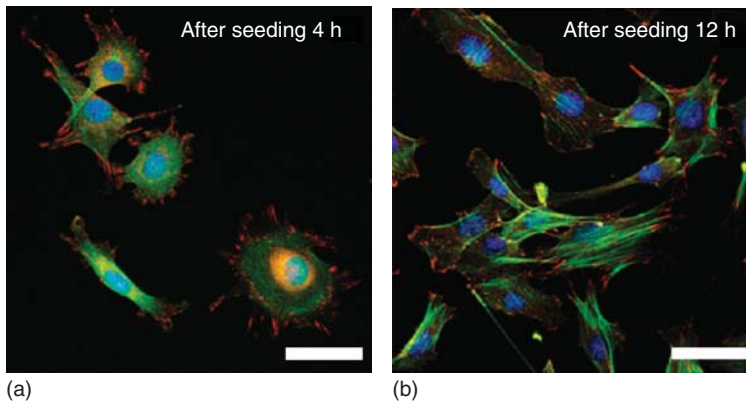
Figure 6.2 (a,b) Myoblasts cells C2C12 was cultivated on the surface of oriented cellulose nanocrystals. Cell was stained for vinculin (red), F-actin (green), and nuclei (blue), scale bar = 50 μm. Reproduced from [66], copyright 2010 © permission from The American Chemical Society.

nontoxicity represent strong drivers for their use as water treatment agents. Boufi *et al.* have attempted to utilize stearic acid chain-modified starch nanocrystals in removing dissolved organic pollutants from water. It was proved that the grafted stearate long chains enhanced the adsorption capacity of aromatic organic compounds on the nanometric substrate, which ranged between 150 and 900 mmol g^{-1} and the maximum adsorption can reach 100 mg g^{-1}. The values of adsorption capacity and the maximum adsorption amount of stearate-modified starch nanocrystals are comparative to nanographite and are half those of the activated carbon [67]. Recently, the ability of CN-based materials in water purification was investigated. A double layer of polyacrylonitrile electrospun membrane reinforced with TEMPO-oxidized CNs was prepared, which showed efficient filtration capacity for 7–40 nm nanoparticles and oil/water separation (with rejection of over 99%) [68].

6.3
Nano-Reinforcing Effects in Functional Nanomaterials

The hierarchical structure of natural fibers, based on their elementary nanofibrilar components, leads to unique strength and high performance properties. Indeed, the most important attributes of PNs are their mechanical properties, in particular, their unusual ability to provide high mechanical strength and high strength-to-weight ratio. The modulus of natural polysaccharide microfibrils is expected to result from a mixing rule between the modulus of the crystalline domains and the amorphous fraction. Therefore, it should be higher for more crystalline regions of polysaccharide nanoparticles [3]. For example, the Young's modulus of CNs of crystalline cellulose with a density of around 1.5–1.6 g cm^{-3}

is much higher than that of glass fibers, around 70 GPa with a density around 2.6 g cm^{-3}, which are classically used in composite applications. It is similar to Kevlar (60–125 GPa, density around 1.45 g cm^{-3}) and potentially stronger than steel (200–220 GPa, density around 8 g cm^{-3}). These impressive mechanical properties make PNs ideal candidates for the processing of reinforced matrices and development of functional nanomaterials.

6.3.1
Soft Matter

6.3.1.1 **Hydrogel**
Hydrogels are defined as three-dimensional polymer networks that are swollen by, and trap, large amounts of solvent (usually water), and that are widely used in the fields of food, biomaterials, agriculture, and so on. Hydrogels from PNs (rod-like CNs or ChWs) are usually divided into two types. One is the direct preparation from a suspension of PNs; another is the composite hydrogels preparation from PN-reinforced matrices. Rod-like CNs or chitin whiskers can form gels by themselves under some conditions resulting from the strong hydrogen bonding interactions between nanoparticles. Aqueous suspensions with 0.4 wt% CNs extracted from softwood flour can form a transparent hydrogel with a unique rigid and uniform morphology, and the elastic solid-like behavior of hydrogel is dependent on the mechanical agitation [69]. With the increase of concentration, ChWs derived from crab shell aqueous dispersions shifted from the flowing sol to nematic solid-like hydrogel [70]. In addition, by involving the solvent exchange process, CNs were proved to be able to form stable macroscopic organogels in glycerol [71], ethanol [72], or acetone [73]. More recently, Way *et al.* reported the different gelation behaviors of surface-modified CNs with either carboxylic acid (–COOH) or amine (–NH$_2$). At low pH, amine-modified nanocrystals formed fluid suspension because of the electrostatic repulsions of the ammonium moieties inhibiting aggregation of nanoparticles. However, a transition to hydrogels was observed at higher pH where the amine-modified nanocrystals are neutral and the attractive forces based on hydrogen bonding dominate. The opposite behavior was observed for carboxylated CNs, which were dispersible in water at high pH and formed stable hydrogels in an acidic environment [74].

On the basis of the cross-linking method, composite hydrogels can be divided into chemical gels and physical gels. Physical gels are formed by molecular self-assembly through ionic or hydrogen bonds, while chemical gels are formed by covalent bonds. The introduction of rigid PNs in polymeric matrices to prepare physical hydrogel nanomaterials generally improves structural stability and enhances the elastic modulus. To date, it is reported that CNs have been used in various synthetic polymeric matrices for the preparation of gel nanomaterials, such as PEG (poly(ethylene glycol)) [75], PVA (poly(vinyl alcohol)) [76, 77], PHEMA (poly(2-hydroxyethylmethacrylate)) [78, 79], PAM (polyacrylamide) [80, 81], poly(NIPAM-*co*-BMA) (poly(*N*-isopropylacrylamide-*co*-butyl methacrylate)) [82], starch-*g*-poly(sodium acrylate) [83], as well as natural

polymeric matrices, for instance, regenerated cellulose [84], agarose [85–87], and cyclodextrin [88].

On the other hand, CN-based hydrogels can also be obtained with chemical cross-linking methods, such as the *in situ* cross-linking of CNs with poly(MVE-*co*-MA)–PEG (poly(methyl vinyl ether-*co*-maleic acid)–polyethylene glycol) [89, 90], gelation [91], PAA (poly(acrylic acid)) [92], and poly(NIPAM) [93]. Lin and Dufresne reported the strategy of *in situ* conjunction of CNs in supramolecular hydrogels with the aid of host–guest inclusion complexation. As shown in Figure 6.3, using grafted *β*-cyclodextrin as target sites, Pluronic polymers have been introduced on the surface of CNs by means of inclusion interaction between *β*-cyclodextrin and the hydrophobic segment of the polymers. Because of a steric stabilization effect, surface PEG chains facilitate the dispersion and compatibility of nanocrystals, which also enhance the loading level of nanocrystals in the hydrogel system. Furthermore, uncovered PEG segments render the participating inclusion of α-cyclodextrin for the architecture of *in situ* hydrogels. With the
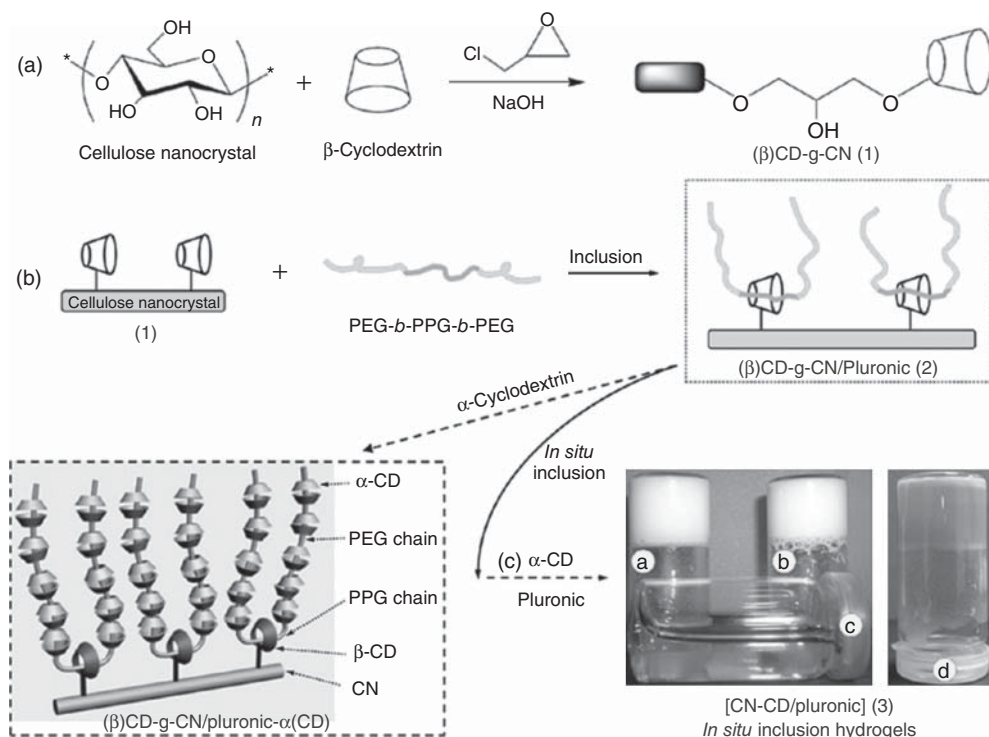
Figure 6.3 Synthesis pathway for (A) β-cyclodextrin grafting on cellulose nanocrystal (β)CD-g-CN; (B) inclusion complex of (β)CD-g-CN and pluronic polymers; and (C) supramolecular hydrogels from *in situ* inclusion between (β)CD-g-CN/Pluronic and α-CD: (a) hydrogel CN-CD/F68, (b) hydrogel CN-CD/F108, (c) water, and (d) drug-loaded hydrogel CN-CD/F108-Dox. Reproduced from [94], copyright 2013 © permission from The American Chemical Society.

introduction of high loading levels of modified nanocrystals (>5 wt%), a significant enhancement in structural and thermal stability of *in situ* hydrogels was observed from rheological analysis [94].

6.3.1.2 Sponge, Foam, Aerogel, and Tissue-Engineering Nanoscaffold

Sponge is a material full of pores and channels allowing water or other molecules to circulate through them. With a similar structure, foam is a substance that is formed by trapping pockets of gas in a liquid or solid. Aerogel is a synthetic porous ultralight material derived from a gel, in which the liquid component of the gel has been replaced with a gas. As nanomaterials of high porosity and specific surface area as well as low density, sponge, foam, and aerogel materials can generally be produced by extracting the liquid component using freeze-drying or supercritical CO_2 drying processing. These treatments allow the liquid to be slowly dried off without causing the solid matrix to collapse from capillary action, as happens with conventional evaporation. Table 6.1 shows diverse PN-based sponge, foam, and aerogel materials prepared with different techniques.

Table 6.1 Diverse PNs-based sponge, foam, aerogel, and nanoscaffold materials.

PNs	Sources	Matrices	Materials	Techniques	References
CNs	Cotton	Alginate	Sponge	Ionic crosslinking/ freeze-casting	[95]
	Cotton	Starch/PVA	Sponge	Freezing/thawing cycles	[96]
	—	Polyurethane	Foam	Evaporation under high vacuum	[97]
	MCC	Xylans	Foam	Freeze-casting	[98]
	Softwood pulp	PVA	Foam	Freeze-casting	[99]
	Ramie fiber	Arabinoxylan	Aerogel	Freeze-casting	[100]
	Cotton wool	—	Aerogel	Supercritical CO_2 drying	[101]
	Tunicate	Clay/PVA	Aerogel	Freeze-casting	[102]
	Cotton	MAH-*g*-PLA	Scaffold	Electrospining	[103]
ChW	Shrimp shell	Silk fibroin	Sponge	Freeze-casting	[104]
	Crab shell	Polylactide	Foam	Two-step batch foaming	[105]
	Crab shell	—	Aerogel	Supercritical CO_2 drying	[106]
	—	Hyaluronan/ gelatin	Scaffold	Freeze-casting	[107]
	—	Chitosan	Scaffold	Supercritical CO_2 drying	[108]
	Shrimp shell	Chitosan	Scaffold	Microwave poly-merization	[109]
	Shrimp shell	Chitosan	Scaffold	Freeze-casting	[110, 111]

MCC, microcrystalline cellulose.

Lin *et al.* reported the preparation of cross-linked polysaccharide sponges by freeze-drying of amorphous alginate and oxidized nanocellulose (CNs and microfibrillated cellulose) in the presence of a Ca^{2+} ionic cross-linking agent. The new carboxyl groups on the surface of nanocellulose induced by chemical oxidization provided the possibility of participating in the construction of an alginate-based sponge's structure and played a fundamental role in the structural and mechanical stability of ensuing sponges [95]. Another study reported the method of repeated cycles of freezing and thawing to prepare sponge materials with homogeneously embedded CNs in the starch/PVA matrix [96]. It was shown that the repeated freezing−thawing cycles induced physically cross-linked chain packing between starch and PVA, which supports the cell proliferation and biocompatibility of the resultant sponges. Chitin whiskers were also used to reinforce silk fibroin-based sponges, which possessed an interconnected pore network with an average pore size of 150 mm, and were used for the cellular cultivation [104]. The presence of chitin whiskers embedded into silk fibroin nano-sponges not only improved dimensional stability but also enhanced compression strength. Moreover, it should be pointed out that the incorporation of chitin whiskers into the sponges was found to promote the viability and proliferation of L929 mouse connective tissue cells, in comparison with neat silk fibroin sponge. The percentage of cell spreading at 24 h of cultivation on chitin whiskers/silk fibroin sponges was almost double (61%) compared to that on the neat silk fibroin sponges (31%), which proved that the incorporation of chitin whiskers into the silk fibroin matrix enabled significant promotion of the percentage of cell spreading of the L929 cells.

Using the freeze-casting method, Ragauskas and coworkers reported the preparation of diverse foams with the reinforcement of CNs in PVA [99], xylan [98], and polyurethane matrices [97]. They found that the parameters for freezing treatment (freezing rate and slurry concentration) will significantly affect the microstructure and morphological features (such as pore size and shape) of foams. Meanwhile, the introduction of rigid CNs will improve the mechanical and thermal performance of the prepared foams. Through a two-step batch-foaming technique, chitin whiskers are also used to fabricate foams, with PLA (poly(lactic acid)) as a support material [105].

Pure CNs and chitin whisker aerogels were reported to be prepared by supercritical carbon dioxide ($scCO_2$) technique. The density and porosity of aerogels varied linearly with varying concentrations of PNs in the initial hydrogel [101]. Particularly, chitin aerogels have promising low densities ($0.043-0.113\ g\ cm^{-3}$), high porosities (up to 97%), and surface areas of $261\ m^2\ g^{-1}$, and showed extraordinarily low shrinkage during drying (with an average shrinkage of only 4%) [106]. Other studies reported the development of aerogels from clay/PVA [102] and xylanase [100] as matrices with the introduction of CNs.

Owing to the properties of porosity, biocompatibility, and right mechanical property similar to those of natural tissue, PN-based biomaterials can also be used as a special tissue bioscaffold, such as for a cell-friendly environment to encourage cell attachment and proliferation. The tissue-engineered porous nanoscaffold is a kind of novel biomedical nanomaterial providing the necessary template

and physical support to guide the differentiation and proliferation of cells into targeted functional tissues or organs. The components of diverse PN-based scaffolds are summarized in Table 6.1, and their use in the cultivation of cells has been discussed in Section 6.2.3.1. Chirachanchai *et al.* first developed a chitosan nanoscaffold with the direct one-pot deacetylation of ChWs via an alkaline treatment method [110, 111]. The rigid rod-like ChWs develop themselves to form a network in the nanoscale and a porous chitosan nanoscaffold. When compared to the original chitosan flakes, the surface area, pore volume, and pore size of the nanoscaffold increased over 7 times, 26 times, and 4 times, respectively, which will support its advanced biomedical-based applications. In another work, a microwave technique was developed for the alkaline deacetylation conditions of chitin whiskers for the preparation of a chitosan nanoscaffold [109]. The introduction of the microwave technique made the preparation procedure more efficient and seven times shorter than the conventional method. Recently, scCO$_2$ technique was also used to prepare the chitosan nanoscaffold during the reaction of ChWs with alkali solution [108]. Compared to the freeze-drying method, the scCO$_2$ technique was found to be time and energy efficient, and the prepared nanoscaffolds exhibited promising antibacterial activity, high surface area, and better cellular attachment and proliferation, which indicated the potential applicability in tissue engineering materials. In another study, Haririraksapitak and Supaphol developed the hyaluronan/gelatin-based tissue scaffolds containing different contents of chitin whiskers with the freeze-drying method, and it was shown that with the introduction of 10 wt% ChWs the scaffold showed a significant supporting effect for the viability and proliferation of cultured human osteosarcoma cells [107]. Blaker *et al.* developed a technique of combining the ice-microsphere template with thermally induced phase separation lining the pore walls with bacterial CNs to produce *in situ* porous PLA/CNs scaffolds. The resultant nanoscaffolds showed porous morphology with controlled porosities up to 97% of spherical interconnected pore walls lined by CNs, which can be more suitable for expansion and direct interaction with cells in three-dimensional culture [112]. Electrospun fibrous nanoscaffolds reinforced with CNs for MAH-grafted-PLA (maleic anhydride) matrix with improved interfacial adhesion were also reported [103].

6.3.2
Special Mechanical Materials

Special mechanical materials based on CNs are mainly referred as mechanically switchable, stimuli-responsive materials, such as mechanically adaptive materials and mechanical gradient materials. Inspired by biological creatures such as sea cucumbers, which have the ability to reversibly change the stiffness of their dermis, three-dimensional percolating networks based on rigid CNs were introduced in various polymeric matrices, such as poly(EO−EPI) (ethyleneoxide−epichlorohydrin) copolymer (1 : 1), PVA, and PBMA (poly(butyl-methacrylate)). The first generation of percolating CN nanomaterials were based

on the poly(EO−EPI) and PVA matrix [113]. In the rubbery zone, the tensile storage moduli (E'_c) of the dry matrix materials at 25 °C increased by over two orders of magnitude from 3.7 MPa (neat matrix) to about 800 MPa for a nanocrystal content of 19% (v/v). However, upon exposure to water, these CNs/matrix nanomaterials exhibit a pronounced and reversible modulus reduction (40-fold), from 800 to 20 MPa, for the materials with the same CN content of 19% (v/v) at room temperature. The second generation of mechanically adaptive nanomaterials was based on PVA or PBMA matrices, which are dynamically sensitive to the thermal transition (from the ambient (about 23 °C) to the physiological (37 °C)) [114–116]. For instance, below the glass-transition temperature (T_g), the tensile storage moduli of the dry nanomaterials increased only 2- to 2.5-folds when adding 16.5% (v/v) nanocrystals, while E' increased 1000-folds above T_g. At the same time, when being exposed to physiological conditions (immersion in artificial cerebrospinal fluid, 37 °C) these nanomaterials displayed a significant decrease of E' from several gigapascals to several megapascals. Recently, the effects of cotton CNs introduced in rubbery polyurethane matrix to produce mechanically adaptive nanocomposites, which can change the mechanical properties upon exposure to water and display a water-activated shape-memory effect, were also reported [117].

A theoretical model for the mechanically adaptive nanomaterial mechanism has been proposed, as shown in Figure 6.4 [1, 118]. The mechanical properties of these chemoresponsive materials can selectively and reversibly be controlled through the formation and decoupling of a three-dimensional network of well-individualized rigid nanocrystals in response to specific chemical triggers. In the "on" state, strong hydrogen bonds between rigid, percolating nanocrystals maximize stress transfer and induce the reinforcement of the nanomaterials. In contrast, with environmental stimuli such as exposure to water or the increase of temperature, hydrogen bonding interactions among nanocrystals are disrupted and the nanocrystals dissociated from each other, which are switched "off" by the introduction of the chemical regulators.

Recently, inspired by the water-enhanced mechanical gradient character of the squid beak, Fox *et al.* reported mechanical gradient nanocomposites made from CNs where the degree of cross-linking can be controlled along the length of the materials. Tunicate cellulose nanocrystals were modified with allyl moieties and
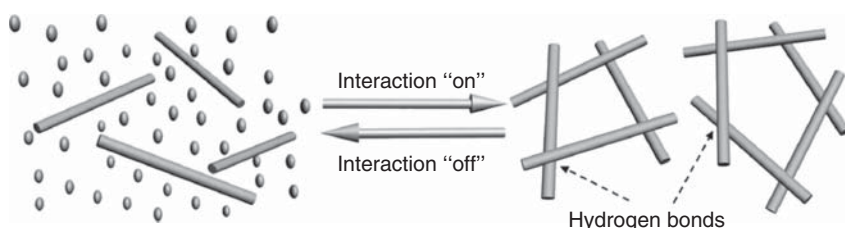
Figure 6.4 Schematic representation of the architecture and switching mechanism in the mechanically adaptive nanomaterials. Reproduced from [1], copyright 2012 © permission from Royal Society of Chemistry.

cross-linked using photoinduced thiol-ene chemistry. With the reaction between modified CNs and photoinitiator, the varying degrees of cross-linking degrees of nanocrystals were controlled by UV irradiation. The gradient in UV exposure was simply achieved using an aluminum foil mask that was wrapped around different length and regions of the film exposed to different amounts of UV irradiation (0, 4, 8, 12, 16, and 20 min), as shown in Figure 6.5a. Under different states (dry or wet) and temperatures, different lengths and regions from the film exhibited different mechanical properties, with an increase in irradiation time consistent with increased cross-linking. A dramatic increase in the mechanical contrast is

(a)
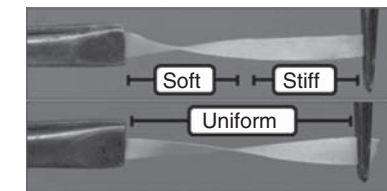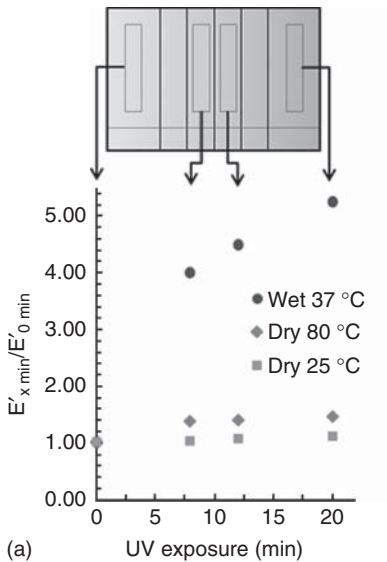
(b)

Figure 6.5 (a) Schematic of the gradient film of 15 wt% allyl-modified cellulose nanocrystals reinforced PVA nanocomposite with solid lines dividing increments of UV exposure. Dashed lines in the shape of rectangle represent samples cut out for mechanical testing. The horizontal long dashed line represents the gradient film sample cut from bottom of film (and shown in the top picture of (b). Mechanical testing results plotted to highlight the contrast in gradient between the samples dry at 25 °C (squares), dry at 80 °C (diamonds), and wet at 37 °C (circles). (b) Twisting by half turn of wet nanocomposite samples of a gradient exposed film (top picture, gradient as shown in (a)) and a uniform cross-linked film (bottom picture, 4 min exposure across the length of the film). Reproduced from [119], copyright 2013 © permission from The American Chemical Society.

observed for the wet film ($E'_{stiff}/E'_{soft} > 5$) over the dry film either below or above T_g (E'_{stiff}/E'_{soft} of about 1.1 and 1.5, respectively). To visually demonstrate the mechanical gradient along the film, a strip of the nanocomposite was cut in parallel with the gradient (so as to include each irradiation increment) and soaked in water for 6 h. This gradient film strip was pictured in the top panel of Figure 6.5b and showed a soft to stiff transition from left to right; performing a half twist on this film resulted in the twist being concentrated at the soft end. In contrast, a uniformly irradiated sample (taken from the 4 min irradiated section of the same nanocomposite) showed uniform twisting (bottom panel of Figure 6.5b) under the same half twist conditions [119].

6.3.3
Self-Healable and Shape-Memory Materials

Named as "self-healable materials" and "shape-memory materials," these two kinds of materials are repairable or revertible after being damaged or after a change in shape, and are attractive for many applications because their features can improve the reliability, functionality, and lifetime of a broad range of products. The introduction of CNs in these functional materials will significantly enhance the mechanical performance.

The self-healable property of materials is generally realized with the division and re-conjunction of the supramolecular structure in materials under external stimulus, such as ultraviolet radiation or heating energy. Biyani *et al.* reported light-healable nanocomposites based on a telechelic poly(ethylene-*co*-butylene) that was functionalized by hydrogen bonding ureidopyrimidone (UPy) and CNs decorated with the same binding motif. When these materials were exposed to ultraviolet radiation, the UPy motifs were excited and the absorbed energy was converted into heat, which caused temporary disengagement of the hydrogen-bonding motifs, concomitant with a reversible decrease in molecular weight and viscosity. Meanwhile, these nanocomposites showed significantly improved mechanical properties from the reinforcement of CNs when compared to neat materials. As a result, deliberately introduced defects could be healed quickly and efficiently and exhibited high strength and stiffness. As shown in Figure 6.6, the nanocomposite samples containing 10 wt% CNs were found to heal considerably faster, requiring less than 20 s of UV exposure (image a). AFM (atomic force microscopy) images taken before, during, and after healing further confirmed that on the nanoscale, the original topology of the prepared nanocomposites can be restored (image b) [120]. In another study, a supramolecular polymer blend, formed via $\pi-\pi$ interactions between a π-electron-rich pyrenyl end-capped oligomer and a chain-folding oligomer containing pairs of π-electron-poor naphthalene-diimide units, has been reinforced with CNs (from 1.25 to 20.0 wt%) to afford a healable nanocomposite material. All the nanocomposites could be rehealed upon exposure to elevated temperatures. The best combination of healing efficiency and mechanical properties was obtained with the 7.5 wt% CN nanocomposite that
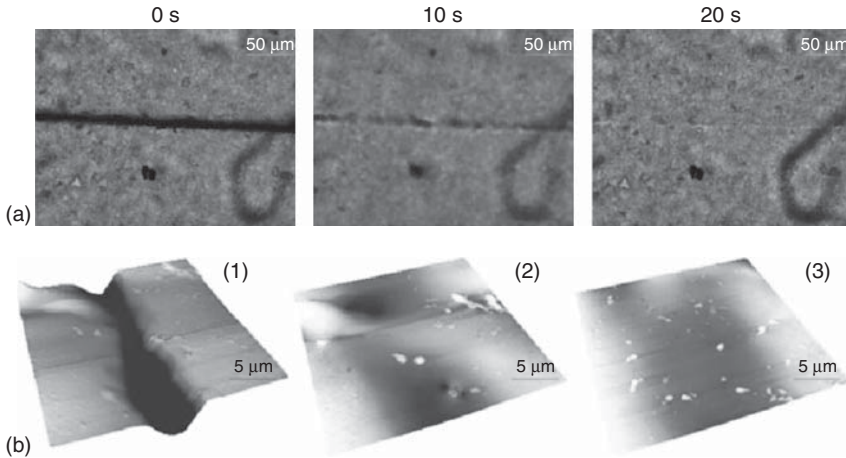
Figure 6.6 (a) Optical microscope images of deliberately damaged ureidopyrimidone-cellulose nanocrystals materials (with 10 wt% nanocrystal content) before, during, and after exposure to UV light (320–390 nm, 350 mW cm^{-2}, 20 s). (b) Atomic force micrographs of ureidopyrimidone-cellulose nanocrystals materials (with 10 wt% nanocrystal content) in the deliberately damaged (1), partially healed (2), and completely healed (3) state (color range; black = 7 μm, white = 0 μm). Reproduced from [120], copyright 2013 © permission from The American Chemical Society.

exhibited a tensile modulus enhanced by as much as a factor of 20 over the matrix material alone and could be fully rehealed at 85 °C within 30 min [121].

Through the regulation of reversible formation and disruption of CNs percolation network, elastomeric polyurethane nanocomposites containing CNs (from 1.1 to 29.6 wt%) can be prepared, which are rapidly switchable shape-memory materials activated by water. The CNs percolation network reformed after drying to provide a fixing force for the temporary shape. The entropy elasticity of polyurethane matrix then enabled rapid shape recovery when the percolation network was disrupted again during wetting. On using plasticizers to lower the glass transition temperature of shape-memory polymers, water molecules will trigger the shape recovery at room temperature or less for these shape-memory materials [122, 123].

6.3.4
Polymeric Electrolytes and Battery

Polymer-based ion-conducting materials have generated remarkable interest in the field of lithium batteries because of their application as an electrolyte. A high specific energy density can be reached at medium temperature using a dry polymer electrolyte and lithium metal as the negative electrode. Moreover, the high flexibility of polymers allows processing of batteries with various sizes and geometries. In this application, the incorporation of ion-conducting solid

polymer electrolytes into PNs allows a combination of both the mechanical function of a separator and the high ionic conductivity of the medium. Dufresne *et al.* have investigated a series of PEO-based (polyoxyethylene) polymer electrolytes reinforced with CNs, which displayed high ionic conductivity as well as electrochemical, thermal, and mechanical stability. Solid polymer electrolytes with CNs were generally prepared in two steps: the first step consisting of the preparation of a polymeric matrix–nanocrystal mixture and the second one consisting of the introduction of a lithium salt, such as lithium trifluoromethyl sulfonyl imide (LiTFSI) or $LiClO_4$ into the swelling nanocrystal-reinforced polymer nanomaterial in a concentrated acetonitrile salt solution [124–126]. Recently, electrospinning and hot-pressing technique without solvent was also reported to be of use in preparing composite polymer electrolytes with the reinforcement of CNs [127] and nanochitin [128–130].

Generally, the addition of rigid nanocrystals in polymer electrolytes leads to high mechanical performance with a high increase in the storage modulus at high temperature, and a slight decrease of ionic conductivity. For instance, by adding 10 wt% tunicin nanocrystals in PEO composite materials, the gain in storage modulus exceeded by a factor of 100 with respect to the unfilled polymer electrolyte; however, the values of ionic conductivity still remained higher than $10^{-4}\,S\,cm^{-1}$ above 60 °C (melting point of PEO) [125, 131]. On the other hand, to further enhance the performance of polymer electrolytes, different solvents (water or organic medium) for the dispersion of nanocrystals, cross-linking agent [132], plasticizer [133], or different polymeric matrices [129, 134] were chosen to develop and investigate the effects in the solid polymer electrolyte system.

CNs are reported to be used as optically transparent substrates for the preparation of recyclable organic solar cells. The solar cells fabricated on CN substrates displayed good rectification in the dark and reached a power conversion efficiency of 2.7%. Meanwhile, this solar cell can be easily separated and recycled into its major components using low-energy processes at room temperature [135].

6.3.5
Semi-conducting Material

On the basis of the combination of anionic surface charged CNs and positively charged π-conjugated polymers, functional semi-conducting materials can be prepared. A stable suspension of CNs and PANI-PPE (polyaniline–poly(*p*-phenylene ethynylene)) derivative mixture can be used to produce the semi-conducting film by solution-casting treatment. Further investigations on electrical conductivity, photoluminescence, and mechanical properties revealed that this semiconducting material synergistically combined the electronic characteristics from the conjugated polymers with the outstanding mechanical reinforcement from CNs [136]. In another study, the introduction of CNs in PEDOT (poly(3,4-ethylenedioxythiophene))/PSS (poly(styrene sulfonate))-based PS (polystyrene) conductive polymer matrix extremely reduced electrical percolation threshold,

by five times that of ensuing nanocomposites. It was reported that the percolation threshold of PEDOT:PSS in PEDOT:PSS/PS blends, being 2.2 wt%, was lowered to 0.4 wt% by adding 0.8 wt% of nonconducting CNs. Such a low percolation threshold of PEDOT:PSS was attributed to the templating effect of CNs, which would adsorb the conductive polymers on the surface and cover the electrical percolation with the network formed by CNs [137].

6.4
Optical Materials Derived from Liquid Crystalline Property

Owing to their anisotropic rod-like morphology, CNs and chitin whiskers display a specific property. In suspension, these nanoparticles have a lyotropic liquid crystalline behavior, that is, a phase transition from an isotropic liquid to an ordered liquid crystal when the concentration changes [138]. Indeed, above a given concentration, a chiral nematic phase forms. Under certain conditions, the suspension may be slowly evaporated to obtain semi-translucent films that maintain the chiral nematic liquid crystal order formed in the suspension. These films exhibit iridescence reflecting polarized light in a narrow wavelength range determined by the chiral nematic pitch and the refractive index of the film [3]. Derived from the liquid crystalline behavior, tunable optical nanomaterials can be prepared on the basis of rod-like CNs with two strategies. The first strategy is the slow evaporation of CNs suspension to preserve the chiral nematic ordering phase. Another strategy is the combination of liquid crystalline CNs and inorganic matrix to produce optical materials.

Ultrasound treatment was found to increase the chiral nematic pitch in suspension and red-shift the reflection wavelength of CN films as the applied energy increased [139]. Figure 6.7 shows solid films cast from aliquots of 2.8 wt% CN suspensions prepared from bleached softwood kraft pulp and sonicated with increasing (left to right) energy inputs. The energy was measured in joules per gram of CNs. The films exhibit reflected iridescence with colors ranging from blue-violet to red. By combining sonication and electrolyte addition the reflective properties of the film can be predictably tuned. The effects of sonicating a CN suspension were shown to be cumulative and permanent. Moreover, suspensions sonicated with different energy inputs can be mixed to prepare films having a reflection band intermediate between those obtained from the individual suspensions. Recently, the differential heating rates of aqueous CN suspension during film casting were investigated [140]. Placing materials of different temperatures beneath an evaporating CN suspension resulted in watermark-like patterns of different reflection wavelengths incorporated within the final film structure. The patterned areas are of different thickness and different chiral nematic pitch than the surrounding film; heating results in thicker areas of longer pitch. Thermal pattern creation in CN films is proposed to be caused by differences in evaporation rates and thermal motion in the areas of the suspension. These CN-based optical materials with tunable iridescence were proposed to have the potential

1 cm
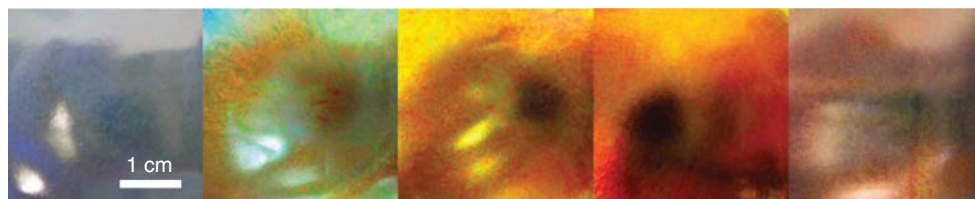
Figure 6.7 Cellulose nanocrystal films produced from suspensions treated with increasing applied ultrasonic energy (0, 250, 700, 1800, and 7200 J g^{-1} of nanocrystals) from left to right. Viewing is normal to the film surface under diffuse lighting. Samples of cellulose nanocrystals suspension were sonicated using a Sonics vibra-cell 130 W 20 kHz ultrasonic processor with a 6 mm diameter probe: typically, 15 ml of a 2–3 wt% cellulose nanocrystals suspension was placed in a 50 ml plastic tube and sonicated at 60% of the maximum power. Prolonged sonication (to an energy input of over 3600 J g^{-1} cellulose nanocrystals) was performed in an ice bath to prevent desulfation caused by heating of the suspension. Reproduced from [139], copyright 2011 © permission from The American Chemical Society.

for covert encryption as an anti-counterfeiting measure and an intrinsic level of covert encryption since the reflection of left-circularly polarized light [141].

Although the mechanism of CN-based optical materials is commonly recognized as the chiral nematic liquid crystal ordering from nanocrystal suspension, another new explanation and model are also proposed. Picard *et al.* observed a solid multilamellar structure for CN suspension after evaporation, with each lamella made of roughly parallel rows of bundles. Consequently, they explained the iridescence of CN optical films as a multilamellar structure inducing light interference, not a helical cholesteric liquid crystal [142].

MacLachlan and his team developed a series of photonic, mesoporous, inorganic (silica) optical materials, which were a cast of a chiral nematic liquid crystals formed from CNs. Inspired by the brilliant iridescent colors of beetle exoskeletons, their first study prepared the freestanding mesoporous silica films with tunable chiral nematic structures from CNs [143, 144]. As shown in Figure 6.8a, the peak reflected wavelength of the biomimetic optical nanomaterials can be varied across the entire visible spectrum and into the near-infrared through simple changes under synthetic conditions. Figure 6.8b shows photographs of the different colors of mesoporous silica nanomaterials. With CN content increasing from samples S1 to S4, the mesoporous films exhibited blue, green, yellow, and red color respectively. The colors in these films can be attributed to the chiral nematic pore structure arising from CNs present in the materials. Moreover, the addition of a drop of water will cause the wet part of the film to become completely transparent, as shown in Figure 6.8d. With the elimination of water (or other common solvents) upon drying, these optical nanomaterials can fully regain their iridescence, which results in a reversible decrease in the circular dichroism (CD) signal to 30 millidegrees (Figure 6.8c). Furthermore, some mesoporous silica and carbon films decorated with CNs and metal nanoparticles through calcination and carbonization are developed [145–147]. Recently, responsive photonic hydrogels from the self-assembly of CNs and hydrogel precursors were reported.
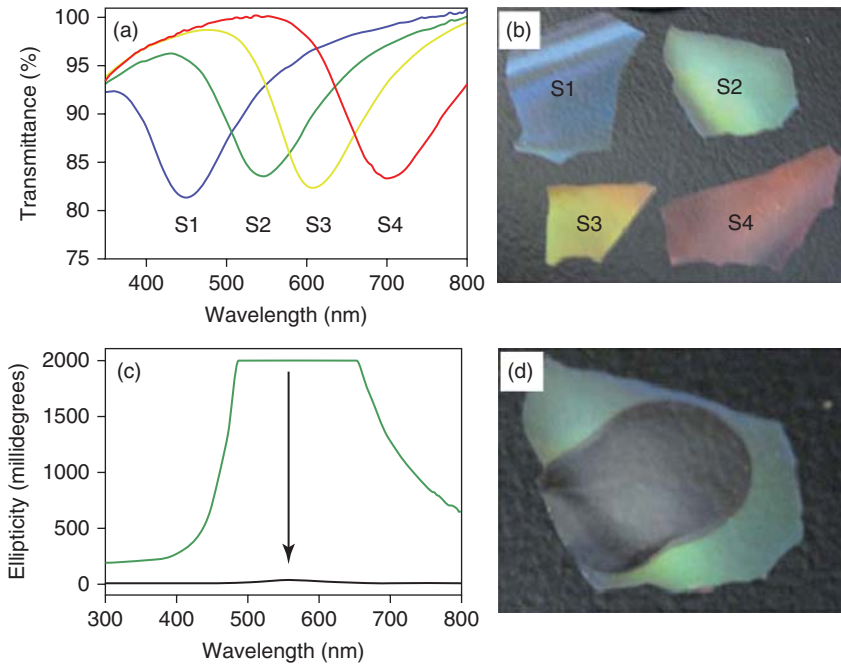
Figure 6.8 Optical characterization of cellulose nanocrystals/silica composite films. (a) Transmission spectra; (b) photographs showing the different colors of mesoporous films S1 to S4 with gradual increase of nanocrystals contents; (c) circular dichroism spectra of a green mesoporous film before (green curve) and after (black curve) infiltration with water; and (d) photograph of the transparent green film after the addition of a drop of water. Reproduced from [143], copyright 2010 © permission from Nature Publishing Group.

Because of the long-range chiral nematic order from the CN component, this kind of hydrogel showed iridescence and rapid response to various stimuli [148].

6.5
Special Films and Systems Ascribed to Barrier Property

There is an increasing interest in the barrier properties of PN films or related functional materials. Indeed, because of its small size, the surface-to-volume ratio of nanoparticles is significantly greater than that for microparticles, which will increase tortuosity for the diffusion of molecules. Moreover, the low permeability of materials can be enhanced by the highly crystalline nature of PNs and their ability to form a dense percolating network. Provided that strong particle–polymer molecular interactions exist, the smaller nanoparticles have a greater ability to bond to the surrounding polymer material, thereby reducing the chain segmental mobility and thus the penetrant diffusivity [3].

6.5.1
Drug Delivery – Barrier for Drug Molecules

Cellulose, with excellent compaction behavior, has a long history of application in the pharmaceutical industry, in particular, as pharmaceutical excipients to condense drug-loaded matrices as tablets suitable for oral administration. Despite an extended history of use in tableting, the research of cellulose on the basis of nanotechnology (especially in the types of nanocellulose) in advanced drug-loaded systems attracted much attention during recent 10 years. The attempts of nanocellulose in the drug delivery included the control of tablet disintegration rate as special excipients, or prolonged drug release as novel drug carriers. Burt *et al.* investigated the capability of pure CNs as drug delivery excipients to bind water-soluble antibiotics (tetracycline and doxorubicin) and the potential of cationic CNs to bind nonionized hydrophobic anticancer agents (docetaxel, paclitaxel, and etoposide) [149]. Besides direct use as excipients, CNs can also be used as co-stabilizer to improve the physicochemical and flow properties of polymeric excipients. Acrylic beads prepared via emulsion polymerization using CNs as co-stabilizer were proved to be a suitable excipient. The presence of CNs affected positively the size and size distribution of the bead excipient, which formed a stable structure together with low flow time and reduced cotangent of angle [150].

The biomaterial application of PNs in drug delivery can be mainly divided into two aspects, as microspheres (or microparticles) [151] and as hydrogels (or gels) [88, 94, 152]. Table 6.2 summarizes various drug carrier systems based on CNs. It was reported that solid carriers formed from CNs and different matrices spatially trapped drug molecules and imparted the regulation of drug release. Lin *et al.* developed a pH-sensitive CN/sodium alginate microsphere-based controlled release system for drug delivery. The presence of CNs in alginate-based microspheres showed more consistent swelling patterns, higher encapsulation efficiency, and promising sustained release profiles of the drug. Analysis of the drug release mechanism indicated that physical cross-linking through hydrogen bonding between CNs and alginate in microspheres could restrict the diffusion of drug molecules, and slow down the dissolution and collapse of microspheres, facilitating improved drug load and release behavior [151]. As for the example of CNs in the fabrication of hydrogels, nanocrystals were chemically grafted with β-cyclodextrin, and participated in the architecture of hydrogels via *in situ* inclusion interactions (the synthesis pathway was shown in Figure 6.3). A drug release study revealed the performance of hydrogels as drug carrier for *in vitro* release of doxorubicin and exhibited prolonged drug release with special release kinetics and mechanisms, which were due to the "obstruction effect" and "locking effect" attributed to the good dispersion of nanoparticles and rigid network of CNs [94]. With similar strategy, another work developed a polyelectrolyte macroion complex via the conjunction between cationic chitosan and anionic CNs, which has the potential for multiparticulate oral drug delivery, but unfortunately without drug loading or drug release results [84].

Table 6.2 Dug carrier systems based on cellulose nanocrystals.

Sources	Matrices	Carrier form	Model drugs	Release time and medium	Mechanism models	References
Cotton	Sodium alginate	Microsphere	Theophylline	16 h in pH = 7.4 PBS solution	Ritger– Peppas equation	[151]
Cotton	Cyclodextrin/ pluronic	Hydrogel	DOX	6.5 days in water	Ritger– Peppas equation	[94]
Cotton	Cyclodextrin/ pluronic	Hydrogel	BSA	20 h in pH = 7.4 PBS solution	—	[88]
MCC	PLA	Fiber	*Columbia Blue*	48 h in water	Higuchi equation	[153]
Cotton pulp	Regenerated cellulose	Gel	BSA	48 h in simulated body fluid	Fickian diffusion law	[152]
Euca- lyptus wood pulp	EA; MMA; BMA	Bead	Propranolol hydrochloride	12 h in pH = 6.8 PBS solution	—	[150]
Commer- cial soft- wood	CTAB	Suspension	DOX; TET; etoposide; paclitaxel; docetaxel	1–4 days in PBS solution	—	[149]

PBS, polybutylene succinate; DOX, doxorubicin hydrochloride; BSA, bovine serum albumin; EA, ethyl acrylate; MMA, methylmethacrylate; BMA, butylmetacrylate; and TET, tetracycline hydrochloride.

Recently, some researchers attempted to directly attach drug molecules on CNs, which was achieved using covalent coupling between modified CNs and drugs, unlike the traditional trapping strategy. With a series of oxidation, reductive amination, and esterification reactions in aqueous media, a novel CN-based delivery system attached to the syringyl alcohol linker through a γ-aminobutyric acid spacer molecule can be produced, on which small model amine drugs (e.g., phenyl-propanolamine) can be covalently connected [154]. Similarly, with the binding of bifunctional fusion protein on CNs, hydrophobic solid drug nanoparticles can be adsorbed by the packed protein film on nanocrystals and can improve the long-term stability of drugs under physiological conditions [155]. The concept of conjunction between CNs and drug is attractive, but many issues need further investigations, such as the influence and regulation of drug release and reduction or destruction of drug structure and activity.

6.5.2
Barrier Nanocomposites – Barrier for Water and Oxygen

Barrier properties using bio-based materials are becoming increasingly desirable in our society to develop environmentally friendly and efficient materials in different applications, such as those used for biodegradable food packaging to replace traditional petrochemical-based materials.

Cellulose is a hydrophilic polymer and it obviously absorbs water when immersed in liquid water or conditioned in moist atmosphere. However, the water vapor permeability is decreased when the cellulose fibers are disintegrated to the nanoscale level, such as CNs [156]. Moreover, the sensitivity of the nanoparticles to moisture can be tuned via pre-treatment before homogenization or post-treatment (polymer impregnation, or chemical grafting) [3, 157]. The gas permeability is also reduced in dry atmospheres when decreasing the size of the cellulosic particles because of the crystalline and dense structure of the nanoparticle film. Platelet-like starch nanocrystals were also reported as promising barriers for water and oxygen gas in nanocomposites in natural rubber matrix [158, 159], and attempts were made to use these in tires to replace traditional carbon black fillers. Whatever the treatment or the experimental conditions used to produce cellulose or starch nanocrystals, it is seen as a new biomaterial for the creation of a good barrier for extending food shelf-life, and it also improves food quality for antioxidants and antimicrobials.

6.6
Other Functional Applications

CN (1 – 3 wt%) was used to improve the performance of PVA as a wood adhesive. With the measurement of block shear tests, wood failure value increased from 59% for pure PVA to 84% for adhesive with 1 wt% CNs and finally to 97% for adhesive with 3 wt% CNs. Fluctuations in properties of PVA as a wood adhesive and a polymer at different loadings of CNs can be attributed to the effect of homogeneous dispersion of nanocrystals on the change of PVA structure [160].

6.7
Concluding Remarks

PNs, the resource and gift provided by nature, are a new ageless bionanomaterials in the field of functional nanomaterials, which is on the threshold of a breakthrough. Overall, research and challenges in the future of PNs in functional nanomaterials application include several aspects. First, in order to introduce more functional molecules on the surface, it is important to develop active and controllable methods for physical or chemical modification of nanocrystals under milder or "green" reactive conditions, keeping the initial morphological integrity

and native crystallinity. Second, all the applications of PNs in the field of functional nanomaterials are based on their inherent physical or chemical properties, such as chiral nematic property, chemical reactivity, nano-effects, biocompatibility, and so on. Therefore, for the development and exploration of PNs in the field of functional nanomaterials, these unique properties should be used to the fullest with the combination of research in multidisciplinary fields, with contributions from chemistry, physics, biology, and materials science. For instance, the piezoelectric effect of CN thin films was reported recently [161]. Meanwhile, the investigation of other potential properties of PNs is an interesting topic deserving study, such as the transformation and change of crystalline properties of PNs with physical/chemical modification. It should be noted that the analysis and investigation of inherent properties of PNs can significantly support and promote their application in the field of functional nanomaterials. Finally, it should be pointed out that the current research on PNs in the field of functional nanomaterials mainly focuses on the utilization of CN, which may be attributed to its higher structural stability and easy chemical modification in comparison with the other two PNs. In fact, starch nanocrystals and chitin whiskers also possess unique properties and characteristics, which could be potentially used to develop special functional nanomaterials, such as the unique platelet-like morphology for starch nanocrystals and different active groups on chitin whiskers.

List of Abbreviations

BMA	butylmethacrylate
BSA	bovine serum albumin
CTAB	cetyl trimethylammonium bromide
DOX	doxorubicin hydrochloride
EA	ethyl acrylate
EO–EPI	ethyleneoxide–epichlorohydrin
FAM-SE	5-(and-6)-carboxyfluorescein succinimidyl ester
FITC	fluorescein-5′-isothiocyanate
MAH	maleic anhydride
MCC	microcrystalline cellulose
MMA	methylmethacrylate
OG-SE	Oregon Green 488 carboxylic acid, succinimidyl ester
PAA	poly(acrylic acid)
PAM	polyacrylamide
PANI	polyaniline
PBMA	poly(butylmethacrylate)
PEDOT	poly(3,4-ethylenedioxythiophene)
PEG	poly(ethylene glycol)
PEI	polyethylenimine
PEO	polyoxyethylene
PHEMA	poly(2-hydroxyethylmethacrylate)

poly(MVE-*co*-MA)−PEG poly(methyl vinyl ether-*co*-maleic acid)−polyethylene glycol
poly(NIPAM)   poly(*N*-isopropylacrylamide)
poly(NIPAM-*co*-BMA)   poly(*N*-isopropylacrylamide-*co*-butyl methacrylate)
PPE   poly(*p*-phenylene ethynylene)
PS   polystyrene
PSS   poly(styrene sulfonate)
PVA   poly(vinyl alcohol)
PSE   1-pyrenebutyric acid *N*-hydroxysuccinimide ester
RBITC   rhodamine B isothiocyanate
TAMRA-SE   5-(and-6)-carboxytetramethylrhod-amine succinimidyl ester
TET   tetracycline hydrochloride

References

1. Lin, N., Huang, J., and Dufresne, A. (2012) Preparation, properties and applications of polysaccharide nanocrystals in advanced functional nanomaterials: a review. *Nanoscale*, **4**, 3274−3294.

2. Persin, Z., Stana-Kleinschek, K., Foster, T.J., van Dam, J.E.G., Boeriu, C.G., and Navard, P. (2011) Challenges and opportunities in polysaccharides research and technology: the EPNOE views for the next decade in the areas of materials, food and health care. *Carbohydr. Polym.*, **84**, 22−32.

3. Dufresne, A. (2013) Nanocellulose: a new ageless bionanomaterial. *Mater. Today*, **16**, 220−227.

4. Dong, S. and Roman, M. (2007) Fluorescently labeled cellulose nanocrystals for bioimaging applications. *J. Am. Chem. Soc.*, **129**, 13810−13811.

5. Mahmoud, K.A., Mena, J.A., Male, K.B., Hrapovic, S., Kamen, A., and Luong, J.H.T. (2010) Effect of surface charge on the cellular uptake and cytotoxicity of fluorescent labeled cellulose nanocrystals. *ACS Appl. Mater. Interfaces*, **2**, 2924−2932.

6. Zhang, L., Li, Q., Zhou, J., and Zhang, L. (2012) Synthesis and photophysical behavior of pyrene-bearing cellulose nanocrystals for Fe^{3+} sensing. *Macromol. Chem. Phys.*, **213**, 1612−1617.

7. Hassan, M.L., Moorefield, C.M., Elbatal, H.S., and Newkomeb, G.R. (2012) New metallo-supramolecular terpyridine-modified cellulose functional nanomaterials. *J. Macromol. Sci. Part A*, **49**, 298−305.

8. Hassan, M.L., Moorefield, C.M., Elbatal, H.S., Newkomeb, G.R., Modarelli, D.A., and Romano, N.C. (2012) Fluorescent cellulose nanocrystals via supramolecular assembly of terpyridine-modified cellulose nanocrystals and terpyridine-modified perylene. *Mater. Sci. Eng., B*, **177**, 350−358.

9. Barazzouk, S. and Daneault, C. (2012) Tryptophan-based peptides grafted onto oxidized nanocellulose. *Cellulose*, **19**, 481−493.

10. Yang, Q. and Pan, X. (2010) A facile approach for fabricating fluorescent cellulose. *J. Appl. Polym. Sci.*, **117**, 3639−3644.

11. Nielsen, L.J., Eyley, S., Thielemans, W., and Aylott, J.W. (2010) Dual fluorescent labelling of cellulose nanocrystals for pH sensing. *Chem. Commun.*, **46**, 8929−8931.

12. Drogat, N., Granet, R., Morvan, C.L., Bégaud-Grimaud, G., Krausz, P., and Sol, V. (2012) Chlorin-PEI-labeled cellulose nanocrystals: synthesis, characterization and potential application in PDT. *Bioorg. Med. Chem. Lett.*, **22**, 3648−3652.

13. Edwards, J.V., Prevost, N., Condon, B., French, A., and Wu, Q. (2012) Immobilization of lysozyme-cellulose

amide-linked conjugates on cellulose I and II cotton nanocrystalline preparations. *Cellulose*, **19**, 495–506.

14. Yang, R., Tan, H., Wei, F., and Wang, S. (2008) Peroxidase conjugate of cellulose nanocrystals for the removal of chlorinated phenolic compounds in aqueous solution. *Biotechnology*, **7**, 233–241.

15. Mahmoud, K.A., Male, K.B., Hrapovic, S., and Luong, J.H.T. (2009) Cellulose nanocrystal/gold nanoparticle composite as a matrix for enzyme immobilization. *ACS Appl. Mater. Interfaces*, **1**, 1383–1386.

16. Incani, V., Danumah, C., and Boluk, Y. (2013) Nanocomposites of nanocrystalline cellulose for enzyme immobilization. *Cellulose*, **20**, 191–200.

17. Mahmoud, K.A., Lam, E., Hrapovic, S., and Luong, J.H.T. (2013) Preparation of well-dispersed gold/magnetite nanoparticles embedded on cellulose nanocrystals for efficient immobilization of papain enzyme. *ACS Appl. Mater. Interfaces*, **5**, 4978–4985.

18. Liu, H., Wang, D., Shang, S., and Song, Z. (2011) Preparation of silver nanoparticles on cellulose nanocrystals and the application in electrochemical detection of DNA hybridization. *Cellulose*, **18**, 67–74.

19. Cerclier, C., Guyomard-Lack, A., Moreau, C., Cousin, F., Beury, N., Bonnin, E., Jean, B., and Cathala, B. (2011) Coloured semi-reflective thin films for biomass-hydrolyzing enzyme detection. *Adv. Mater.*, **23**, 3791–3795.

20. Edwards, J.V., Prevost, N., Sethumadhavan, K., Ullah, A., and Condon, B. (2013) Peptide conjugated cellulose nanocrystals with sensitive human neutrophil elastase sensor activity. *Cellulose*, **20**, 1223–1235.

21. Cateto, C.A. and Ragauskas, A. (2011) Amino acid modified cellulose whiskers. *RSC Adv.*, **1**, 1695–1697.

22. Mangalam, A.P., Simonsen, J., and Benight, A.S. (2009) Cellulose/DNA hybrid nanomaterials. *Biomacromolecules*, **10**, 497–504.

23. Eyley, S., Shariki, S., Dale, S.E.C., Bending, S., Marken, F., and Thielemans, W. (2012) Ferrocene – decorated nanocrystalline cellulose with charge carrier mobility. *Langmuir*, **28**, 6514–6519.

24. Eyley, S. and Thielemans, W. (2011) Imidazolium grafted cellulose nanocrystals for ion exchange applications. *Chem. Commun.*, **47**, 4177–4179.

25. Feese, E., Sadeghifar, H., Gracz, H.S., Argyropoulos, D.S., and Ghiladi, R.A. (2011) Photobactericidal porphyrin-cellulose nanocrystals: synthesis, characterization, and antimicrobial properties. *Biomacromolecules*, **12**, 3528–3539.

26. Carpenter, B.L., Feese, E., Sadeghifar, H., Argyropoulos, D.S., and Ghiladi, R.A. (2012) Porphyrin-cellulose nanocrystals: a photobactericidal material that exhibits broad spectrum antimicrobial activity. *Photochem. Photobiol.*, **88**, 527–536.

27. Dujardin, E., Blaseby, M., and Mann, S. (2003) Synthesis of mesoporous silica by sol–gel mineralisation of cellulose nanorod nematic suspensions. *J. Mater. Chem.*, **13**, 696–699.

28. Scheel, H., Zollfrank, C., and Greil, P. (2009) Luminescent silica nanotubes and nanowires: preparation from cellulose whisker templates and investigation of irradiation-induced luminescence. *J. Mater. Res.*, **24**, 1709–1715.

29. Gruber, S., Gottschlich, A., Scheel, H., Aresipathi, C., Bannat, I., Zollfrank, C., and Wark, M. (2010) Molecular and supramolecular templating of silica-based nanotubes and introduction of metal nanowires. *Phys. Status Solidi B*, **247**, 2401–2411.

30. Gruber, S., Taylor, R.N.K., Scheel, H., Greil, P., and Zollfrank, C. (2011) Cellulose-biotemplated silica nanowires coated with a dense gold nanoparticle layer. *Mater. Chem. Phys.*, **129**, 19–22.

31. Shin, Y., Bae, I.-T., Arey, B.W., and Exarhos, G.J. (2007) Simple preparation and stabilization of nickel nanocrystals on cellulose nanocrystal. *Mater. Lett.*, **61**, 3215–3217.

32. Gebauer, D., Oliynyk, V., Salajkova, M., Sort, J., Zhou, Q., Bergström, L., and Salazar-Alvarez, G. (2011) A transparent hybrid of nanocrystalline cellulose and amorphous calcium carbonate nanoparticles. *Nanoscale*, **3**, 3563–3566.

33. Drogat, N., Granet, R., Sol, V., Memmi, A., Saad, N., Koerkamp, C.K., Bressollier, P., and Krausz, P. (2011) Antimicrobial silver nanoparticles generated on cellulose nanocrystals. *J. Nanopart. Res.*, **13**, 1557–1562.

34. Ifuku, S., Tsuji, M., Morimoto, M., Saimoto, H., and Yano, H. (2009) Synthesis of silver nanoparticles templated by TEMPO-mediated oxidized bacterial cellulose nanofibers. *Biomacromolecules*, **10**, 2714–2717.

35. Koga, H., Tokunaga, E., Hidaka, M., Umemura, Y., Saito, T., Isogai, A., and Kitaoka, T. (2010) Topochemical synthesis and catalysis of metal nanoparticles exposed on crystalline cellulose nanofibers. *Chem. Commun.*, **46**, 8567–8569.

36. Lam, E., Hrapovic, S., Majid, E., Chong, J.H., and Luong, J.H.T. (2012) Catalysis using gold nanoparticles decorated on nanocrystalline cellulose. *Nanoscale*, **4**, 997–1002.

37. Shin, Y., Bae, I.-T., Arey, B.W., and Exarhos, G.J. (2008) Facile stabilization of gold-silver alloy nanoparticles on cellulose nanocrystal. *J. Phys. Chem. C*, **112**, 4844–4848.

38. Liu, H., Wang, D., Shang, S., and Song, Z. (2011) Synthesis and characterization of Ag–Pd alloy nanoparticles/carboxylated cellulose nanocrystals nanocomposites. *Carbohydr. Polym.*, **83**, 38–43.

39. Padalkar, S., Capadona, J.R., Rowan, S.J., Weder, C., Won, Y.-H., Stanciu, L.A., and Moon, R.J. (2010) Natural biopolymers: novel templates for the synthesis of nanostructures. *Langmuir*, **26**, 8497–8502.

40. Benaissi, K., Johnson, L., Walsh, D.A., and Thielemans, W. (2010) Synthesis of platinum nanoparticles using cellulosic reducing agents. *Green Chem.*, **12**, 220–222.

41. Johnson, L., Thielemans, W., and Walsh, D.A. (2011) Synthesis of carbon-supported Pt nanoparticle electrocatalysts using nanocrystalline cellulose as reducing agent. *Green Chem.*, **13**, 1686–1693.

42. Shin, Y., Blackwood, J.M., Bae, I.-T., Arey, B.W., and Exarhos, G.J. (2007) Synthesis and stabilization of selenium nanoparticles on cellulose nanocrystal. *Mater. Lett.*, **61**, 4297–4300.

43. Cirtiu, C.M., Dunlop-Brière, A.F., and Moores, A. (2011) Cellulose nanocrystallites as an efficient support for nanoparticles of palladium: application for catalytic hydrogenation and Heck coupling under mild conditions. *Green Chem.*, **13**, 288–291.

44. Padalkar, S., Capadona, J.R., Rowan, S.J., Weder, C., Moon, R.J., and Stanciu, L.A. (2011) Self-assembly and alignment of semiconductor nanoparticles on cellulose nanocrystals. *J. Mater. Sci.*, **46**, 5672–5679.

45. Nelson, K. and Deng, Y. (2006) The shape dependence of core–shell and hollow titania nanoparticles on coating thickness during layer-by-layer and sol–gel synthesis. *Nanotechnology*, **17**, 3219–3225.

46. Zhou, Y., Ding, E.-Y., and Li, W.-D. (2007) Synthesis of TiO_2 nanocubes induced by cellulose nanocrystal (CNC) at low temperature. *Mater. Lett.*, **61**, 5050–5052.

47. Peng, X. and Ding, E. (2011) Low-temperature synthesis of flower-like TiO_2 nanocrystals. *Micro Nano Lett.*, **6**, 998–1001.

48. Liu, S., Tao, D., Bai, H., and Liu, X. (2012) Cellulose-nanowhisker-templated synthesis of titanium dioxide/cellulose nanomaterials with promising photocatalytic abilities. *J. Appl. Polym. Sci.*, **126**, E281–E289.

49. Xiong, R., Lu, C., Zhang, W., Zhou, Z., and Zhang, X. (2013) Facile synthesis of tunable silver nanostructures for antibacterial application using cellulose nanocrystals. *Carbohydr. Polym.*, **95**, 214–219.

50. Liu, H., Song, J., Shang, S., Song, Z., and Wang, D. (2012) Cellulose nanocrystal/silver nanoparticle composites as bifunctional nanofillers within water-borne polyurethane. *ACS Appl. Mater. Interfaces*, **4**, 2413–2419.

51. Kalashnikova, I., Bizot, H., Cathala, B., and Capron, I. (2011) New pickering emulsions stabilized by bacterial cellulose nanocrystals. *Langmuir*, **27**, 7471–7479.

52. Kalashnikova, I., Bizot, H., Cathala, B., and Capron, I. (2012) Modulation of cellulose nanocrystals amphiphilic properties to stabilize oil/water interface. *Biomacromolecules*, **13**, 267–275.

53. Capron, I. and Cathala, B. (2013) Surfactant-free high internal phase emulsions stabilized by cellulose nanocrystals. *Biomacromolecules*, **14**, 291–296.

54. Zoppe, J.O., Venditti, R.A., and Rojas, O.J. (2012) Pickering emulsions stabilized by cellulose nanocrystals grafted with thermo-responsive polymer brushes. *J. Colloid Interface Sci.*, **369**, 202–209.

55. Tzoumaki, M.V., Moschakis, T., Kiosseoglou, V., and Biliaderis, C.G. (2011) Oil-in-water emulsions stabilized by chitin nanocrystal particles. *Food Hydrocolloids*, **25**, 1521–1529.

56. Tzoumaki, M.V., Moschakis, T., Scholten, E., and Biliaderis, C.G. (2013) *In vitro* lipid digestion of chitin nanocrystal stabilized o/w emulsions. *Food Funct.*, **4**, 121–129.

57. Li, C., Sun, P., and Yang, C. (2012) Emulsion stabilized by starch nanocrystals. *Starch/Stärke*, **64**, 497–502.

58. BelHaaj, S., Mabrouk, A.B., Thielemans, W., and Boufi, S. (2013) A one-step miniemulsion polymerization route towards the synthesis of nanocrystal reinforced acrylic nanocomposites. *Soft Matter*, **9**, 1975–1984.

59. Ma, H., Burger, C., Hsiao, B.S., and Chu, B. (2011) Ultrafine polysaccharide nanofibrous membranes for water purification. *Biomacromolecules*, **12**, 970–976.

60. Ma, H., Hsiao, B.S., and Chu, B. (2012) Ultrafine cellulose nanofibers as efficient adsorbents for removal of UO_2^{2+} in water. *ACS Macro Lett.*, **1**, 213–216.

61. Ma, H., Burger, C., Hsiao, B.S., and Chu, B. (2012) Nanofibrous microfiltration membrane based on cellulose nanowhiskers. *Biomacromolecules*, **13**, 180–186.

62. Thielemans, W., Warbey, C.R., and Walsh, D.A. (2009) Permselective nanostructured membranes based on cellulose nanowhiskers. *Green Chem.*, **11**, 531–537.

63. Liebert, T., Kostag, M., Wotschadlo, J., and Heinze, T. (2011) Stable cellulose nanospheres for cellular uptake. *Macromol. Biosci.*, **11**, 1387–1392.

64. Male, K.B., Leung, A.C.W., Montes, J., Kamen, A., and Luong, J.H.T. (2012) Probing inhibitory effects of nanocrystalline cellulose: inhibition *versus* surface charge. *Nanoscale*, **4**, 1373–1379.

65. Dugan, J.M., Collins, R.F., Gough, J.E., and Eichhorn, S.J. (2013) Oriented surfaces of adsorbed cellulose nanowhiskers promote skeletal muscle myogenesis. *Acta Biomater.*, **9**, 4707–4715.

66. Dugan, J.M., Gough, J.E., and Eichhorn, S.J. (2010) Directing the morphology and differentiation of skeletal muscle cells using oriented cellulose nanowhiskers. *Biomacromolecules*, **11**, 2498–2504.

67. Alila, S., Aloulou, F., Thielemans, W., and Boufi, S. (2011) Sorption potential of modified nanocrystals for the removal of aromatic organic pollutant from aqueous solution. *Ind. Crops Prod.*, **33**, 350–357.

68. Cao, X., Huang, M., Ding, B., Yu, J., and Sun, G. (2013) Robust polyacrylonitrile nanofibrous membrane reinforced with jute cellulose nanowhiskers for water purification. *Desalination*, **316**, 120–126.

69. Gong, G., Mathew, A.P., and Oksman, K. (2011) Strong aqueous gels of cellulose nanofibers and nanowhiskers isolated from softwood flour. *Tappi J.*, **2**, 7–14.

70. Tzoumaki, M.V., Moschakis, T., and Biliaderis, C.G. (2010) Metastability of nematic gels made of aqueous chitin nanocrystal dispersions. *Biomacromolecules*, **11**, 175–181.

71. Dorris, A. and Gray, D.G. (2012) Gelation of cellulose nanocrystal suspensions in glycerol. *Cellulose*, **19**, 687–694.

72. Siqueira, G., Mathew, A.P., and Oksman, K. (2011) Processing of cellulose nanowhiskers/cellulose acetate butyrate nanocomposites using sol–gel process to facilitate dispersion. *Compos. Sci. Technol.*, **71**, 1886–1892.

73. Capadona, J.R., Shanmuganathan, K., Triftschuh, S., Seidel, S., Rowan, S.J., and Weder, C. (2009) Polymer nanocomposites with nanowhiskers isolated from microcrystalline cellulose. *Biomacromolecules*, **10**, 712–716.

74. Way, A.E., Hsu, L., Shanmuganathan, K., Weder, C., and Rowan, S.J. (2012) pH-responsive cellulose nanocrystal gels and nanocomposites. *ACS Macro Lett.*, **1**, 1001–1006.

75. Yang, J., Han, C.-R., Duan, J.-F., Xu, F., and Sun, R.-C. (2013) Mechanical and viscoelastic properties of cellulose nanocrystals reinforced poly(ethylene glycol) nanocomposite hydrogels. *ACS Appl. Mater. Interfaces*, **5**, 3199–3207.

76. Abitbol, T., Johnstone, T., Quinn, T.M., and Gray, D.G. (2011) Reinforcement with cellulose nanocrystals of poly(vinyl alcohol) hydrogels prepared by cyclic freezing and thawing. *Soft Matter*, **7**, 2373–2379.

77. Mihranyan, A. (2013) Viscoelastic properties of cross-linked polyvinyl alcohol and surface-oxidized cellulose whisker hydrogels. *Cellulose*, **20**, 1369–1376.

78. Zhou, C., Wu, Q., Yue, Y., and Zhang, Q. (2011) Application of rod-shaped cellulose nanocrystals in polyacrylamide hydrogels. *J. Colloid Interface Sci.*, **353**, 116–123.

79. Zhou, C., Wu, Q., and Zhang, Q. (2011) Dynamic rheology studies of in situ polymerization process of polyacrylamide–cellulose nanocrystal composite hydrogels. *Colloid Polym. Sci.*, **289**, 247–255.

80. Karaaslan, M.A., Tshabalala, M.A., Yelle, D.J., and Buschle-Diller, G. (2011) Nanoreinforced biocompatible hydrogels from wood hemicelluloses and cellulose whiskers. *Carbohydr. Polym.*, **86**, 192–201.

81. Yang, J., Han, C.-R., Duan, J.-F., Ma, M.-G., Zhang, X.-M., Xu, F., and Sun, R.-C. (2013) Synthesis and characterization of mechanically flexible and tough cellulose nanocrystals–polyacrylamide nanocomposite hydrogels. *Cellulose*, **20**, 227–237.

82. Wu, L., Zhou, H., Sun, H.-J., Zhao, Y., Yang, X., Cheng, S.Z.D., and Yang, G.

(2013) Thermoresponsive bacterial cellulose whisker/poly(NIPAM-co-BMA) nanogel complexes: synthesis, characterization, and biological evaluation. *Biomacromolecules*, **14**, 1078–1084.

83. Spagnol, C., Rodrigues, F.H.A., Pereira, A.G.B., Fajardo, A.R., Rubira, A.F., and Muniz, E.C. (2012) Superabsorbent hydrogel nanocomposites based on starch-g-poly(sodium acrylate) matrix filled with cellulose nanowhiskers. *Cellulose*, **19**, 1225–1237.

84. Wang, H. and Roman, M. (2011) Formation and properties of chitosan/cellulose nanocrystal polyelectrolyte macroion complexes for drug delivery applications. *Biomacromolecules*, **12**, 1585–1593.

85. Bica, C.I.D., Borsali, R., Geissler, E., and Rochas, C. (2001) Dynamics of cellulose whiskers in agarose gels. 1. Polarized dynamic light scattering. *Macromolecules*, **34**, 5275–5279.

86. Bica, C.I.D., Borsali, R., Rochas, C., and Geissler, E. (2006) Dynamics of cellulose whiskers spatially trapped in agarose hydrogels. *Macromolecules*, **39**, 3622–3627.

87. Osorio-Madrazo, A., Eder, M., Rueggeberg, M., Pandey, J.K., Harrington, M.J., Nishiyama, Y., Putaux, J.-L., Rochas, C., and Burgert, I. (2012) Reorientation of cellulose nanowhiskers in agarose hydrogels under tensile loading. *Biomacromolecules*, **13**, 850–856.

88. Zhang, X., Huang, J., Chang, P.R., Li, J., Chen, Y., Wang, D., Yu, J., and Chen, J. (2010) Structure and properties of polysaccharide nanocrystal-doped supramolecular hydrogels based on Cyclodextrin inclusion. *Polymer*, **51**, 4398–4407.

89. Goetz, L., Foston, M., Mathew, A.P., Oksman, K., and Ragauskas, A.J. (2010) Poly(methyl vinyl ether-co-maleic acid)-polyethylene glycol nanocomposites cross-linked in situ with cellulose nanowhiskers. *Biomacromolecules*, **11**, 2660–2666.

90. Goetz, L., Mathew, A.P., Oksman, K., Gatenholm, P., and Ragauskas, A.J. (2009) A novel nanocomposite film prepared from crosslinked cellulosic whiskers. *Carbohydr. Polym.*, **75**, 85–89.

91. Dash, R., Foston, M., and Ragauskas, A.J. (2013) Improving the mechanical and thermal properties of gelatin hydrogels cross-linked by cellulose nanowhiskers. *Carbohydr. Polym.*, **91**, 638–645.

92. Yang, J., Han, C.-R., Duan, J.-F., Ma, M.-G., Zhang, X.-M., Xu, F., Sun, R.-C., and Xie, X.-M. (2012) Studies on the properties and formation mechanism of flexible nanocomposite hydrogels from cellulose nanocrystals and poly(acrylic acid). *J. Mater. Chem.*, **22**, 22467–22480.

93. Cha, R., He, Z., and Ni, Y. (2012) Preparation and characterization of thermal/pH-sensitive hydrogel from carboxylated nanocrystalline cellulose. *Carbohydr. Polym.*, **88**, 713–718.

94. Lin, N. and Dufresne, A. (2013) Supramolecular hydrogels from in situ host–guest inclusion between chemically modified cellulose nanocrystals and cyclodextrin. *Biomacromolecules*, **14**, 871–880.

95. Lin, N., Bruzzese, C., and Dufresne, A. (2012) TEMPO-oxidized nanocellulose participating as crosslinking aid for alginate-based sponges. *ACS Appl. Mater. Interfaces*, **4**, 4948–4959.

96. Wang, Y., Chang, C., and Zhang, L. (2010) Effects of freezing/thawing cycles and cellulose nanowhiskers on structure and properties of biocompatible starch/PVA sponges. *Macromol. Mater. Eng.*, **295**, 137–145.

97. Li, Y. and Ragauskas, A.J. (2012) Ethanol organosolv lignin-based rigid polyurethane foam reinforced with cellulose nanowhiskers. *RSC Adv.*, **2**, 3347–3351.

98. Köhnke, T., Lin, A., Elder, T., Theliander, H., and Ragauskas, A.J. (2012) Nanoreinforced xylan–cellulose composite foams by freeze-casting. *Green Chem.*, **14**, 1864–1869.

99. Dash, R., Li, Y., and Ragauskas, A.J. (2012) Cellulose nanowhisker foams by freeze casting. *Carbohydr. Polym.*, **88**, 789–792.

100. Paës, G. and Chabbert, B. (2012) Characterization of arabinoxylan/cellulose nanocrystals gels to investigate fluorescent probes mobility in bioinspired models of plant secondary cell wall. *Biomacromolecules*, **13**, 206–214.

101. Heath, L. and Thielemans, W. (2010) Cellulose nanowhisker aerogels. *Green Chem.*, **12**, 1448–1453.

102. Gawryla, M.D., van den Berg, O., Weder, C., and Schiraldi, D.A. (2009) Clay aerogel/cellulose whisker nanocomposites: a nanoscale wattle and daub. *J. Mater. Chem.*, **19**, 2118–2124.

103. Zhou, C., Shi, Q., Guo, W., Terrell, L., Qureshi, A.T., Hayes, D.J., and Wu, Q. (2013) Electrospun bio-nanocomposite scaffolds for bone tissue engineering by cellulose nanocrystals reinforcing maleic anhydride grafted PLA. *ACS Appl. Mater. Interfaces*, **5**, 3847–3854.

104. Wongpanit, P., Sanchavanakit, N., Pavasant, P., Bunaprasert, T., Tabata, Y., and Rujiravanit, R. (2007) Preparation and characterization of chitin whisker-reinforced silk fibroin nanocomposite sponges. *Eur. Polym. J.*, **43**, 4123–4135.

105. Rizvi, R., Cochrane, B., Naguib, H., and Lee, P.C. (2011) Fabrication and characterization of melt-blended polylactide–chitin composites and their foams. *J. Cell. Plast.*, **47**, 283–300.

106. Heath, L., Zhu, L., and Thielemans, W. (2013) Chitin nanowhisker aerogels. *ChemSusChem*, **6**, 537–544.

107. Hariraksapitak, P. and Supaphol, P. (2010) Preparation and properties of α-chitin-whisker-reinforced hyaluronan–gelatin nanocomposite scaffolds. *J. Appl. Polym. Sci.*, **117**, 3406–3418.

108. Rinki, K., Tripathi, S., Dutta, P.K., Dutta, J., Hunt, A.J., Macquarrie, D.J., and Clark, J.H. (2009) Direct chitosan scaffold formation *via* chitin whiskers by a supercritical carbon dioxide method: a green approach. *J. Mater. Chem.*, **19**, 8651–8655.

109. Lertwattanaseri, T., Ichikawa, N., Mizoguchi, T., Tanaka, Y., and Chirachanchai, S. (2009) Microwave technique for efficient deacetylation of chitin nanowhiskers to a chitosan nanoscaffold. *Carbohydr. Res.*, **344**, 331–335.

110. Phongying, S., Aiba, S., and Chirachanchai, S. (2006) A novel

soft and cotton-like chitosan-sugar nanoscaffold. *Biopolymers*, **83**, 280–288.

111. Phongying, S., Aiba, S., and Chirachanchai, S. (2007) Direct chitosan nanoscaffold formation via chitin whiskers. *Polymer*, **48**, 393–400.

112. Blaker, J.J., Lee, K.-Y., Mantalaris, A., and Bismarck, A. (2010) Ice-microsphere templating to produce highly porous nanocomposite PLA matrix scaffolds with pores selectively lined by bacterial cellulose nano-whiskers. *Compos. Sci. Technol.*, **70**, 1879–1888.

113. Capadona, J.R., Shanmuganathan, K., Tyler, D.J., Rowan, S.J., and Weder, C. (2008) Stimuli-responsive polymer nanocomposites inspired by the sea cucumber dermis. *Science*, **319**, 1370–1374.

114. Shanmuganathan, K., Capadona, J.R., Rowan, S.J., and Weder, C. (2010) Bio-inspired mechanically-adaptive nanocomposites derived from cotton cellulose whiskers. *J. Mater. Chem.*, **20**, 180–186.

115. Shanmuganathan, K., Capadona, J.R., Rowan, S.J., and Weder, C. (2010) Stimuli-responsive mechanically adaptive polymer nanocomposites. *ACS Appl. Mater. Interfaces*, **2**, 165–174.

116. Rusli, R., Shanmuganathan, K., Rowan, S.J., Weder, C., and Eichhorn, S.J. (2010) Stress-transfer in anisotropic and environmentally adaptive cellulose whisker nanocomposites. *Biomacromolecules*, **11**, 762–768.

117. Mendez, J., Annamalai, P.K., Eichhorn, S.J., Rusli, R., Rowan, S.J., Foster, E.J., and Weder, C. (2011) Bioinspired mechanically adaptive polymer nanocomposites with water-activated shape-memory effect. *Macromolecules*, **44**, 6827–6835.

118. Shanmuganathan, K., Capadona, J.R., Rowan, S.J., and Weder, C. (2010) Biomimetic mechanically adaptive nanocomposites. *Prog. Polym. Sci.*, **35**, 212–222.

119. Fox, J.D., Capadona, J.R., Marasco, P.D., and Rowan, S.J. (2013) Bioinspired water-enhanced mechanical gradient nanocomposite films that mimic the architecture and properties of the squid beak. *J. Am. Chem. Soc.*, **135**, 5167–5174.

120. Biyani, M.V., Foster, E.J., and Weder, C. (2013) Light-healable supramolecular nanocomposites based on modified cellulose nanocrystals. *ACS Macro Lett.*, **2**, 236–240.

121. Fox, J., Wie, J.J., Greenland, B.W., Burattini, S., Hayes, W., Colquhoun, H.M., Mackay, M.E., and Rowan, S.J. (2012) High-strength, healable, supramolecular polymer nanocomposites. *J. Am. Chem. Soc.*, **134**, 5362–5368.

122. Zhu, Y., Hu, J., Luo, H., Young, R.J., Deng, L., Zhang, S., Fan, Y., and Ye, G. (2012) Rapidly switchable water-sensitive shape-memory cellulose/elastomer nano-composites. *Soft Matter*, **8**, 2509–2517.

123. Luo, H., Hu, J., and Zhu, Y. (2012) Path-dependent and selective multi-shape recovery of a polyurethane/cellulose-whisker nanocomposite. *Mater. Lett.*, **89**, 172–175.

124. Alloin, F., Azizi Samir, M.A.S., Cavaillé, J.-Y., Dufresne, A., Paillet, M., and Sanchez, J.-Y. (2002) Materiau a conduction ionique renforce, son utilisation dans les electrodes et les electrolytes. French Patent FR0207746.

125. Azizi Samir, M.A.S., Alloin, F., Gorecki, W., Sanchez, J.-Y., and Dufresne, A. (2004) Nanocomposite polymer electrolytes based on poly(oxyethylene) and cellulose nanocrystals. *J. Phys. Chem. B*, **108**, 10845–10852.

126. Alloin, F., D'Aprea, A., Kissi, N.E., Dufresne, A., and Bossard, F. (2010) Nanocomposite polymer electrolyte based on whisker or microFIbrils polyoxyethylene nanocomposites. *Electrochim. Acta*, **55**, 5186–5194.

127. Lalia, B.S., Samad, Y.A., and Hashaikeh, R. (2013) Nanocrystalline cellulose-reinforced composite mats for lithium-ion batteries: electrochemical and thermomechanical performance. *J. Solid State Electrochem.*, **17**, 575–581.

128. Angulakshmi, N., Thomas, S., Nair, J.R., Bongiovanni, R., Gerbaldi, C., and Stephan, A.M. (2013) Cycling profile of innovative nanochitin-incorporated poly(ethylene oxide) based electrolytes for

lithium batteries. *J. Power Sources*, **228**, 294–299.

129. Angulakshmi, N., Thomas, S., Nahm, K.S., Stephan, A.M., and Elizabeth, R.N. (2011) Electrochemical and mechanical properties of nanochitin-incorporated PVDF-HFP-based polymer electrolytes for lithium batteries. *Ionics*, **17**, 407–414.

130. Angulakshmi, N., Kumar, T.P., Thomas, S., and Stephan, A.M. (2010) Ionic conductivity and interfacial properties of nanochitin-incorporated polyethylene oxide–LiN(C₂F₅SO₂)₂ polymer electrolytes. *Electrochim. Acta*, **55**, 1401–1406.

131. Azizi Samir, M.A.S., Chazeau, L., Alloin, F., Cavaillé, J.-Y., Dufresne, A., and Sanchez, J.-Y. (2005) POE-based nanocomposite polymer electrolytes reinforced with cellulose whiskers. *Electrochim. Acta*, **50**, 3897–3903.

132. Azizi Samir, M.A.S., Alloin, F., Sanchez, J.-Y., and Dufresne, A. (2004) Cross-linked nanocomposite polymer electrolytes reinforced with cellulose whiskers. *Macromolecules*, **37**, 4839–4844.

133. Azizi Samir, M.A.S., Mateos, A.M., Alloin, F., Sanchez, J.-Y., and Dufresne, A. (2004) Plasticized nanocomposite polymer electrolytes based on poly(oxyethylene) and cellulose whiskers. *Electrochim. Acta*, **49**, 4667–4677.

134. Schroers, M., Kokil, A., and Weder, C. (2004) Solid polymer electrolytes based on nanocomposites of ethylene oxide–epichlorohydrin copolymers and cellulose whiskers. *J. Appl. Polym. Sci.*, **93**, 2883–2888.

135. Zhou, Y., Fuentes-Hernandez, C., Khan, T.M., Liu, J.-C., Hsu, J., Shim, J.W., Dindar, A., Youngblood, J.P., Moon, R.J., and Kippelen, B. (2013) Recyclable organic solar cells on cellulose nanocrystal substrates. *Sci. Rep.*, **3**, 1536 (5 pages).

136. van den Berg, O., Schroeter, M., Capadona, J.R., and Weder, C. (2007) Nanocomposites based on cellulose whiskers and (semi)conducting conjugated polymers. *J. Mater. Chem.*, **17**, 2746–2753.

137. Tkalya, E., Ghislandi, M., Thielemans, W., van der Schoot, P., de With, G., and Koning, C. (2013) Cellulose nanowhiskers templating in conductive polymer nanocomposites reduces electrical percolation threshold 5-fold. *ACS Macro Lett.*, **2**, 157–163.

138. Majoinen, J., Kontturi, E., Ikkala, O., and Gray, D.G. (2012) SEM imaging of chiral nematic films cast from cellulose nanocrystal suspensions. *Cellulose*, **19**, 1599–1605.

139. Beck, S., Bouchard, J., and Berry, R. (2011) Controlling the reflection wavelength of iridescent solid films of nanocrystalline cellulose. *Biomacromolecules*, **12**, 167–172.

140. Beck, S., Bouchard, J., Chauve, G., and Berry, R. (2013) Controlled production of patterns in iridescent solid films of cellulose nanocrystals. *Cellulose*, **20**, 1401–1411.

141. Zhang, Y.P., Chodavarapu, V.P., Kirk, A.G., and Andrews, M.P. (2012) Nanocrystalline cellulose for covert optical encryption. *J. Nanophotonics*, **6**, 063516.

142. Picard, G., Simon, D., Kadiri, Y., LeBreux, J.D., and Ghozayel, F. (2012) Cellulose nanocrystal iridescence: a new model. *Langmuir*, **28**, 14799–14807.

143. Shopsowitz, K.E., Qi, H., Hamad, W.Y., and MacLachlan, M.J. (2010) Free-standing mesoporous silica films with tunable chiral nematic structures. *Nature*, **468**, 422–426.

144. Shopsowitz, K.E., Hamad, W.Y., and MacLachlan, M.J. (2012) Flexible and iridescent chiral nematic mesoporous organosilica films. *J. Am. Chem. Soc.*, **134**, 867–870.

145. Shopsowitz, K.E., Hamad, W.Y., and MacLachlan, M.J. (2011) Chiral nematic mesoporous carbon derived from nanocrystalline cellulose. *Angew. Chem. Int. Ed.*, **50**, 10991–10995.

146. Shopsowitz, K.E., Kelly, J.A., Hamad, W.Y., and MacLachlan, M.J. (2013) Biopolymer templated glass with a twist: controlling the chirality, porosity, and photonic properties of silica with cellulose nanocrystals. *Adv. Funct. Mater.* doi: 10.1002/adfm.201301737

147. Kelly, J.A., Shopsowitz, K.E., Ahn, J.M., Hamad, W.Y., and MacLachlan, M.J. (2012) Chiral nematic stained glass: controlling the optical properties of nanocrystalline cellulose-templated materials. *Langmuir*, **28**, 17256–17262.

148. Kelly, J.A., Shukaliak, A.M., Cheung, C.C.Y., Shopsowitz, K.E., Hamad, W.Y., and MacLachlan, M.J. (2013) Responsive photonic hydrogels based on nanocrystalline cellulose. *Angew. Chem. Int. Ed.*, **52**, 8912–8916.

149. Jackson, J.K., Letchford, K., Wasserman, B.Z., Ye, L., hamad, W.Y., and Burt, H.M. (2011) The use of nanocrystalline cellulose for the binding and controlled release of drugs. *Int. J. Nanomed.*, **6**, 321–330.

150. Villanova, J.C.O., Ayres, E., Carvalho, S.M., Patrício, P.S., Pereira, F.V., and Oréfice, R.L. (2011) Pharmaceutical acrylic beads obtained by suspension polymerization containing cellulose nanowhiskers as excipient for drug delivery. *Eur. J. Pharm. Sci.*, **42**, 406–415.

151. Lin, N., Huang, J., Chang, P.R., Feng, L., and Yu, J. (2011) Effect of polysaccharide nanocrystals on structure, properties, and drug release kinetics of alginate-based microspheres. *Colloids Surf., B*, **85**, 270–279.

152. Wang, Y. and Chen, L. (2011) Impacts of nanowhisker on formation kinetics and properties of all-cellulose composite gels. *Carbohydr. Polym.*, **83**, 1937–1946.

153. Xiang, C., Taylor, A.G., Hinestroza, J.P., and Frey, M.W. (2013) Controlled release of nonionic compounds from poly(lactic acid)/cellulose nanocrystal nanocomposite fibers. *J. Appl. Polym. Sci.*, **127**, 79–86.

154. Dash, R. and Ragauskas, A.J. (2012) Synthesis of a novel cellulose nanowhisker-based drug delivery system. *RSC Adv.*, **2**, 3403–3409.

155. Varjonen, S., Laaksonen, P., Paananen, A., Valo, H., Hähl, H., Laaksonen, T., and Linder, M.B. (2011) Self-assembly of cellulose nanofibrils by genetically engineered fusion proteins. *Soft Matter*, **7**, 2402–2411.

156. Minellia, M., Baschettia, M.G., Doghieria, F., Ankerforsb, M., Lindströmb, T., Siróc, I., and Plackett, D. (2010) Investigation of mass transport properties of microfibrillated cellulose (MFC) films. *J. Membr. Sci.*, **358**, 67–75.

157. Lin, N. and Dufresne, A. (2013) Physical and/or chemical compatibilization of extruded cellulose nanocrystal reinforced polystyrene nanocomposites. *Macromolecules*, **46**, 5570–5583.

158. Angellier, H., Molina-Boisseau, S., Lebrun, L., and Dufresne, A. (2005) Processing and structural properties of waxy maize starch nanocrystals reinforced natural rubber. *Macromolecules*, **38**, 3783–3792.

159. Angellier, H., Molina-Boisseau, S., and Dufresne, A. (2005) Mechanical properties of waxy maize starch nanocrystal reinforced natural rubber. *Macromolecules*, **38**, 9161–9170.

160. Kaboorani, A., Riedl, B., Blanchet, P., Fellin, M., Hosseinaei, O., and Wang, S. (2012) Nanocrystalline cellulose (NCC): a renewable nano-material for polyvinyl acetate (PVA) adhesive. *Eur. Polym. J.*, **48**, 1829–1837.

161. Csoka, L., Hoeger, I.C., Rojas, O.J., Peszlen, I., Pawlak, J.J., and Peralta, P.N. (2012) Piezoelectric effect of cellulose nanocrystals thin films. *ACS Macro Lett.*, **1**, 867–870.

7
Characterization of Polysaccharide Nanocrystal-Based Materials

Alain Dufresne and Ning Lin

7.1
Introduction

Biological materials such as wood, plants, and exoskeleton of crustaceans and insects boast of outstanding performances and multifunctionality that surpass our engineering materials. As a result, they have emerged as models for bio-inspired synthetic materials with superior performance. For example, plants are cellular hierarchical biocomposites designed by nature, and they are basically semicrystalline cellulose microfibril-reinforced amorphous matrices made of hemicellulose, lignin, waxes, extractive, and trace elements. In nature, cellulose is a ubiquitous structural polymer that confers its mechanical properties to higher plant cells. The hierarchical structure of natural fibers, based on their elementary nanofibrillar components, leads to the unique strength and high performance properties of different species of plants. Indeed, the most important attribute of wood and other lignocellulosic materials is their mechanical properties, in particular their unusual ability to provide high mechanical strength and high strength-to-weight ratio while allowing for flexibility to counter large dimensional changes due to swelling and shrinking. In all terrestrial and aquatic plant species, the primary cell wall is a dynamic structure and its constituting material must be synthesized in a form that is competent to undergo extension.

Similarly, chitin is a naturally abundant polysaccharide and the supporting material of crustaceans, insects, and so on. It is biosynthesized by a large number of living organisms and can be easily obtained from crab or shrimp shells. The exocuticle and endocuticle layers of the shells are designed to resist mechanical loads, and they consist of a hard fibrous chitin-protein tissue containing calcium carbonate minerals (mostly crystalline, sometimes amorphous). Both layers present a twisted plywood structure, characteristic of cuticles. The presence of microfibrils suggests that cellulose and chitin have characteristics that make them good candidates for the development of nanocomposites. Starch is another natural, renewable, biodegradable polymer produced by many plants as a source of storage energy. It is found in plant roots, stalks, crop seeds, and staple crops such as rice, corn, wheat, tapioca, and potato.

These three abundant renewable polysaccharides share rather similar building blocks, but they exhibit quite different properties because the existing differences in molecular structure lead to different arrangements and supramolecular structures. Owing to their hierarchical structure and semicrystalline nature, nanoparticles can be extracted from these naturally occurring polymers using a top-down mechanically or chemically induced deconstructing strategy. The potential of these nanoparticles has been proved for special functional nanomaterials [1] but it is as a bio-based reinforcing nanofiller that they have attracted significant interest during the last 20 years [2–5]. Meanwhile, nanocomposites show unique properties because of the nanometric size effect, compared to conventional composites even at low filler content. Nanofillers have strong reinforcing effects, and studies have also shown their positive impact in barrier packaging. However, for decades, studies have been conducted with non-renewable inorganic fillers and petroleum-based matrix. Increasing environmental concerns have led to developing new flexible barrier bio-based packaging and investigating the potential uses of renewable resources for such application. For instance, scientific publications and patents related to nanocellulose have begun to increase markedly after 2003 and 2004, respectively [6].

7.2
Mechanical Properties of Polysaccharide Nanocrystals

7.2.1
Intrinsic Mechanical Properties of Polysaccharide Nanocrystals

The elastic modulus of the crystalline region of cellulose and chitin is an important property of these materials, especially with respect to the ultimate aim of exploiting their full potential in composite materials. The elastic properties of cellulose crystalline regions have been investigated since the mid-1930s either by theoretical evaluations or by experimental measurements (wave propagation, X-ray diffraction, Raman spectroscopy, and atomic force microscopy (AFM)). It was shown in 1936 [7] that the modulus of elasticity corresponding to the principal chain direction of a polymer crystal of specified nature may be calculated from the force constants of the chemical bonds of the chain derived from vibration frequencies of molecules. Appling the method to the cellulose crystal, the authors obtained for two different estimates of force constants longitudinal modulus values of 7.7×10^{11} and 12.1×10^{11} dyn·cm^{-2}, that is, 77 and 121 GPa.

The cellulose crystal modulus has been first experimentally studied in 1962 for cellulose I [8] and cellulose II [9]. For cellulose I, the modulus value was determined from the crystal deformation of highly oriented fibers of bleached ramie. The lattice extension was measured by X-ray diffraction under a constant stress, so that the relaxation had no influence on the result. The stress in the crystalline regions was assumed to be equal to the stress applied to the sample,

and this assumption of a homogeneous stress distribution was proven experimentally. The lattice extension was measured under this constant stress and similar experiments were carried out by varying the thickness of the fiber and the applied weight. Then, the stress–strain curves were plotted. The calculation of the elastic modulus was based on the assumption of the series model in which crystalline and amorphous regions alternate along the length of the fiber. A value of $134 \times 10^4 \, kg \cdot cm^{-2}$, that is, 134 GPa, was reported for cellulose I. X-ray measurements of the elastic modulus of cellulose II crystals was performed using Fortisan H fibers [9]. The position of the 040 reflection has been measured with and without load on the fibers. The crystallographic 040 planes are perpendicular to the chain axes of the cellulosic molecules and the 040 spacing gave a measure of the length of the repeating unit of the chain. An apparent modulus value ranging between 7 and $9 \times 10^{11} \, dyn \cdot cm^{-2}$, that is, 70 and 90 GPa, was calculated for crystalline regions on the basis of a series model.

The different values reported so far for the stiffness of crystalline cellulose are collected in Table 7.1. It evidenced the important role of intramolecular bonding on the determination of the crystallite modulus and chain deformation mechanism. The lower values observed for form II compared to cellulose I were ascribed to lower intramolecular hydrogen bonds, showing again the importance of intramolecular hydrogen bonds, whereas the intermolecular hydrogen bonds were found to play a minor role. For cellulose I, the average value is within the range 130–150 GPa. These values are comparable to those reported for aromatic ring polymers such as poly-*p*-phenylene terephthalamide (153–200 GPa) and poly-*m*-phenylene isophthalamide (88 GPa) [10]. However, it is much lower than that (235 GPa) of polyethylene, which possesses the maximum elastic modulus of the crystalline regions in the direction parallel to the chain axis [11]. However, if the cross-sectional area of each individual molecule is considered, it is found that the modulus value is similar for cellulose and polyethylene.

The different values reported for the crystal of cellulose are comparable to those reported for pure crystalline β-chitin produced by the marine diatom *Thalassiosira fluviatilis* [32]. For example, the Young's modulus of chitin crystal was estimated to be at least 150 GPa [33]. However, lower values, that is, 41 GPa [34] and 59.3 GPa [35], were also reported for α-chitin, which were ascribed to the contracted skeletons of α-chitin in the crystal lattice and larger cross-sectional area of the single molecule in the crystalline lattice.

These impressive mechanical properties make cellulose and chitin nanocrystals ideal candidates for the processing of reinforced polymer composites. Their Young's modulus with a density for crystalline cellulose or chitin around $1.5–1.6 \, g \cdot cm^{-3}$ is much higher than the one for glass fibers, around 70 GPa with a density around $2.6 \, g \cdot cm^{-3}$, which are classically used in composite applications. It is similar to Kevlar (60–125 GPa, density around $1.45 \, g \cdot cm^{-3}$) and potentially stronger than steel (200–220 GPa, density around $8 \, g \cdot cm^{-3}$). Indeed, the specific Young's modulus, which is the ratio between the Young's modulus and the density, of cellulose nanocrystals is around $85 \, J \cdot g^{-1}$ whereas it is around $25 \, J \cdot g^{-1}$ for steel [36]. Incorporating these nanoparticles in a synthetic or natural polymeric matrix

Table 7.1 Longitudinal (E_L) and transverse (E_T) moduli of crystalline cellulose.

Material	Method	E_L (GPa)	E_T (GPa)	References
Cellulose I	Calculation	77–121		[7]
		56		[12]
Bleached ramie fibers (cellulose I)	X-ray diffraction	134		[8]
Fortisan H fibers (cellulose II)	X-ray diffraction	70–90		[9]
Cellulose I	Calculation	172.9[a]		[13]
		70.8[b]		[13]
		76	51–57	[14]
Cellobiose (two hydrogen bonds – cellulose I)	Calculation	136±6		[15]
Cellobiose (one hydrogen bond – cellulose II)		89±4		
Ramie fibers (cellulose I)	X-ray diffraction	122–135		[16]
Mercerized ramie fibers (cellulose II)		106–112		
Cellulose I	Calculation	167.5	11	[17]
Cellulose II		162.1	50	
Purified ramie fibers (cellulose I)	X-ray diffraction	138		[18]
Polynosics (cellulose II)		88		
Cellulose III$_\mathrm{I}$		87		
Cellulose III$_\mathrm{II}$		58		
Cellulose IV$_\mathrm{I}$		75		
Cellulose I	Calculation	134–135		[19]
Cellulose II		83		
Cellulose II	Calculation	155	24–51	[20]
Cellulose I$_\alpha$	Calculation	127.8		[21]
Cellulose I$_\beta$		115.2		
Cellulose I$_\beta$	Raman	143		[22]
Cellulose I$_\beta$	Calculation	124–155		[23]
Cellulose I$_\alpha$	Calculation	136–155[a]		[24]
		114–117[b]		
Cellulose I$_\beta$		116–149[a]		
		124–127[b]		
Cellulose II		109–166[a]		
		101–106[b]		
Cellulose I$_\beta$	Calculation	156 at 300 K		[25]
		117 at 500 K		
Cellulose I	Raman	57–105		[26]
Ramie fibers (cellulose I)	Inelastic X-ray scattering	220	15	[27]
TEMPO-oxidized cellulose I$_\beta$	AFM	145		[28]

(continued overleaf)

Table 7.1 (*Continued.*)

Material	Method	E_L (GPa)	E_T (GPa)	References
Acid-hydrolyzed cellulose I$_\beta$		150		
Wood	AFM		18–50	[29]
Disaccharide cellulose I$_\beta$	Calculation	85.2^a/37.6^b		[30]
Disaccharide cellulose I$_\beta$		99.7^a/33.0^b		
Extended cellulose I$_\beta$ chains (10–40 glucoses)		126.0^a/63.3^b		
Cellulose I$_\beta$	Calculation	206	19	[31]

^{a}With intramolecular hydrogen bonding.
^{b}Without intramolecular hydrogen bonding.

consists therefore in biomimeting nature. All that scientists need to do is to try to mimic nature or to exploit natural biocomposites in order to develop novel materials that can be suitable to our needs without being harmful to the environment.

Obviously, the mechanical properties of crystalline starch should be much lower than for cellulose and chitin because it does not consist of aligned macro-molecules but of parallel-stranded left-handed double helices arranged in a monoclinic (allomorph A) or hexagonal (allomorph B) packing. Moreover, it was found that roughly half of the dextrins in starch nanocrystals are branched mole-cules [37].

7.2.2
Mechanical Properties of Polysaccharide Nanocrystal Films

The high intrinsic stiffness of polysaccharide nanocrystals is not their only asset. The high specific surface area ensuing from their nanoscale dimensions and high density of surface hydroxyl groups result in potential strong interactions between the nanoparticles through hydrogen bonding. The outstanding mechanical properties of polysaccharide nanocrystal-reinforced polymer nanocomposites can be well understood from the formation of a continuous nanoparticle network. The formation of this rigid network, resulting from strong interactions between nanocrystals, is assumed to be governed by a percolation mechanism. In this approach, an important parameter is the modulus of the percolating nanoparticle network, which is obviously different from that of individual nanocrystals. This modulus can be assumed to be similar, in principle, to that of a paper sheet for which the hydrogen bonding forces provide the basis of its stiffness. However, because of the nanoscale effect stronger interactions are expected. This modulus can be experimentally determined from tensile tests performed on films prepared by water evaporation of a suspension of nanocrystals. Figure 7.1 shows the surface of a film obtained by casting/evaporation of a cellulose nanocrystal suspension
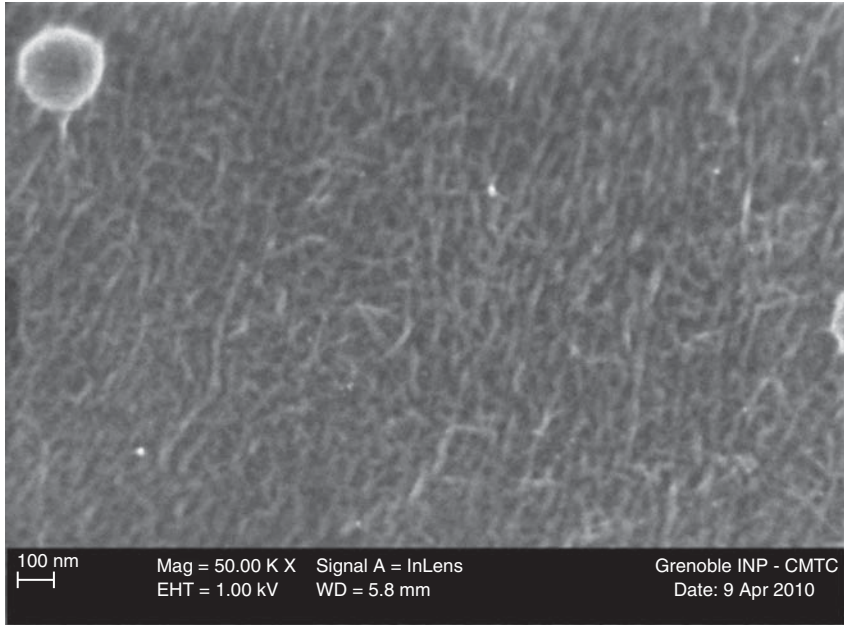
Figure 7.1 Scanning electron micrograph (SEM-FEG) of a sisal cellulose nanocrystal film. Reproduced from [38], copyright 2011 © permission from Elsevier.

extracted from sisal and observed by scanning electron microscopy with field emission gun (SEM-FEG).

Some data have been reported in the literature but more values are available for nanofibrillated cellulose (NFC) [5]. For tunicin [39, 40] and wheat straw cellulose nanocrystals [41], the tensile modulus was around 15 and 6 GPa, respectively. For tunicin nanocrystals lower values (8; 5; 2; 4 GPa) were also reported [42–45]. These values are much higher than those obtained for films made of chitin nanocrystals. Tensile modulus values around 0.5 and 2 GPa were reported for chitin nanocrystals extracted from squid pen [46] and *Riftia* tubes [47], respectively. As suggested from these values and from the literature [44], the reinforcing capacity of cellulose nanocrystals is related to the aspect ratio of the nanoparticles. The benchmarking of cellulose nanocrystals from different sources and the impact of the geometrical characteristics on the specific mechanical properties of the percolating network were reported [48]. Even if other factors are controlling the mechanical properties of this network, such as porosity, density, orientation, and organization of the nanoparticles, it seems that a weak correlation exists between the aspect ratio of the nanocrystals and mechanical stiffness of the mat as shown in Figure 7.2. The stiffness of the film was found to increase with the aspect ratio of the nanocrystals. The experimental testing conditions (temperature, humidity, and cross-head speed) also affect the measured characteristics. Indeed, water present in the film acts as a plasticizer, reducing the intermolecular interactions between the nanoparticles, thus reducing the stiffness of the material.
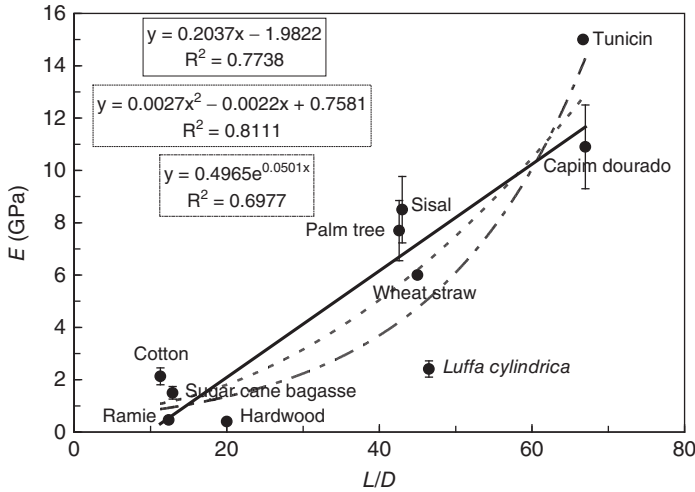
Figure 7.2 Evolution of the Young's modulus of cellulose nanocrystals films determined from tensile tests as a function of the aspect ratio of the constituting nanocrystals. Reproduced from [48], copyright 2011 © permission from Elsevier.

7.3
Dispersion of Polysaccharide Nanocrystals

The homogeneous dispersion of polysaccharide nanocrystals within a continuous medium (polymeric matrix in the case of nanocomposites) is the key step to benefiting from their outstanding properties. It is fixed during the processing of the material.

Polysaccharide nanoparticles have a strong tendency for self-association because of the omnipresence of interacting surface hydroxyl groups. This property, which is the basis of the strength of paper sheets, is a desirable feature for the formation of load-bearing percolating architectures within the host polymer matrix. However, these interparticle interactions can cause aggregation during the preparation of the nanocomposite, thus inducing the loss of the nanoscale and limiting the potential of mechanical reinforcement. This aggregation phenomenon is magnified when the specific surface area increases and then when the size of the particle decreases. Different strategies have been reported in the literature to homogeneously mix cellulose nanoparticles with a polymeric matrix. These different strategies are summarized in Figure 7.3 and are briefly described below. More detailed information can be found elsewhere [5, 49].

Because of the good dispersion level of polysaccharide nanoparticles in water, it is obviously the most suitable processing medium. Both water-soluble polymers and polymer aqueous dispersions (latex) can be used. After mixing the polysaccharide nanoparticle dispersion with the polymer solution/dispersion, a solid nanocomposite film can be obtained by simple casting and water
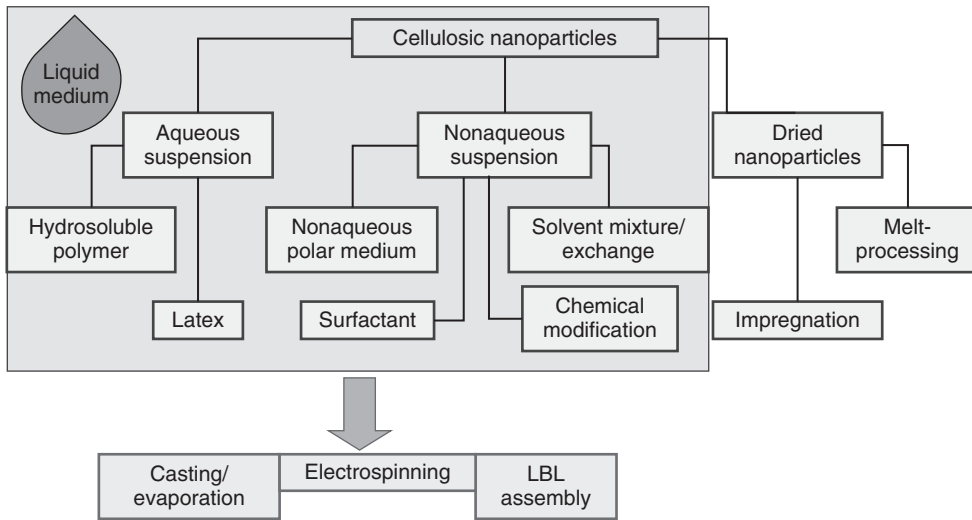
Figure 7.3 The different strategies applied for the processing of cellulose nanocrystal reinforced polymer nanocomposites. (Adapted from Ref. [36].)

evaporation. This mode of processing allows preserving the individualization state of the nanoparticles resulting from their colloidal dispersion in water and has therefore been extensively used in literature. A copolymer of styrene and butyl acrylate (poly(S-co-BuA)) in latex form and cellulose nanocrystals extracted from tunicin were used in the pioneering work [39, 40].

However, stable suspensions of polysaccharide nanocrystals with negatively charged surface groups, commonly produced by hydrolysis of the native polysaccharide with sulfuric acid, can be obtained in various polar liquid media. For instance, stable cellulose nanocrystal suspensions have been prepared in dimethylformamide (DMF) [50], dimethyl sulfoxide (DMSO), *N*-methyl pyrrolidine (NMP), formic acid, and *m*-cresol [51]. Nanocomposites can be prepared by mixing these suspensions with a polymer solution. Casting from a mixture of solvents can also be used to prepare polysaccharide nanocrystal-reinforced nanocomposites. By this method, the aqueous suspension of nanoparticles is mixed with a polymer solution involving a solvent miscible with water, for example, tetrahydrofuran (THF) [52]. Solvent exchange procedure can be applied to suspend the nanoparticles in the proper liquid medium for further surface chemical modification, or mixing with a polymer solution or monomer for subsequent *in situ* polymerization [53]. In this method, the aqueous suspension is progressively solvent exchanged in liquids of decreasing polarity by several successive centrifugation and redispersion operations, using sonication after each solvent exchange step to avoid aggregation. Acetone is routinely used for the first solvent exchange step.

Stable polysaccharide nanoparticle dispersions in apolar or low polarity solvent can be obtained by physically coating the surface with a surfactant [54, 55] or

chemically grafting apolar moieties onto the surface. Both methods allow tuning the surface and decreasing the surface energy of the nanoparticle to fit with the one of the liquid. The surface chemical modification of polysaccharide nanoparticles obviously involves the ample surface hydroxyl groups resulting from their nanoscale dimensions and ensuing high surface area. Experimental conditions should avoid swelling media and the peeling effect of surface-grafted chains, which would otherwise induce their dissolution in the reaction medium. Therefore, the chemical grafting process has to be mild enough in order to preserve the integrity of the nanoparticle. The possible surface chemical modifications of polysaccharide nanocrystals are reported in Chapter 3. The chemically modified nanoparticles can be dispersed in organic liquids of low polarity and mixed with polymer solution or eventually directly added in the polymer melt after drying. However, two conflicting effects arise from this procedure. On the one hand, it allows improving the dispersion of the modified nanoparticles in the continuous apolar medium, which is beneficial to optimize the mechanical properties of the ensuing nanocomposite. On the other hand, it restricts the interactions between nanoparticles through hydrogen bonding, which is the basis of the outstanding mechanical properties of polysaccharide nanocrystal-based nanocomposites.

The previous processing techniques used mainly a liquid as the processing medium and are mainly restricted to wet processing methods such as casting/evaporation, which has been extensively used. The main advantage of this strategy relies in the fact that it allows preserving the dispersion state of the nanoparticles in the liquid. However, it limits the number of polymer matrices that can be used in association with polysaccharide nanocrystals. Moreover, this procedure is both non-industrial and non-economic. It should be used for niche applications. A number of organizations have announced nanocellulose demonstration plants [5]. Therefore, more industrial nanocomposite processing techniques should be developed. Melt-compounding techniques, such as extrusion or injection molding, are commonly used to process thermoplastic polymers. They are "green" (solvent-free), and industrially and economically viable. However, these conventional processing techniques are infrequently employed for the preparation of polysaccharide nanocrystal-reinforced polymer nanocomposites. This is ascribed to inherent incompatibility and thermal stability issues. The hydrophilic nature of polysaccharides causes irreversible agglomeration during drying and aggregation in nonpolar matrices because of the formation of additional hydrogen bonds between nanoparticles. Few solutions have been proposed to address this challenge. A glance at literature allows discerning different strategies [49].

7.3.1
Observation of Polysaccharide Nanocrystals in Matrix

The extremely small dimensions of polysaccharide nanocrystals make it difficult to directly observe their degree of dispersion in the polymeric matrix.

(a)

(b)

(c)

(d)

(e)

(f)
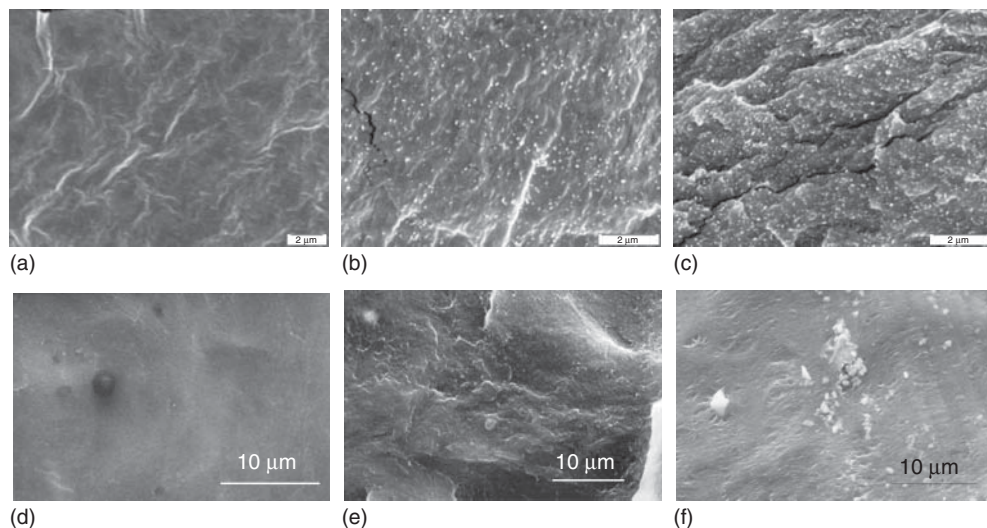
Figure 7.4 Scanning electron micrographs of the cryofractured surface of unfilled glycerol plasticized starch (a) and related nanocomposites reinforced with 6.2 wt% (b) and 25 wt% (c) tunicin nanocrystals. Reproduced from [56], copyright 2000 © permission from American Chemical Society and unfilled PEO (d) and related nanocomposites reinforced with 6 wt% ramie nanocrystals obtained by casting evaporation (e) or extrusion (f). Reproduced from [57], copyright 2011 © permission from Springer.

Generally, scanning electron microscopy (SEM) observation of the cryofractured surface of the sample is performed to check the presence or absence of nanoparticle aggregates. If no aggregate is observed a good dispersion level is concluded. Examples are given in Figure 7.4 showing SEM of the cryofractured surface of glycerol plasticized starch [56] and poly(oxyethylene) PEO [57] reinforced with cellulose nanocrystals. In each case, observation of the matrix is provided for comparison. By comparing the micrographs showing the surface of fracture of unfilled starch (panel a) and of composites (panels b and c), it is easy to identify cellulose nanocrystals. They appear as white dots, the concentration of which is a direct function of the cellulose content in the composite. These shiny dots correspond to the transversal sections of cellulose nanocrystals. Their diameter, around 62 ± 2 nm, was much higher than the nanocrystal diameter (around 10 nm). This results from a charge concentration effect due to the emergence of the nanorods from the observed surface. It is worth noting the homogeneous distribution of the filler within the starch matrix. This is ascribed to the processing method used in this study involving an aqueous medium. Figure 7.4(e,f) show the cryofractured surface of PEO films reinforced with 6 wt% cellulose nanocrystals extracted from ramie fibers. Panel (e) corresponds to nanocomposite films obtained by casting/evaporation from an aqueous suspension whereas panel (f) corresponds to films obtained by extrusion. The surface of the cast/evaporated film is more chaotic than for the PEO matrix
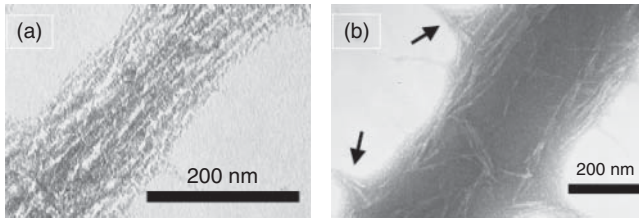
Figure 7.5 Transmission electron micrographs of electrospun PEO-based nanofibers prepared from 5 wt% (a) and 7 wt% (b) solutions reinforced with 20 wt% cellulose nanocrystals (arrows pointing to typical secondary nanofibers). Reproduced from [58], copyright 2011 © permission from American Chemical Society.

(Figure 7.4d) but shows again a homogeneous dispersion of white dots. The morphology of the extruded nanocomposites film is similar but less chaotic than its cast/evaporated counterpart. Large domains of white dots, much larger than those obtained for the cast/evaporated film, are observed, indicating that the nanoparticles are not well dispersed in the PEO matrix. It was concluded that the nanocrystal aggregates may have been induced by the extrusion process.

Transmission electron microscopy (TEM) observation of ultra-thin cryomicrotomed specimens is a better option but more difficult to implement. Direct electrospinning of PEO/cellulose nanocrystal suspensions onto a carbon-coated copper grid was also reported [58]. The uranyl acetate staining procedure is generally used to observe the nanoparticles within the matrix by increasing the contrast between the different phases. Drop casting of a very diluted polyvinyl alcohol (PVA)/cellulose nanocrystal suspension on carbon-coated copper grid was also carried out for TEM observations [59]. Figure 7.5 shows that rod-shaped cellulose nanocrystals without obvious aggregation were well dispersed in the electrospun PEO-based nanofibers [58].

AFM can also be used to investigate the dispersion of polysaccharide nanocrystals in a polymer matrix. For instance, the morphology of segmented thermoplastic elastomeric polyurethane (STPUE) reinforced with cellulose nanocrystals prepared from DMF medium was imaged using tapping-mode AFM and following two protocols, namely, spin-coating/annealing and casting evaporation/cryo-ultramicrotomy [60].

Both phase and height features were reported as shown in Figures 7.6 and 7.7 for spin-coated/annealed and cast-evaporated/cryo-ultramicrotomed specimens, respectively. In the phase image (right), lighter regions correspond to hard phase material (crystalline domains in polyurethane matrix or hard segments) and darker regions are associated to soft phase material (polyol or soft segments). AFM images for the neat STPUE matrix revealed very small size of hard segment domains due to the low quantity of hard segments involved. For nanocomposites the proportion of lighter segments increased as the cellulose nanocrystal content increased as expected. A relatively uniform dispersion of cellulose nanocrystals was observed in the polyurethane matrix using both processing procedures.
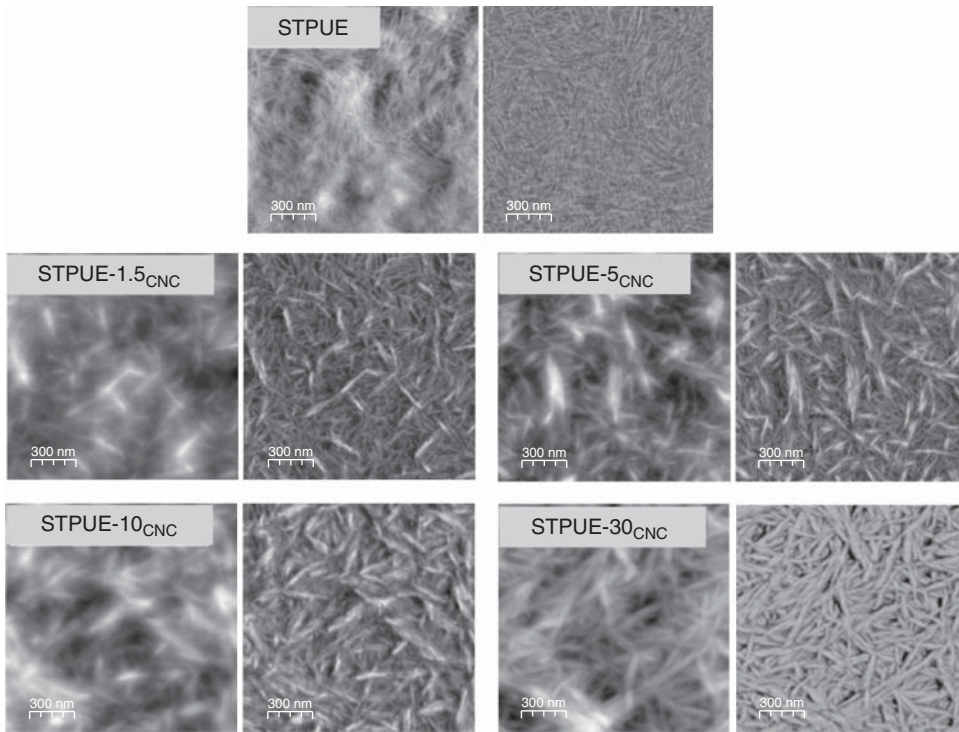
Figure 7.6 AFM height (left) and phase (right) images of spin-coated/annealed (100 °C for 12 h) polyurethane (STPUE) and cellulose nanocrystal reinforced polyurethane nanocomposites (STPUE-X$_{CNC}$; where X corresponds to the cellulose nanocrystal weight content). Reproduced from [60], copyright 2013 © permission from Elsevier.

7.3.2
Three-Dimensional Network of Polysaccharide Nanocrystals

As mentioned in Section 7.2.2 interactions through strong hydrogen bonding between nanocrystals result in high mechanical property materials. This continuous network can be easily formed from evaporation of an aqueous dispersion of polysaccharide nanoparticles but it can be absent or destroyed when the filler is embedded in a polymeric matrix.

In the pioneering works on the reinforcing effect of cellulose nanocrystals [39, 40], poly(S-co-BuA) in the latex form was reinforced with cellulose nanocrystals extracted from tunicate. The reinforcing effect of the nanoparticles was accessed by dynamic mechanical analysis (DMA) experiments in the shear mode. The authors measured a spectacular improvement in the storage modulus after adding tunicin nanocrystals into the host polymer even at low contents. This increase was especially significant above the glass–rubber transition temperature of the thermoplastic matrix because of its poor mechanical properties in this
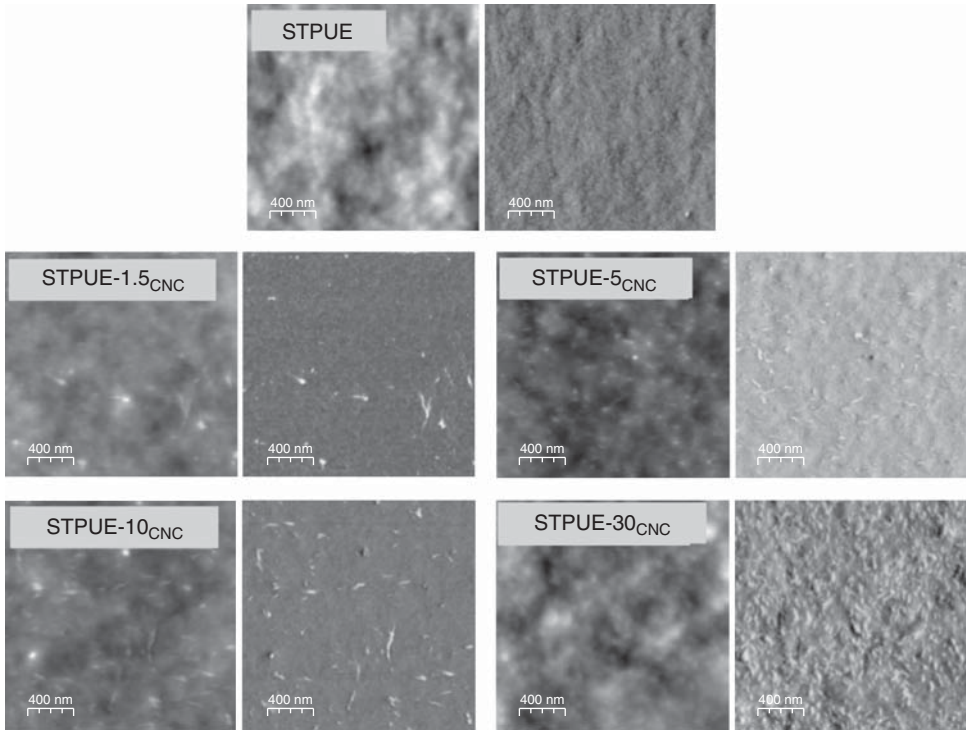
Figure 7.7 AFM height (left) and phase (right) images of cast-evaporated/cryo-ultramicrotomed polyurethane (STPUE) and cellulose nanocrystal reinforced polyurethane nanocomposites (STPUE-X$_{CNC}$; where X corresponds to the cellulose nanocrystal weight content). Reproduced from [60], copyright 2013 © permission from Elsevier.

temperature range. In the rubbery state of the thermoplastic matrix, the modulus of the composite with a loading level as low as 6 wt%, that is, 4 vol%, was more than two orders of magnitude higher than that of the unfilled matrix. Moreover, the introduction of 3 wt% or more cellulosic nanocrystals provided an outstanding thermal stability of the matrix modulus up to the temperature at which cellulose started to degrade (500 K).

A good agreement between experimental and predicted data was reported when using the series–parallel model of Takayanagi modified to include a percolation approach [39, 40]. In this approach the percolating filler network is set in parallel with a series part composed of the matrix and the non-percolating filler phase (Figure 7.8) and the elastic tensile modulus E_c of the composite is given by the following equation:

$$E_c = \frac{(1 - 2\psi + \psi\nu_R)E_S E_R + (1 - \nu_R)\psi E_R^2}{(1 - \nu_R)E_R + (\nu_R - \psi)E_S}$$

The subscripts S and R refer to the soft (polymer matrix) and rigid (cellulose nanocrystal) phase, respectively. The adjustable parameter, ψ, involved in the
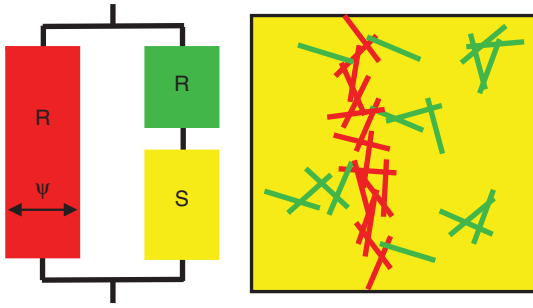
Figure 7.8 Schematic representation of the series–parallel model. R and S refer to the rigid (cellulosic filler) and (polymeric matrix) phases, respectively, and ψ is the volume fraction of the percolating rigid phase. Red and green rods correspond to percolating and unpercolating nanoparticles, respectively. (Adapted from Ref. [5].)

series–parallel model corresponds in the adapted prediction to the volume fraction of the percolating rigid phase. With b being the critical percolation exponent, ψ can be written as:

$$\psi = 0 \qquad \qquad \text{for } v_R < v_{Rc}$$

$$\psi = v_R \left(\frac{v_R - v_{Rc}}{1 - v_{Rc}} \right)^b \qquad \text{for } v_R > v_{Rc}$$

where $b = 0.4$ for a 3D network [61, 62].

At high temperatures when the polymeric matrix could be assumed to have zero stiffness ($E_S \sim 0$), the calculated stiffness of the composites is simply the product of that of the percolating filler network by the volume fraction of percolating filler phase:

$$E_c = \psi E_R$$

It was therefore suspected that all the stiffness of the material was due to infinite aggregates of cellulose nanocrystals. Above the percolation threshold the cellulosic nanoparticles can connect and form a 3D continuous pathway through the nanocomposite film. The formation of this cellulose network was supposed to result from strong interactions between nanocrystals, such as hydrogen bonds. This mechanical percolation effect allowed explaining both the high reinforcing effect and the thermal stabilization of the composite modulus up to 500 K for tunicin nanocrystal reinforced poly(S-co-BuA) films. For cylindrical shaped particles, the volume fraction required to achieve the geometrical percolation threshold v_{Rc} can be determined from the following relation [63]:

$$v_{Rc} = \frac{0.7}{L/d}$$

where L/d corresponds to the aspect ratio of the rod.

The existence of such a three-dimensional percolating nanoparticle network was evidenced by performing successive tensile tests on crab shell chitin
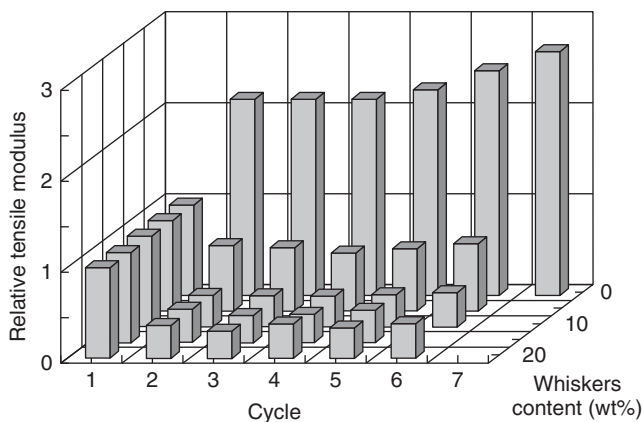
Figure 7.9 Evolution of the relative tensile modulus, viz. the modulus of the composite measured during cycle i divided by the one measured for the same sample during the first stretching cycle, E_i/E_1, of natural rubber films as a function of i and of the chitin nanocrystal content. Reproduced from [64], copyright 2003 © permission from American Chemical Society.

nanocrystals reinforced-natural rubber (NR) [64]. The experiment consisted in stretching the material up to a given elongation and then releasing the force, and stretching the material again up to a higher elongation, and so on. From these experimental data, the true stress and the true strain were calculated. For each cycle, the tensile modulus was determined and the relative tensile modulus, that is the ratio of the modulus measured during a given cycle by the one measured during the first cycle, was plotted as a function of both the number of cycles and the nanocrystal content (Figure 7.9). For the unfilled NR matrix, an increase of the relative modulus during successive tensile tests was observed. It was ascribed to the well-known strain-induced crystallization of the NR matrix. For composites the behavior was reported to be totally different. During successive tensile tests, the relative tensile modulus first decreased and then slowly increased. The initial decrease of the modulus for composite materials was ascribed to the progressive damaging of the polysaccharide nanocrystal network. This is an indication that the tensile behavior of the composites wais mainly governed by the percolating nanoparticle network. After the complete destruction of the network, the modulus started to slowly increase as a result of the strain-induced crystallization of the matrix already observed for the unfilled sample. In this strain range, the composite modulus became matrix-dominated.

7.4
Mechanical Properties of Polysaccharide Nanocrystal-Based Materials

The mechanical properties of polysaccharide nanocrystals are their most important and most investigated asset, especially for cellulose and chitin nanocrystals. Indeed, these properties are profitably exploited by Mother Nature since cellulose

and chitin are structural polymers that provide the mechanical strength and stiffness to living organisms. Impressive mechanical properties, nanoscale dimensions, and high aspect ratio of crystalline rod-like polysaccharide nanoparticles therefore make them ideal candidates for the reinforcement of polymeric materials. To improve the mechanical properties of the host material and take advantage of this property, special care needs to be paid to the processing of the nanocomposite. Indeed, it is well-known that the macroscopic mechanical properties of heterogeneous materials depend on the specific behavior of each phase and the composition (volume fraction of each phase), and also on the morphology (spatial arrangement of the phases) and interfacial properties.

We have shown previously (see Sections 7.2.2 and 7.3.2) that the establishment of a percolating polysaccharide nanocrystal network is an important issue for the reinforcement of a polymeric matrix. It corresponds actually to the highest mechanical performance that can be reached for a given system. Comparison between experimental mechanical data and prediction from the percolation approach (see Section 7.3.2) is a simple method to verify if a percolating polysaccharide network is effectively formed within the polymeric matrix. This is well exemplified in Figure 7.10 showing the temperature dependence of the storage tensile modulus of unfilled PEO and composites reinforced with tunicin nanocrystals [42]. The main relaxation associated with the glass–rubber transition of PEO amorphous phase was observed around −60 °C. Above this temperature, a higher rubbery modulus was observed for composites. It was ascribed to a reinforcing effect of the nanoparticles since no change in the degree of crystallinity of the matrix was reported in this filler content range. However, the main effect of tunicin nanocrystals on the mechanical behavior of PEO was observed at higher temperatures, above the melting point of the matrix. While the modulus of the unfilled matrix dropped irremediably with the melting of the
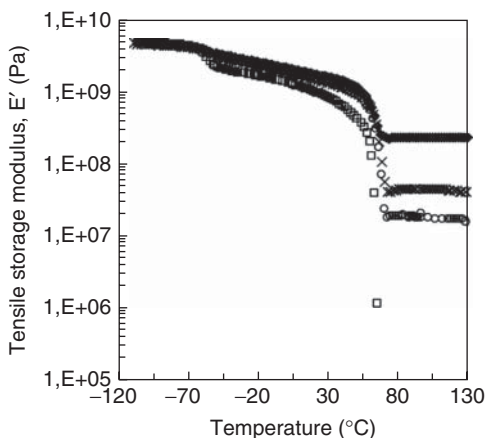
Figure 7.10 Evolution of the storage tensile modulus as a function of temperature at 1 Hz for PEO reinforced with 0 wt% (□), 3 wt% (○), 6 wt% (×), and 10 wt% (◇) tunicin nanocrystals. Reproduced from [42], copyright 2004 © permission from Elsevier

crystalline PEO domains, nanocrystals brought a thermal stabilization effect. Similar observation was reported for polycaprolactone (PCL) reinforced with chitin nanocrystals [47] and poly(hydroxyoctanoate) (PHO) reinforced with cellulose nanocrystals [65]. This effect was ascribed to the formation of a percolating cellulose network, and the high temperature modulus, which increased with increasing nanoparticle/nanoparticle interaction probability and density of the cellulose network, was well predicted from the percolation approach. Indeed, experimental high temperature storage modulus values were around 18, 45, and 235 MPa for nanocomposites filled with 3, 6, and 10 wt% tunicin nanocrystals, respectively, whereas the predicted values were 35, 106, and 255 MPa, respectively. The establishment of this rigid percolating nanocrystal network was not influenced when using PEO-lithium trifluoromethyl sulfonyl imide (LiTFSI) polymer electrolyte plasticized with tetra(ethylene) glycol dimethyl ether (TEGDME) [66] or cross-linked polyether-LiTFSI [67] as matrix. Neither processing medium (water or DMF) altered the percolation of the nanocrystals [50].

In another study [68], biomimetic, stimuli-responsive nanocomposites were made using either poly(styrene-co-butadiene) (SBR) or polybutadiene (PBD) as the hydrophobic, low-modulus matrix, and hydrophilic cellulose nanocrystals isolated from tunicate, i.e. tunicate cellulose nanocrystals (TCNs), as the high-modulus filler. These materials were prepared using a template approach [44, 45], which involved the formation of a percolating TCN network, and filling this template with either of the matrix polymers. Mechanical analysis of the dry nanocomposite films revealed that despite the lack of specific matrix–filler interactions, the incorporation of cellulose nanocrystals into the rubbery polymers increased the tensile storage modulus E′ significantly as shown in Figure 7.11. The experimentally determined moduli of the dry nanocomposites matched well with the values predicted from the percolation model. The reinforcement was therefore brought about by the formation of a three-dimensional percolating filler network within the SBR and PBD matrices with strong filler–filler interactions.

The tensile storage moduli E′ of the nanocomposites after equilibrium swelling in deionized water were also determined using a submersion clamp, which allowed the preconditioned samples to remain submerged in deionized water during isothermal testing at room temperature. Submersion of these hydrophobic matrix nanocomposites in water resulted in dramatic softening (Figure 7.11). Given the hydrophobic nature of the matrices, it was proposed that the TCNs created a percolating network of hydrophilic channels within the hydrophobic SBR and PBD matrices. The E′ values of water-swollen SBR/TCN and PBD/TCN nanocomposite samples closely matched the calculations made on the basis of the Halpin–Kardos model [69], which was successfully used to predict and describe the modulus of nanocomposites in which the filler is homogeneously dispersed in a polymer matrix and does not display pronounced filler–filler interactions. It is consistent with disengagement of the nanocrystal network as a consequence of competitive hydrogen bonding with water. Thus, both the SBR/TCN and PBD/TCN nanocomposites exhibit stimuli-responsive mechanically dynamic behavior with water as the stimulus. Consistent with this interpretation was the
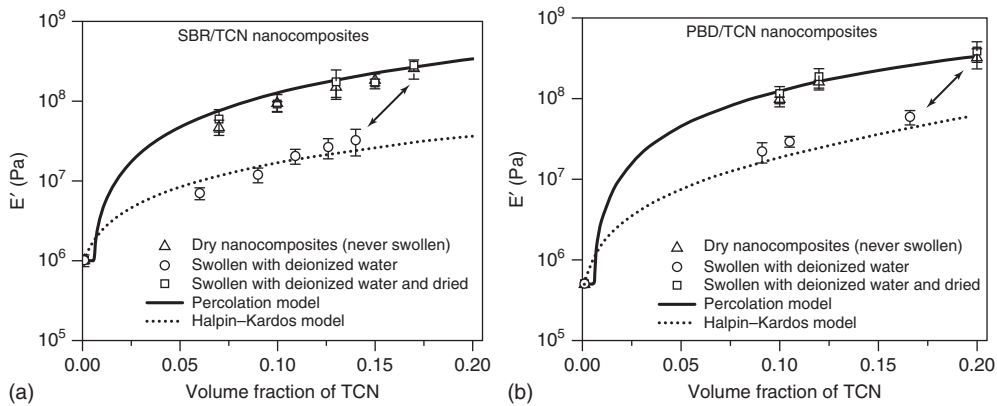
Figure 7.11 Tensile storage moduli E' of films of poly(styrene-co-butadiene) (SBR) (a) and polybutadiene (PBD) (b) reinforced with tunicin nanocrystals (TCN) as a function of TCN content at 25 °C. The materials were conditioned by either drying in vacuo at 50 °C for 24 h, equilibrium swelling in deionized water for 10 days (SBR nanocomposites) or 5 days (PBD nanocomposites), or swelling to saturation as before followed by redrying in vacuo at 50 °C for 48 h. The solid lines show the values predicted by the percolation model for dry materials, whereas the dotted lines represent those predicted by the Halpin–Kardos model for wet state moduli. The arrows indicate changes in modulus and volume fraction of TCN resulting from aqueous swelling of two selected nanocomposite samples (note that water-swollen samples have a lower volume fraction of TCNs, on account of the water uptake). Reproduced from [68], copyright 2012 © permission from American Chemical Society.

fact that the mechanical switching was completely reversible: drying the materials restores their original mechanical properties (Figure 7.11).

Therefore, any factor that affects the formation of the percolating nanocrystal network or interferes with it is a critical issue that changes dramatically the mechanical performances of the composite [70]. Three main parameters were identified to affect the mechanical properties of such materials, namely, the morphology and dimensions of the nanoparticles, the processing method, and the microstructure of the matrix and matrix/filler interactions. This last parameter is developed in Section 7.5. Obviously, the potential relative reinforcing effect of polysaccharide nanoparticles increases as the stiffness of the neat matrix decreases. Indeed, for semicrystalline polymers the rubbery modulus is known to depend on the degree of crystallinity of the material. The crystalline regions act as physical cross-links for the elastomer and in this physically cross-linked system, the crystalline regions would also act as filler particles because of their finite size, which would increase the modulus substantially and therefore blur the reinforcing capacity of the nanoparticles. A simple mixing rule allows accounting for this phenomenon.

An abundant and flourishing literature is devoted to the mechanical properties of polysaccharide (mainly cellulose) nanocrystal-reinforced polymer nanocomposites. In most cases, a reinforcing effect of the nanoparticles is

claimed even if their potential is not always fully exploited, that is, if the formation of a three-dimensional polysaccharide nanocrystal network within the polymeric matrix is not achieved.

7.4.1
Influence of the Morphology and Dimensions of the Nanocrystals

Polysaccharide nanocrystals occur in two forms, namely, platelet-like nanoparticles for starch nanocrystals and rod-like nanoparticles for cellulose and chitin nanocrystals.

Starch nanocrystals were first used as reinforcements in elastomer-based matrices such as poly(S-co-BuA) [71–73] and NR [74–78]. Then, most work has been oriented toward the use of bio-based polymers such as waterborne polyurethane (WPU) [79, 80], thermoplastic starch [81–84], pullulan [85], polylactic acid (PLA) [86], PVA [87], PCL [88], poly(butylene succinate) (PBS) [89], and soy protein isolate (SPI) [90]. For most systems, the introduction of starch nanocrystals resulted in an increase in both the modulus and strength, whereas the strain at break decreased. However, for higher filler contents possible self-aggregation of the nanoparticles induced a leveling or even reduction of their reinforcing capability.

As for other polysaccharide nanocrystals, the reinforcing mechanism of starch nanocrystals is generally ascribed to the formation of a hydrogen bonded percolating filler network above a given starch content corresponding to the percolation threshold. This percolation phenomenon was evidenced in the case of NR reinforced with waxy maize starch nanocrystals from swelling experiments (toluene and water uptake) for which changing behavior was reported above a certain filler concentration [75]. In that case, the percolation threshold was estimated at 10 wt% [74]. The percolation mechanism has been verified by successive tensile experiments, which consisted in stretching the material to a given elongation, releasing the force, stretching again to a higher elongation, and repeating [75]. It was shown that for the unfilled NR matrix, the tensile modulus continuously increased during successive cycles due to the strain-induced crystallization of NR, whereas for highly filled nanocomposite materials the tensile modulus decreased during the five first cycles. This was ascribed to the progressive disruption of the continuous starch nanocrystals network. The establishment of a percolating network was further confirmed by the same authors. They showed that any deterioration of these filler–filler interactions, for example, induced by the surface chemical modification of starch nanocrystals, resulted in a dramatic decrease in the mechanical performances of the ensuing composites [74, 75].

However, new highlights have been given concerning the reinforcing mechanisms of starch nanocrystals in NR matrix [77]. The presence of both Mullins and Payne effects was demonstrated, even for low filler contents, suggesting that the strain dependence of the viscoelastic properties of filler non-vulcanized NR could not be only related to the development of filler–filler interactions. Two phenomenological models were used to predict the Payne effect and thus discriminate the possible origins of the nonlinear viscoelastic behavior: (i) the Kraus model

considering that filler–filler interactions are preponderant and (ii) the Maier and Göritz model that is based on matrix–filler interactions. The use of the Kraus model lay with the confirmation of the formation of a percolating network for filler contents higher than 6.7 vol% (10 wt%). However, the Kraus model was unable to predict the dissipative properties of the different nanocomposites. The use of the Maier and Goritz model allowed demonstrating that nonlinear viscoelastic properties were governed by phenomena of adsorption and desorption of NR chains on the filler surface, even if the formation of a percolating network for filler contents higher than 6.7 vol% (10 wt%) was evidenced.

As expected and in agreement with their respective roles in nature, the reinforcing effect of elongated rod-like nanocrystals extracted from cellulose and chitin is higher than for starch nanocrystals. This has been proved in a comparative study of starch and cellulose nanocrystals [91]. For these nanorods, the geometrical aspect ratio is of course an important factor since it determines the percolation threshold value. This factor is linked to the source of cellulose or chitin and acid hydrolysis conditions. The stiffness of the percolating nanocrystal network is also influenced by the aspect ratio of the nanoparticles (see Figure 7.2). Therefore, nanorods with high aspect ratio should give the highest reinforcing effect. For instance, the rubbery storage tensile modulus was systematically lower for poly(S-co-BuA) reinforced with wheat straw nanocrystals (with an aspect ratio of 45) than for the same matrix reinforced with tunicin nanocrystals (aspect ratio of 67) [70]. Similar observation was reported when comparing the mechanical properties of poly(S-co-BuA) reinforced with squid pen chitin nanocrystals with an aspect ratio of 15 [46] or *Riftia* tubes with an aspect ratio of 120 [47].

7.4.2
Influence of the Processing Method

The processing method of the polysaccharide nanocrystal-reinforced nanocomposite governs the homogeneous dispersion and possible formation of a continuous nanoparticle network and then the final properties of the nanocomposite material. As seen in Section 7.3, in most studies nanocomposites are prepared in liquid medium by a casting/evaporation method, using polymer solution or polymer dispersion (latex). The main advantage is that it allows preserving the dispersion state of the nanoparticles in the liquid medium. This dispersion state is very good in aqueous medium and can be acceptable in some organic solvents. This slow wet process was reported to give the highest mechanical performance materials compared to other processing techniques. Indeed, during liquid evaporation strong interactions between nanoparticles can settle and promote the formation of a strong percolating network. During slow water (or organic liquid) evaporation, because of Brownian motions in the suspension or solution (whose viscosity remains low, up to the end of the process when the latex particle or polymer concentration becomes very high), rearrangement of the nanoparticles is possible. They have time enough to interact and connect to form a percolating network that is the basis of their reinforcing effect. The resulting structure (after the coalescence

of latex particles and/or interdiffusion of polymeric chains) is completely relaxed and direct contacts between nanocrystals are then created.

To broaden the range of polymeric matrices that can be used in association with polysaccharide nanocrystals, homogeneous dispersion of the nanoparticles in any liquid medium, regardless of its polarity, is desirable. To promote this dispersion, it is necessary to lower the surface energy of the nanoparticles to fit with that of the liquid. This is generally achieved by coating their surface with a surfactant or replacing part of the surface hydroxyl groups by less polar groups (surface chemical modification). However, even if the dispersion of the nanoparticles in the liquid medium (in which the polymeric matrix is generally solubilized) is improved, hindered interactions between physically or chemically modified nanocrystals limit the formation of a strong percolating nanoparticle network and then the reinforcing effect. This effect was reported for chitin [92] and starch nanocrystal [93]-reinforced NR. However, in both studies, processing of the nanocomposites involving chemically modified nanoparticles was carried out in toluene (a good solvent for NR) and the mechanical performances of ensuing materials were compared to those of unmodified nanocrystal/NR nanocomposite materials made from an aqueous medium (NR being in the form of a latex) that displayed very high mechanical properties. In other studies, the assessment of the reinforcing ability of unmodified and modified nanoparticles was performed by processing the nanocomposites in the same conditions. For instance, enhancement of the dispersion and mechanical properties was reported for *N*-octadecyl isocyanate- [53] and PCL-grafted cellulose nanocrystals blended with PCL using a grafting onto [88] or grafting from approach [94]. The nanocomposites involving both unmodified and chemically modified nanocrystals were prepared by a casting/evaporation method in dichloromethane (a solvent of PCL). Similarly, improved mechanical properties were observed when mixing by extrusion chemically modified cellulose nanocrystals with a PCL [95] and PLA [96] matrix in comparison with unmodified nanoparticles processed in under similar conditions. Obviously, strong self-aggregation of the unmodified nanocrystals in dichloromethane or polymer melt was the source of the poor mechanical properties of the nanocomposites prepared from these particles.

Apart from the wet processing methods, conventional melt-compounding techniques that are commonly used to process thermoplastic polymers have been infrequently employed for the preparation of polysaccharide nanocrystal-reinforced polymer composites. This is ascribed to inherent incompatibility and thermal issues. The hydrophilic nature of polysaccharides induces almost irreversible agglomeration upon drying and aggregation in nonpolar matrices. For example, the effect of processing technique on mechanical properties was reported for tunicin [97] and wheat straw [98] nanocrystal-reinforced poly(S-co-BuA). Three types of composite films were prepared from an aqueous mixture of the nanoparticle suspension and polymer latex by (i) casting/evaporation, (ii) freeze-drying and hot-pressing, and (iii) freeze-drying, extruding, and then hot-pressing. The processing methods have been classified in ascending order of their reinforcement efficiency as extrusion < hot-pressing < evaporation.

(a)

(b)
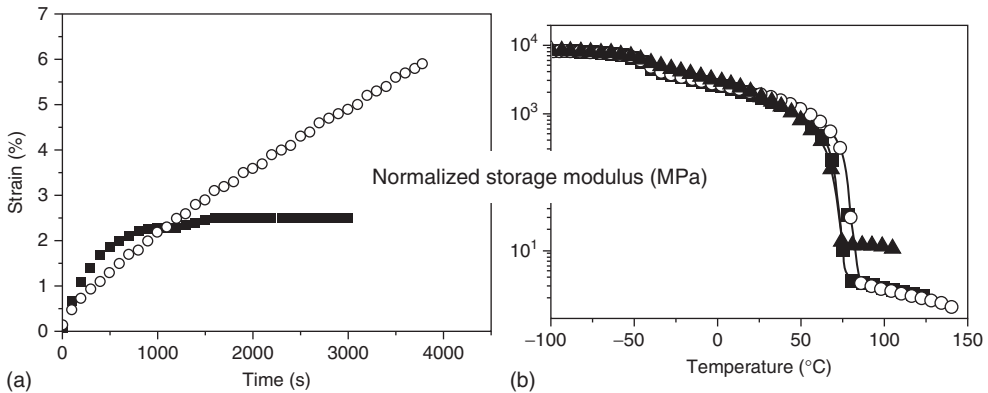
Figure 7.12 Creep measurements (torque = 5 μNm) at 90 °C under inert atmosphere for cast-evaporated (●) and freeze-dried/extruded (○) (a), and normalized storage modulus as a function of temperature for cast-evaporated (▲) and freeze-dried/ extruded in the extrusion direction (○) and cross-sectional direction (■) for PEO nanocomposite films reinforced with 6 wt% ramie nanocrystals (b). (Adapted from Ref. [57].)

It was ascribed to a breaking and/or orientation effect of the nanoparticles induced during shear stresses induced by freeze-drying/molding or freeze-drying/extruding/molding techniques.

The mechanical behavior of cellulose nanocrystal-reinforced PEO films prepared by casting/evaporation or freeze-drying/extrusion was also compared [57]. Rheological characterization of the nanocomposites in the melt showed that the film obtained by casting/evaporation had the typical behavior of a solid material with stabilization of the strain during creep experiments whereas the extruded specimen behaved as a liquid with a continuous evolution of the strain as a function of time (Figure 7.12a). As a consequence, the reinforcing effect of nanocrystals in the extruded sample was dramatically reduced, suggesting the absence of a strong mechanical network or at least, the presence of a weak percolating network (Figure 7.12b). Moreover, no significant orientation of the nanocrystals was observed during extrusion as shown by the overlapping of the DMA curves obtained for the sample cut in the extrusion and cross-sectional directions (Figure 7.12b). On the contrary, an increase in the tensile strength due to shear alignment of cellulose nanocrystals in extruded starch was reported [99]. Similarly, cellulose nanocrystal orientation induced by a strong magnetic film was found to increase the modulus in the orientation direction [100].

7.5
Polysaccharide Nanocrystal/Matrix Interfacial Interactions

The filler/matrix interactions can be tuned by appropriate surface modification treatment of the nanoparticles. This strategy is classically used in

composite science to compatibilize the reinforcing phase with the matrix for optimal performance. However, as reported in Section 7.4.2, for polysaccharide nanocrystal-reinforced nanocomposites the opposite trend can be observed depending on the processing conditions of the reference material (consisting of unmodified or uncompatibilized nanoreinforcement). It means that the higher the affinity between the polysaccharide filler and the host matrix is the lower the mechanical performances are when comparing the mechanical behavior to well-dispersed unmodified nanoparticle-based nanocomposites. This unusual behavior is ascribed to the originality of the reinforcing phenomenon of polysaccharide nanocrystals resulting from the formation of a percolating network thanks to hydrogen bonding forces. The challenge consists therefore in promoting the homogeneous dispersion of the polysaccharide nanoparticles and avoiding agglomeration during processing, thus requiring eventually favorable filler/matrix interactions, and at the same time promoting filler/filler interactions to allow the beneficial formation of a percolating network of nanoparticles. These two requirements are simply conflicting and no suitable strategy has been proposed so far.

The interfacial interactions between the polymeric matrix and polysaccharide nanocrystals can be investigated by different methods. Interactions between cellulose nanocrystals and PEO have been quantified using heat flow microcalorimetry [42]. The heat of immersion was directly measured by mixing tunicin nanocrystals with water, dodecane, and oligoethers. Dodecane was used to evaluate the contribution of the alkane part of PEO to the global interactions. Obviously, the highest heat of immersion was observed for water whereas dodecane displayed the weakest interactions with cellulose. For oligoethers, intermediate values were obtained and stronger affinity of cellulose nanocrystal surface with hydroxyl end groups of PEO rather than its ether oxygen groups was reported.

Interactions between cellulose nanocrystals and PEO have been evidenced in aqueous medium [101]. Upon adding cellulosic nanoparticles in the PEO solution, the viscosity of the suspension first decreased and then increased (Figure 7.13). Interaction of PEO chains with OH groups from the surface of the nanoparticles has been suspected. In the experimental conditions investigated (1 wt% high molecular weight PEO in water), it appeared that a cotton nanocrystal concentration around 6 wt% corresponded to a critical concentration, sufficient to attract all the PEO chains available in the suspension. Above this critical value, the viscosity increased with filler content and the suspension displayed a typical suspension behavior, with the viscosity increasing with suspension concentration. These interactions can be boosted when using polyethylene glycol (PEG)-grafted cellulose nanocrystals [102].

However, investigation of the nanocrystal/matrix interactions *in situ* directly from the processed nanocomposite is a better option. Fourier transform infrared (FTIR) can be used in this regard. FTIR characterization of PCL-based WPU reinforced with flax cellulose nanocrystals was reported [103]. For the neat matrix, a prominent peak band centered at $1722 \, \text{cm}^{-1}$ was observed, assigned to the stretching vibration of both urethane and ester carbonyl, confirming the existence of the integrated phase between hard and soft segments in the matrix. This peak
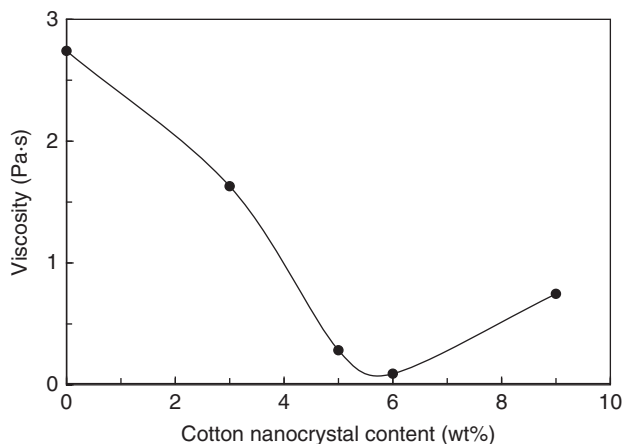
Figure 7.13 Steady shear viscosity for 1 wt% PEO ($M_w = 5 \times 10^6$ g·mol^{-1}) solution as a function of cellulose nanocrystal content (on the PEO basis). Reproduced from [101], copyright 2012 © permission from American Chemical Society.

shifted to 1731 cm^{-1} when adding cellulose nanocrystals, suggesting that the nanoparticles disturbed the hydrogen bonding between –NH and –CO, and favored microphase separation due to the strong interaction between cellulose nanocrystals and matrix chains. FTIR was also used to characterize starch–starch nanocomposites consisting of a glycerol-plasticized matrix reinforced with starch nanocrystals [83]. The bands related to the absorptions of hydroxyl groups at 3260 and 1650 cm^{-1} showed a very slight broadening for composites suggesting an increase in the number of oscillation modes, which could be associated to the presence of different types of hydrogen bonding interactions.

The extent of filler–matrix interactions can also be determined from swelling experiments in a good solvent of the matrix. For instance, the relative weight loss and fraction of bounded matrix after 48 h immersion in toluene and subsequent drying was investigated for chitin nanocrystal-reinforced NR [104].

DMA is a powerful tool to investigate the linear mechanical behavior of materials in a broad temperature/frequency range and it is strongly sensitive to the morphology of heterogeneous systems. Information on the interfacial interactions in composite systems can also be accessed from DMA experiments, especially through the evolution of the loss angle. A shift of the main relaxation process associated with the glass–rubber transition of the matrix toward higher temperatures is an indication of an increase in the glass transition temperature (Tg) value resulting from strong filler/matrix interactions. However, this effect can be affected by the so-called mechanical coupling effect because the temperature position of the relaxation depends on both the Tg value and the associated magnitude of the modulus drop. A broadening of the main relaxation process can also be observed, or even a splitting into two peaks. This effect was observed for NR reinforced with NFC obtained through mechanical disintegration of cellulosic fibers [105]. The main relaxation was found to split into two well-defined peaks, and the relative

magnitude of the high temperature peak was found to increase when the filler content was increased. This splitting was not observed for cellulose nanocrystals extracted from the same source (date palm tree) and it was ascribed to stronger interactions between NFC and the NR matrix. The presence of residual lignin, extractive substances, and fatty acids at the surface of NFC was suggested to compatibilize it with the matrix. These favorable interactions could lead to the formation of an interfacial layer surrounding the filler, the mobility of which is restricted compared to the bulk matrix.

Strong interactions between cellulose nanocrystals [106–110] or starch nanocrystals [81, 82] and polar matrices such as glycerol-plasticized starch matrix were reported to play a key role in reinforcing properties. Similar behavior was observed for sorbitol-plasticized starch reinforced with cellulose nanocrystals [111] or WPU-reinforced with chitin nanocrystals [112]. Strong interactions with cellulose have also been suggested to contribute to the reinforcing effect of PVA [113–116] and SPI plastics [117] on adding nanocrystals.

Nanocomposite materials were also prepared from copolymers of PVA and polyvinyl acetate (PVAc) and cellulose nanocrystals obtained from cotton linter [118]. The degree of hydrolysis of the matrix was varied in order to vary the hydrophilic character of the polymer matrix and then the degree of interaction between the filler and the matrix. Nanocomposite films were conditioned at various moisture contents, and the mechanical properties were characterized in both the linear and nonlinear range. The order of magnitude of experimental mechanical data agreed with the percolation approach. Figure 7.14 shows the evolution of the relative tensile modulus, defined as the ratio of the modulus of the composite to that of the unfilled matrix, of these copolymers reinforced with 12 wt% nanocrystals and conditioned at 0% relative humidity (RH) as a function of the degree of hydrolysis of the matrix. An increase in the relative tensile modulus was observed with the degree of hydrolysis assigned to stronger
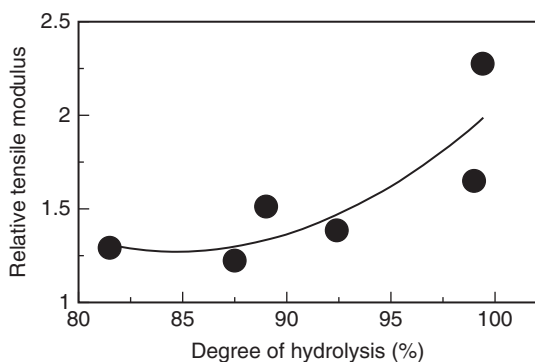
Figure 7.14 Evolution of the relative tensile modulus of poly(vinyl alcohol-co-vinyl acetate) reinforced with 12 wt% cotton nanocrystals and conditioned at 0% RH as a function of the degree of hydrolysis of the matrix. The solid line serves to guide the eye. Reproduced from [118], copyright 2008 © permission from Elsevier.

filler – matrix interactions. However, as the water content in the film increased, a lower reinforcing effect was observed. It was ascribed to strong water/cellulose interactions that hinder the inter-nanocrystal connections.

In non-percolating systems, for instance, for materials processed in toluene from freeze-dried cellulose nanocrystals, strong matrix/filler interactions can enhance the reinforcing effect of the filler as observed classically for composite materials. This observation was reported using random copolymers of poly(ethylene-co-vinyl acetate) (EVA) matrices with different vinyl acetate contents and then different polarities [119]. The more polar matrices exhibited higher storage modulus values. It also appeared that a minimum number of acetate groups were needed to observe a reinforcing effect above the melting point of the matrix and prevent the flow of the matrix. Moreover, a leveling-off of this effect appeared for copolymers with vinyl acetate content of 40 and 100 wt% for which the storage modulus was approximately the same.

Strong interfacial interactions are often associated with the existence of an interphase. By definition, the interphase exists from some point in the filler where the local properties begin to change from the filler bulk properties, through the actual interface into the matrix where the local properties again equal the bulk properties. The usual question is to quantify the magnitude of the interactions between filler and polymer chains and the distance away from the surface where the force field may be still in effect. Local change in the properties of the polymer by adsorption onto the filler particle affects the magnitude of the loss angle peak associated to Tg. For example, a strong decrease in the loss angle peak was observed for starch nanocrystal-reinforced acrylic resin processed via a one-pot miniemulsion polymerization [120].

If significant specific interactions between polymer and filler exist, this will tend to immobilize a layer of polymer around each solid particle. This immobilized polymer layer contributes to the effective filler volume fraction in the compound. Evaluation of the effective volume fraction from the measured volume fraction requires knowledge of the geometry of the particle and the effective thickness, ΔR, of the interfacial region. Such estimation was reported for nanocomposite materials obtained by reinforcing either amorphous or semi-crystalline PHO with tunicin nanocrystals [121]. A physical model based on a percolation approach, suitable for the prediction of the reinforcing effect of cellulose nanocrystals, was used to predict the mechanical loss angle. The ratio of the experimental and predicted magnitude of the relaxation process associated with Tg of the composite was used to calculate the thickness of the interphase. Significant differences were found depending on the nature of the matrix. The molecular mobility of amorphous macromolecular chains was slightly affected by the presence of cellulose nanocrystals, owing to a possible transcrystallization phenomenon leading to a coating of the filler with the crystalline phase, when a semi-crystalline PHO was used as the matrix. In contrast, the flexibility of chains in the surface layer was lowered by the conformational restrictions imposed by the cellulose surface, when an amorphous PHO was used as the matrix. This resulted in a broader interphase and in a broadening of the main relaxation process.

7.6
Thermal Properties of Polysaccharide Nanocrystal-Based Materials

7.6.1
Thermal Properties of Polysaccharide Nanocrystals

The thermal properties of five types of starches (waxy maize, normal maize, high amylose maize, potato, and wheat) and their corresponding starch nanocrystals were characterized by differential scanning calorimetry (DSC) [122]. Native starches showed only one thermal transition, whereas nanocrystals showed two transitions. In excess water, the first peak was attributed to the first stage of crystallites melting (unpacking of the double helixes) and the second transition to the second stage of crystallites melting (unwinding of the helixes). B-type crystallinity starch nanocrystals gained more stability than A-type nanocrystals as they consist of more rigid crystallites. In the dry state, the peaks were attributed to crystallites melting, with a direct transition from packed helixes to unwound helixes. The presence of two peaks was attributed to the heterogeneity in crystallites quality. Limited influence of the amylose content of starch was observed. This study gave important information for the processing conditions of starch nanocrystal-based nanocomposites. It showed that starch nanocrystals can be used in wet processes, such as coating, if the temperature remains lower than $80-100\,°C$, and in dry processes at temperatures below $150-200\,°C$.

Thermal stability of polysaccharide nanocrystals and nanocomposites is a crucial factor in assessing their processing and use conditions. This characteristic is generally determined using thermogravimetric analysis (TGA), which typically consists of heating the sample from room temperature to $600\,°C$ at a given heating rate (typically $10\,°C\cdot min^{-1}$) in a nitrogen, air, or helium atmosphere, and recording the weight loss as a function of temperature. Use of an inert atmosphere avoids thermo-oxidation degradation.

Regardless f the source of cellulose, cellulose nanocrystals display a significantly reduced thermal stability compared to the raw starting material [5]. This effect is ascribed to the acid hydrolysis step, which generally involves sulfuric acid for suspension stability issues. During the hydrolysis reaction sulfate groups are introduced on the surface of the nanoparticles, promoting at the same time improved stability of the aqueous suspension and lowering the thermal stability. A detailed investigation on the thermostability of cellulose nanocrystals acid-hydrolyzed from bacterial cellulose has been reported [123]. Different acid hydrolysis conditions with H_2SO_4 were used to elucidate the relationship between the number of sulfate groups introduced and the thermal degradation behavior. Increasing surface sulfate group content led to degradation at lower temperatures, and a broader temperature range was observed as compared to unhydrolyzed samples. The degradation was described as a two-step process, namely, low temperature process and high temperature process. The low temperature process involved the degradation of most accessible amorphous

regions that were also highly sulfated. The high temperature process involved the degradation of less accessible interior crystalline regions that were comparatively less sulfated. For highly sulfated samples, an extra step involving the degradation of sulfated ends of crystalline regions was observed. Moreover, increasing the number of sulfate groups on nanocrystals increased the amount of charred residue at 350 °C, indicating that sulfate groups were flame retardant in nature. Through the regulation of reactant ratio and reactive conditions for postsulfation and desulfation, gradient contents of sulfate groups have been introduced on the surface of cellulose nanocrystals [124]. It was clearly shown that the lowering of sulfated group content on nanocrystals resulted in higher degradation temperature.

To increase the thermal stability of H_2SO_4-hydrolyzed nanocrystals, neutralization of the nanoparticles by NaOH can be carried out [125]. A marked increase by 50 °C of the degradation temperature for neutralized samples has been observed compared to untreated samples as shown in Figure 7.15 [94]. An isothermal TGA test performed at 185 °C for 40 min also provided evidence of the higher thermal stability of NaOH-neutralized cellulose nanocrystals [126].

7.6.2
Glass Transition of Polysaccharide Nanocrystal-Based Nanocomposites

For most nanocomposite systems reinforced with polysaccharide nanocrystals, the addition of the nanoparticles did not affect appreciably the Tg value of the host polymer [5]. This observation is quite surprising considering the highly reactive
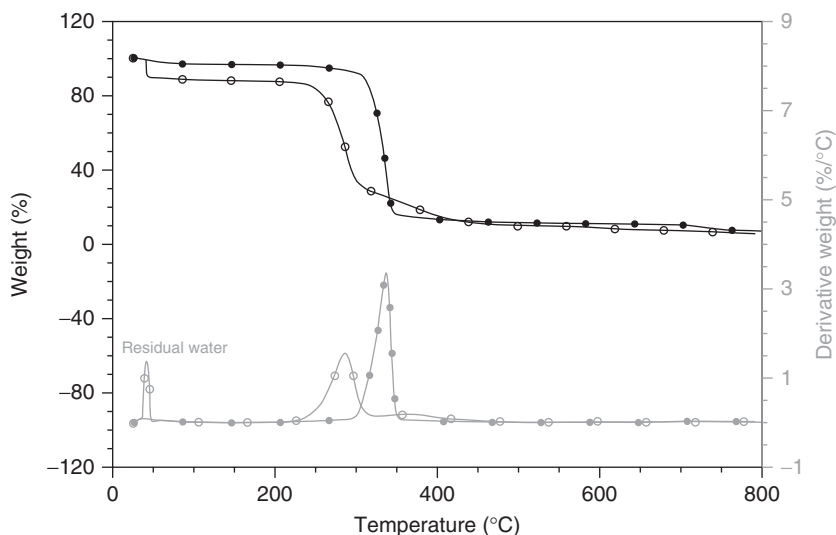
Figure 7.15 Thermogravimetric analysis (TGA) curves of untreated (○) and neutralized (●) cellulose nanocrystals extracted from ramie fibers (under helium flow). Reproduced from [94], copyright 2008 © permission from Royal Society of Chemistry.

nature and high specific area of polysaccharide nanocrystals. Nevertheless, it can be well understood for hydrophobic polymers because of the poor filler/matrix adhesion. However, even some polar polymers that display a good affinity for polysaccharides, such as PEO, did not show any increase in Tg [42].

An increase in Tg was reported for some nanocomposite systems, mostly when using plasticized starch as matrix. It was ascribed to interfacial hydrogen bonding forces inducing a reduction in the mobility of the matrix chains. Such effect was observed for starch nanocrystal-reinforced thermoplastic starch [81, 82], pullu-lan [85] and WPU [79], and cellulose nanocrystal-reinforced thermoplastic starch [56, 106–109, 127]. Limitation of the water uptake of PVAc [128] and PVA [118] when adding cellulose nanocrystals was also found to induce an increase of Tg. Nanocrystal-induced crystallization of PCL chains was also reported and suspected to increase the Tg of the PCL matrix [129].

For a few nanocomposite systems, a decrease in Tg was observed when adding cellulose nanocrystals. For flax cellulose nanocrystals-reinforced WPU, this depression of Tg was assigned to enhanced degree of freedom of the soft segments in WPU as a result of improved microphase separation between soft and hard segments [103]. In the case of polystyrene/cellulose nanocrystal composite microfibers prepared by electrospinning, the reduction observed in Tg was explained by the plasticizing effect of the surfactant used to disperse the nanoparticles in THF [130]. A plasticizing effect of PLA chains grafted on the surface of cellulose nanocrystals was also suggested to interpret the decrease in the Tg of the PLA matrix [96]. For PCL-grafted cellulose nanocrystal-reinforced PLA the increased mobility of PLA chains was ascribed to the rubbery PCL phase [131].

7.6.3
Melting/Crystallization Temperature of Polysaccharide Nanocrystal-Based Nanocomposites

The melting point Tm of semicrystalline polymers is directly correlated with the thickness of the crystalline lamellae. An increase in Tm reveals the formation of thicker crystalline lamellae. However, for most nanocomposite systems reinforced with polysaccharide nanocrystals no variation in the melting point was observed [5].

When a semicrystalline polymer is cooled from the melt, crystallization occurs at a temperature which is lower than the melting point. The crystallization temperature (Tc) value is directly correlated with the ease of polymer chains to form crystalline domains, that is, its value increases as the easiness of crystallization is enhanced. It is generally associated with a nucleating agent action of the polysaccharide nanoparticles. Such effect has been reported for poly(3-hydroxybutyrate-co-3-hydroxyvalerate) (PHBV) reinforced with acetylated chitin nano-crystals [132].

During heating DSC scans an exothermic peak is sometimes observed, attributed to the so-called cold crystallization during the heating process.

This phenomenon has been observed for some polysaccharide nanocrystal-reinforced polymer nanocomposites. For PHBV, cold crystallization was observed at 66 °C, which decreased to 37 °C when adding 2 or 5 wt% cellulose nanocrystals [133]. It was ascribed to an enhanced crystallization ability of PHBV, the nanocrystals acting as nucleation agent and inducing crystallization of the polymer at lower temperatures [134]. A similar trend was reported for PLA reinforced with cellulose nanocrystals prepared from microcrystalline cellulose [126, 135]. Moreover, the heat of cold crystallization increased for nanocomposites [126, 135] or the cold crystallization transition appeared while it was absent for the neat matrix [96].

7.6.4
Thermal Stability of Polysaccharide Nanocrystal-Based Nanocomposites

The effect of polysaccharide nanocrystals on the thermal stability of nanocomposites depends obviously on the initial thermal stability of the neat polymer. The char residue can also be altered by the nanofiller. Different situations can be observed.

Enhanced thermal stability of the host polymer results from favorable interactions with the cellulosic filler. For example, for PVA [113] and regenerated cellulose [136] reinforced with cellulose nanocrystals, strong hydrogen bonding between hydroxyl groups of cellulose and the polar matrix was suggested to improve the thermal stability of the host polymer. Similarly, the formation of a confined structure in PU matrix was supposed to improve the thermal stability of the matrix on cellulose nanocrystal addition [137]. However, for higher filler contents a decrease in thermal stability is sometimes observed because of aggregation [136]. Improved thermal stability of hyaluronan-gelatin scaffolds upon chitin nanocrystal addition was also reported [138].

The low onset degradation temperature of H_2SO_4-prepared cellulose nanocrystals was supposed to decrease the degradation temperature of polysulfone [139], glycerol-plasticized starch [110], NR [140], polymethylmethacrylate (PMMA) [141], PVA [114], and PEO [57]. For PLA-based nanocomposites the higher water content induced by the presence of the cellulosic nanofiller was expected to decrease the thermal stability of the polymer [142]. Acetylation of the nanoparticles can limit this effect [143]. The increased thermal conductivity of the polymer after cellulose nanocrystal addition was also suggested as the reason for reduced thermal stability of the composite [134].

7.7
Barrier Properties of Polysaccharide Nanocrystal-Based Materials

Most studies of polysaccharide nanocrystal-based materials focus on their mechanical properties. However, there is an increasing interest in their barrier properties because of the increased tortuosity provided by nanoparticles.

Indeed, because of their small size, the surface-to-volume ratio of the nanoparticles is significantly greater than that of microparticles. Moreover, the low permeability of polysaccharides can be enhanced by the highly crystalline nature of polysaccharide nanocrystals and the ability to form a dense percolating network. Provided that strong particle–polymer molecular interactions exist, the smaller particles have a greater ability to bond to the surrounding polymer material, thereby reducing the chain segmental mobility and thus the penetrant diffusivity. Barrier properties are commonly in connection with particular permeable objects, which include common gases, water vapor, liquid and organic substance, and so on. In polymers, they are necessarily associated to their inherent ability to permit the exchange, to a higher or lower extent, of low molecular weight substances through mass transport processes such as permeation. The whole transmitting process includes adsorption, dissolution, diffusion, and desorption. Gases or water vapor enter the surface of the material from the higher density side. After diffusing inside the material, it desorbs on the low-density side. The permeation of low molecular weight chemical species usually takes place through the polymer amorphous phase, and the crystalline phase is considered impenetrable.

7.7.1
Barrier Properties of Polysaccharide Nanocrystal Films

Barrier properties are important properties for packaging applications because increased shelf life by protecting the inside product from deteriorations through oxidation, humidity, or bacteria is often needed.

The swelling and barrier properties of neat cellulose nanocrystal films have been much less investigated than those of NFC. The swelling of cellulose nanocrystal films was reported to be higher than for NFC films [38, 144]. It was ascribed to water penetration between the nanocrystals, causing their separation, and allowing for further imbibition into the film. Moreover, the sulfuric acid-prepared nanocrystals contain sulfate groups aiding in creating an osmotic pressure separating the crystals in the film and exposure to liquid water [144]. The water diffusion coefficient was also higher for nanocrystal films compared to NFC films [38]. It was attributed to the presence of residual lignin, extractive substances, and fatty acids at the surface of NFC. Nanocrystal films also showed significantly higher permeability to gases and diffusion coefficients than NFC films. It was suspected that gas molecules penetrate much more slowly in the NFC films because of a longer diffusion path. In addition to a different surface chemistry, it was supposed that entanglements of the fibrils and lower porosity of the NFC films represented barrier domains increasing the tortuosity of the diffusion pathway.

Because of surface negatively charged surface groups resulting from the sulfuric acid hydrolysis step cellulose nanocrystal membranes present permselective properties. The transfer of negatively charged species through the nanocrystal membrane is inhibited, while positively charged species are adsorbed by the film

[145]. Cellulose nanocrystals were also used to prepare ultrafine membranes for water purification [146].

7.7.2
Swelling and Sorption Properties of Polysaccharide Nanocrystal-Based Nanocomposites

The interaction of polymeric materials with solvents can be a problem from a technological point of view because the dimensions and physical properties of the material may change with the penetration of solvent molecules into the specimen.

The water resistance of nanocomposite films reinforced with polysaccharide nanocrystals depends on the hydrophilicity of the matrix. For hydrophilic matrices such as plasticized starch [56, 106–110, 127, 147, 148], SPI [117], glycerin plasticized carboxymethyl cellulose (CMC) [149], carrageenan [150], and chitosan [151] both the water uptake and diffusion coefficient of water were found to decrease upon adding cellulose nanocrystals. Similar observations were reported for SPI [90] and sorbitol-plasticized pullulan [85] reinforced with starch nanocrystals, as well as SPI [152], chitosan [153], and PVA [154] reinforced with chitin nanocrystals. This behavior was ascribed to the existence of strong hydrogen bonding interactions between nanoparticles and between the polar matrix and nanoparticles. However, in some cases higher nanocrystal contents resulted in agglomeration and increase of the water uptake [150]. Nevertheless, for starch nanocrystal-reinforced glycerol-plasticized thermoplastic starch an increase in the water uptake was reported compared to the neat matrix [83] because of a relocalization of glycerol around the nanoparticles, leaving more hydroxyl groups in the matrix that were able to interact with water molecules.

For hydrophobic matrices, the opposite trend is obviously observed as expected. This behavior was reported for PVAc [128, 155], PMMA [156], and NR [105, 140] reinforced with cellulose nanocrystals, and also poly(S-co-BuA) [72] and NR [75, 78] reinforced with starch nanocrystals. Diffusion of water molecules toward the hydrophilic polysaccharide nanoparticles and localization in the weak interfacial zones were of course set out as the main explanation for this phenomenon. Therefore, the possible formation of a continuous percolation polysaccharide nanocrystal network and then the aspect ratio of the nanoparticles are important parameters with two regimes, below and above the percolation threshold. Above this critical value the diffusion of water molecules is facilitated. When a solvent of the polymeric matrix is used as swelling medium instead of water, the addition of polysaccharide nanocrystals decreases the swelling of the material as shown for cellulose nanocrystals [105, 157], starch nanocrystals [75, 78], and chitin nanocrystals [104]. For the latter system, the influence of the nanocomposite processing method was also investigated and the material processed by casting/evaporation was found to be more resistant to swelling compared to the material obtained by freeze-drying/hot-pressing because of the presence of a percolating chitin nanocrystal network in the former (Figure 7.16).

Sample	Before swelling	After swelling
NCH10ev		
NCH10L		
NCH15ev		
NCH15L		
NCH20ev		
NCH20L		
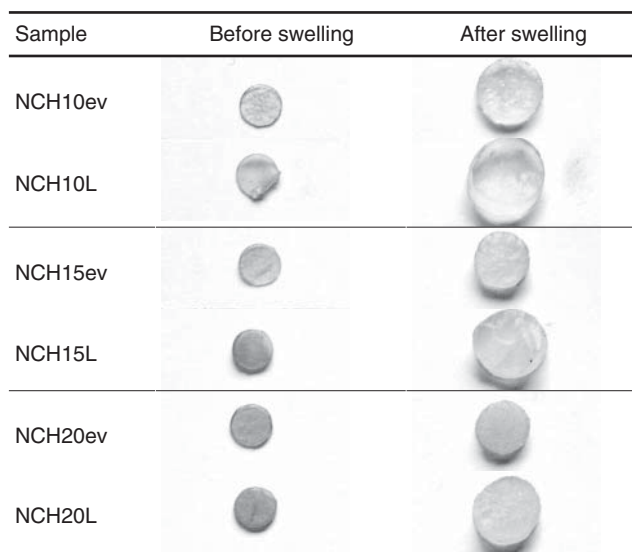
Figure 7.16 Photographs of natural rubber films reinforced with chitin nanocrystals prepared by evaporation (NCHxev samples) and hot-pressing (NCHxL samples) methods, where *x* corresponds to the weight content of chitin nanocrystals. Photographs were taken before and just after swelling in toluene for 24 h at room temperature (25 °C). The diameter of all samples before swelling was 7.5 mm. Reproduced from [101], copyright 2003 © permission from American Chemical Society .

7.7.3
Water Vapor Transfer and Permeability of Polysaccharide Nanocrystal-Based Nanocomposites

The evolution of the water vapor transmission rate (WVTR) or water vapor permeability (WVP) when adding polysaccharide nanocrystals also strongly depends on the hydrophilic character of the matrix. Decreased WVTR or WVP values were reported for hydrophilic matrices such as PVA [158], alginate-acerola [159], mango puree [160], glycerol-plasticized chitosan [161], and methylcellulose (MC) [162] when reinforced with cellulose nanocrystals, as well as for glycerol-plasticized thermoplastic starch [83] and sorbitol-plasticized pullulan [85] when reinforced with starch nanocrystals. This behavior was attributed to the physical barrier role provided by nanocrystals creating a tortuous path for the permeating moisture. However, an unexpected increase of WVP for glycerol-plasticized waxy maize starch matrix on addition of starch nanocrystals was reported [84] that was ascribed to a close association between starch nanoparticles and glycerol-rich domains.

For hydrophobic matrices, opposing tendencies have been reported. For starch nanocrystal-reinforced NR both a continuous and significant reduction [75] and an increase [78] of the permeability to water vapor have been reported. However, in the latter study WVP was measured under tropical conditions (38 °C, 90%

RH) and it was suggested that the hydrophilic nature of starch nanocrystals was predominant under these conditions. For NR reinforced with cellulose nanocrystals an increase of WVP was observed when adding the nanoparticles up to a concentration of 7.5 wt% followed by a decrease [140]. The former increase was ascribed to the hydrophilic nature of cellulose and the decrease for higher cellulose nanocrystal contents was associated with the formation of a percolating nanoparticle network. Reduction of the WVP value of PLA [135], carrageenan [150], xylan [163], and PCL [164] was also reported when adding cellulose nanocrystals. For PLA-based systems nanocrystal-induced crystallization of the matrix was suspected to contribute to the reduction of water transmission [135]. Moreover, the reduction in water transmission of xylan films was found to be more significant with sulfuric acid-hydrolyzed than with hydrochloric acid-hydrolyzed cellulose nanocrystals [163]. Further decrease of WVP was observed with 10 kGy gamma irradiation treatment [64]. A continuous increase of the WVTR of nanocomposite films made of polysulfone and cellulose nanocrystals was observed when increasing the nanoparticle content [139]. It was associated with the formation of a percolating cellulose network within the polymeric matrix acting as a channel for the diffusion of water through the film. However, as cellulose crystals are rather impermeable to water, the formation of a weak interphase in which diffusion is facilitated compared to the bulk matrix was suggested. This was supported by the low compatibility between cellulose and the polysulfone matrix.

7.7.4
Gas Permeability of Polysaccharide Nanocrystal-Based Nanocomposites

A continuous and significant decrease of the oxygen permeability (OP) was reported for NR films on adding starch nanocrystals [75]. It was attributed to the platelet-like morphology of the nanoparticles. The OP was also characterized at 24 °C and 80% RH for cellulose nanocrystal-reinforced PLA films [135]. A reduction of OP value was observed when adding up to 5 wt% nanocrystals, with an optimal value around 2–3 wt% filler loading. As for WVP experiments, this effect was attributed to the nanocrystal-induced crystallinity of the PLA matrix. This experimental permeability drop was higher than the one predicted by Nielsen and Fricke models even if experimental data were corrected by crystallinity alterations. Because experiments were conducted at 80% RH, it was hypothesized that sorbed moisture was thought to fill in the existing free volume, thereby reducing the gas permeability. Decreased oxygen transmission rate (OTR) and carbon dioxide transmission rate of PCL were observed with 5 wt% cellulose nanocrystal incorporation and further improvement was reported upon gamma irradiation treatment [164].

The barrier properties to oxygen and carbon dioxide of ternary systems consisting of NR reinforced with cellulose nanocrystals and natural montmorillonite (MMT) were also investigated [165]. The total filler content was kept constant and

equal to 5 wt% but changing the weight content of each filler. Improved gas barrier properties were reported and explained by a tortuosity effect. For binary systems, a more efficient barrier effect was observed for MMT compared to cellulose nanocrystals. The tortuosity values calculated from permeability and diffusion coefficients indicated that the simultaneous use of both fillers greatly slowed down the gas diffusion, leading to a synergistic effect. This phenomenon was ascribed to the formation of MMT-cellulose nanocrystal subassembly, the most efficient effect being observed for MMT contents higher than 2.5 wt%.

7.8
Concluding Remarks

Cost-effective and environmentally benign alternatives to petroleum for energy and engineering material demands are required in order to realize a future with sustainable economy and environment. Abundant and renewable semicrystalline polysaccharides such as cellulose, chitin, and starch consisting of crystalline and amorphous domains are possible candidates for organic nanofillers because the amorphous domains can be removed under certain conditions such as controlled acid hydrolysis. Crystalline polysaccharide domains with high modulus can therefore be isolated in nanoscale. Ensuing nanosized crystalline particles, usually known as polysaccharide nanocrystals, can be used as reinforcing nanofillers in polymer nanocomposites. These nanoparticles possess the potential to act as high-performance reinforcement in polymeric nanocomposites, thereby creating opportunities to develop high-performance and highly durable engineering materials from a renewable resource that could be suitable for potential consumer, structural, and biomedical applications. Even despite the lack of specific matrix–filler interactions, improved mechanical, thermal, and barrier properties have been reported when dispersing these hydrophilic polysaccharide nanocrystals homogeneously in a (mostly hydrophobic) polymeric matrix. Most of these enhancements are brought about by the formation of a percolating filler network with strong filler–filler interactions (presumably via hydrogen bonding of the surface hydroxyl groups). So, we are facing a paradox: the need to promote the filler–matrix interactions to avoid self-aggregation of the nanoreinforcement and then favor their homogeneous dispersion, and simultaneously the need to allow free filler–filler interactions ensuring optimal performances of the nanocomposite. To date, the potential of polysaccharide nanocrystal-reinforced nanocomposites has been primarily realized in materials prepared either by wet processing methods, such as casting or by template impregnation. The challenge over the next years is probably to transfer the successful potential of polysaccharide nanoreinforcements to industrially available and viable polymer processing techniques such as extrusion or injection-molding through the development of cost-effective, scalable compatibilization and dispersion techniques.

List of Abbreviations

AFM	atomic force microscopy
DMA	dynamic mechanical analysis
DMF	dimethylformamide
DMSO	dimethyl sulfoxide
DSC	differential scanning calorimetry
EVA	poly(ethylene-co-vinyl acetate)
FTIR	Fourier transform infrared
LiTFSI	lithium trifluoromethyl sulfonyl imide
MMT	montmorillonite
NCHxev samples	chitin nanocrystals prepared by evaporation
NCHxL samples	chitin nanocrystals prepared by hot-pressing
NFC	nanofibrillated cellulose
NR	natural rubber
OP	oxygen permeability
OTR	oxygen transmission rate
PBD	polybutadiene
PCL	polycaprolactone
PEO	poly(oxyethylene)
PHBV	poly(3-hydroxybutyrate-co-3-hydroxyvalerate)
PHO	poly(hydroxyoctanoate)
PLA	polylactic acid
PMMA	polymethylmethacrylate
poly(S-co-BuA)	copolymer of styrene and butyl acrylate
PVA	polyvinyl alcohol
PVAc	polyvinyl acetate
RH	relative humidity
SBR	poly(styrene-co-butadiene)
SEM	scanning electron microscopy
SEM-FEG	scanning electron microscopy with field emission gun
SPI	soy protein isolate
STPUE	segmented thermoplastic elastomeric polyurethane
Tc	crystallization temperature
TEGDME	tetra(ethylene) glycol dimethyl ether
TEM	Transmission electron microscopy
Tg	glass transition temperature
TGA	thermogravimetric analysis
THF	tetrahydrofuran
TCN	tunicate cellulose nanocrystal
WPU	waterborne polyurethane
WVP	water vapor permeability
WVTR	water vapor transmission rate

References

1. Lin, N., Huang, J., and Dufresne, A. (2012) Preparations, properties and applications of polysaccharide nanocrystals in advanced functional nanomaterials: a review. *Nanoscale*, **4**, 3274–3294.

2. Azizi Samir, M.A.S., Alloin, F., and Dufresne, A. (2005) A review of recent research into cellulosic whiskers, their properties and their application in nanocomposite field. *Biomacromolecules*, **6**, 612–626.

3. Eichhorn, S.J., Dufresne, A., Aranguren, M., Marcovich, N.E., Capadona, J.R., Rowan, S.R., Weder, C., Thielemans, W., Roman, M., Renneckar, S., Gindl, W., Veigel, S., Yano, H., Abe, K., Nogi, M., Nakagaito, A.N., Mangalam, A., Simonsen, J., Benight, A.S., Bismarck, A., Berglund, L.A., and Peijs, T. (2010) Review: current international research into cellulose nanofibres and nanocomposites. *J. Mater. Sci.*, **45**, 1–33.

4. Moon, R.J., Martini, A., Nairn, J., Simonsen, J., and Youngblood, J. (2011) Cellulose nanomaterials review: structure, properties and nanocomposites. *Chem. Soc. Rev.*, **40**, 3941–3994.

5. Dufresne, A. (2012) *Nanocellulose: From Nature to High Performance Tailored Materials*, Walter de Gruyter GmbH & Co. KG, Berlin, Boston, MA, 475 pp.

6. Milanez, D.H. and do Amaral, R.M. (2013) Assessing nanocellulose developments using science and technology indicators. *Mater. Res.*, **16**, 635–641.

7. Meyer, K. and Lotmar, W. (1936) Sur l'élasticité de la cellulose. *Helv. Chim. Acta*, **19**, 68–86.

8. Sakurada, I., Nukushina, Y., and Ito, T. (1962) Experimental determination of the elastic modulus of crystalline regions oriented polymers. *J. Polym. Sci.*, **57**, 651–660.

9. Mann, J. and Roldan-Gonzales, L. (1962) X-ray measurements of the elastic modulus of cellulose crystals. *Polymer*, **3**, 549–553.

10. Tashiro, K., Kobayashi, M., and Tadokoro, H. (1977) Elastic moduli and molecular structures of several crystalline polymers, including aromatic polyamides. *Macromolecules*, **10**, 413–420.

11. Nakamae, K., Nishino, T., and Okubo, M. (1991) Elastic modulus of crystalline regions of polyethylene with different microstructures: experimental proof of homogeneous stress distribution. *J. Macromol. Sci. Phys.*, **B30**, 1–7.

12. Treloar, L.R.G. (1960) Calculations of elastic moduli of polymer crystals: III. *Cellul. Polym.*, **1**, 290–303.

13. Tashiro, K. and Kobayashi, M. (1985) Calculation of crystallite modulus of native cellulose. *Polym. Bull.*, **14**, 213–218.

14. Jaswon, M.A., Gillis, P.P., and Mark, R.E. (1968) The elastic constants of crystalline native cellulose. *Proc. R. Soc.*, **306**, 389–412.

15. Kroon-Batenburg, L.M.J., Kroon, J., and Northolt, M.G. (1986) Chain modulus and intermolecular hydrogen bonding in native and regenerated cellulose fibers. *Polym. Commun.*, **27**, 290–292.

16. Matsuo, M., Sawatari, C., Iwai, Y., and Ozaki, F. (1990) Effect of orientation distribution and crystallinity on the measurement by X-ray diffraction of the crystal lattice moduli of cellulose I and II. *Macromolecules*, **23**, 3266–3275.

17. Tashiro, K. and Kobayashi, M. (1991) Theoretical evaluation of three-dimensional elastic constants of native and regenerated celluloses: role of hydrogen bonds. *Polymer*, **32**, 1516–1526.

18. Nishino, T., Takano, K., and Nakamae, K. (1995) Elastic modulus of the crystalline regions of cellulose polymorphs. *J. Polym. Sci. Part B: Polym. Phys.*, **33**, 1647–1651.

19. Reiling, S. and Brickmann, J. (1995) Theoretical investigations on the structure and physical properties of cellulose. *Macromol. Theory Simul.*, **4**, 725–743.

20. Ganster, J. and Blackwell, J. (1996) NpH-MD-simulations of the elastic moduli of cellulose II at room temperature. *J. Mol. Model.*, **2**, 278–285.

21. Neyertz, S., Pizzi, A., Merlin, A., Maigret, B., Borwn, D., and Deglise, X. (2000) A new all-atom force field for crystalline cellulose I. *J. Appl. Polym. Sci.*, **78**, 1939–1946.

22. Šturcova, A., Davies, G.R., and Eichhorn, S.J. (2005) Elastic modulus and stress-transfer properties of tunicate cellulose whiskers. *Biomacromolecules*, **6**, 1055–1061.

23. Tanaka, F. and Iwata, T. (2006) Estimation of the elastic modulus of cellulose crystal by molecular mechanics simulation. *Cellulose*, **13**, 509–517.

24. Eichhorn, S.J. and Davies, G.R. (2006) Modelling the crystalline deformation of native and regenerated cellulose. *Cellulose*, **13**, 291–307.

25. Bergenstråhle, M., Berglund, L.A., and Mazeau, K. (2007) Thermal response in crystalline I cellulose: a molecular dynamics study. *J. Phys. Chem. B*, **111**, 9138–9145.

26. Rusli, R. and Eichhorn, S.J. (2008) Determination of the stiffness of cellulose nanowhiskers and the fiber-matrix interface in a nanocomposite using Raman spectroscopy. *Appl. Phys. Lett.*, **93**, 033111.

27. Diddens, I., Murphy, B., Krisch, M., and Müller, M. (2008) Anisotropic elastic properties of cellulose measured using inelastic X-ray scattering. *Macromolecules*, **41**, 9755–9759.

28. Iwamoto, S., Kai, W., Isogai, A., and Iwata, T. (2009) Elastic modulus of single cellulose microfibrils from tunicate measured by atomic force microscopy. *Biomacromolecules*, **10**, 2571–2576.

29. Lahiji, R.R., Xu, X., Reifenberger, R., Raman, A., Rudie, A., and Moon, R.J. (2010) Atomic force microscopy characterization of cellulose nanocrystals. *Langmuir*, **26**, 4480–4488.

30. Cintrón, M.S., Johnson, G.P., and French, A.D. (2011) Young's modulus calculations for cellulose I by MM3 and quantum mechanics. *Cellulose*, **18**, 505–516.

31. Dri, F.L., Hector, L.G. Jr., Moon, R.J., and Zavattieri, P.D. (2013) Anisotropy of the elastic properties of crystalline cellulose I_β from first principles density functional theory with Van der Waals interactions. *Cellulose*, **20**, 2703–2718.

32. Xu, W., Mulhern, P.J., Blackford, B.L., Jericho, M.H., and Templeton, I. (1994) A new atomic force microscopy technique for the measurement of the elastic properties of biological materials. *Scanning Microsc.*, **8**, 499–506.

33. Vincent, J. and Wegst, U. (2004) Design and mechanical properties of insect cuticle. *Arthrop Struct. Dev.*, **33**, 187–199.

34. Nishino, T., Matsui, R., and Nakamae, K. (1999) Elastic modulus of the crystalline regions of chitin and chitosan. *J. Polym. Sci. Part B: Polym. Phys.*, **37**, 1191–1196.

35. Ogawa, Y., Hori, R., Kim, U.-J., and Wada, M. (2011) Elastic modulus in the crystalline region and the thermal expansion coefficients of α-chitin determined using synchrotron radiated X-ray diffraction. *Carbohydr. Polym.*, **83**, 1213–1217.

36. Dufresne, A. (2013) Nanocellulose - a new ageless bionanomaterial. *Mater. Today*, **16**, 220–227.

37. Angellier-Coussy, H., Putaux, J.L., Molina-Boisseau, S., Dufresne, A., Bertoft, E., and Perez, S. (2009) The molecular structure of waxy maize starch nanocrystals. *Carbohydr. Res.*, **344**, 1558–1566.

38. Belbekhouche, S., Bras, J., Siqueira, G., Chappey, C., Lebrun, L., Khelifi, B., Marais, S., and Dufresne, A. (2011) Water sorption behavior and gas barrier properties of cellulose whiskers and microfibrils films. *Carbohydr. Polym.*, **83**, 1740–1748.

39. Favier, V., Canova, G.R., Cavaillé, J.Y., Chanzy, H., Dufresne, A., and Gauthier, C. (1995) Nanocomposites materials from latex and cellulose whiskers. *Polym. Adv. Technol.*, **6**, 351–355.

40. Favier, V., Chanzy, H., and Cavaillé, J.Y. (1995) Polymer nanocomposites reinforced by cellulose whiskers. *Macromolecules*, **28**, 6365–6367.

41. Helbert, W., Cavaillé, J.Y., and Dufresne, A. (1996) Thermoplastic nanocomposites filled with wheat straw

cellulose whiskers. Part I: processing and mechanical behavior. *Polym. Compos.*, **17**, 604–611.

42. Azizi Samir, M.A.S., Alloin, F., Sanchez, J.-Y., and Dufresne, A. (2004) Cellulose nanocrystals reinforced poly(oxyethylene). *Polymer*, **45**, 4149–4157.

43. Ljungberg, N., Bonini, C., Bortolussi, F., Boisson, C., Heux, L., and Cavaillé, J.Y. (2005) New nanocomposite materials reinforced with cellulose whiskers in atactic polypropylene: effect of surface and dispersion characteristics. *Biomacromolecules*, **6**, 2732–2739.

44. Capadona, J.R., Van den Berg, O., Capadona, L., Schroeter, M., Tyler, D., Rowan, S.J., and Weder, C. (2007) A versatile approach for the processing of polymer nanocomposites with self assembled nanofibre templates. *Nat. Nanotechnol.*, **2**, 765–769.

45. Capadona, J.R., Shanmuganathan, K., Tyler, D.J., Rowan, S.J., and Weder, C. (2008) Stimuli-responsive polymer nanocomposites inspired by the sea cucumber dermis. *Science*, **319**, 1370–1374.

46. Paillet, M. and Dufresne, A. (2001) Chitin whisker reinforced thermoplastic nanocomposites. *Macromolecules*, **34**, 6527–6530.

47. Morin, A. and Dufresne, A. (2002) Nanocomposites of chitin whiskers from *Riftia* tubes and poly(caprolactone). *Macromolecules*, **35**, 2190–2199.

48. Bras, J., Viet, D., Bruzzese, C., and Dufresne, A. (2011) Correlation between stiffness of sheets prepared from cellulose whiskers and nanoparticles dimensions. *Carbohydr. Polym.*, **84**, 211–215.

49. Dufresne, A. (2012) Processing of polymer nanocomposites reinforced with cellulose nanocrystals: a challenge. *Int. Polym. Proc.*, **27**, 557–564.

50. Azizi Samir, M.A.S., Alloin, F., Sanchez, J.Y., El Kissi, N., and Dufresne, A. (2004) Preparation of cellulose whiskers reinforced nanocomposites from an organic medium suspension. *Macromolecules*, **37**, 1386–1393.

51. Van den Berg, O., Capadona, J.R., and Weder, C. (2007) Preparation of homogeneous dispersions of tunicate cellulose whiskers in organic solvents. *Biomacromolecules*, **8**, 1353–1357.

52. Schroers, M., Kokil, A., and Weder, C. (2004) Solid polymer electrolytes based on nanocomposites of ethylene oxide-epichlorohydrin copolymers and cellulose whiskers. *J. Appl. Polym. Sci.*, **93**, 2883–2888.

53. Siqueira, G., Bras, J., and Dufresne, A. (2009) New process of chemical grafting of cellulose nanoparticles with a long chain isocyanate. *Langmuir*, **26**, 402–411.

54. Heux, L., Chauve, G., and Bonini, C. (2000) Nonflocculating and chiral-nematic self-ordering of cellulose microcrystals suspensions in nonpolar solvents. *Langmuir*, **16**, 8210–8212.

55. Kvien, I., Tanem, B.S., and Oksman, K. (2005) Characterization of cellulose whiskers and their nanocomposites by atomic force and electron microscopy. *Biomacromolecules*, **6**, 3160–3165.

56. Anglès, M.N. and Dufresne, A. (2000) Plasticized starch/tunicin whiskers nanocomposites: 1. Structural analysis. *Macromolecules*, **33**, 8344–8353.

57. Alloin, F., d'Aprea, A., Dufresne, A., El Kissi, N., and Bossard, F. (2011) Poly(oxyethylene) and ramie whiskers based nanocomposites. Influence of processing: extrusion and casting/evaporation. *Cellulose*, **18**, 957–973.

58. Zhou, C., Chu, R., Wu, R., and Wu, Q. (2011) Electrospun polyethylene oxide/cellulose nanocrystal composite nanofibrous mats with homogeneous and heterogeneous microstructures. *Biomacromolecules*, **12**, 2617–2625.

59. George, J., Sajeevkumar, A.V., Ramana, K.V., Sabapathy, S.N., and Siddaramaiah, (2012) Augmented properties of PVA hybride nanocomposites containing cellulose nanocrystals and silver nanoparticles. *J. Mater. Chem.*, **22**, 22433–22439.

60. Rueda, L., Saralegui, A., Fernández d'Arlas, B., Zhou, Q., Berglund, L.A., Corcuera, M.A., Mondragon, I., and Eceiza, A. (2013)

Cellulose nanocrystals/polyurethane nanocomposites. Study from the point of view of microphase separated structure. *Carbohydr. Polym.*, **92**, 751–757.

61. de Gennes, P.G. (1979) *Scaling Concepts in Polymer Physics*, Cornell University Press, Ithaca, NY.

62. Stauffer, D. (1985) *Introduction to Percolation Theory*, Taylor & Francis, London, Philadelphia, PA.

63. Favier, V., Dendievel, R., Canova, G., Cavaillé, J.Y., and Gilormini, P. (1997) Simulation and modeling of three-dimensional percolating structures: case of a latex matrix reinforced by a network of cellulose fibers. *Acta Mater.*, **45**, 1557–1565.

64. Gopalan Nair, K. and Dufresne, A. (2003) Crab shell chitin whisker reinforced natural rubber nanocomposites. 2. Mechanical behaviour. *Biomacromolecules*, **4**, 666–674.

65. Dufresne, A., Kellerhals, M.B., and Witholt, B. (1999) Transcrystallization in mcl-PHAs/cellulose whiskers composites. *Macromolecules*, **32**, 7396–7401.

66. Azizi Samir, M.A.S., Montero Mateos, A., Alloin, F., Sanchez, J.-Y., and Dufresne, A. (2004) Plasticized nanocomposite polymer electrolytes based on poly(oxyethylene) and cellulose whiskers. *Electrochim. Acta*, **49**, 4667–4677.

67. Azizi Samir, M.A.S., Alloin, F., Sanchez, J.Y., and Dufresne, A. (2004) Cross-linked nanocomposite polymer electrolytes reinforced with cellulose whiskers. *Macromolecules*, **37**, 4839–4844.

68. Dagnon, K.L., Shanmuganathan, K., Weder, C., and Rowan, S.J. (2012) Water-triggered modulus changes of cellulose nanofiber nanocomposites with hydrophobic polymer matrices. *Macromolecules*, **45**, 4707–4715.

69. Halpin, J.C. and Kardos, J.L. (1972) Moduli of crystalline polymers employing composite theory. *J. Appl. Phys.*, **43**, 2235–2241.

70. Dufresne, A. (2006) Comparing the mechanical properties of high performances polymer nanocomposites from biological sources. *J. Nanosci. Nanotechnol.*, **6**, 322–330.

71. Dufresne, A., Cavaillé, J.Y., and Helbert, W. (1996) New nanocomposite materials: microcrystalline starch reinforced thermoplastic. *Macromolecules*, **29**, 7624–7626.

72. Dufresne, A. and Cavaillé, J.-Y. (1998) Clustering and percolation effects in microcrystalline starch-reinforced thermoplastic. *J. Polym. Sci. Polym. Phys.*, **36**, 2211–2224.

73. Angellier, H., Putaux, J.L., Molina-Boisseau, S., Dupeyre, D., and Dufresne, A. (2005) Starch nanocrystal fillers in an acrylic polymer matrix. *Macromol. Symp.*, **221**, 95–104.

74. Angellier, H., Molina-Boisseau, S., and Dufresne, A. (2005) Mechanical properties of waxy maize starch nanocrystals reinforced natural rubber. *Macromolecules*, **38**, 9161–9170.

75. Angellier, H., Molina-Boisseau, S., Lebrun, L., and Dufresne, A. (2005) Processing and structural properties of waxy maize starch nanocrystals reinforced natural rubber. *Macromolecules*, **38**, 3783–3792.

76. Angellier, H., Molina-Boisseau, S., and Dufresne, A. (2006) Waxy maize starch nanocrystals as filler in natural rubber. *Macromol. Symp.*, **233**, 132–136.

77. Mélé, P., Angellier-Coussy, H., Molina-Boisseau, S., and Dufresne, A. (2011) Reinforcing mechanisms of starch nanocrystals in a non-vulcanized natural rubber matrix. *Biomacromolecules*, **12**, 1487–1493.

78. LeCorre, D., Bras, J., and Dufresne, A. (2012) Influence of the botanic origin of starch nanocrystals on the morphological and mechanical properties of natural rubber nanocomposites. *Macromol. Mater. Eng.*, **297**, 969–978.

79. Chen, G., Wei, M., Chen, J., Huang, J., Dufresne, A., and Chang, P.R. (2008) Simultaneous reinforcing and toughening: new nanocomposites of waterbone polyurethane filled with low loading level of starch nanocrystals. *Polymer*, **49**, 1860–1870.

80. Chang, P.R., Ai, F., Chen, Y., Dufresne, A., and Huang, J. (2009)

Effects of starch nanocrystal-graft-polycaprolactone on mechanical properties of waterbone polyurethane-based nanocomposites. *J. Appl. Polym. Sci.*, **111**, 619–627.

81. Angellier, H., Molina-Boisseau, S., Dole, P., and Dufresne, A. (2006) Thermoplastic starch-waxy maize starch nanocrystals nanocomposites. *Biomacromolecules*, **7**, 531–539.

82. Viguié, J., Molina-Boisseau, S., and Dufresne, A. (2007) Processing and characterization of waxy maize starch films plasticized by sorbitol and reinforced with starch nanocrystals. *Macromol. Biosci.*, **7**, 1206–1216.

83. Garcia, N.L., Ribba, L., Dufresne, A., Aranguren, M., and Goyanes, S. (2009) Physico-mechanical properties of biodegradable starch nanocomposites. *Macromol. Mater. Eng.*, **294**, 169–177.

84. Garcia, N.L., Ribba, L., Dufresne, A., Aranguren, M., and Goyanes, S. (2011) Effect of glycerol on the morphology of nanocomposites made from thermoplastic starch and starch nanocrystals. *Carbohydr. Polym.*, **84**, 203–210.

85. Kristo, E. and Biliaderis, C.G. (2007) Physical properties of starch nanocrystal-reinforced pullulan films. *Carbohydr. Polym.*, **68**, 146–158.

86. Yu, J., Ai, F., Dufresne, A., Gao, S., Huang, J., and Chang, P.R. (2008) Structure and mechanical properties of poly(lactic acid) filled with (starch nanocrystal)-graft-poly(ε-caprolactone). *Macromol. Mater. Eng.*, **293**, 763–770.

87. Chen, Y., Cao, X., Chang, P.R., and Huneault, M.A. (2008) Comparative study on the films of poly(vinyl alcohol)/pea starch nanocrystals and poly(vinyl alcohol)/native pea starch. *Carbohydr. Polym.*, **73**, 8–17.

88. Habibi, Y. and Dufresne, A. (2008) Highly filled bionancomposites from functionalized polysaccharide nanocrystals. *Biomacromolecules*, **9**, 1974–1980.

89. Lin, N., Yu, J., Chang, P.R., Li, J., and Huang, J. (2011) Poly(butylene succinate)-based biocomposites filled with polysaccharide nanocrystals: structure and properties. *Polym. Compos.*, **32**, 472–482.

90. Zheng, H., Ai, F., Chang, P.R., Huang, J., and Dufresne, A. (2009) Structure and properties of starch nanocrystal-reinforced soy protein plastics. *Polym. Compos.*, **30**, 474–480.

91. Dubief, D., Samain, E., and Dufresne, A. (1999) Polysaccharide micro-crystals reinforced amorphous poly(β-hydroxyoctanoate) nanocomposite materials. *Macromolecules*, **32**, 5765–5771.

92. Gopalan Nair, K., Dufresne, A., Gandini, A., and Belgacem, M.N. (2003) Crab shell chitin whisker reinforced natural rubber nanocomposites. 3. Effect of chemical modification of chitin whiskers. *Biomacromolecules*, **4**, 1835–1842.

93. Angellier, H., Molina-Boisseau, S., Belgacem, M.N., and Dufresne, A. (2005) Surface chemical modification of waxy maize starch nanocrystals. *Langmuir*, **21**, 2425–2433.

94. Habibi, Y., Goffin, A.L., Schiltz, N., Duquesne, E., Dubois, P., and Dufresne, A. (2008) Bionanocomposites based on poly(ε-caprolactone)-grafted cellulose nanocrystals by ring opening polymerization. *J. Mater. Chem.*, **18**, 5002–5010.

95. Goffin, A.-L., Raquez, J.-M., Duquesne, E., Siqueira, G., Habibi, Y., Dufresne, A., and Dubois, P. (2011) Poly(ε-caprolactone) based nanocomposites reinforced by surface-grafted cellulose nanowhiskers via extrusion processing: morphology, rheology, and thermo-mechanical properties. *Polymer*, **52**, 1532–1538.

96. Goffin, A.-L., Raquez, J.-M., Duquesne, E., Siqueira, G., Habibi, Y., Dufresne, A., and Dubois, P. (2011) From interfacial ring-opening polymerization to melt processing of cellulose nanowhisker-filled polylactide-based nanocomposites. *Biomacromolecules*, **12**, 2456–2465.

97. Hajji, P., Cavaillé, J.Y., Favier, V., Gauthier, C., and Vigier, G. (1996) Tensile behavior of nanocomposites from latex and cellulose whiskers. *Polym. Compos.*, **17**, 612–619.

98. Dufresne, A., Cavaillé, J.Y., and Helbert, W. (1997) Thermoplastic nanocomposites filled with wheat straw cellulose whiskers. Part II: effect of processing and modeling. *Polym. Compos.*, **18**, 198–210.

99. Orts, W.J., Shey, J., Imam, S.H., Glenn, G.M., Guttman, M.E., and Revol, J.F. (2005) Application of cellulose microfibrils in polymer nanocomposites. *J. Polym. Environ.*, **13**, 301–306.

100. Kvien, S. and Oksman, K. (2007) Orientation of cellulose nanowhiskers in polyvinyl alcohol (PVA). *Appl. Phys. A*, **87**, 641–643.

101. Ben Azouz, K., Ramires, E.C., Van den Fonteyne, W., El Kissi, N., and Dufresne, A. (2012) Simple method for the melt extrusion of a cellulose nanocrystal reinforced hydrophobic polymer. *ACS Macro Lett.*, **1**, 236–240.

102. Lin, N. and Dufresne, A. (2013) Physical and/or chemical compatibilization of extruded cellulose nanocrystal reinforced polystyrene nanocomposites. *Macromolecules*, **46**, 5570–5583.

103. Cao, X., Dong, H., and Li, C.M. (2007) New nanocomposite materials reinforced with flax cellulose nanocrystals in waterborne polyurethane. *Biomacromolecules*, **8**, 899–904.

104. Gopalan Nair, K. and Dufresne, A. (2003) Crab shell chitin whisker reinforced natural rubber nanocomposites. 1. Processing and swelling behaviour. *Biomacromolecules*, **4**, 657–665.

105. Bendahou, A., Kaddami, H., and Dufresne, A. (2010) Investigation on the effect of cellulosic nanoparticles' morphology on the properties of natural rubber based nanocomposites. *Eur. Polym. J.*, **46**, 609–620.

106. Lu, Y., Weng, L., and Cao, X. (2005) Biocomposites of plasticized starch reinforced with cellulose crystallites from cottonseed linter. *Macromol. Biosci.*, **5**, 1101–1107.

107. Lu, Y., Weng, L., and Cao, X. (2006) Morphological, thermal and mechanical properties of ramie crystallites - reinforced plasticized starch biocomposites. *Carbohydr. Polym.*, **63**, 198–204.

108. Cao, X., Chen, Y., Chang, P.R., Stumborg, M., and Huneault, M.A. (2008) Green composites reinforced with hemp nanocrystals in plasticized starch. *J. Appl. Polym. Sci.*, **109**, 3804–3810.

109. Cao, X., Chen, Y., Chang, P.R., Muir, A.D., and Falk, G. (2008) Starch-based nanocomposites reinforced with flax cellulose nanocrystals. *eXPRESS Polym. Lett.*, **2**, 502–510.

110. Chen, Y., Liu, C., Chang, P.R., Cao, X., and Anderson, D.P. (2009) Bionanocomposites based on pea starch and cellulose nanowhiskers hydrolyzed from pea hull fibre: effect of hydrolysis time. *Carbohydr. Polym.*, **76**, 607–615.

111. Mathew, A.P., Thielemans, W., and Dufresne, A. (2008) Mechanical properties of nanocomposites from sorbitol plasticized starch and tunicin whiskers. *J. Appl. Polym. Sci.*, **109**, 4065–4074.

112. Huang, J., Zou, J.W., Chang, P.R., Yu, J.H., and Dufresne, A. (2011) New waterborne polyurethane-based nanocomposites reinforced with low loading levels of chitin whiskers. *eXPRESS Polym. Lett.*, **5**, 362–373.

113. Lee, S.Y., Mohan, D.J., Kang, I.A., Doh, G.H., Lee, S., and Han, N.O. (2009) Nanocellulose reinforced PVA composite films: effects of acid treatment and filler loading. *Fibers Polym.*, **10**, 77–82.

114. Peresin, M.S., Habibi, Y., Zoppe, J.O., Pawlak, J.J., and Rojas, O.J. (2010) Nanofiber composites of polyvinyl alcohol and cellulose nanocrystals: manufacture and characterization. *Biomacromolecules*, **11**, 674–681.

115. Uddin, A.J., Araki, J., and Gotoh, Y. (2011) Toward "strong" green nanocomposites: polyvinyl alcohol reinforced with extremely oriented cellulose whiskers. *Biomacromolecules*, **12**, 617–624.

116. Frone, A.N., Panaitescu, D.M., Donescu, D., Spataru, C.I., Radovici, C., Trusca, R., and Somoghi, R. (2011) Preparation and characterization of PVA composites with cellulose nanofibers obtained by ultrasonication. *BioResources*, **6**, 487–512.

117. Wang, Y., Cao, X., and Zhang, L. (2006) Effects of cellulose whiskers on properties of soy protein thermoplastics. *Macromol. Biosci.*, **6**, 524–531.

118. Roohani, M., Habibi, Y., Belgacem, N.M., Ebrahim, G., Karimi, A.N., and Dufresne, A. (2008) Cellulose whiskers reinforced polyvinyl alcohol copolymers nanocomposites. *Eur. Polym. J.*, **44**, 2489–2498.

119. Chauve, G., Heux, L., Arouini, R., and Mazeau, K. (2005) Cellulose poly(ethylene-co-vinyl acetate) nanocomposites studied by molecular modeling and mechanical spectroscopy. *Biomacromolecules*, **6**, 2025–2031.

120. BelHaaj, S., Ben Mabrouk, A., Thielemans, W., and Boufi, S. (2013) A one-step miniemulsion polymerization route towards the synthesis of nanocrystal acrylic nanocomposites. *Soft Matter*, **9**, 1975–1984.

121. Dufresne, A. (2000) Dynamic mechanical analysis of the interphase in bacterial polyester/cellulose whiskers natural composites. *Compos. Interfaces*, **7**, 53–67.

122. LeCorre, D., Bras, J., and Dufresne, A. (2012) Influence of native starch's properties on starch nanocrystals thermal properties. *Carbohydr. Polym.*, **87**, 658–666.

123. Roman, M. and Winter, W.T. (2004) Effect of sulphate groups from sulphuric acid hydrolysis on the thermal degradation behaviour of bacterial cellulose. *Biomacromolecules*, **5**, 1671–1677.

124. Lin, N. and Dufresne, A. (2014) Surface chemistry, morphological analysis and properties of cellulose nanocrystals with gradient sulfation degrees. *Nanoscale.* doi: 10.1039/C3NR06761K

125. Wang, N., Ding, E., and Cheng, R. (2007) Thermal degradation behavior of spherical cellulose nanocrystals with sulfate groups. *Polymer*, **48**, 3486–3493.

126. Fortunati, E., Armentano, I., Zhou, Q., Iannoni, A., Saino, E., Visai, L., Berglund, L.A., and Kenny, J.M. (2012) Multifunctional bionanocomposite films of poly(lactic acid), cellulose nanocrystals and silver nanoparticles. *Carbohydr. Polym.*, **87**, 1596–1605.

127. Mathew, A.P. and Dufresne, A. (2002) Morphological investigation of nanocomposites from sorbitol plasticized starch and tunicin whiskers. *Biomacromolecules*, **3**, 609–617.

128. Garcia de Rodriguez, N.L., Thielemans, W., and Dufresne, A. (2006) Sisal cellulose whiskers reinforced polyvinyl acetate nanocomposites. *Cellulose*, **13**, 261–270.

129. Siqueira, G., Bras, J., and Dufresne, A. (2009) Cellulose whiskers vs. microfibrils: influence of the nature of the nanoparticle and its surface functionalization on the thermal and mechanical properties of nanocomposites. *Biomacromolecules*, **10**, 425–432.

130. Rojas, O.J., Montero, G.A., and Habibi, Y. (2009) Electronspun nancomposites from polystyrene loaded with cellulose nanowhiskers. *J. Appl. Polym. Sci.*, **113**, 927–935.

131. Lin, N., Chen, G., Huang, J., Dufresne, A., and Chang, P.R. (2009) Effects of polymer-grafted natural nanocrystals on the structure and mechanical properties of poly(lactic acid): a case of cellulose whisker-graft-polycaprolactone. *J. Appl. Polym. Sci.*, **113**, 3417–3425.

132. Wang, B., Li, J., Zhang, J., Li, H., Chen, P., Gu, Q., and Wang, Z. (2013) Thermo-mechanical properties of the composite made of poly(3-hydroxybutyrate-co-3-hydroxyvalerate) and acetylated chitin nanocrystals. *Carbohydr. Polym.*, **95**, 100–106.

133. Jiang, L., Morelius, E., Zhang, J., Wolcott, M., and Holbery, J. (2008) Study of the poly(3-hydroxybutyrate-co-3-hydroxyvalerate)/cellulose nanowhiskers composites prepared by solution casting and melt processing. *J. Compos. Mater.*, **42**, 2629–2645.

134. Ten, E., Turtle, J., Bahr, D., Jiang, L., and Wolcott, M. (2010) Thermal and mechanical properties of poly(3-hydroxybutyrate-co-3-hydroxyvalerate)/cellulose nanowhiskers composites. *Polymer*, **51**, 2652–2660.

135. Sanchez-Garcia, M.D. and Laragon, J.M. (2010) On the use of plant cellulose nanowhiskers to enhance the barrier properties of polylactic acid. *Cellulose*, **17**, 987–1004.

136. Ma, H., Zhou, B., Li, H.S., Li, Y.Q., and Ou, S.Y. (2011) Green composite films

composed of nanocrystalline cellulose and a cellulose matrix regenerated from functionalized ionic liquid solution. *Carbohydr. Polym.*, **84**, 383–389.

137. Cao, X., Habibi, Y., and Lucia, L.A. (2009) One-pot polymerization, surface grafting, and processing of waterborne polyurethane-cellulose nanocrystal nanocomposites. *J. Mater. Chem.*, **19**, 7137–7145.

138. Hariraksapitak, P. and Supaphol, P. (2010) Preparation and properties of α-chitin-whisker-reinforced hyaluronan-gelatin nanocomposite scaffolds. *J. Appl. Polym. Sci.*, **117**, 3406–3418.

139. Noorani, S., Simonsen, J., and Atre, S. (2007) Nano-enabled microtechnology: polysulfone nanocomposites incorporating cellulose nanocrystals. *Cellulose*, **14**, 577–584.

140. Bras, J., Hassan, M.L., Bruzesse, C., Hassan, E.A., El-Wakil, N.A., and Dufresne, A. (2010) Mechanical, barrier, and biodegradability properties of bagasse cellulose whiskers reinforced natural rubber nanocomposites. *Ind. Crops Prod.*, **32**, 627–633.

141. Liu, H., Liu, D., Yao, F., and Wu, Q. (2010) Fabrication and properties of transparent polymethylmethacrylate/cellulose nanocrystals composites. *Bioresour. Technol.*, **101**, 5685–5692.

142. Pandey, J.K., Chu, W.S., Kim, C.S., Lee, C.S., and Ahn, S.H. (2009) Bio-nano reinforcement of environmentally degradable polymer matrix by cellulose whiskers from grass. *Composites Part B*, **40**, 676–680.

143. Tingaut, P., Zimmermann, T., and Lopez-Suevos, F. (2010) Synthesis and characterization of bionanocomposites with tunable properties from poly(lactic acid) and acetylated microfibrillated cellulose. *Biomacromolecules*, **11**, 454–464.

144. Aulin, C., Ahola, S., Josefsson, P., Nishino, T., Hirose, Y., Österberg, M., and Wågberg, L. (2009) Nanoscale cellulose films with different crystallinities and mesostructures - their surface properties and interaction with water. *Langmuir*, **25**, 7675–7685.

145. Thielemans, W., Warbey, C.R., and Walsh, D.A. (2009) Permselective nanostructured membranes based on cellulose nanowhiskers. *Green Chem.*, **11**, 531–537.

146. Ma, H., Burger, C., Hsiao, B.S., and Chu, B. (2011) Ultrafine polysaccharide nanofibrous membranes for water purification. *Biomacromolecules*, **12**, 970–976.

147. Liu, D., Zhong, T., Chang, P.R., Li, K., and Wu, Q. (2010) Starch composites reinforced by bamboo cellulosic crystals. *Bioresour. Technol.*, **101**, 2529–2536.

148. Teixeira, E.M., Pasquini, D., Curvelo, A.A.S., Corradini, E., Belgacem, M.N., and Dufresne, A. (2009) Cassava bagasse cellulose nanofibrils reinforced thermoplastic cassava starch. *Carbohydr. Polym.*, **78**, 422–431.

149. Choi, Y.J. and Simonsen, J. (2006) Cellulose nanocrystal-filled carboxymethyl cellulose nanocomposites. *J. Nanosci. Nanotechnol.*, **6**, 633–639.

150. Sanchez-Garcia, M.D., Hilliou, L., and Laragon, J.M. (2010) Morphology and water barrier properties of nanobiocomposites of κ/ι-hybrid carrageenan and cellulose nanowhiskers. *J. Agric. Food Chem.*, **58**, 12847–12857.

151. de Mesquita, J.P., Donnici, C.L., Teixeira, I.F., and Pereira, F.V. (2012) Bio-based nanocomposites obtained through covalent linkage between chitosan and cellulose nanocrystals. *Carbohydr. Polym.*, **90**, 210–217.

152. Lu, Y., Weng, L., and Zhang, L. (2004) Morphology and properties of soy protein isolate thermoplastics reinforced with chitin whiskers. *Biomacromolecules*, **5**, 1046–1051.

153. Sriupayo, J., Supaphol, P., Blackwell, J., and Rujiravanit, R. (2005) Preparation and characterization of α-chitin whisker-reinforced chitosan nanocomposite films with or without heat treatment. *Carbohydr. Polym.*, **62**, 130–136.

154. Sriupayo, J., Supaphol, P., Blackwell, J., and Rujiravanit, R. (2005) Preparation and characterization of α-chitin whisker-reinforced poly(vinyl alcohol) nanocomposite films with or without heat treatment. *Polymer*, **46**, 5637–5644.

155. Shanmuganathan, K., Capadona, J.R., Rowan, S.J., and Weder, C. (2010) Bio-inspired mechanically-adaptive nanocomposites derived from cotton cellulose whiskers. *J. Mater. Chem.*, **20**, 180–186.

156. Shanmuganathan, K., Capadona, J.R., Rowan, S.J., and Weder, C. (2010) Stimuli-responsive mechanically adaptive polymer nanocomposites. *ACS Appl. Mater. Interfaces*, **2**, 165–174.

157. Chazeau, L., Cavaillé, J.Y., Canova, G.R., Dendievel, R., and Boutherin, B. (1999) Viscoelastic properties of plasticized PVC reinforced with cellulose whiskers. *J. Appl. Polym. Sci.*, **71**, 1797–1808.

158. Paralikar, S.A., Simonsen, J., and Lombardi, J. (2008) Poly(vinyl alcohol)/cellulose nanocrystal barrier membranes. *J. Membr. Sci.*, **320**, 248–258.

159. Azeredo, H.M.C., Miranda, K.W.E., Rosa, M.F., Nascimento, D.M., and de Moura, M.R. (2012) Edible films from alginate-acerola puree reinforced with cellulose whiskers. *Food Sci. Technol.*, **46**, 294–297.

160. Azeredo, H.M.C., Mattoso, L.H.C., Wood, D., Williams, T.G., Avena-Bustillos, R.J., and McHugh, T.H. (2009) Nanocomposite edible films from mango puree reinforced with cellulose nanofibers. *J. Food Sci.*, **74**, N31–N35.

161. Azeredo, H.M.C., Mattoso, L.H.C., Avena-Bustillos, R.J., Filho, G.C., Munford, M.L., Wood, D., and McHugh, T.H. (2010) Nanocellulose reinforced chitosan composite films as affected by nanofiller loading and plasticizer content. *J. Food Sci.*, **75**, N1–N7.

162. Khan, R.A., Salmieri, S., Dussault, D., Uribe-Calderon, J., Kamal, M.R., Safrany, A., and Lacroix, M. (2010) Production and properties of nanocellulose-reinforced methylcellulose-based biodegradable films. *J. Agric. Food Chem.*, **58**, 7878–7885.

163. Saxena, A., Elder, T.J., and Ragauskas, A.J. (2011) Moisture barrier properties of xylan composite films. *Carbohydr. Polym.*, **84**, 1371–1377.

164. Khan, R.A., beck, S., Dussault, D., Salmieri, S., Bouchard, J., and Lacroix, M. (2013) Mechanical and barrier properties of nanocrystalline cellulose reinforced poly(caprolactone) composites: effect of gamma radiation. *J. Appl. Polym. Sci.*, **129**, 3038–3046.

165. Bendahou, A., Kaddami, H., Espuche, E., Gouanvé, F., and Dufresne, A. (2011) Synergism effect of montmorillonite and cellulose whiskers on the mechanical and barrier properties of natural rubber. *Macromol. Mater. Eng.*, **296**, 760–769.

Index

WILEY END USER LICENSE AGREEMENT

Go to www.wiley.com/go/eula to access Wiley's ebook EULA.